The Influence of High Harmonic Force on Fatigue Life and its Prediction via Coupled Inline-Crossflow VIV Modeling

by

Haining Zheng

B.E., Mechanical Engineering and Automation (2004)
B.E., Computer Application (2004)
Shanghai Jiao Tong University
S.M., Computation for Design and Optimization (2008)
Massachusetts Institute of Technology

Submitted to the Department of Mechanical Engineering
in partial fulfillment of the requirements for the degree of

Doctor of Philosophy

at the

MASSACHUSETTS INSTITUTE OF TECHNOLOGY

February 2014

© Massachusetts Institute of Technology 2014. All rights reserved.

Signature redacted

Author .....
Department of Mechanical Engineering
September 27, 2013

Signature redacted

Certified by .....
Michael S. Triantafyllou
William I. Koch Professor of Marine Technology
Professor of Mechanical and Ocean Engineering
Thesis Supervisor

Accepted by .....
David E. Hardt
Ralph E. and Eloise F. Cross Professor of Mechanical Engineering
Chairman, Department Committee on Graduate Students

The Influence of High Harmonic Force on Fatigue Life and its Prediction via Coupled Inline-Crossflow VIV Modeling

by

Haining Zheng

Submitted to the Department of Mechanical Engineering
on September 27, 2013, in partial fulfillment of the
requirements for the degree of
Doctor of Philosophy

Abstract

Vortex Induced Vibrations (VIV) of a flexibly mounted rigid cylinder placed in a flow is a canonical problem of fluid-structure interactions and the study of VIV and the resulting material fatigue is particularly important in design for ultra-deep water oil exploration and development. Long cylindrical structures such as risers and mooring lines can be outfitted with VIV-cancellation systems or subjected to aggressive replacement schedules. However, the cost of these measures can be high. Effective VIV and fatigue prediction programs offer the potential for design and replacement schedule optimization.

For a long time, researchers believed that these oscillations were mainly in the crossflow direction (a direction perpendicular to the flow direction) and were purely harmonic ones with only one major frequency close to the Strouhal frequency (a dimensionless representative of the frequency of vortex shedding). The study of inline motion of long flexible cylinders caused by VIV has been long neglected due to its small amplitude compared to the cross-flow response amplitude. However, it is shown that the inline motion has a major impact on fatigue life due to its higher frequency (second harmonic). More importantly, it triggers a third harmonic stress component in the crossflow direction along with a chaotic frequency stress component.

In this thesis, first the impact of the higher harmonic components and the chaotic response on the resulting fatigue damage of the flexible cylinders was first systematically assessed. Statistical methods were employed to generate a stress time series based on the power spectrum density (PSD) plots similar to those of the experimental signals. It is shown that the high harmonic signal has a significant influence on the fatigue life, while the wide-band chaotic components have limited effects. Thus, prediction of high harmonic forces through coupled inline-crossflow VIV modeling is the key to the problem.

Thereafter, the semi-empirical crossflow VIV prediction model was revisited. Pre-

diction results from VIVA - a VIV response prediction program widely used in the offshore industry - were improved through the systematical adjustment of hydrodynamics coefficients based on field and laboratory experiments. The results were benchmarked with controlled laboratory experiments, including the Norwegian Deepwater Programme (NDP) Riser High Mode VIV test, the Chaplin experiment, the ExxonMobil 10m long riser model datasets, and field experiments including the Miami experiment (MIT-DeepStar datasets) and the BP bare full-scale riser datasets in the Gulf of Mexico.

Afterwards, pure inline VIV was studied using both experiments and a semi-empirical model. A pure inline VIV hydrodynamic force coefficients database was constructed from forced motion experiments in the towing tank. A spring-damper rigid cylinder VIV model was created and the pure inline hydrodynamic database was employed to calculate the fluid forces to the system. The motion predicted by the model was compared with free vibration experiments. Additionally, an inline response prediction module was introduced to VIVA to predict the inline response of flexible cylinders. The results were benchmarked with the Norwegian Deepwater Programme (NDP) Riser High Mode VIV test data.

Finally, the coupled Inline-crossflow VIV problem was systematically addressed. Extensive forced inline-crossflow experiments were designed and carried out in the MIT towing tank, which provided hydrodynamic coefficient databases for VIV prediction models. The constructed 2D VIV hydrodynamics coefficients database 'ZDMiT' was thoroughly studied and is expected to be useful for semi-empirical programs predicting coupled inline-crossflow VIV in the field. Additionally, a rigid cylinder VIV prediction model was developed to estimate the coupled inline-crossflow VIV response and the high harmonic VIV forces.

Thesis Supervisor: Michael S. Triantafyllou
Title: William I. Koch Professor of Marine Technology
Professor of Mechanical and Ocean Engineering

Acknowledgments

I would first like to thank my thesis advisor, Professor Michael Triantafyllou, for his guidance and support during my thesis work. It is my great fortune to have him as my advisor. I am truly grateful for his insights and his vision on the research topic and his hand-on approach to problem solving. His passion and dedication to the research encourages me continually, and I strongly believe that his influence will benefit me tremendously in my future work.

I am also very thankful to my thesis committee members. Professor Nicholas Patrikalakis has always been encouraging and took good care of me. Professor Kim Vandiver's devotion towards teaching and research inspire me greatly. I really appreciate the many invaluable discussions with Prof. Yahya Modarres-Sadeghi. I am also highly grateful to Prof. Jason Dahl for help with my experiment setup and insightful discussions.

I must also acknowledge my lab colleagues: Alex, Rachel, Dilip, Felipe, Heather, Stephanie, Jeff, Audrey, James, Jacob, Amy and my other friends in the community of the OE program: Bryce, Yulin, Meng, Wenting, Themis, Zhibiao, Zao, Georgios, and Shmuel. The friendship we built during these years will last for a lifetime.

Finally, above all, I want to express my gratitude for my parents Ruxin Zheng, Suzhen Ding and my wife Shan Xu. Their encouragement and love have always been the motivation for my progress. Without their understanding and strong support, I would never have been able to go after my interests and survive the most difficult time during my pursuit of a Ph.D.

Nomenclatures

Abbreviations

CF	Crossflow
IL	Inline
Re	Reynolds number, real part of a complex number
St	Strouhal number
VIV	Vortex induced vibration

Symbols

A	Amplitude
A_y	Amplitude in CF direction
A_x	Amplitude in IL direction
b_y	Damping constant in CF direction
b_x	Damping constant in IL direction
$C_{m,CF}$	Added mass coefficient in CF direction
$C_{m,IL}$	Added mass coefficient in IL direction
C_D	Drag coefficient
C_{Dv}	Fluctuating drag coefficient in phase with velocity
C_L	Lift coefficient
C_{L1}	First Harmonic of Lift coefficient
C_{L3}	Third Harmonic of Lift coefficient
C_{Lv}	Lift coefficient in phase with velocity
D	Cylinder diameter
D_f	Fluid force in inline direction
F	Force
F_o	Force amplitude
f	Frequency
f_n	Natural frequency
f_o	Oscillation frequency

$f*$	Oscillation frequency/Natural frequency
k_x	Spring constant in IL direction
k_y	Spring constant in CF direction
L_f	Fluid force in crossflow direction
m	Cylinder mass
$m*$	Mass ratio
m_x	Cylinder mass in IL direction
m_y	Cylinder mass in CF direction
U	Flow velocity
U_{rn}	Nominal reduced velocity U/f_nD
U_r	Response reduced velocity U/f_nD
θ	Phase difference
θ_{12}	Phase difference between inline and crossflow motion
θ_{13}	Phase difference between the first harmonic and the third harmonic
x	Cylinder inline displacement
$\dot{x}$	Cylinder inline velocity
$\ddot{x}$	Cylinder inline acceleration
y	Cylinder crossflow displacement
$\dot{y}$	Cylinder crossflow velocity
$\ddot{y}$	Cylinder crossflow acceleration
ζ	Damping ratio
ρ	Density of water
ω	Circular frequency, $2\pi f$

Contents

1 Introduction **39**

1.1 Motivations 40

1.2 Major Challenges to Address 41

1.3 Thesis Scope 41

2 Vortex Induced Vibration **43**

2.1 Theoretical Background of Vortex Induced Vibration 43

2.2 Vortex Induced Vibration Prediction in Crossflow Direction 48

2.3 Vortex Induced Vibration Studies in Inline Direction 49

2.4 Inline-Crossflow Vortex Induced Vibration Studies 51

3 The Influence of High Harmonic and Chaotic Force Components on Fatigue Damage of Long Flexible Cylinders Due to Vortex-Induced Vibrations **53**

3.1 Introduction 54

3.2 Experimental Data 55

3.3 The Methodology of Constructing Stress Time Series 59

3.4 The Influence of High Harmonic Components on Fatigue Damage of Type-I Signals 70

3.5 The Influence of Spreading and Time-varying Frequency Content on Fatigue Life of Type-II Signals 73

3.5.1 The Influence of Spreading Width 73

3.5.2 The Influence of Spreading Symmetry 81

3.5.3 The Influence of Non-Stationarity 89
3.6 Conclusions 94

4 Crossflow VIV Prediction and Optimization 97

4.1 Introduction 98
4.2 Methodology of Database Optimization 99
4.3 Experimental Database and Processing 103
4.4 Database Optimization Results 103
4.5 Crossflow VIV Prediction Results Analysis 107
4.5.1 NDP38 Experiment 107
4.5.2 Chaplin Experiment 116
4.5.3 NDP10 Experiment 118
4.5.4 Miami Experiment 134
4.6 Conclusions 140

5 Inline VIV Prediction 141

5.1 Methodology 141
5.2 Pure Inline VIV Experiment 143
5.2.1 Pure Inline VIV Experiment Design 143
5.2.2 Comparison with Higher Re Pure Inline Database 149
5.3 Inline Rigid Cylinder VIV Prediction 151
5.3.1 Validation with Pure Crossflow Database 152
5.3.2 Prediction Comparison with Rigid Cylinder Free Vibration Experiment 158
5.4 Inline Flexible Cylinder VIV Prediction using VIVA 164
5.4.1 Inline Hydrodynamic Coefficients Database to VIVA 165
5.4.2 Prediction Comparison with Flexible Cylinder Free Vibration Experiment 167
5.5 Conclusions 169

6 Inline-Crossflow VIV Prediction **171**

6.1 High Resolution 2D Forced VIV Motion Experiment Design 171

6.2 'ZDMiT' 2D VIV Force Coefficients Database Analysis 177

6.2.1 Hydrodynamic Force Coefficients in the Database 177

6.2.2 Force Coefficients in Phase with Velocity 180

6.2.3 Added Mass Coefficients 191

6.3 Case Study on Added Mass Coefficients 206

6.3.1 Observations on Added Mass Coefficients 206

6.3.2 Force Analysis 209

6.3.3 Particle Image Velocimetry (PIV) 215

6.4 Inline-Crossflow Rigid Cylinder Modeling and Prediction 222

6.5 High Harmonic Force Prediction Based on the Inline-Crossflow Model 231

7 Conclusions **233**

7.1 Overview 233

7.2 Principal Contributions 233

7.2.1 Systematically Quantified the Influence of High Frequency and Chaotic Stress Components on Fatigue Damage of Risers . . . 233

7.2.2 Optimized Crossflow Hydrodynamic Coefficient Database Based on Lab and Field Experiments 234

7.2.3 Designed and Carried Out Forced Pure Inline VIV Experiments. 234

7.2.4 Developed and Benchmarked a Semi-Empirical Rigid Cylinder Inline VIV model 235

7.2.5 Designed and Carried Out Fine Grid Forced Crossflow-Inline VIV Experiments 235

7.2.6 Created 2D VIV Hydrodynamics Coefficients Database 'ZDMiT' to be Used by Semi-empirical Programs to Predict Coupled Inline-Crossflow VIV. 235

7.2.7 Developed a Coupled Inline-crossflow Rigid Cylinder Response Model to Predict Coupled Inline-Crossflow VIV Motion and Higher Harmonic VIV Forces 236
7.3 Future Work 236
7.3.1 Coupled IL-CF VIV Prediction Extension to Flexible Cylinder 236
7.3.2 Combination of Numerical Virtual Tests with Semi-Empirical Models 236

A Additional Figures for Hydrodynamic Force Coefficients in the 2D VIV Database 237
A.1 Lift Coefficients in Phase with Velocity C_{Lv} 237
A.2 Drag Coefficients in Phase with Velocity C_{Dv} 274
A.3 Crossflow Added Mass Coefficients $C_{m,CF}$ 310
A.4 Inline Added Mass Coefficients $C_{m,IL}$ 346

List of Figures

2-1 Pressure field and separation point for flow past a cylinder. [27] . . . 44

2-2 Types of offshore oil and gas structures by NOAA 46

2-3 Subsea Pipelines by EcoPrasinos 46

2-4 Altered picture from An Album of Fluid Motion [26]. 47

3-1 A sample scalogram of the NDP experimental data for a case with linearly sheared flow profile and with a maximum flow velocity of 0.8 m/s (case 2460). 56

3-2 (left) A sample case of the PSD plot of a measured strain signal with spreading, and (right) A sample case of the PSD plot of a measured strain signal without spreading 57

3-3 Relative power stored in each harmonic for (top) linearly sheared flow cases, and (bottom) uniform flow cases. 58

3-4 The PSD (top) and time series (bottom) of signal with energy lumped at the first harmonic 61

3-5 The PSD (top) and time series (bottom) of signal with energy lumped at the first and third harmonics 62

3-6 Generated frequencies and amplitudes 66

3-7 Distribution of generated amplitudes and frequencies 67

3-8 The power spectral density (top) and time serials (bottom) of generated type II signal 67

3-9 The time serials (first and third rows) and power spectral density (second and fourth rows) of ten generated non-stationary segments . 68

3-10 Time serials of the generated Type II signal 69

3-11 Scalogram of the generated Type II signal 69

3-12 The influence of energy distribution and phase angle between the first and the third harmonic on fatigue life (years). 71

3-13 Slices of Figure 3-12 for a constant phase difference of 180 72

3-14 Slices of Figure 3-12 for a constant third harmonic contribution of 33.3 %, i.e., $P_3/P_1 = 1/2$ 72

3-15 Deterministic PSD shape: signals with first harmonic only. The x-axis is the multiplier of original peak first harmonic frequency (1Hz in this case). 74

3-16 Deterministic PSD shape: signals with first and third harmonics. The x-axis is the multiplier of original peak first harmonic frequency (1Hz in this case). 75

3-17 The influence of spread width on fatigue life of broadband stationary signal with deterministic PSD shape: signals with first harmonic only. The fatigue life is normalized by the fatigue life of Type I signal with only the first harmonics. 76

3-18 The influence of spread width on fatigue life of broadband stationary signal with deterministic PSD shape: signals with first and third harmonics. The fatigue life is normalized by the fatigue life of Type I signal with both the first and third harmonics. 77

3-19 Random Frequency/Amplitude PSD shape with different width (0.1 to 1 Hz as indicated in the titles) 78

3-20 The influence of spread width on fatigue life of broadband stationary signal with random PSD shape: first harmonic only. The x-axis is the multiplier of original harmonic spread. The fatigue life is normalized by the fatigue life of Type I signal with only the first harmonics. . . 79

3-21 The influence of spread width on fatigue life of broadband stationary signal with random PSD shape: first and third harmonics . The x-axis is the multiplier of original harmonic spread. The fatigue life is normalized by the fatigue life of Type I signal with both the first and third harmonics 80

3-22 Deterministic PSD shape: signals with first harmonic only. The x-axis indicates the degree of asymmetry (spread width ratio of right part of spread vs left part). 82

3-23 Deterministic PSD shape: signals with first and third harmonics. The x-axis indicates the degree of asymmetry (spread width ratio of right part of spread vs left part). 83

3-24 The influence of asymmetry of spread distribution on fatigue life of broadband stationary signal with deterministic PSD shape: signals with first harmonic only. The x-axis indicates the degree of asymmetry (spread width ratio of right part of spread vs left part). The fatigue life is normalized by the fatigue life of Type I signal with only the first harmonics. 84

3-25 The influence of asymmetry of spread distribution on fatigue life of broadband stationary signal with deterministic PSD shape: signals with first and third harmonics. The x-axis indicates the degree of asymmetry (spread width ratio of right part of spread vs left part). The fatigue life is normalized by the fatigue life of Type I signal with both the first and third harmonics. 85

3-26 Random Frequency/Amplitude PSD shape with different asymmetry (spread width ratio of right part of spread vs left part from 0.1 to 10, as indicated in the titles) 86

3-27 The influence of symmetry of spread distribution on fatigue life of broadband stationary signal with random PSD: first harmonic only. The x-axis indicates the degree of asymmetry (spread width ratio of right part of spread vs left part). The fatigue life is normalized by the fatigue life of Type I signal with only the first harmonics. 87

3-28 The influence of symmetry of spread distribution on fatigue life of broadband stationary signal with random PSD: first and third harmonics. The x-axis indicates the degree of asymmetry (spread width ratio of right part of spread vs left part). The fatigue life is normalized by the fatigue life of Type I signal with both the first and third harmonics. 88

3-29 The influence of spread width on fatigue life of non-stationary signal with random PSD shape: first harmonic only. The x-axis is the multiplier of original harmonic spread. The fatigue life is normalized by the fatigue life of Type I signal with only the first harmonics. 90

3-30 The influence of spread width on fatigue life of non-stationary signal with random PSD shape: first and third harmonics (right). The x-axis is the multiplier of original harmonic spread. The fatigue life is normalized by the fatigue life of Type I signal with both the first and third harmonics. 91

3-31 The influence of symmetry of spread distribution on the fatigue life of a non-stationary signal with random PSD shape: first harmonic only. The x-axis indicates the degree of asymmetry (spread width ratio of right part of spread vs left part). The fatigue life is normalized by the fatigue life of Type I signal with only the first harmonics. 92

3-32 The influence of symmetry of spread distribution on the fatigue life of a non-stationary signal with random PSD shape: first and third harmonics. The x-axis indicates the degree of asymmetry (spread width ratio of right part of spread vs left part). The fatigue life is normalized by the fatigue life of Type I signal with both the first and third harmonics 93

3-33 The influence of non-stationarity of spread distribution on the fatigue life. The x-axis is the percentage of third harmonic power. The fatigue life is normalized by the fatigue life of Type I signal with both the first and third harmonics. 94

4-1 Surface plots of lift coefficient C_{lv} (left) and added mass coefficient C_m (right) as functions of reduced velocity (x-axis) and non-dimensional amplitude (y-axis) [28]. 100

4-2 Two dimensional representation of the lift coefficient C_{lv} and added mass coefficient C_m surfaces. 100

4-3 Two-dimensional linear plots of lift coefficient C_{lv} and added mass coefficient C_m curves for a bare cylinder. 101

4-4 Two-dimensional linear plots of lift coefficient C_{lv} and added mass coefficient C_m curves for straked cylinder. 102

4-5 Optimal 2D linear plots of lift coefficient C_{lv} and added mass coefficient C_m curves for bare cylinder. 104

4-6 Optimal 2D linear plots of lift coefficient C_{lv} and added mass coefficient C_m curves for straked cylinder. 105

4-7 Optimal 3D linear plots of lift coefficient C_{lv} curves for bare cylinder. 105

4-8 Optimal 3D linear plots of added mass coefficient C_m curves for bare cylinder. 106

4-9 VIV RMS amplitude (A/D) versus length (x/L) comparison between VIVA prediction and experimental data; VIVA prediction (continuous line), experimental data (circles). Current profile in green dotted line. NDP38 dataset for bare riser in uniform flow. 107

4-10 Ratio of VIV dominant frequency of VIVA prediction and experimental data. NDP38 dataset for bare riser in uniform flow. 108

4-11 VIV RMS amplitude (A/D) versus length (x/L) comparison between VIVA prediction and experimental data; VIVA prediction (continuous line), experimental data (circles). Current profile in green dotted line. NDP38 dataset for bare riser in sheared flow. 109

4-12 Ratio of VIV dominant frequency of VIVA prediction and experimental data. NDP38 dataset for bare riser in sheared flow. 110

4-13 VIV RMS amplitude (A/D) versus length (x/L) comparison between VIVA prediction and experimental data; VIVA prediction (continuous line), experimental data (circles). Current profile in green dotted line. NDP38 dataset for 50% straked riser in uniform flow. 111

4-14 Ratio of VIV dominant frequency of VIVA prediction and experimental data. NDP38 dataset for 50% straked riser in uniform flow. . . . 112

4-15 VIV RMS amplitude (A/D) versus length (x/L) comparison between VIVA prediction and experimental data; VIVA prediction (continuous line), experimental data (circles). Current profile in green dotted line. NDP38 dataset for 50% straked riser in sheared flow. 113

4-16 Ratio of VIV dominant frequency of VIVA prediction and experimental data. NDP38 dataset for 50% straked riser in sheared flow. . . . 114

4-17 VIVA prediction of first harmonic stress (in Pa) as a function of frequency (solid curve) and the corresponding third harmonic stress component (dotted line) for a bare riser in linearly sheared flow (NDP38 data). 115

4-18 VIV RMS amplitude (A/D) versus length (x/L) comparison between VIVA prediction and experimental data; VIVA prediction (continuous line), experimental data (circles). Current profile in green dotted line. Chaplin Experiment. 116
4-19 Ratio of VIV dominant frequency of VIVA prediction and experimental data. Chaplin Experiment. 117
4-20 VIV RMS amplitude (A/D) versus length (x/L) comparison between VIVA prediction and experimental data; VIVA prediction (continuous line), experimental data (circles). Current profile in green dotted line. NDP 10m bare riser in uniform flow. 118
4-21 Ratio of VIV dominant frequency of VIVA prediction. NDP 10m bare riser in uniform. 119
4-22 VIV RMS amplitude (A/D) versus length (x/L) comparison between VIVA prediction and experimental data; VIVA prediction (continuous line), experimental data (circles). Current profile in green dotted line. NDP 10m bare riser in sheared flow. 120
4-23 Ratio of VIV dominant frequency of VIVA prediction. NDP 10m bare riser in sheared flow. 121
4-24 VIV RMS amplitude (A/D) versus length (x/L) comparison between VIVA prediction and experimental data; VIVA prediction (continuous line), experimental data (circles). Current profile in green dotted line. NDP 10m 25% strake riser in uniform flow. 122
4-25 Ratio of VIV dominant frequency of VIVA prediction. NDP 10m 25% strake riser in unform flow. 123
4-26 VIV RMS amplitude (A/D) versus length (x/L) comparison between VIVA prediction and experimental data; VIVA prediction (continuous line), experimental data (circles). Current profile in green dotted line. NDP 10m 25% strake riser in sheared flow. 124
4-27 Ratio of VIV dominant frequency of VIVA prediction. NDP 10m 25% strake riser in sheared flow. 125

4-28 VIV RMS amplitude (A/D) versus length (x/L) comparison between VIVA prediction and experimental data; VIVA prediction (continuous line), experimental data (circles). Current profile in green dotted line. NDP 10m 50% strake riser in uniform flow. 126

4-29 Ratio of VIV dominant frequency of VIVA prediction. NDP 10m 50% strake riser in uniform flow. 127

4-30 VIV RMS amplitude (A/D) versus length (x/L) comparison between VIVA prediction and experimental data; VIVA prediction (continuous line), experimental data (circles). Current profile in green dotted line. NDP 10m 50% strake riser in sheared flow. 128

4-31 Ratio of VIV dominant frequency of VIVA prediction. NDP 10m 50% strake riser in sheared flow. 129

4-32 VIV RMS amplitude (A/D) versus length (x/L) comparison between VIVA prediction and experimental data; VIVA prediction (continuous line), experimental data (circles). Current profile in green dotted line.NDP 10m 75% strake riser in uniform flow. 130

4-33 Ratio of VIV dominant frequency of VIVA prediction. NDP 10m 75% strake riser in uniform flow. 131

4-34 VIV RMS amplitude (A/D) versus length (x/L) comparison between VIVA prediction and experimental data; VIVA prediction (continuous line), experimental data (circles). Current profile in green dotted line. NDP 10m 75% strake riser in sheared flow. 132

4-35 Ratio of VIV dominant frequency of VIVA prediction. NDP 10m 75% strake riser in sheared flow. 133

4-36 VIV RMS strain versus length (x/L) comparison between VIVA prediction and experimental data; VIVA prediction (continuous line), experimental data (circles). Current profile in green dotted line. Miami field experiment bare riser. 134

4-37 VIV RMS strain versus length (x/L) comparison between VIVA prediction and experimental data; VIVA prediction (continuous line), experimental data (circles). Current profile in green dotted line. Miami field experiment bare riser (continued). 135

4-38 VIV RMS strain versus length (x/L) comparison between VIVA prediction and experimental data; VIVA prediction (continuous line), experimental data (circles). Current profile in green dotted line. Miami field experiment bare riser (continued). 136

4-39 Ratio of VIV dominant frequency of VIVA prediction. Miami field experiment bare riser. 137

4-40 VIV RMS strain versus length (x/L) comparison between VIVA prediction and experimental data; VIVA prediction (continuous line), experimental data (circles). Current profile in green dotted line. Miami field experiment 40% strake riser. 138

4-41 Ratio of VIV dominant frequency of VIVA prediction. Miami field experiment 40% strake riser. 139

5-1 VIV response regions, crossflow motion dominant region is marked with – on the right, Inline-Crossflow motion region is marked by in the middle and Inline motion dominant region is marked by -.- on the left. (figure altered from Jauvtis and Williamson [32]) 142

5-2 MIT small towing tank. 143

5-3 Test Matrix. 144

5-4 Samples of experimental signals. 144

5-5 Experiment data processing diagram 145

5-6 Original added mass coefficients (C_m) for pure inline oscillations. . . 145

5-7 Smoothed added mass coefficients (C_m) for pure inline oscillations. . 146

5-8 Excitation coefficients in phase with velocity (C_{Dv}) for pure inline oscillations. 147

5-9 $C_{e,IL}$ in 3D zoomed at positive part. 148

5-10 Contour plot of excitation coefficients in phase with velocity (c_{Dv}) for pure inline oscillations. 148
5-11 $C_{a,IL}$ in 3D regenerated from Aronsen [3] 149
5-12 $C_{e,IL}$ in 3D regenerated from Aronsen [3]. 150
5-13 $C_{e,IL}$ in 3D zoomed-in at positive part, regenerated from Aronsen [3]. 150
5-14 Response reduced velocity vs. nominal reduced velocity for a flexibly mounted rigid cylinder [62]. 152
5-15 Nondimensional Amplitude of Oscillations vs. Reduced Velocity for a Flexibly Mounted Rigid Cylinder [62]. 153
5-16 Response reduced velocity vs. nominal reduced velocity for a flexibly mounted rigid cylinder of different damping ratio. 154
5-17 Nondimensional amplitude vs. nominal reduced velocity for a flexibly mounted rigid cylinder of different damping ratio. 154
5-18 Nondimensional amplitude vs. nominal reduced velocity for a flexibly mounted rigid cylinder of different mass ratio. 155
5-19 Response reduced velocity vs. nominal reduced velocity for a flexibly mounted rigid cylinder of different mass ratio. 155
5-20 Response reduced velocity vs. nominal reduced velocity for a flexibly mounted rigid cylinder [19]. 156
5-21 Nondimensional amplitude of oscillations vs. reduced velocity for a flexibly mounted rigid cylinder [19]. 157
5-22 Oscillation frequency vs. reduced velocity for a flexibly mounted rigid cylinder. 159
5-23 Nondimensional amplitude of the inline oscillations vs. reduced velocity for a flexibly mounted rigid cylinder. 159
5-24 Nondimensional amplitude of the inline oscillations vs. reduced velocity for a flexibly mounted rigid cylinder adjusted for Reynolds number effects. 160
5-25 Nondimensional amplitude of the inline oscillations vs. reduced velocity for a flexibly mounted rigid cylinder. 162

5-26 Nondimensional amplitude of the inline oscillations vs. reduced velocity for a flexibly mounted rigid cylinder adjusted for Reynolds number effects. 163
5-27 The inline hydrodynamic coefficients database input to VIVA. 166
5-28 Inline VIVA predicted frequencies versus NDP 38m experimental values. 168
5-29 Inline VIVA predicted amplitude versus NDP 38m experimental values. 168

6-1 VIV response regions, crossflow motion dominant region is marked with – on the right, inline-crossflow motion region is marked by in the middle and Inline motion dominant region is marked by -.- on the left. The x-axis reduced velocity U^* is defined as $U/(f_N D)$ (Figure altered from Jauvtis and Williamson [32]) 173
6-2 2D motion regions in free vibration experiments. The x-axis reduced velocity U_{rn} is defined as $U/(f_N D)$ (Figure altered from Dahl [19]) . 174
6-3 Amp range of 2011 vs 2007 experiments. 175
6-4 Phase range of 2011 vs 2007 experiments. 176
6-5 Lift coefficients extracted from the experiments at a reduced velocity of 4.5 as iso-surfaces. 178
6-6 Lift coefficients extracted from the experiments at a reduced velocity of 4.5 as contours at different phases. 179
6-7 Orbits shape for various phases btw inline and crossflow motion. . . 180
6-8 Lift coefficients in phase with velocity C_{Lv} with inline motion amplitude 0.05 and crossflow motion amplitude 0.15 181
6-9 Lift coefficients C_{Lv} with inline motion amplitude 0.05 and crossflow motion amplitude 0.15 182
6-10 Lift coefficients C_{Lv} for all amplitude of inline and crossflow motions. The x-axis is the nondimensional amplitude of inline motion 0.05, 0.1, 0.15, 0.2, 0.25, 0.3, 0.45, 0.6 and 0.75. The y-axis is the nondimensional amplitudes of crossflow motion: 0.15, 0.25, 0.5, 0.75, 1, 1.25 and 1.5. 183

6-11 Lift coefficients C_{Lv} for all amplitude of inline and crossflow motions with same colorbar.The x-axis is the nondimensional amplitude of inline motion 0.05, 0.1, 0.15, 0.2, 0.25, 0.3, 0.45, 0.6 and 0.75. The y-axis is the nondimensional amplitudes of crossflow motion: 0.15, 0.25, 0.5, 0.75, 1, 1.25 and 1.5. 184

6-12 Fluctuating drag coefficient in phase with velocity C_{Dv} with inline motion amplitude 0.05 and crossflow motion amplitude 0.15 186

6-13 Fluctuating drag coefficient in phase with velocity C_{Dv} with inline motion amplitude 0.05 and crossflow motion amplitude 0.15 187

6-14 Fluctuating drag coefficient in phase with velocity C_{Dv}. The x-axis is the nondimensional amplitude of inline motion 0.05, 0.1, 0.15, 0.2, 0.25, 0.3, 0.45, 0.6 and 0.75. The y-axis is the nondimensional amplitudes of crossflow motion: 0.15, 0.25, 0.5, 0.75, 1, 1.25 and 1.5. . . . 188

6-15 Fluctuating drag coefficient in phase with velocity C_{Dv} with same colorbar. The x-axis is the nondimensional amplitude of inline motion 0.05, 0.1, 0.15, 0.2, 0.25, 0.3, 0.45, 0.6 and 0.75. The y-axis is the nondimensional amplitudes of crossflow motion: 0.15, 0.25, 0.5, 0.75, 1, 1.25 and 1.5. 189

6-16 Added mass coefficient in the crossflow direction C_{my} with inline motion amplitude 0.05 and crossflow motion amplitude 0.15 191

6-17 Added mass coefficient in the crossflow direction C_{my} with inline motion amplitude 0.05 and crossflow motion amplitude 0.15 192

6-18 Added mass coefficient in the crossflow direction C_{my}. The x-axis is the nondimensional amplitude of inline motion 0.05, 0.1, 0.15, 0.2, 0.25, 0.3, 0.45, 0.6 and 0.75. The y-axis is the nondimensional amplitudes of crossflow motion: 0.15, 0.25, 0.5, 0.75, 1, 1.25 and 1.5. . . . 193

6-19 Added mass coefficient in the crossflow direction C_{my} with same colorbar. The x-axis is the nondimensional amplitude of inline motion 0.05, 0.1, 0.15, 0.2, 0.25, 0.3, 0.45, 0.6 and 0.75. The y-axis is the nondimensional amplitudes of crossflow motion: 0.15, 0.25, 0.5, 0.75, 1, 1.25 and 1.5. 194

6-20 Added mass coefficient in the crossflow direction C_{my} with inline motion amplitude 0.05 and crossflow motion amplitude 0.5 195

6-21 Added mass coefficient in the crossflow direction C_{my} with inline motion amplitude 0.05 and crossflow motion amplitude 1 195

6-22 Added mass coefficient in the crossflow direction C_{my} with inline motion amplitude 0.05 and crossflow motion amplitude 1.5 196

6-23 Added mass coefficient in the crossflow direction C_{my} with inline motion amplitude 0.15 and crossflow motion amplitude 0.15 197

6-24 Added mass coefficient in the crossflow direction C_{my} with inline motion amplitude 0.25 and crossflow motion amplitude 0.25 198

6-25 Added mass coefficient in the crossflow direction C_{my} with inline motion amplitude 0.15 and crossflow motion amplitude 0.75 199

6-26 Added mass coefficient in the crossflow direction C_{my} with inline motion amplitude 0.25 and crossflow motion amplitude 1.25 200

6-27 Added mass coefficient in the inline direction C_{mx} with inline motion amplitude 0.05 and crossflow motion amplitude 0.15 201

6-28 Added mass coefficient in the inline direction C_{mx} with inline motion amplitude 0.05 and crossflow motion amplitude 0.15 202

6-29 Added mass coefficient in the inline direction C_{mx}. The x-axis is the nondimensional amplitude of inline motion 0.05, 0.1, 0.15, 0.2, 0.25, 0.3, 0.45, 0.6 and 0.75. The y-axis is the nondimensional amplitudes of crossflow motion: 0.15, 0.25, 0.5, 0.75, 1, 1.25 and 1.5. 203

6-30 Added mass coefficient in the inline direction C_{mx} with same colorbar. The x-axis is the nondimensional amplitude of inline motion 0.05, 0.1, 0.15, 0.2, 0.25, 0.3, 0.45, 0.6 and 0.75. The y-axis is the nondimensional amplitudes of crossflow motion: 0.15, 0.25, 0.5, 0.75, 1, 1.25 and 1.5. 204
6-31 Added mass coefficient in the crossflow direction C_{my} with inline motion amplitude 0.3 and crossflow motion amplitude 1 207
6-32 Added mass coefficient in the inline direction C_{mx} with inline motion amplitude 0.3 and crossflow motion amplitude 1 207
6-33 Time series of drag coefficients and inline displacement of 90° motion. 210
6-34 Time series of drag coefficients and inline displacement of -90° motion. 211
6-35 Time series of lift coefficients and inline displacement of 90° motion. 213
6-36 Time series of lift coefficients and inline displacement of 90° motion. 214
6-37 PIV of 90° motion. 215
6-38 PIV of -90° motion. 216
6-39 PIV of 90° motion. 218
6-40 Lift force from vortex. 220
6-41 Drag force from vortex. 221
6-42 Uncoupled Response Prediction vs Free Vibration Experiment Measurement at Natural Frequency Ratio 1.9 225
6-43 Coupled response prediction vs free vibration experiment measurement 228
6-44 Added mass coefficients comparison. The magenta triangle is the added mass predicted from the forced vibration model, the green diamond is added mass measured from the free vibration experiment, and the blue circle is derived from the free vibration motion following equation 6.32. 229
6-45 Lift and drag force coefficients comparison. The magenta triangle is the added mass predicted from the forced vibration model and the blue circle is derived from free vibration motion following equation 6.33. 230

6-46 First harmonic force prediction vs free vibration experiment measurement at natural frequency ratio 1.9 231
6-47 Third harmonic force prediction vs free vibration experiment measurement at natural frequency ratio. 232

A-1 Lift coefficients in phase with velocity C_{Lv} X 0.05 Y 0.15 238
A-2 Lift coefficients in phase with velocity C_{Lv} X 0.05 Y 0.25 238
A-3 Lift coefficients in phase with velocity C_{Lv} X 0.05 Y 0.5 239
A-4 Lift coefficients in phase with velocity C_{Lv} X 0.05 Y 0.75 239
A-5 Lift coefficients in phase with velocity C_{Lv} X 0.05 Y 1 240
A-6 Lift coefficients in phase with velocity C_{Lv} X 0.05 Y 1.25 240
A-7 Lift coefficients in phase with velocity C_{Lv} X 0.05 Y 1.5 241
A-8 Lift coefficients in phase with velocity C_{Lv} X 0.1 Y 0.15 242
A-9 Lift coefficients in phase with velocity C_{Lv} X 0.1 Y 0.25 242
A-10 Lift coefficients in phase with velocity C_{Lv} X 0.1 Y 0.5 243
A-11 Lift coefficients in phase with velocity C_{Lv} X 0.1 Y 0.75 243
A-12 Lift coefficients in phase with velocity C_{Lv} X 0.1 Y 1 244
A-13 Lift coefficients in phase with velocity C_{Lv} X 0.1 Y 1.25 244
A-14 Lift coefficients in phase with velocity C_{Lv} X 0.1 Y 1.5 245
A-15 Lift coefficients in phase with velocity C_{Lv} X 0.15 Y 0.15 246
A-16 Lift coefficients in phase with velocity C_{Lv} X 0.15 Y 0.25 246
A-17 Lift coefficients in phase with velocity C_{Lv} X 0.15 Y 0.5 247
A-18 Lift coefficients in phase with velocity C_{Lv} X 0.15 Y 0.75 247
A-19 Lift coefficients in phase with velocity C_{Lv} X 0.15 Y 1 248
A-20 Lift coefficients in phase with velocity C_{Lv} X 0.15 Y 1.25 248
A-21 Lift coefficients in phase with velocity C_{Lv} X 0.15 Y 1.5 249
A-22 Lift coefficients in phase with velocity C_{Lv} X 0.2 Y 0.15 250
A-23 Lift coefficients in phase with velocity C_{Lv} X 0.2 Y 0.25 250
A-24 Lift coefficients in phase with velocity C_{Lv} X 0.2 Y 0.5 251
A-25 Lift coefficients in phase with velocity C_{Lv} X 0.2 Y 0.75 251

A-26 Lift coefficients in phase with velocity C_{Lv} X 0.2 Y 1 252
A-27 Lift coefficients in phase with velocity C_{Lv} X 0.2 Y 1.25 252
A-28 Lift coefficients in phase with velocity C_{Lv} X 0.2 Y 1.5 253
A-29 Lift coefficients in phase with velocity C_{Lv} X 0.25 Y 0.15 254
A-30 Lift coefficients in phase with velocity C_{Lv} X 0.25 Y 0.25 254
A-31 Lift coefficients in phase with velocity C_{Lv} X 0.25 Y 0.5 255
A-32 Lift coefficients in phase with velocity C_{Lv} X 0.25 Y 0.75 255
A-33 Lift coefficients in phase with velocity C_{Lv} X 0.25 Y 1 256
A-34 Lift coefficients in phase with velocity C_{Lv} X 0.25 Y 1.25 256
A-35 Lift coefficients in phase with velocity C_{Lv} X 0.25 Y 1.5 257
A-36 Lift coefficients in phase with velocity C_{Lv} X 0.3 Y 0.15 258
A-37 Lift coefficients in phase with velocity C_{Lv} X 0.3 Y 0.25 258
A-38 Lift coefficients in phase with velocity C_{Lv} X 0.3 Y 0.5 259
A-39 Lift coefficients in phase with velocity C_{Lv} X 0.3 Y 0.75 259
A-40 Lift coefficients in phase with velocity C_{Lv} X 0.3 Y 1 260
A-41 Lift coefficients in phase with velocity C_{Lv} X 0.3 Y 1.25 260
A-42 Lift coefficients in phase with velocity C_{Lv} X 0.3 Y 1.5 261
A-43 Lift coefficients in phase with velocity C_{Lv} X 0.45 Y 0.15 262
A-44 Lift coefficients in phase with velocity C_{Lv} X 0.45 Y 0.25 262
A-45 Lift coefficients in phase with velocity C_{Lv} X 0.45 Y 0.5 263
A-46 Lift coefficients in phase with velocity C_{Lv} X 0.45 Y 0.75 263
A-47 Lift coefficients in phase with velocity C_{Lv} X 0.45 Y 1 264
A-48 Lift coefficients in phase with velocity C_{Lv} X 0.45 Y 1.25 264
A-49 Lift coefficients in phase with velocity C_{Lv} X 0.45 Y 1.5 265
A-50 Lift coefficients in phase with velocity C_{Lv} X 0.6 Y 0.15 266
A-51 Lift coefficients in phase with velocity C_{Lv} X 0.6 Y 0.25 266
A-52 Lift coefficients in phase with velocity C_{Lv} X 0.6 Y 0.5 267
A-53 Lift coefficients in phase with velocity C_{Lv} X 0.6 Y 0.75 267
A-54 Lift coefficients in phase with velocity C_{Lv} X 0.6 Y 1 268
A-55 Lift coefficients in phase with velocity C_{Lv} X 0.6 Y 1.25 268

A-56 Lift coefficients in phase with velocity C_{Lv} X 0.6 Y 1.5 269
A-57 Lift coefficients in phase with velocity C_{Lv} X 0.75 Y 0.15 270
A-58 Lift coefficients in phase with velocity C_{Lv} X 0.75 Y 0.25 270
A-59 Lift coefficients in phase with velocity C_{Lv} X 0.75 Y 0.5 271
A-60 Lift coefficients in phase with velocity C_{Lv} X 0.75 Y 0.75 271
A-61 Lift coefficients in phase with velocity C_{Lv} X 0.75 Y 1 272
A-62 Lift coefficients in phase with velocity C_{Lv} X 0.75 Y 1.25 272
A-63 Lift coefficients in phase with velocity C_{Lv} X 0.75 Y 1.5 273
A-64 Drag coefficients in phase with velocity C_{Dv} X 0.05 Y 0.15 274
A-65 Drag coefficients in phase with velocity C_{Dv} X 0.05 Y 0.25 274
A-66 Drag coefficients in phase with velocity C_{Dv} X 0.05 Y 0.5 275
A-67 Drag coefficients in phase with velocity C_{Dv} X 0.05 Y 0.75 275
A-68 Drag coefficients in phase with velocity C_{Dv} X 0.05 Y 1 276
A-69 Drag coefficients in phase with velocity C_{Dv} X 0.05 Y 1.25 276
A-70 Drag coefficients in phase with velocity C_{Dv} X 0.05 Y 1.5 277
A-71 Drag coefficients in phase with velocity C_{Dv} X 0.1 Y 0.15 278
A-72 Drag coefficients in phase with velocity C_{Dv} X 0.1 Y 0.25 278
A-73 Drag coefficients in phase with velocity C_{Dv} X 0.1 Y 0.5 279
A-74 Drag coefficients in phase with velocity C_{Dv} X 0.1 Y 0.75 279
A-75 Drag coefficients in phase with velocity C_{Dv} X 0.1 Y 1 280
A-76 Drag coefficients in phase with velocity C_{Dv} X 0.1 Y 1.25 280
A-77 Drag coefficients in phase with velocity C_{Dv} X 0.1 Y 1.5 281
A-78 Drag coefficients in phase with velocity C_{Dv} X 0.15 Y 0.15 282
A-79 Drag coefficients in phase with velocity C_{Dv} X 0.15 Y 0.25 282
A-80 Drag coefficients in phase with velocity C_{Dv} X 0.15 Y 0.5 283
A-81 Drag coefficients in phase with velocity C_{Dv} X 0.15 Y 0.75 283
A-82 Drag coefficients in phase with velocity C_{Dv} X 0.15 Y 1 284
A-83 Drag coefficients in phase with velocity C_{Dv} X 0.15 Y 1.25 284
A-84 Drag coefficients in phase with velocity C_{Dv} X 0.15 Y 1.5 285
A-85 Drag coefficients in phase with velocity C_{Dv} X 0.2 Y 0.15 286

A-86 Drag coefficients in phase with velocity C_{Dv} X 0.2 Y 0.25 286
A-87 Drag coefficients in phase with velocity C_{Dv} X 0.2 Y 0.5 287
A-88 Drag coefficients in phase with velocity C_{Dv} X 0.2 Y 0.75 287
A-89 Drag coefficients in phase with velocity C_{Dv} X 0.2 Y 1 288
A-90 Drag coefficients in phase with velocity C_{Dv} X 0.2 Y 1.25 288
A-91 Drag coefficients in phase with velocity C_{Dv} X 0.2 Y 1.5 289
A-92 Drag coefficients in phase with velocity C_{Dv} X 0.25 Y 0.15 290
A-93 Drag coefficients in phase with velocity C_{Dv} X 0.25 Y 0.25 290
A-94 Drag coefficients in phase with velocity C_{Dv} X 0.25 Y 0.5 291
A-95 Drag coefficients in phase with velocity C_{Dv} X 0.25 Y 0.75 291
A-96 Drag coefficients in phase with velocity C_{Dv} X 0.25 Y 1 292
A-97 Drag coefficients in phase with velocity C_{Dv} X 0.25 Y 1.25 292
A-98 Drag coefficients in phase with velocity C_{Dv} X 0.25 Y 1.5 293
A-99 Drag coefficients in phase with velocity C_{Dv} X 0.3 Y 0.15 294
A-100 Drag coefficients in phase with velocity C_{Dv} X 0.3 Y 0.25 294
A-101 Drag coefficients in phase with velocity C_{Dv} X 0.3 Y 0.5 295
A-102 Drag coefficients in phase with velocity C_{Dv} X 0.3 Y 0.75 295
A-103 Drag coefficients in phase with velocity C_{Dv} X 0.3 Y 1 296
A-104 Drag coefficients in phase with velocity C_{Dv} X 0.3 Y 1.25 296
A-105 Drag coefficients in phase with velocity C_{Dv} X 0.3 Y 1.5 297
A-106 Drag coefficients in phase with velocity C_{Dv} X 0.45 Y 0.15 298
A-107 Drag coefficients in phase with velocity C_{Dv} X 0.45 Y 0.25 298
A-108 Drag coefficients in phase with velocity C_{Dv} X 0.45 Y 0.5 299
A-109 Drag coefficients in phase with velocity C_{Dv} X 0.45 Y 0.75 299
A-110 Drag coefficients in phase with velocity C_{Dv} X 0.45 Y 1 300
A-111 Drag coefficients in phase with velocity C_{Dv} X 0.45 Y 1.25 300
A-112 Drag coefficients in phase with velocity C_{Dv} X 0.45 Y 1.5 301
A-113 Drag coefficients in phase with velocity C_{Dv} X 0.6 Y 0.15 302
A-114 Drag coefficients in phase with velocity C_{Dv} X 0.6 Y 0.25 302
A-115 Drag coefficients in phase with velocity C_{Dv} X 0.6 Y 0.5 303

A-116 Drag coefficients in phase with velocity C_{Dv} X 0.6 Y 0.75 303
A-117 Drag coefficients in phase with velocity C_{Dv} X 0.6 Y 1 304
A-118 Drag coefficients in phase with velocity C_{Dv} X 0.6 Y 1.25 304
A-119 Drag coefficients in phase with velocity C_{Dv} X 0.6 Y 1.5 305
A-120 Drag coefficients in phase with velocity C_{Dv} X 0.75 Y 0.15 306
A-121 Drag coefficients in phase with velocity C_{Dv} X 0.75 Y 0.25 306
A-122 Drag coefficients in phase with velocity C_{Dv} X 0.75 Y 0.5 307
A-123 Drag coefficients in phase with velocity C_{Dv} X 0.75 Y 0.75 307
A-124 Drag coefficients in phase with velocity C_{Dv} X 0.75 Y 1 308
A-125 Drag coefficients in phase with velocity C_{Dv} X 0.75 Y 1.25 308
A-126 Drag coefficients in phase with velocity C_{Dv} X 0.75 Y 1.5 309
A-127 Crossflow added mass coefficients $C_{m,CF}$ X 0.05 Y 0.15 310
A-128 Crossflow added mass coefficients $C_{m,CF}$ X 0.05 Y 0.25 310
A-129 Crossflow added mass coefficients $C_{m,CF}$ X 0.05 Y 0.5 311
A-130 Crossflow added mass coefficients $C_{m,CF}$ X 0.05 Y 0.75 311
A-131 Crossflow added mass coefficients $C_{m,CF}$ X 0.05 Y 1 312
A-132 Crossflow added mass coefficients $C_{m,CF}$ X 0.05 Y 1.25 312
A-133 Crossflow added mass coefficients $C_{m,CF}$ X 0.05 Y 1.5 313
A-134 Crossflow added mass coefficients $C_{m,CF}$ X 0.1 Y 0.15 314
A-135 Crossflow added mass coefficients $C_{m,CF}$ X 0.1 Y 0.25 314
A-136 Crossflow added mass coefficients $C_{m,CF}$ X 0.1 Y 0.5 315
A-137 Crossflow added mass coefficients $C_{m,CF}$ X 0.1 Y 0.75 315
A-138 Crossflow added mass coefficients $C_{m,CF}$ X 0.1 Y 1 316
A-139 Crossflow added mass coefficients $C_{m,CF}$ X 0.1 Y 1.25 316
A-140 Crossflow added mass coefficients $C_{m,CF}$ X 0.1 Y 1.5 317
A-141 Crossflow added mass coefficients $C_{m,CF}$ X 0.15 Y 0.15 318
A-142 Crossflow added mass coefficients $C_{m,CF}$ X 0.15 Y 0.25 318
A-143 Crossflow added mass coefficients $C_{m,CF}$ X 0.15 Y 0.5 319
A-144 Crossflow added mass coefficients $C_{m,CF}$ X 0.15 Y 0.75 319
A-145 Crossflow added mass coefficients $C_{m,CF}$ X 0.15 Y 1 320

A-146 Crossflow added mass coefficients $C_{m,CF}$ X 0.15 Y 1.25 320
A-147 Crossflow added mass coefficients $C_{m,CF}$ X 0.15 Y 1.5 321
A-148 Crossflow added mass coefficients $C_{m,CF}$ X 0.2 Y 0.15 322
A-149 Crossflow added mass coefficients $C_{m,CF}$ X 0.2 Y 0.25 322
A-150 Crossflow added mass coefficients $C_{m,CF}$ X 0.2 Y 0.5 323
A-151 Crossflow added mass coefficients $C_{m,CF}$ X 0.2 Y 0.75 323
A-152 Crossflow added mass coefficients $C_{m,CF}$ X 0.2 Y 1 324
A-153 Crossflow added mass coefficients $C_{m,CF}$ X 0.2 Y 1.25 324
A-154 Crossflow added mass coefficients $C_{m,CF}$ X 0.2 Y 1.5 325
A-155 Crossflow added mass coefficients $C_{m,CF}$ X 0.25 Y 0.15 326
A-156 Crossflow added mass coefficients $C_{m,CF}$ X 0.25 Y 0.25 326
A-157 Crossflow added mass coefficients $C_{m,CF}$ X 0.25 Y 0.5 327
A-158 Crossflow added mass coefficients $C_{m,CF}$ X 0.25 Y 0.75 327
A-159 Crossflow added mass coefficients $C_{m,CF}$ X 0.25 Y 1 328
A-160 Crossflow added mass coefficients $C_{m,CF}$ X 0.25 Y 1.25 328
A-161 Crossflow added mass coefficients $C_{m,CF}$ X 0.25 Y 1.5 329
A-162 Crossflow added mass coefficients $C_{m,CF}$ X 0.3 Y 0.15 330
A-163 Crossflow added mass coefficients $C_{m,CF}$ X 0.3 Y 0.25 330
A-164 Crossflow added mass coefficients $C_{m,CF}$ X 0.3 Y 0.5 331
A-165 Crossflow added mass coefficients $C_{m,CF}$ X 0.3 Y 0.75 331
A-166 Crossflow added mass coefficients $C_{m,CF}$ X 0.3 Y 1 332
A-167 Crossflow added mass coefficients $C_{m,CF}$ X 0.3 Y 1.25 332
A-168 Crossflow added mass coefficients $C_{m,CF}$ X 0.3 Y 1.5 333
A-169 Crossflow added mass coefficients $C_{m,CF}$ X 0.45 Y 0.15 334
A-170 Crossflow added mass coefficients $C_{m,CF}$ X 0.45 Y 0.25 334
A-171 Crossflow added mass coefficients $C_{m,CF}$ X 0.45 Y 0.5 335
A-172 Crossflow added mass coefficients $C_{m,CF}$ X 0.45 Y 0.75 335
A-173 Crossflow added mass coefficients $C_{m,CF}$ X 0.45 Y 1 336
A-174 Crossflow added mass coefficients $C_{m,CF}$ X 0.45 Y 1.25 336
A-175 Crossflow added mass coefficients $C_{m,CF}$ X 0.45 Y 1.5 337

A-176 Crossflow added mass coefficients $C_{m,CF}$ X 0.6 Y 0.15 338
A-177 Crossflow added mass coefficients $C_{m,CF}$ X 0.6 Y 0.25 338
A-178 Crossflow added mass coefficients $C_{m,CF}$ X 0.6 Y 0.5 339
A-179 Crossflow added mass coefficients $C_{m,CF}$ X 0.6 Y 0.75 339
A-180 Crossflow added mass coefficients $C_{m,CF}$ X 0.6 Y 1 340
A-181 Crossflow added mass coefficients $C_{m,CF}$ X 0.6 Y 1.25 340
A-182 Crossflow added mass coefficients $C_{m,CF}$ X 0.6 Y 1.5 341
A-183 Crossflow added mass coefficients $C_{m,CF}$ X 0.75 Y 0.15 342
A-184 Crossflow added mass coefficients $C_{m,CF}$ X 0.75 Y 0.25 342
A-185 Crossflow added mass coefficients $C_{m,CF}$ X 0.75 Y 0.5 343
A-186 Crossflow added mass coefficients $C_{m,CF}$ X 0.75 Y 0.75 343
A-187 Crossflow added mass coefficients $C_{m,CF}$ X 0.75 Y 1 344
A-188 Crossflow added mass coefficients $C_{m,CF}$ X 0.75 Y 1.25 344
A-189 Crossflow added mass coefficients $C_{m,CF}$ X 0.75 Y 1.5 345
A-190 Inline added mass coefficients $C_{m,IL}$ X 0.05 Y 0.15 346
A-191 Inline added mass coefficients $C_{m,IL}$ X 0.05 Y 0.25 346
A-192 Inline added mass coefficients $C_{m,IL}$ X 0.05 Y 0.5 347
A-193 Inline added mass coefficients $C_{m,IL}$ X 0.05 Y 0.75 347
A-194 Inline added mass coefficients $C_{m,IL}$ X 0.05 Y 1 348
A-195 Inline added mass coefficients $C_{m,IL}$ X 0.05 Y 1.25 348
A-196 Inline added mass coefficients $C_{m,IL}$ X 0.05 Y 1.5 349
A-197 Inline added mass coefficients $C_{m,IL}$ X 0.1 Y 0.15 350
A-198 Inline added mass coefficients $C_{m,IL}$ X 0.1 Y 0.25 350
A-199 Inline added mass coefficients $C_{m,IL}$ X 0.1 Y 0.5 351
A-200 Inline added mass coefficients $C_{m,IL}$ X 0.1 Y 0.75 351
A-201 Inline added mass coefficients $C_{m,IL}$ X 0.1 Y 1 352
A-202 Inline added mass coefficients $C_{m,IL}$ X 0.1 Y 1.25 352
A-203 Inline added mass coefficients $C_{m,IL}$ X 0.1 Y 1.5 353
A-204 Inline added mass coefficients $C_{m,IL}$ X 0.15 Y 0.15 354
A-205 Inline added mass coefficients $C_{m,IL}$ X 0.15 Y 0.25 354

A-206 Inline added mass coefficients $C_{m,IL}$ X 0.15 Y 0.5 355
A-207 Inline added mass coefficients $C_{m,IL}$ X 0.15 Y 0.75 355
A-208 Inline added mass coefficients $C_{m,IL}$ X 0.15 Y 1 356
A-209 Inline added mass coefficients $C_{m,IL}$ X 0.15 Y 1.25 356
A-210 Inline added mass coefficients $C_{m,IL}$ X 0.15 Y 1.5 357
A-211 Inline added mass coefficients $C_{m,IL}$ X 0.2 Y 0.15 358
A-212 Inline added mass coefficients $C_{m,IL}$ X 0.2 Y 0.25 358
A-213 Inline added mass coefficients $C_{m,IL}$ X 0.2 Y 0.5 359
A-214 Inline added mass coefficients $C_{m,IL}$ X 0.2 Y 0.75 359
A-215 Inline added mass coefficients $C_{m,IL}$ X 0.2 Y 1 360
A-216 Inline added mass coefficients $C_{m,IL}$ X 0.2 Y 1.25 360
A-217 Inline added mass coefficients $C_{m,IL}$ X 0.2 Y 1.5 361
A-218 Inline added mass coefficients $C_{m,IL}$ X 0.25 Y 0.15 362
A-219 Inline added mass coefficients $C_{m,IL}$ X 0.25 Y 0.25 362
A-220 Inline added mass coefficients $C_{m,IL}$ X 0.25 Y 0.5 363
A-221 Inline added mass coefficients $C_{m,IL}$ X 0.25 Y 0.75 363
A-222 Inline added mass coefficients $C_{m,IL}$ X 0.25 Y 1 364
A-223 Inline added mass coefficients $C_{m,IL}$ X 0.25 Y 1.25 364
A-224 Inline added mass coefficients $C_{m,IL}$ X 0.25 Y 1.5 365
A-225 Inline added mass coefficients $C_{m,IL}$ X 0.3 Y 0.15 366
A-226 Inline added mass coefficients $C_{m,IL}$ X 0.3 Y 0.25 366
A-227 Inline added mass coefficients $C_{m,IL}$ X 0.3 Y 0.5 367
A-228 Inline added mass coefficients $C_{m,IL}$ X 0.3 Y 0.75 367
A-229 Inline added mass coefficients $C_{m,IL}$ X 0.3 Y 1 368
A-230 Inline added mass coefficients $C_{m,IL}$ X 0.3 Y 1.25 368
A-231 Inline added mass coefficients $C_{m,IL}$ X 0.3 Y 1.5 369
A-232 Inline added mass coefficients $C_{m,IL}$ X 0.45 Y 0.15 370
A-233 Inline added mass coefficients $C_{m,IL}$ X 0.45 Y 0.25 370
A-234 Inline added mass coefficients $C_{m,IL}$ X 0.45 Y 0.5 371
A-235 Inline added mass coefficients $C_{m,IL}$ X 0.45 Y 0.75 371

A-236 Inline added mass coefficients $C_{m,IL}$ X 0.45 Y 1 372
A-237 Inline added mass coefficients $C_{m,IL}$ X 0.45 Y 1.25 372
A-238 Inline added mass coefficients $C_{m,IL}$ X 0.45 Y 1.5 373
A-239 Inline added mass coefficients $C_{m,IL}$ X 0.6 Y 0.15 374
A-240 Inline added mass coefficients $C_{m,IL}$ X 0.6 Y 0.25 374
A-241 Inline added mass coefficients $C_{m,IL}$ X 0.6 Y 0.5 375
A-242 Inline added mass coefficients $C_{m,IL}$ X 0.6 Y 0.75 375
A-243 Inline added mass coefficients $C_{m,IL}$ X 0.6 Y 1 376
A-244 Inline added mass coefficients $C_{m,IL}$ X 0.6 Y 1.25 376
A-245 Inline added mass coefficients $C_{m,IL}$ X 0.6 Y 1.5 377
A-246 Inline added mass coefficients $C_{m,IL}$ X 0.75 Y 0.15 378
A-247 Inline added mass coefficients $C_{m,IL}$ X 0.75 Y 0.25 378
A-248 Inline added mass coefficients $C_{m,IL}$ X 0.75 Y 0.5 379
A-249 Inline added mass coefficients $C_{m,IL}$ X 0.75 Y 0.75 379
A-250 Inline added mass coefficients $C_{m,IL}$ X 0.75 Y 1 380
A-251 Inline added mass coefficients $C_{m,IL}$ X 0.75 Y 1.25 380
A-252 Inline added mass coefficients $C_{m,IL}$ X 0.75 Y 1.5 381

List of Tables

3.1 Cylinder properties in the NDP data 56

3.2 Occurrence of Type II signals (spreading) in uniform and linearly sheared flow cases in the NDP data 59

5.1 Cagney and Balabani 2013 free vibration experiment parameters [10] 158

5.2 King free vibration experiment parameters [36] 161

6.1 2D Experiment Amplitude Matrix. The first column is the crossflow nondimensional amplitude and the first row is the inline nondimensional amplitude. 175

6.2 2D experiment phase matrix. 176

Chapter 1

Introduction

Vortex Induced Vibrations (VIV) of a flexibly mounted rigid cylinder placed in the flow is a canonical problem of the fluid-structure interactions. Vortex shedding is a phenomenon observed for bluff bodies in a free stream above Reynolds Number 50. Since real fluids have viscosity, the flow around the cylinder will form the boundary layer. The boundary layer can separate from the body and vortices are shed from the body because of its excessive curvature and instability. Asymmetrical vortex shedding results in an oscillating force acting on the body transversely and inline to the flow, causing the cylinder to vibrate. On the other hand, the vibrations of the cylinder change the flow field around it, which in turn alters the vortex and the forces on the body. This fluid-structure interaction process is complicated because of the high nonlinearity and complexity of the Navier-Stokes Equations.

Many researchers have studied this phenomenon from various points of view and techniques, ranging from purely experimental studies to purely numerical ones. Bearman [5], Sarpkaya [61] and Williamson and Govardhan [78] give a complete review of studies conducted on a flexibly mounted cylinder. The interest in VIV studies, besides the inherent fundamental understanding they provide, comes from the various industrial applications where vortex-induced vibrations are observed. Although vortex-induced vibrations are of rather low amplitude (up to one cylinder diameter), they can lead to failure of the structure due to fatigue. Examples range from the

risers used in the ocean oil platforms, to the mooring lines used in conceptual designs of floating wind turbines, to the cables used in cable-stayed bridges. In all of these examples, the structure is flexible with a large slenderness ratio. The study of VIV and the resulting material fatigue is particularly important for ultra-deep water oil exploration and development. Long cylindrical structures, such as risers and mooring lines, can experience severe fatigue life damage due to VIV. In the engineering practice, they are usually outfitted with VIV-cancellation systems or subjected to aggressive replacement schedules; however, the cost of these measures can be high due to the large safety factor employed.

This problem calls for studies on vortex-induced vibrations of structures placed in the flow. A deeper understanding of the physics behind the VIV phenomena and the resulting effective VIV and fatigue prediction programs offer the prospect of optimizing the design and replacement schedule, eventually reducing the cost while increasing the safety of such engineering projects.

1.1 Motivations

Research on VIV has been ongoing in the past few decades [73]. For a long time, it was believed that these oscillations were mainly in the crossflow direction (a direction perpendicular to the flow direction) and were purely harmonic ones, with only one major frequency close to the Strouhal frequency (a dimensionless representative of the frequency of vortex shedding). The inline motion of cylinders caused by VIV has been long neglected due to its small amplitude compared to the cross-flow response amplitude. However, it was shown recently [32], [77], [20] that for both rigid and flexible cylinders, the inline oscillations cause drastic changes in the wake and the resulting fluid forces. This includes a significant 3rd and, in some cases, 5th harmonic component in the measured crossflow fluid force signals and even-harmonics in the inline force. The inclusion of these higher harmonic components of stress in the

fatigue analysis can increase the predicted damage by an order of magnitude [44]. Thus, a thorough quantification of the influence of both high harmonic and chaotic components and modeling of vortex induced vibrations in both inline and crossflow directions are crucial to advancing our understanding of the fatigue life damage caused by VIV and will improve the predictions of VIV.

1.2 Major Challenges to Address

This thesis is organized around the following key challenges that emerged from the frontier VIV research related to high harmonic fatigue life damage and VIV prediction modeling.

- What is the influence of high harmonic and chaotic components on fatigue life?
- How to improve the existing crossflow VIV prediction model?
- How to model and predict inline VIV?
- How to model the interaction of the inline motion and the crossflow motion?
- How to predict coupled inline-crossflow VIV motions and high harmonic forces?

1.3 Thesis Scope

In Chapter 2, previous work on VIV, especially prediction, was systematically reviewed.

In Chapter 3, the impact of the higher harmonic components and the chaotic response on the resulting fatigue damage of the flexible cylinders was systematically assessed. Statistical methods were employed to generate a stress time series based on the PSD plots similar to those of experimental signals. It is shown that the high harmonic signal significantly influences the fatigue life, while the wide- band chaotic components have limited effects. Thus, prediction of high harmonic forces through

coupled Inline-crossflow model holds the key to the problem.

In Chapter 4, the semi-empirical crossflow VIV prediction model was revisited. Prediction results from VIVA, a VIV response prediction program widely used in the offshore industry, were improved through a systematical adjustment of hydrodynamics coefficients based on filed and lab experiments. The results were benchmarked with controlled lab experiments, including the Norwegian Deepwater Programme (NDP) Riser High Mode VIV test, the Chaplin experiment, and the ExxonMobil 10m long riser model experiment, and field experiments including the Miami experiment (MIT-DeepStar datasets) and the BP bare full-scale riser test in the Gulf of Mexico.

In Chapter 5, pure inline VIV was studied using both experiments and a semi- empirical model. A pure inline VIV hydrodynamic force coefficients database was constructed from forced motion experiments in the towing tank. A spring-damper rigid cylinder VIV model was created, and the above pure inline hydrodynamic database was employed to calculate the fluid forces to the system. The motion predicted by the model was compared with free vibration experiments. Additionally, an inline response prediction module was introduced to VIVA to predict the inline response of flexible cylinders and the results were benchmarked with Norwegian Deepwater Programme (NDP) Riser High Mode VIV tests data.

In Chapter 6, the coupled Inline-crossflow VIV problem was systematically addressed. Extensive forced inline and combined inline-crossflow experiments were designed and carried out in the MIT towing tank, which subsequently was employed to provide hydrodynamic coefficient databases for VIV prediction models. The constructed 2D VIV hydrodynamics coefficients database ZDMiT was thoroughly studied and semi-empirical programs are expected to widely use it to predict coupled Inline- Crossflow VIV in the field. Additionally, a coupled inline-crossflow rigid cylinder response prediction model was developed to predict coupled Inline-Crossflow VIV motion and the higher harmonic VIV forces.

In Chapter 7, the major contribution of this thesis work is summarized and future work is recommended.

Chapter 2

Vortex Induced Vibration

Fluid passing a bluff body, defined as cross sectional shapes that have a span-to-chord ratio near one, is considered a fundamental problem in the field of fluid-body interaction. The problem has a simple formulation but has a wide range of engineering applications due to the prevalence of bluff bodies in structures and occurrence of vortex-induced vibrations. Vortex shedding in the wake of the bluff bodies can excite their natural frequencies, thus resulting in severe fatigue damage to structures. In this chapter, the theoretical background of Vortex Induced Vibration, as well as literature review on both crossflow and inline direction VIV, are discussed.

2.1 Theoretical Background of Vortex Induced Vibration

When a bluff body is placed in a free stream of fluid, the fluid field will be altered, especially surrounding the body. To satisfy the continuity, the streamlines become denser around the body, which indicates the ow speeds up from D to E in Figure 2-1. There exists a pressure gradient $\frac{\partial p}{\partial x} < 0$ to accelerate the fluid along the surface from D to E. When passing the top edge of the cylinder, the streamlines begin to spread out again and the pressure gradient switches signs, (gradient $\frac{\partial p}{\partial x} > 0$), to decelerate it again between E and F.

Since real fluids have viscosity, the flow around the body will be slowed down while in contact with its surface, thus forming a boundary layer. Because pressure does not vary across the thickness of the layer [52, 81], the variation of the pressure along the inside the boundary layer must be the same as that predicted by the inviscid theory. Since the fluid in the inner part of the boundary layer is relatively slower, it is more affected by the increasing pressure gradient. For a large enough pressure increase passing the top of the bluff body, the fluid may slow to zero velocity or even become reversed. When flow reversal occurs, the flow is said to be separated from the surface. As the Reynolds number increases, the wake becomes unstable and small perturbations in the flow or on the surface of the cylinder will cause the boundary layer separate from the body and vortices to break off from the cylinder, therefore shedding from the body.

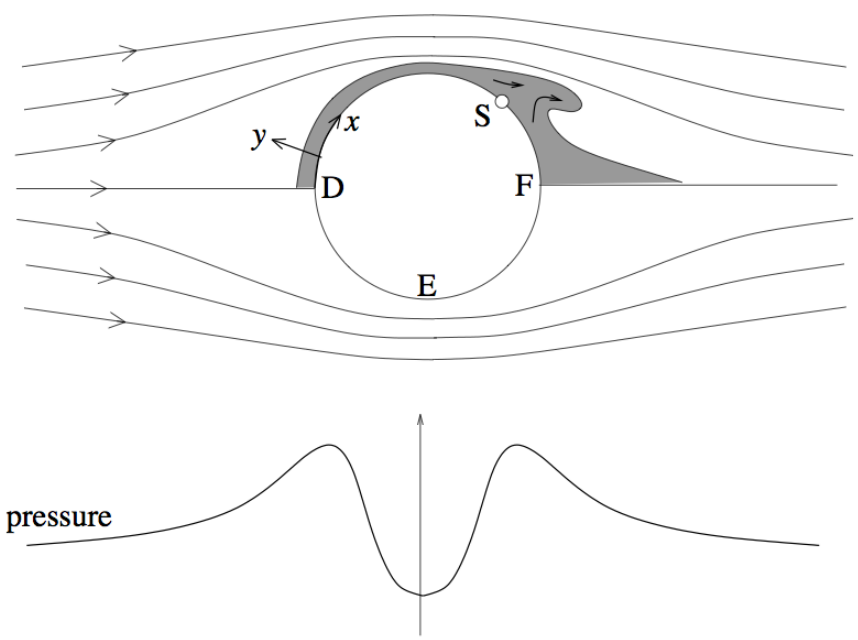

Figure 2-1: Pressure field and separation point for flow past a cylinder. [27]

When the cylinder is flexibly mounted or flexible, the natural frequency of the cylinder can be excited by vortex shedding. When the frequency of vortex shedding is near the natural frequency of the cylinder, large amplitude vibrations of the cylinder may occur. The motions caused by vortex shedding are called vortex-induced

vibrations (VIV) and are essentially resulting from the interaction of the cylinder structure with the fluid wake.

Vortex-induced vibrations are a subdivision of flow-induced vibrations [7]. Unlike unstable oscillations, such as galloping, vortex-induced vibrations generally are stable and self-limiting. The self-limiting nature of vortex-induced vibrations is caused by a balance between excitation forces and fluid damping [68, 66, 75].

Vortex-induced vibrations are typically moderate in amplitude (on the order of one cylinder diameter), resulting in structural oscillations that are not large enough to cause structure failure abruptly, but that accumulate fatigue damage over time. Material fatigue is caused by stresses on the structure and is directly related to the frequency and the amplitude of the vibrations. Therefore, accurately predicting the vibration frequency and amplitude of a structure due to vortex-induced vibrations is very important in defining the design criteria.

There are many long, slender structures in ocean engineering applications, which are exposed to a large number of natural frequencies and are frequently subject to vortex-induced vibrations. On the ocean surface, a floating structure such as an oil rig or ship can be connected to the ocean floor via long cylindrical structures in the form of drilling risers and mooring lines, as shown in Figure 2-2. Below sea level, sub-sea structures like pipes (e.g. in Figure 2-3), jumpers, and cables exist on the ocean floor to transport natural resources and transmit data across the ocean floor. These structures can be up to several miles long and are susceptible to vibrations caused by ocean currents. These structures in ocean engineering can be very costly to design, construction, install and maintain. Because these ocean engineering structures are typically built to last in excess of 20 years, the fatigue life of these structures are very important in defining the design criteria. Therefore, it is important to accurately estimate the fatigue damage due to VIV before installation.

Vibrations of these structures in the field can be very complicated because of the high number of natural modes and complex ocean currents. To better understand the vortex-induced vibrations of fluid flow around a long, slender body, it is desirable

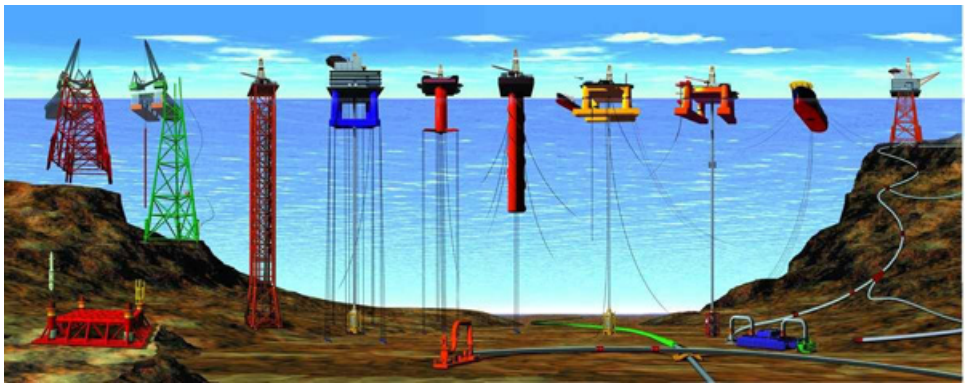

Figure 2-2: Types of offshore oil and gas structures by NOAA

Figure 2-3: Subsea Pipelines by EcoPrasinos

to simplify the problem with strip theory and analyze the flow over a small section of the body first [67]. This simplification allows the fluid mechanics to be analyzed as though the flow is nearly two-dimensional. By looking at only a small portion of a long cylinder, the cylinder appears to be as a flexibly mounted rigid cylinder and a complex current will appear as a free stream of fluid with constant velocity.

Figure 2-4 shows a flexibly mounted rigid cylinder in a free stream. The crossflow (lift) direction is defined as the direction perpendicular to the free stream direction and the inline (drag) direction is defined as the direction parallel to the free stream direction. Since one vortex sheds above the cylinder once per cycle and one vortex sheds below the cylinder once per cycle, the forcing frequency in the crossflow direction occurs at the frequency of vortex shedding. In the inline direction, the drag force associated with vortex shedding occurs at twice the frequency of vortex shedding because all vortices are shed downstream, the same side of the cylinder in the inline direction. Thus the force frequency in the inline direction is twice that of the crossflow

direction.

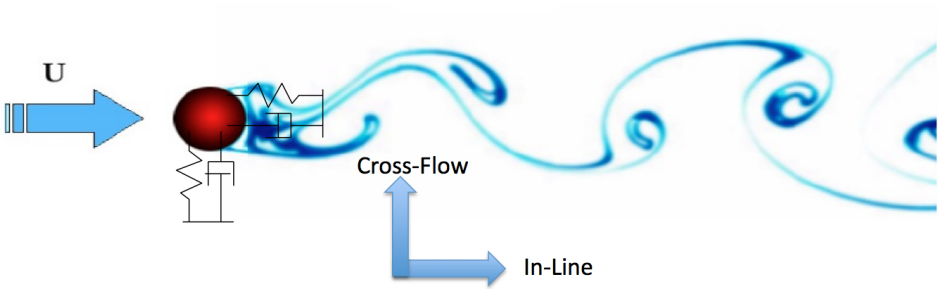

Figure 2-4: Altered picture from An Album of Fluid Motion [26].

When the vortex shedding frequency is near the natural frequency of the elastically mounted cylinder, the response motions resulting from these fluctuating forces cause relatively large cross-flow motion on the order of one cylinder diameter. On the other hand, the inline vibrations are not as large as cross-flow motions and are typically less than 0.3 diameters. For this reason, many studies have simplified the problem further by only considering cross-flow vibrations of the structure. However, it is shown that the inline motion has a major impact on fatigue life due to its higher frequency (second harmonic). More importantly, it triggers a third harmonic stress component in the crossflow direction along with a chaotic frequency stress component [20, 19]. Thus, the inline direction VIV is significant and both the inline and crossflow VIV should be modeled. In the rest of this chapter, the literature review on Vortex Induced Vibration in the crossflow direction, Vortex Induced Vibration in the inline direction, and coupled Vortex Induced Vibration in both crossflow direction and inline direction, are given.

2.2 Vortex Induced Vibration Prediction in Crossflow Direction

In the past 40 years, Vortex Induced Vibration in the crossflow direction has been extensively studied by both experimental model testing and numerical simulation. The reviews of [59], [5], [61], and [78] give comprehensive summaries of the major achievements in the field. In the following section, the prediction of Vortex Induced Vibration is emphasized.

Experimental studies have two major approaches: free vibrations and forced vibrations. In free vibration experiments, a rigid or flexible cylinder is allowed to oscillate purely due to fluid excitation and its motions are measured. In the forced vibration experiments, the cylinder′s motions are predefined and forced, with the resulting fluid forces being measured. Experimental studies of a cylinder oscillating in the crossflow direction show that the forcing function can be represented as a sinusoid of the same form as the cylinder motion ([59]). Thus, hydrodynamic coefficients derived through forced vibration experiments can be employed to predict the response from free vibrations, which is in the same situation of real engineering applications [58]. The results of this method is in agreement with free vibration measurements [30]. Several hydrodynamic coefficients databases of force coefficients derived through forced rigid cylinder vibration have since been reported. Among these, Gopalkrishnan [28] constructed a large database of lift and added mass coefficients to extend the motion predictions beyond just the elastically mounted rigid cylinder in uniform flow to flexible cylinder in a complex flow. The hydrodynamic coefficients databases of prevailing semi-empirical VIV prediction programs (VIVA [70], SHEAR7 [74], and VIVANA [37]) are still largely based on this study.

The semi-empirical VIV prediction programs typically consist of two parts: (1) a fluid-structure interaction model and (2) laboratory-derived or empirical databases. The fluid-structure interaction model consists of a fluid force model and the equations of structural dynamics. The hydrodynamic databases primarily contain hydrodynamic information in the form of the lift coefficient in phase with velocity and added

mass coefficient. It is a common practice [70, 74, 48] to use a strip theory approach to subdivide the riser into small segments, which act similar to a series of interconnected, elastically mounted rigid cylinders, and estimate the vortex-induced forces on each of these segments: the excitation force in phase with velocity and the excitation force in phase with acceleration. As shown by Triantafyllou [65], estimating these forces requires lift coefficient databases of added mass coefficient and lift coefficient in phase with velocity. From a structural dynamics viewpoint, a riser is adequately modeled as a tensioned beam with the appropriate boundary conditions and acted upon by the external hydrodynamic force.

Chaplin [14] compared laboratory measurements of vortex-induced vibrations of a tension riser to blind predictions of prevailing VIV prediction programs, both semi-empirical softwares and CFD codes. His results showed that the semi-empirical programs still have more accurate predictions compared to CFD results. Recently, Direct Numerical Simulation has had some success in predicting VIV motion and resolving wake behind the cylinder [33, 51, 24, 25, 8] but the Reynolds number is very low, generally in the 100-1000 range, due to its enormous computation cost.

Several flexible cylinder experiments have also been done in the lab and the field by academia and the offshore industry [41], including the Norwegian Deepwater Programme (NDP) 38 meter experiment [71] in Marintek′s Ocean Basin in Trondheim and Deepstar-MIT Gulf Stream tests on a 500-foot long and 1.43-inch diameter pipe in the Gulf of Mexico [76].

2.3 Vortex Induced Vibration Studies in Inline Direction

The inline motion of long flexible cylinders caused by VIV has been long neglected due to its small amplitude compared to the crossflow response amplitude. However, it is starting to draw more attention because research indicates that inline motion has a major impact on fatigue life due to its higher frequency [4] and its coupling to

the crossflow direction [19]. Dahl′s study shows the inline motion also triggers a third harmonic stress component in the crossflow direction [20]. Due to its high similarity to the crossflow VIV, the research methods used for studyling the traditional crossflow VIV are employed to explore the inline VIV.

Regarding the forced experiment to extract hydrodynamic coefficients, Aronsen studied pure inline rigid cylinder forced vibration experiments in his PhD thesis [1] and reported hydrodynamic coefficients at a Reynolds number, 24,000. Zheng [82] reported hydrodynamic coefficients from pure inline rigid cylinder forced vibration experiments at a lower Reynolds number, 7,600. Szwalek [63] studied the Reynolds number effects on hydrodynamic coefficients for inline vortex induced vibrations. She found within the Reynolds number range of 9,200 to 46,000, there is a dependence on Reynolds number for all four coefficients: lift force in phase with velocity, lift force in phase with acceleration, mean drag, and RMS coefficient of the hydrodynamic force.

In his rigid cylinder free vibration experimental study, King [36] reported two pure inline free vibration experiments at the Reynolds numbers 60,000 and 600,000 and discussed the influence of Reynolds number in these two particular setups. Recently, Cagney and Balabani [10] have described two pure inline free vibration experiments at the Reynolds number 450-3,700 and reported observing different wake patterns behind the inline vibrations.

Regarding flexible cylinder experiments, Lee reported pure inline experiments of different materials done in 2009 at the Shell Westhollow current tank [38]. He concluded that at low reduced velocities, the modal stiffness - among a number of structural or hydrodynamic parameters - is identified as the primary factor for a number of equal-diameter cylinders with different rigidities. If the other parameters are similar in quantity, the modal and physical displacements are inversely proportional to the modal stiffness.

Passano [55] described a series of flexible riser experiments including pure inline VIV response done in Marintek of different lengths. She also compared predictions from semi-empirical code VIVANA to the model test results.

2.4 Inline-Crossflow Vortex Induced Vibration Studies

Sarpkaya [60] carried out experiments on an elastically mounted rigid cylinder with freedom in both the inline and crossflow directions. He discussed the possible problems associated with having a cylinder with a natural frequency of inline motion twice that of the natural frequency in the crossflow direction. In his experiment, the inline mass of the system was not equal to the crossflow mass of the system and springs were used to tune the natural frequencies to the proper ratio. VIV of the structure occurred in both directions and results from experiments with inline-crossflow frequency ratios of 1 and 2 are reported. Sarpkaya [60] observed that the crossflow oscillation amplitudes were largely different from the free vibrations of a cylinder in crossflow only. While a natural frequency ratio of 1 resulted in much larger oscillation amplitudes, when the frequency ratio was increased to 2, the amplitude response displayed two peaks in crossflow amplitudes at different reduced velocities.

Jauvtis and Williamson [31, 32] developed a system with equal mass ratios and equal natural frequencies in both the inline and crossflow directions to study the vortex induced vibration of a cylinder rigid in two degrees of freedom motion. For high mass ratios in both the inline and crossflow directions, Jauvtis and Williamson [31] found that the crossflow motions of the cylinder were not largely different from the motions of a cylinder oscillating with cross-flow motion only. However, when the mass ratio was reduced to values comparable with ocean structures, Jauvtis and Williamson [32] observed very large amplitudes of crossflow cylinder oscillations, as large as 1.5 times the diameter of the cylinder. In addition, they [32] noted a significant third harmonic force component in lift that they attributed to a specific triplet vortex shedding mode in the wake of the cylinder.

Another recent study of free and forced vibrations in two degrees of freedom was performed by Aronsen [1]. Aronsen [1] found that the free vibration of a cylinder with freedom both in the inline and crossflow direction resembles motions observed for vibrating flexible cantilevered beams. Additionally, it is shown that using a strip

theory assumption, the two degree of freedom free vibration of a flexible riser may be predicted using coefficients obtained from forced oscillations of the cylinder. Aronsen′s experiment did not cover the whole range of two degree of freedom VIV parameters and limited results were reported at phase. The results reported in his thesis have a phase angle of either 0 or 180 degrees.

Dahl performed experiments on both free and forced vibration in two degree of freedom to construct a hydrodynamic database[19]. The natural frequency ratio of inline and crossflow in Dahl′s experiments varied from 1.23 to 1.9. The inline mass of the system was not equal to the crossflow mass of the system and springs were used to tune the natural frequencies to the proper ratio. He reported third harmonic forces increase almost linearly as a function of inline motion in the region that free vibrations may occur. He also showed that the wake of the cylinder is largely affected by the phasing between inline and crossflow motions of the cylinder. The resolution in Dahl′s experiment is relatively coarse, especially the phase between inline and crossflow motions.

Chapter 3

The Influence of High Harmonic and Chaotic Force Components on Fatigue Damage of Long Flexible Cylinders Due to Vortex-Induced Vibrations

Recent experimental data has revealed that the vortex-induced vibrations of long flexible cylinders are characterized by time intervals of chaotic response, followed by or preceded by periods of statistically stationary response. A chaotic response is characterized by a broad-band PSD, while the steady response can be classified as a periodic or quasi-periodic signal with possible large higher harmonic stress components. These phenomena are observed in both sheared and uniform current profiles. Regions of chaotic response and the steady regions with large higher harmonic stress components contain distinctly different response features and have significant implications for the fatigue analysis. To quantify the effect of the higher harmonic force components and chaotic oscillations on fatigue damage of long flexible structures, stress time series are generated such that the higher harmonics can be included or

removed, and using either a narrow-band or broad-band PSD. This approach enables conducting a systematic study on the influence of each of these phenomena on the resulting fatigue damage. It is shown that a dramatic increase in fatigue damage for signals containing higher harmonics. On the other hand, for stress signals with a significantly spread-out PSD and statistical non-stationarity, the damage to the riser is increased moderately, relative to the stress with a narrow-band PSD containing the same total power. In general, it is found that the increase in fatigue damage caused by a response with a widely-spread PSD plot is not as significant as that caused by the high harmonic components.

3.1 Introduction

For a long time, Vortex-Induced Vibrations (VIV) were considered only in the cross-flow direction (a direction perpendicular to the flow direction) and were treated as purely harmonic oscillations with only one major frequency close to the Strouhal frequency (a dimensionless representative of the frequency of vortex shedding). Recently, it has been shown [20, 85] that both for the rigid and flexible cylinders, the inline oscillations cause drastic changes in the wake and the resulting fluid forces, including a significant third, and in some cases 5th, harmonic component in the measured crossflow fluid force signals and even-harmonics in the inline force. The inclusion of these high harmonic components of stress in the fatigue analysis can increase the predicted damage by an order of magnitude [17, 56].

On the other hand, it is shown [45] that the observed cylinder response is characterized by time intervals of chaotic response, followed by or preceded by periodic response. Furthermore, the periodic motion consists of cases with purely first harmonic oscillations, as well as cases where higher harmonic components have strongly contribute. While in a traditional view of such experiments, the chaotic responses and the higher harmonic components of the periodic signals are normally ignored, it is observed that these components have a normallyn-negligible influence on the forces acting on the structure [46, 84]. We call the statistically stationary regions, mainly

periodic, or Type-I signals, and the regions with qualitatively chaotic characteristics (e.g., rather broad-banded PSD), Type-II signals. If a Type-II signal is approximated through an equivalent Type-I signal, fatigue calculations seriously underpredict the fatigue damage.

In this chapter, we will separately assess the impact of the higher harmonic components and the Type-II responses on the resulting fatigue damage of the flexible cylinders. In order to achieve this goal, we use statistical methods to generate stress time series based on the PSD plots similar to those of the experimental signals. Using this method, we can systematically alter the signal spectrum, from a purely first harmonic signal to a signal with sharp peaks at the higher harmonics and the main (first) harmonic, and also to a signal with increasing frequency spreading, toward a completely Type-II signal.

3.2 Experimental Data

We have used the Norwegian Deepwater Programme (NDP) Riser High Mode VIV tests [9] in order to come up with proper ranges of the various parameters used in our study. The riser properties for those tests are given in Table 3.1. The tests were conducted both for a uniform flow case and for a linearly sheared flow profile (zero flow velocity at one end, and a maximum flow at the other end). In these tests, the maximum flow velocities were varied from 0.3 m/s to 2.2 m/s, in increments of 0.1 m/s, and measurements of the crossflow and inline strain and acceleration were taken at various points.

The experimental VIV response can be quite complex. The scalogram of Figure 3-1 belongs to a case where a multiple-frequency response is observed. Besides the widespread frequency content at each instant of time, the frequency content also varies over time. Large third harmonic components with a rather broad frequency spectrum are observed too.

Figure 3-2 (left) shows a typical PSD plot of a signal from the NDP tests (shear bare 2360 crossflow sensor 4), where the signal consists of a first harmonic component

Table 3.1: Cylinder properties in the NDP data

Length between pinned ends	38 m
Outer Diameter	0.027 m
Wall Thickness	0.003 m
Young's Modulus	36.2 x 109 N/m^2
Mass per Unit Length (air filled)	0.761 kg/m
Mass per Unit Length (water filled)	0.933 kg/m
Weight in Water	2.79 N/m

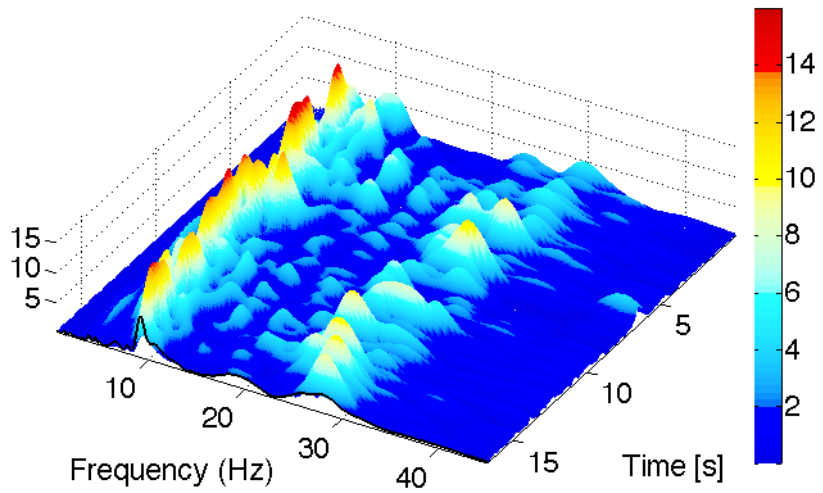

Figure 3-1: A sample scalogram of the NDP experimental data for a case with linearly sheared flow profile and with a maximum flow velocity of 0.8 m/s (case 2460).

at around 3.4 Hz (closest to the Strouhal frequency), with some higher harmonic components at around 10.2 Hz (third harmonic). Every peak is spread over a range of frequencies; e.g., the third harmonic component has its maximum amplitude at 10 Hz, and is spread over the range of frequencies from 9 Hz to 12 Hz. This is an example of a Type II signal. Figure 3-2 (right) shows another case (shear bare 2350 crossflow sensor 4) in which the frequency contents are single peaks located at the first and the third harmonic frequencies. This is an example of a Type-I signal.

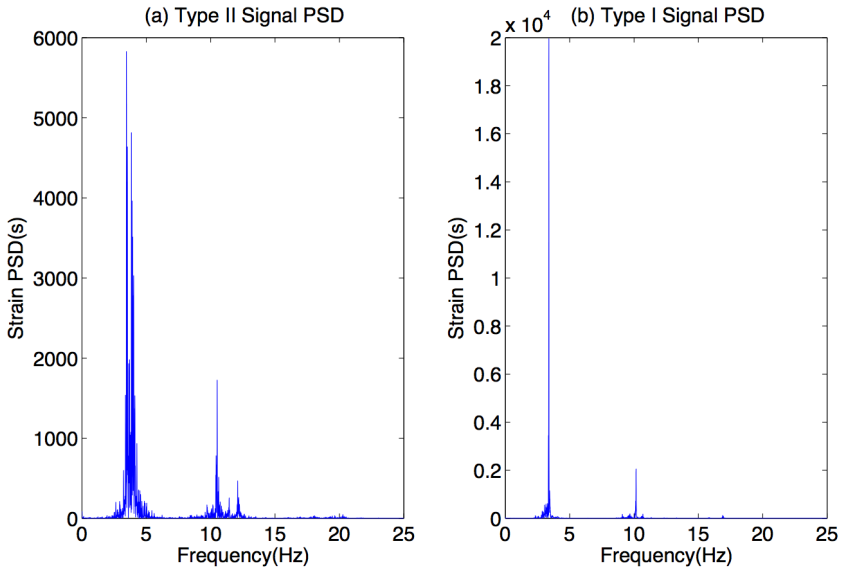

Figure 3-2: (left) A sample case of the PSD plot of a measured strain signal with spreading, and (right) A sample case of the PSD plot of a measured strain signal without spreading

Before conducting any stress-signal construction, we use the measured strain signals in order to calculate the relative power stored in each of the strain signal harmonics. Figure 3-3 shows the ratio of power stored in each harmonic component of the signal based on the average PSD plots, for the linearly sheared flow and uniform flow cases. Obviously at some measurement points, the higher harmonic components could be larger (before averaging) than what is shown in this figure. It is observed that for the sheared cases, on average around 20% of the total power belongs to the third harmonic component, while for the uniform flow cases, up to 40% of the power is due to the third harmonic component. This suggests that neglecting the third harmonic components will result in a major underestimation of the fatigue damage of these cases - in agreement with previous findings [44]. Also as summarized in Table 3.2, in the majority of the NDP experimental cases, Type-II signals (signals with some spreading around the main frequency peaks) are observed, as discussed in details previously [43].

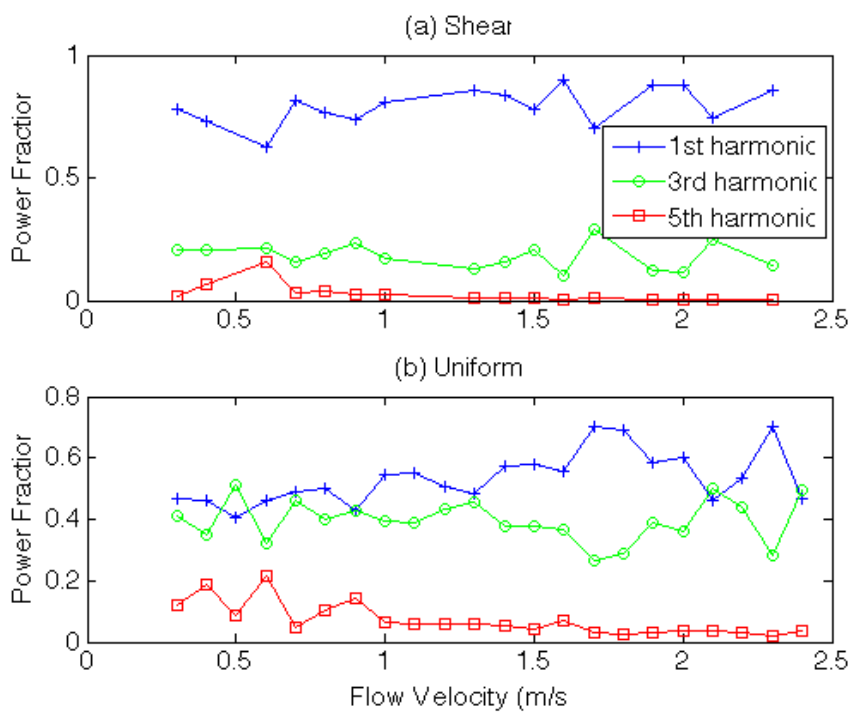

Figure 3-3: Relative power stored in each harmonic for (top) linearly sheared flow cases, and (bottom) uniform flow cases.

Table 3.2: Occurrence of Type II signals (spreading) in uniform and linearly sheared flow cases in the NDP data

Uniform Bare		Sheared Bare	
Case	Spreading	Case	Spreading
2010	N	2310	N
2020	Y	2320	Y
2030	N	2330	Y
2040	Y	2340	Y
2050	N	2350	N
2060	Y	2360	N
2070	Y	2370	Y
2080	Y	2380	Y
2090	Y	2390	Y
2100	Y	2400	Y
2110	Y	2410	Y
2120	Y	2420	Y
2130	Y	2430	Y
2141	Y	2440	Y
2150	Y	2450	Y
2160	Y	2460	Y
2170	Y	2470	N
2182	Y	2480	Y
2191	Y	2490	Y
2201	Y	2500	Y
2210	Y	2510	Y
2220	Y	2520	Y

3.3 The Methodology of Constructing Stress Time Series

In order to study the influence of the frequency content on the calculated fatigue damage, we need to be able to construct stress time histories based on a given PSD plot. For a PSD plot with only one frequency peak, f, the constructed stress signal is simply,

$$\sigma(t) = Asin(2\pi ft) \tag{3.1}$$

where f and A are the frequency and stress amplitudes, respectively, and the signals power, P, is

$$P = \frac{1}{2}A^2 = \int Sdf \tag{3.2}$$

where S is the magnitude of the PSD at the frequency f with a frequency increment of df.

Figure 3-4 shows a sample case. A PSD plot with a peak frequency at f = 1 Hz is considered as the starting point (Figure 3-4 a) and its corresponding time history is constructed (Figure 3-4 b). In this Type-I signal, the stress consists of only the first harmonic components, and that the total power (PT) of the signal is lumped at only one point (f). This means that we ignore the higher harmonic components, as well as the frequency spreading of the first harmonic.

For the next step, we assume that the higher harmonic components do exist, but the total power of each harmonic is lumped at one point. This means that we ignore the frequency spreading in all harmonics. For a PSD plot with two lumped peaks at the first and the third harmonics only, the constructed stress signal is,

$$\sigma(t) = A_1 sin(2\pi ft) + A_3 sin(6\pi ft + \phi) \tag{3.3}$$

where f is the first harmonic frequency, $A1$ and $A3$ are stress amplitudes of the first and the third harmonics, respectively, and ϕ is the phase difference between the third and the first harmonic components. The total power in this signal, PT, is distributed between the first and the third harmonic powers: $P_T = P_1 + P_3$.

Figure 3-5 shows a sample PSD plot with two peaks at the first and the third harmonics, with its corresponding time history. This signal is also Type-I, and its

total power is equal to the total power of the signal with only the first harmonic in Figure 3-4. Comparing the fatigue life of the signals of Figure 3-4 and Figure 3-5 will shed light on the influence of the third harmonic component as discussed in chapter 3.4.

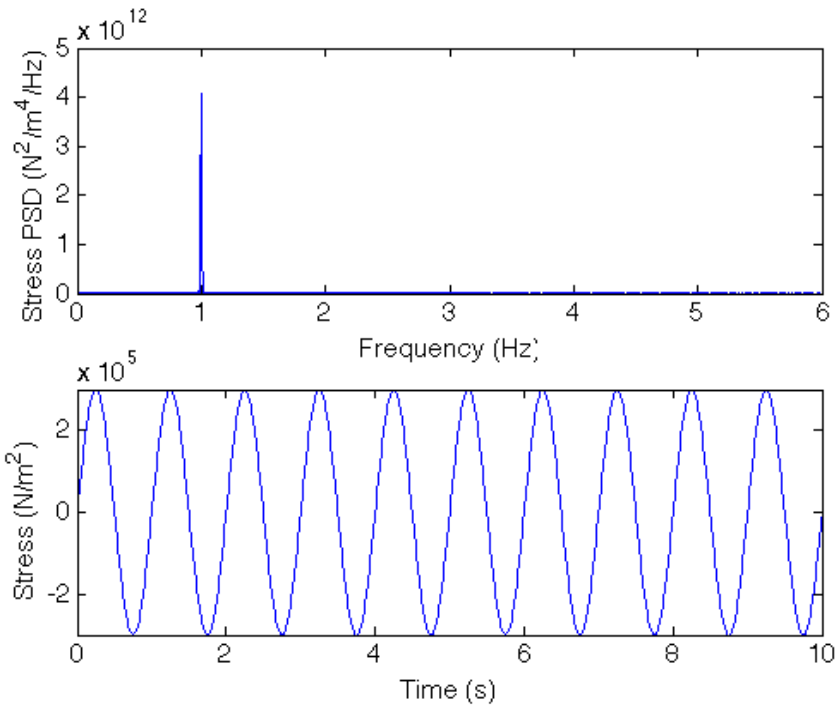

Figure 3-4: The PSD (top) and time series (bottom) of signal with energy lumped at the first harmonic

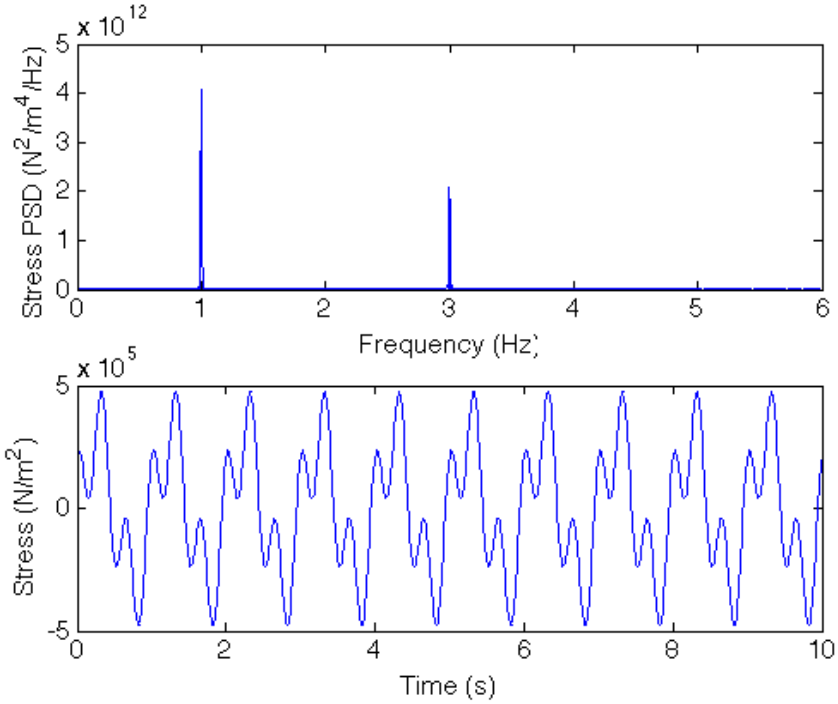

Figure 3-5: The PSD (top) and time series (bottom) of signal with energy lumped at the first and third harmonics

Then, we assume that in the stress signal, the higher harmonic components do exist and that the power for each harmonic is spread in a manner similar to that of the experimental data (Type-II Signals). In order to construct signals with a wide spectrum PSD, we assume that the signal has its first harmonic at f_1 and its third harmonic at f_3. However, the frequency content in each of these harmonics is spread over a range, instead of being lumped at f_1 and f_3 only. This means that there are several frequency peaks around the mean frequency of each harmonic:

$$\sigma(t) = \sum_{i=1}^{N} A_i sin(2\pi f_i t + \phi_i) + \sum_{j=1}^{N} A_j sin(2\pi f_j t + \phi_j) \tag{3.4}$$

where, f_i and f_j are the frequencies around the first and the third harmonics, respectively; i and j are randomly-generated phase differences between frequency peaks around the first and the third harmonic components, respectively; N is the number of peak frequencies around each harmonic; A_i and A_j are stress spectral amplitudes around the first and the third harmonics, respectively; and

$$A_i = \sqrt{\frac{S_i df}{2\pi}}, A_j = \sqrt{\frac{S_j df}{2\pi}} \tag{3.5}$$

in which S_i is the value of the PSD at frequency f_i separated from f_{i+1} by a space of df. The modal frequencies are randomly selected within narrow bands of width df, to avoid periodicity of the signal.

We define the range of frequency contents spreading around the peak harmonic as spread width, which consists of the contents on the left of the peak harmonic with a width and the contents on the right of the peak harmonic with a width.

$$S_{width} = W_{right} + W_{left} \tag{3.6}$$

Furthermore, we define the ratio of the right width and the left width as the asym-

metry of the spread.

$$S_{asymmetry} = W_{right}/W_{left} = N_{right}/N_{left} = P_{right}/P_{left} \tag{3.7}$$

We first assume that the spectral peak frequencies follow a uniform distribution

$$f_i \sim U(f_1 - W_{left}, f_1 + W_{right}), f_j \sim U(f_3 - W_{left}, f_3 + W_{right}), \tag{3.8}$$

and the phases follow a uniform distribution:

$$\phi_i \sim U(0, 2\pi), \phi_j \sim U(0, 2\pi) \tag{3.9}$$

To simulate the spread shape from experimental data, we assume that the spectral peak amplitudes decrease as its distance to the peak harmonic increases:

$$\begin{aligned} A_{i_left} \sim linspace(0, c_1, N_{left}), A_{j_left} \sim linspace(0, c_2, N_{left}) \\ A_{i_right} \sim linspace(c_1, 0, N_{right}), A_{j_right} \sim linspace(c_2, 0, N_{right}) \end{aligned} \tag{3.10}$$

where A_1 and A_3 are the peak amplitudes of the first and third harmonics of the equivalent Type-I signal, and c_1 and c_2 are constants that control the power of the signal. The total energy associated with each harmonic is kept constant:

$$\begin{aligned} \sum_{i=1}^{N} A_i^2 = A_1^2 = C_1 \\ \sum_{j=1}^{N} A_j^2 = A_3^2 = C_3 \end{aligned} \tag{3.11}$$

At last, we assume that the spectral peak frequencies follow a normal distribution:

and

$$
\begin{aligned}
f_{i_left} \sim N(f_1, (\frac{W_{left}}{2})^2), f_{j_left} \sim N(f_3, (\frac{W_{left}}{2})^2) \\
f_{i_right} \sim N(f_1, (\frac{W_{right}}{2})^2), f_{j_right} \sim N(f_3, (\frac{W_{right}}{2})^2) \\
f_{i_left}, f_{i_right}, f_{j_left}, f_{j_right} > 0
\end{aligned}
\tag{3.12}
$$

The spectral peak amplitudes still decrease as its distance to the peak harmonic increases, but follows normal distributions and $A_i, A_j > 0$

$$
\begin{aligned}
A_i \sim N(\frac{A_1(1 - \left|\frac{f_i - f_1}{W_{right/left}}\right|)}{2c}, (\frac{A_1(1 - \left|\frac{f_i - f_1}{W_{right/left}}\right|)}{8c})^2) \\
A_j \sim N(\frac{A_3(1 - \left|\frac{f_j - f_3}{W_{right/left}}\right|)}{2c}, (\frac{A_3(1 - \left|\frac{f_j - f_3}{W_{right/left}}\right|)}{8c})^2) \\
f_i, f_j > 0
\end{aligned}
\tag{3.13}
$$

and the phases follow a uniform distribution:

$$
\phi_i \sim U(0, 2\pi), \phi_j \sim U(0, 2\pi), \tag{3.14}
$$

After generating the amplitudes and frequencies following these assumptions, the negative amplitudes and frequencies are removed to obtain physically meaningful signals. Figure 3-6 shows a sample for these randomly-generated amplitudes and frequencies. Figure 3-7 shows that the amplitude and frequency still have a normal distribution even after removing their negative values. The top of Figure 3-8 shows a sample Type-II PSD plot that is used to generate the corresponding Type-II stress signal at the bottom of Figure 3-8, following the method discussed here.

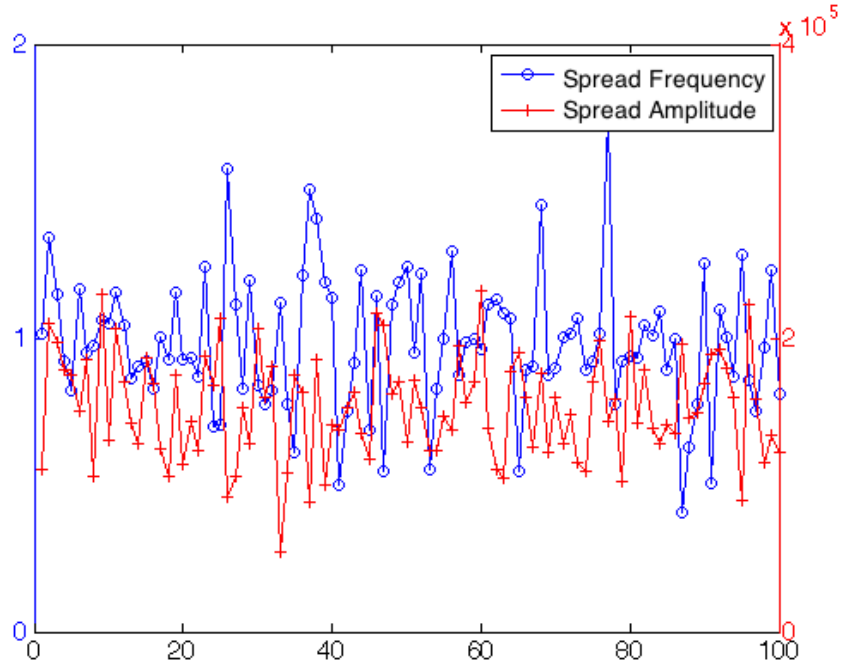

Figure 3-6: Generated frequencies and amplitudes

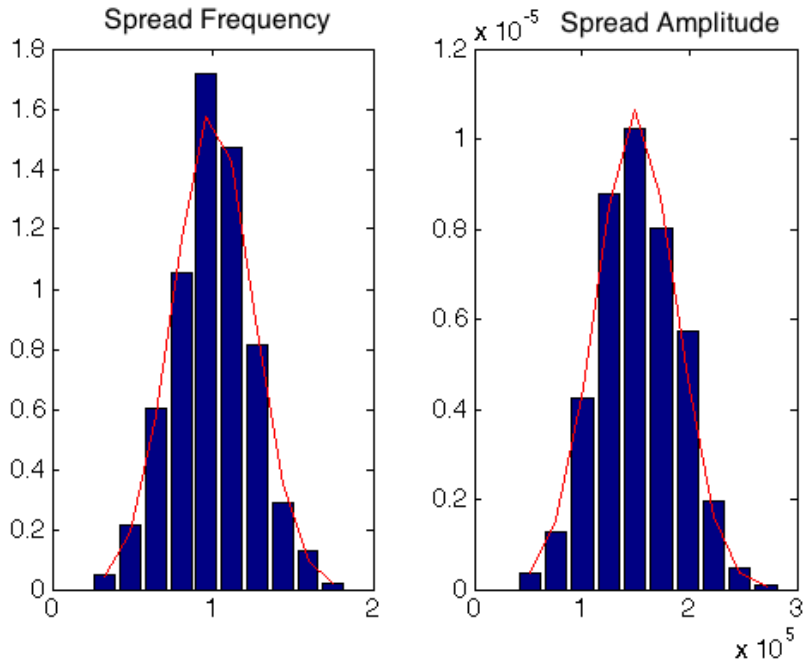

Figure 3-7: Distribution of generated amplitudes and frequencies

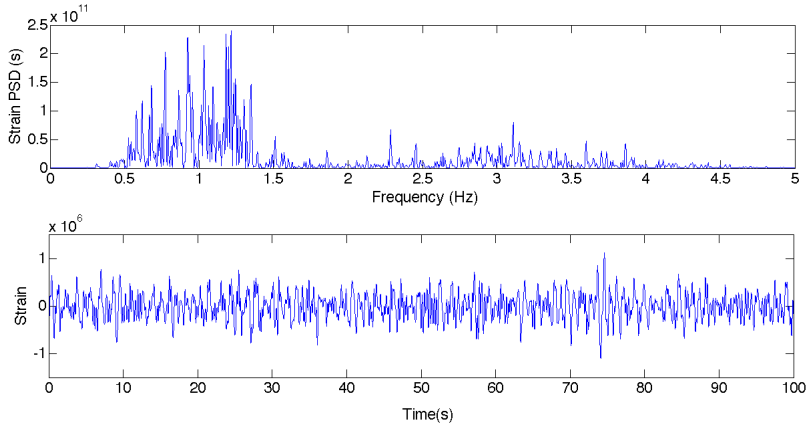

Figure 3-8: The power spectral density (top) and time serials (bottom) of generated type II signal

Besides a wide spectrum PSD, the Type-II experimental VIV signals have frequency contents that vary with time. This is well observed in the scalogram of Figure 3-1, a sample of the NDP tests. In order to construct a signal which follows the same trend, we construct several segments of the signal using Equation (4). Each segment has a different spectral peak amplitude, spectral peak frequency, and phase. Figure 3-9 shows ten signal segments generated using this method. While the PSDs of the ten signal segments follow the same distribution, they are random in nature, and therefore each segment has a different PSD plot. The segments are connected to each other to form a long time history without losing continuity, following the method discussed by [42]. The resulting time history and its corresponding scalogram are shown in Figure 3-10 and Figure 3-11.

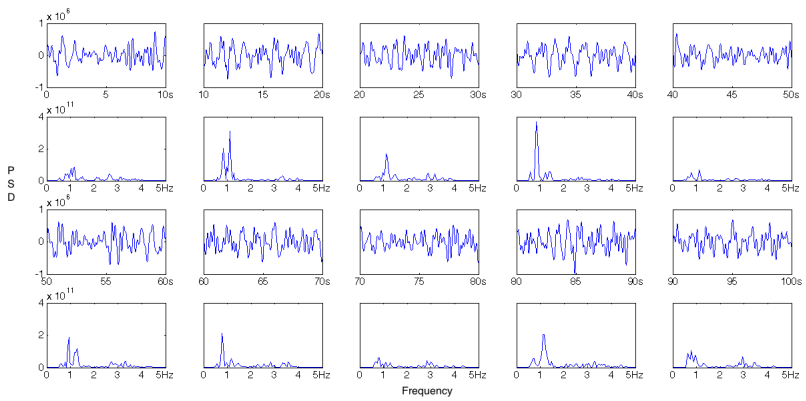

Figure 3-9: The time serials (first and third rows) and power spectral density (second and fourth rows) of ten generated non-stationary segments

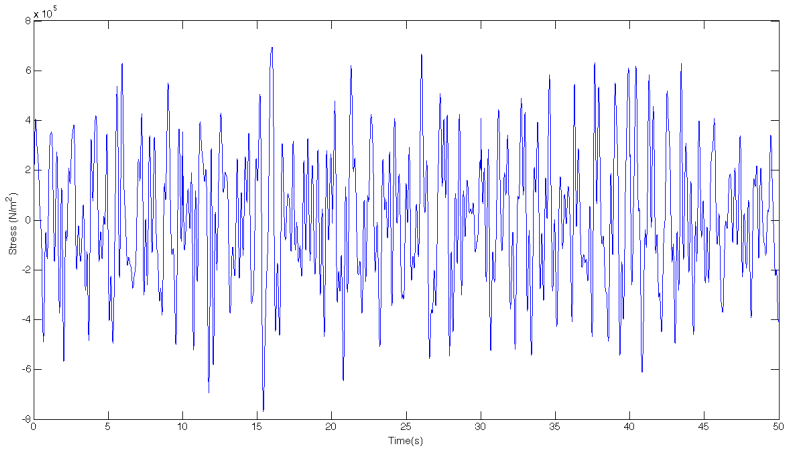

Figure 3-10: Time serials of the generated Type II signal

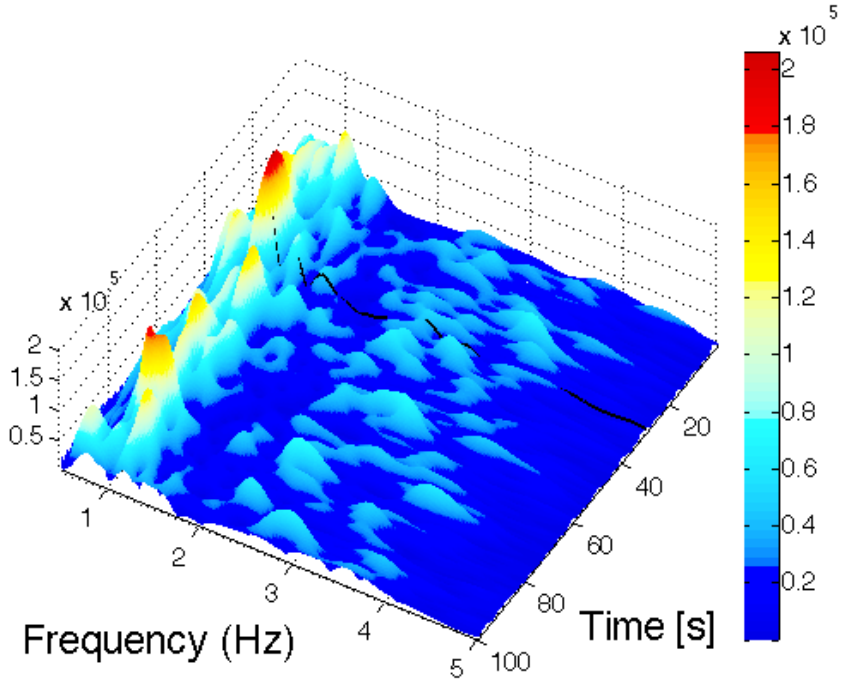

Figure 3-11: Scalogram of the generated Type II signal

3.4 The Influence of High Harmonic Components on Fatigue Damage of Type-I Signals

In this section, signals with the first and the third harmonic components will be constructed. The frequencies will be lumped at the two harmonics so as to focus on the power distribution between the first and the third harmonic, with no influence from the Type-II signals. For all the cases in this section, the total power of the signal is kept constant, and only the distribution between the first and the third harmonics is altered.

We first construct the stress time series with all the power lumped at the first harmonic (f_1). This means that we ignore the higher harmonic components, as well as the frequency spreading of the first harmonic. The PSD plot and its corresponding time history will be similar to what is shown Figure 3-4. The total power in this signal is assumed to be PT. Then, we assume that the higher harmonic components do exist, and we transfer a portion of the total power from the first harmonic to the third harmonic, while keeping the total power constant: $P_T = P_1 + P_3$, where P_1 and P_3 are the powers associated with the first and the third components, respectively. The third harmonic component will be lumped at the frequency of $f_3 = 3f_1$. This means we ignore the frequency spreading in all harmonics. The PSD plot and its corresponding time history are shown in Figure 3-5 for a case where $P_3/P_1 = 2$.

The reconstructed signals will be used to calculate the structures fatigue life using the rainflow method [18]. The $S - N$ curve used here is

$$S = e^{\frac{log(a) - log(N)}{m}} \tag{3.15}$$

where N is the number of cycles to failure, S is the stress range (in MPa), and m is the inverse slope of the $S - N$ curve. Here we have used $log(a) = 11.63, m = 3.0$ [71].

Figure 3-12 shows the influence of power distribution between the first and the

third harmonic as well as the phasing between them on the resulting fatigue life. The signals total power is kept constant. The fatigue life is normalized by the fatigue life of a case with a first harmonic component only. Overall, larger higher harmonic components result in a larger fatigue damage. In fact, by transferring more power from the first harmonic to the third harmonic (with a constant phase between the third and the first components), fatigue life decreases due to a higher frequency of the stress signal relative to the first harmonic. This is shown in a slice of Figure 3-12, shown in Figure 3-13 for a phase difference of 180. The phasing between the first and the third harmonic stress also influences the resulting fatigue life. For a constant higher harmonic component, the minimum life occurs for a phase difference of 180. A slice of Figure 3-12 for a constant higher harmonic component ratio of $P_3/P_1 = 1/2$ in Figure 3-14 shows that the fatigue life can vary greatly with the phasing.

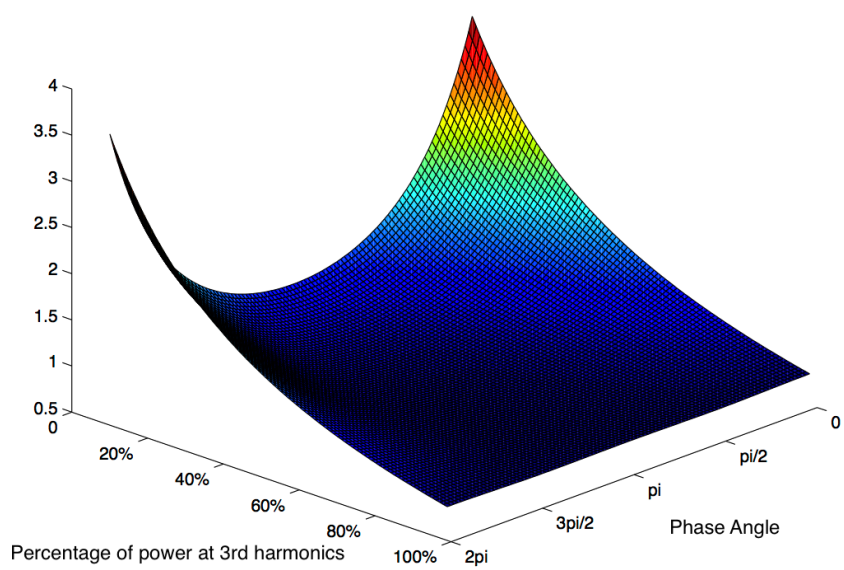

Figure 3-12: The influence of energy distribution and phase angle between the first and the third harmonic on fatigue life (years).

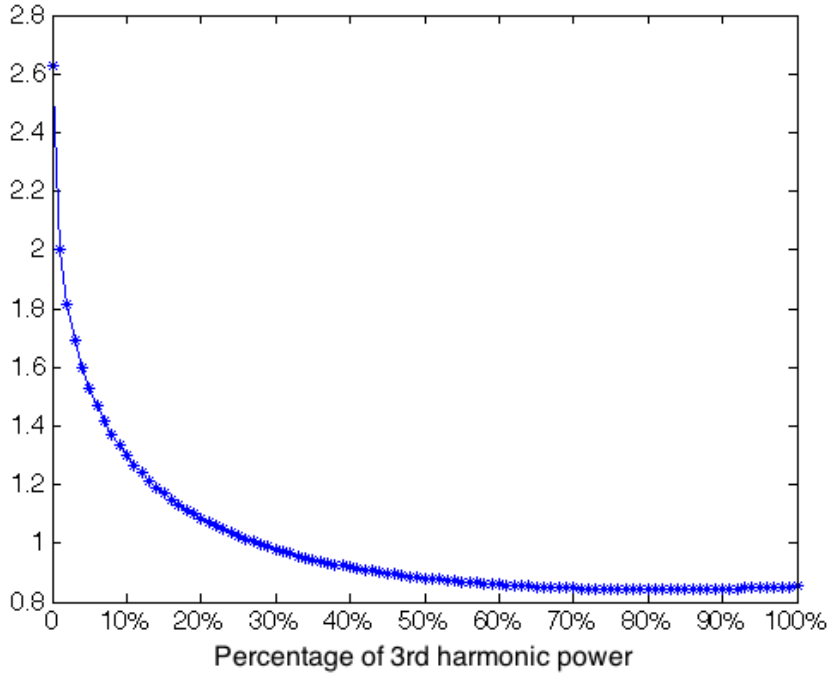

Figure 3-13: Slices of Figure 3-12 for a constant phase difference of 180

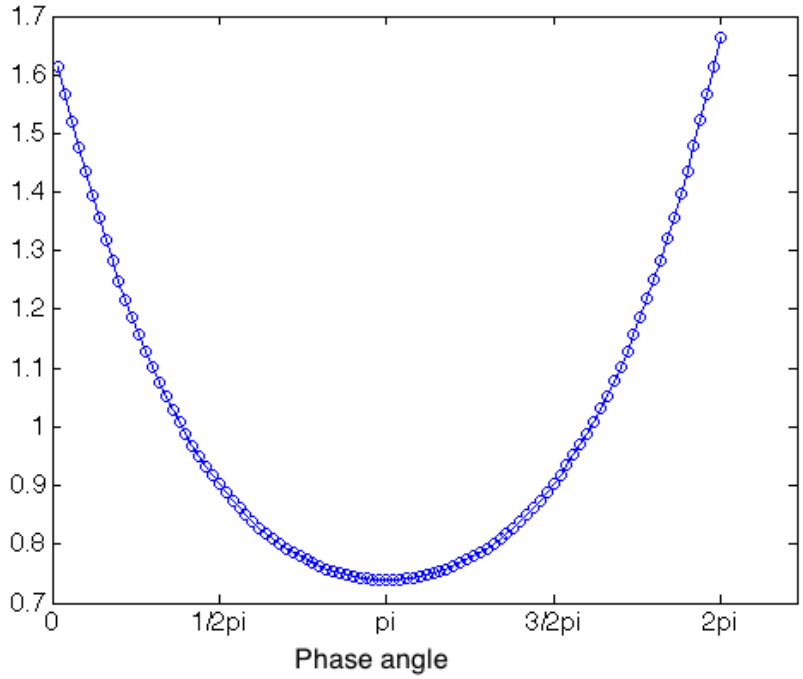

Figure 3-14: Slices of Figure 3-12 for a constant third harmonic contribution of 33.3 %, i.e., $P_3/P_1 = 1/2$

3.5 The Influence of Spreading and Time-varying Frequency Content on Fatigue Life of Type-II Signals

In the previous section, we showed that the higher harmonic stress components could decrease the fatigue life of a flexible cylinder undergoing VIV. In this section we consider Type-II signals and quantify the influence of frequency spreading on the cylinders fatigue life. More specifically, the spreading width and the spreading symmetry of the frequency content will be studied. In general, we assume that in the stress signal both the first and the third harmonic components exist. We then assume that the power for each harmonic is spread over a range of frequencies around each harmonic, instead of being lumped at one single frequency. For all these cases, the total power in the signal is kept constant.

3.5.1 The Influence of Spreading Width

Signals with small spreading width tend to have a distinct peak near the mean, as opposed to the signals with large spreading width. Figure 3-15 shows the PSD plot of a signal with only the first harmonic component. The influence of the spreading width on the resulting fatigue life is shown in the plot of Figure 3-17. In this plot, the vertical axis is the ratio of the fatigue life of the signals with spreading normalized by the fatigue life of a signal with no spreading (where only one frequency peak that exists in the PSD). The total power is kept constant for all signals. For all the cases with some spreading, the fatigue life ratio deceases to around 80%, contrary to Wirsching's remark that type-I signal assumption produces conservative results [80, 79] . It seems that the width of the spreading does not affect the results dramatically and it is just the existence of the spreading that reduces the fatigue life.

Figure 3-16 shows another PSD plot, where both the first and the third harmonics exist in the signal. Figure 3-18 shows the ratio of the fatigue life for the signals corresponding to these PSD plots with various spreading width, normalized by the

equivalent Type-I signal (a signal with a PSD where the peaks are lumped only at the first and the third harmonics). The spreading decreases the fatigue life ratio to 90%, but similarly to the previous case, its width does not affect the results dramatically.

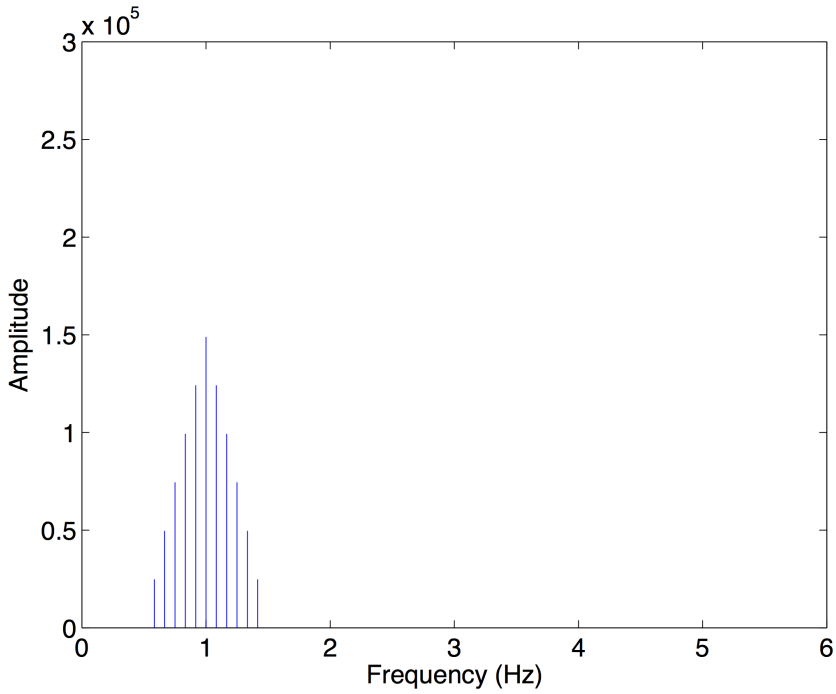

Figure 3-15: Deterministic PSD shape: signals with first harmonic only. The x-axis is the multiplier of original peak first harmonic frequency (1Hz in this case).

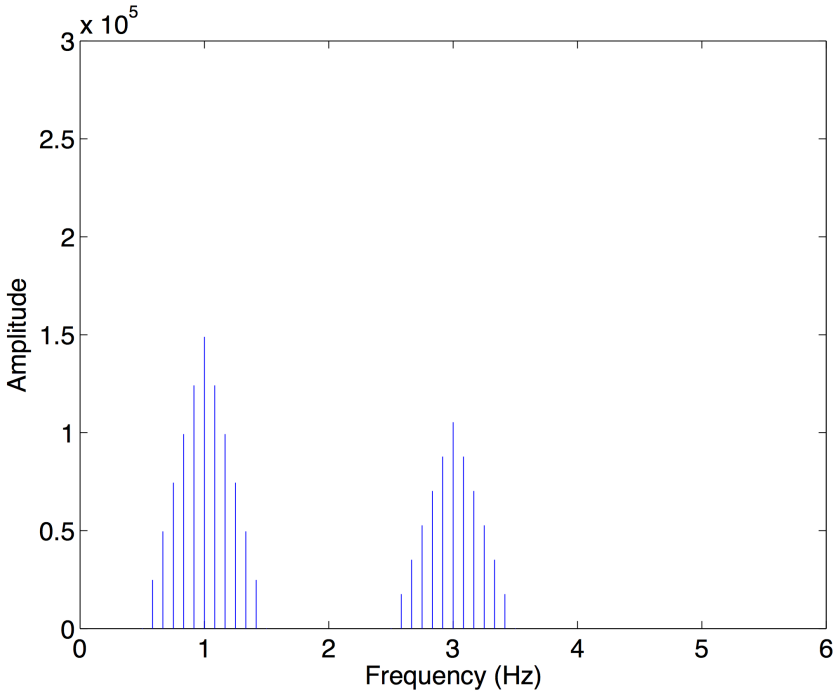

Figure 3-16: Deterministic PSD shape: signals with first and third harmonics. The x-axis is the multiplier of original peak first harmonic frequency (1Hz in this case).

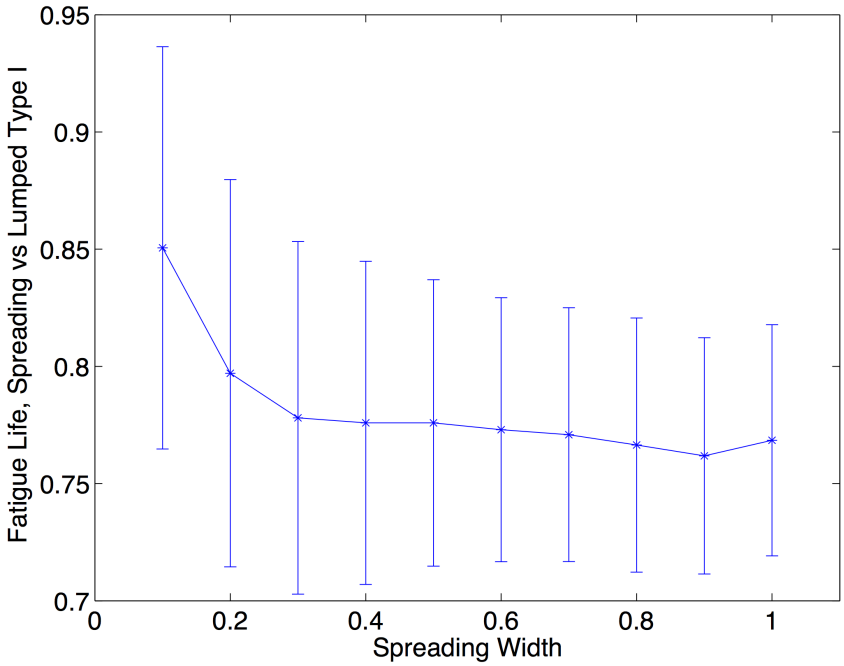

Figure 3-17: The influence of spread width on fatigue life of broadband stationary signal with deterministic PSD shape: signals with first harmonic only. The fatigue life is normalized by the fatigue life of Type I signal with only the first harmonics.

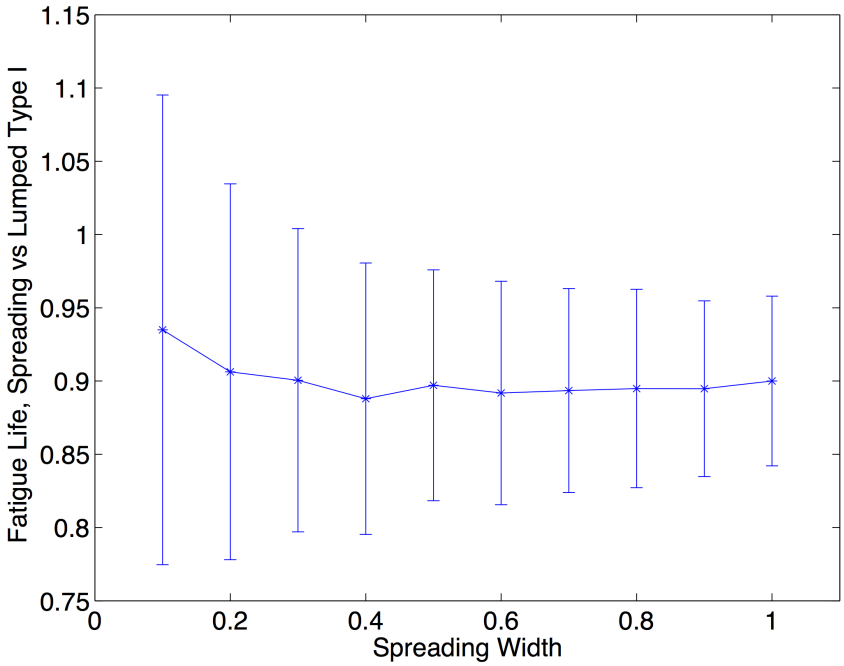

Figure 3-18: The influence of spread width on fatigue life of broadband stationary signal with deterministic PSD shape: signals with first and third harmonics. The fatigue life is normalized by the fatigue life of Type I signal with both the first and third harmonics.

We further evaluate the influence of spreading width on fatigue life when the signal′s PSD is not as deterministic, following the methodology in equations 9 to 11 of chapter 3, as that shown in Figure 3-15 and Figure 3-16. The PSD shapes of various width are plotted in Figure 3-19, and the frequency and magnitude of the peaks around each harmonic are randomly generated, following the methodology in equations 12 to 14 of chapter 3. Figure 3-20 and Figure 3-21 show a decrease of fatigue life to 80% and 90% respectively for the cases with only the first harmonic contribution and both the first and third harmonic contribution. Thus, the spread width does not affect the results dramatically as well.

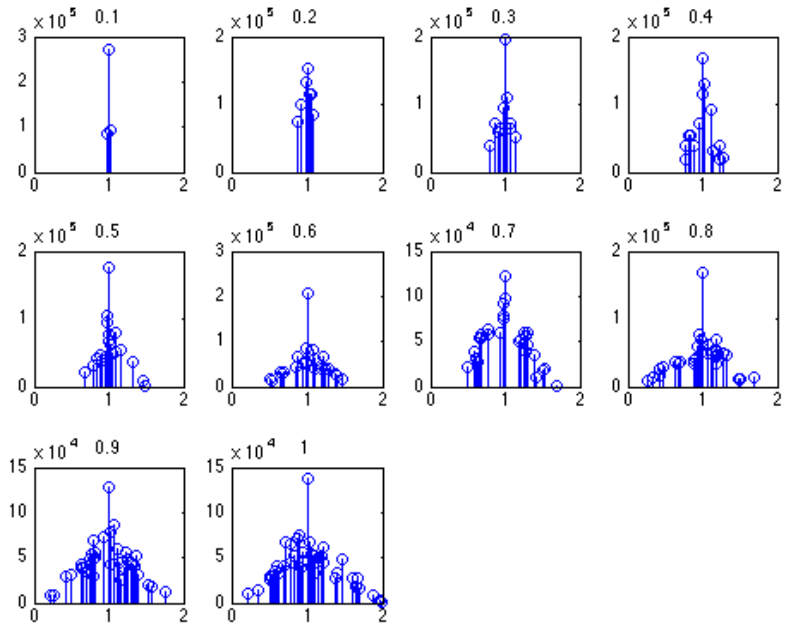

Figure 3-19: Random Frequency/Amplitude PSD shape with different width (0.1 to 1 Hz as indicated in the titles)

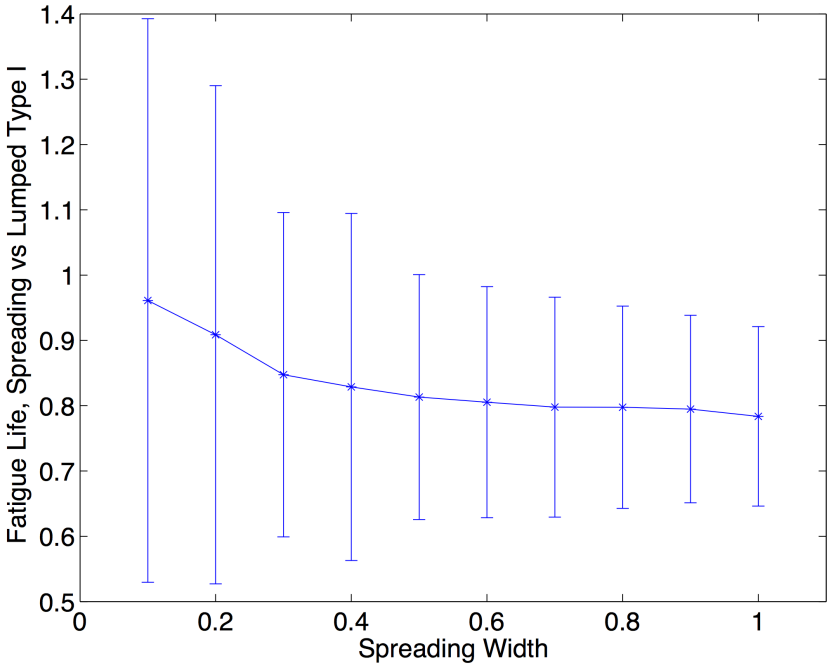

Figure 3-20: The influence of spread width on fatigue life of broadband stationary signal with random PSD shape: first harmonic only. The x-axis is the multiplier of original harmonic spread. The fatigue life is normalized by the fatigue life of Type I signal with only the first harmonics.

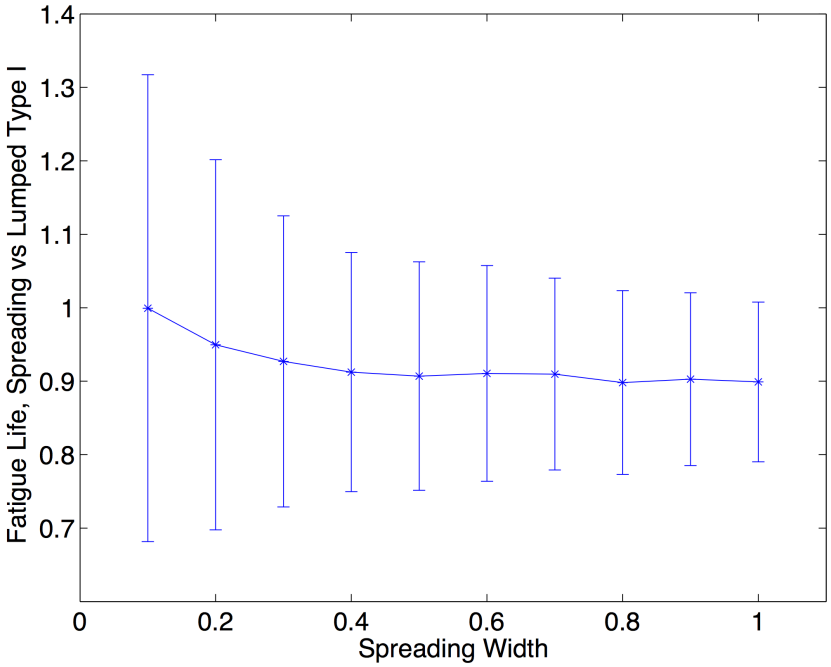

Figure 3-21: The influence of spread width on fatigue life of broadband stationary signal with random PSD shape: first and third harmonics . The x-axis is the multiplier of original harmonic spread. The fatigue life is normalized by the fatigue life of Type I signal with both the first and third harmonics

3.5.2 The Influence of Spreading Symmetry

The symmetry of a PSD plot can be broken by having a larger frequency content on either side of the center point of each harmonic. A right spreading corresponds to a signal with more frequency content on the right-hand side of the center point (higher frequencies), and a left spreading corresponds to more frequency content on the left-hand side of the center point.

Figure 3-22 shows the PSD plot of a signal with only the first harmonic component and a left asymmetric spreading. Figure 3-24 shows the ratio of the fatigue life of such signals, normalized by the fatigue life of a signal with only a single peak at the first harmonic, versus the degree of asymmetry (the ratio of the right spreading width to the left spreading width). When the ratio is 1, the spreading is perfectly symmetric. It is seen that the fatigue life ratio decreases as the spreading becomes more asymmetric towards the right, including higher frequency content. Fatigue life decreases by more than 20%, compared with a perfectly symmetric case, when a right spreading exists. It increases by up to 20%, when left spreading exists.

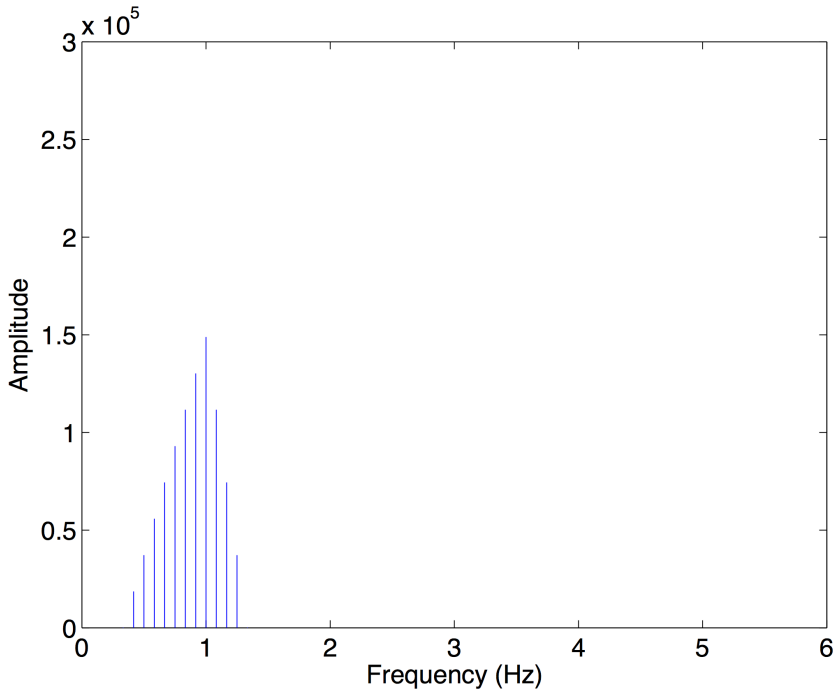

Figure 3-22: Deterministic PSD shape: signals with first harmonic only. The x-axis indicates the degree of asymmetry (spread width ratio of right part of spread vs left part).

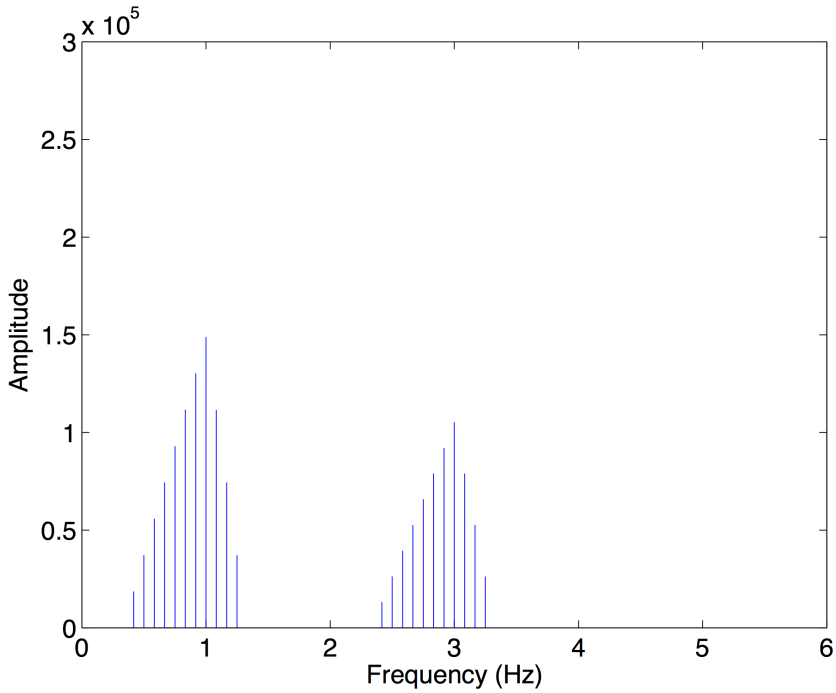

Figure 3-23: Deterministic PSD shape: signals with first and third harmonics. The x-axis indicates the degree of asymmetry (spread width ratio of right part of spread vs left part).

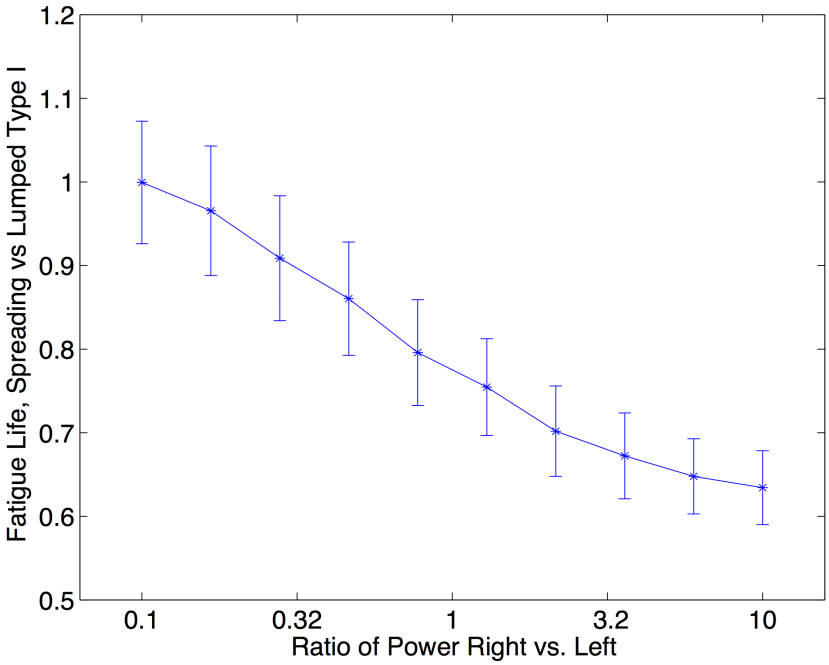

Figure 3-24: The influence of asymmetry of spread distribution on fatigue life of broadband stationary signal with deterministic PSD shape: signals with first harmonic only. The x-axis indicates the degree of asymmetry (spread width ratio of right part of spread vs left part). The fatigue life is normalized by the fatigue life of Type I signal with only the first harmonics.

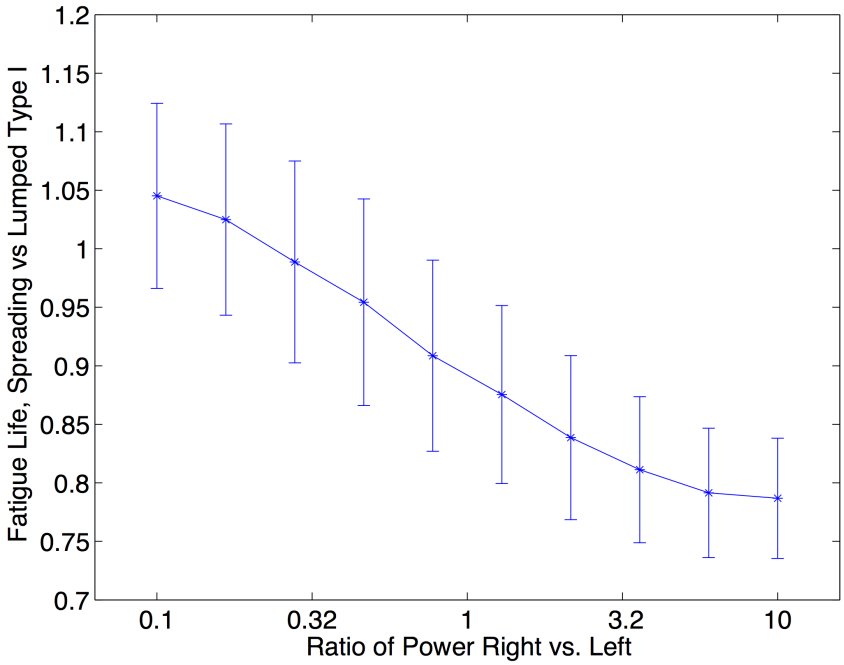

Figure 3-25: The influence of asymmetry of spread distribution on fatigue life of broadband stationary signal with deterministic PSD shape: signals with first and third harmonics. The x-axis indicates the degree of asymmetry (spread width ratio of right part of spread vs left part). The fatigue life is normalized by the fatigue life of Type I signal with both the first and third harmonics.

Figure 3-23 shows a PSD with both the first and the third harmonics, with asymmetric spreading. The ratio of the fatigue life for these signals, normalized by the fatigue life of a Type-I signal with both the first and the third harmonics, versus the spreading ratio (the ratio of the right spreading to the left spreading) is plotted in Figure 3-25. Fatigue life decreases to 90% of the symmetrical signal in these cases.

We further evaluate the influence of spreading symmetry on fatigue life when the PSD shape of the signal is not as deterministic, following the methodology in equations 9 to 11 of chapter 3.3, as Figure 3-22 and Figure 3-23, but are generated using the methodology in equations 12 to 14 of chapter 3.3. The PSD shapes of various asymmetry (spread width ratio of the right part of the spread versus the left part from 0.1 to 10) are plotted in Figure 3-26. The results in Figure 3-27 and Figure 3-28 show the trend of decreasing fatigue life for both the first harmonics only and the first harmonics plus the third harmonics cases, although the increased randomness enlarged the standard deviation (error bar in the figure).

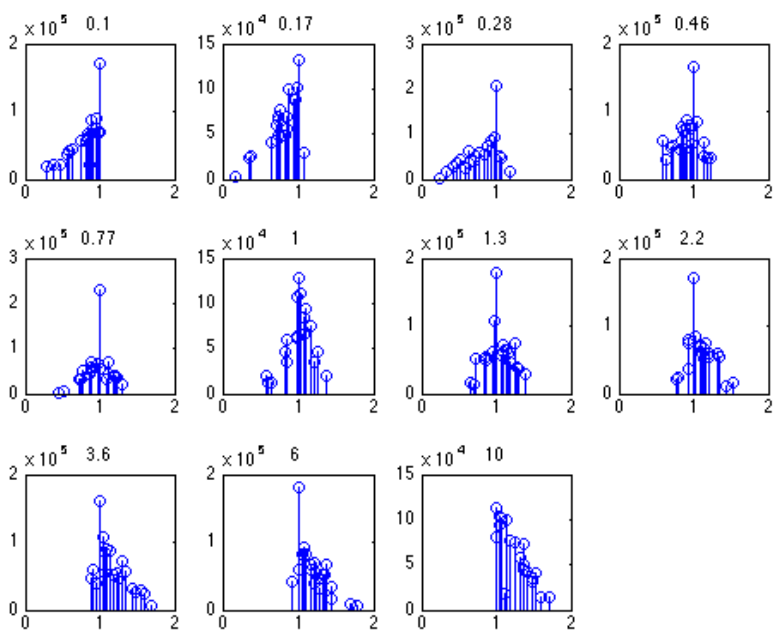

Figure 3-26: Random Frequency/Amplitude PSD shape with different asymmetry (spread width ratio of right part of spread vs left part from 0.1 to 10, as indicated in the titles)

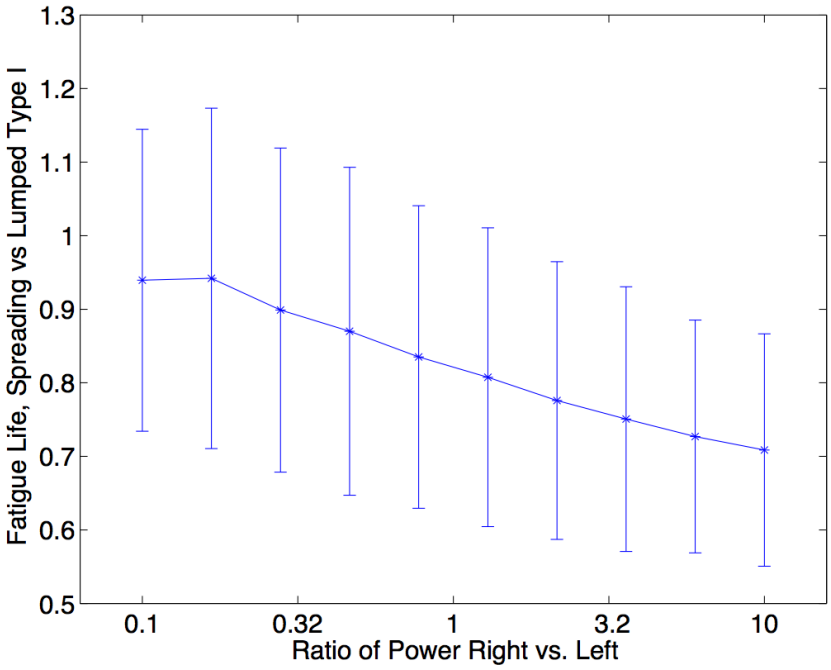

Figure 3-27: The influence of symmetry of spread distribution on fatigue life of broadband stationary signal with random PSD: first harmonic only. The x-axis indicates the degree of asymmetry (spread width ratio of right part of spread vs left part). The fatigue life is normalized by the fatigue life of Type I signal with only the first harmonics.

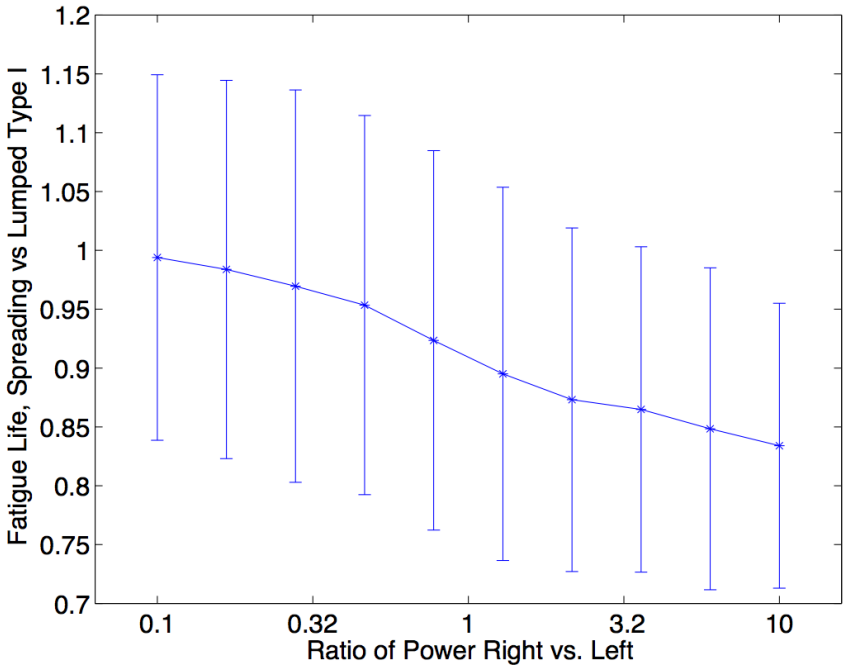

Figure 3-28: The influence of symmetry of spread distribution on fatigue life of broadband stationary signal with random PSD: first and third harmonics. The x-axis indicates the degree of asymmetry (spread width ratio of right part of spread vs left part). The fatigue life is normalized by the fatigue life of Type I signal with both the first and third harmonics.

3.5.3 The Influence of Non-Stationarity

As discussed in the last paragraph of chapter 3.3 and shown in Figure 3-1, the frequency content of the experimental VIV signals varies with time. In order to investigate the influence of the time-dependence frequency contents on the resulting fatigue life, we construct time histories, which follow this trend, as discussed in chapter 3.3. We generate 10 Type-II signals as segments of the main signal and then connect them smoothly to construct a non-stationary signal. We repeated the process 1000 times using random phase following a uniform distribution. We studied the influence of spreading width and asymmetry following the same methodology in chapter 3.5.1 and 3.5.2.

The influence of the spreading width on the resulting fatigue life is shown in the plot of Figure 3-29, first harmonic only, and 3-30, first and third harmonics. In these plots, the vertical axis is the ratio of the fatigue life of the signals with spreading normalized by the fatigue life of a signal with no spreading (where there is only one frequency peak in the PSD). The total power is kept constant for all signals. For all the cases with some spreading, the fatigue life ratio deceases to around 80%. It seems that the width of the spreading does not affect the results dramatically and it is just the existence of the spreading that reduces the fatigue life. Similar to the previous case, the spreading decreases the fatigue life ratio to 90%, but its width does not affect the results dramatically.

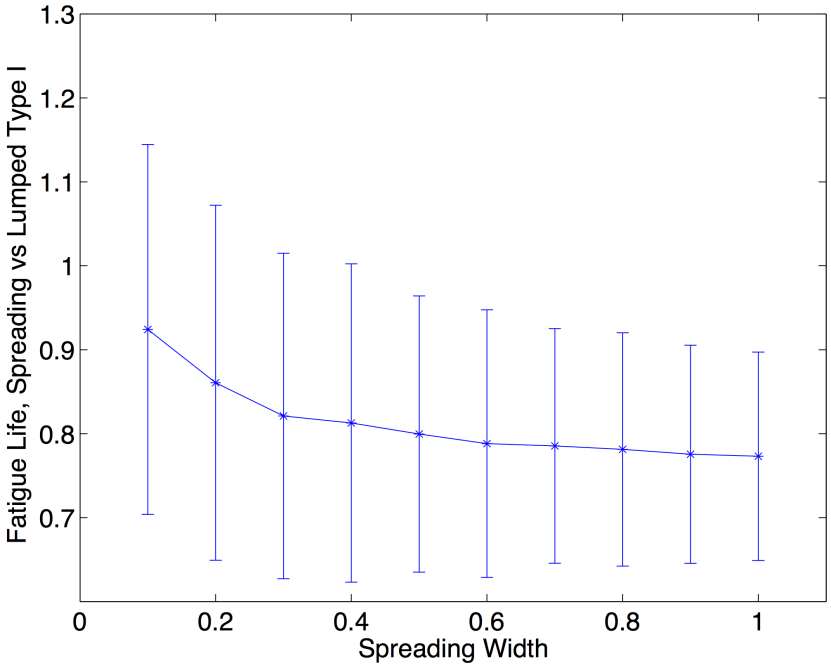

Figure 3-29: The influence of spread width on fatigue life of non-stationary signal with random PSD shape: first harmonic only. The x-axis is the multiplier of original harmonic spread. The fatigue life is normalized by the fatigue life of Type I signal with only the first harmonics.

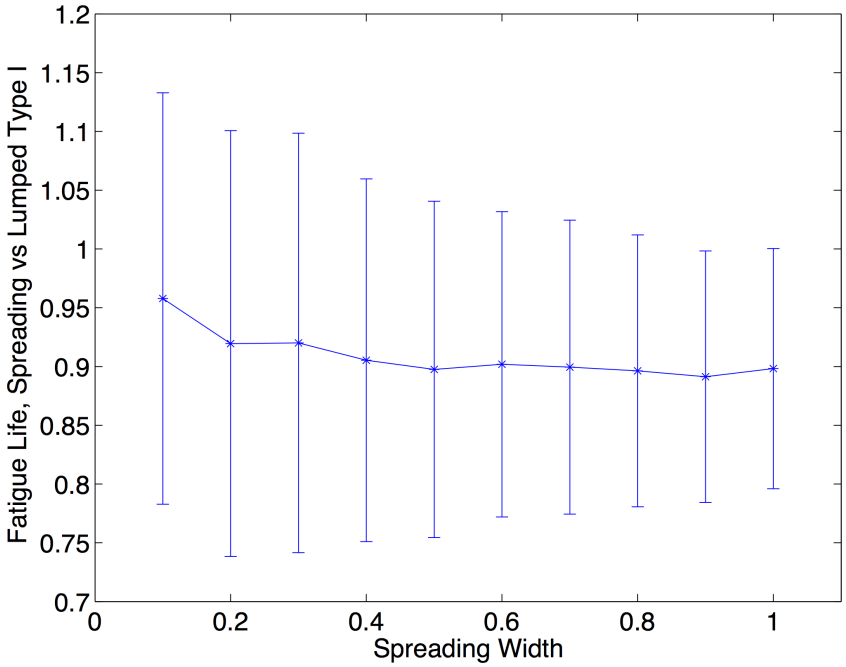

Figure 3-30: The influence of spread width on fatigue life of non-stationary signal with random PSD shape: first and third harmonics (right). The x-axis is the multiplier of original harmonic spread. The fatigue life is normalized by the fatigue life of Type I signal with both the first and third harmonics.

Figure 3-31 shows the ratio of the fatigue life of such signals normalized by the fatigue life of a signal with only a single peak at the first harmonic versus the degree of asymmetry, which is the ratio of the right spreading width to the left spreading width. When the ratio is one, the spreading is perfectly symmetric. It is seen that the fatigue life ratio decreases as the spreading becomes more asymmetric towards the right. Fatigue life decreases by more than 19% when a right asymmetric spreading exists and increases 22% when left asymmetric spreading exists. The ratios of the fatigue life for these signals normalized by the fatigue life of a Type-I signal with both the first and the third harmonics are plotted versus the spread width ratio of the right part with the left part. The fatigue life is plotted in Figure 3-32. Fatigue life decreases down to 90% of the symmetric case in these cases.

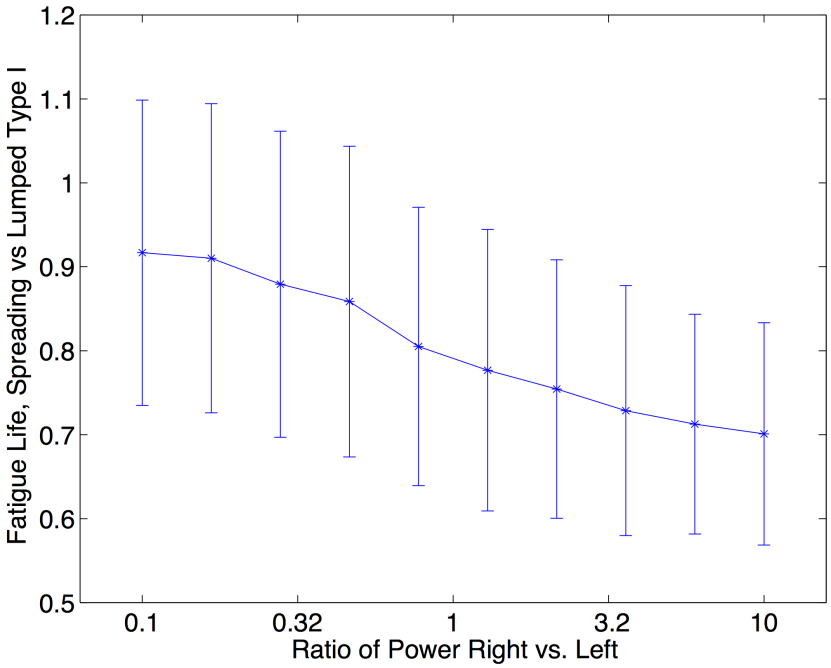

Figure 3-31: The influence of symmetry of spread distribution on the fatigue life of a non-stationary signal with random PSD shape: first harmonic only. The x-axis indicates the degree of asymmetry (spread width ratio of right part of spread vs left part). The fatigue life is normalized by the fatigue life of Type I signal with only the first harmonics.

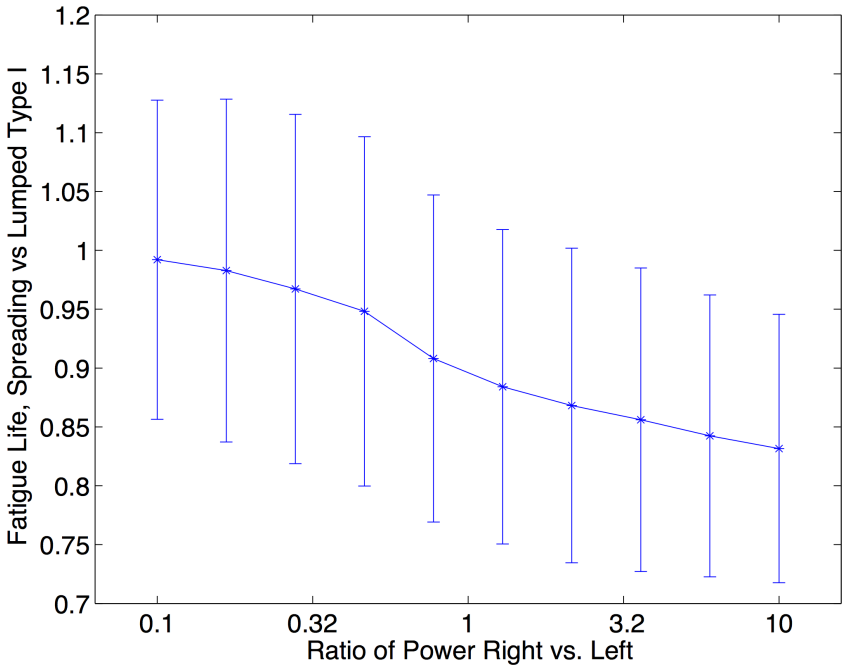

Figure 3-32: The influence of symmetry of spread distribution on the fatigue life of a non-stationary signal with random PSD shape: first and third harmonics. The x-axis indicates the degree of asymmetry (spread width ratio of right part of spread vs left part). The fatigue life is normalized by the fatigue life of Type I signal with both the first and third harmonics

We further investigate the influence of non-stationarity on the fatigue life of a non-stationarity Type II signals with different energy distributions between the first and third harmonics and the results are shown in Figure 3-33. The error bar shows the mean and standard deviation of the fatigue life, and the x-axial is the percentage of the third harmonic power over the whole signal power. The results show a fatigue life reduction of 15 -20% in most cases and the influence is the same magnitude as the influence of spreading width and symmetry.

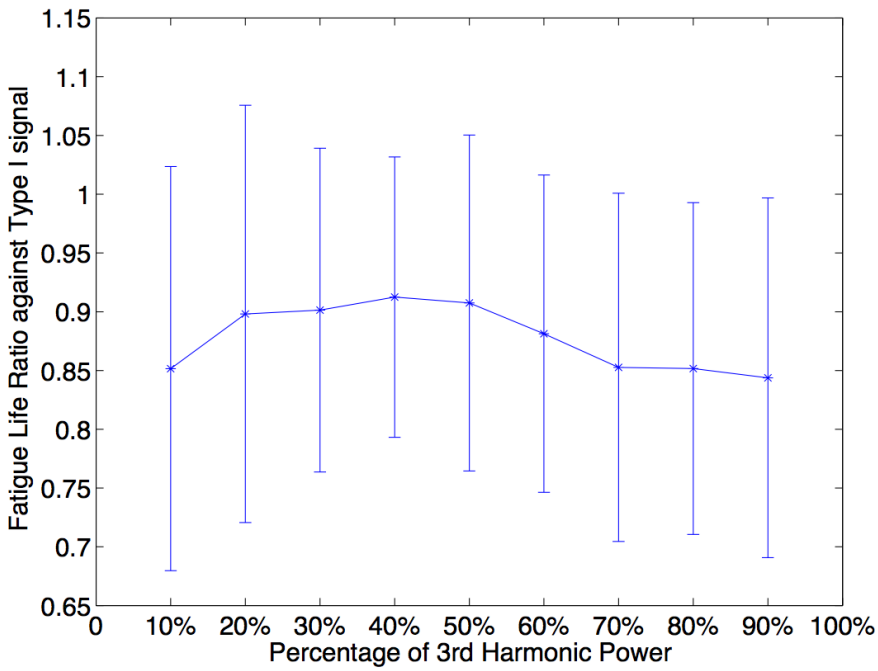

Figure 3-33: The influence of non-stationarity of spread distribution on the fatigue life. The x-axis is the percentage of third harmonic power. The fatigue life is normalized by the fatigue life of Type I signal with both the first and third harmonics.

3.6 Conclusions

Higher harmonic force components in VIV signals have been observed relatively recently. Besides being an inherently interesting finding, these higher harmonics have practical significance due to the increase they cause in fatigue damage of marine risers. It has been shown previously that this increase can be up to two orders of magnitude.

Another recent discovery, viz. the fact that VIV signals contain regions of chaotic-like oscillations, is shown to be important in this chapter, because such chaotic oscillations can also increase the fatigue damage substantially. Chaotic signals have a broad-band PSD and are non-stationary.

In this chapter, we have studied the impact of (a) the presence of higher harmonic stress components, (b) the frequency spreading of the power spectral density (PSD) on fatigue damage, and (c) the initial investigation of non-stationarity of the chaotic signal. We use the NDP experimental data to calculate the stress PSDs and also the corresponding relative importance of the higher harmonic power. Then, we use this information to construct time series that have the same total power but different PSD shapes: (i) containing only the first harmonic with the energy lumped at one frequency point, (ii) containing the first and the third harmonics with the energy lumped at two frequencies only, and (iii) containing the first and the third harmonics with their energy spread over a frequency range. The rainflow fatigue algorithm is applied to the time series to estimate the fatigue damage on the riser. To assess the impact of the variations introduced, we calculate the ratio of the fatigue damage resulting from the changes introduced relative to the fatigue damage of the original signal.

We find that by including the higher harmonic components, there is a damage increase of 50% with respect to the damage due the first harmonic stress only. The fatigue damage increases by another 20% due to a spread PSD, characteristic of Type-II (chaotic) behavior of the riser. This shows that the influence of the frequency spreading on the increase in fatigue damage is as crucial as the influence of adding the higher harmonic components.

Chapter 4

Crossflow VIV Prediction and Optimization

The prediction of VIV using a hydrodynamic database has two major components: the structural response can be modeled accurately, whereas the hydrodynamic loads are predicted using laboratory data, which require significant corrections before being applied. Field data is used systematically to make such corrections in a meaningful way, and data from numerical simulations provide further insight into the mechanisms of VIV as they apply to long structures. Hence, there is a continuous dialogue between predictions using the experiment-based codes on one hand and field and experimental data on the other, as well as computational data.

This chapter outlines the procedures used by the program VIVA developed over the last sixteen years, as modified through comparison against experimental and field data. The program by construction can handle standing as well as traveling waves, or a combination of the two types of waves, through the use of complex modes. Considerable effort was expended to develop a hydrodynamic methodology that is suitable for long risers and cables, and which also provides results in agreement with recently observed mechanisms. In particular, we outline changes that need to be taken into account: (i) the influence of in-line as well as cross-flow oscillations, (ii) the modeling of lock-in in a sheared flow and (iii) the modeling of straked sections. The methodology is illustrated through several examples where predictions are compared

with field and experimental data.

4.1 Introduction

The semi-empirical VIV prediction programs model the structure part using beam theory and modal superposition and also employ experiment-based hydrodynamic coefficients databases to calculate the fluid forces instead of solving the Navier-Stokes equation. The most widely used methods for predicting the riser VIV are semi-empirical prediction programs like VIVA [69, 70], SHEAR7 [74], and VIVANA [37]. Such programs typically consist of two parts: (1) a fluid-structure interaction model and (2) laboratory-derived or empirical databases. The fluid-structure interaction model consists of a fluid force model and the equations of structural dynamics. The hydrodynamic databases primarily contain hydrodynamic information in the form of the lift force coefficients (lift coefficient in phase with velocity and added mass coefficient) and drag coefficients. These force coefficients are often obtained from extensive laboratory experiments using an elastically mounted rigid cylinder. It is a common practice (see [70, 74]) to use a strip theory approach to subdivide the riser into small segments, which act similar to a series of interconnected, elastically mounted rigid cylinders, and estimate the vortex-induced forces on each of these segments: the excitation force in phase with velocity and the excitation force in phase with acceleration. As shown by [65], estimating these forces requires lift coefficient databases of added mass coefficient and lift coefficient in phase with velocity. From a structural dynamics viewpoint, a riser is adequately modeled as a tensioned beam with the appropriate boundary conditions, acted upon by the external hydrodynamic force [57].

The available extensive databases used in the original VIVA were obtained in the MIT Towing Tank by Gopalkrishnan [28]. The lift coefficients and added mass coefficients are functions of reduced velocity and amplitude of response. Figure 4-1 shows surface plots of these databases. The databases were obtained: (i) at a Reynolds number around 10,000; (ii) for cylinders undergoing harmonic motion at a single fre-

quency and restricted to the cross-flow direction only. To overcome these limitations, Mukundan [49, 50] developed a systematic method to extract information from field and experimental data and update the existing databases. A formal procedure to optimize this process was discussed by Mukundan [50] and a heuristic method was used by Chasparis [15, 16], whereby a small number of parameters were allowed to vary. In this chapter, I extend this idea by using experimental data obtained from a series of lab and field experiments for both bare and straked cylinders in our optimization methodology to come up with a universal database.

4.2 Methodology of Database Optimization

In semi-empirical VIV predictive tools, strip theory is used, requiring that the fluid force slowly varies along the length and can therefore be locally approximated by a 2-D flow, and also that a force correlation model is available. It also requires that databases provide the sectional lift coefficient and added mass coefficient in terms of the local reduced velocity and the non-dimensional amplitude. The original lift coefficient in phase with velocity, C_{lv}, and the added mass coefficient, C_m, are functions of the reduced (non-dimensional) velocity Vr = U/(fD), where U is the current velocity, f the frequency of vibration, and D the cylinder diameter; and the non-dimensional amplitude $A^* = A/D$, where A is the amplitude of oscillation. Surface plots of C_{lv} and C_m are shown in Figure 4-1.

To avoid computationally expensive 3D interpolations and to help numerical convergence, we consider cross-sections of the above 3D surfaces for various reduced velocities, Vr, as shown in the left figure in Figure 4-2. For convenience, these 2D plots can be parameterized by straight lines, as shown in the two right-hand figures of Figure 4-2. In Figure 4-3, the first subplot shows the C_{lv} at zero non-dimensional amplitude as a function of non-dimensional frequency. The second subplot shows the C_m at zero non-dimensional amplitude as a function of non-dimensional frequency. The 3rd and 4th subplots show the first and second average slopes of C_{lv} as indicated in Figure 4-2. The 5th subplot shows the point where C_{lv} reaches its maximum and

also the transaction points of the above two slopes.

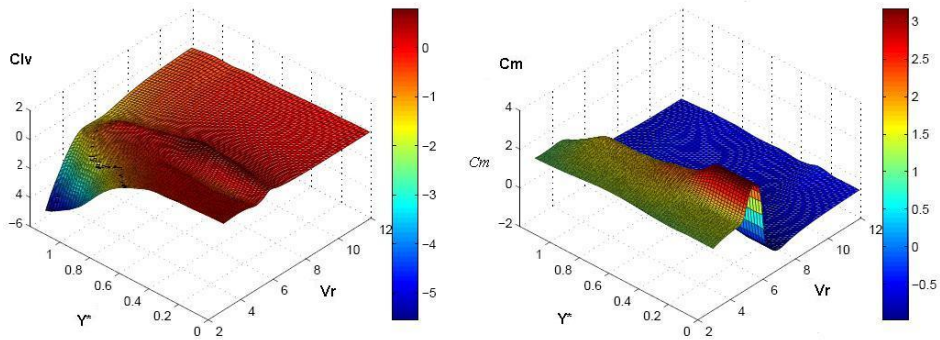

Figure 4-1: Surface plots of lift coefficient C_{lv} (left) and added mass coefficient C_m (right) as functions of reduced velocity (x-axis) and non-dimensional amplitude (y-axis) [28].

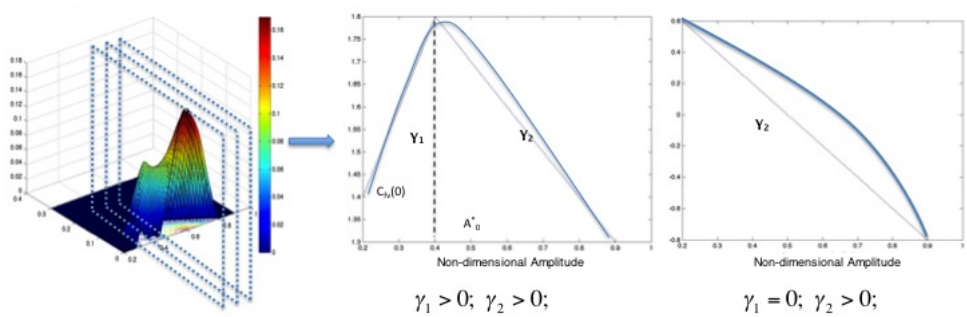

Figure 4-2: Two dimensional representation of the lift coefficient C_{lv} and added mass coefficient C_m surfaces.

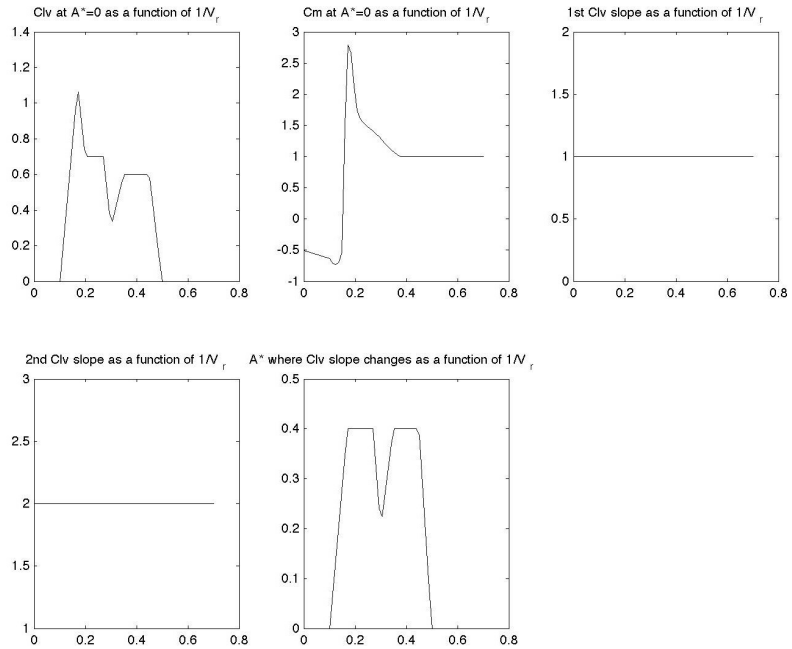

Figure 4-3: Two-dimensional linear plots of lift coefficient C_{lv} and added mass coefficient C_m curves for a bare cylinder.

When we optimized the database, we parameterized the 2D curves of lift and added mass coefficients, allowing (a) the curve of the lift coefficient in phase with velocity as a function of reduced velocity to expand in width and to be adjustable in height so as to accommodate Reynolds number effects and the effect of the in-line motions; (b) the slope of C_{lv} as a function of A^* to be adjustable to accommodate Reynolds number effects; and (c) the transition of the added mass coefficient C_m from high to low values as a function of the reduced velocity to be adjustable [15].

Similar procedures were followed for the hydrodynamic coefficients for straked cylinders. These have a different shape, since the lift coefficient is mostly of the damping type, and the added mass coefficient is practically constant, as shown in Figure 4-4. In order to provide for differences between field data and laboratory data, we allowed the slope of the lift coefficient as a function of A^* to vary, and the added mass coefficient to be adjustable.

In order to extract a set of universal hydrodynamic coefficients, we compared

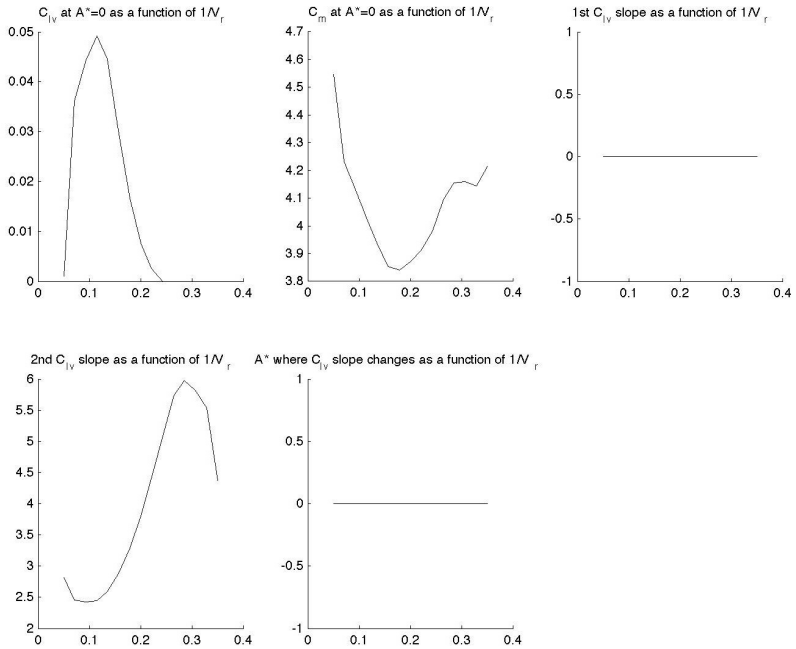

Figure 4-4: Two-dimensional linear plots of lift coefficient C_{lv} and added mass coefficient C_m curves for straked cylinder.

VIVA (multi-mode) predictions with an entire set of experimental data as described in the following section.

4.3 Experimental Database and Processing

In our optimization, we have compared against the following experimental databases, some of which are available online at the MIT VIV Data Repository [41, 83].

NDP38 lab experiments [9] were conducted by the Norwegian Deepwater Programme in December 2003. They were carried out on a 38-meter long riser model for various linearly sheared and uniform flow velocity cases for both the bare and either partially or fully straked riser configurations.

NDP10 lab experiments [39] were conducted on a straked riser model (10m long) for various linearly sheared and uniform flow velocity cases in June 2003. These datasets correspond to experiments conducted with various strake coverage (25%, 50%, 75% and 100%).

Chaplin's [14] lab experiment was carried out with a model vertical tension riser that was 28 mm in diameter, 13.12 m long, and with a mass ratio (mass/displaced mass) of 3.0, in a stepped current in May 2003.

Miami field experiments were part of the Deepstar-MIT Gulf Stream 2006 tests [77] and were conducted on a 500-foot long and 1.43-inch diameter pipe in October 2006.

The derivation of the new database, shown in Figures 4-5 and 4-6, was done heuristically, as this allowed us to ensure that physical mechanisms are adequately represented, especially the effects of the Reynolds number and inline motion. Inline motion drastically changes the shape of the database for all Reynolds numbers [21]. To properly model the effect of the inline motion, we relied on the extensive database by Dahl [19], derived at the MIT Towing Tank.

4.4 Database Optimization Results

Following the optimization methodology, we use the program VIVA to predict the VIV response for the above-mentioned experimental cases. Then we compare the response predicted by VIVA with experimental results and adjust the hydrodynamic

coefficients until the error between prediction and experiment is minimized. The bare cylinder database was obtained using the bare cylinder results and the straked database was obtained using the partially straked riser results in conjunction with the previously optimized bare database. The optimization results of the hydrodynamic force coefficients for bare and straked riser are shown in Figures 4-5 and 4-6, respectively. The surface plots of the optimized C_m and C_{lv} are shown in Figures 4-7 and 4-8.

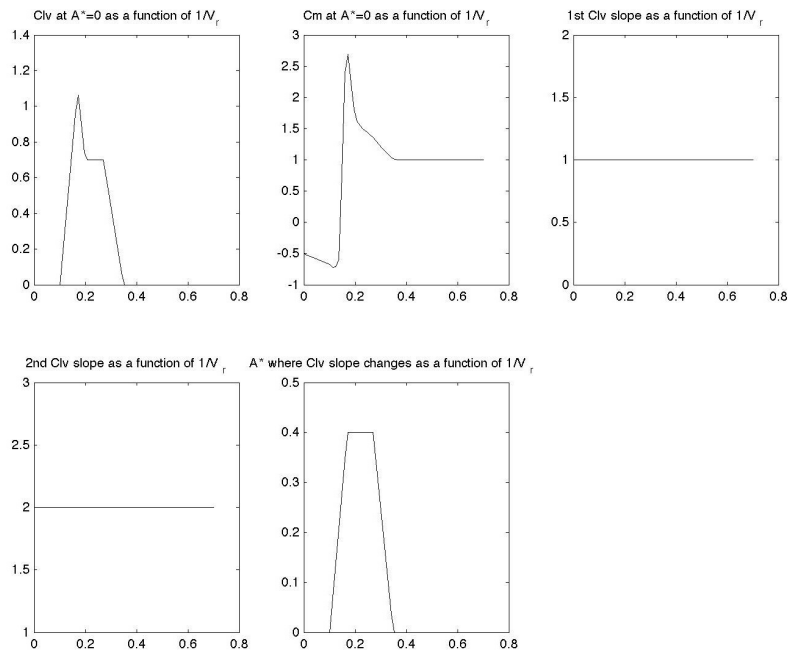

Figure 4-5: Optimal 2D linear plots of lift coefficient C_{lv} and added mass coefficient C_m curves for bare cylinder.

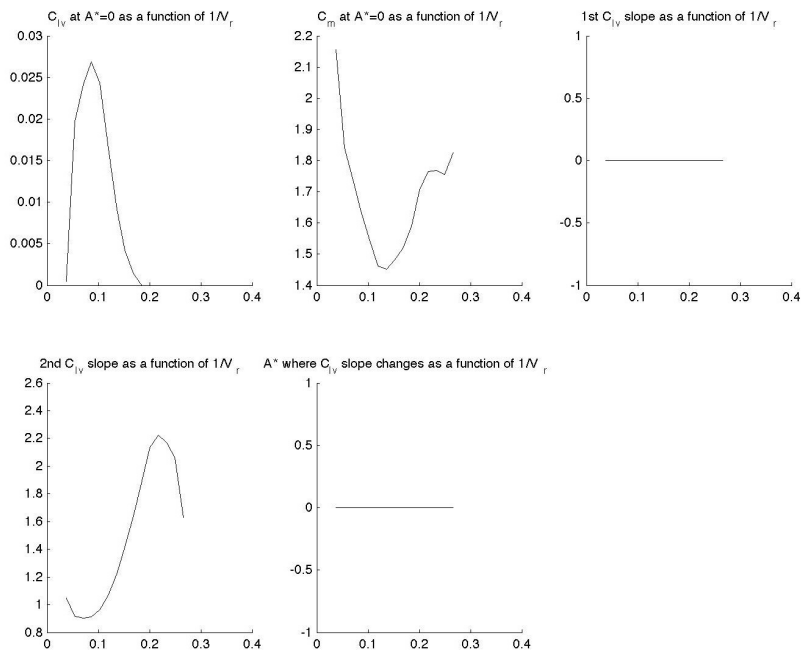

Figure 4-6: Optimal 2D linear plots of lift coefficient C_{lv} and added mass coefficient C_m curves for straked cylinder.

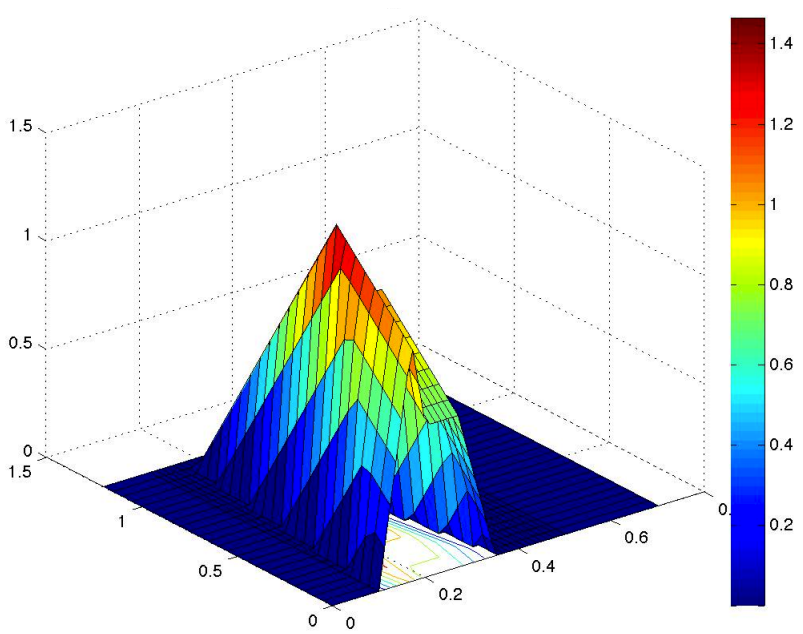

Figure 4-7: Optimal 3D linear plots of lift coefficient C_{lv} curves for bare cylinder.

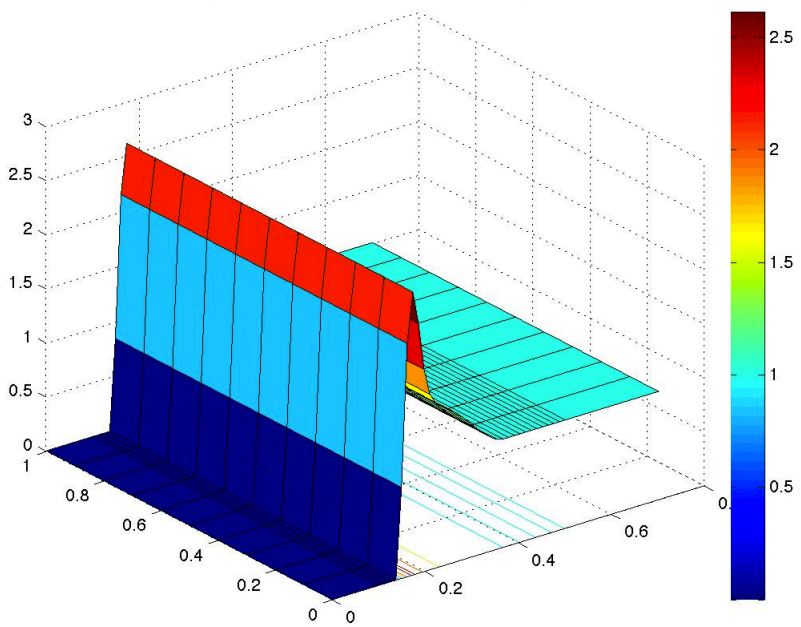

Figure 4-8: Optimal 3D linear plots of added mass coefficient C_m curves for bare cylinder.

4.5 Crossflow VIV Prediction Results Analysis

In this section, some sample results using the optimized databases are given.

4.5.1 NDP38 Experiment

Figure 4-9 shows a comparison between VIVA predicted RMS amplitudes (solid line) and measured values (red dots) for NDP38 data as a function of riser length (x/L) in uniform flow. The ratio of the VIV dominant frequency predicted by VIVA and measured by experiment in uniform flow is given in Figure 4-10. A ratio of one indicates a perfect prediction. The flow is uniform and indicated for each case in m/s; the first half of the riser is covered with triple-start strakes with a pitch to diameter ratio of 16.5 and strake height equal to 25% of the diameter.

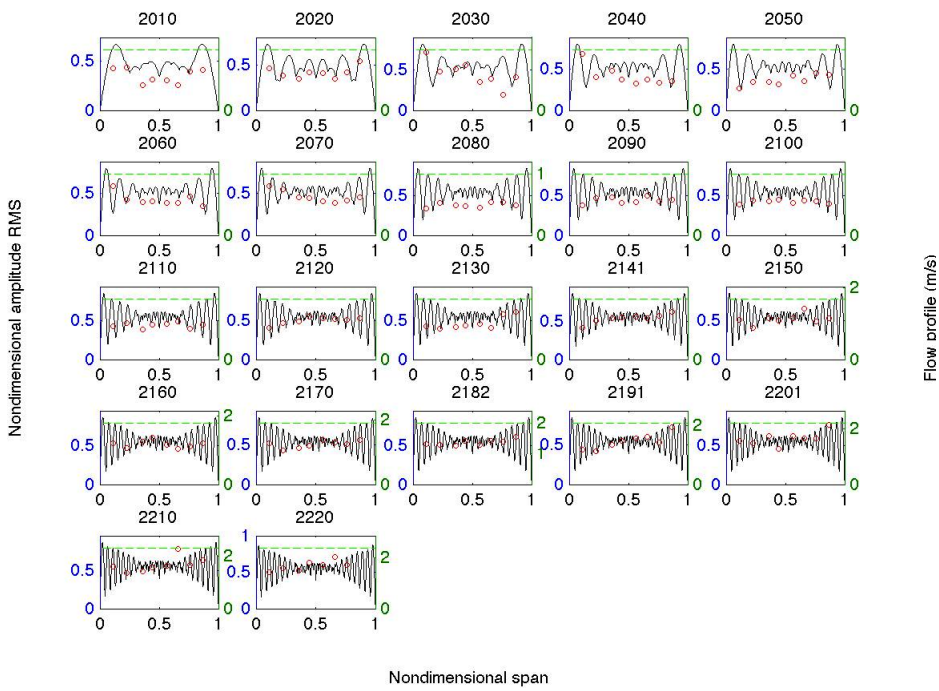

Figure 4-9: VIV RMS amplitude (A/D) versus length (x/L) comparison between VIVA prediction and experimental data; VIVA prediction (continuous line), experimental data (circles). Current profile in green dotted line. NDP38 dataset for bare riser in uniform flow.

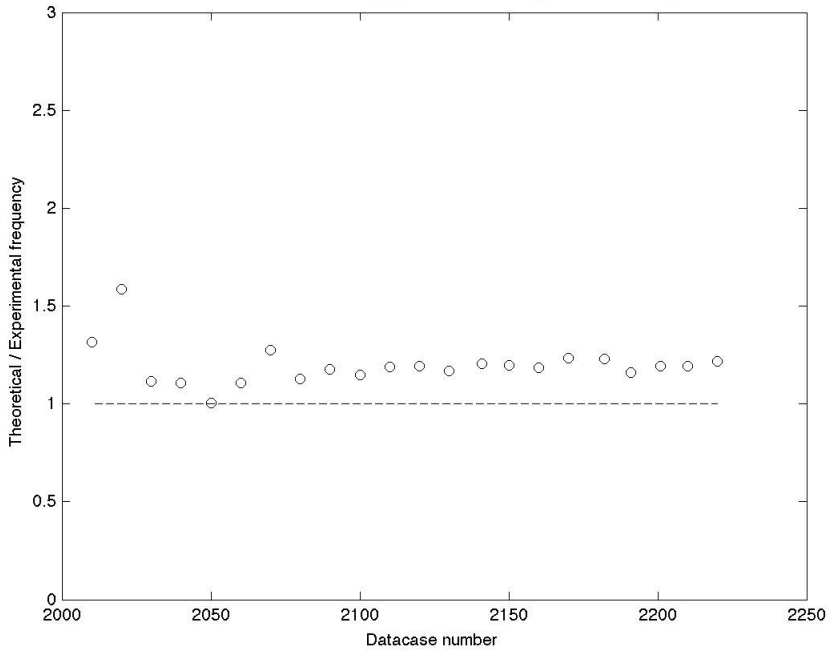

Figure 4-10: Ratio of VIV dominant frequency of VIVA prediction and experimental data. NDP38 dataset for bare riser in uniform flow.

Figure 4-11 shows a comparison between VIVA predicted RMS amplitudes (solid line) and measured values (red dots) for NDP38 data as a function of riser length (x/L) in sheared flow. The ratio of VIV dominant frequency predicted by VIVA and measured in sheared flow experiments is given in Figure 4-12.

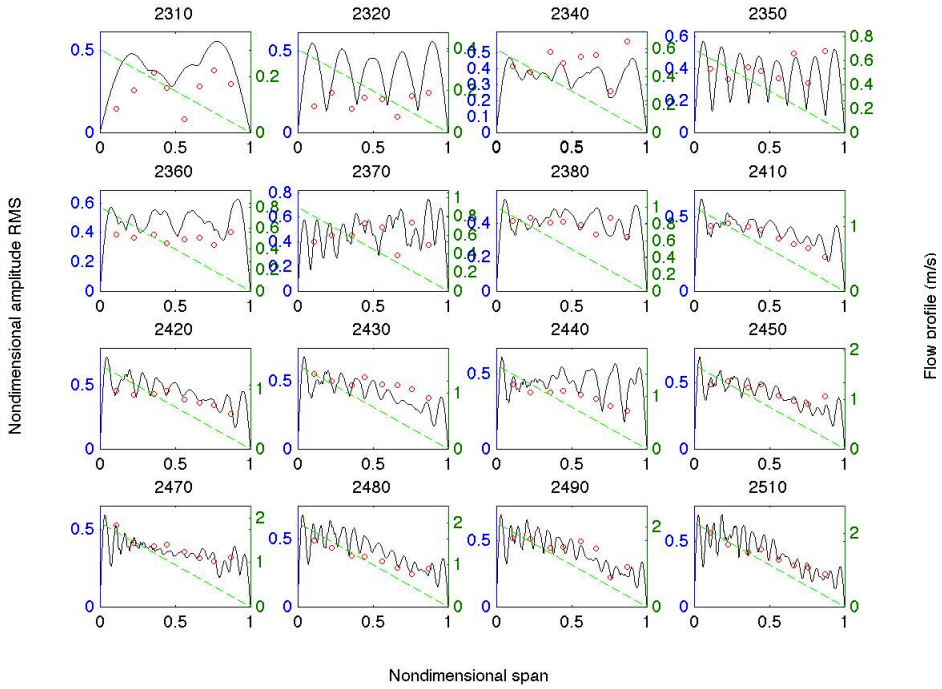

Figure 4-11: VIV RMS amplitude (A/D) versus length (x/L) comparison between VIVA prediction and experimental data; VIVA prediction (continuous line), experimental data (circles). Current profile in green dotted line. NDP38 dataset for bare riser in sheared flow.

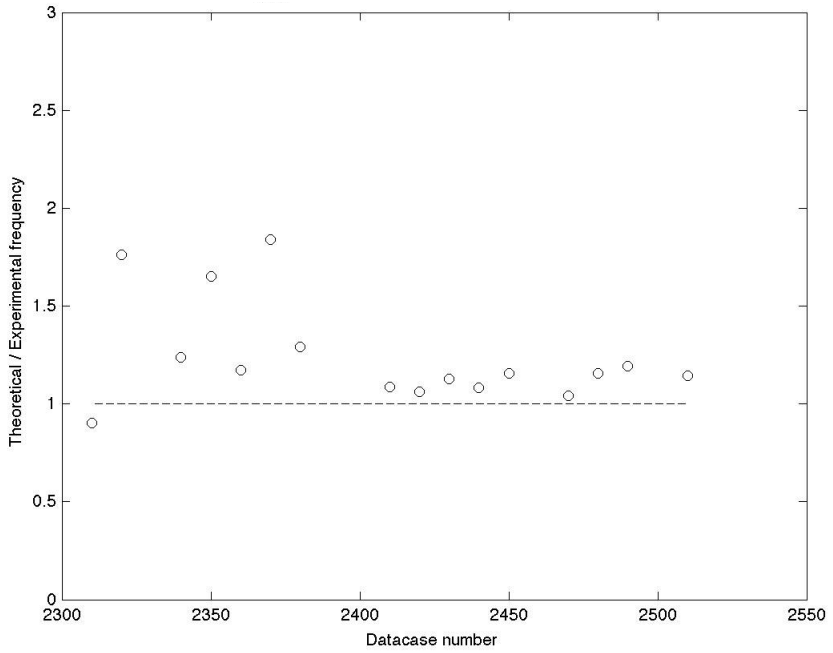

Figure 4-12: Ratio of VIV dominant frequency of VIVA prediction and experimental data. NDP38 dataset for bare riser in sheared flow.

Figure 4-13 provides a comparison between VIVA predicted RMS amplitudes (solid line) and measured values (red dots) for the 50% straked riser in uniform flow, from the NDP38 data. Solid lines denote VIVA predictions and red dots represent experimental data; all are RMS motions. The green line shows the incoming current velocity profile along the riser span, in m/s. The ratio of VIV dominant frequency predicted by VIVA and measured in experiments is given in Figure 4-14. For 50% coverage, 50% of the strakes in the lower end were removed.

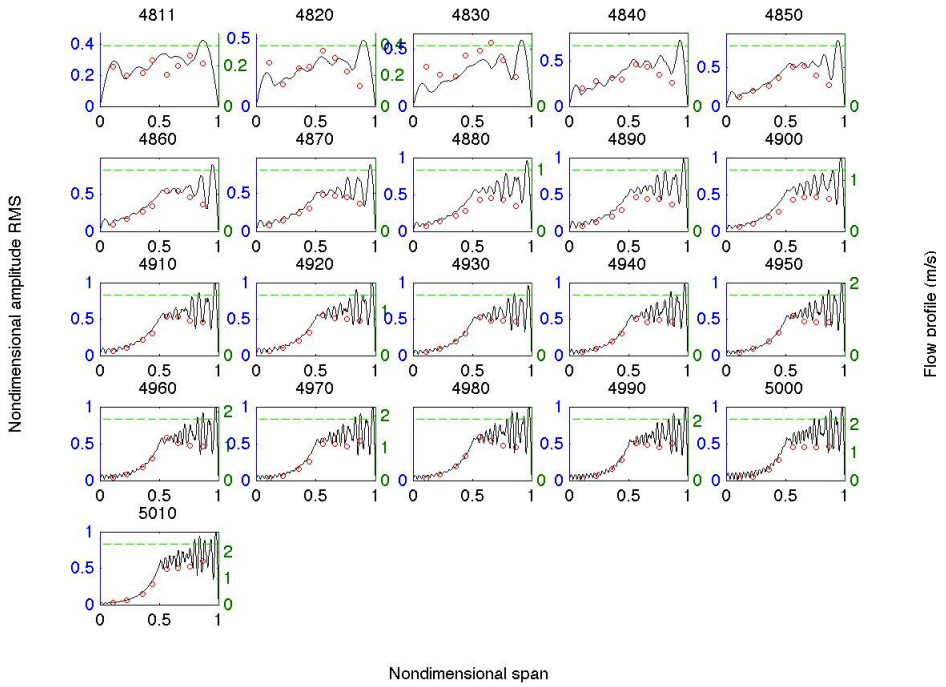

Figure 4-13: VIV RMS amplitude (A/D) versus length (x/L) comparison between VIVA prediction and experimental data; VIVA prediction (continuous line), experimental data (circles). Current profile in green dotted line. NDP38 dataset for 50% straked riser in uniform flow.

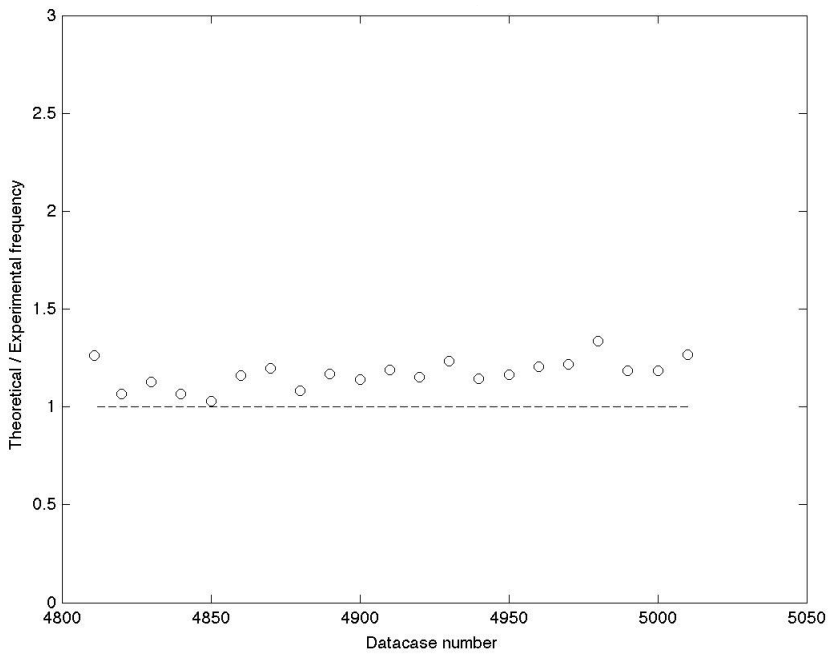

Figure 4-14: Ratio of VIV dominant frequency of VIVA prediction and experimental data. NDP38 dataset for 50% straked riser in uniform flow.

Figure 4-15 provides the same data for the 50% straked riser in linearly sheared flow, from the NDP38 data. Again solid lines denote VIVA predictions and red dots experimental data; all are RMS motions. The green line shows the incoming current velocity profile along the riser span, in meters per second. The ratio of VIV dominant frequency predicted by VIVA and measured in the experiment is given in Figure 4-16. It should be noted that the predictions are very good for modes higher than the first couple of modes; for the first two modes, VIVA over-predicts the response by about 20% due to the assumed worst-case scenario of strong in-line motion. The responses for the mid-range of velocities shown in Figures 4-15 and 4-16 are very good, particularly in capturing the effect of the strakes. For 50% coverage, 50% of the strakes in the lower end were removed.

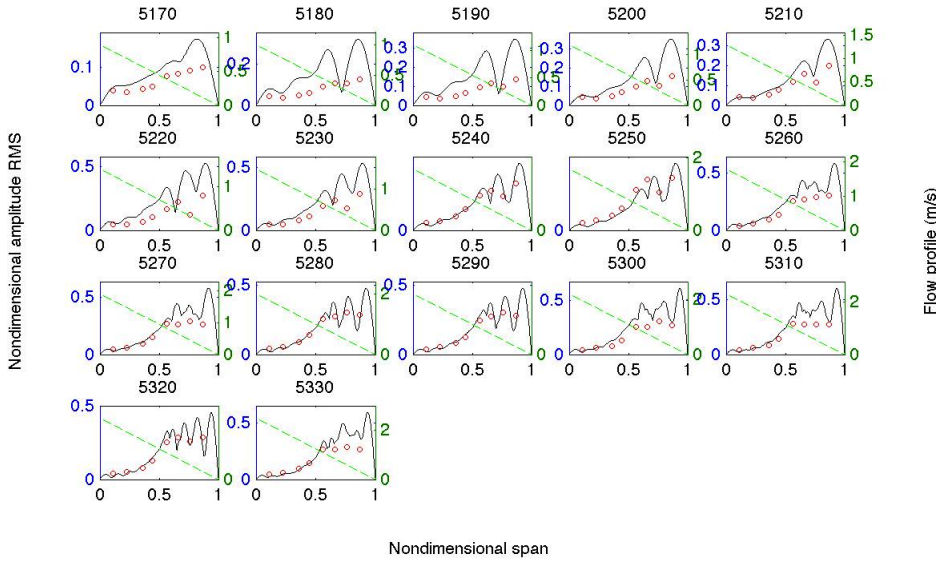

Figure 4-15: VIV RMS amplitude (A/D) versus length (x/L) comparison between VIVA prediction and experimental data; VIVA prediction (continuous line), experimental data (circles). Current profile in green dotted line. NDP38 dataset for 50% straked riser in sheared flow.

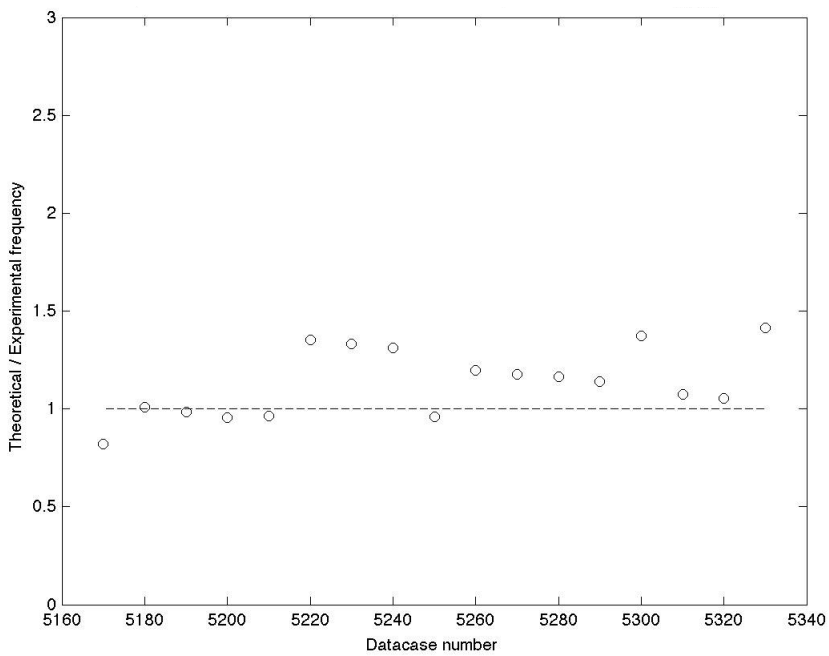

Figure 4-16: Ratio of VIV dominant frequency of VIVA prediction and experimental data. NDP38 dataset for 50% straked riser in sheared flow.

Figure 4-17 provides the predicted first and third harmonics of stress for one particular case of linear shear flow on a bare riser (NDP38 data). VIVA predicts a range of modes that are likely to be excited as a function of frequency in Hz. The first harmonic is shown using a solid line and the third harmonic using a dotted line; they are both parameterized with respect to the frequency of the first harmonic. The multi-frequency algorithm selects the most likely mode which is found at the peak response, at about 5.8 Hz in this case. As shown, the corresponding third harmonic stress component is about 45% of the first harmonic component. The experimental data show a third harmonic component close to 30% of the first harmonic. The agreement is fair given the several assumptions involved in the calculation.

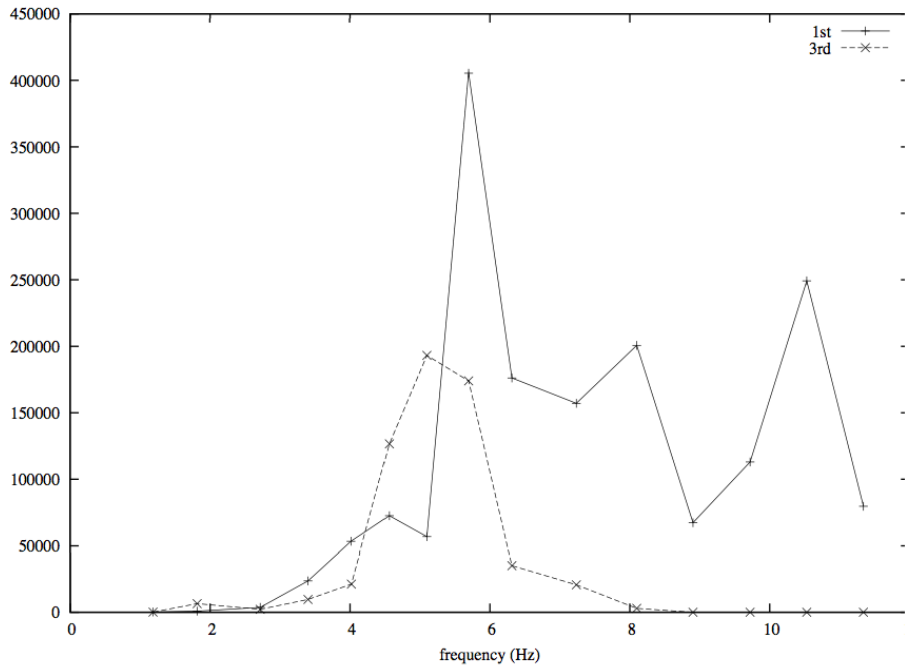

Figure 4-17: VIVA prediction of first harmonic stress (in Pa) as a function of frequency (solid curve) and the corresponding third harmonic stress component (dotted line) for a bare riser in linearly sheared flow (NDP38 data).

4.5.2 Chaplin Experiment

Figure 4-18 provides the predicted RMS amplitude of response along the riser length for four cases from Chaplin [14]. The ratio of VIV dominant frequency predicted by VIVA and measured in the experiment is given in Figure 4-19. There were only 2 accelerometers, at 3.435m and 5.587m from the bottom of the riser. The lower one recorded only cross-flow, but the upper one recorded in both directions. The displacement and flow velocity data is processed to have 32 readings.

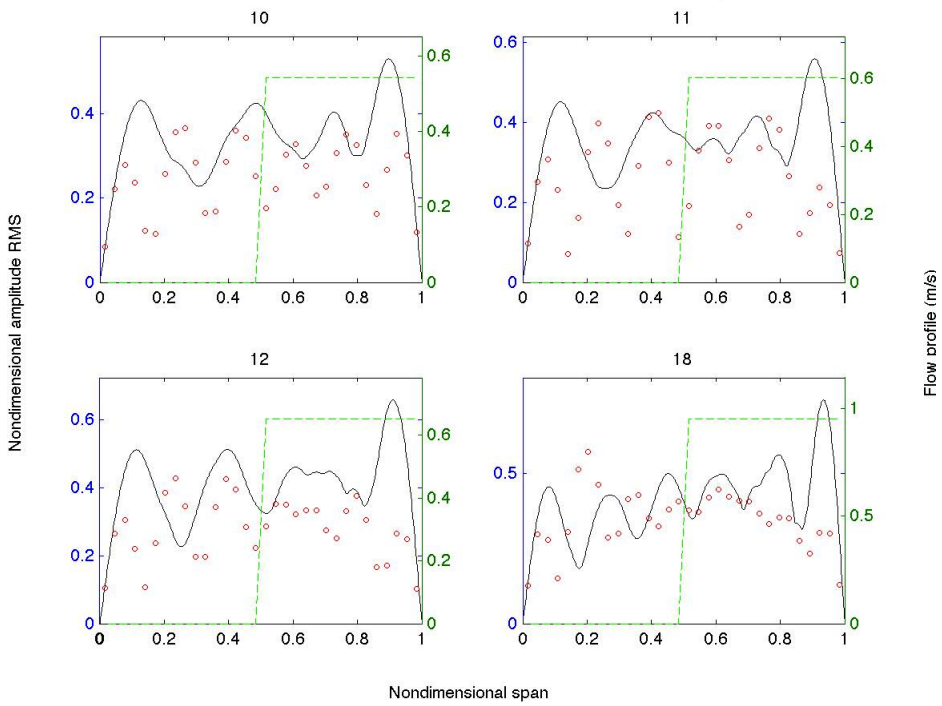

Figure 4-18: VIV RMS amplitude (A/D) versus length (x/L) comparison between VIVA prediction and experimental data; VIVA prediction (continuous line), experimental data (circles). Current profile in green dotted line. Chaplin Experiment.

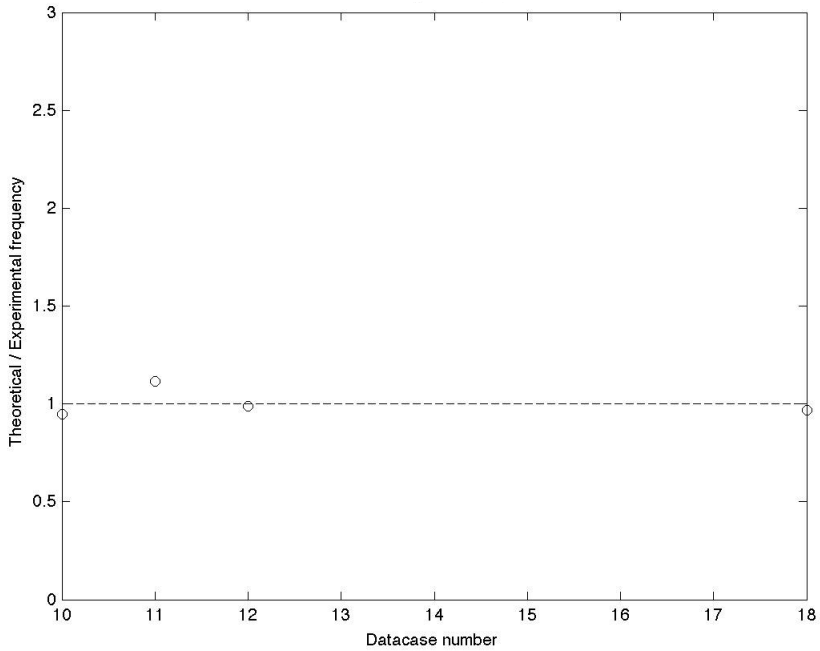

Figure 4-19: Ratio of VIV dominant frequency of VIVA prediction and experimental data. Chaplin Experiment.

4.5.3 NDP10 Experiment

NDP10 lab experiments [39] were measured on a straked riser model (10m long) for various linearly sheared and uniform flow velocity cases. These datasets correspond to experiments conducted with varying strake coverage (25%, 50%, 75% and 100%).

Figure 4-20 provides the predicted RMS amplitude of response along the riser length for a NDP 10m bare riser in uniform flow. The corresponding ratio of the VIV dominant frequency predicted by VIVA and measured in the experiment is given in Figure 4-21.

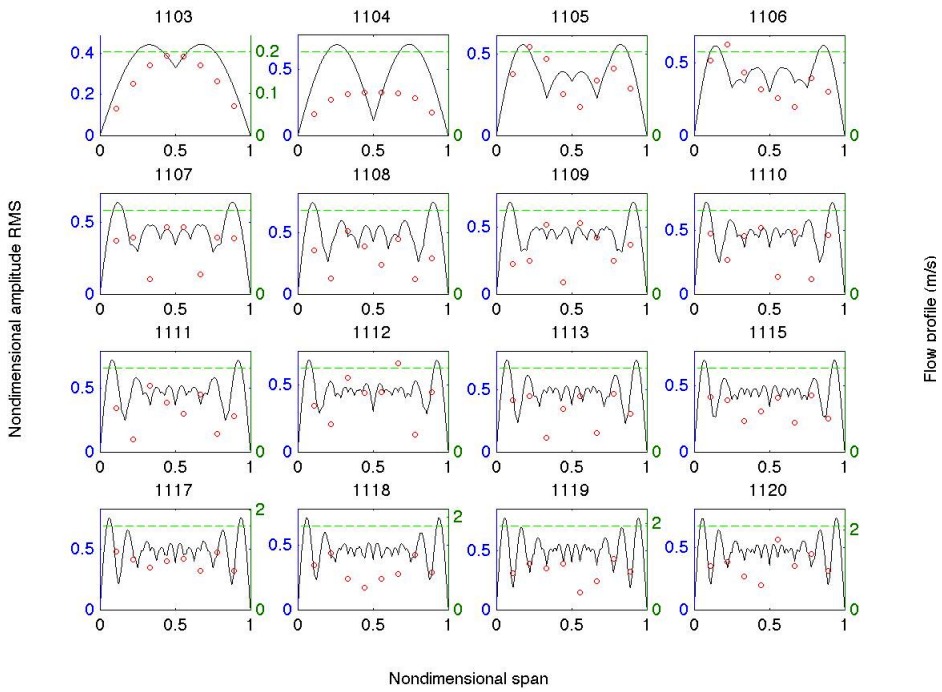

Figure 4-20: VIV RMS amplitude (A/D) versus length (x/L) comparison between VIVA prediction and experimental data; VIVA prediction (continuous line), experimental data (circles). Current profile in green dotted line. NDP 10m bare riser in uniform flow.

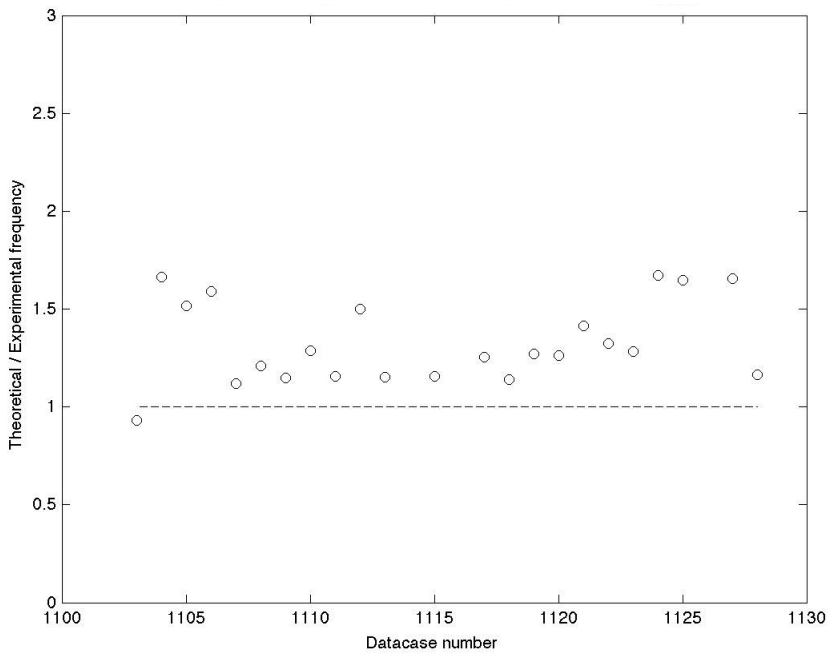

Figure 4-21: Ratio of VIV dominant frequency of VIVA prediction. NDP 10m bare riser in uniform.

Figure 4-22 provides the predicted RMS amplitude of response along the riser length for a NDP 10m bare riser in sheared flow. The corresponding ratio of VIV dominant frequency predicted by VIVA and measured in the experiment is given in Figure 4-23.

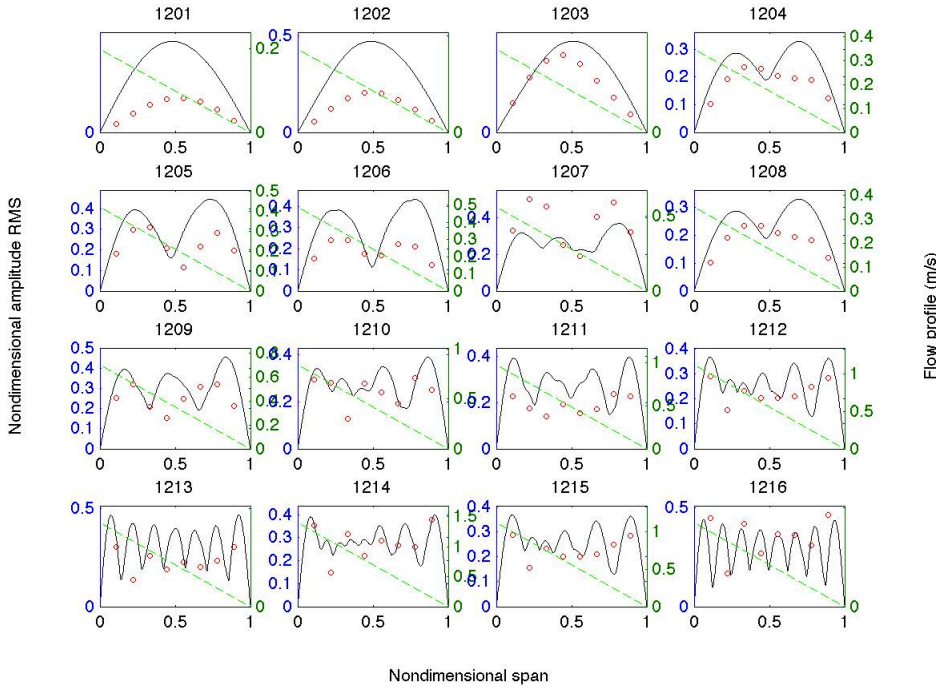

Figure 4-22: VIV RMS amplitude (A/D) versus length (x/L) comparison between VIVA prediction and experimental data; VIVA prediction (continuous line), experimental data (circles). Current profile in green dotted line. NDP 10m bare riser in sheared flow.

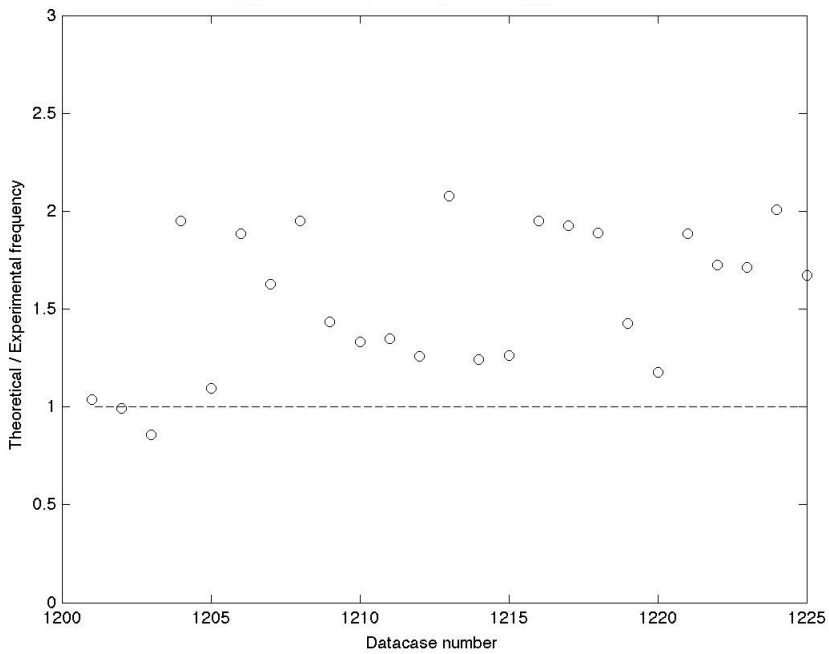

Figure 4-23: Ratio of VIV dominant frequency of VIVA prediction. NDP 10m bare riser in sheared flow.

Figure 4-24 provides the predicted RMS amplitude of response along the riser length for NDP 10m 25% strake riser in uniform flow. The corresponding ratio of VIV dominant frequency predicted by VIVA and measured in the experiment is given in Figure 4-25.

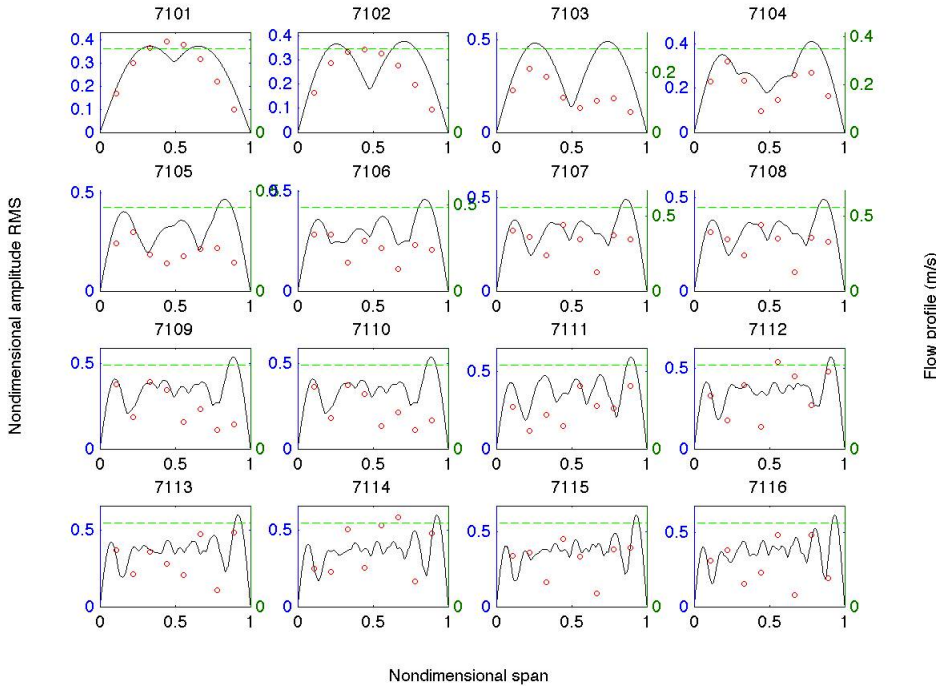

Figure 4-24: VIV RMS amplitude (A/D) versus length (x/L) comparison between VIVA prediction and experimental data; VIVA prediction (continuous line), experimental data (circles). Current profile in green dotted line. NDP 10m 25% strake riser in uniform flow.

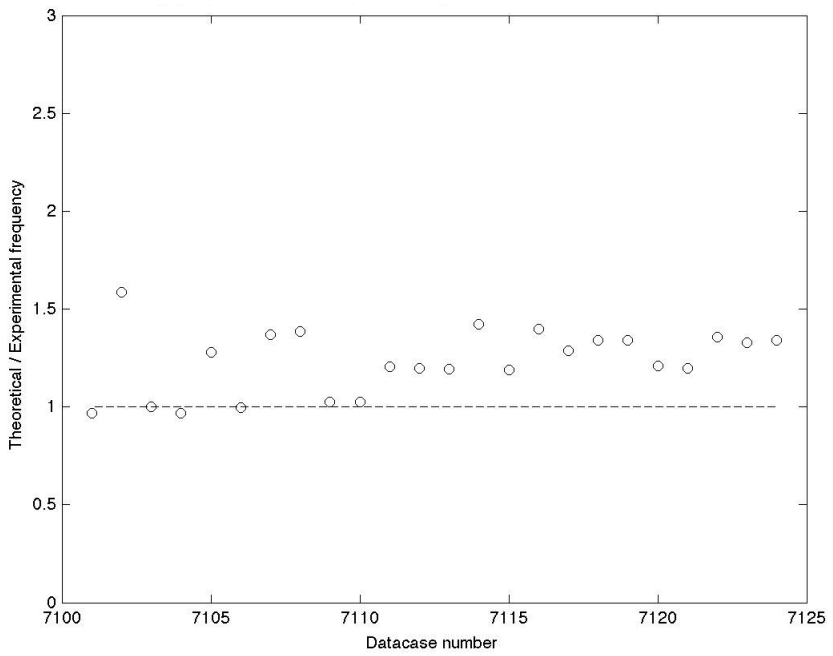

Figure 4-25: Ratio of VIV dominant frequency of VIVA prediction. NDP 10m 25% strake riser in unform flow.

Figure 4-26 provides the predicted RMS amplitude of response along the riser length for NDP 10m 25% strake riser in sheared flow. The corresponding ratio of VIV dominant frequency predicted by VIVA and measured in the experiment is given in Figure 4-27.

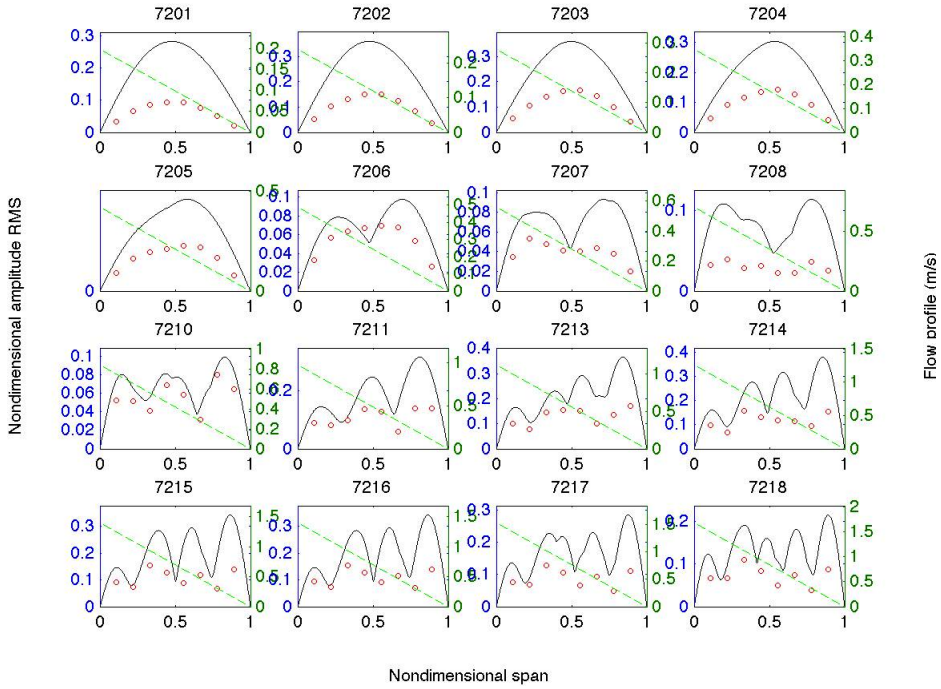

Figure 4-26: VIV RMS amplitude (A/D) versus length (x/L) comparison between VIVA prediction and experimental data; VIVA prediction (continuous line), experimental data (circles). Current profile in green dotted line. NDP 10m 25% strake riser in sheared flow.

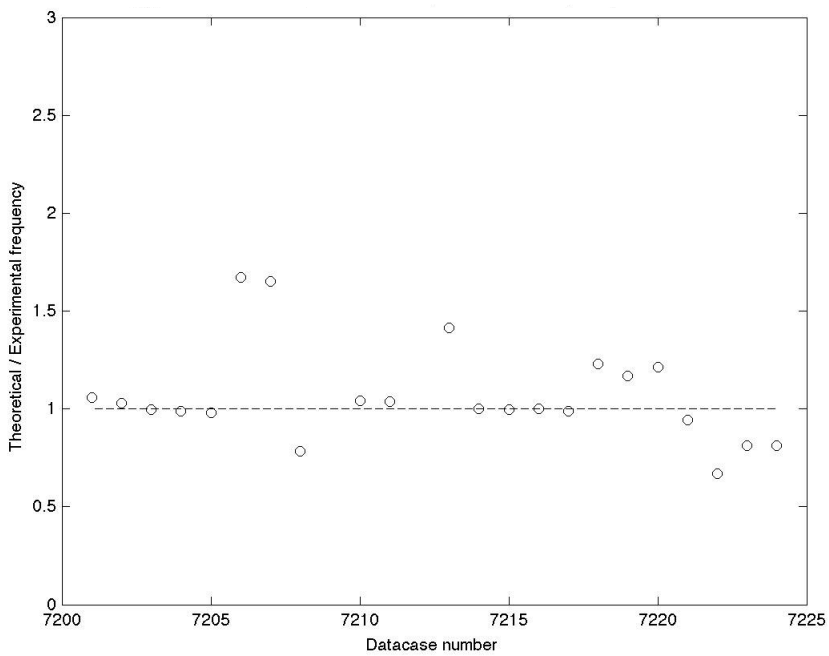

Figure 4-27: Ratio of VIV dominant frequency of VIVA prediction. NDP 10m 25% strake riser in sheared flow.

Figure 4-28 provides the predicted RMS amplitude of response along the riser length for NDP 10m 50% strake riser in uniform flow. The corresponding ratio of VIV dominant frequency predicted by VIVA and measured in the experiment is given in Figure 4-29.

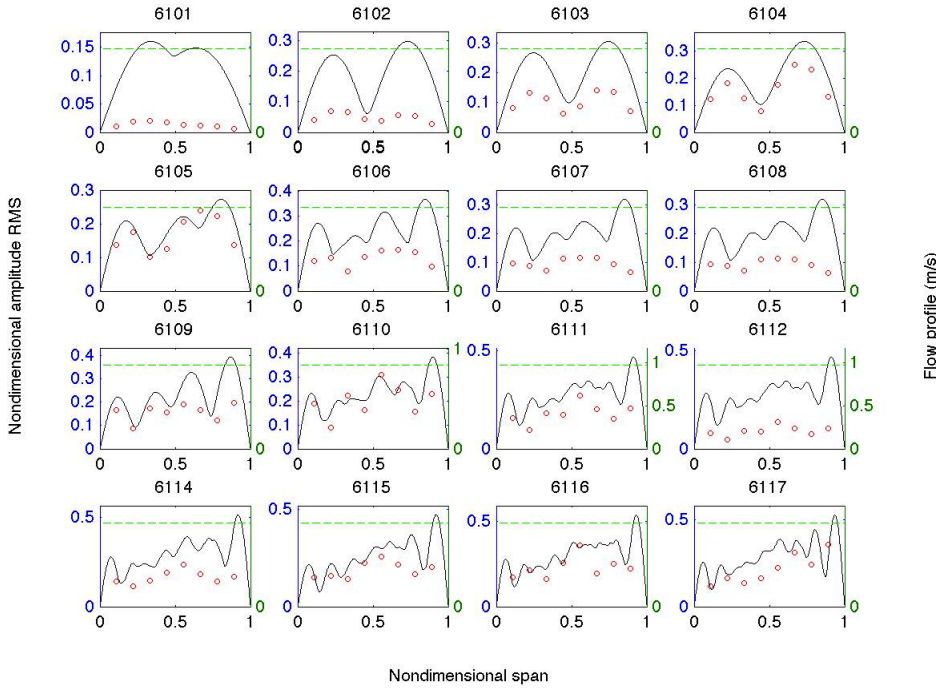

Figure 4-28: VIV RMS amplitude (A/D) versus length (x/L) comparison between VIVA prediction and experimental data; VIVA prediction (continuous line), experimental data (circles). Current profile in green dotted line. NDP 10m 50% strake riser in uniform flow.

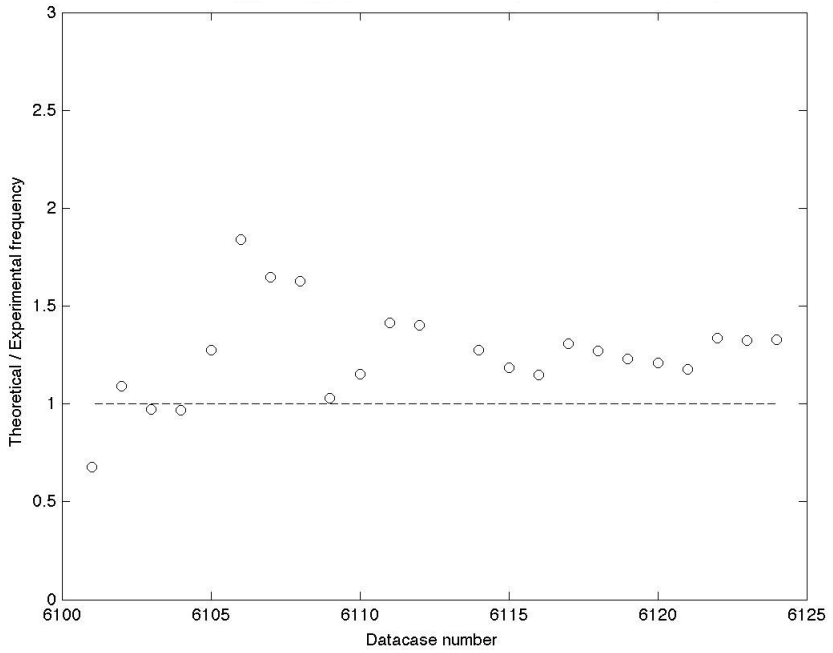

Figure 4-29: Ratio of VIV dominant frequency of VIVA prediction. NDP 10m 50% strake riser in uniform flow.

Figure 4-30 provides the predicted RMS amplitude of response along the riser length for NDP 10m 50% strake riser in sheared flow. The corresponding ratio of VIV dominant frequency predicted by VIVA and measured by experimental is given in Figure 4-31.

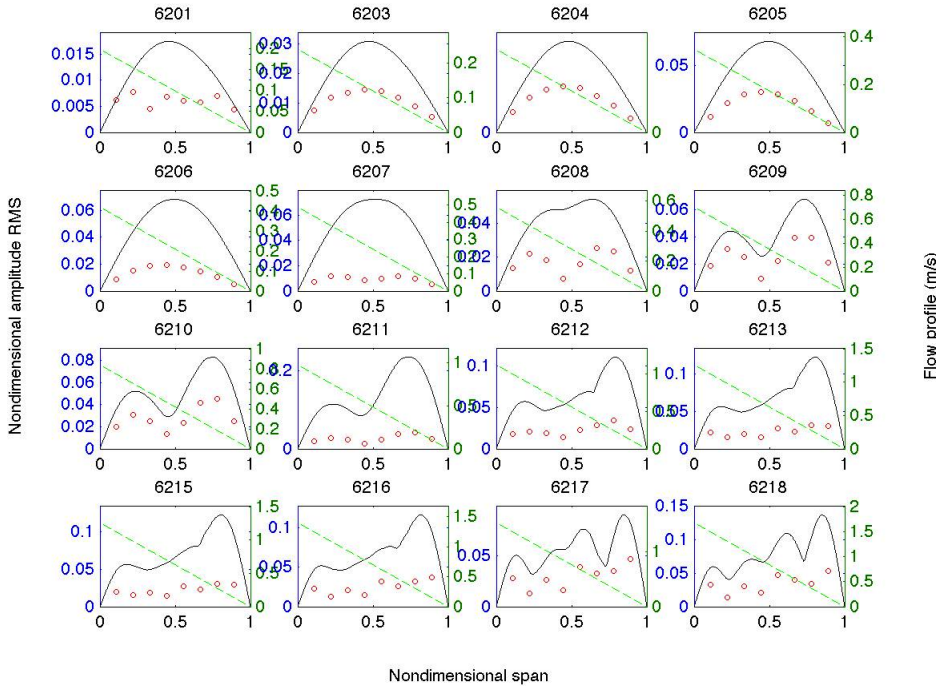

Figure 4-30: VIV RMS amplitude (A/D) versus length (x/L) comparison between VIVA prediction and experimental data; VIVA prediction (continuous line), experimental data (circles). Current profile in green dotted line. NDP 10m 50% strake riser in sheared flow.

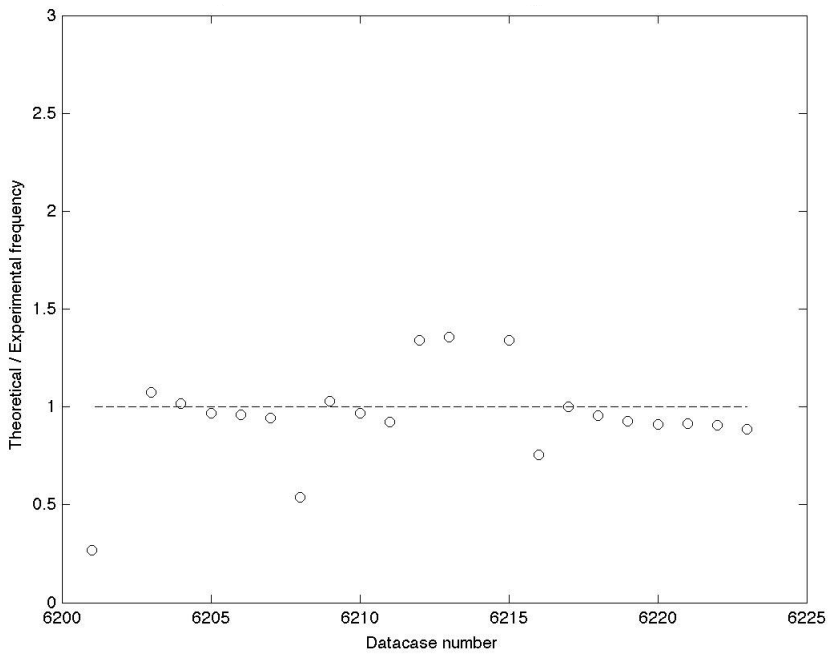

Figure 4-31: Ratio of VIV dominant frequency of VIVA prediction. NDP 10m 50% strake riser in sheared flow.

Figure 4-32 provides the predicted RMS amplitude of response along the riser length for NDP 10m 75% strake riser in uniform flow. The corresponding ratio of VIV dominant frequency predicted by VIVA and measured by experimental is given in Figure 4-33.

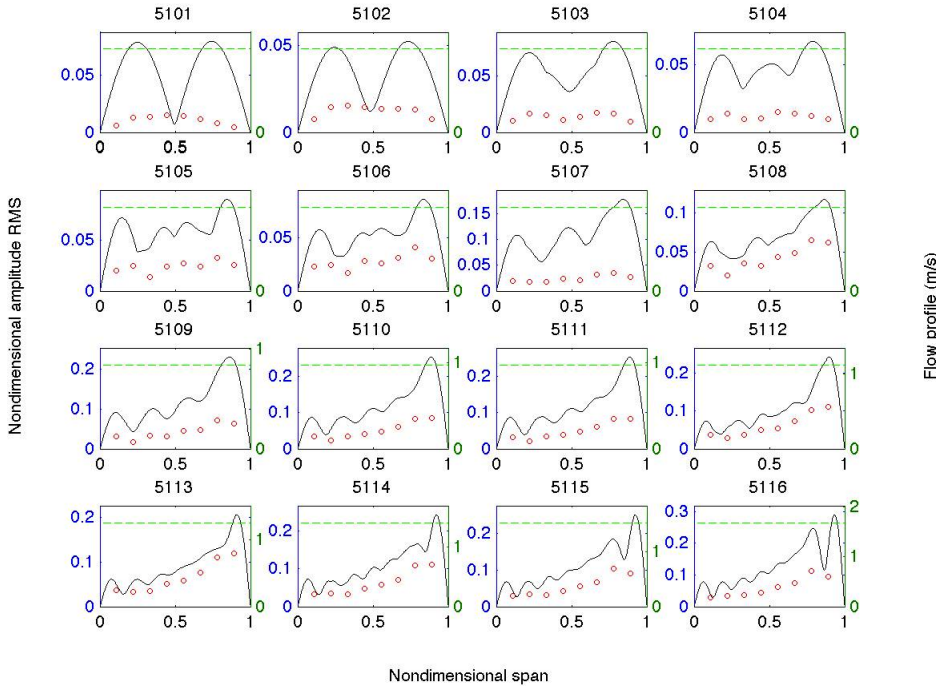

Figure 4-32: VIV RMS amplitude (A/D) versus length (x/L) comparison between VIVA prediction and experimental data; VIVA prediction (continuous line), experimental data (circles). Current profile in green dotted line.NDP 10m 75% strake riser in uniform flow.

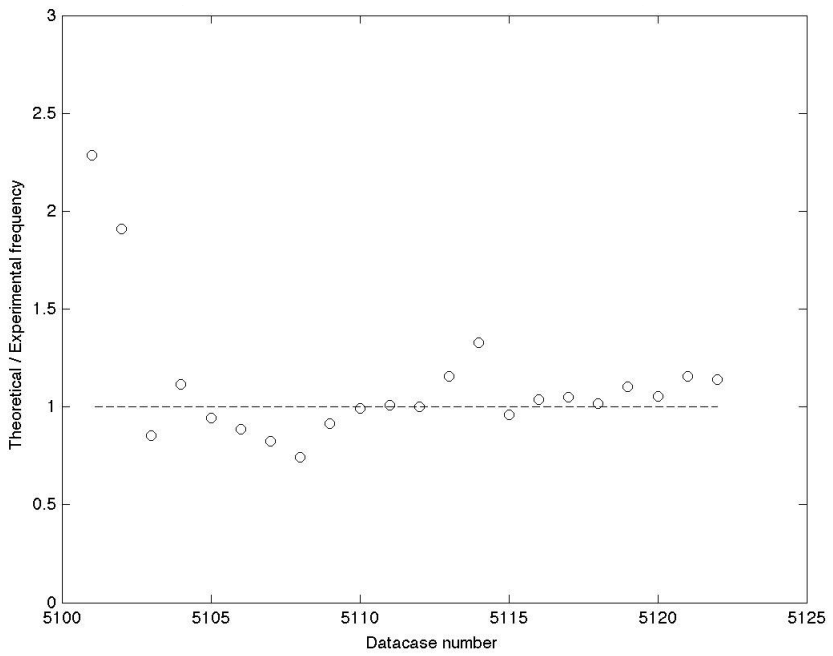

Figure 4-33: Ratio of VIV dominant frequency of VIVA prediction. NDP 10m 75% strake riser in uniform flow.

Figure 4-34 provides the predicted RMS amplitude of response along the riser length for NDP 10m 75% strake riser in sheared flow. The corresponding ratio of VIV dominant frequency predicted by VIVA and measured by experimental is given in Figure 4-35.

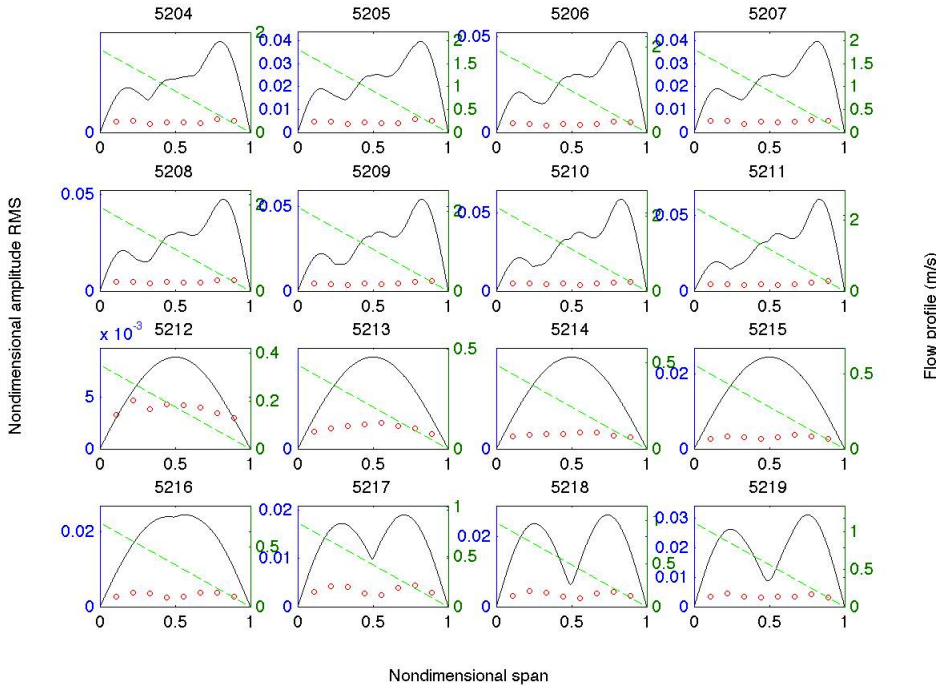

Figure 4-34: VIV RMS amplitude (A/D) versus length (x/L) comparison between VIVA prediction and experimental data; VIVA prediction (continuous line), experimental data (circles). Current profile in green dotted line. NDP 10m 75% strake riser in sheared flow.

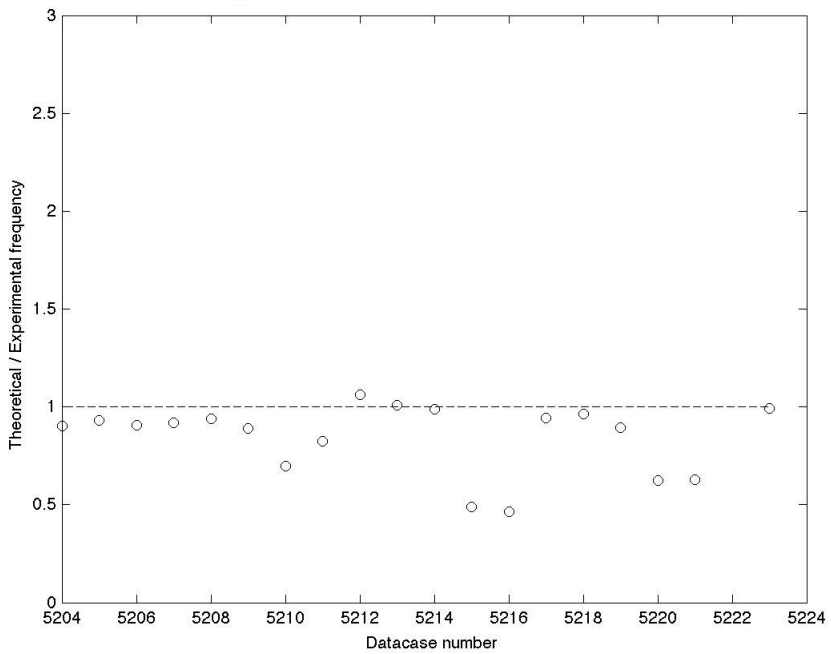

Figure 4-35: Ratio of VIV dominant frequency of VIVA prediction. NDP 10m 75% strake riser in sheared flow.

4.5.4 Miami Experiment

Figure 4-36 , Figure 4-37 and Figure 4-38 provide the predicted RMS strain of response along the riser length from Miami field experiments [77].

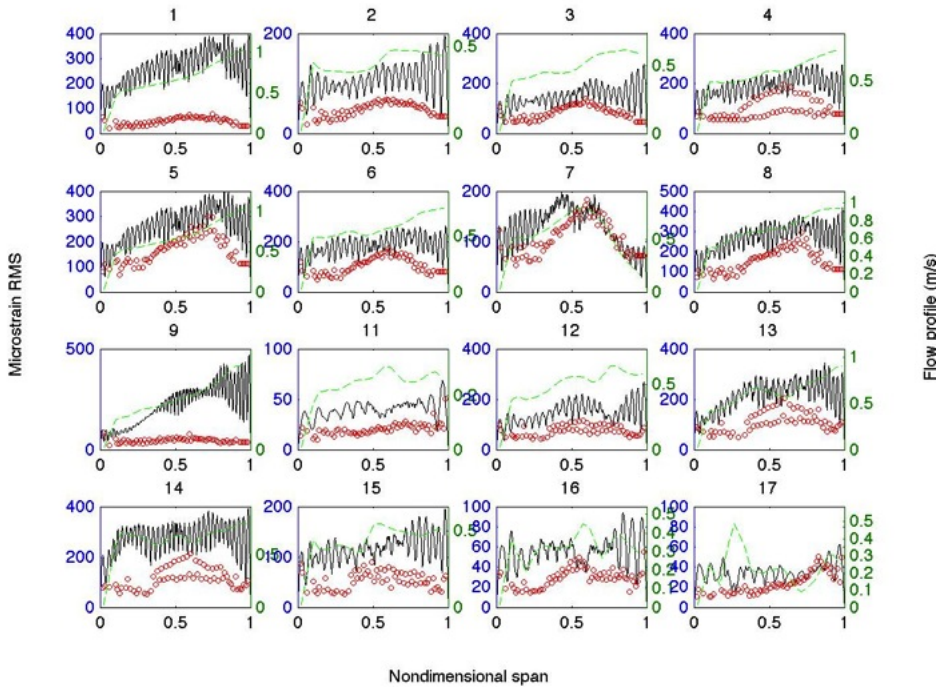

Figure 4-36: VIV RMS strain versus length (x/L) comparison between VIVA prediction and experimental data; VIVA prediction (continuous line), experimental data (circles). Current profile in green dotted line. Miami field experiment bare riser.

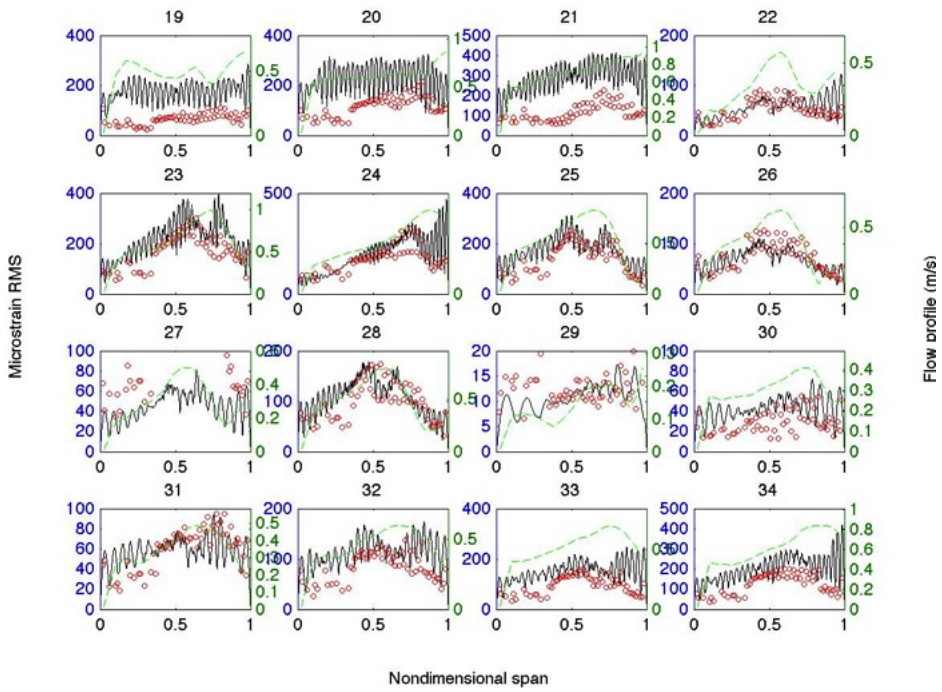

Figure 4-37: VIV RMS strain versus length (x/L) comparison between VIVA prediction and experimental data; VIVA prediction (continuous line), experimental data (circles). Current profile in green dotted line. Miami field experiment bare riser (continued).

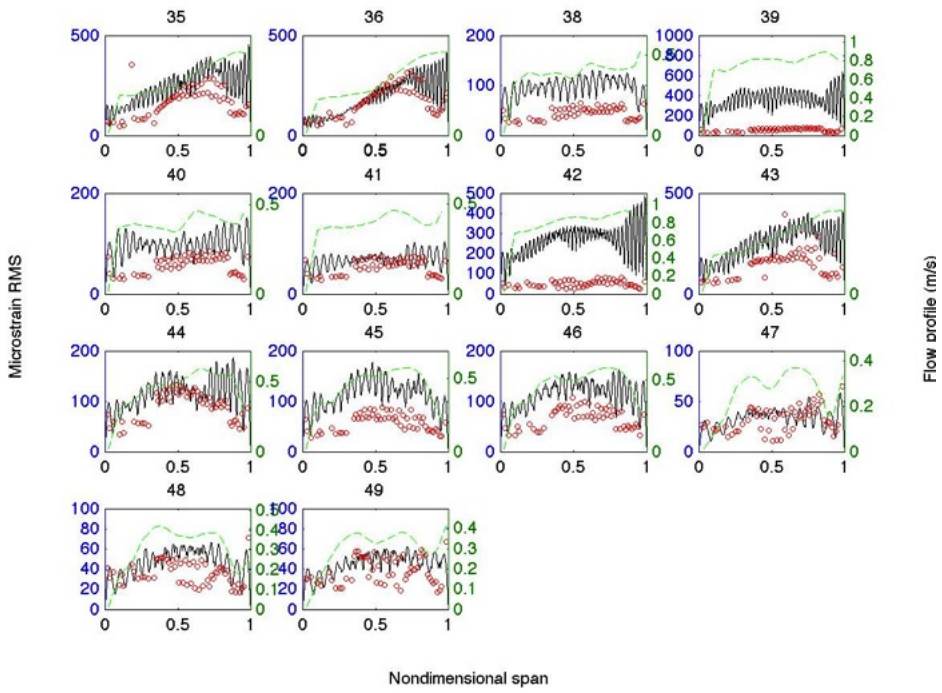

Figure 4-38: VIV RMS strain versus length (x/L) comparison between VIVA prediction and experimental data; VIVA prediction (continuous line), experimental data (circles). Current profile in green dotted line. Miami field experiment bare riser (continued).

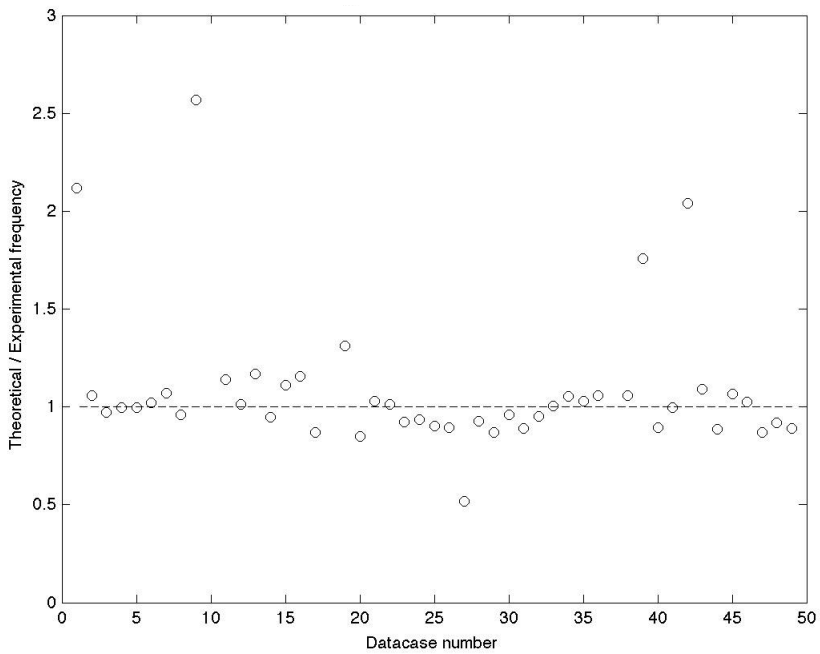

Figure 4-39: Ratio of VIV dominant frequency of VIVA prediction. Miami field experiment bare riser.

Figure 4-40 provides the predicted RMS strain of response of a riser with 40% strakes from Miami field experiments [77].

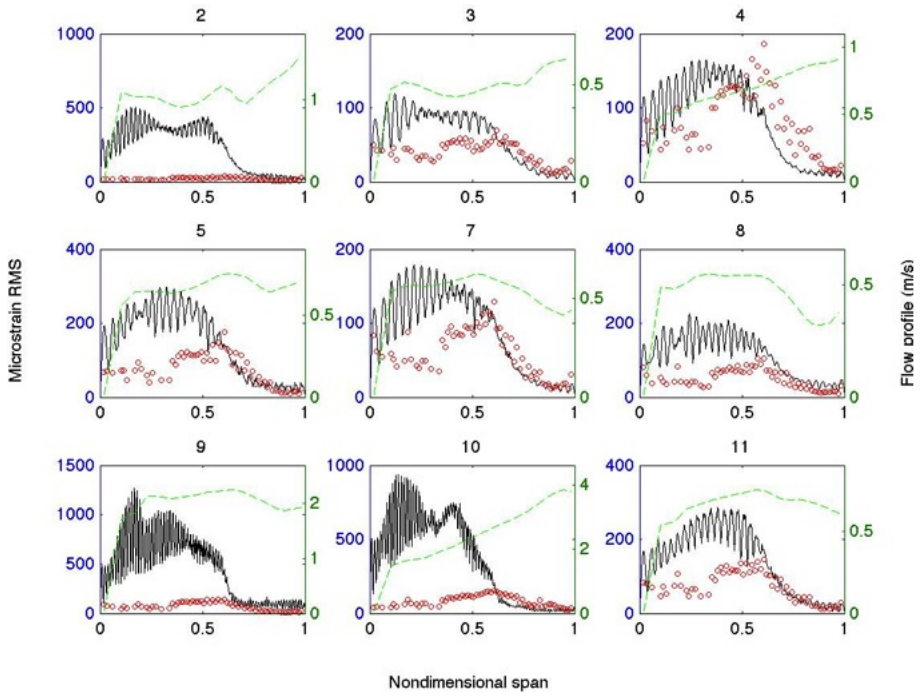

Figure 4-40: VIV RMS strain versus length (x/L) comparison between VIVA prediction and experimental data; VIVA prediction (continuous line), experimental data (circles). Current profile in green dotted line. Miami field experiment 40% strake riser.

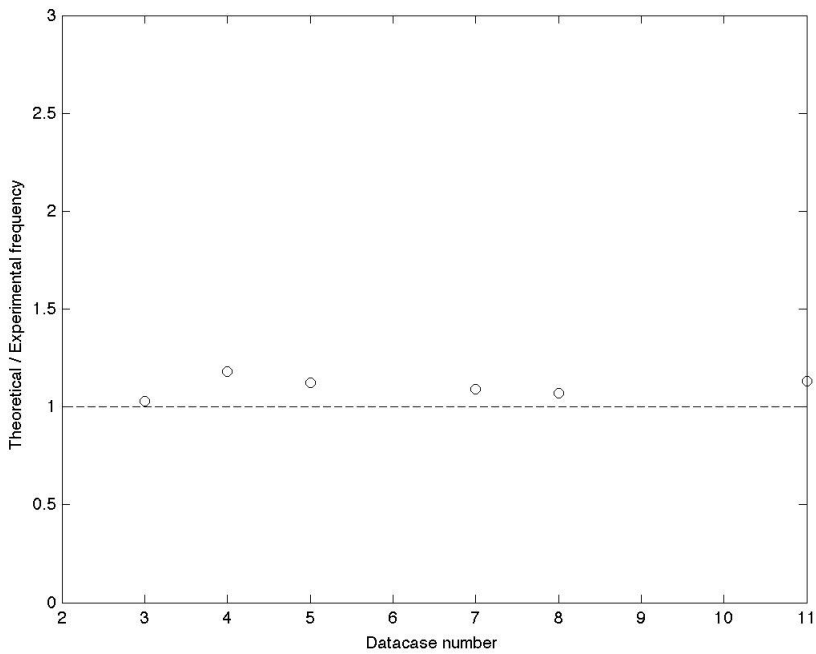

Figure 4-41: Ratio of VIV dominant frequency of VIVA prediction. Miami field experiment 40% strake riser.

4.6 Conclusions

In this chapter, the basic assumptions and working hypotheses employed in the program VIVA - a code developed to calculate the amplitude and the frequency of response, stress, and fatigue damage along the length of a multi-segment riser in sheared flow - is presented. The basic hypothesis is that strip theory can be employed, using data from laboratory databases, combined with a correlation length model, based on wake capture region data from the laboratory. The original database was developed by Gopalkrishan [28] for cylinders at Reynolds number 10,000. Data-mining procedures allowed the identification of trends and quantitative information from field and experimental data. These resulted in the development of new databases for bare and straked cylinders as presented in Figures 4-5 and 4-6. Various VIVA predictions versus lab and field experimental data are presented and the results are consistent.

Chapter 5

Inline VIV Prediction

Vortex-Induced Vibration has been an intensively studied field in the past 30 years; however the significant influence of the inline motion on fluid forcing and stress harmonics has long been ignored until recently, owing to low observed inline amplitudes [44, 85]. In this chapter, the inline VIV response was studied using a semi-empirical method for both the rigid cylinder and the flexible cylinder. An inline hydrodynamics coefficients database was built from a forced pure inline vibration experiment in the tow tank. The elastically mounted rigid cylinder VIV model was extended to the inline direction and VIVA, a widely used program to predict flexible cylinder VIV, was expanded from the crossflow response to the inline response. The expansion of the response prediction capabilities was achieved by including a pure inline hydrodynamic coefficients database, obtained through a series of pure inline forced VIV experiments on a rigid cylinder.

5.1 Methodology

The free vibration of a rigid cylinder that is elastically mounted demonstrates a response that can be divided into three regions, as shown in Figure 5-1 : (i) At reduced velocities less than 4, inline motion is dominant, (ii) if the reduced velocity is larger than 8, the crossflow motion is dominant, and (iii) when the reduced velocity is between 4 and 8, there is a strong coupling effect between the inline and crossflow

vibrations. Thus we will use different hydrodynamic databases to predict VIV motion depending on the dominant reduced velocity, namely the pure inline database, the pure crossflow database, and the inline-crossflow coupled database, corresponding to the regions discussed above.

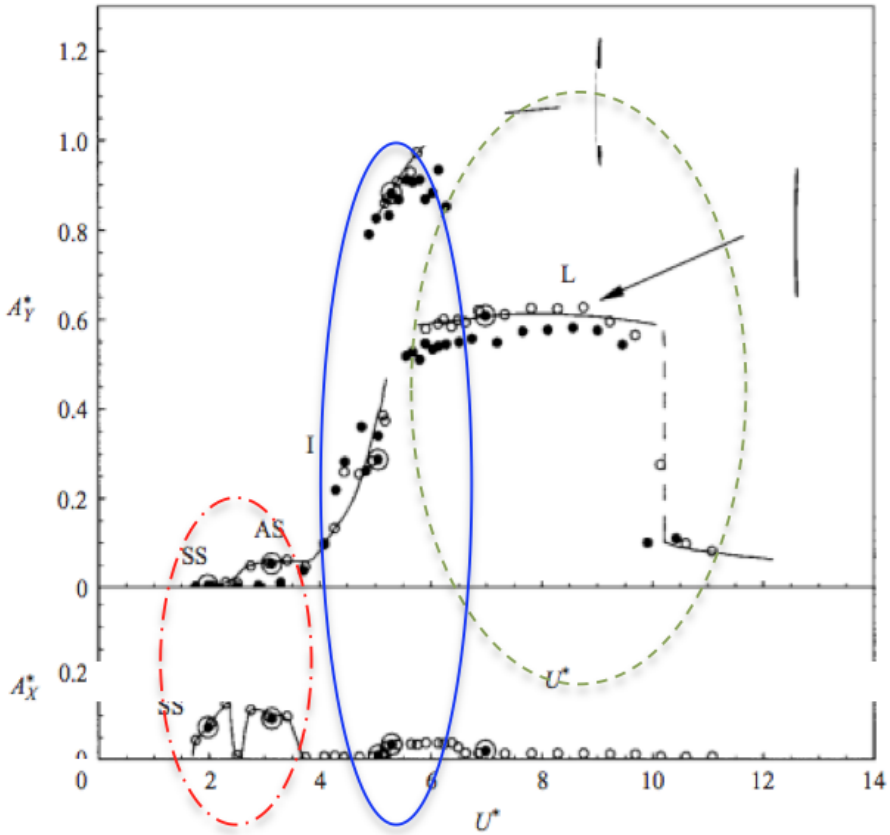

Figure 5-1: VIV response regions, crossflow motion dominant region is marked with – on the right, Inline-Crossflow motion region is marked by in the middle and Inline motion dominant region is marked by -.- on the left. (figure altered from Jauvtis and Williamson [32])

Two very important working hypotheses were extended to inline VIV study from past crossflow VIV research: (i) using the hydrodynamic force coefficients from forced vibration experiment to predict free vibration response, and (ii) applying strip theory to model flexible cylinder response through a series of rigid cylinder sections. Therefore, a pure inline hydrodynamic coefficients database, obtained through pure inline forced VIV experiments on a rigid cylinder, is the key to studying of pure inline VIV.

5.2 Pure Inline VIV Experiment

In order to produce a database for the inline hydrodynamic forces, a series of forced VIV tests were conducted in a small towing tank at MIT. The tank is 2.4 m long, 0.9 m wide, and 0.64 m deep. It is filled with clear, deionized water while a small towing carriage rides along the top of the tank. Figure 5-2 shows a photo of the tank with the carriage. The carriage traverse holds two linear motors that are used to force cylinder motions both in the transverse and inline directions.

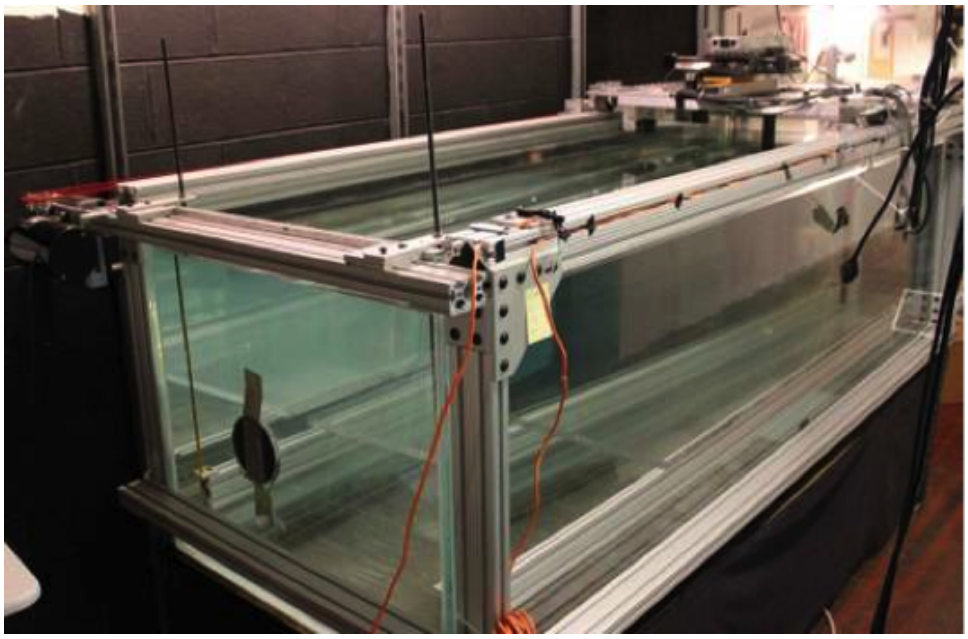

Figure 5-2: MIT small towing tank.

5.2.1 Pure Inline VIV Experiment Design

A six-axis sensor is located on a cantilevered arm connecting the linear motors and the test cylinder and is used to measure forces on the cylinder. A six-axis calibration was performed to correct voltage measurements based on the large moments exerted on the cantilevered test cylinder. The test cylinder, with a diameter of 0.038 m and a wetted span length of 0.64 m, is mounted vertically and extends the entire depth of the towing tank. The tests were conducted following the matrix shown in Figure 6-3 with finer grids at low frequency and amplitude. The Reynolds number (Re) of

the test is 7600.

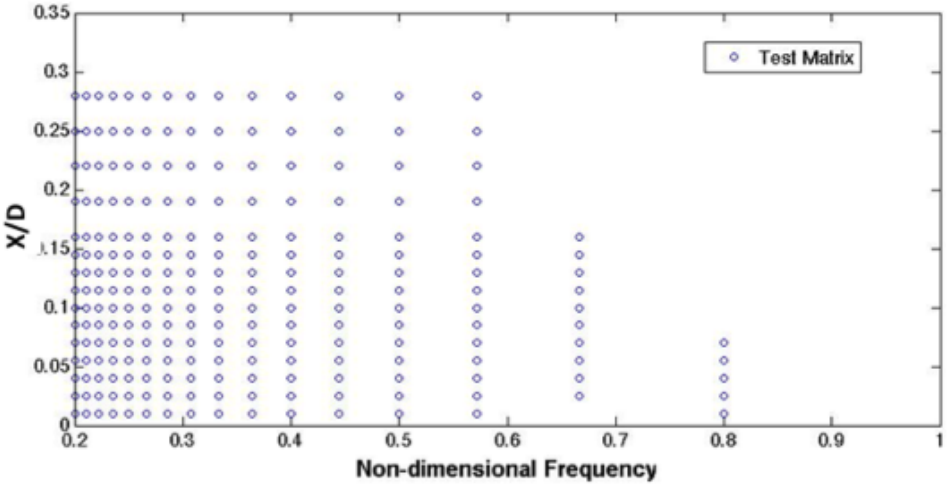

Figure 5-3: Test Matrix.

Figure 5-4 shows a sample of experimental signals. The blue signal is the velocity of the carriage, which represents the relative motion of the current to the cylinder. Two clear jumps observed at the beginning and end of the signal indicate the duration of the experiment. The pink vertical lines indicate the section of signal that is stable and consequently used for hydrodynamic coefficients extraction. The signal in black is the measured linear motor position based on the motor encoder reading. The green signal is force in the inline direction measured from force sensor mounted on the cylinder.

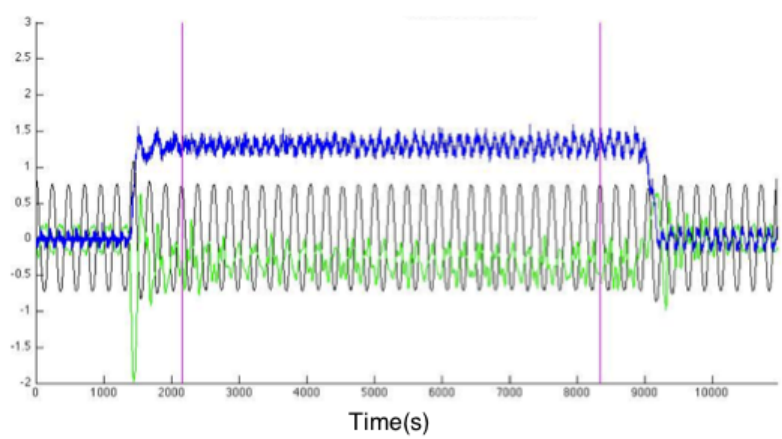

Figure 5-4: Samples of experimental signals.

The experimental data processing diagram is shown in Figure 5-5. The starting point of the signal is determined through the carriage velocity and the linear motor motion, and a Butterworth filter is employed to filter measurement drifting and high frequency noise. After the stable section of force measurement is identified, the data is trimmed and scaled to calculate the lift and drag coefficients.

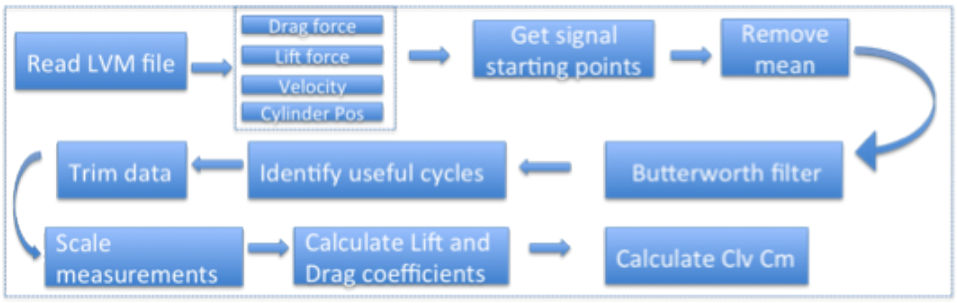

Figure 5-5: Experiment data processing diagram

The resulting added mass coefficients versus the amplitude of inline oscillations and the reduced velocity are shown in Figure 5-7.

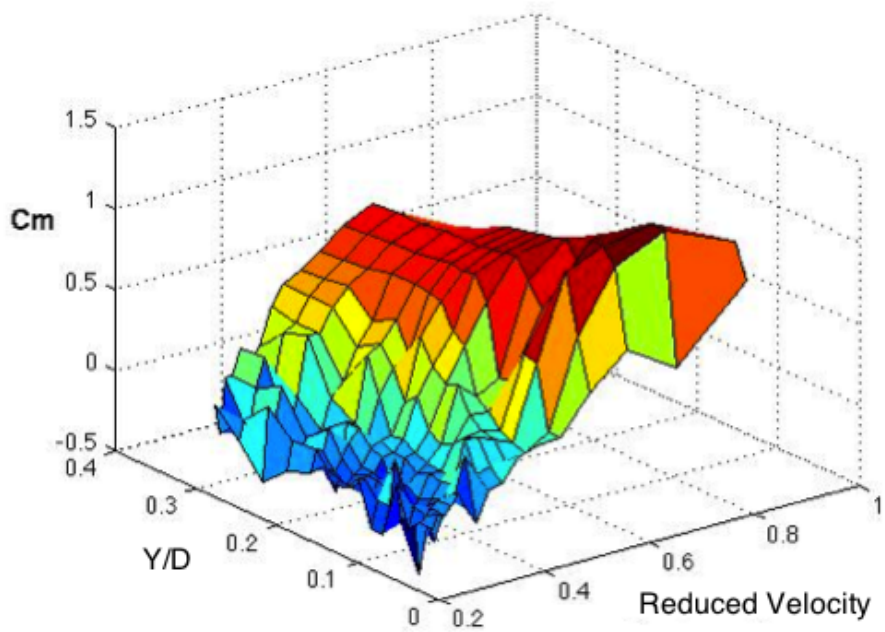

Figure 5-6: Original added mass coefficients (C_m) for pure inline oscillations.

The smoothed added mass coefficients are given in Figure 5-7, and it can be

observed that they are more a function of reduced velocity and that the influence of oscillation amplitude is limited. This observation is consistent with the trend of crossflow added mass coefficients.

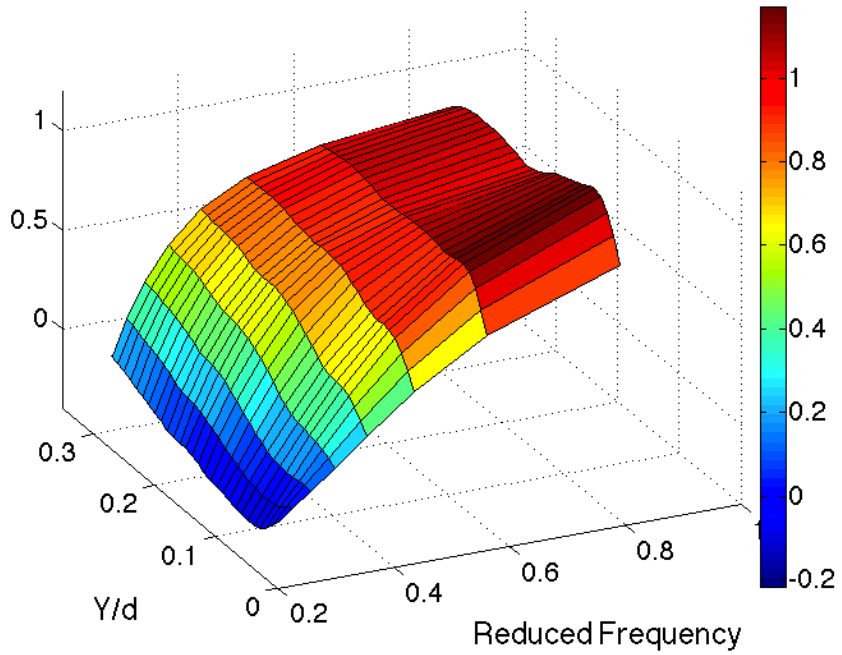

Figure 5-7: Smoothed added mass coefficients (C_m) for pure inline oscillations.

The resulting excitation coefficients in phase with velocity versus the amplitude of the inline oscillations and the reduced velocity are shown in Figure 5-8.

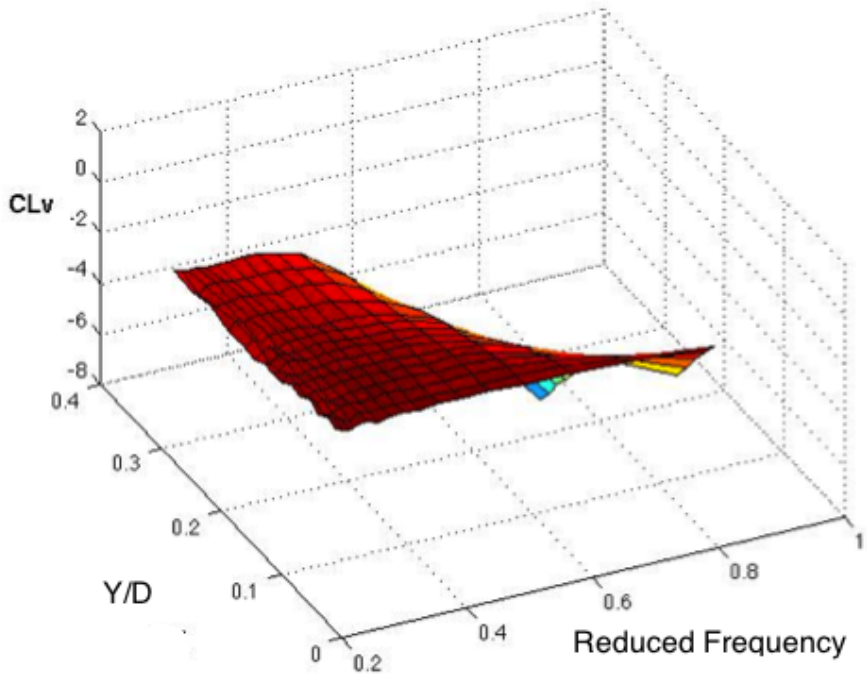

Figure 5-8: Excitation coefficients in phase with velocity (C_{Dv}) for pure inline oscillations.

The positive part of the excitation coefficients in phase with velocity (C_{Dv}) for the pure inline oscillations is given in Figure 5-9.

The contour of excitation coefficients in phase with velocity (C_{Dv}) for pure inline oscillations are given in Figure 5-10

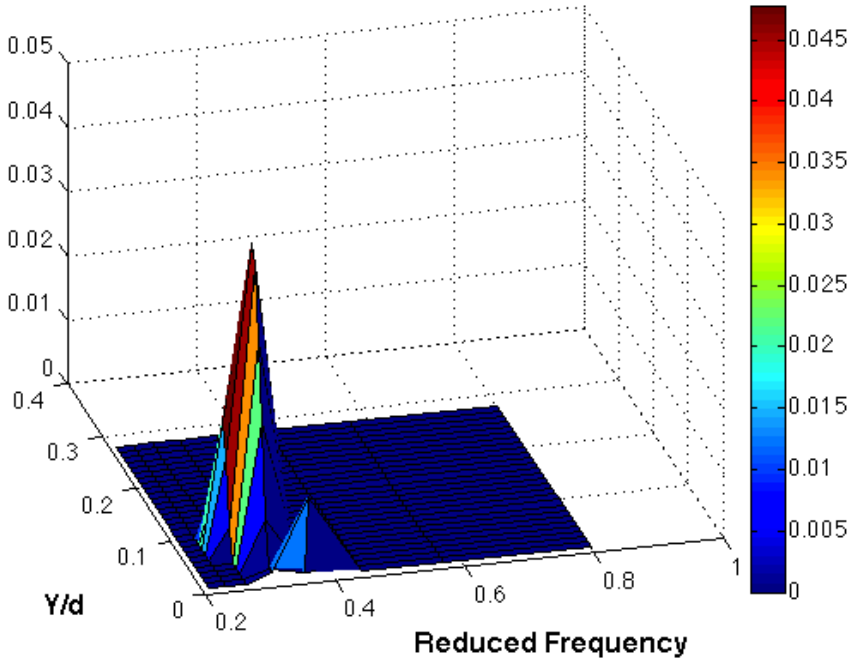

Figure 5-9: $C_{e,IL}$ in 3D zoomed at positive part.

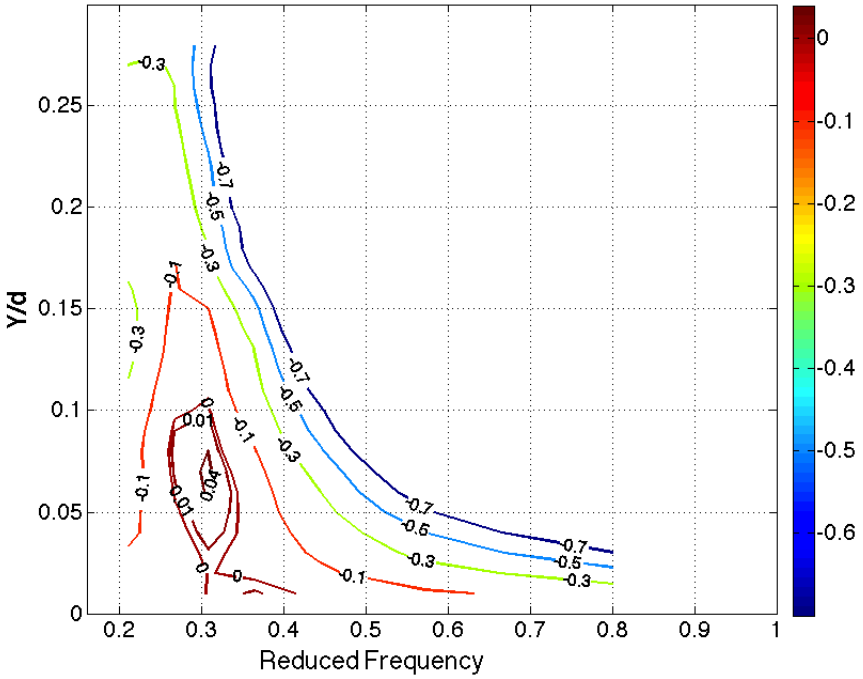

Figure 5-10: Contour plot of excitation coefficients in phase with velocity (c_{Dv}) for pure inline oscillations.

5.2.2 Comparison with Higher Re Pure Inline Database

While the hydrodynamic coefficients from the pure in-line rigid cylinder forced vibration experiments in the last section are at a lower Reynolds number 7,600, Aronsen studied pure in-line rigid cylinder forced vibration experiments in his PhD thesis [1] and reported hydrodynamic coefficients at the higher Reynolds number 24,000 [2, 3]. His hydrodynamic coefficients are as shown in Figure 5-11 and Figure 5-12. A zoomed-in view on the positive part of the excitation coefficients is shown in Figure 5-13.

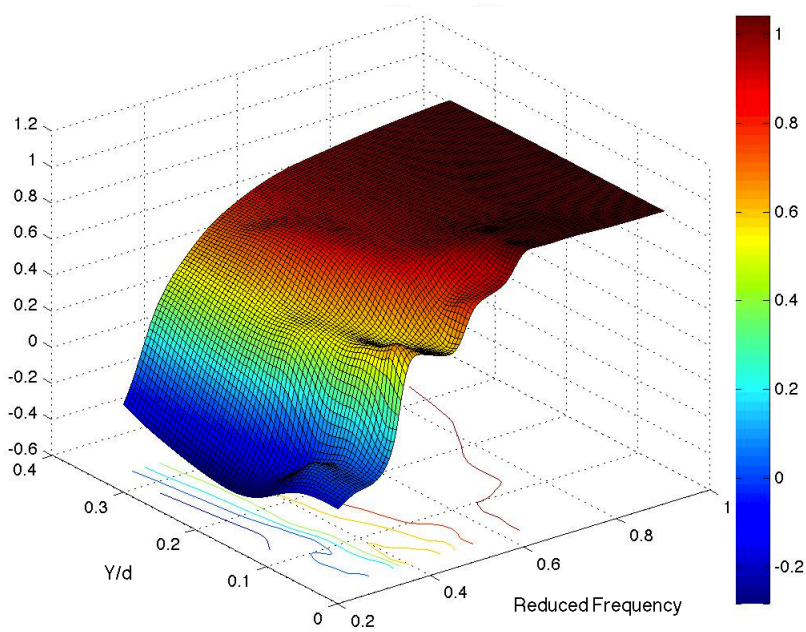

Figure 5-11: $C_{a,IL}$ in 3D regenerated from Aronsen [3] .

It can be observed that, compared with the higher Reynolds number experiment, the excitation coefficients in phase with velocity (C_{Dv}) is relatively small and the excitation region is also smaller. On the other hand, the shape of added mass coefficients are very close.

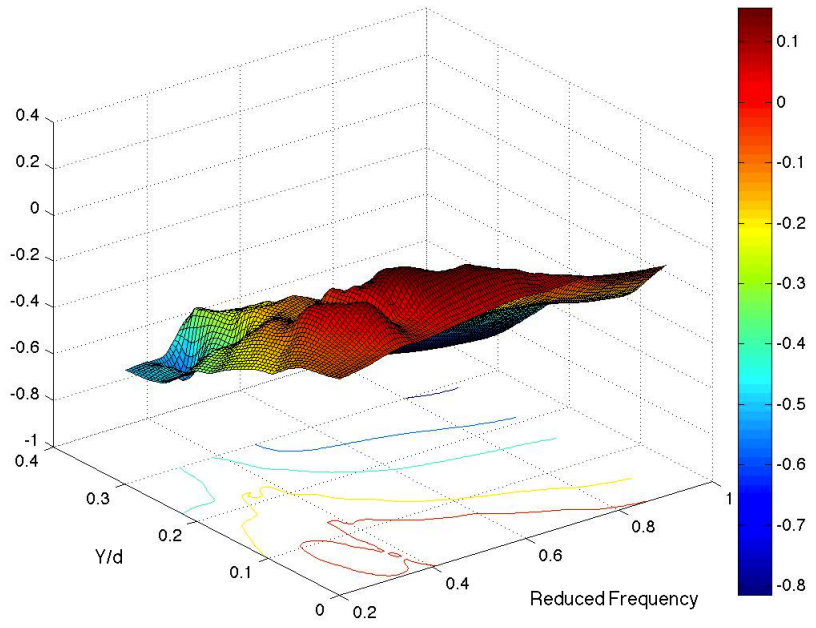

Figure 5-12: $C_{e,IL}$ in 3D regenerated from Aronsen [3].

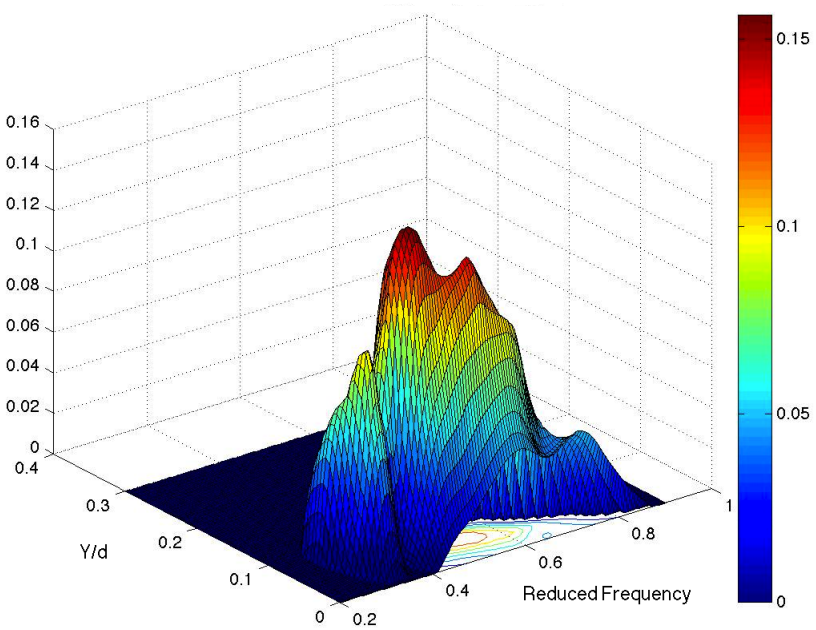

Figure 5-13: $C_{e,IL}$ in 3D zoomed-in at positive part, regenerated from Aronsen [3].

5.3 Inline Rigid Cylinder VIV Prediction

The experimental database of force coefficients is first used to predict the response of an elastically mounted, rigid cylinder. The governing equation of a rigid cylinder [57] of mass, m, mounted on springs with spring constant, k, and dashpots with damping constant, b, under a uniform current of velocity U is

$$m_x\ddot{x} + b_x\dot{x} + k_x x = D_f \tag{5.1}$$

where

$$D_f(t) = Re\left\{(m_{a,IL}A_x(2w)^2 + i_{fv,IL}\frac{\rho_f U^2 DL}{2})e^{i(2wt-\theta)}\right\} \tag{5.2}$$

The hydrodynamic force is decomposed into two terms: one in phase with velocity and one in phase with acceleration (added mass force). The excitation coefficient in phase with velocity $C_{fv,IL}$ and added mass coefficient $C_{a,IL}$ are defined as

$$C_{fv,IL} = \frac{D_f sin(\phi)}{\rho_f U^2 DL/2} \tag{5.3}$$

$$C_{m,IL} = -\frac{D_f cos(\phi)}{\rho_f \pi U^2 L A_w^2/4} \tag{5.4}$$

where F_0 is the magnitude of the hydrodynamic force, f is the density of the fluid, D is diameter of the cylinder, L is the span length of cylinder and A_w is the wet area. The lift and added mass coefficient values correspond to the experimentally obtained coefficients in the previous section.

5.3.1 Validation with Pure Crossflow Database

To validate the approach, the methodology was first applied to make predictions in the crossflow direction and the results are compared with pure crossflow experiment measurements from Smogeli [62].

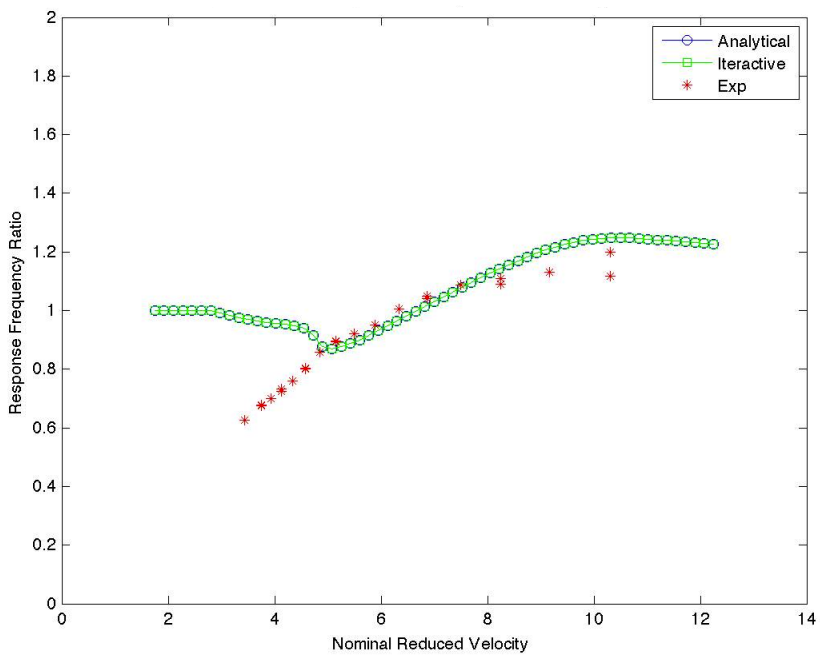

Figure 5-14: Response reduced velocity vs. nominal reduced velocity for a flexibly mounted rigid cylinder [62].

The resulting crossflow response of the cylinder is very similar to the freely vibrating crossflow response observed for a low mass-ratio cylinder allowed to move with crossflow motions.

The influence of the damping ratio on the response frequency and amplitude is given in Figure 5-17 and Figure 5-16. The damping ratio has a direct effect on the maximum amplitude that the cylinder can achieve as shown in 5-17. The larger the damping ratio, the smaller the amplitude. The damping ratio has no influence on the range of the response region. On the other hand, the damping ratio has no influence on the response frequency as indicated in 5-16, which was expected and consistent with previous study.

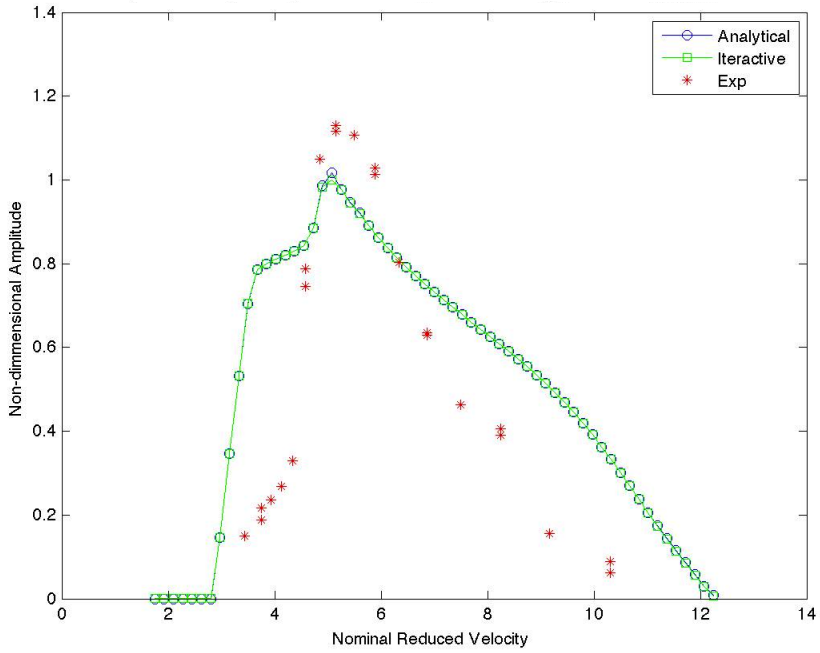

Figure 5-15: Nondimensional Amplitude of Oscillations vs. Reduced Velocity for a Flexibly Mounted Rigid Cylinder [62].

The influence of the mass ratio on the response frequency and amplitude is given in Figure 5-18 and Figure 5-19. The mass ratio has no effect on the maximum amplitude that the cylinder can achieve as shown in 5-17, but it has an influence on the range of the response region. The smaller the mass ratio, the larger the range of response region, as shown in 5-17. The mass ratio has a larger influence on the response frequency in the high reduced velocity region, as shown in Figure 5-19 .

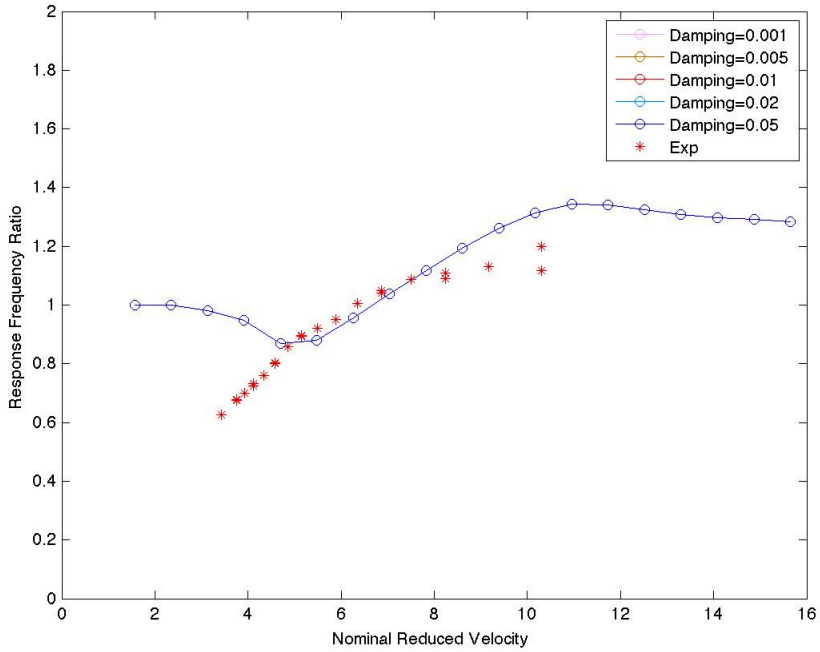

Figure 5-16: Response reduced velocity vs. nominal reduced velocity for a flexibly mounted rigid cylinder of different damping ratio.

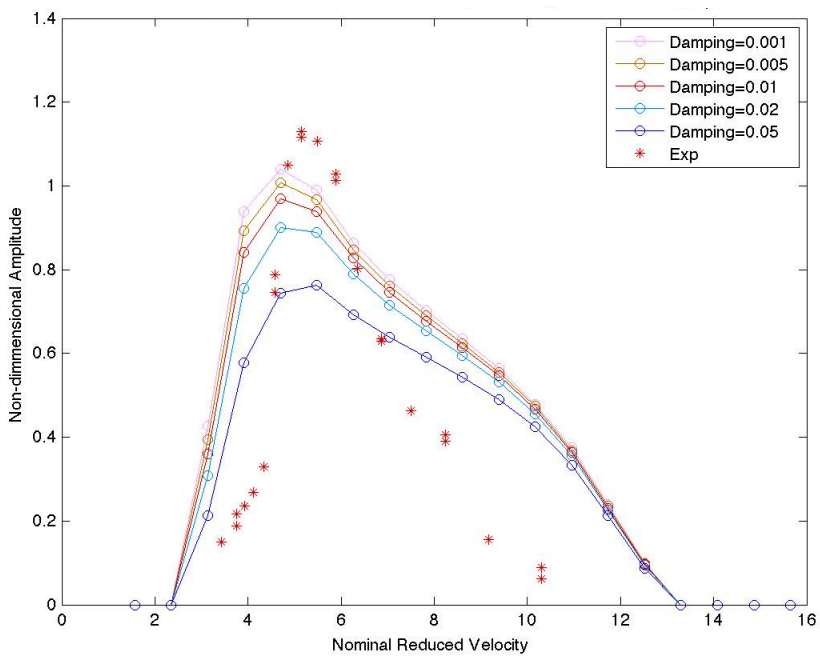

Figure 5-17: Nondimensional amplitude vs. nominal reduced velocity for a flexibly mounted rigid cylinder of different damping ratio.

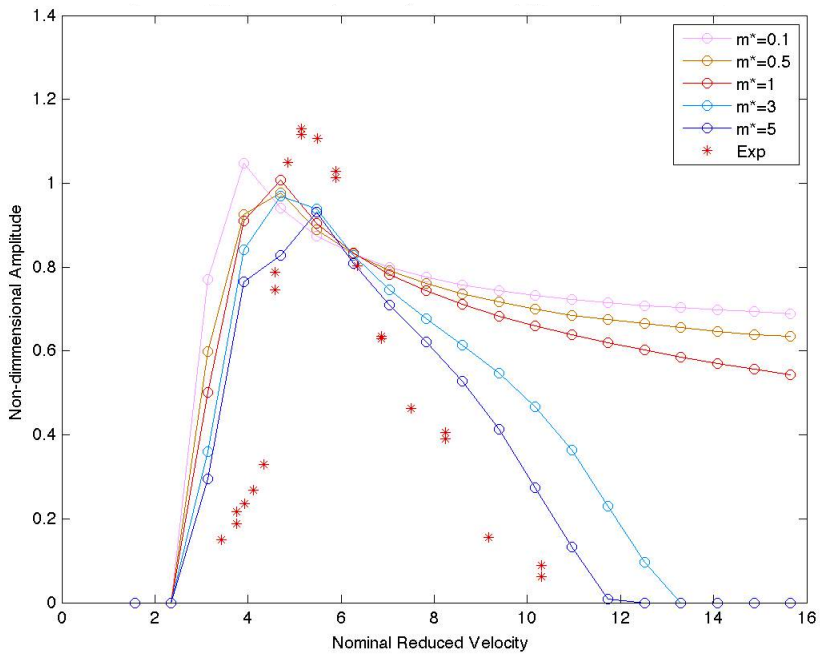

Figure 5-18: Nondimensional amplitude vs. nominal reduced velocity for a flexibly mounted rigid cylinder of different mass ratio.

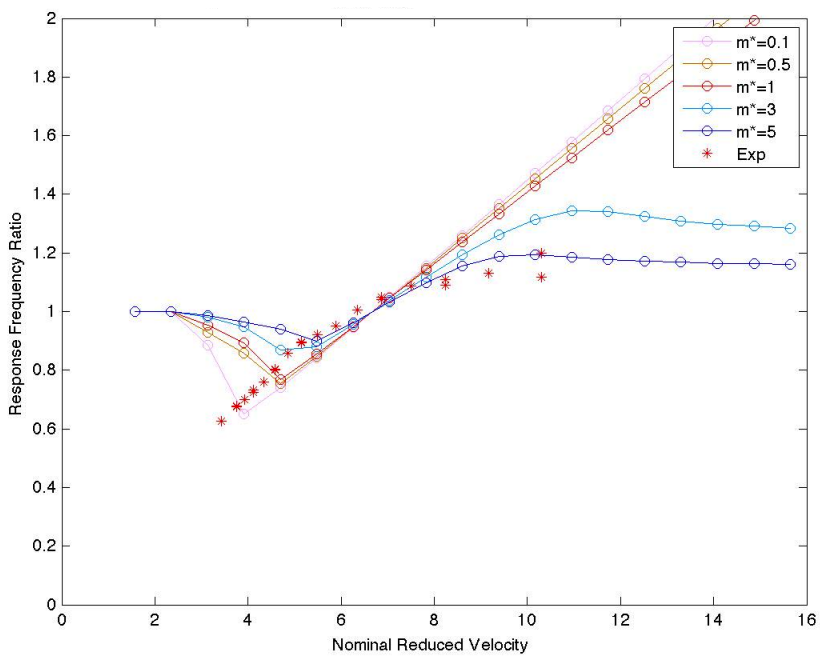

Figure 5-19: Response reduced velocity vs. nominal reduced velocity for a flexibly mounted rigid cylinder of different mass ratio.

A similar comparison is done with crossflow experiment results from Dahl [19]. The resulting crossflow response of the cylinder is very similar to the freely vibrating crossflow response observed for a low mass-ratio cylinder allowed to move with the crossflow motions.

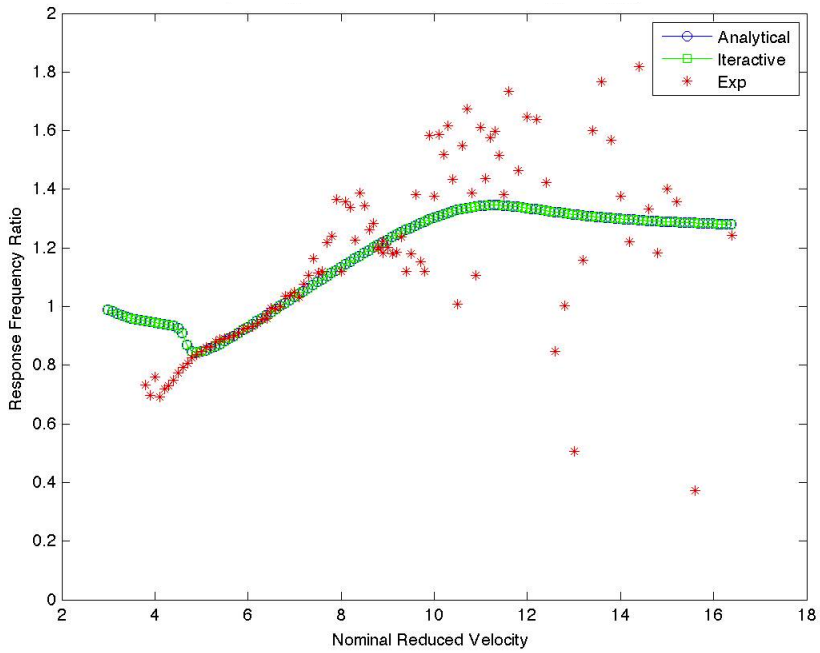

Figure 5-20: Response reduced velocity vs. nominal reduced velocity for a flexibly mounted rigid cylinder [19].

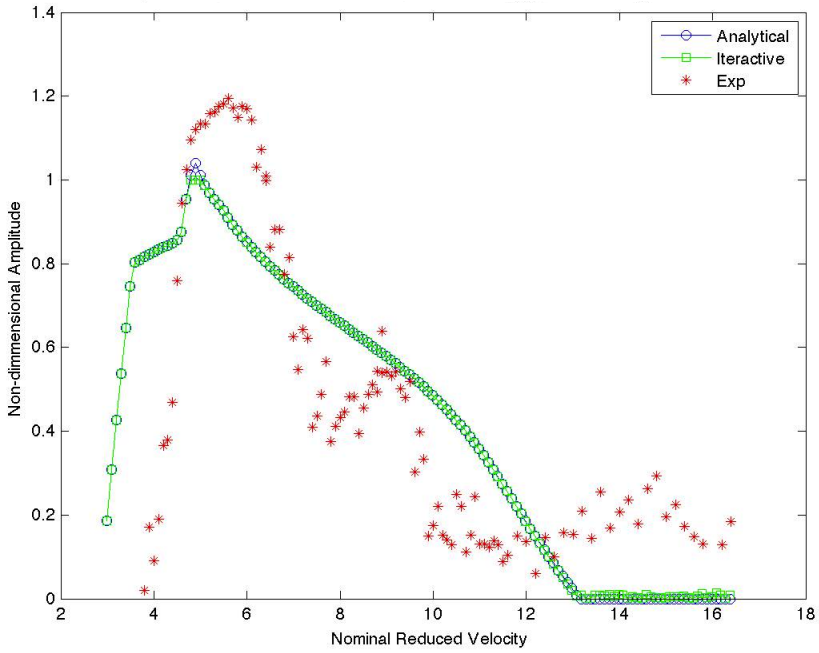

Figure 5-21: Nondimensional amplitude of oscillations vs. reduced velocity for a flexibly mounted rigid cylinder [19].

5.3.2 Prediction Comparison with Rigid Cylinder Free Vibration Experiment

Recently, Cagney and Balabani described two pure in-line free vibration experiments at the Reynolds number 450-3,700 [10]. The key experiment parameters are given in Table 5.1

Table 5.1: Cagney and Balabani 2013 free vibration experiment parameters [10]

Aspect Ratio	10
Length	0.071 m
Reynolds Number	450 to 3700
Flow Velocity	0.06 to 0.52 m/s
Mass Ratio	1.17
Damping Ratio	0.0053
Damper Const	6.1e-3
Natural Frequency in Still Water	15.08 Hz
Spring Constant	54.763
Diameter	0.0071 m

The damping ratio is defined as:

$$\zeta = \frac{b}{4\pi m f_n} \tag{5.5}$$

where m is the mass of the cylinder, b is the damping constant of the dashpots and f_n is the natural frequency of system in still water.

The predicted response reduced velocity and amplitude for the flexibly mounted rigid cylinder setup of Cagney in the inline direction is plotted in Figure 5-22 and Figure 5-23. The predicted oscillation frequency is very close to the experimental measurements as can be observed in Figure 5-22. The shape of the response amplitude predicted by the program is similar to that of experimental data but the magnitude is a little lower as shown in Figure 5-23.

Considering the effects of Reynolds number [29], the predicted amplitude magnitude can be improved greatly, as shown in 5-24.

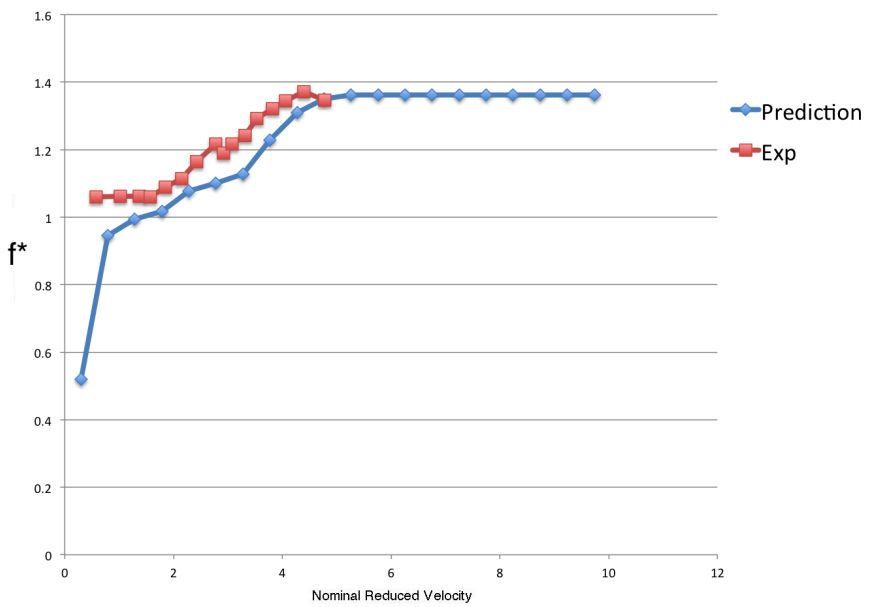

Figure 5-22: Oscillation frequency vs. reduced velocity for a flexibly mounted rigid cylinder.

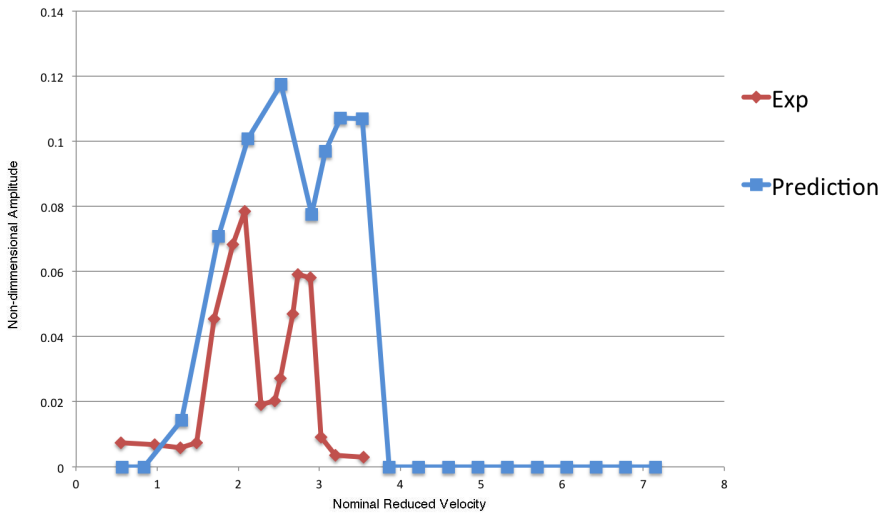

Figure 5-23: Nondimensional amplitude of the inline oscillations vs. reduced velocity for a flexibly mounted rigid cylinder.

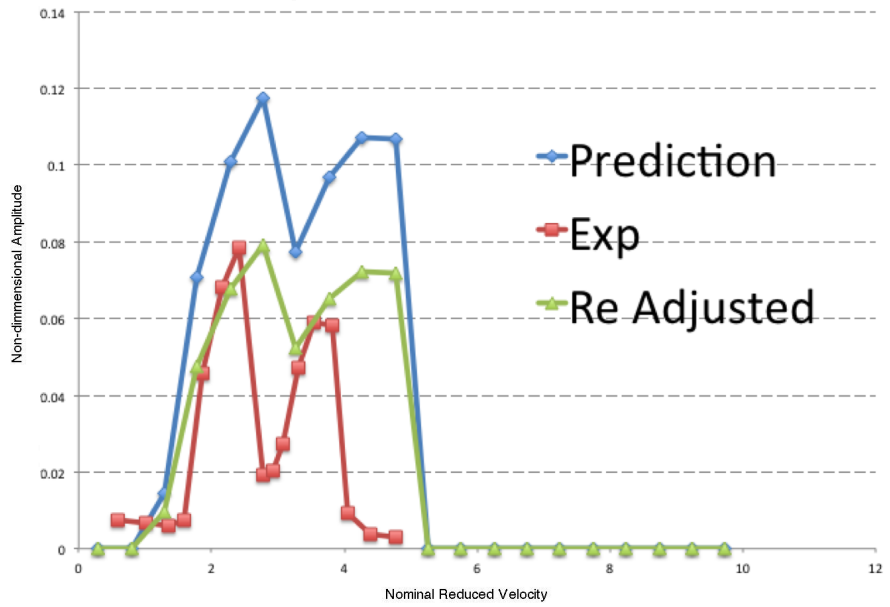

Figure 5-24: Nondimensional amplitude of the inline oscillations vs. reduced velocity for a flexibly mounted rigid cylinder adjusted for Reynolds number effects.

Previously King also reported two pure in-line free vibration experiments at Reynolds number 60,000 and 600,000 [36] and discussed the influence of Reynolds number in these two particular setups. The key experiment parameters are in Table 5.2

Table 5.2: King free vibration experiment parameters [36]

Aspect Ratio	71.1
Reynolds Number	60,000 or 600,000
Mass Ratio	0.6838
Damping Ratio	0.0107
Natural Frequency in Still Water	6.75 Hz
Diameter	0.0171 m
Length	1.2192 m

The damping ratio is defined as:

$$\zeta = \frac{b}{4\pi m f_n} \tag{5.6}$$

where m is the mass of the cylinder, b is the damping constant of the dashpots and f_n is the natural frequency of system in still water.

The predicted response amplitude for the flexibly mounted rigid cylinder setup of Cagney in the inline direction is plotted in Figure 5-25. The shape of the response amplitude predicted by the program is similar to that of experimental data but the magnitude is a little higher.

Considering the effects of Reynolds number [29], the predicted amplitude magnitude can be improved significantly, as shown in 5-26.

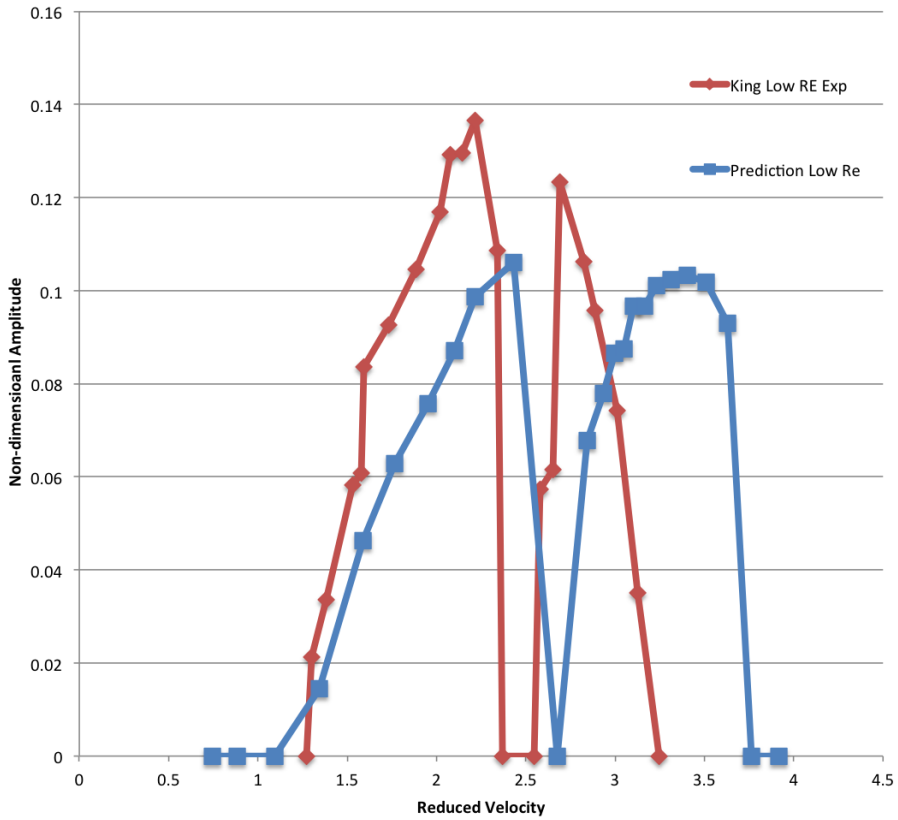

Figure 5-25: Nondimensional amplitude of the inline oscillations vs. reduced velocity for a flexibly mounted rigid cylinder.

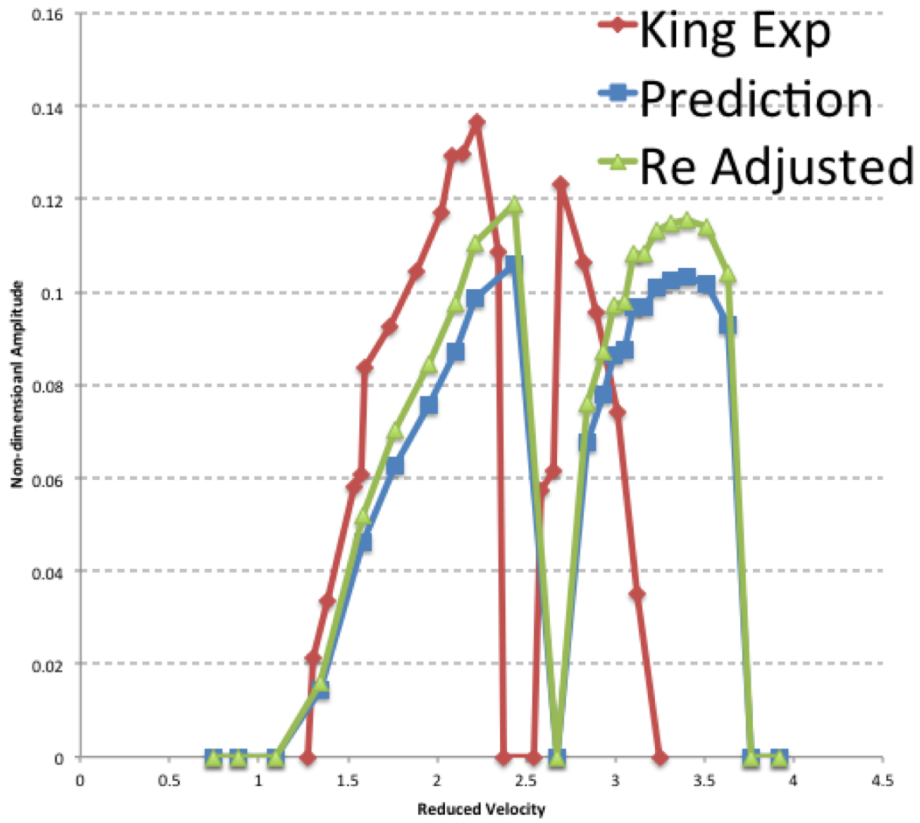

Figure 5-26: Nondimensional amplitude of the inline oscillations vs. reduced velocity for a flexibly mounted rigid cylinder adjusted for Reynolds number effects.

5.4 Inline Flexible Cylinder VIV Prediction using VIVA

The prediction program, VIVA, consists of two parts: (1) a fluid-structure interaction model and (2) laboratory-derived or empirical databases. The fluid-structure interaction model consists of a fluid force model and the equations of structural dynamics. The hydrodynamic databases primarily contain hydrodynamic information in the form of the excitation coefficients (excitation coefficient in phase with velocity and added mass coefficient) and drag coefficients. These force coefficients are often obtained from extensive laboratory experiments using a rigid cylinder.

Upon demonstrating that a purely inline database gives an expected response for an elastically mounted, rigid cylinder, VIVA is adapted to predict the vortex-induced vibrations of a flexible marine riser in the inline direction for low reduced velocities. VIVA uses a linear theory to describe structural oscillations since VIV oscillations have small amplitude relative to the length of the riser. The calculation of the response is done using a strip theory approximation, where the long riser is divided into a number of small sections over which the fluid forces acting on the riser are assumed to be the same as for an elastically mounted rigid cylinder. Using strip theory, the response is combined along the length to form the overall riser response. To simulate a long flexible cylinder, a linear, tensioned beam model is employed:

$$m\frac{\partial^2 x}{\partial t^2} + b\frac{\partial x}{\partial t} - \frac{\partial}{\partial z}(T\frac{\partial x}{\partial z}) + \frac{\partial}{\partial z^2}(T\frac{\partial^2 x}{\partial z^2}) = f(x, z, t) \tag{5.7}$$

where m is the mass per unit length of the structure; b is the structural damping; T is the tension; EI is the flexural rigidity; and f is the fluid load per unit length, which is a function of the motion of the structure.

5.4.1 Inline Hydrodynamic Coefficients Database to VIVA

The database for the IL oscillations is introduced to VIVA through 5 inputs that describe the shape of the surfaces defining the added mass and lift in phase with velocity as functions of the amplitude response and the reduced frequency (inverse of the reduced velocity). These input surfaces are shown in Figures 5-8 and 5-7. Since manipulating the complete 3D surfaces is computationally expensive, the surfaces are divided into cross-sections for various reduced frequencies which act as a standard input for VIVA. Figure 5-27 shows the five input functions, which describe the input surface for a particular cross-section. In general, for a constant amplitude of motion, the excitation coefficient in phase with velocity can be described by a point-wise linear function with an initial slope at low reduced frequencies, a transition point at a particular reduced frequency, and a second slope at higher reduced frequencies. For example in Figure 5-27, the following are shown from the top left:

a) C_{Dv} at zero nondimensional amplitude as a function of nondimensional frequency;

b) C_m at zero nondimensional amplitude as a function of nondimensional frequency;

c) the average slope of C_{Dv} for low reduced frequency indicated in a);

d) the average slope of C_{Dv} for high reduced frequency as indicated in a); and

e) the point where C_{Dv} reaches its maximum and transitions between the two linear slopes.

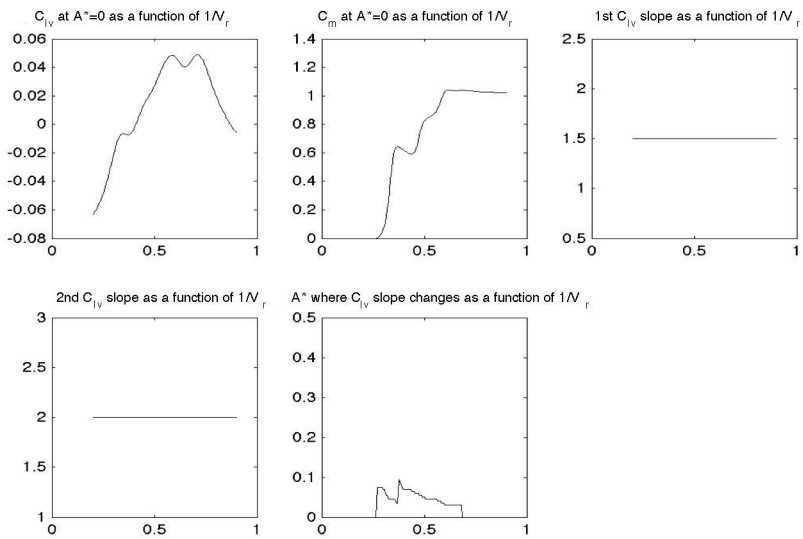

Figure 5-27: The inline hydrodynamic coefficients database input to VIVA.

5.4.2 Prediction Comparison with Flexible Cylinder Free Vibration Experiment

Prediction Comparison with NDP38 Inline Data

A prediction of the inline vibration of a flexible riser was made using the structural characteristics of a riser from the Norwegian Deepwater Programme (NDP) Riser High Mode VIV tests [9]. This allowed for a direct comparison between the prediction method and the observed vibrations from experiments. The experimental tests were conducted on a 38-meter riser with the characteristics shown in Table 3.1, and were kept under tension and towed horizontally at varying speeds with either uniform or sheared flow profiles. In the uniform flow cases, the flow velocity was varied from 0.3 to 2.2 m/s, in 0.1 m/s increments. Measurements of the in-line strain were taken at 40 points along the riser, while measurements of the cross-flow strain were taken at 24 points.

Figure 5-28 shows the ratio between the theoretical predicted dominant frequency of inline motion and the observed frequency of inline motion from experiments for a number of cases. The dotted line indicates the condition over which there is a perfect match between the predicted frequency and the observed experimental frequency. One can see that there is very good agreement between the predicted frequency and the observed frequency from experiments.

The amplitudes of the predicted and the observed VIV response in the inline direction are shown in Figure 5-29. The red circles represent the experimental data obtained from the NDP experiments at discrete locations and blue solid lines show the prediction from VIVA. In general, VIVA tends to underpredict the amplitude in the in-line direction. The inline amplitude is relatively small from the experimental cases, so the assumption used in the prediction method that there is no crossflow motion may have an impact on the resulting prediction of inline motion, since there are likely still coupling effects between the inline and crossflow response in this region.

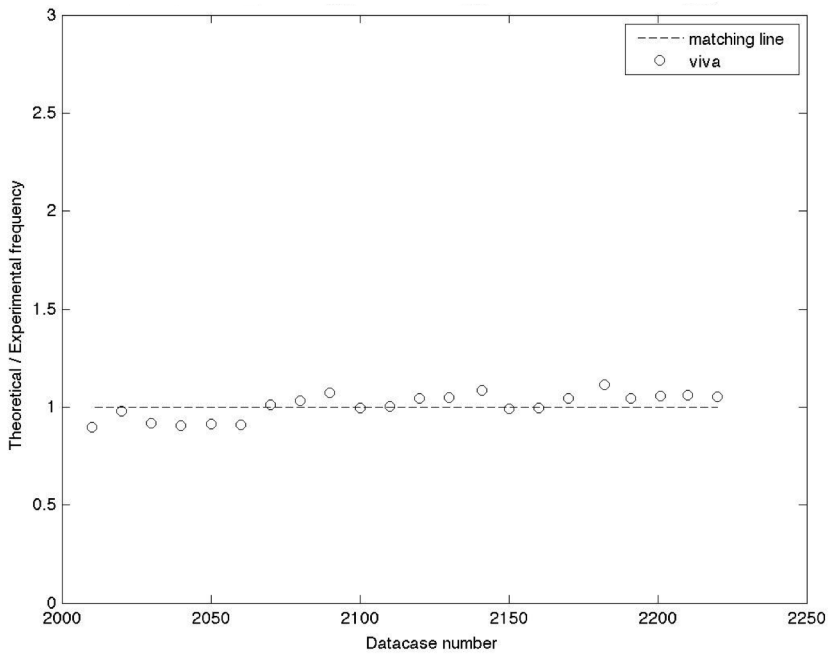

Figure 5-28: Inline VIVA predicted frequencies versus NDP 38m experimental values.

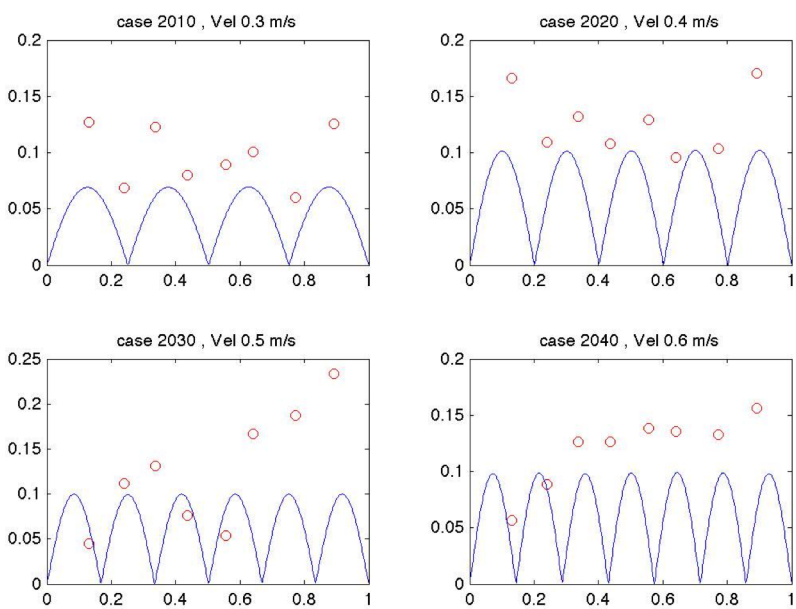

Figure 5-29: Inline VIVA predicted amplitude versus NDP 38m experimental values.

5.5 Conclusions

In this chapter, we address the coupled inline and crossflow VIV prediction through systematic modeling and extensive experiments. The ultimate goal is to include the inline prediction module to VIVA and extend its capabilities to predict the coupled crossflow-inline VIV of flexible cylinders. We conducted a series of experiments on a rigid cylinder forced to oscillate in the inline direction only and measured the excitation coefficient in phase with velocity and the added mass coefficient for various inline amplitudes and frequencies, and used these measurements to make a hydrodynamic database for the inline VIV. We used this database to predict the inline oscillation of a flexibly mounted rigid cylinder, and then extended this method to the case of a flexible cylinder and obtained reasonable agreement with the experimental results from the NDP tests.

Chapter 6

Inline-Crossflow VIV Prediction

After studying pure crossflow and pure inline Vortex Induced Vibrations in the previous two chapters, the coupled inline-crossflow VIV is addressed in this chapter. The inline motion is coupled with the crossflow motion and it triggers a third harmonic stress component in the crossflow direction, which has a significant influence on fatigue life. In this chapter, the problem of an elastically mounted rigid cylinder is systematically studied. Extensive forced inline and combined inline-crossflow experiments were employed to provide the hydrodynamic coefficient database, in addition to existing pure crossflow and pure inline hydrodynamic coefficients. Several important physical phenomena are found from the database and are studied. A coupled inline-crossflow VIV model of an elastically mounted rigid cylinder was built to predict the inline and crossflow motion and its coupling. Consequently, higher harmonic forces were predicted. Rigid cylinder free vibration experimental data were used to validate this prediction methodology.

6.1 High Resolution 2D Forced VIV Motion Experiment Design

An experimental database is necessary to extend the capabilities of VIV prediction to allow the prediction of coupled 2D inline-crossflow response. A series of 2D forced vi-

bration experiments were conducted at the MIT towing tank to produce this database with a total of 3402 experimental runs, covering 6 crossflow amplitudes, from 0.25 to 1.5, in increments of 0.25; 6 inline amplitudes, from 0 to 0.75, in increments of 0.15; 8 phases, from -180 to 180 degrees, in increments of 45 degrees; and 8 reduced velocities, from 4.5 to 8, in increments of 0.5. One challenge with extending the prediction method to include combined inline and crossflow motions is that the number of variable parameters increases, making a large number of experiments necessary to define the hydrodynamic coefficients governing the problem. The experiments described in [22, 23] were an initial attempt to characterize the force coefficients over a relatively small range of reduced velocities, and this series of experiments resulted in a very sparse representation of the hydrodynamic forces governing a combined crossflow and inline response. While this set of experiments provides useful information on the forces exerted on a rigid cylinder undergoing combined crossflow and inline motion, in order to be able to use it as a hydrodynamic database, it is necessary to increase the resolution of the experimental grid. The same experimental set up used for the pure inline forced VIV experiments is employed with the additional usage of a second linear motor in the crossflow direction.

From the free vibration experiments [32, 23], the inline and crossflow motions are significant in the reduced velocity region of 4 to 8, as shown in Figure 6-1; therefore, the experiments are conducted in this range of reduced velocities. Also, from Dahl's free vibration experiments [19], reproduced in Figure 6-2, the ratio of the inline to crossflow amplitude in this region is less than 1/3. In order to limit the number of experiments necessary to expand the resolution of the experimental database, experiments are conducted only for ratios smaller than 1/3, as show in Table 6.1.

It was observed by Jauvtis and Williamson [32] and Dahl [19] that for the free vibration of cylinders with two degrees of freedom, the phase between the inline and crossflow motion can vary greatly, from -180 to 180 degrees, especially if the nominal natural frequency ratio between inline and crossflow motions is variable (as may exist on a long riser). Since the entire range of phases is shown to exist for freely vibrating

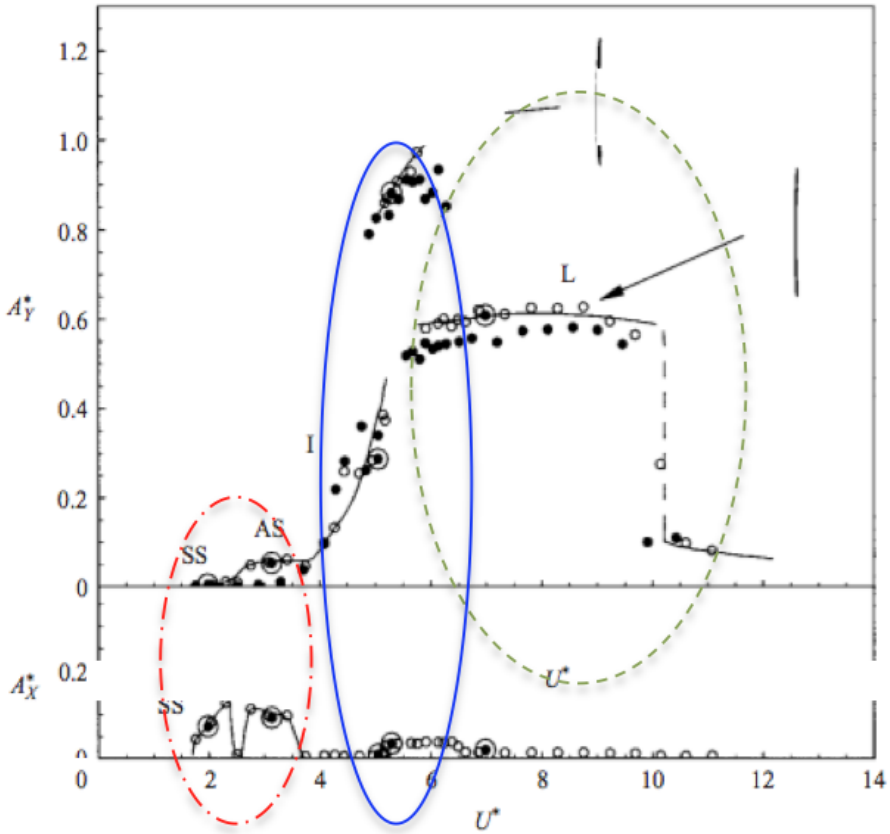

Figure 6-1: VIV response regions, crossflow motion dominant region is marked with – on the right, inline-crossflow motion region is marked by in the middle and Inline motion dominant region is marked by -.- on the left. The x-axis reduced velocity U^* is defined as $U/(f_N D)$ (Figure altered from Jauvtis and Williamson [32])

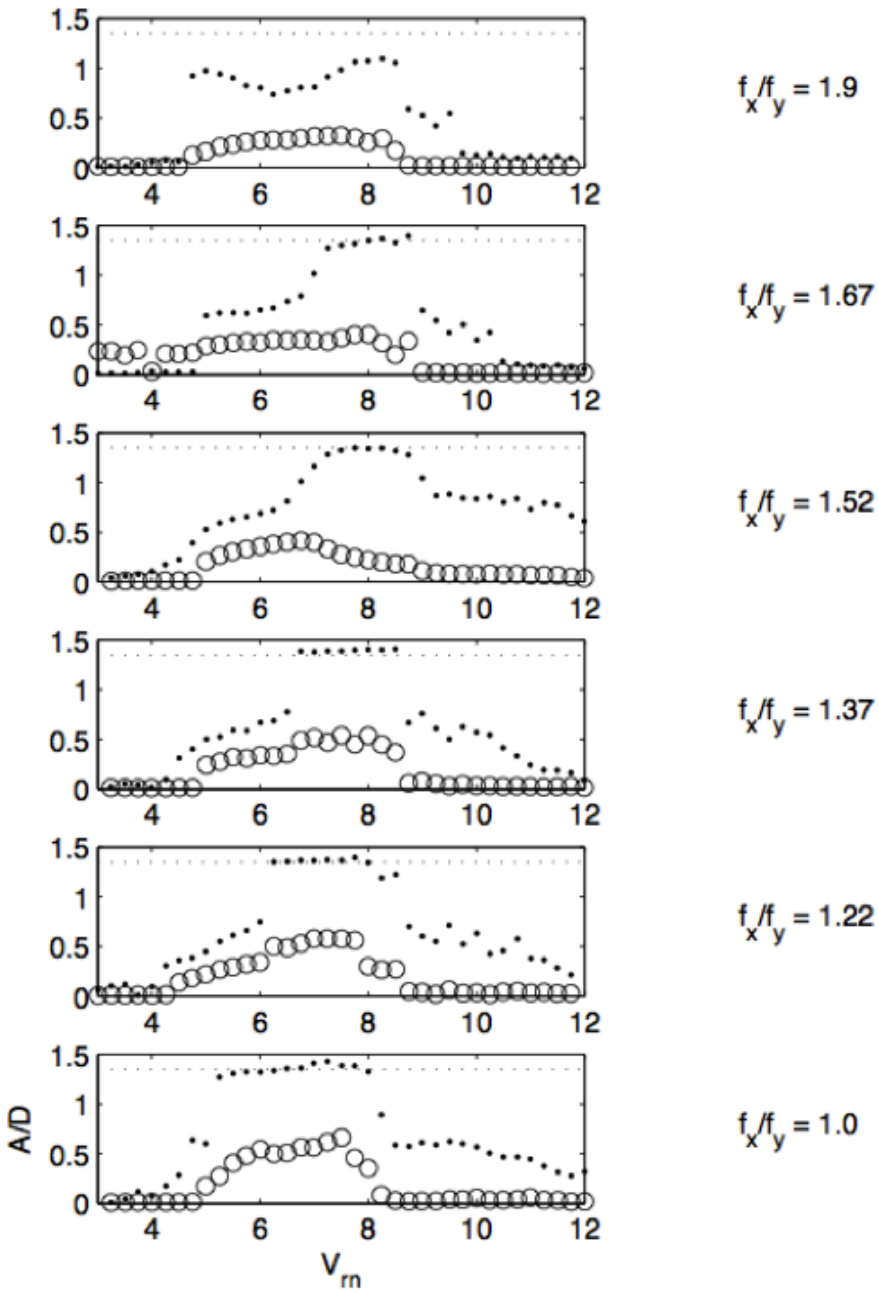

Figure 6-2: 2D motion regions in free vibration experiments. The x-axis reduced velocity U_{rn} is defined as $U/(f_N D)$ (Figure altered from Dahl [19])

Table 6.1: 2D Experiment Amplitude Matrix. The first column is the crossflow nondimensional amplitude and the first row is the inline nondimensional amplitude.

y/x	0.05	0.1	0.15	0.2	0.25	0.3
0.15	1	x	x	x	x	x
0.25	1	1	x	x	x	x
0.5	1	1	1	1	x	x
0.75	1	1	1	1	x	x
1	1	1	1	1	1	1

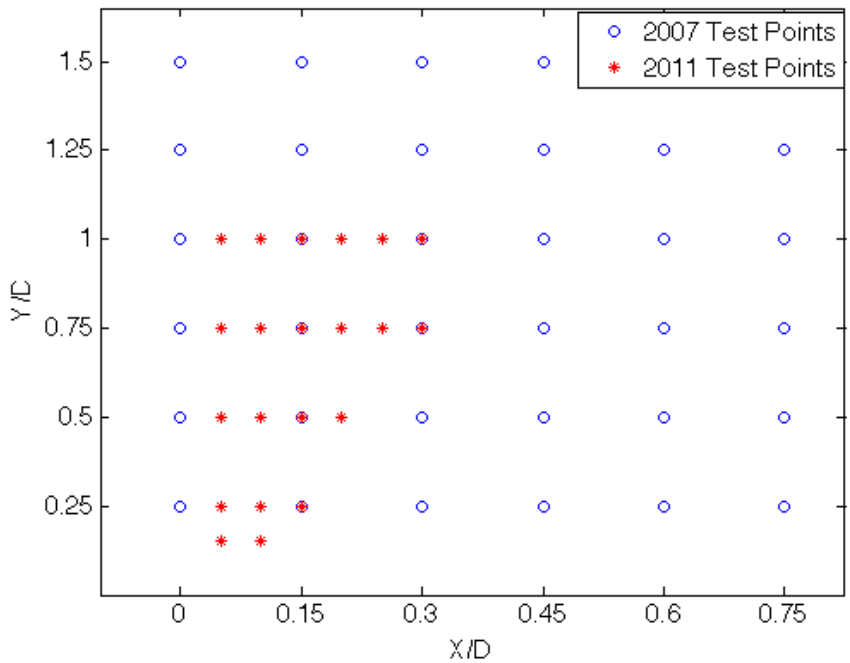

Figure 6-3: Amp range of 2011 vs 2007 experiments.

rigid cylinders, 18 phases are chosen from -180 to 180 degrees, in increments of 15 degrees from -45 to 45 degree, and in increments of 22.5 degrees otherwise, in order to expand the phase resolution of the database, which previously only included data for 8 phases.

In summary, a total of 3402 experimental runs were scheduled covering 6 inline amplitudes, from 0.05 to 0.3, in increments of 0.05; 5 crossflow amplitudes, from 0.15 to 1 (0.15, 0.25, 0.5, 0.75, 1); 18 phases, from -180 to 180 degrees, in increments of 15 degrees from -45 to 45 degree and in increments of 22.5 degrees otherwise; and 9

Table 6.2: 2D experiment phase matrix.

1	-180	-180
2		-157.5
3	-135	-135
4		-120
5		-105
6	-90	-90
7		-75
8		-60
9	-45	-45
10		-22.5
11	0	0
12		22.5
13	45	45
14		67.5
15	90	90
16		112.5
17	135	135
18		157.5

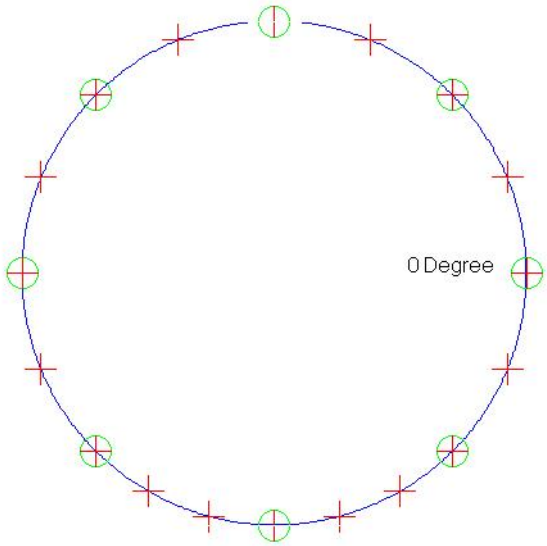

Figure 6-4: Phase range of 2011 vs 2007 experiments.

reduced velocities, from 4 to 8, in increments of 0.5. These data points are chosen in order to expand the existing database of values from [19], including some overlapping

points in order to verify previous results.

6.2 'ZDMiT' 2D VIV Force Coefficients Database Analysis

The 'ZDMiT' 2D VIV hydrodynamics coefficients database is named after the research team under the supervision of Professor Triantafyllou, Zheng -Dahl - Modarres-Sadeghi - Triantafyllou, and is based on the Dahl 2006 [19] and the Zheng 2011 [82] forced vibration VIV experiments at MIT towing tank.

6.2.1 Hydrodynamic Force Coefficients in the Database

The key hydrodynamic force coefficients in the database are listed below:

- Added mass
  - Cmx - Added mass in inline direction
  - Cmy - Added mass in crossflow direction
- Drag force
  - CDa - Fluctuating drag in phase with acceleration from inner product calculation
  - CDv - Fluctuating drag in phase with velocity from inner product calculation
- Lift force
  - CL1 - 1st harmonic component of lift
  - CL3 - 3rd harmonic component of lift
  - CLa - Lift in phase with acceleration determined from inner product calculation
  - CLv - Lift in phase with velocity from inner product calculation

- Phase
  - Phase - Phase between 1st harmonic lift force and crossflow position
  - Phi2 - Phase between 2nd harmonic fluctuating drag and inline position
  - Psi - Calculated phase between third harmonic lift and first harmonic lift

The resulting lift coefficients in phase with velocity and the added mass coefficients at a reduced velocity 4.5 are shown as the iso-surfaces of lift coefficients as a function of inline amplitude, crossflow amplitude, and phase between inline and crossflow motion in Figure 6-5. The same results are shown as contours in Figure 6-6 for fixed values of the phase between inline and crossflow motion.

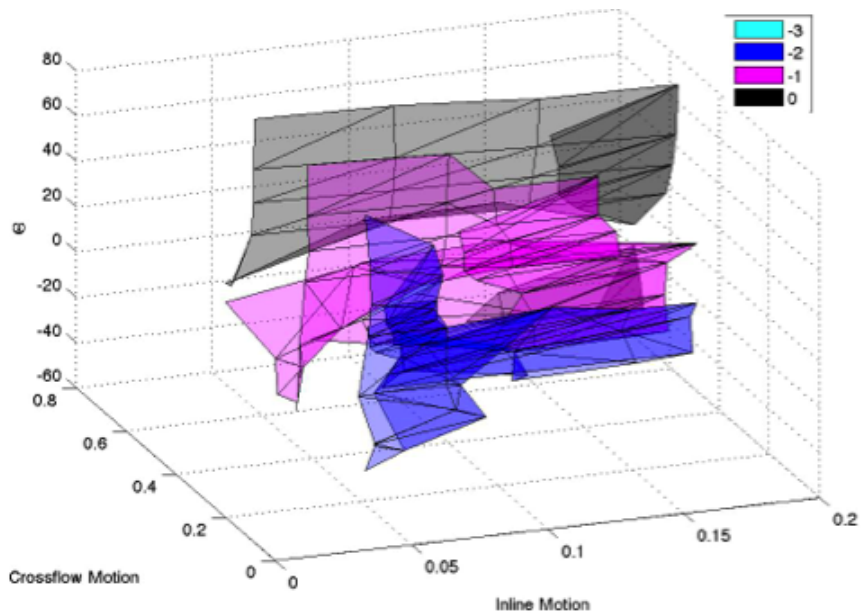

Figure 6-5: Lift coefficients extracted from the experiments at a reduced velocity of 4.5 as iso-surfaces.

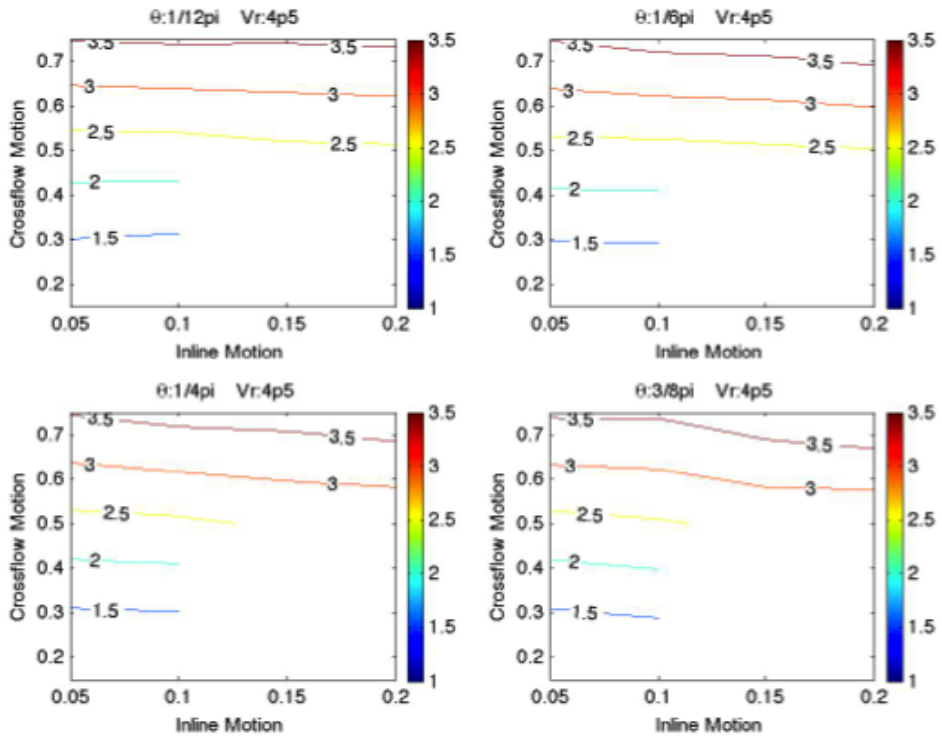

Figure 6-6: Lift coefficients extracted from the experiments at a reduced velocity of 4.5 as contours at different phases.

One important new parameter in the 2D VIV hydrodynamic coefficients database is the phase between crossflow and inline motions. The crossflow and inline motions are defined as the following:

$$y = sin(wt) \tag{6.1}$$

$$x = sin(2wt + \phi) \tag{6.2}$$

The orbit shapes for various phases between inline and crossflow motions are plotted in Figure 6-7.

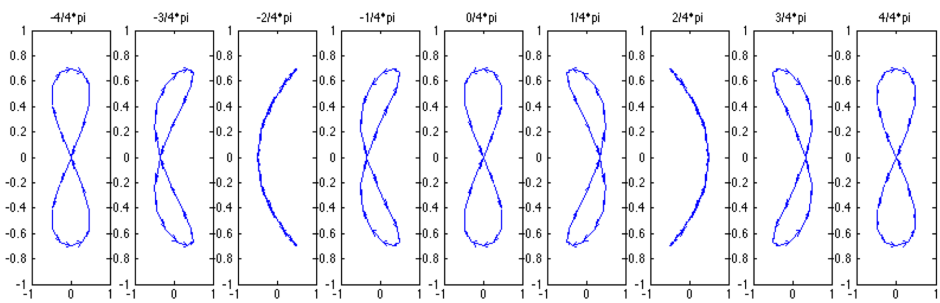

Figure 6-7: Orbits shape for various phases btw inline and crossflow motion.

Counter-clockwise motion is defined for the orbits shape with phases in [-90, 90], while clockwise motion is defined for the orbits shape with phases in [-180 -90] and [90 180] [19]. The phases between the inline and crossflow motions play a significant role for the hydrodynamic force coefficients in the database.

6.2.2 Force Coefficients in Phase with Velocity

Besides the traditional lift in phase with velocity in the crossflow direction C_{Lv}, there is also a fluctuating drag force in phase with velocity in the inline direction C_{Dv} in the new 2D VIV hydrodynamic coefficients database.

Lift Coefficients in Phase with Velocity

Lift coefficients C_{Lv} are mostly positive for the counter-clockwise motion while mostly negative in clockwise motion as shown in Figure 6-8 and Figure 6-9. Figure 6-8 and Figure 6-9 are plotted for C_{Lv} with the inline motion amplitude equal to 0.05 times the diameter of the cylinder and the crossflow motion amplitude equal to 0.15 times the diameter of the cylinder.

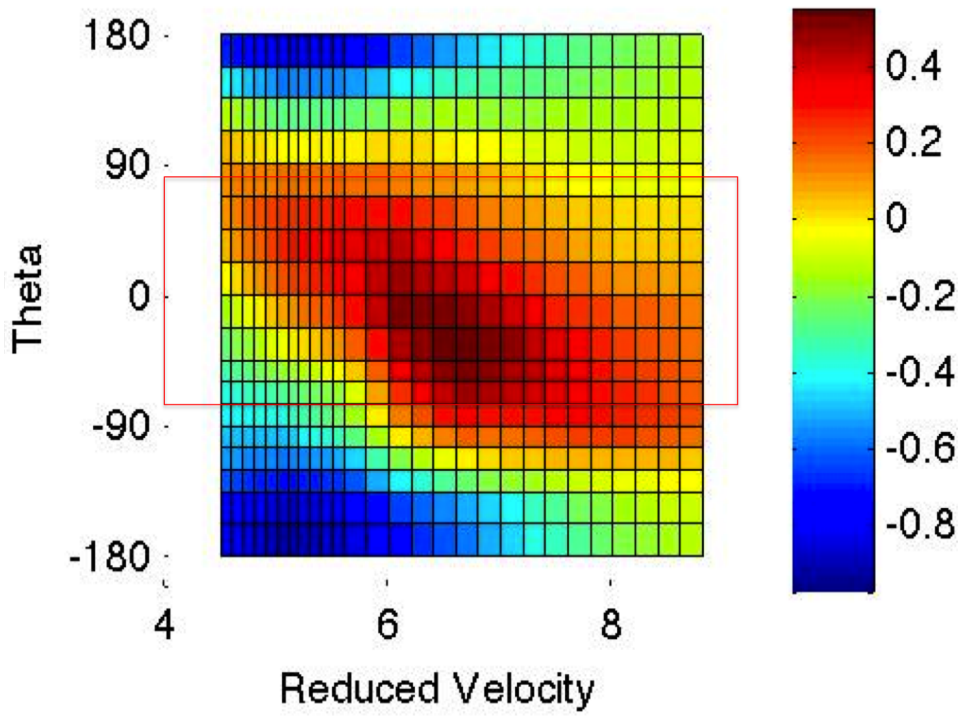

Figure 6-8: Lift coefficients in phase with velocity C_{Lv} with inline motion amplitude 0.05 and crossflow motion amplitude 0.15

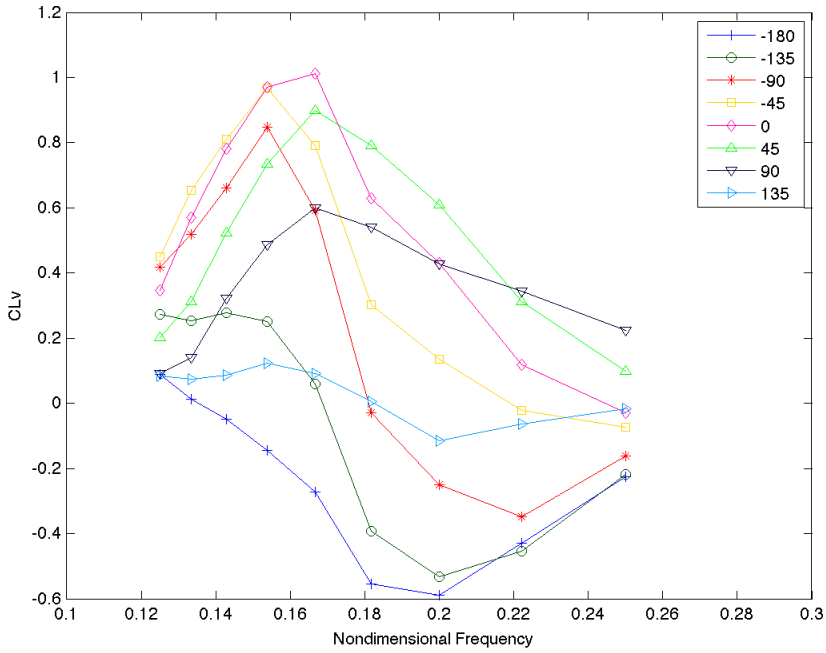

Figure 6-9: Lift coefficients C_{Lv} with inline motion amplitude 0.05 and crossflow motion amplitude 0.15

Figure 6-10 shows C_{Lv} for all amplitudes of inline and crossflow motions in the hydrodynamic coefficients database, ranging from 0.05 times the diameter of the cylinder to 0.75 times the diameter of the cylinder in the inline direction (0.05, 0.1, 0.15, 0.2, 0.25, 0.3, 0.45, 0.6, 0.75) and ranging from 0.15 times the diameter of the cylinder to 1.5 times the diameter of the cylinder in the crossflow direction (0.15, 0.25, 0.5, 0.75, 1, 1.25, 1.5).

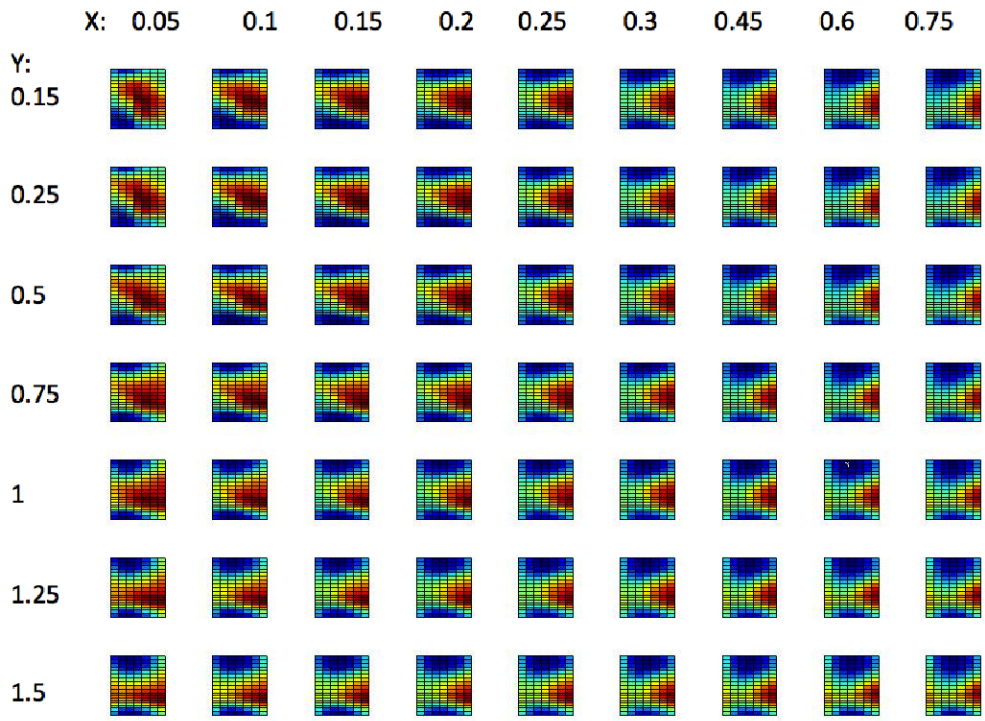

Figure 6-10: Lift coefficients C_{Lv} for all amplitude of inline and crossflow motions. The x-axis is the nondimensional amplitude of inline motion 0.05, 0.1, 0.15, 0.2, 0.25, 0.3, 0.45, 0.6 and 0.75. The y-axis is the nondimensional amplitudes of crossflow motion: 0.15, 0.25, 0.5, 0.75, 1, 1.25 and 1.5.

From Figure 6-10 , it can be observed that the lift coefficients C_{Lv} show the same trend as shown in Figure 6-8. The lift coefficients C_{Lv} are mostly positive for counter-clockwise motion while being mostly negative for clockwise motion for all combinations of inline and crossflow motion amplitudes.

The color map in Figure 6-10 is tailored to each individual subplot and thus the scale of lift coefficients C_{Lv} is different from subplot to subplot. If the color map is unified as shown in Figure 6-11, the absolute value of the lift coefficient C_{Lv} are more clearly shown and another important trend can be observed: as the inline or crossflow motion amplitude increases, the lift coefficient C_{Lv} quickly decreases below 0. When crossflow motion amplitude is larger than 1.25 times the diameter of the cylinder, all C_{Lv} values become negative.

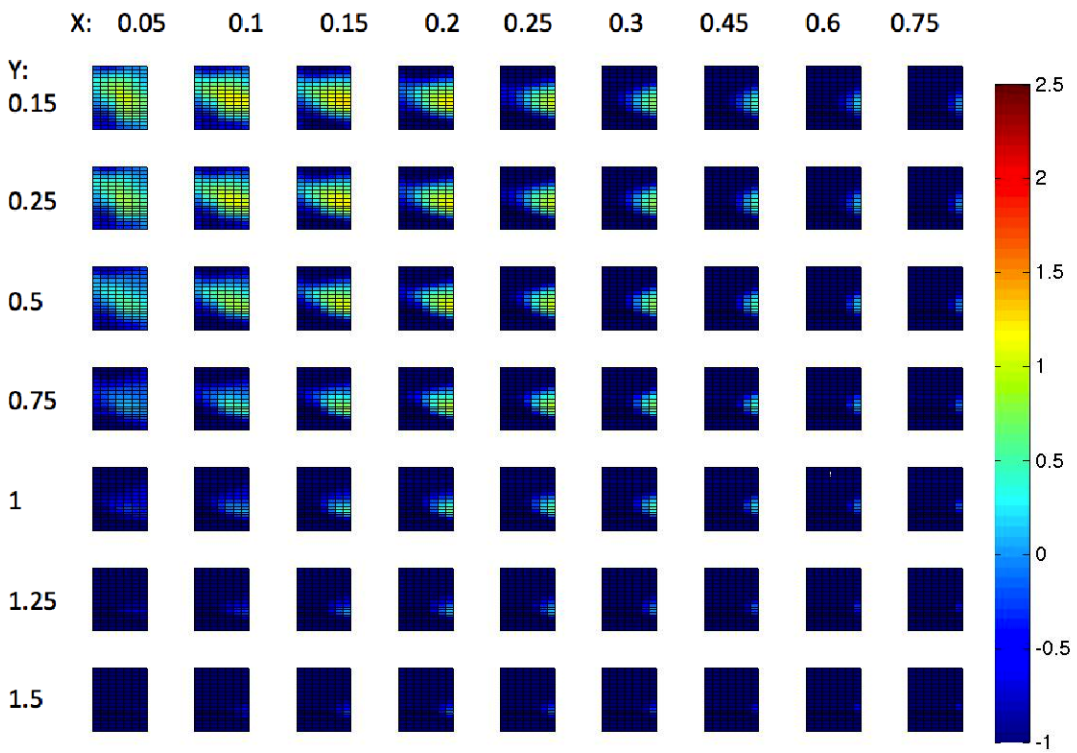

Figure 6-11: Lift coefficients C_{Lv} for all amplitude of inline and crossflow motions with same colorbar.The x-axis is the nondimensional amplitude of inline motion 0.05, 0.1, 0.15, 0.2, 0.25, 0.3, 0.45, 0.6 and 0.75. The y-axis is the nondimensional amplitudes of crossflow motion: 0.15, 0.25, 0.5, 0.75, 1, 1.25 and 1.5.

It can also be observed that the peak frequency of lift coefficients C_{Lv} stays stable when the crossflow motion amplitude increases while the inline motion amplitude is kept constant, but decreases when the inline motion amplitude increases while the

crossflow motion amplitude is kept constant. A complete set of lift coefficients C_{Lv} with different combination of inline and crossflow motion amplitudes can be found in appendix A.

Fluctuating Drag Coefficients in Phase with Velocity

Fluctuating drag coefficients C_{Dv} are mostly Positive in [-90, 180] (the whole counter-clockwise motion region and half of Clock wise motion region), and mostly negative in [-180, -90](half of clockwise motion region) as shown in Figure 6-12 and Figure 6-13. The Figure 6-12 and Figure 6-13 are plotted for C_{Dv} with the inline motion amplitude equal to 0.05 times the diameter of the cylinder and the crossflow motion amplitude equal to 0.15 times the diameter of the cylinder.

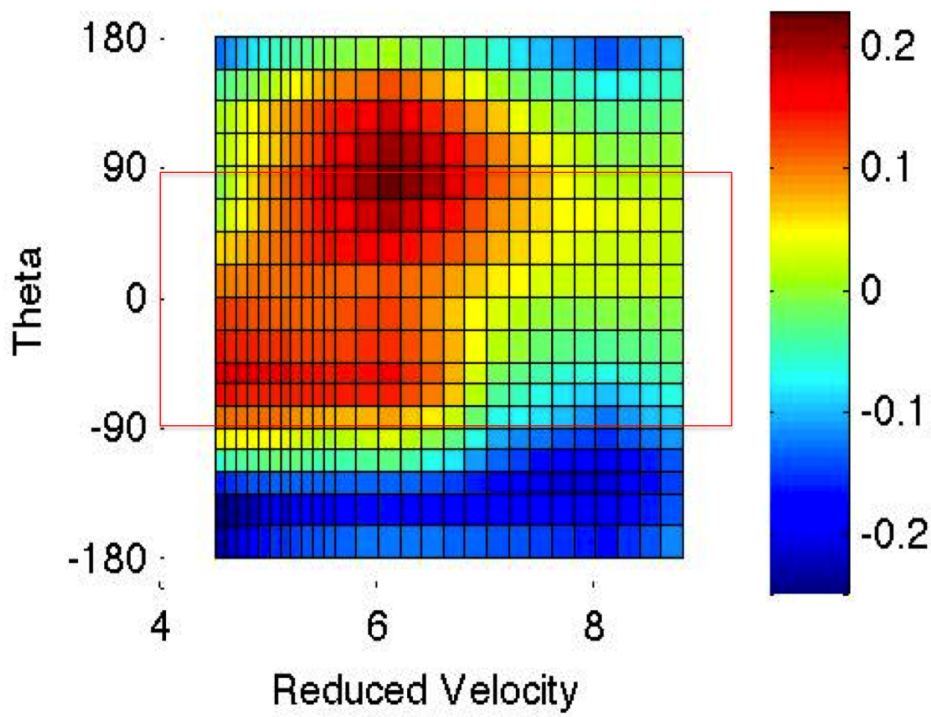

Figure 6-12: Fluctuating drag coefficient in phase with velocity C_{Dv} with inline motion amplitude 0.05 and crossflow motion amplitude 0.15

Figure 6-14 shows C_{Dv} for all amplitudes of inline and crossflow motions in the hydrodynamic coefficients database, ranging from 0.05 times the diameter of the cylinder to 0.75 times the diameter of the cylinder in the inline direction (0.05, 0.1, 0.15, 0.2, 0.25, 0.3, 0.45, 0.6, 0.75) and ranging from 0.15 times the diameter of the cylinder to 1.5 times the diameter of the cylinder in the crossflow direction (0.15, 0.25, 0.5, 0.75, 1, 1.25, 1.5).

From Figure 6-14 , it can be observed that the fluctuating drag coefficients in

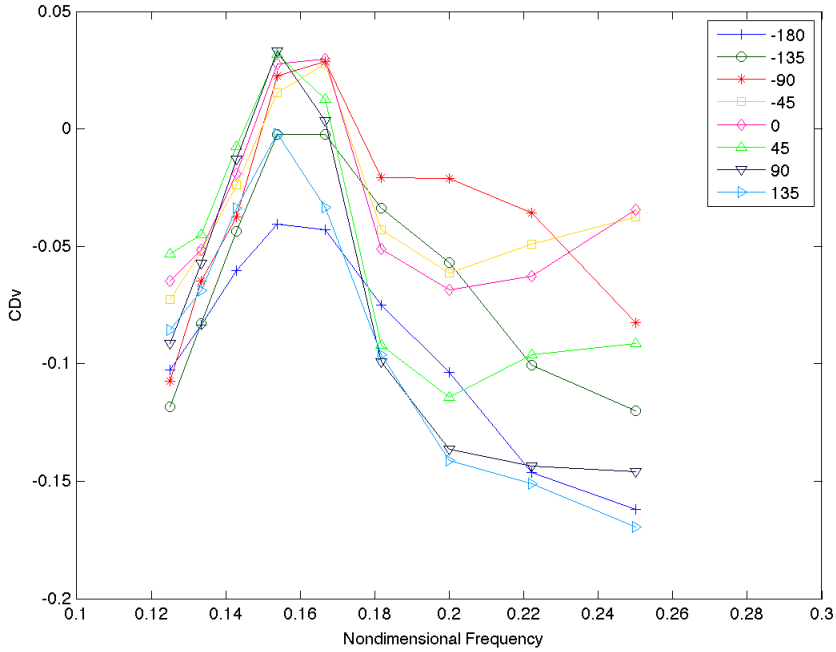

Figure 6-13: Fluctuating drag coefficient in phase with velocity C_{Dv} with inline motion amplitude 0.05 and crossflow motion amplitude 0.15

phase with velocity C_{Dv} show the same trend as shown in Figure 6-12. The fluctuating drag coefficients in phase with velocity C_{Dv} are mostly positive in counter-clockwise motion while mostly negative in clockwise motion at all combinations of inline and crossflow motion amplitudes.

The color map in Figure 6-14 is tailored to each individual subplot and thus the scale of fluctuating drag coefficients in phase with velocity C_{Dv} is different from subplot to subplot. If the color map is unified as shown in Figure 6-15, the absolute value of the fluctuating drag coefficients in phase with velocity C_{Dv} are more clearly shown and another important trend can be observed: as the inline motion amplitude increases, the fluctuating drag coefficients in phase with velocity C_{Dv} quickly decrease below 0. When inline motion amplitude is larger than 0.3 times the diameter of the cylinder, all C_{Dv} values become negative.

It can also be observed that the peak frequency of fluctuating drag coefficients in phase with velocity C_{Dv} remains stable when the inline motion amplitude increases

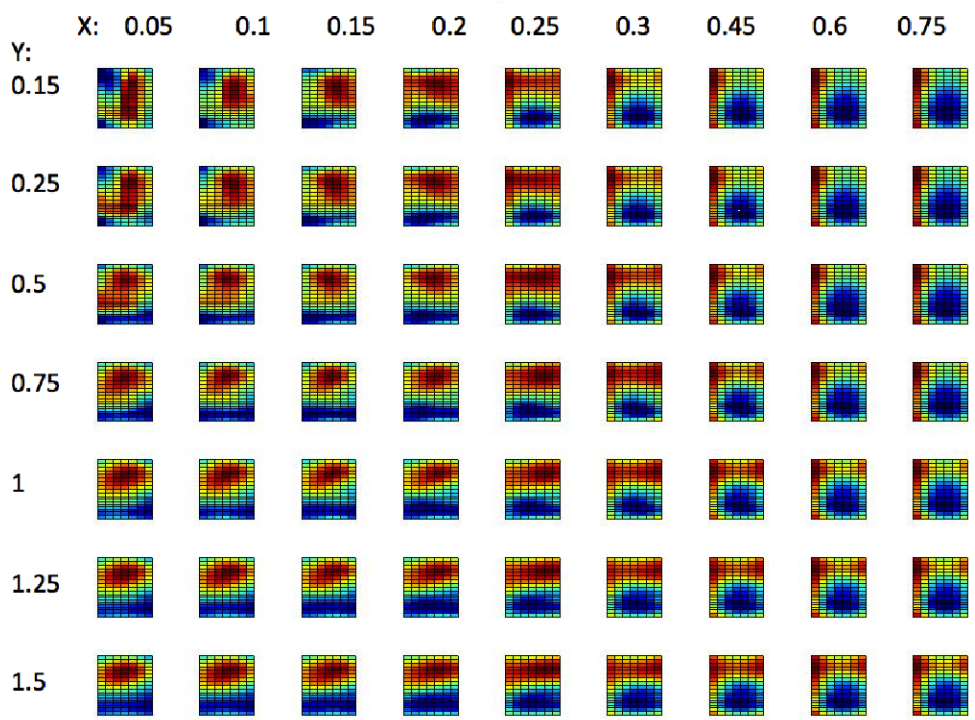

Figure 6-14: Fluctuating drag coefficient in phase with velocity C_{Dv}. The x-axis is the nondimensional amplitude of inline motion 0.05, 0.1, 0.15, 0.2, 0.25, 0.3, 0.45, 0.6 and 0.75. The y-axis is the nondimensional amplitudes of crossflow motion: 0.15, 0.25, 0.5, 0.75, 1, 1.25 and 1.5.

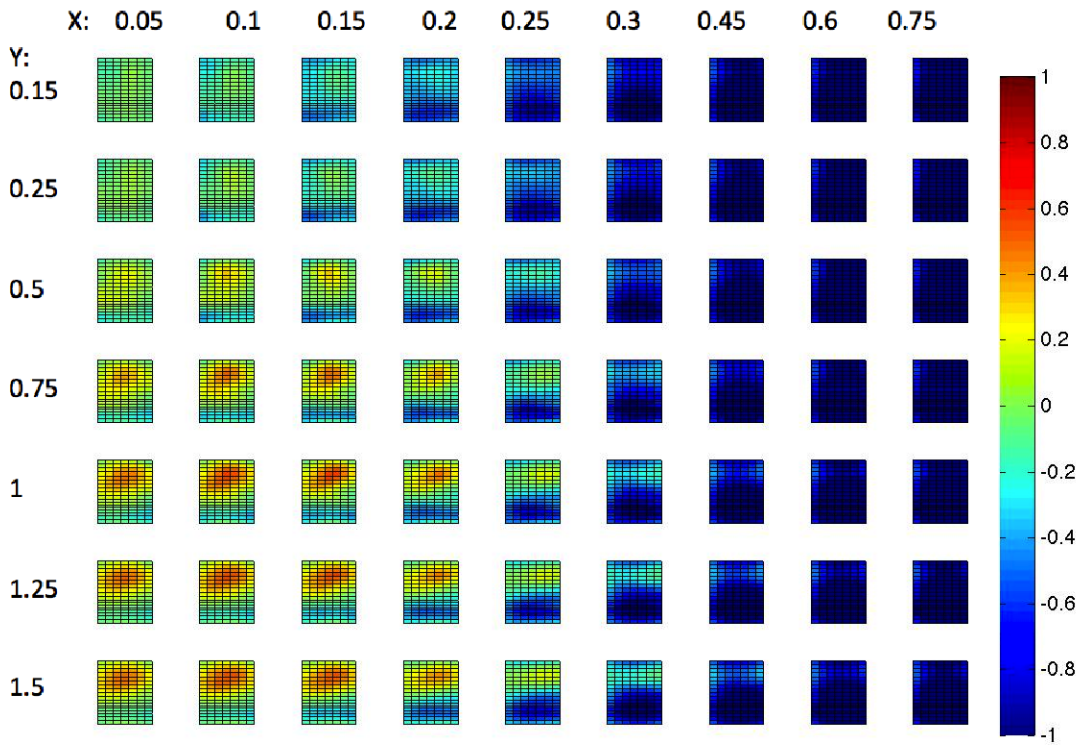

Figure 6-15: Fluctuating drag coefficient in phase with velocity C_{Dv} with same colorbar. The x-axis is the nondimensional amplitude of inline motion 0.05, 0.1, 0.15, 0.2, 0.25, 0.3, 0.45, 0.6 and 0.75. The y-axis is the nondimensional amplitudes of crossflow motion: 0.15, 0.25, 0.5, 0.75, 1, 1.25 and 1.5.

while the crossflow motion amplitude is kept constant, but it decreases when the crossflow motion amplitude increases while the inline motion amplitude is kept constant. This is a reversal of the lift coefficients C_{Lv} trend. A complete set of fluctuating drag coefficients in phase with velocity C_{Dv} with different combinations of inline and crossflow motion amplitudes can be found in appendix A.

6.2.3 Added Mass Coefficients

Besides the traditional added mass coefficients in the crossflow direction C_{my}, there are also an added mass coefficients in the inline direction C_{mx} in the new 2D VIV hydrodynamic coefficients database.

Added Mass Coefficient in Crossflow Direction

The added mass coefficient in the crossflow direction C_{my} is a strong function of reduced velocity and is mostly larger for the counter-clockwise motion as shown in Figure 6-16 and Figure 6-17. Figure 6-16 and Figure 6-17 are plotted for C_{my} with the inline motion amplitude equal to 0.05 times the diameter of the cylinder and the crossflow motion amplitude equal to 0.15 times the diameter of the cylinder.

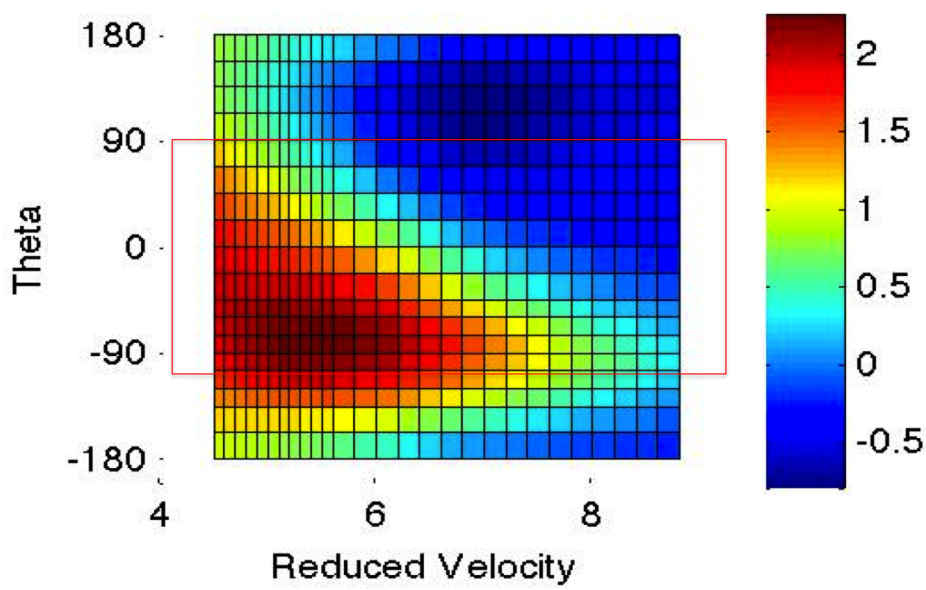

Figure 6-16: Added mass coefficient in the crossflow direction C_{my} with inline motion amplitude 0.05 and crossflow motion amplitude 0.15

Figure 6-18 shows C_{my} for all amplitudes of inline and crossflow motions in the hydrodynamic coefficients database, ranging from 0.05 times the diameter of the cylinder to 0.75 times the diameter of the cylinder in the inline direction (0.05, 0.1, 0.15, 0.2, 0.25, 0.3, 0.45, 0.6, 0.75) and ranging from 0.15 times the diameter of the

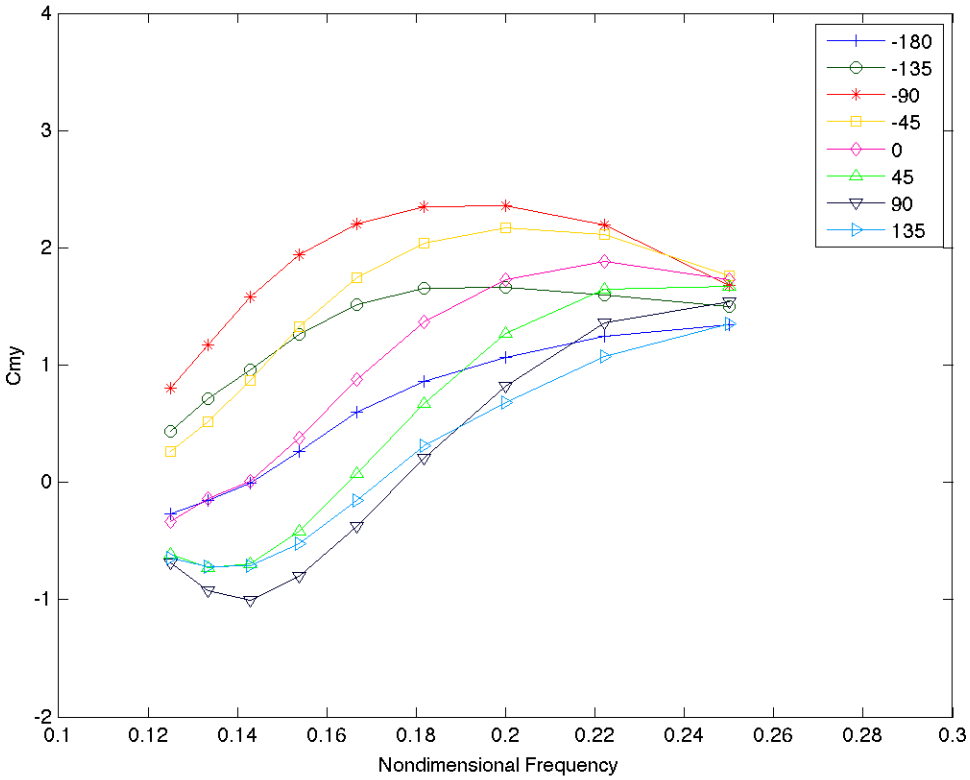

Figure 6-17: Added mass coefficient in the crossflow direction C_{my} with inline motion amplitude 0.05 and crossflow motion amplitude 0.15

cylinder to 1.5 times the diameter of the cylinder in the crossflow direction (0.15, 0.25, 0.5, 0.75, 1, 1.25, 1.5).

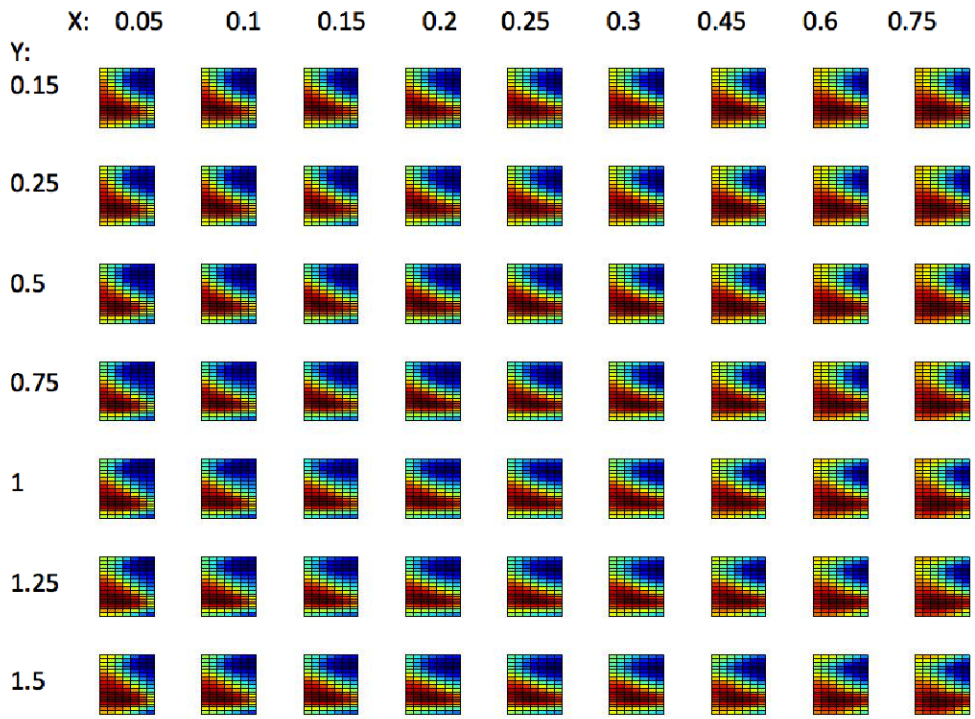

Figure 6-18: Added mass coefficient in the crossflow direction C_{my}. The x-axis is the nondimensional amplitude of inline motion 0.05, 0.1, 0.15, 0.2, 0.25, 0.3, 0.45, 0.6 and 0.75. The y-axis is the nondimensional amplitudes of crossflow motion: 0.15, 0.25, 0.5, 0.75, 1, 1.25 and 1.5.

From Figure 6-18 , it can be observed that the added mass coefficients in the crossflow direction C_{my} show the same trend as shown in Figure 6-16. The added mass coefficient in the crossflow direction C_{my} is a strong function of reduced velocity and is generally larger for the counter-clockwise motion.

The color map in Figure 6-18 is tailored to each individual subplot and thus the scale of lift coefficients C_{Lv} is different from subplot to subplot. If the color map is unified as shown in Figure 6-19, the absolute values of the lift coefficient C_{my} is more clearly shown and another important trend can be observed: as the inline

motion amplitude increases, the added mass coefficient in the crossflow direction C_{my} increases while as the crossflow motion amplitude increases, the added mass coefficient in the crossflow direction C_{my} decreases.

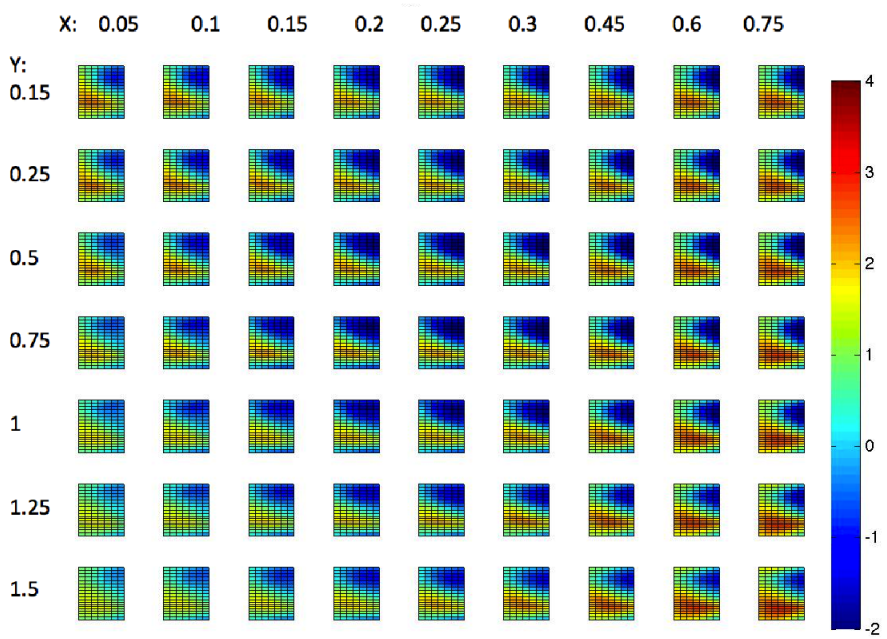

Figure 6-19: Added mass coefficient in the crossflow direction C_{my} with same colorbar. The x-axis is the nondimensional amplitude of inline motion 0.05, 0.1, 0.15, 0.2, 0.25, 0.3, 0.45, 0.6 and 0.75. The y-axis is the nondimensional amplitudes of crossflow motion: 0.15, 0.25, 0.5, 0.75, 1, 1.25 and 1.5.

The ratio of the inline motion amplitude to the crossflow motion amplitude is 1:3 in Figure 6-17 with 0.05 times the diameter of the cylinder in the inline direction and 0.15 times the diameter of the cylinder in the crossflow direction. Figure 6-20 has an inline-crossflow amplitude ratio of 1:10. Figure 6-21 has an inline-crossflow amplitude ratio of 1:20. Figure 6-22 has an inline-crossflow amplitude ratio of 1:30. From these four figures, it can be observed that as the inline-crossflow ratio decreases, the phase influence decreases and the range of C_{my} decreases.

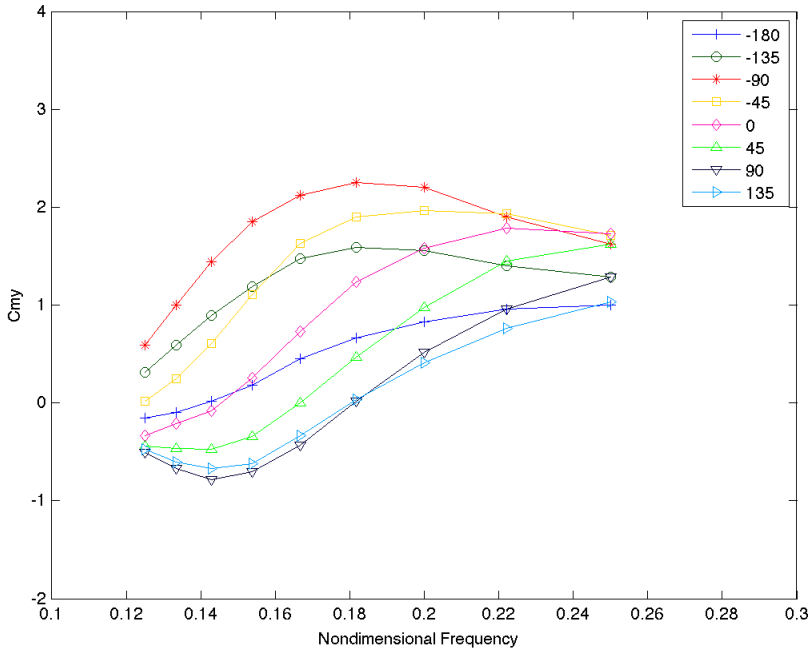

Figure 6-20: Added mass coefficient in the crossflow direction C_{my} with inline motion amplitude 0.05 and crossflow motion amplitude 0.5

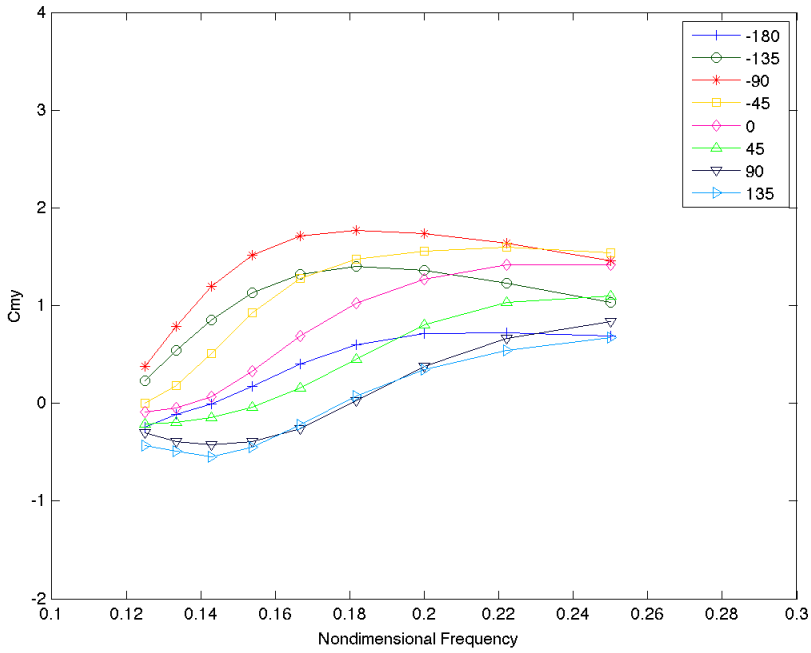

Figure 6-21: Added mass coefficient in the crossflow direction C_{my} with inline motion amplitude 0.05 and crossflow motion amplitude 1

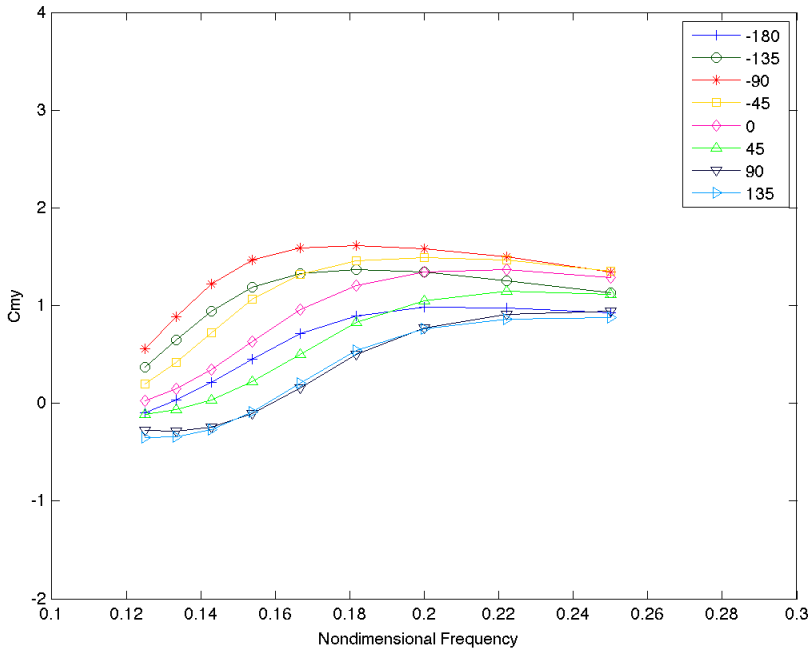

Figure 6-22: Added mass coefficient in the crossflow direction C_{my} with inline motion amplitude 0.05 and crossflow motion amplitude 1.5

Meanwhile, if the inline-crossflow amplitude ratio is the same, then the phase influence will be similar. Figure 6-23 has 0.15 times the diameter of the cylinder in the inline direction and 0.15 times the diameter of the cylinder in the crossflow direction. Figure 6-24 has 0.25 times the diameter of the cylinder in the inline direction and 0.25 times the diameter of the cylinder in the crossflow direction. They both have a inline-crossflow motion amplitude ratio of 1:1 and the shape of the added mass curve is very close.

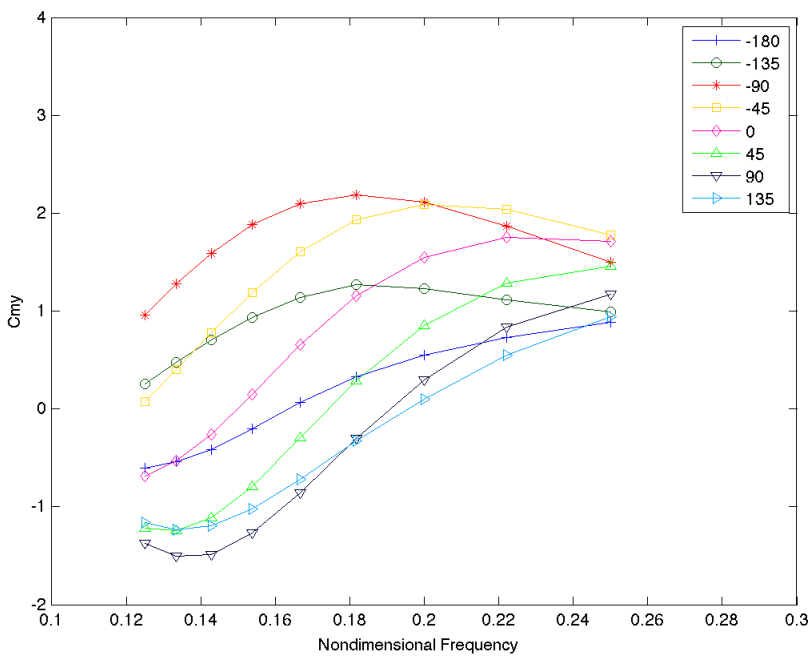

Figure 6-23: Added mass coefficient in the crossflow direction C_{my} with inline motion amplitude 0.15 and crossflow motion amplitude 0.15

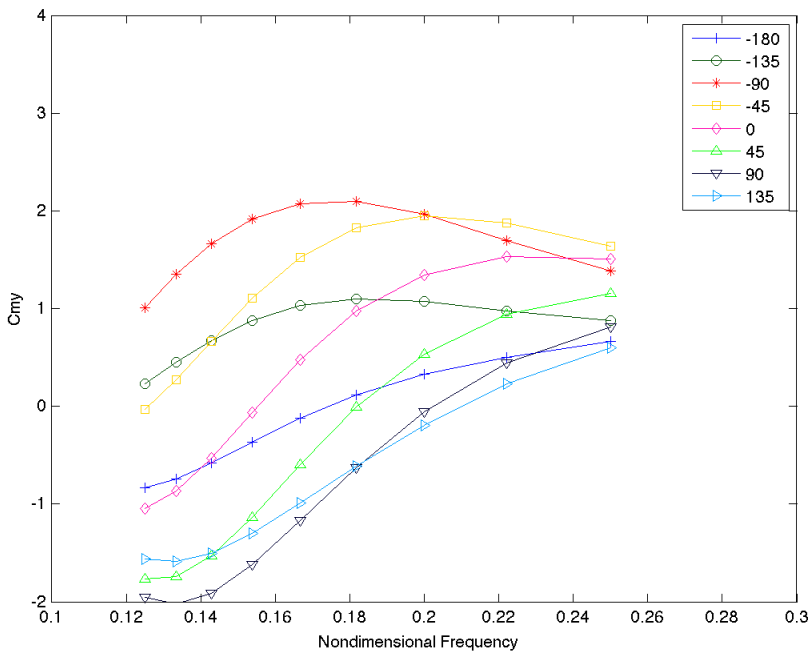

Figure 6-24: Added mass coefficient in the crossflow direction C_{my} with inline motion amplitude 0.25 and crossflow motion amplitude 0.25

On the other hand, Figure 6-25 has 0.15 times the diameter of the cylinder in the inline direction and 0.75 times the diameter of the cylinder in the crossflow direction. Figure 6-26 has 0.25 times the diameter of the cylinder in the inline direction and 1.25 times the diameter of the cylinder in the crossflow direction. They both have a inline-crossflow amplitude ratio of 1:5 and the shape of the added mass curve is very close. Their shapes are wider compared with those in Figure 6-23 and Figure 6-24 which have a inline-crossflow amplitude ratio of 1:1.

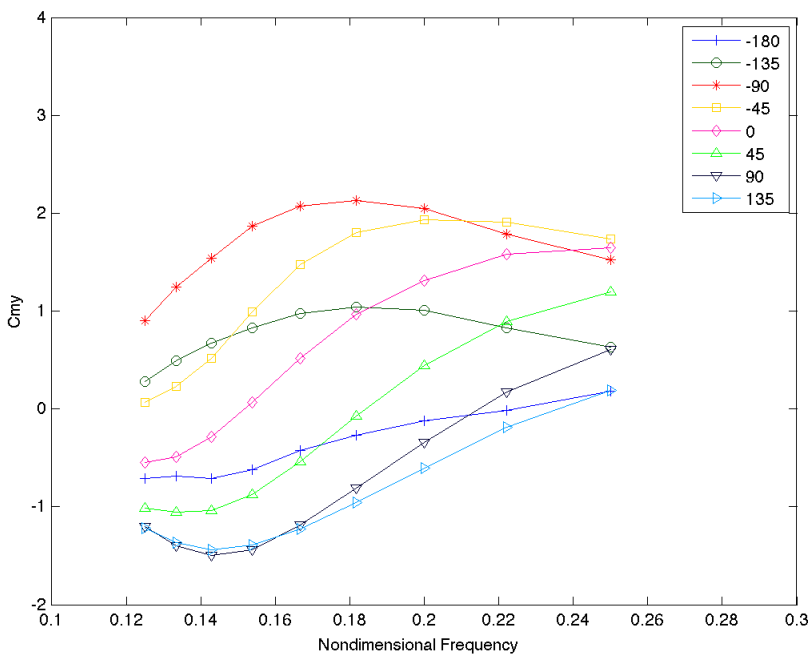

Figure 6-25: Added mass coefficient in the crossflow direction C_{my} with inline motion amplitude 0.15 and crossflow motion amplitude 0.75

It can be surmised from the above figures that the shapes of the added mass coefficient in the crossflow direction C_{my} are consistent across different inline and crossflow motion amplitudes. A complete set of the added mass coefficients in the crossflow direction C_{my} with different combinations of inline and crossflow motion amplitudes can be found in appendix A.

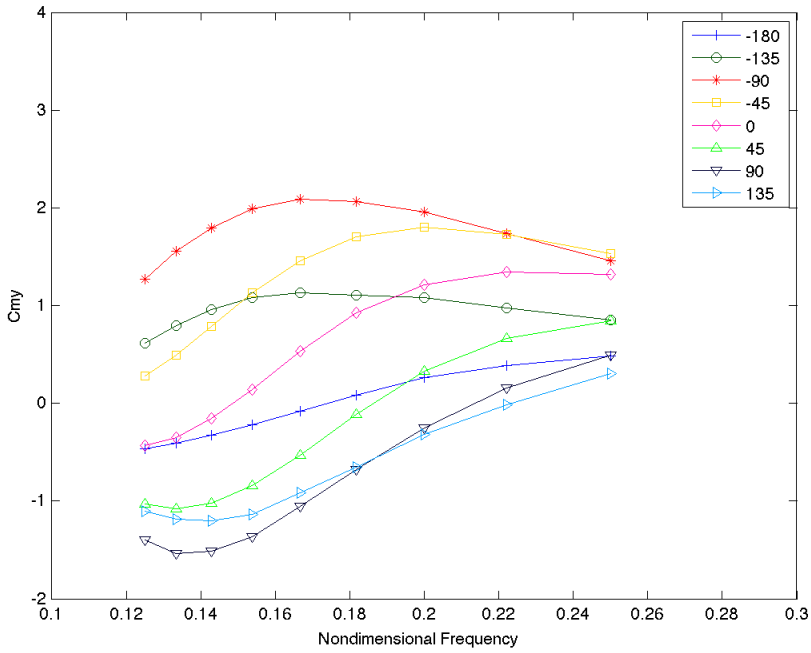

Figure 6-26: Added mass coefficient in the crossflow direction C_{my} with inline motion amplitude 0.25 and crossflow motion amplitude 1.25

Added Mass Coefficient in Inline Direction

The added mass coefficient in the inline direction C_{mx} is a strong function of reduced velocity and is mostly smaller in counter-clockwise motion as shown in Figure 6-28 and Figure 6-27. Figure 6-28 and Figure 6-27 are plotted for C_{mx} with the inline motion amplitude equal to 0.05 times the diameter of the cylinder and the crossflow motion amplitude equal to 0.15 times the diameter of the cylinder.

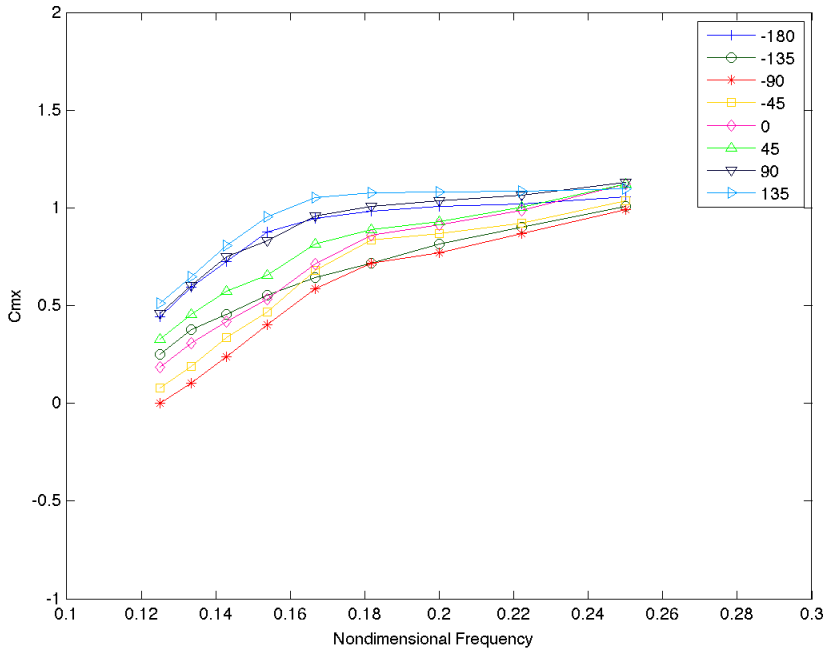

Figure 6-27: Added mass coefficient in the inline direction C_{mx} with inline motion amplitude 0.05 and crossflow motion amplitude 0.15

Figure 6-29 shows C_{mx} for all amplitude of inline and crossflow motions in the hydrodynamic coefficients database, ranging from 0.05 times the diameter of the cylinder to 0.75 times the diameter of the cylinder in the inline direction (0.05, 0.1, 0.15, 0.2, 0.25, 0.3, 0.45, 0.6, 0.75) and ranging from 0.15 times the diameter of the cylinder to 1.5 times the diameter of the cylinder in the crossflow direction (0.15, 0.25, 0.5, 0.75, 1, 1.25, 1.5).

From Figure 6-29 , it can be observed that the added mass coefficients in the inline direction C_{mx} show the same trend as shown in Figure 6-28. The added mass

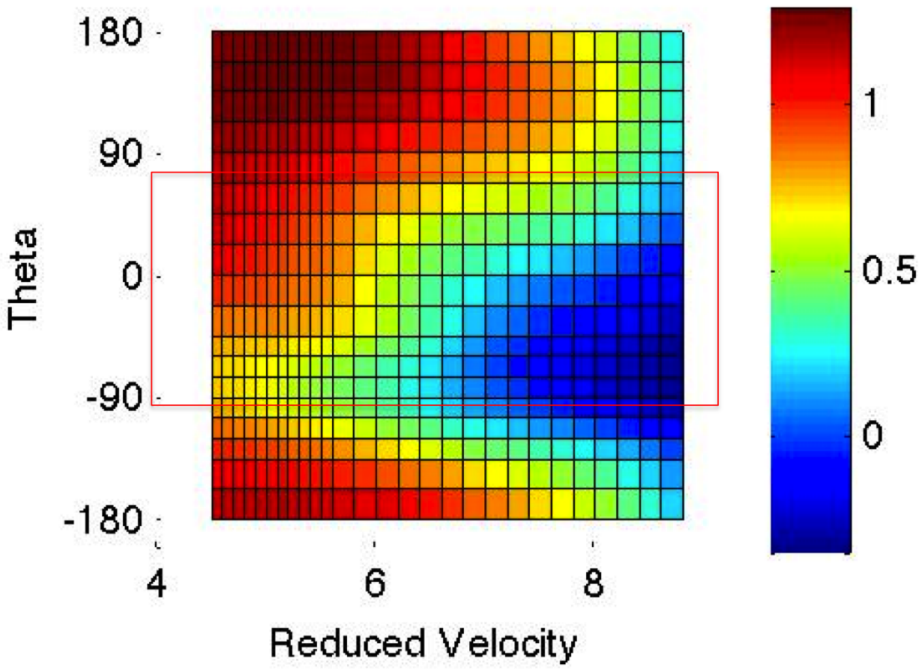

Figure 6-28: Added mass coefficient in the inline direction C_{mx} with inline motion amplitude 0.05 and crossflow motion amplitude 0.15

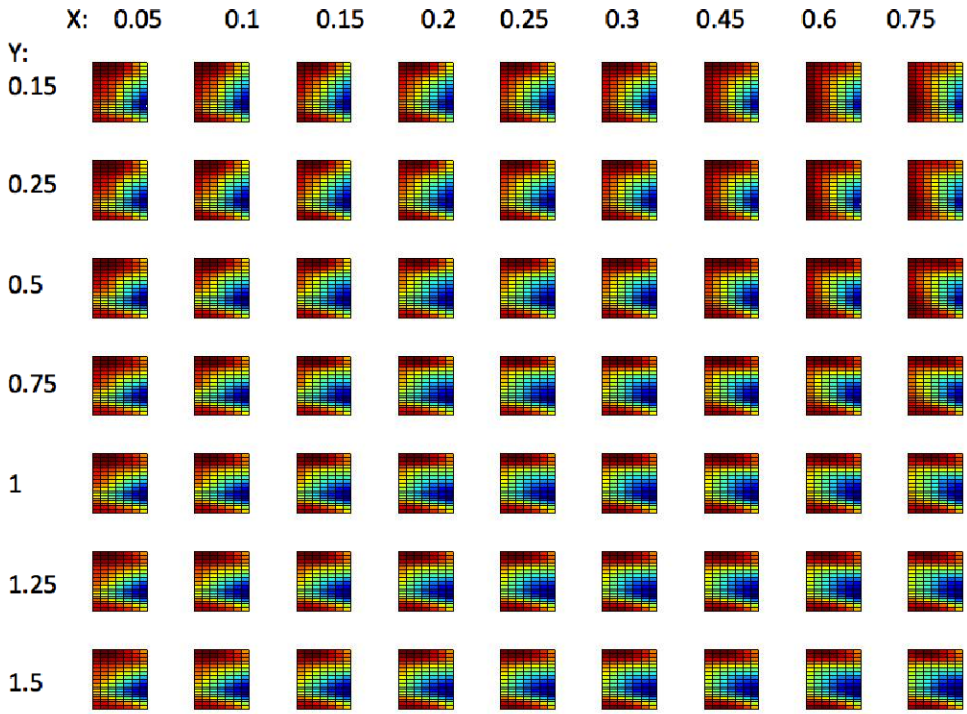

Figure 6-29: Added mass coefficient in the inline direction C_{mx}. The x-axis is the nondimensional amplitude of inline motion 0.05, 0.1, 0.15, 0.2, 0.25, 0.3, 0.45, 0.6 and 0.75. The y-axis is the nondimensional amplitudes of crossflow motion: 0.15, 0.25, 0.5, 0.75, 1, 1.25 and 1.5.

coefficient in the inline direction C_{mx} is a strong function of reduced velocity and is mostly smaller for counter-clockwise motion.

The color map in Figure 6-29 is tailored to each individual subplot and thus the scale of lift coefficients C_{Lv} is different from subplot to subplot. If the color map is unified as shown in Figure 6-30, the absolute value of the lift coefficient C_{mx} is more clearly shown and another important trend can be observed: as the inline motion amplitude increases, the added mass coefficient in the inline direction C_{mx} increases while as the crossflow motion amplitude decreases, the added mass coefficient in the inline direction C_{mx} increases.

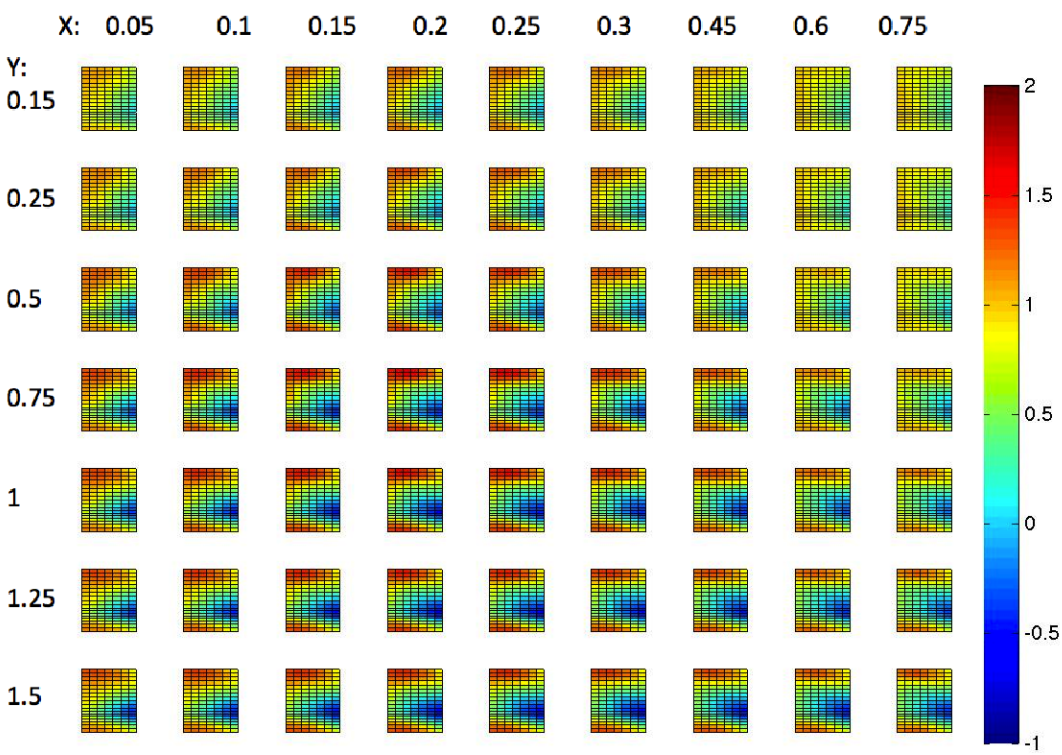

Figure 6-30: Added mass coefficient in the inline direction C_{mx} with same colorbar. The x-axis is the nondimensional amplitude of inline motion 0.05, 0.1, 0.15, 0.2, 0.25, 0.3, 0.45, 0.6 and 0.75. The y-axis is the nondimensional amplitudes of crossflow motion: 0.15, 0.25, 0.5, 0.75, 1, 1.25 and 1.5.

A complete set of the added mass coefficients in the inline direction C_{mx} with

different combinations of inline and crossflow motion amplitudes can be found in appendix A.

6.3 Case Study on Added Mass Coefficients

As discussed In the previous chapter, the added mass coefficients in the crossflow and inline directions were found to have a strong dependency on the phase between Inline and crossflow motion and behave adversely in the crossflow and inline directions. This is especially true when the added mass coefficients in the inline direction C_{mx} is larger (positive) in 90 degree IL-CF motion while the added mass coefficient in the crossflow direction C_{my} is larger (positive) in -90 degree IL-CF motion. To reveal the physics behind the observations, force analysis was conducted from the time series of cylinder forced motion and force measurement. The phase and magnitude of lift and drag force were also analyzed. Furthermore, Particle Image Velocimetry (PIV) observations provide qualitative discussions on the vortex forces and their influence on the added mass. Additionally, the potential flow solution of vortex forces on the body is computed and the measured forces were validated. Lastly, universality of added mass coefficients rules was proven with different amplitudes in the inline and crossflow directions and at different reduced velocities.

6.3.1 Observations on Added Mass Coefficients

The added mass coefficient in the crossflow direction C_{my} and the added mass coefficient in the inline direction C_{mx} are shown in Figure 6-31 and Figure 6-32. The inline motion amplitude equals 0.3 times the diameter of the cylinder and the crossflow motion amplitude equals the diameter of the cylinder.

It can be observed that C_{mx} has a smaller range of change compared with C_{my}. As the ratio of the inline motion amplitude and the crossflow motion amplitude decreases, the phase influence on C_{mx} increases, and the range of C_{mx} increases. As the ratio of the inline motion amplitude and the crossflow motion amplitude decreases, the phase influence to C_{my} decreases, and the range of C_{my} decreases. C_{mx} converges much faster to 1 at a high nondimensional frequency. In particular, the added mass coefficient in the inline direction C_{mx} is larger (positive) in the 90 degree IL-CF motion while the added mass coefficient in the crossflow direction C_{my} is larger (positive) in

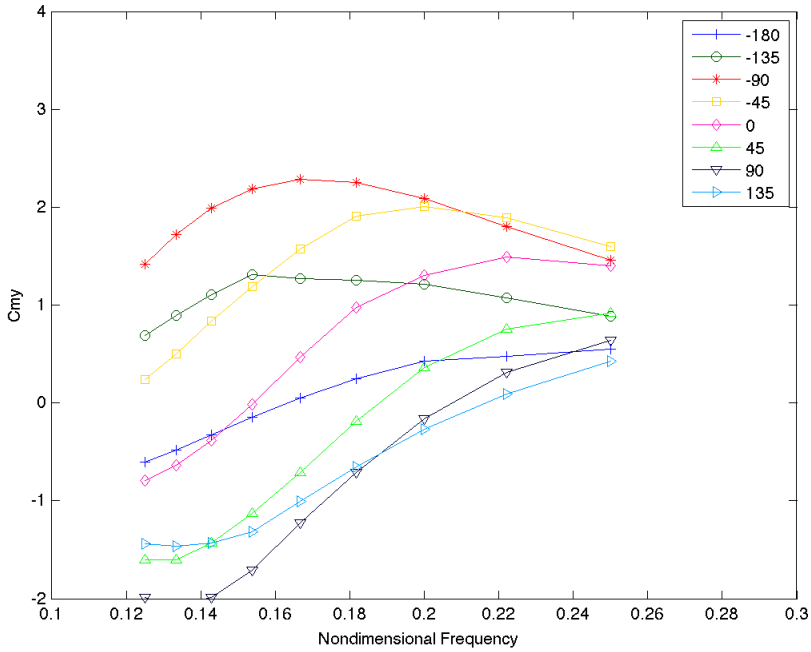

Figure 6-31: Added mass coefficient in the crossflow direction C_{my} with inline motion amplitude 0.3 and crossflow motion amplitude 1

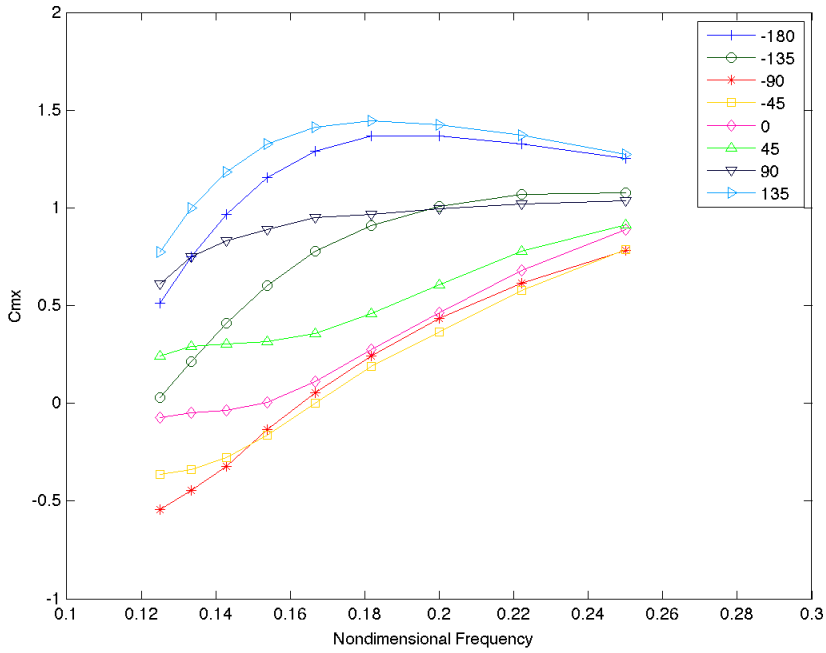

Figure 6-32: Added mass coefficient in the inline direction C_{mx} with inline motion amplitude 0.3 and crossflow motion amplitude 1

the -90 degree IL-CF motion.

6.3.2 Force Analysis

The lift and drag forces on a circular cylinder played a very important role in studying the fluid-body interaction [6, 47]. To reveal the physics behind these observations, force analysis was conducted from the time series of cylinder forced motion and force measurement, and phase and magnitude of lift and drag force were analyzed.

Phase and Magnitude of Drag Force

The added mass coefficient in the inline direction is calculated using the following formula:

$$C_{m,IL} = \frac{2U^2 C_{D2} cos(\phi)}{\pi X D (2w)^2} \tag{6.3}$$

It can be found that the phase ϕ determines the signs of the added mass.

Time series of cylinder forced motion and force of 90° motion are given in Figure 6-33.

Fluctuating drag direction is upstream at the 90° motion apex and is against inline motion, thus a large or positive C_{mx} value is expected. Meanwhile, it was calculated from Figure 6-33 that the ϕ is equal to -40°, which gives a positive C_{mx} value from the above equation and validates the above qualitative results.

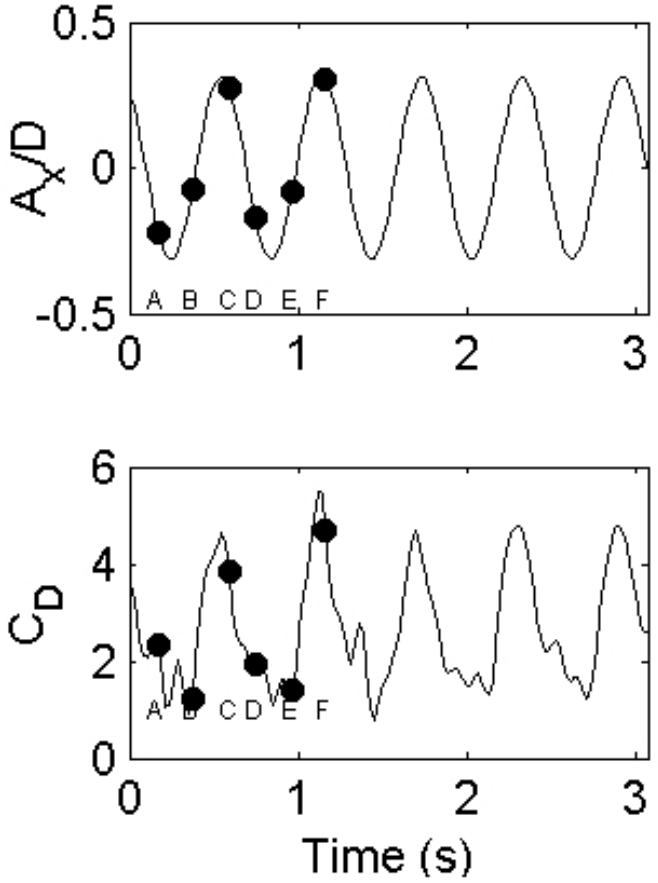

Figure 6-33: Time series of drag coefficients and inline displacement of 90° motion.

Time series of cylinder forced motion and force of -90° motion are given in Figure 6-34.

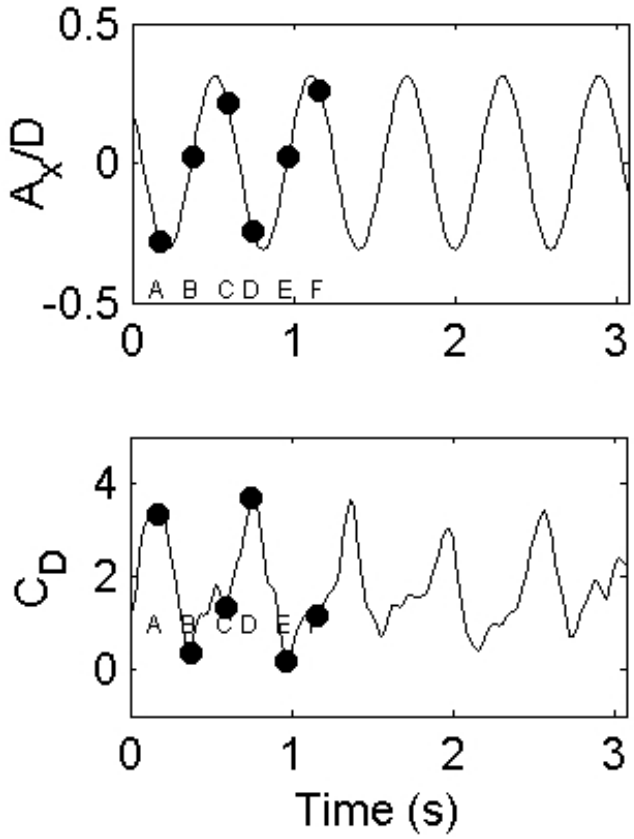

Figure 6-34: Time series of drag coefficients and inline displacement of -90° motion.

Fluctuating drag direction is downstream at the -90° motion apex, and it is along the inline motion, thus a small or negative C_{mx} value is expected. Meanwhile, it was calculated from Figure 6-34 that the phase ϕ is equal to -135°, which gives a negative C_{mx} from the above equation and validates the above qualitative results.

Phase and Magnitude of Lift Force

Phase shift and mode transitions in the near wake of a cylinder under controlled oscillations were studied in the crossflow direction in the past [35, 12, 13] and they provide powerful tools to reveal the mechanisms of fluid-solid interaction [54].

The added mass coefficient in the inline direction is calculated using the following formula:

$$C_{m,CF} = \frac{2U^2 C_{L1} cos(\phi)}{\pi Y D w^2} \tag{6.4}$$

Time series of cylinder forced motion and force of 90° motion are given in Figure 6-35.

Fluctuating lift direction is downwards at the 90° motion apex, and thus along crossflow motion, so a small or negative C_{my} value is expected. Meanwhile, it was calculated from Figure 6-35 that the phase ϕ is equal to -137°, which gives negative C_{my} from above equation and validates the above qualitative results.

Time series of cylinder forced motion and force of -90° motion are given in Figure 6-36.

Fluctuating lift direction is upwards at the -90° motion apex, and thus against crossflow motion; therefore, a large or positive C_{my} value is expected. Meanwhile, it was calculated from Figure 6-36 that the phase ϕ is equal to -15°, which gives a positive C_{my} from the above equation and validated the above qualitative results.

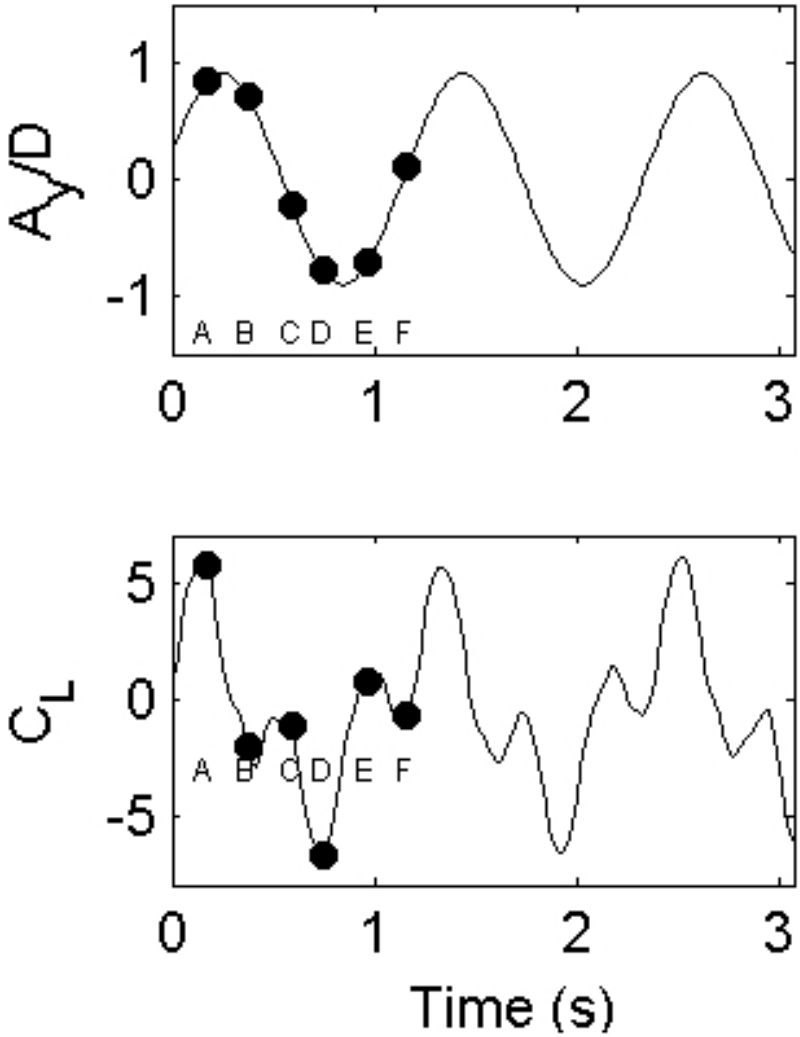

Figure 6-35: Time series of lift coefficients and inline displacement of 90° motion.

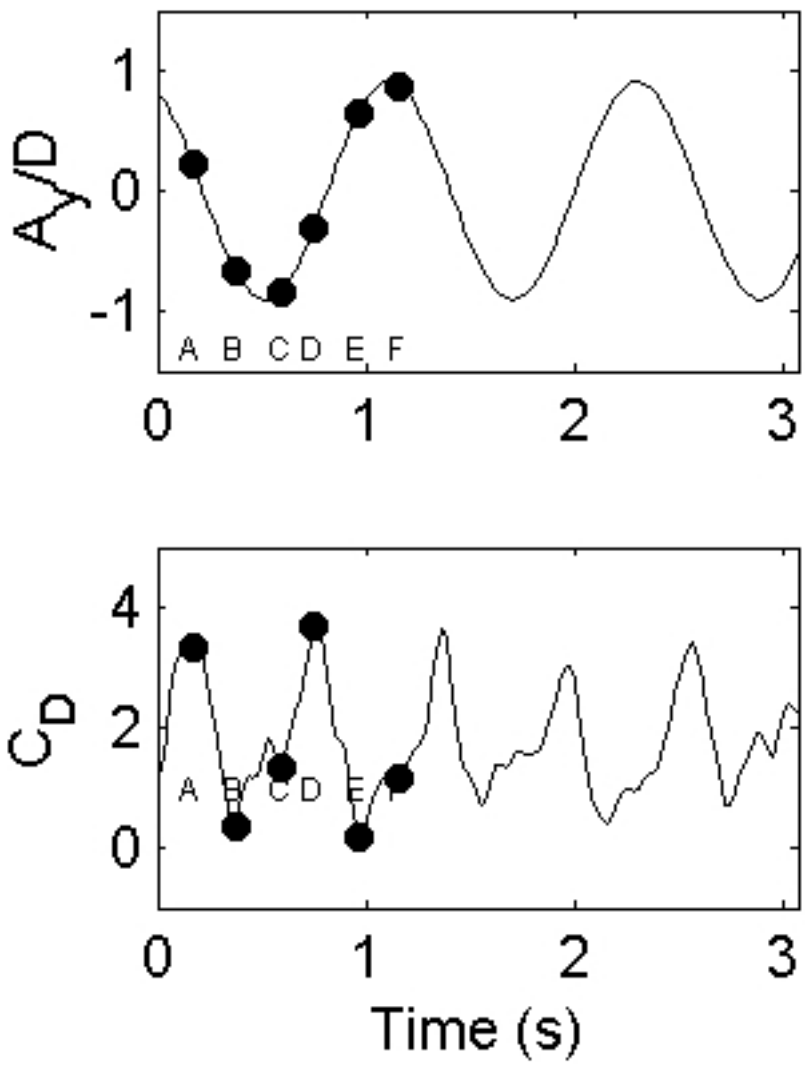

Figure 6-36: Time series of lift coefficients and inline displacement of 90° motion.

6.3.3 Particle Image Velocimetry (PIV)

Particle Image Velocimetry (PIV) is a very powerful tool [64, 72] for revealing the fluid field behind the cylinder and provides both qualitative information and quantitative data on the vorticity.

Qualitative Discussions

The PIV of a cylinder following 90° figure 8 motion is given in Figure 6-37.

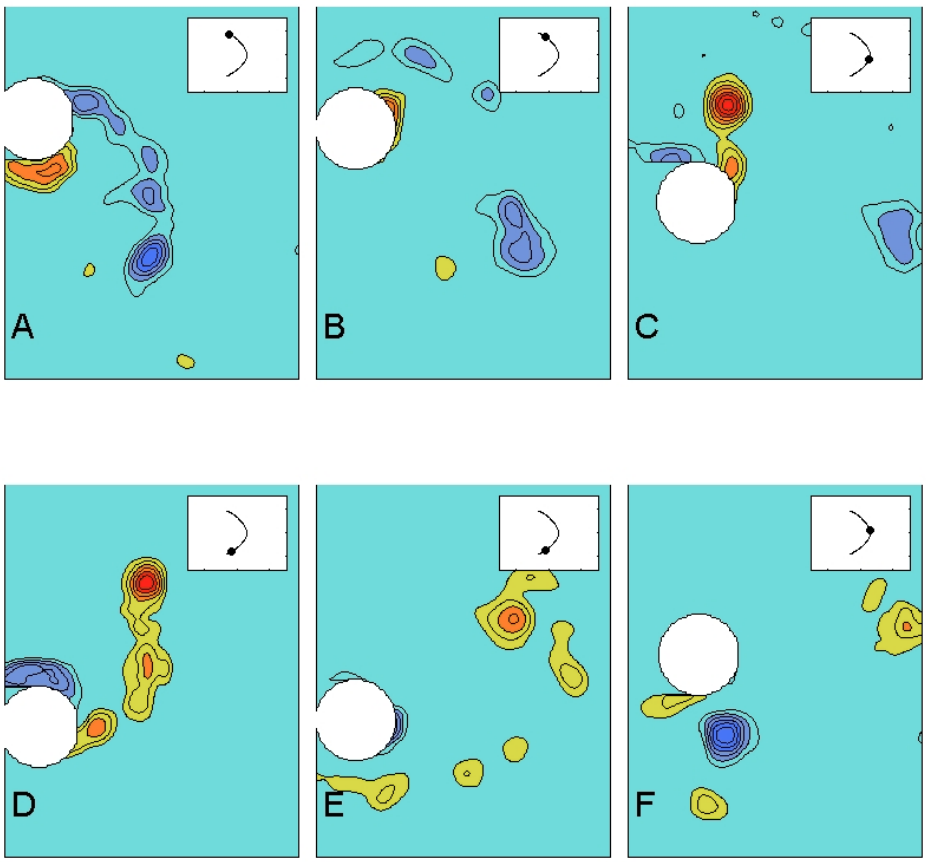

Figure 6-37: PIV of 90° motion.

The PIV of a cylinder following -90° figure 8 motion is given in Figure 6-38.

Generally the closer the distance is, the larger the force. In the inline direction, the cylinder runs into the vortex due to the 90° motion, so a larger force amplitude occurs. The cylinder runs away from the vortex due to the -90° motion, and thus exhibits a smaller force amplitude. In the crossflow direction, the cylinder runs into the vortex

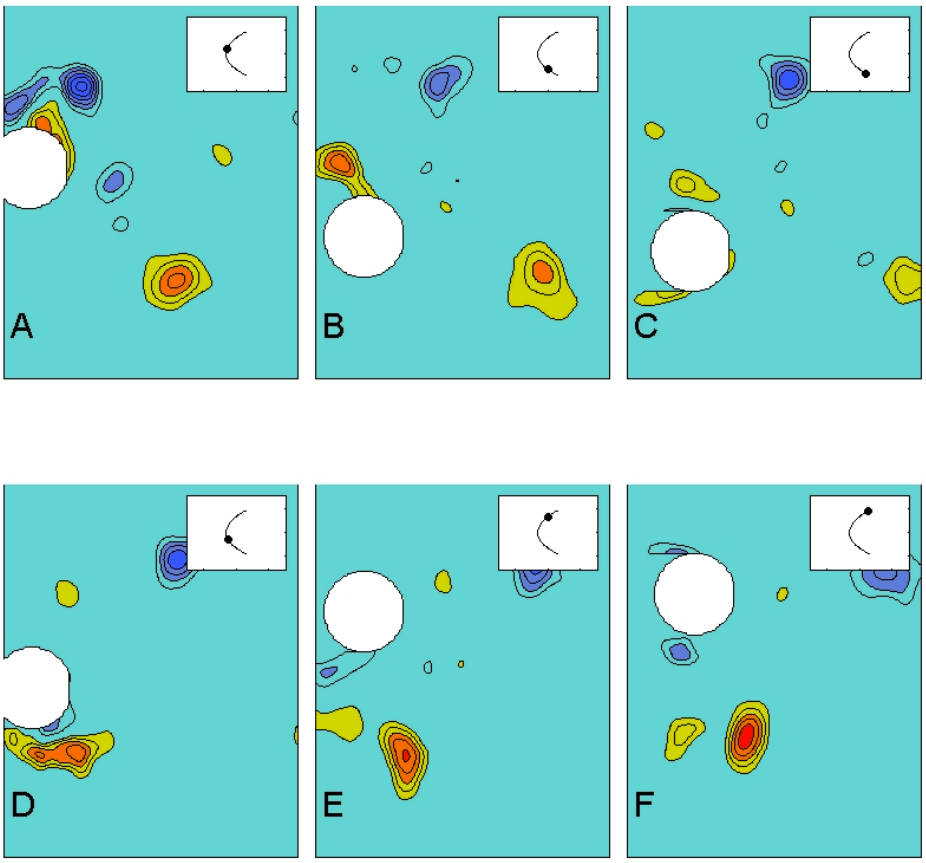

Figure 6-38: PIV of -90° motion.

due to the 90° motion which causes a larger force amplitude. The cylinder runs away from the vortex due to the -90° motion, resulting in a smaller force amplitude.

Forces from Vortices

PIV also provides quantitative data to calculate the fluid forces from vortex [53, 11, 34].

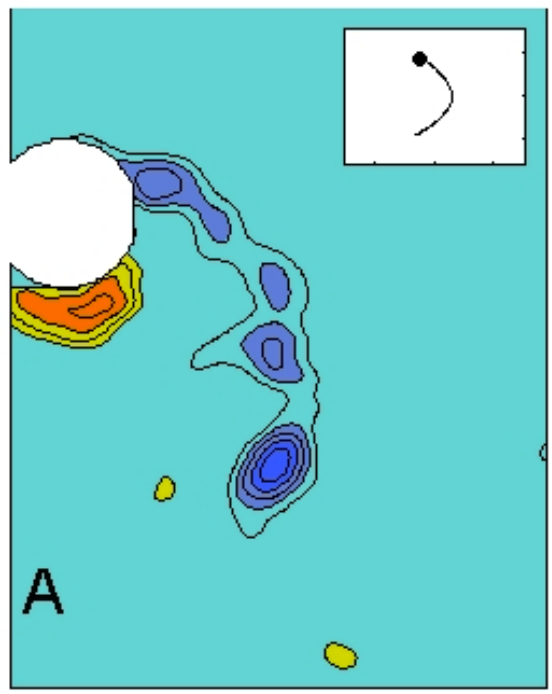

Figure 6-39: PIV of 90° motion.

In this section, the distributed vorticity model for vortex forces on a rigid cylinder is derived from scratch.

From Blasius Theorem [40], the vortex force is given by:

$$F = F_x - jF_y = -i\rho \oint \frac{\partial \bar{w}}{\partial t} d\bar{w} + i\frac{\rho}{2} \oint (\frac{\partial w}{\partial z})^2 dz \tag{6.5}$$

The complex potential of the fluid field is

$$w = -U(z + \frac{R^2}{z}) + \sum (jk_i ln(z - z_i) - jk_i ln(z - \frac{R^2}{\bar{z}_i}) + jk_i ln(z)) \tag{6.6}$$

$$\frac{\partial w}{\partial z} = -U(1 - \frac{R^2}{z^2}) + \sum(\frac{jk_i}{(z - z_i)} - \frac{jk_i}{(z - \frac{R^2}{\bar{z}_i})} + \frac{jk_i}{ln(z)}) \tag{6.7}$$

$$(\frac{\partial w}{\partial z})^2 = (-U(1 - \frac{R^2}{z^2}) + \sum(\frac{jk_i}{(z - z_i)} - \frac{jk_i}{(z - \frac{R^2}{\bar{z}_i})} + \frac{jk_i}{ln(z)}))^2 \tag{6.8}$$

$$\oint(\frac{\partial w}{\partial z})^2 dz = 2\pi j * 2UR^2 * \sum(\frac{1}{-z_i^2}) + \oint(\sum(\frac{jk_i}{(z - z_i)} - \frac{jk_i}{(z - \frac{R^2}{\bar{z}_i})} + \frac{jk_i}{ln(z)}))^2 dz \tag{6.9}$$

The vortex force is given by:

$$\begin{aligned} F &= F_x - jF_y \\ &= -j\rho * 2\pi R^2 \sum(\frac{k_i \dot{z}_i}{-{z_i}^2}) \\ &+ 0.5j\rho(2\pi j * 2UR^2 \sum(\frac{1}{-z_i^2}) + \oint(\sum(\frac{jk_i}{(z - z_i)} - \frac{jk_i}{(z - \frac{R^2}{\bar{z}_i})} + \frac{jk_i}{ln(z)}))^2 dz) \end{aligned} \tag{6.10}$$

The calculated vortex force is shown in Figure 6-40 and Figure 6-41 for lift and drag respectively.

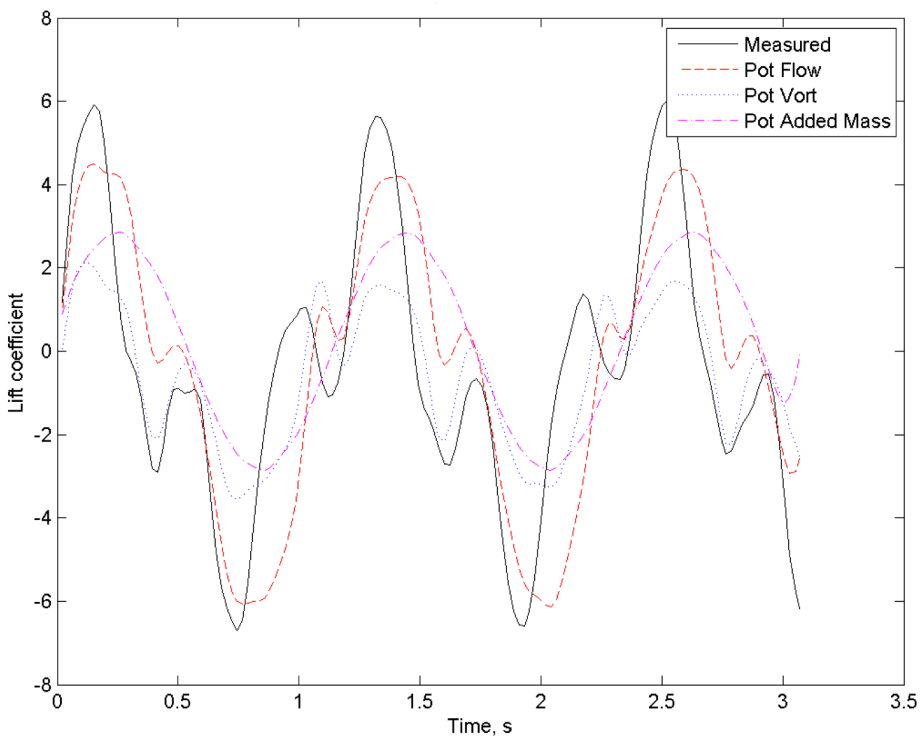

Figure 6-40: Lift force from vortex.

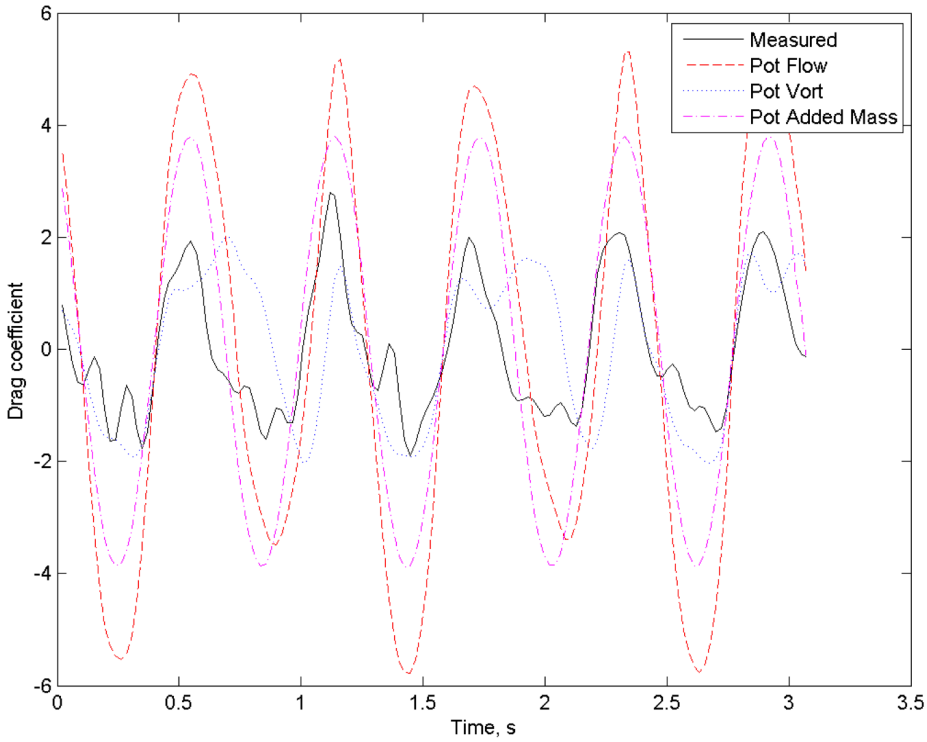

Figure 6-41: Drag force from vortex.

6.4 Inline-Crossflow Rigid Cylinder Modeling and Prediction

The experimental database of force coefficients is first used to predict the response of an elastically mounted, rigid cylinder. The governing equation of a rigid cylinder [57] of mass, m, mounted on springs with spring constant, k, and dashpots with damping constant, b, under a uniform current of velocity U is

$$m_y\ddot{y} + b_y\dot{y} + k_y y = L_f \tag{6.11}$$

$$m_x\ddot{x} + b_x\dot{x} + k_x x = D_f \tag{6.12}$$

where

$$L_f(t) = Re\left\{(m_{a,CF}A_y(w)^2 + i_{lv,IL}\frac{\rho_f U^2 DL}{2})e^{i(wt)}\right\} \tag{6.13}$$

and

$$D_f(t) = Re\left\{(m_{a,IL}A_x(2w)^2 + i_{lv,IL}\frac{\rho_f U^2 DL}{2})e^{i(2wt-\theta)}\right\} \tag{6.14}$$

The hydrodynamic force is decomposed into two terms: one in phase with velocity and one in phase with acceleration (added mass force). The lift coefficient in phase with velocity $C_{fv,IL}$ and added mass coefficient $C_{a,IL}$ are defined as

$$C_{lv,CF} = \frac{L_f sin(\phi)}{\rho_f U^2 DL/2} \tag{6.15}$$

$$C_{fv,IL} = \frac{D_f sin(\phi)}{\rho_f U^2 DL/2} \tag{6.16}$$

$$C_{m,CF} = -\frac{L_f cos(\phi)}{\rho_f \pi U^2 L A_w^2/4} \tag{6.17}$$

$$C_{m,IL} = -\frac{D_f cos(\phi)}{\rho_f \pi U^2 L A_w^2/4} \tag{6.18}$$

where F_0 is the magnitude of hydrodynamic force, f is the density of the fluid, D is the diameter of the cylinder, L is the span length of the cylinder, and A_w is the wet area. The lift and added mass coefficient values correspond to the experimentally obtained coefficients in the previous section:

$$\begin{cases} V_{r,CF} = V_{rn,CF}\sqrt{\frac{m^*_{CF}+C_{m,CF}(A^*_{CF},A^*_{IL},\theta,V_r)}{m^*_{CF}+1}} \\ A^*_{CF} = \frac{C_{lv,CF}(A^*_{CF},A^*_{IL},\theta,V_{r,CF})V_{r,CF}V_{rn,CF}}{4\pi^3 m^*_{CF}+C_{m,CF}(A^*_{CF},A^*_{IL},\theta,V_r)\zeta_{CF}} \\ V_{r,IL} = V_{rn,IL}\sqrt{\frac{m^*_{IL}+C_{m,IL}(A^*_{CF},A^*_{IL},\theta,V_r)}{m^*_{IL}+1}} \\ A^*_{IL} = \frac{C_{fv,IL}(A^*_{CF},A^*_{IL},\theta,V_{r,IL})V_{r,IL}V_{rn,IL}}{4\pi^3 m^*_{IL}+C_{m,IL}(A^*_{CF},A^*_{IL},\theta,V_r)\zeta_{IL}} \\ V_r = V_{r,CF} = 2V_{r,IL} \end{cases} \tag{6.19}$$

where the variables are defined as the following:

$$V_{rn,CF} = \frac{U}{f_{n,CF}D} \tag{6.20}$$

$$V_{rn,IL} = \frac{U}{f_{n,IL}D} \tag{6.21}$$

$$m^*_{CF} = \frac{m_{CF}}{\rho_f \frac{\pi D^2 L}{4}} \tag{6.22}$$

$$m^*_{IL} = \frac{m_{IL}}{\rho_f \frac{\pi D^2 L}{4}} \tag{6.23}$$

$$\zeta_{CF} = \frac{b_{CF}}{2(m^*_{CF} + C_{m,CF})\rho_f \frac{\pi D^2 L}{4} w_{n,CF}} \tag{6.24}$$

$$\zeta_{IL} = \frac{b_{IL}}{2(m^*_{IL} + C_{m,IL})\rho_f \frac{\pi D^2 L}{4} w_{n,IL}} \tag{6.25}$$

$$f_{n,CF} = \frac{1}{2\pi}\sqrt{\frac{k_{CF}}{m_{CF}(1 + \frac{1}{m^*_{CF}})}} \tag{6.26}$$

$$f_{n,IL} = \frac{1}{2\pi}\sqrt{\frac{k_{IL}}{m_{IL}(1 + \frac{1}{m^*_{IL}})}} \tag{6.27}$$

There are five equations and five unknowns. However, due to high non-linearity of the equations and hydrodynamic coefficients database, there is no guarantee from a mathematical point of view that there is a single or unique solution. To solve the above equation, we first try to get the initial values using the two uncoupled databases in the inline and crossflow directions.

$$\begin{cases} V^0_{r,CF} = V_{rn,CF}\sqrt{\frac{m^*_{CF} + C_{m,CF}(A^0_{CF}, V_r)}{m^*_{CF} + 1}} \\ A^0_{CF} = \frac{C_{lv,CF}(A^*_{CF}, V_{r,CF}) V_{r,CF} V_{rn,CF}}{4\pi^3 m^*_{CF} + C_{m,CF}(A^*_{CF}, V_r)\zeta_{CF}} \end{cases} \tag{6.28}$$

$$\begin{cases} V^0_{r,IL} = V_{rn,IL}\sqrt{\frac{m^*_{IL}+C_{m,IL}(A^0_{IL},V_{r,IL})}{m^*_{IL}+1}} \\ A^0_{IL} = \frac{C_{lv,IL}(A^*_{IL},V_{r,IL})V_{r,IL}V_{rn,IL}}{4\pi^3 m^*_{IL}+C_{m,IL}(A^*_{IL},V_r)\zeta_{IL}} \end{cases} \tag{6.29}$$

The calculated responses are given in Figure 6-42.

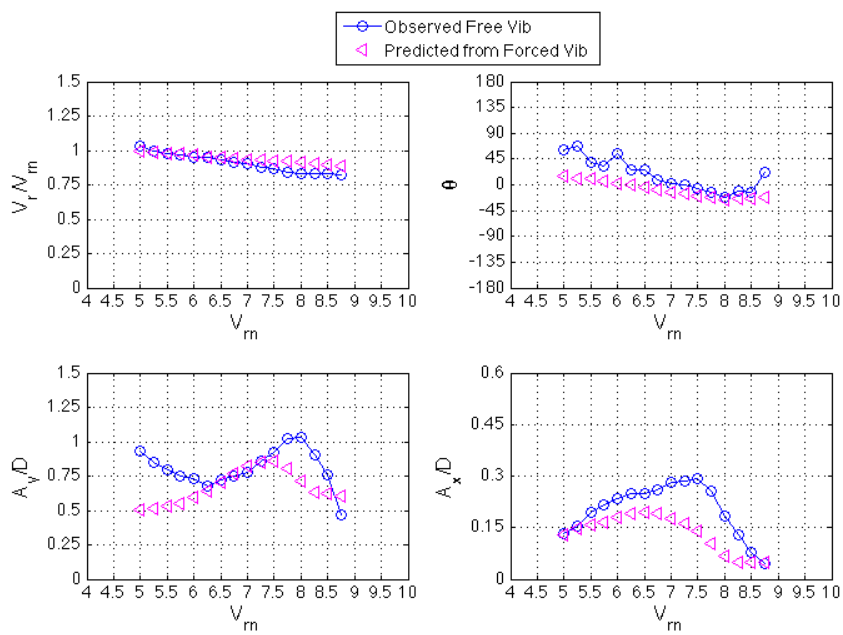

Figure 6-42: Uncoupled Response Prediction vs Free Vibration Experiment Measurement at Natural Frequency Ratio 1.9

The next step is solving the non-linear equations by setting up a system of 11 equations and 11 unknowns. The 11 unknowns are defined as:

$$\begin{bmatrix} \\ x_1 \\ x_2 \\ x_3 \\ x_4 \\ x_5 \\ x_6 \\ x_7 \\ x_8 \\ x_9 \\ x_{10} \\ x_{11} \\ \\ \end{bmatrix} = \begin{bmatrix} \\ A^*_{CF} \\ A^*_{IL} \\ \theta \\ V_{r,CF} \\ V_{r,IL} \\ C_{m,CF} \\ C_{m,IL} \\ C_{lv,CF} \\ C_{fv,IL} \\ \zeta_{CF} \\ \zeta_{IL} \\ \\ \end{bmatrix} \tag{6.30}$$

The governing equations are further decomposed as:

$$
\begin{cases}
A^*_{CF} - \frac{C_{lv,CF}(A^*_{CF},A^*_{IL},\theta,V_{r,CF})V_{r,CF}V_{rn,CF}}{4\pi^3 m^*_{CF}+C_{m,CF}(A^*_{CF},A^*_{IL},\theta,V_r)\zeta_{CF}} = 0 \\
A^*_{IL} - \frac{C_{fv,IL}(A^*_{CF},A^*_{IL},\theta,V_{r,IL})V_{r,IL}V_{rn,IL}}{4\pi^3 m^*_{IL}+C_{m,IL}(A^*_{CF},A^*_{IL},\theta,V_r)\zeta_{IL}} = 0 \\
V_{r,CF} - V_{rn,CF}\sqrt{\frac{m^*_{CF}+C_{m,CF}(A^*_{CF},A^*_{IL},\theta,V_r)}{m^*_{CF}+1}} = 0 \\
V_{r,IL} - V_{rn,IL}\sqrt{\frac{m^*_{IL}+C_{m,IL}(A^*_{CF},A^*_{IL},\theta,V_r)}{m^*_{IL}+1}} = 0 \\
V_{r,CF} - 2V_{r,IL} = 0 \\
C_{m,CF} - C_{m,CF}(A^*_{CF}, A^*_{IL}, \theta, V_r) = 0 \\
C_{m,IL} - C_{m,IL}(A^*_{CF}, A^*_{IL}, \theta, V_r) = 0 \\
C_{lv,CF} - C_{lv,CF}(A^*_{CF}, A^*_{IL}, \theta, V_{r,CF}) = 0 \\
C_{fv,IL} - C_{fv,IL}(A^*_{CF}, A^*_{IL}, \theta, V_{r,IL}) = 0 \\
\zeta_{CF} - \frac{b_{CF}}{2(m^*_{CF}+C_{m,CF})\rho_f \frac{\pi D^2 L}{4} w_{n,CF}} = 0 \\
\zeta_{IL} - \frac{b_{IL}}{2(m^*_{IL}+C_{m,IL})\rho_f \frac{\pi D^2 L}{4} w_{n,IL}} = 0
\end{cases}
\tag{6.31}
$$

The calculated final coupled responses are given in Figure 6-43.

It can be observed that the predicted response frequency is very close to the experimental data in general, although there is slight deviation in the high reduced velocity region. To investigate the difference, the added mass coefficients are plotted in

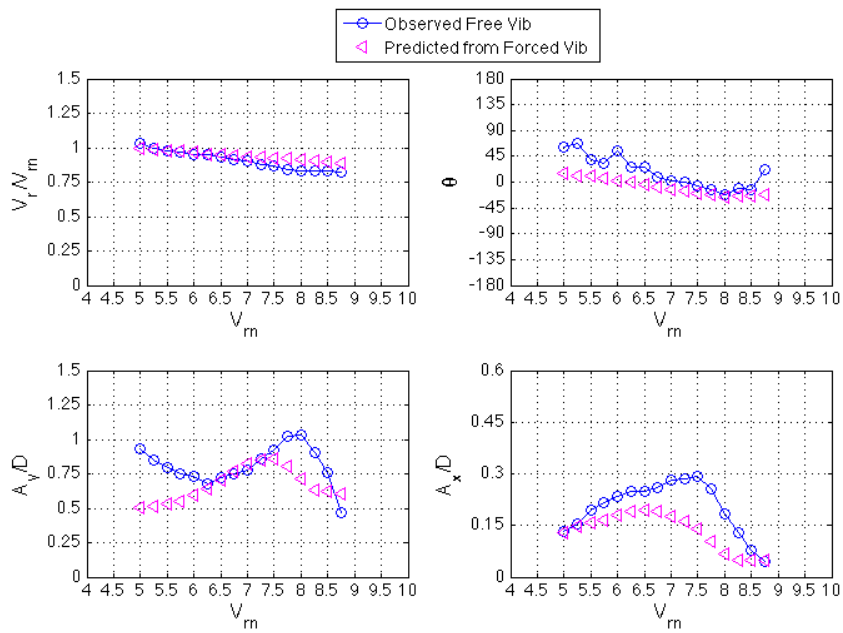

Figure 6-43: Coupled response prediction vs free vibration experiment measurement

Figure 6-44. The added mass is also derived from the free vibration motion following the equation 6.32. There is a very good match between the predicted added mass coefficients and the measured added mass coefficients in the lower and middle reduced velocity range, but they have observable differences at a higher reduced velocity. In order to have a perfect match of response frequency, the added mass coefficients in both the crossflow and the inline direction need to be as low as -1 as indicated by the blue circles in Figure 6-44. However, both the direct measurement from force sensors and the values in the coefficients database are only as low as -0.5. One possible scenario is that there was an error in the measurement of mass ratio and response velocity in the pluck tests before the free vibration experiment.

$$\begin{cases} C_{m,CF} = (m^*_{CF} + 1)(\frac{V_{r,CF}}{V_{rn,CF}})^2 - m^*_{CF} \\ \\ C_{m,IL} = (m^*_{IL} + 1)(\frac{V_{r,IL}}{V_{rn,IL}})^2 - m^*_{IL} \end{cases} \tag{6.32}$$

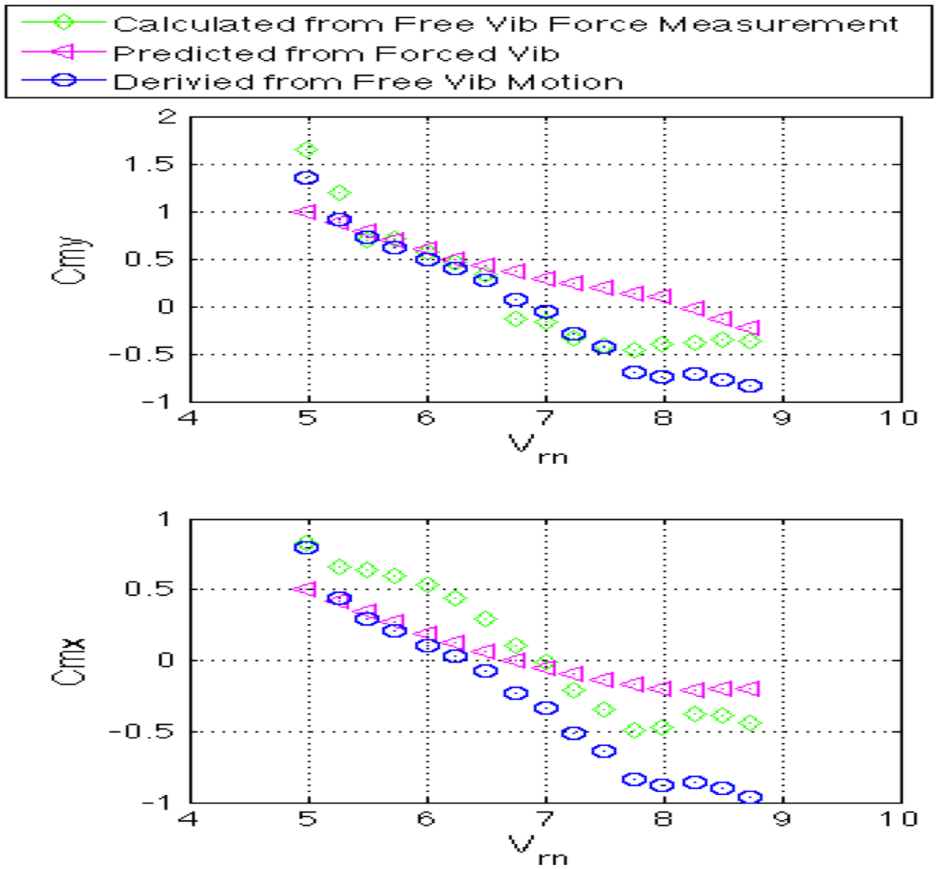

Figure 6-44: Added mass coefficients comparison. The magenta triangle is the added mass predicted from the forced vibration model, the green diamond is added mass measured from the free vibration experiment, and the blue circle is derived from the free vibration motion following equation 6.32.

The predicted response amplitude in the inline direction is very close to the experimental data in shape, but the peak response is lower. This trend is also true for the fluctuating drag coefficients in phase with the velocity shown in Figure 6-45. The blue circle is derived from the free vibration motion following the equation 6.33. In fact, the damping was not perfectly linear as assumed in the prediction model and is a function of the response amplitude. The larger the response amplitude, the smaller the damping. Thus the non-linearity of the damping enhanced the peak response and made it different from the predictions. Similar trends can be observed and possibly explained for the response amplitude and lift coefficients in the crossflow direction.

$$\begin{cases} C_{lv,CF} = \frac{4\pi^3(m^*_{CF}+C_{m,CF})\zeta_{CF}A^*_{CF}}{V_{r,CF}V_{rn,CF}} \\ \\ C_{lv,IL} = \frac{4\pi^3(m^*_{IL}+C_{m,IL})\zeta_{IL}A^*_{IL}}{V_{r,IL}V_{rn,IL}} \end{cases} \tag{6.33}$$

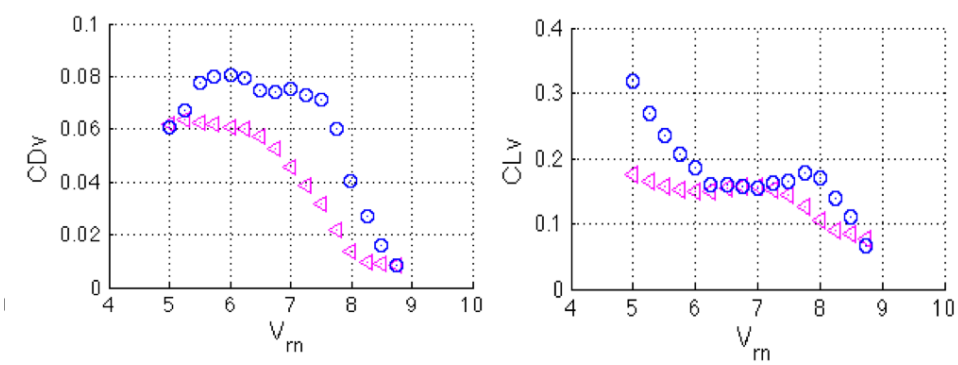

Figure 6-45: Lift and drag force coefficients comparison. The magenta triangle is the added mass predicted from the forced vibration model and the blue circle is derived from free vibration motion following equation 6.33.

6.5 High Harmonic Force Prediction Based on the Inline-Crossflow Model

High harmonic VIV stresses were identified relatively recently [32], [77], [20]. They are closely associated with strong inline motions and they can be very significant for fatigue.

With the crossflow motion, inline motion, response frequency and the phase between inline and crossflow motion calculated from the model in previous section, the first and higher harmonic forces are predicted on the basis of the 'ZDMiT' hydrodynamic coefficients database.

The first harmonic force predicted is very close to the experimental data as shown in Figure 6-46.

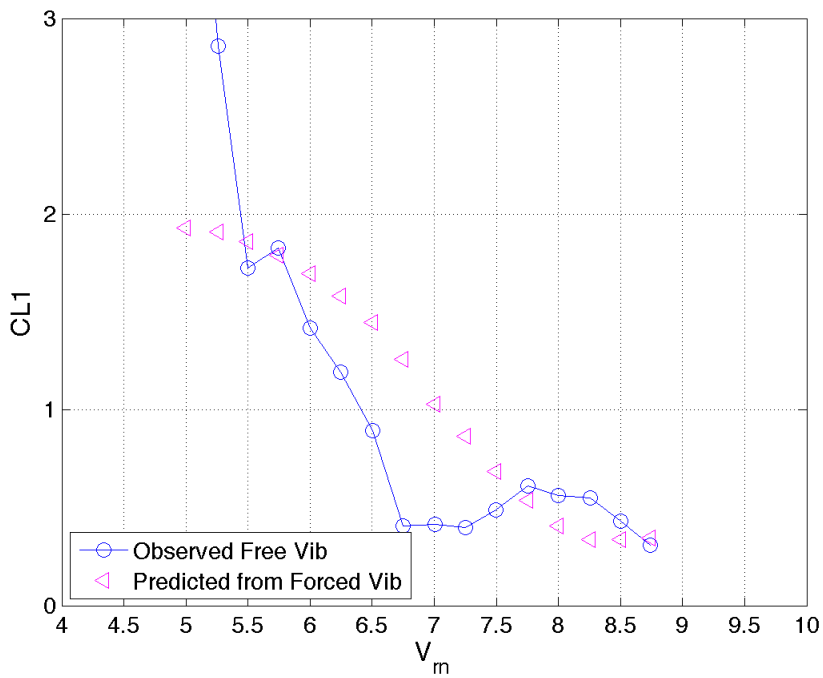

Figure 6-46: First harmonic force prediction vs free vibration experiment measurement at natural frequency ratio 1.9

The third harmonic predicted is similar to the experimental data as shown in Figure 6-47 but the peak value is smaller. When compared back to the inline response

amplitude in Figure 6-43, a similar trend is observed. In fact, the inline response amplitude dominantly effects the third harmonic in the crossflow. Considering the experimental uncertainty discussed above, if the free vibration is used as an input to the database, a very good third harmonic is predicted, as illustrated by the red curve in Figure 6-47. This validates the methodology of using the forced vibration experiment database to predict high harmonic forces.

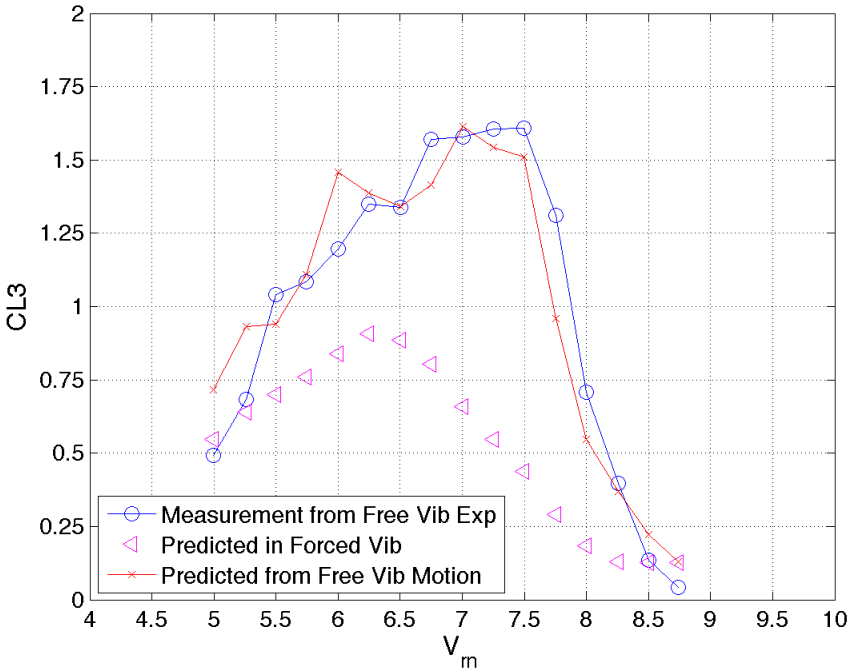

Figure 6-47: Third harmonic force prediction vs free vibration experiment measurement at natural frequency ratio.

Chapter 7

Conclusions

7.1 Overview

The main focus of this thesis is on the high harmonic force starting from quantifying its impact on fatigue damage and ending with its prediction through the coupled inline-crossflow VIV model. VIV prediction in the crossflow direction is improved through the optimization of the hydrodynamic coefficients database and extended to the inline VIV prediction via the pure inline experimental database. The coupled inline-crossflow VIV problem was attacked using a 2D VIV hydrodynamics coefficients database 'ZDMiT' developed from extensive inline-crossflow experiments and a coupled inline-crossflow rigid cylinder response prediction model.

7.2 Principal Contributions

7.2.1 Systematically Quantified the Influence of High Frequency and Chaotic Stress Components on Fatigue Damage of Risers

Higher harmonic force components in VIV signals have been observed relatively recently. Besides being an inherently interesting finding, these higher harmonics have practical significance due to the increase they cause in fatigue damage of marine

risers. It has been shown previously that this increase can be up to two orders of magnitude. In this thesis, the impact of the higher harmonic components as well as the chaotic response on the resulting fatigue damage of the flexible cylinders was systematically quantified using statistical methods to reconstruct a stress time series based on the PSD plots similar to those of the experimental signals. It is concluded that the high harmonic signal has a significant influence on the fatigue life while the wide-band chaotic components have limited effects. Thus, the prediction of high harmonic forces through the coupled inline-crossflow model is the key to the problem.

7.2.2 Optimized Crossflow Hydrodynamic Coefficient Database Based on Lab and Field Experiments

The prediction results of the semi-empirical crossflow VIV prediction model VIVA, a VIV response prediction program widely used in offshore industry, was improved through systematically adjusting the hydrodynamics coefficients based on field and lab experiments. The program with the optimized database was benchmarked with controlled lab experiments and field experiments.

7.2.3 Designed and Carried Out Forced Pure Inline VIV Experiments.

A pure inline forced motion experiment was designed and carried out in the MIT towing tank in 2010. The extracted VIV hydrodynamic force coefficients were compared with higher Reynolds number experiments and a pure inline database was constructed for semi-empirical rigid cylinder Inline VIV models.

7.2.4 Developed and Benchmarked a Semi-Empirical Rigid Cylinder Inline VIV model

A spring-damper rigid cylinder VIV model was developed and the above pure inline hydrodynamic database was employed to calculate the fluid forces on the system. The motion predicted by the model matched well with free vibration experiments. Furthermore, an inline response prediction module was introduced to VIVA to predict the inline response of flexible cylinders and the results were benchmarked with Norwegian Deepwater Programme (NDP) Riser High Mode VIV tests data.

7.2.5 Designed and Carried Out Fine Grid Forced Crossflow-Inline VIV Experiments

Fine grid extensive forced inline and combined inline-crossflow experiments were designed and carried out in the MIT towing tank in 2011. They cover most of the response region in fine resolution and can be employed to provide hydrodynamic coefficients for VIV prediction models.

7.2.6 Created 2D VIV Hydrodynamics Coefficients Database 'ZDMiT' to be Used by Semi-empirical Programs to Predict Coupled Inline-Crossflow VIV.

'ZDMiT', also known as the 2D VIV hydrodynamics coefficients database, is named after the research team under the supervision of Professor Triantafyllou, Zheng Dahl Modarres-Sadeghi Triantafyllou and based on the Dahl 2006 and Zheng 2011 inline-crossflow forced vibration VIV experiments at the MIT towing tank. The constructed 2D VIV hydrodynamics coefficients database ZDMiT was throughly studied and it is expected to be widely used by semi-empirical programs to predict coupled inline-crossflow VIV in the field.

7.2.7 Developed a Coupled Inline-crossflow Rigid Cylinder Response Model to Predict Coupled Inline-Crossflow VIV Motion and Higher Harmonic VIV Forces

A coupled inline-crossflow VIV model of an elastically mounted rigid cylinder was built to predict the inline and crossflow motion frequency, amplitude, and the phase between the inline and crossflow motion. The higher harmonic force was also predicted using the coupled model. Rigid cylinder free vibration experimental data was used to validate this prediction methodology.

7.3 Future Work

7.3.1 Coupled IL-CF VIV Prediction Extension to Flexible Cylinder

Long flexible cylinders are widely used in the industry applications, thus extending the coupled IL-CF VIV prediction method to flexible cylinders is very important. One of the major challenges is resolving the phase between the inline and crossflow motion along different positions of the cylinder span.

7.3.2 Combination of Numerical Virtual Tests with Semi-Empirical Models

As the computation capability of modern cluster computers increases, it will become feasible to calculate the hydrodynamic coefficients at a relatively high Reynolds number and a much finer grid. Therefore, a more complete database can be built for semi-empirical models, without using towing tank experiments.

Appendix A

Additional Figures for Hydrodynamic Force Coefficients in the 2D VIV Database

A.1 Lift Coefficients in Phase with Velocity C_{Lv}

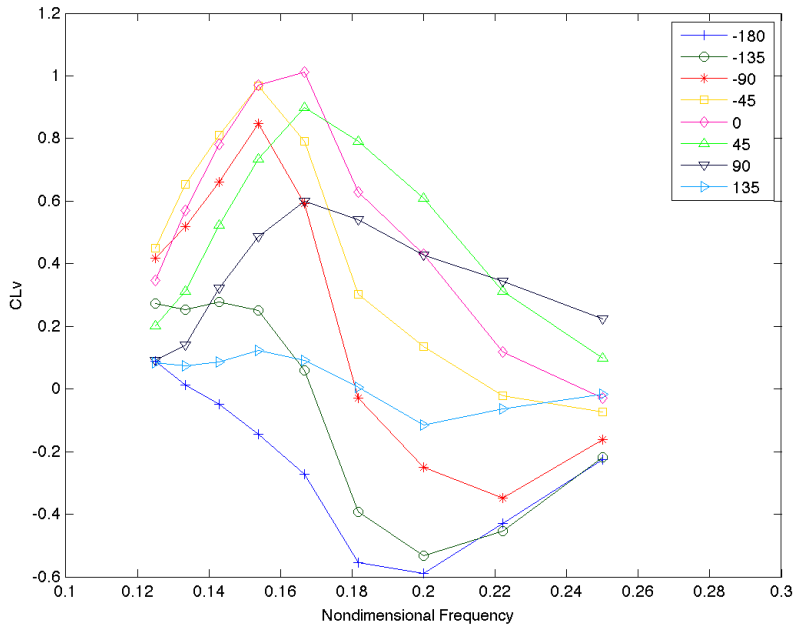

Figure A-1: Lift coefficients in phase with velocity C_{Lv} X 0.05 Y 0.15

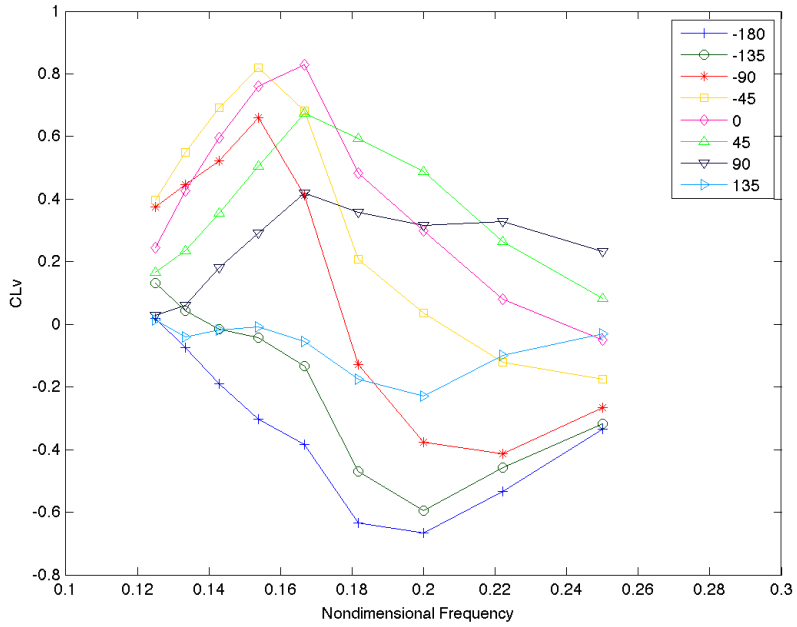

Figure A-2: Lift coefficients in phase with velocity C_{Lv} X 0.05 Y 0.25

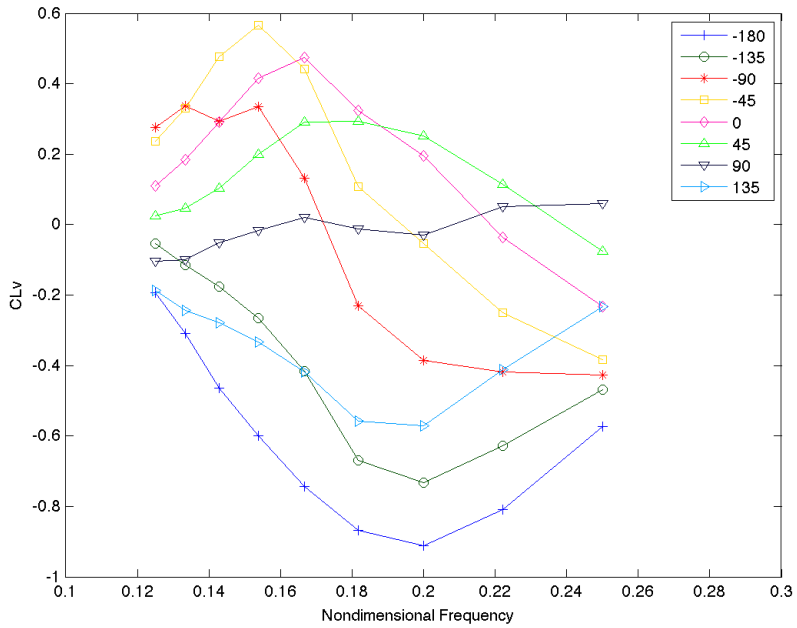

Figure A-3: Lift coefficients in phase with velocity C_{Lv} X 0.05 Y 0.5

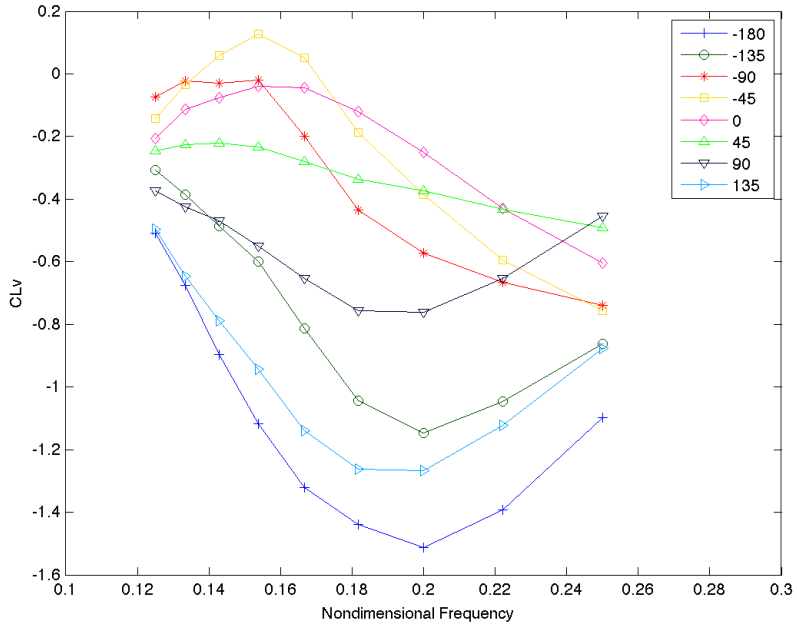

Figure A-4: Lift coefficients in phase with velocity C_{Lv} X 0.05 Y 0.75

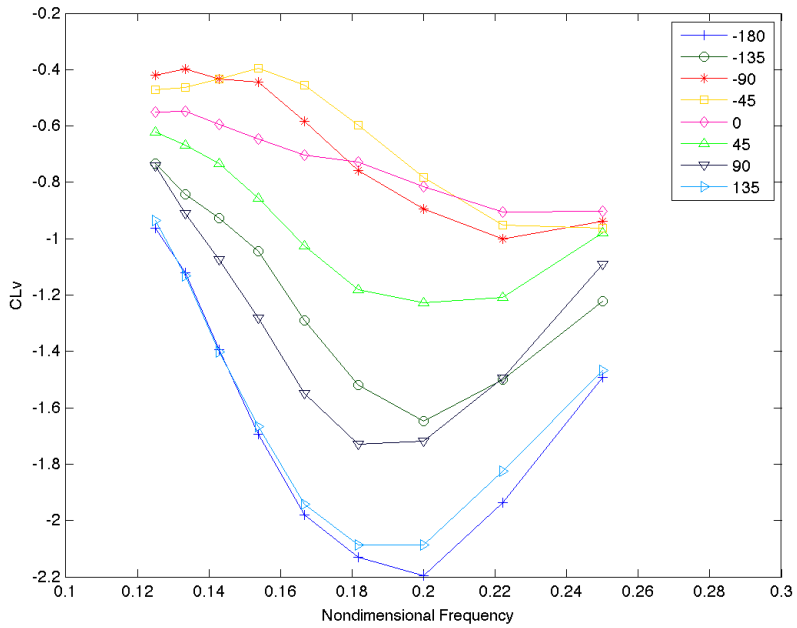

Figure A-5: Lift coefficients in phase with velocity C_{Lv} X 0.05 Y 1

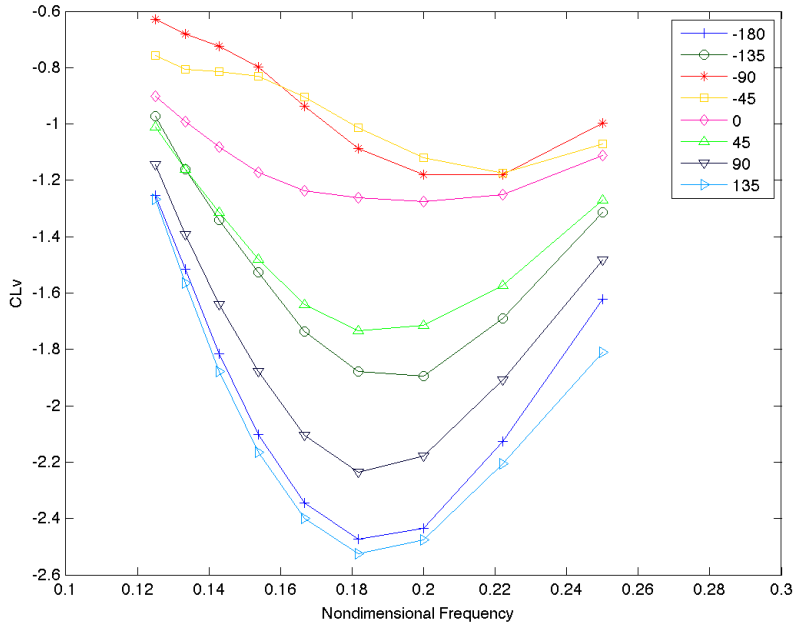

Figure A-6: Lift coefficients in phase with velocity C_{Lv} X 0.05 Y 1.25

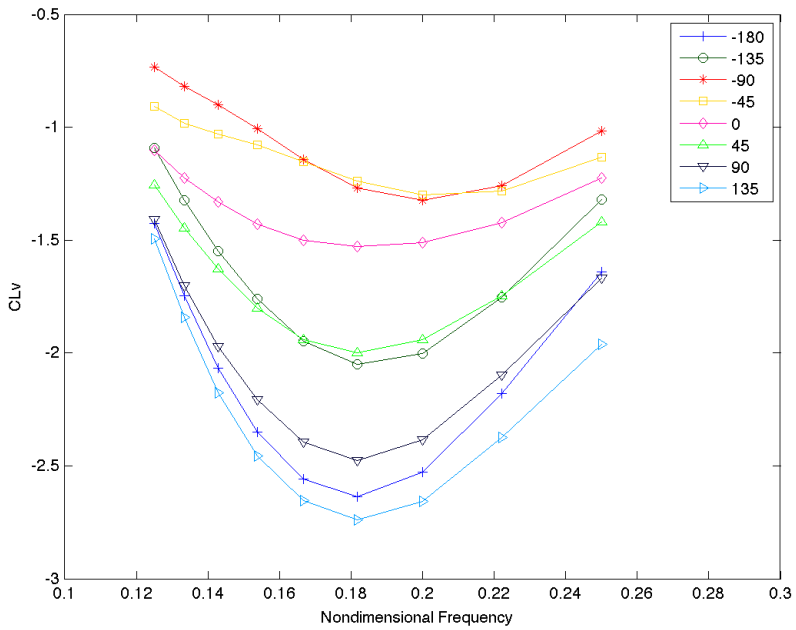

Figure A-7: Lift coefficients in phase with velocity C_{Lv} X 0.05 Y 1.5

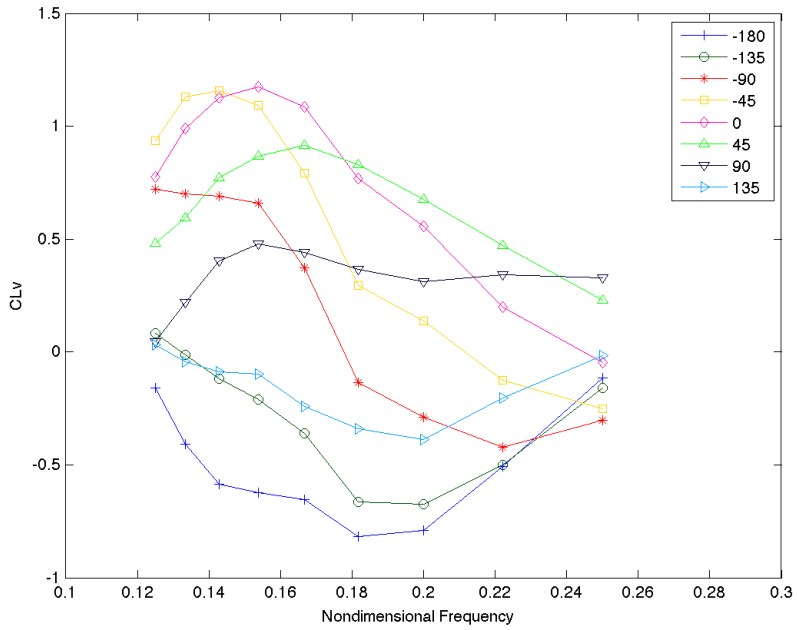

Figure A-8: Lift coefficients in phase with velocity C_{Lv} X 0.1 Y 0.15

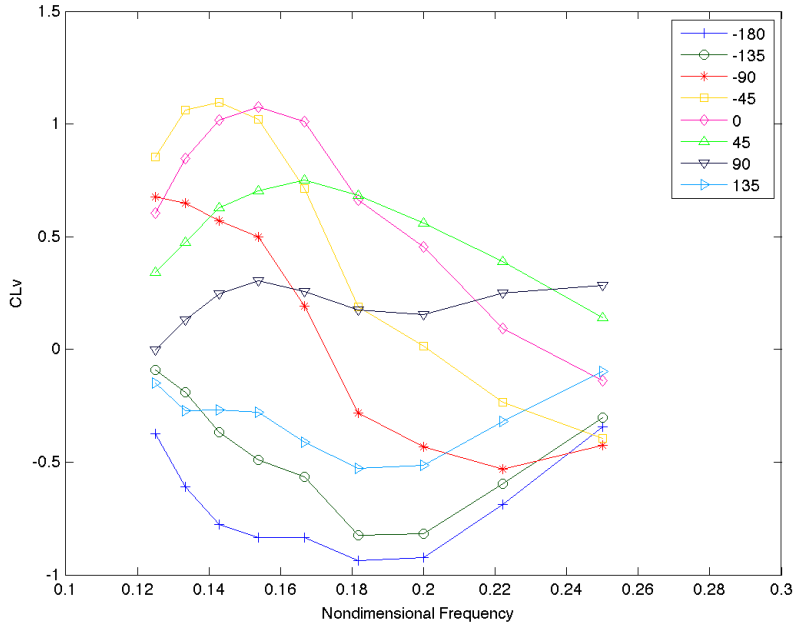

Figure A-9: Lift coefficients in phase with velocity C_{Lv} X 0.1 Y 0.25

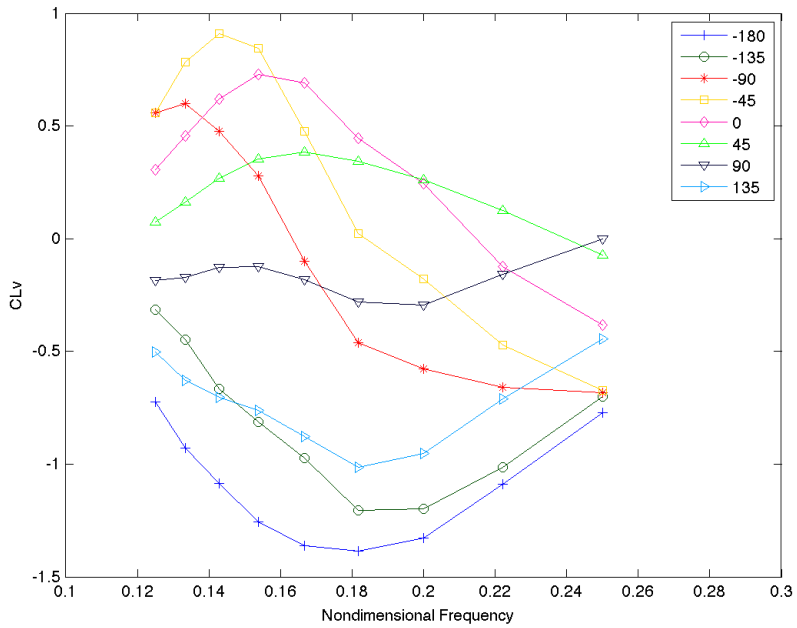

Figure A-10: Lift coefficients in phase with velocity C_{Lv} X 0.1 Y 0.5

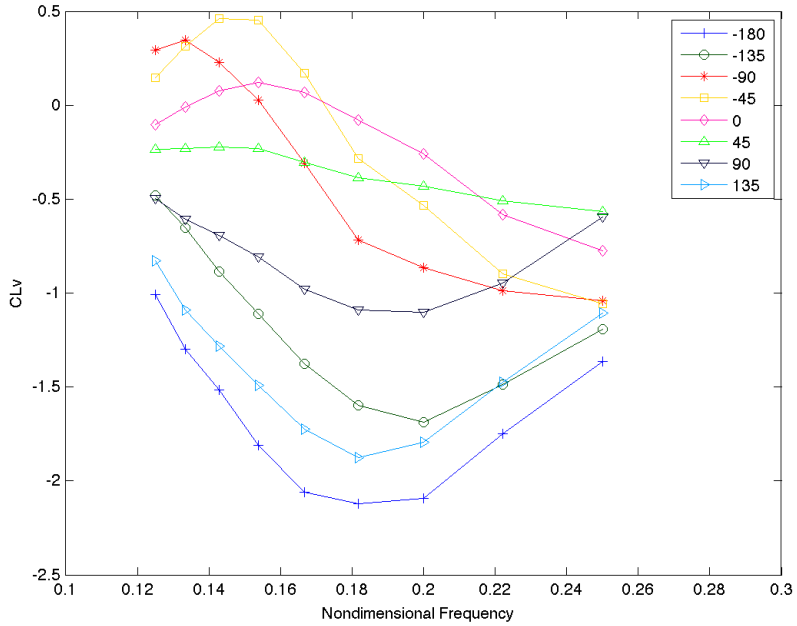

Figure A-11: Lift coefficients in phase with velocity C_{Lv} X 0.1 Y 0.75

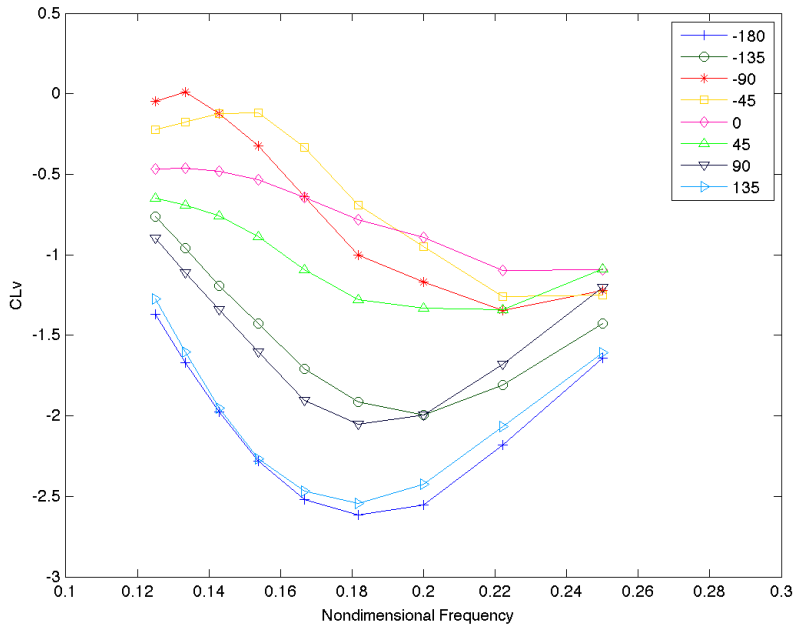

Figure A-12: Lift coefficients in phase with velocity C_{Lv} X 0.1 Y 1

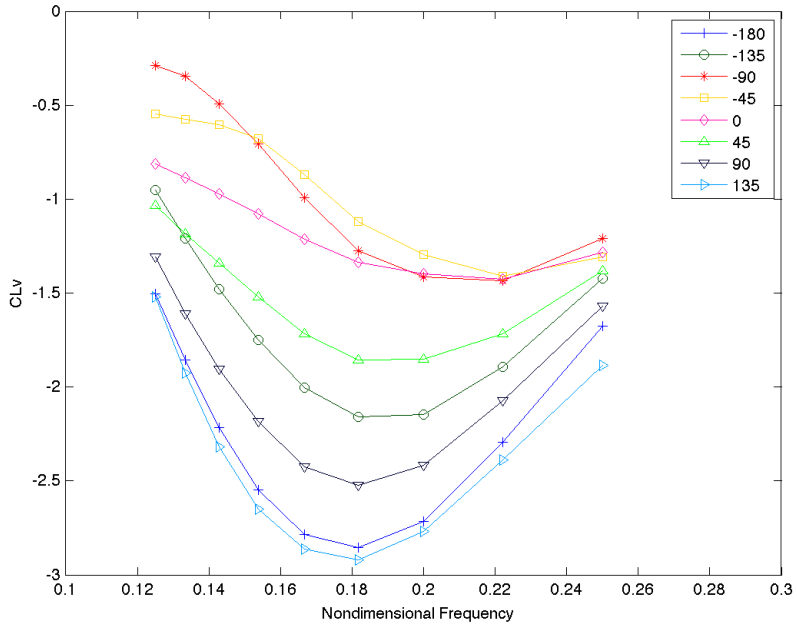

Figure A-13: Lift coefficients in phase with velocity C_{Lv} X 0.1 Y 1.25

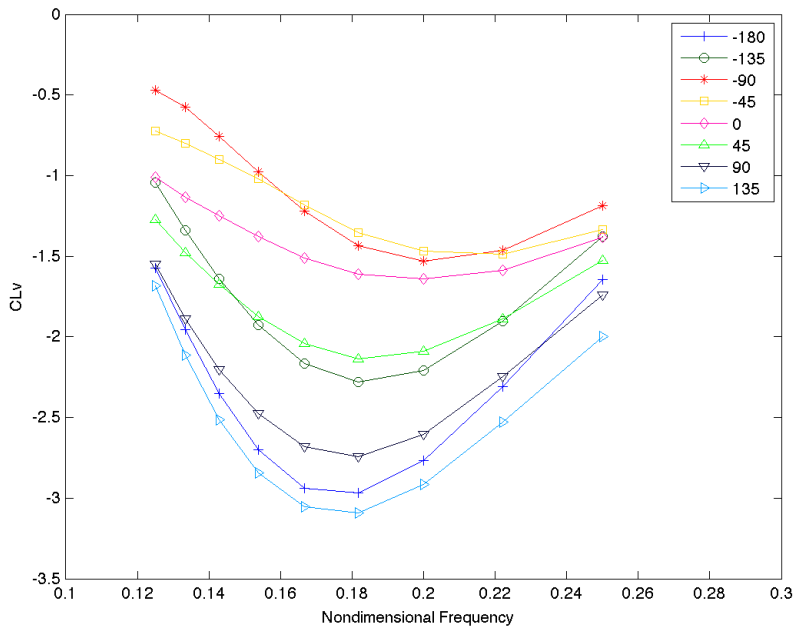

Figure A-14: Lift coefficients in phase with velocity C_{Lv} X 0.1 Y 1.5

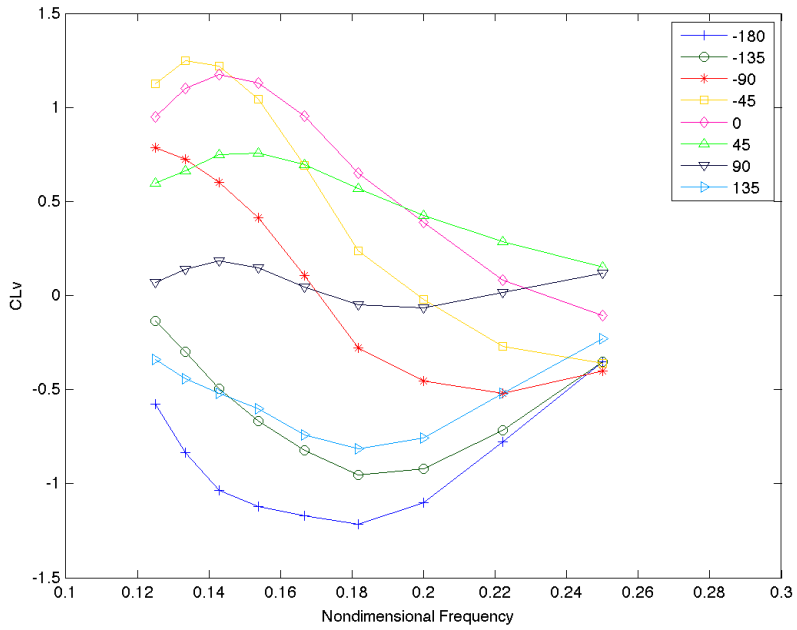

Figure A-15: Lift coefficients in phase with velocity C_{Lv} X 0.15 Y 0.15

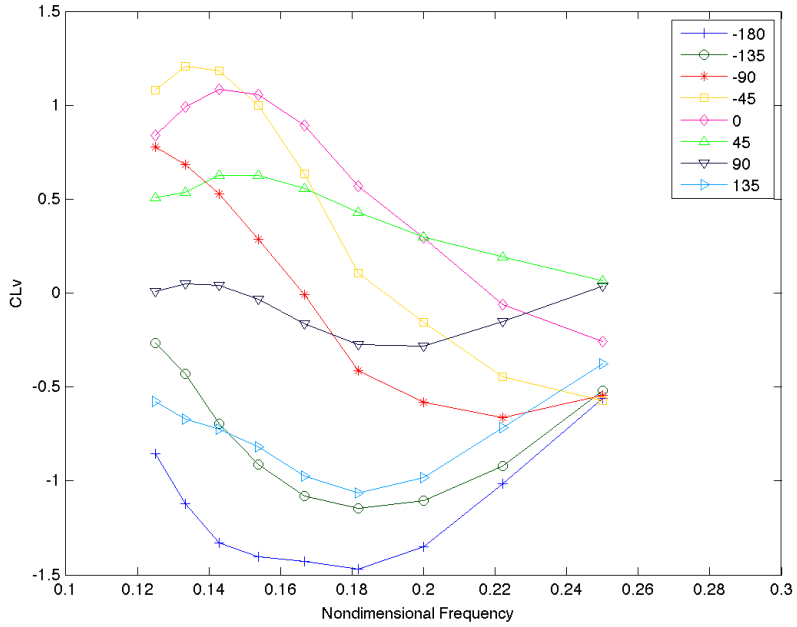

Figure A-16: Lift coefficients in phase with velocity C_{Lv} X 0.15 Y 0.25

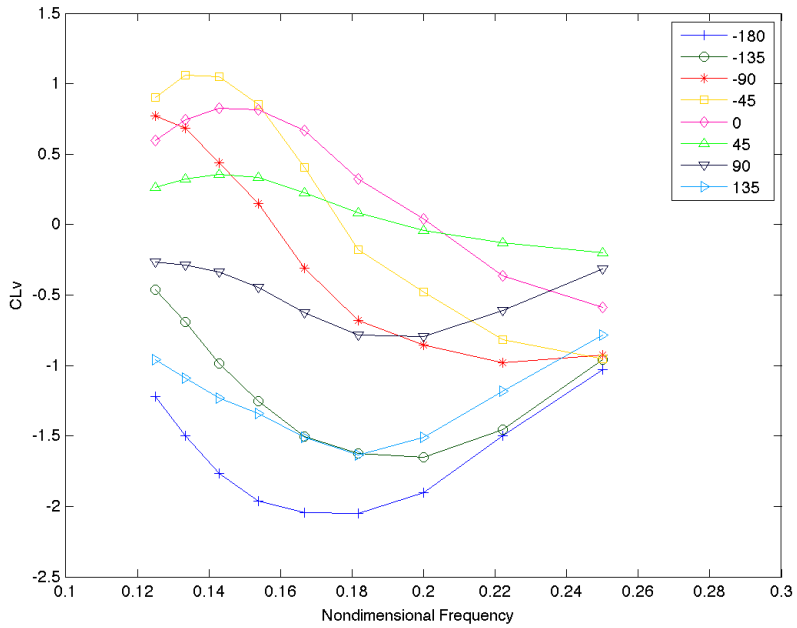

Figure A-17: Lift coefficients in phase with velocity C_{Lv} X 0.15 Y 0.5

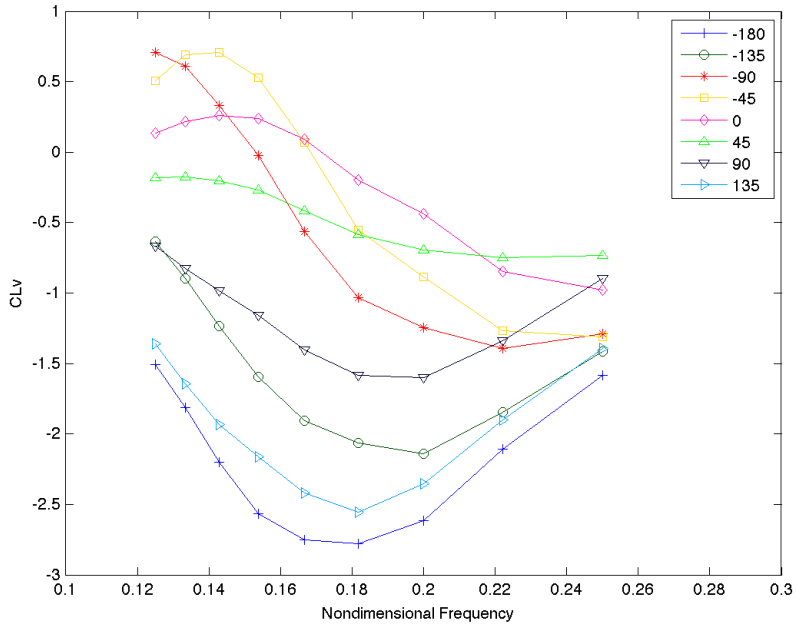

Figure A-18: Lift coefficients in phase with velocity C_{Lv} X 0.15 Y 0.75

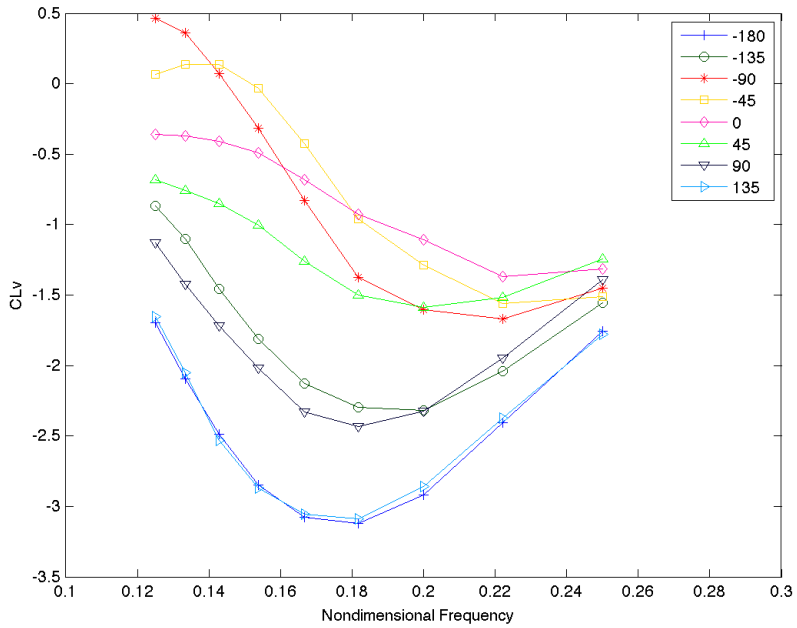

Figure A-19: Lift coefficients in phase with velocity C_{Lv} X 0.15 Y 1

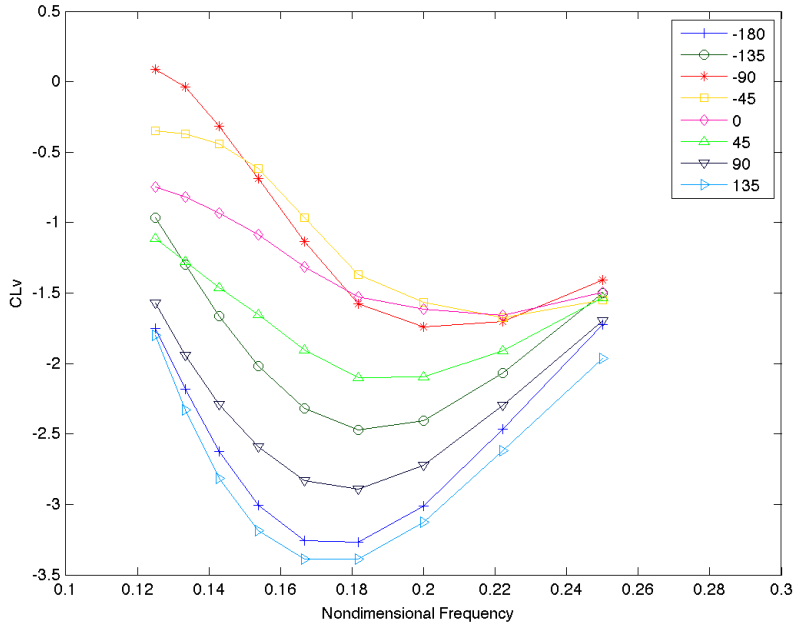

Figure A-20: Lift coefficients in phase with velocity C_{Lv} X 0.15 Y 1.25

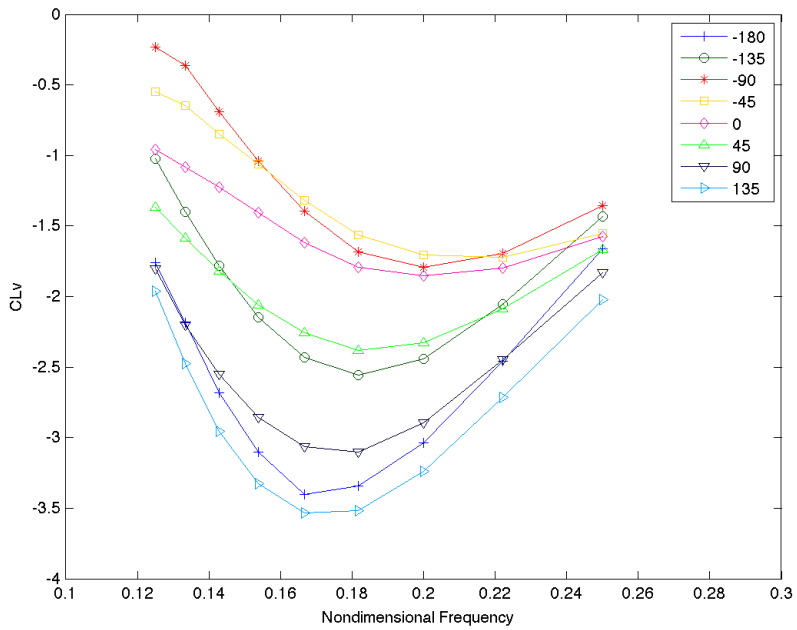

Figure A-21: Lift coefficients in phase with velocity C_{Lv} X 0.15 Y 1.5

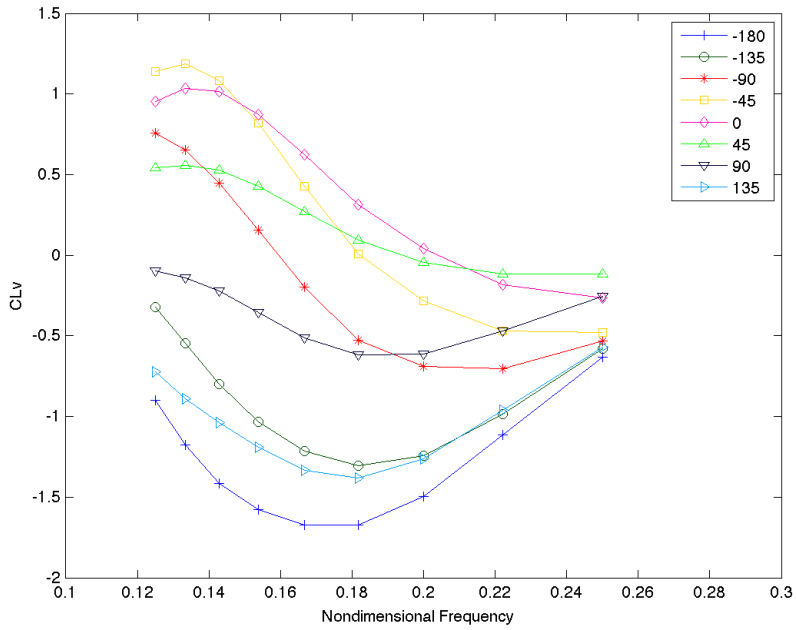

Figure A-22: Lift coefficients in phase with velocity C_{Lv} X 0.2 Y 0.15

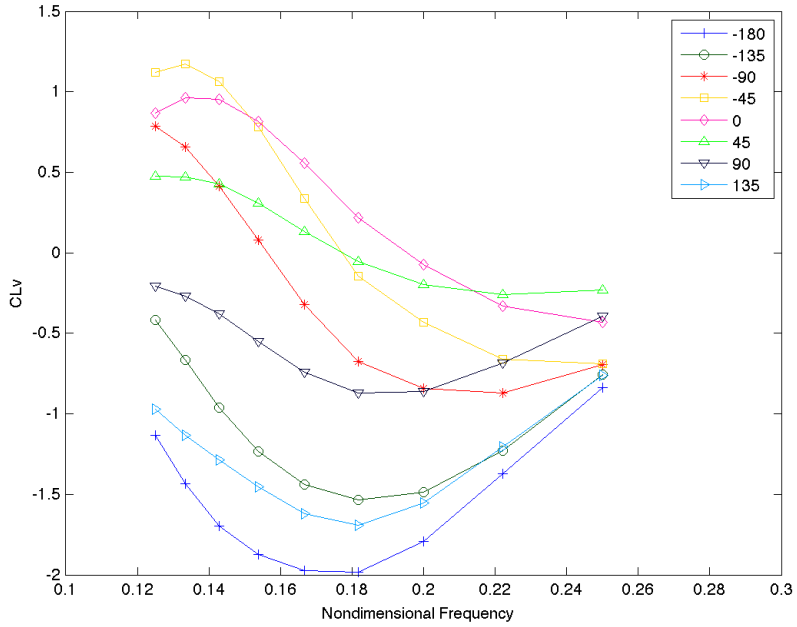

Figure A-23: Lift coefficients in phase with velocity C_{Lv} X 0.2 Y 0.25

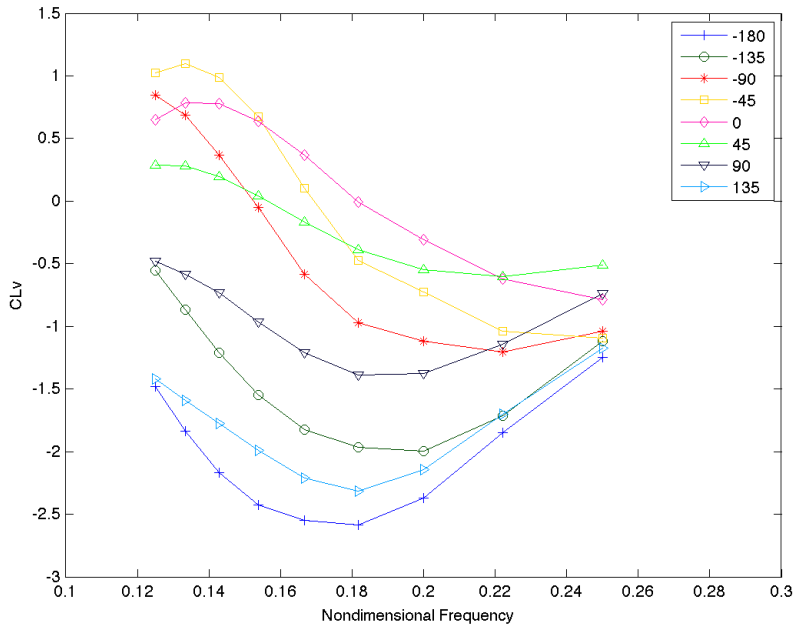

Figure A-24: Lift coefficients in phase with velocity C_{Lv} X 0.2 Y 0.5

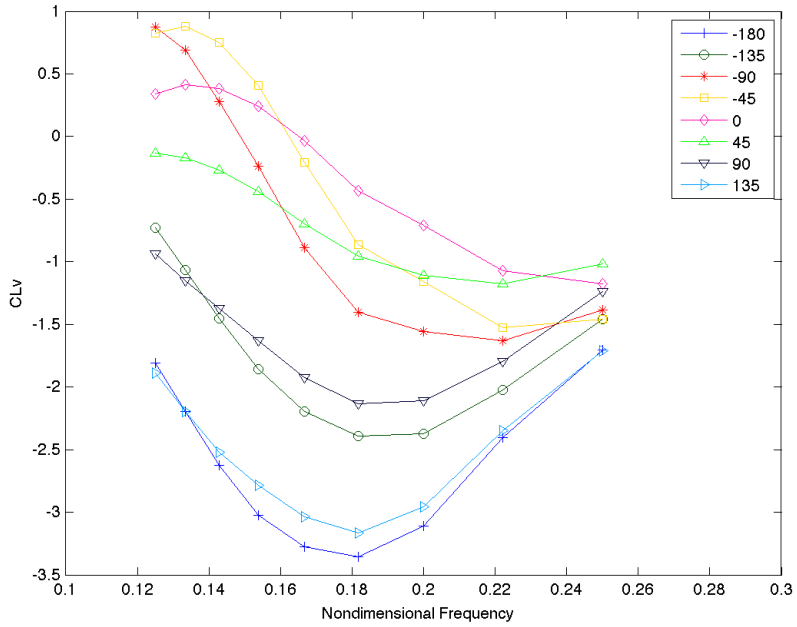

Figure A-25: Lift coefficients in phase with velocity C_{Lv} X 0.2 Y 0.75

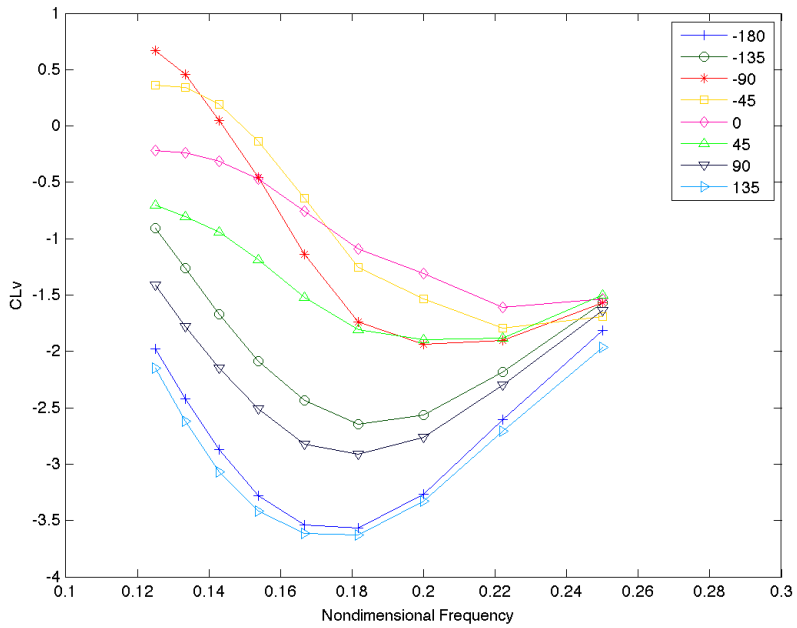

Figure A-26: Lift coefficients in phase with velocity C_{Lv} X 0.2 Y 1

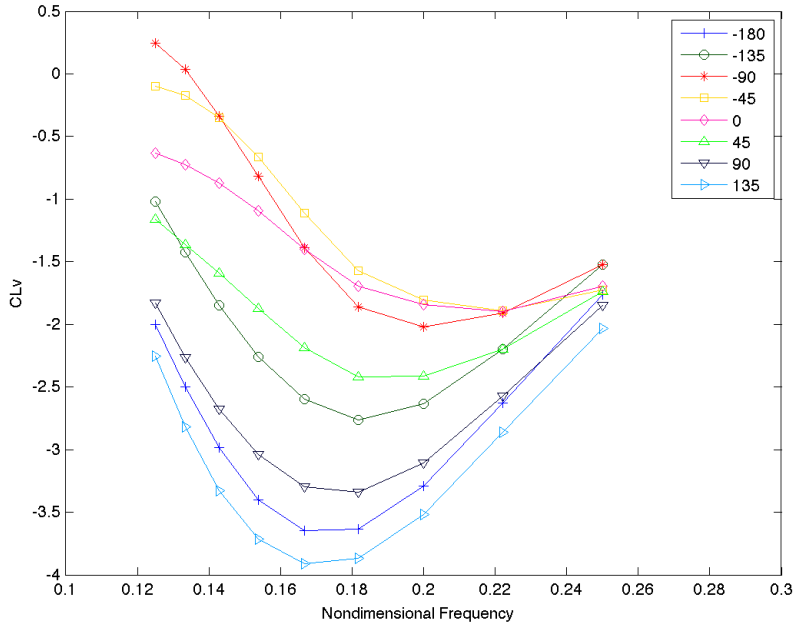

Figure A-27: Lift coefficients in phase with velocity C_{Lv} X 0.2 Y 1.25

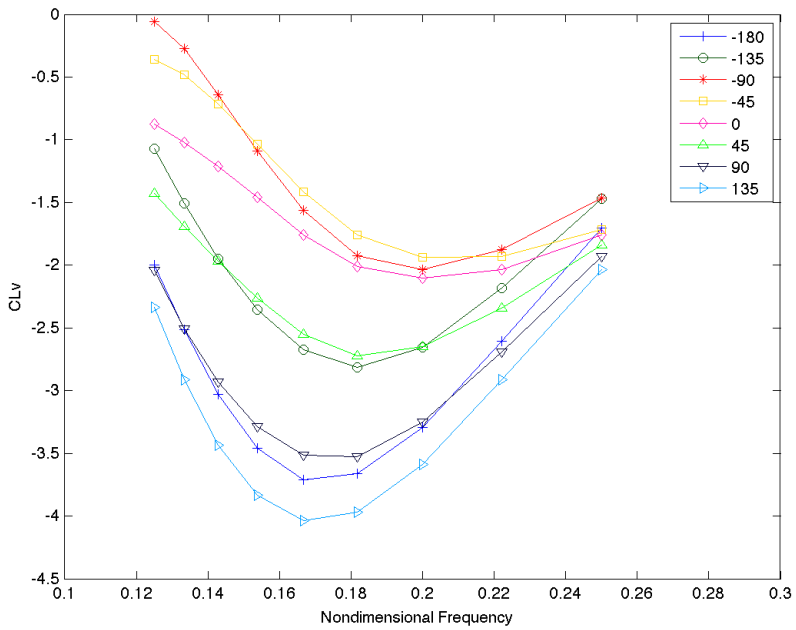

Figure A-28: Lift coefficients in phase with velocity C_{Lv} X 0.2 Y 1.5

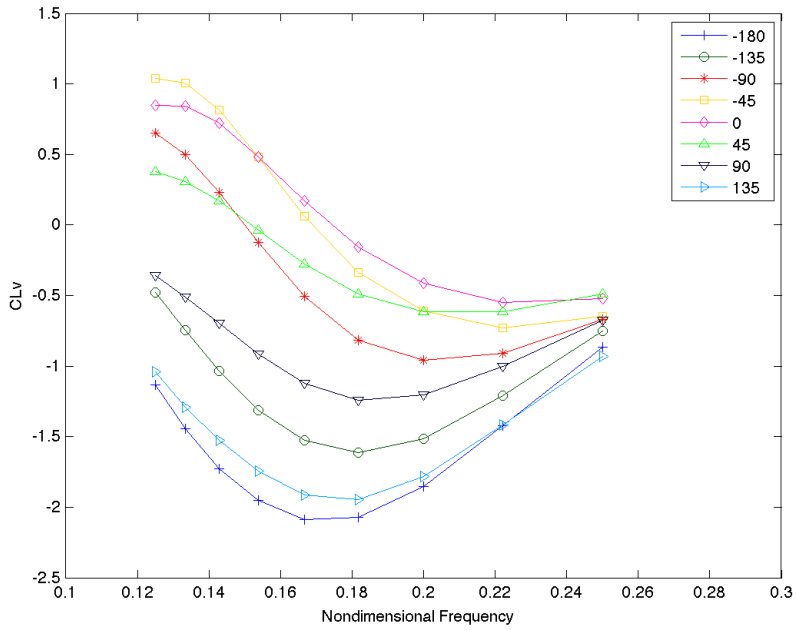

Figure A-29: Lift coefficients in phase with velocity C_{Lv} X 0.25 Y 0.15

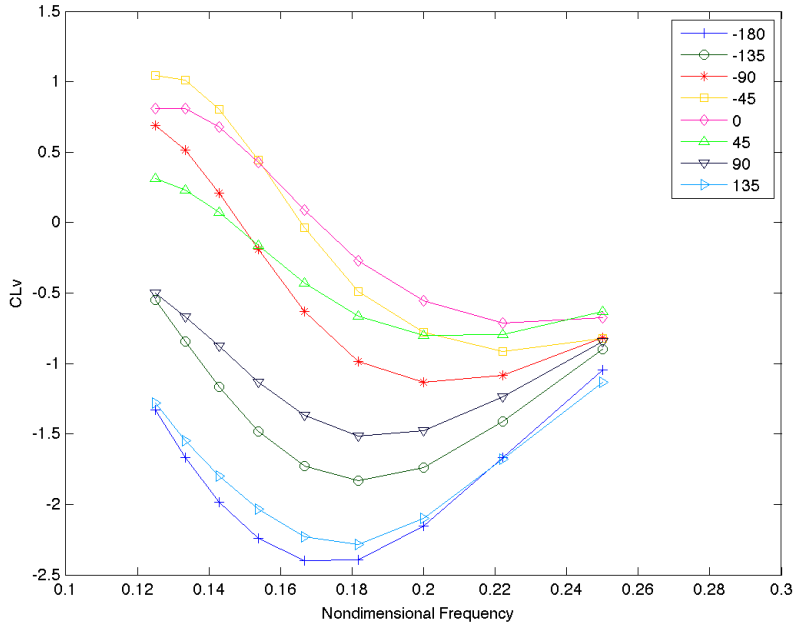

Figure A-30: Lift coefficients in phase with velocity C_{Lv} X 0.25 Y 0.25

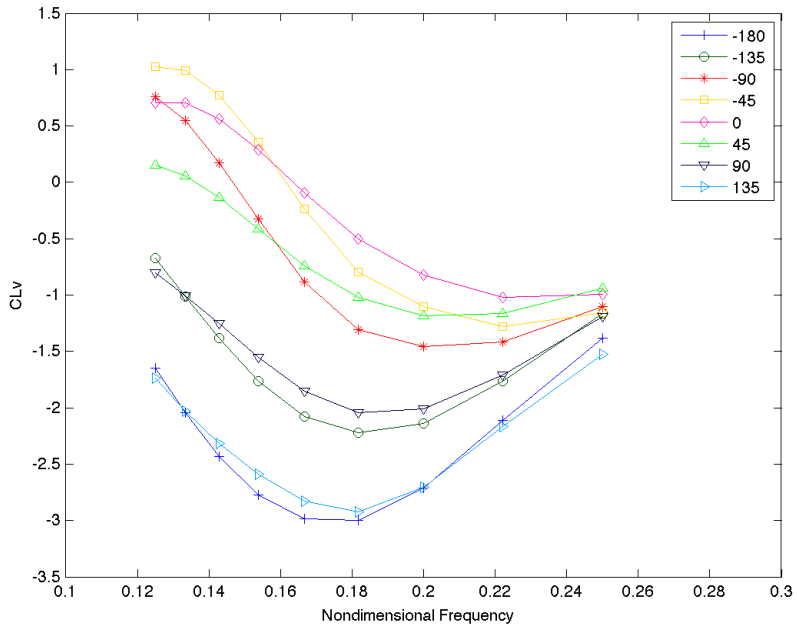

Figure A-31: Lift coefficients in phase with velocity C_{Lv} X 0.25 Y 0.5

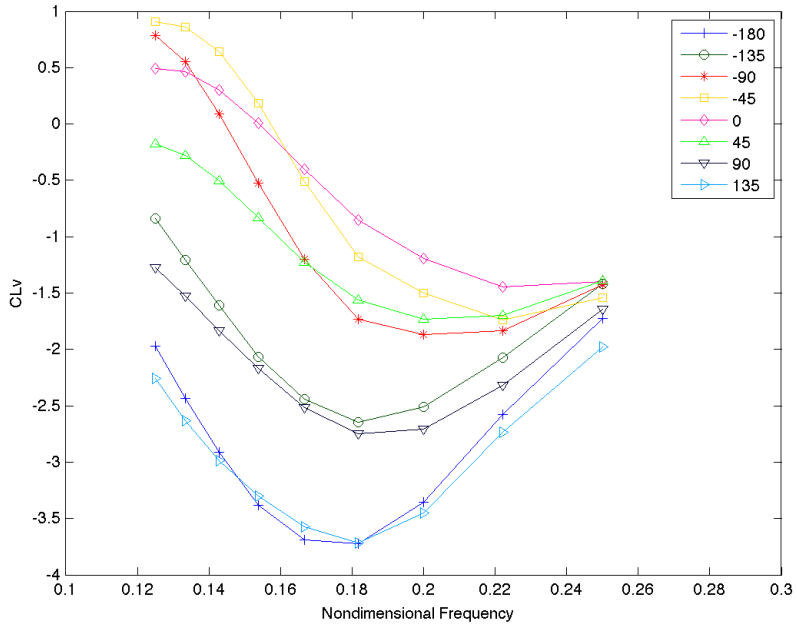

Figure A-32: Lift coefficients in phase with velocity C_{Lv} X 0.25 Y 0.75

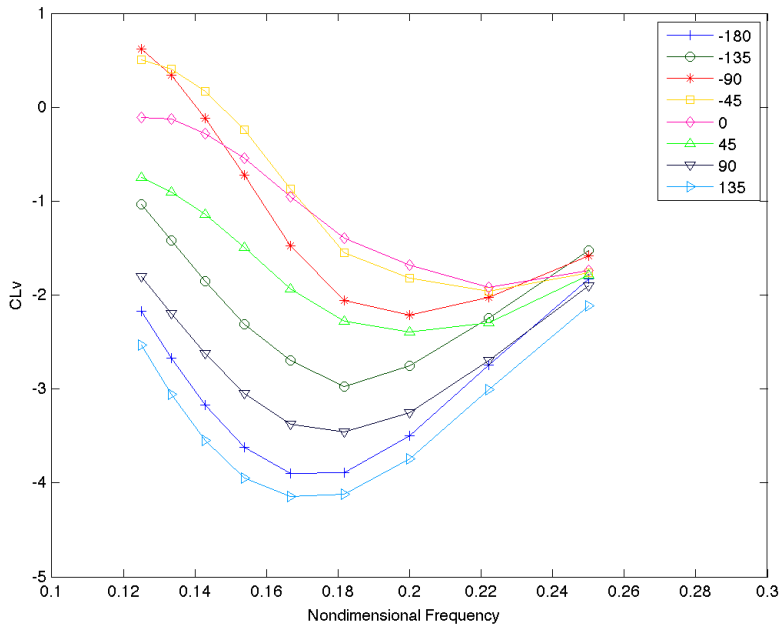

Figure A-33: Lift coefficients in phase with velocity C_{Lv} X 0.25 Y 1

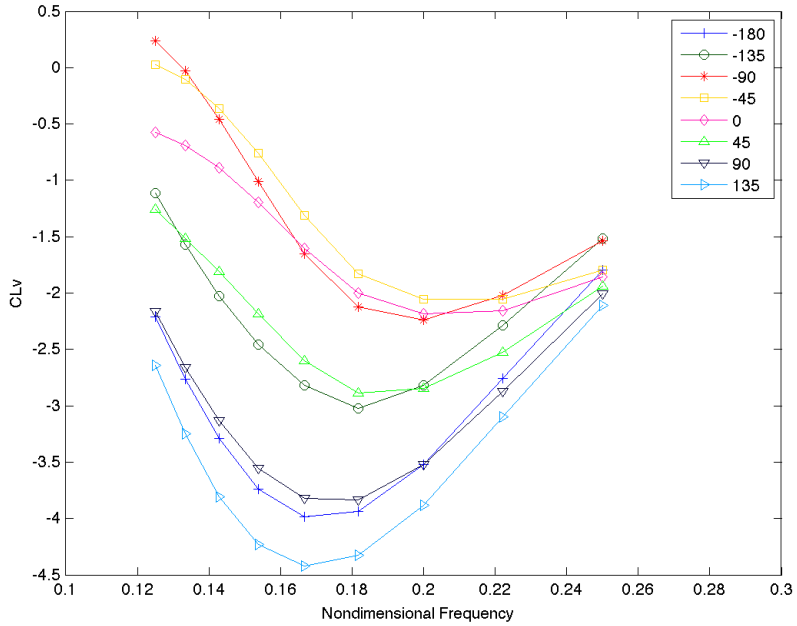

Figure A-34: Lift coefficients in phase with velocity C_{Lv} X 0.25 Y 1.25

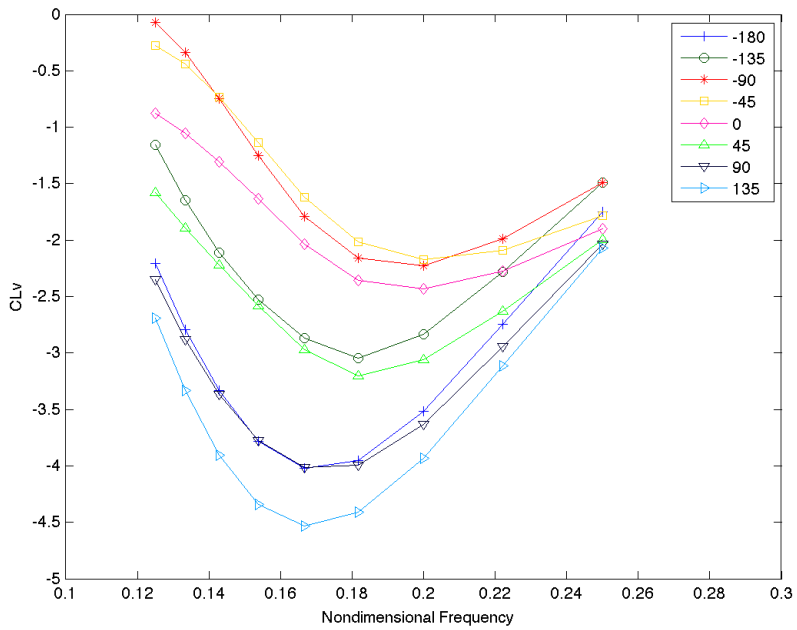

Figure A-35: Lift coefficients in phase with velocity C_{Lv} X 0.25 Y 1.5

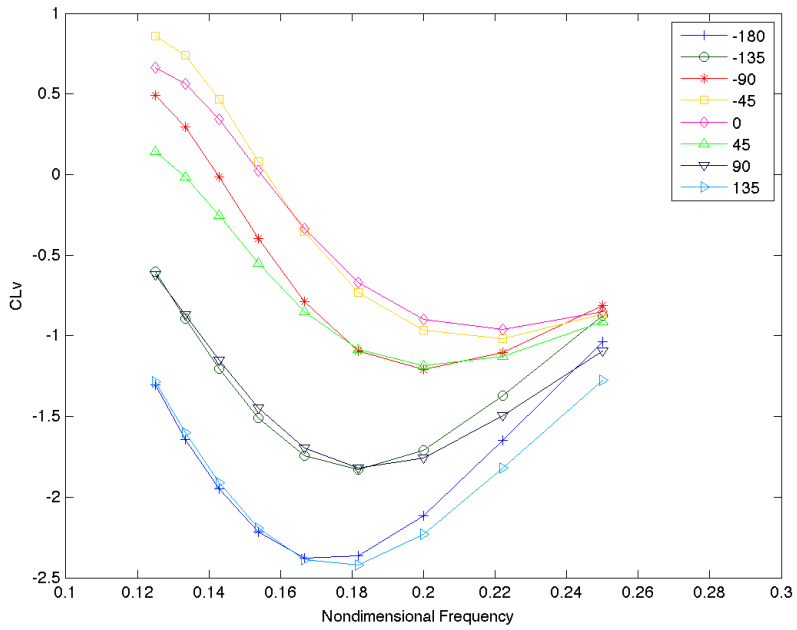

Figure A-36: Lift coefficients in phase with velocity C_{Lv} X 0.3 Y 0.15

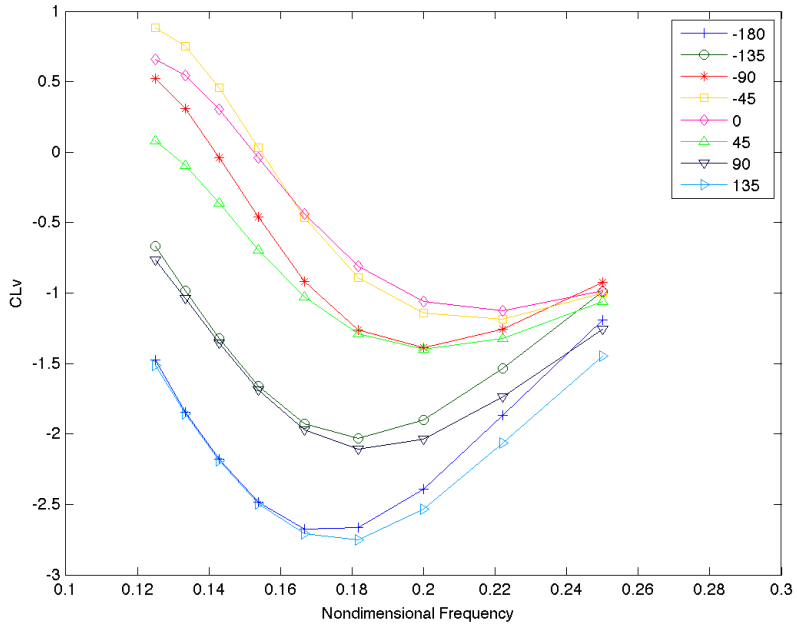

Figure A-37: Lift coefficients in phase with velocity C_{Lv} X 0.3 Y 0.25

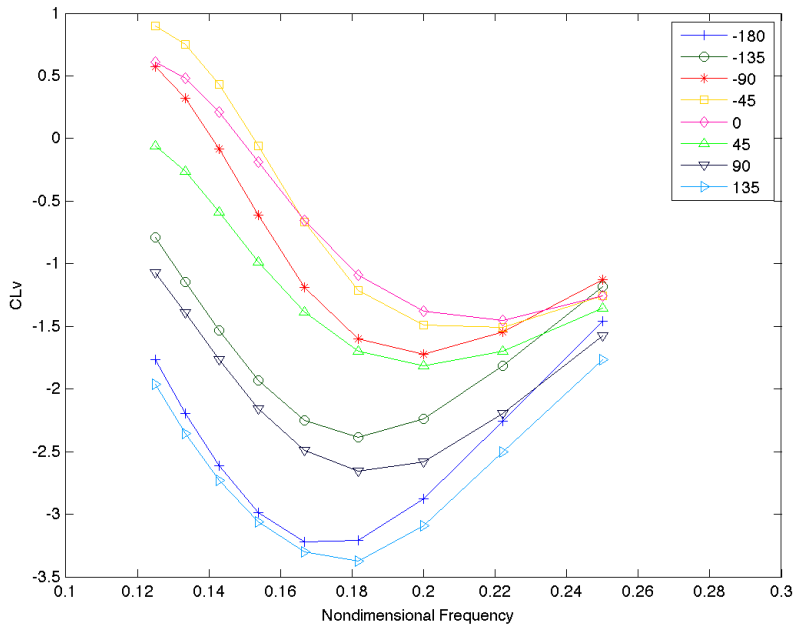

Figure A-38: Lift coefficients in phase with velocity C_{Lv} X 0.3 Y 0.5

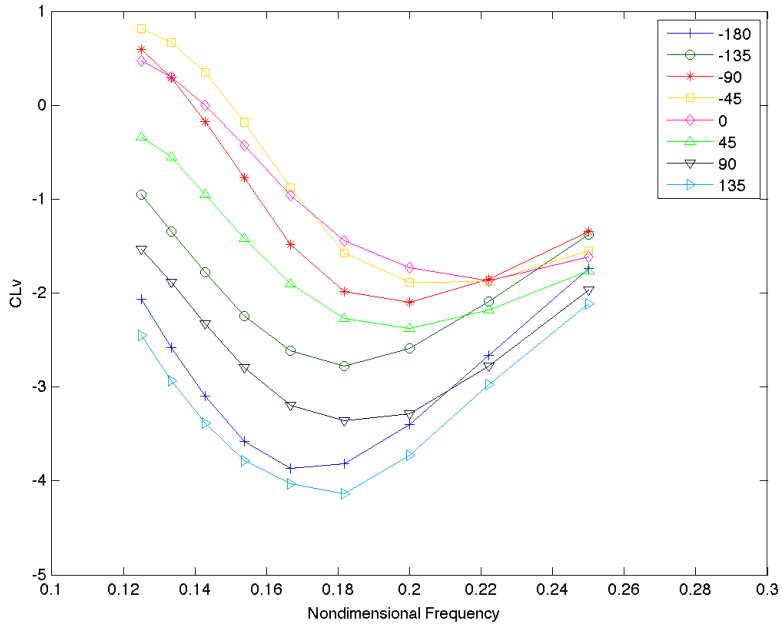

Figure A-39: Lift coefficients in phase with velocity C_{Lv} X 0.3 Y 0.75

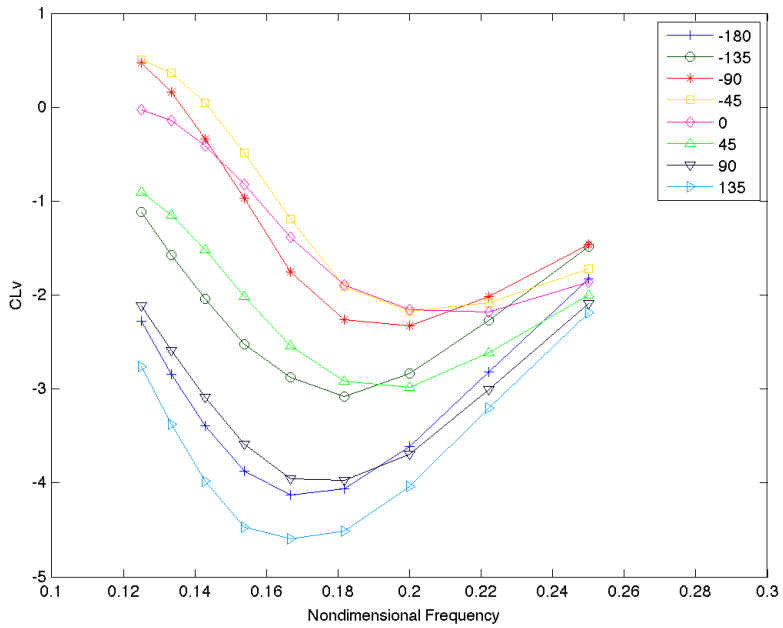

Figure A-40: Lift coefficients in phase with velocity C_{Lv} X 0.3 Y 1

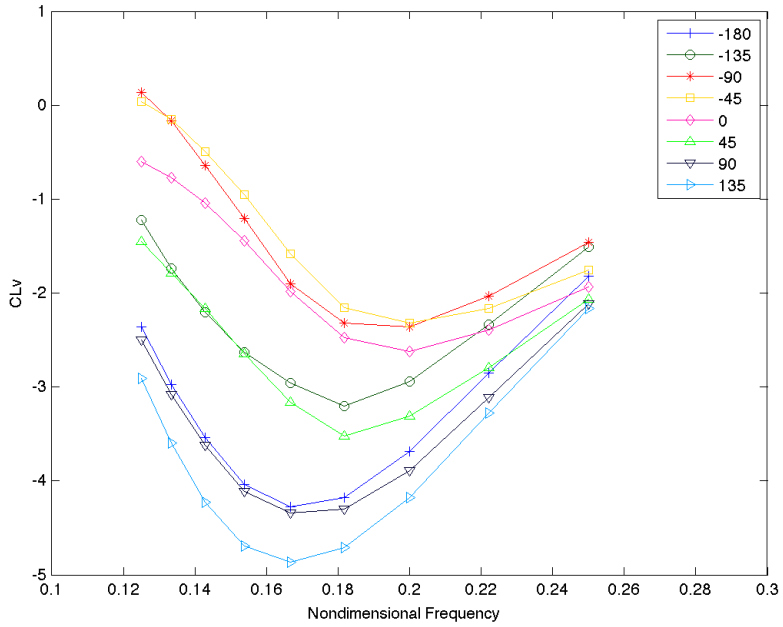

Figure A-41: Lift coefficients in phase with velocity C_{Lv} X 0.3 Y 1.25

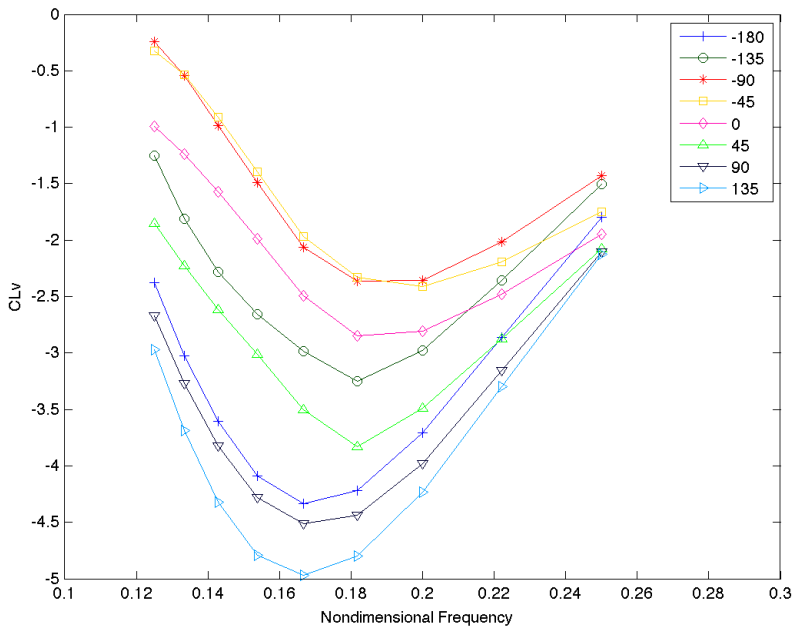

Figure A-42: Lift coefficients in phase with velocity C_{Lv} X 0.3 Y 1.5

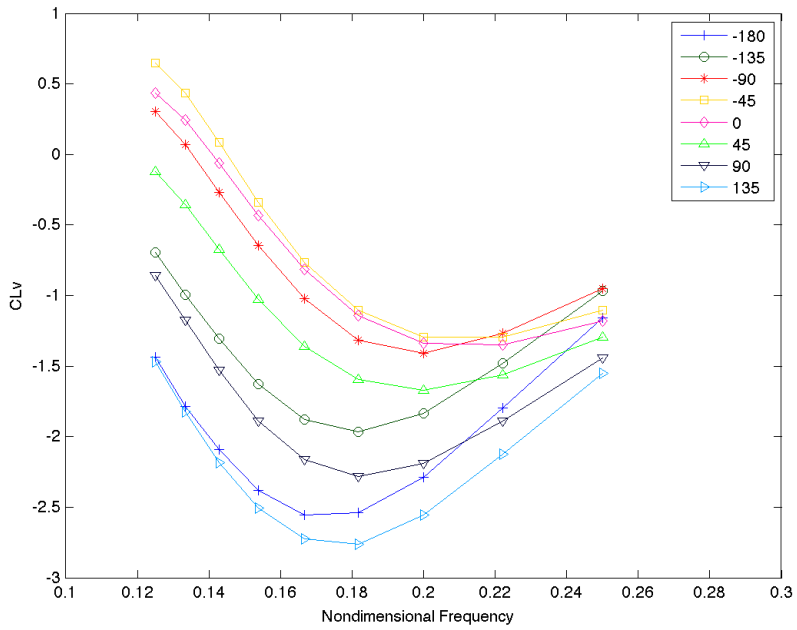

Figure A-43: Lift coefficients in phase with velocity C_{Lv} X 0.45 Y 0.15

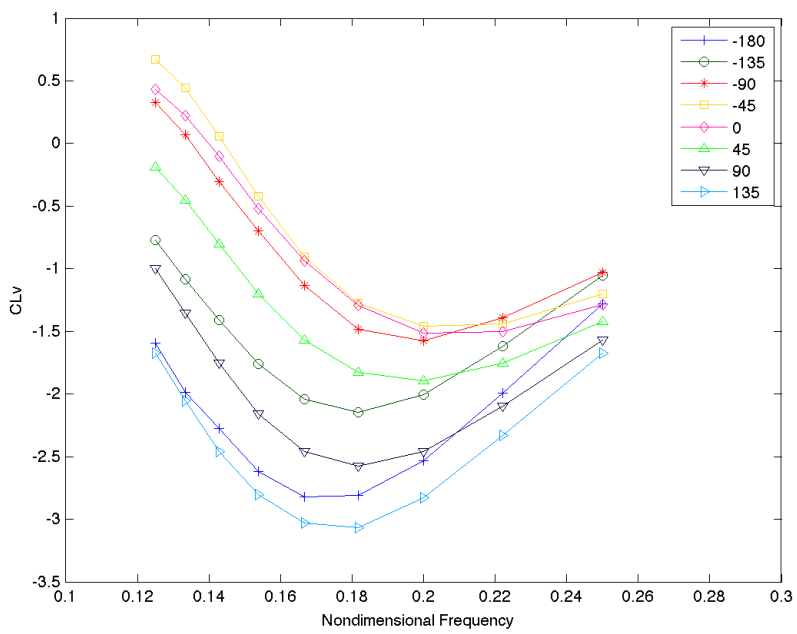

Figure A-44: Lift coefficients in phase with velocity C_{Lv} X 0.45 Y 0.25

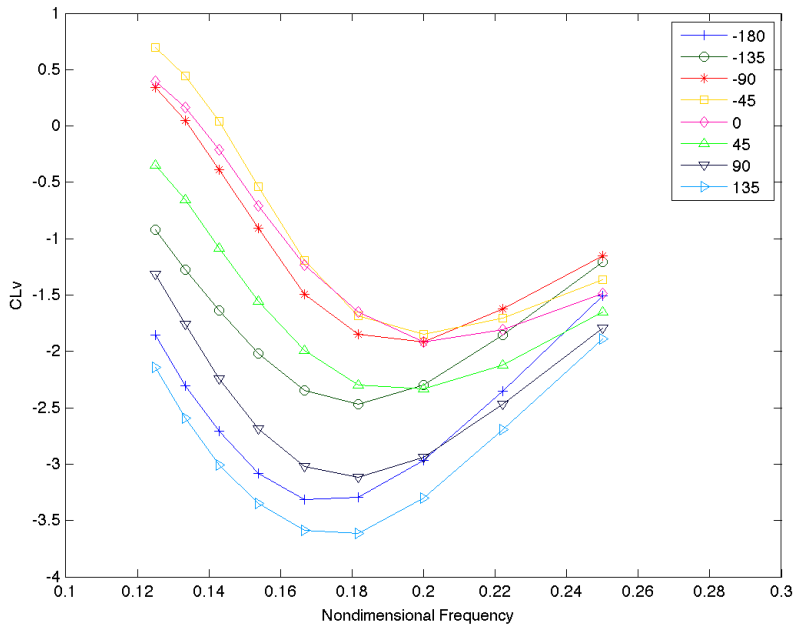

Figure A-45: Lift coefficients in phase with velocity C_{Lv} X 0.45 Y 0.5

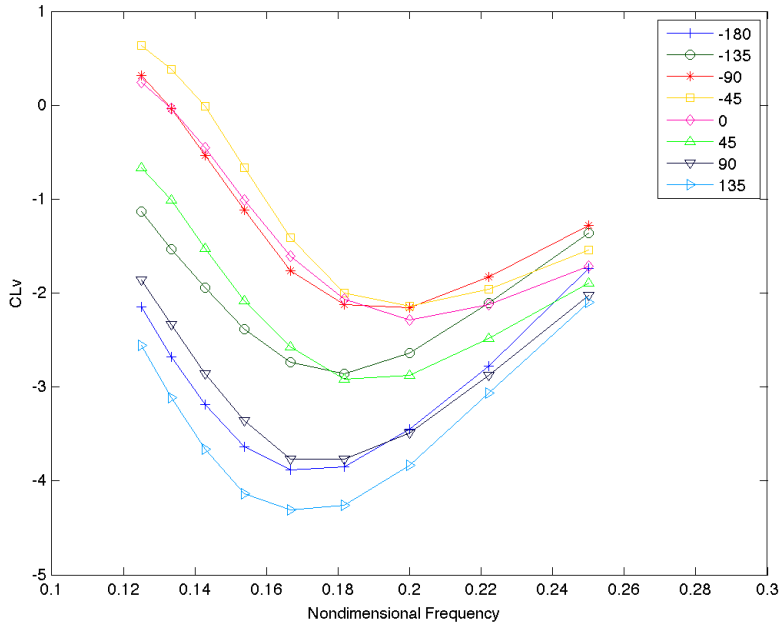

Figure A-46: Lift coefficients in phase with velocity C_{Lv} X 0.45 Y 0.75

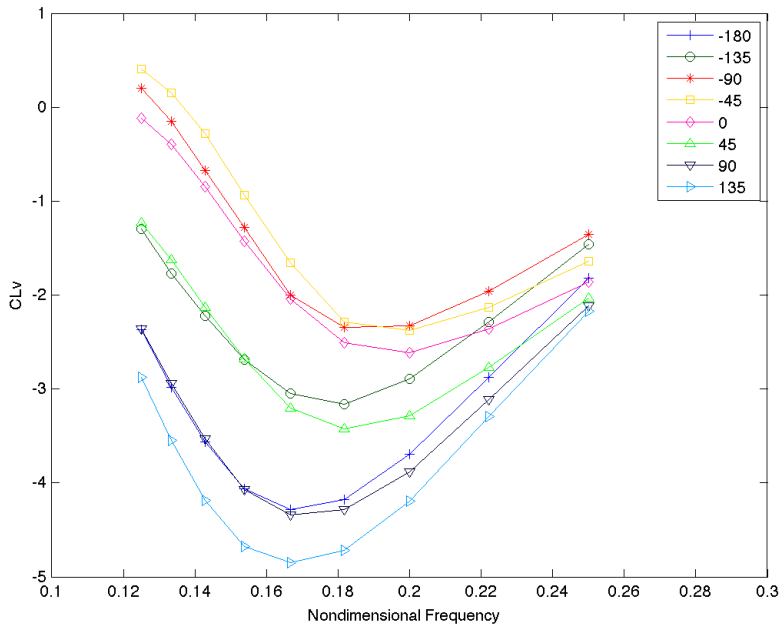

Figure A-47: Lift coefficients in phase with velocity C_{Lv} X 0.45 Y 1

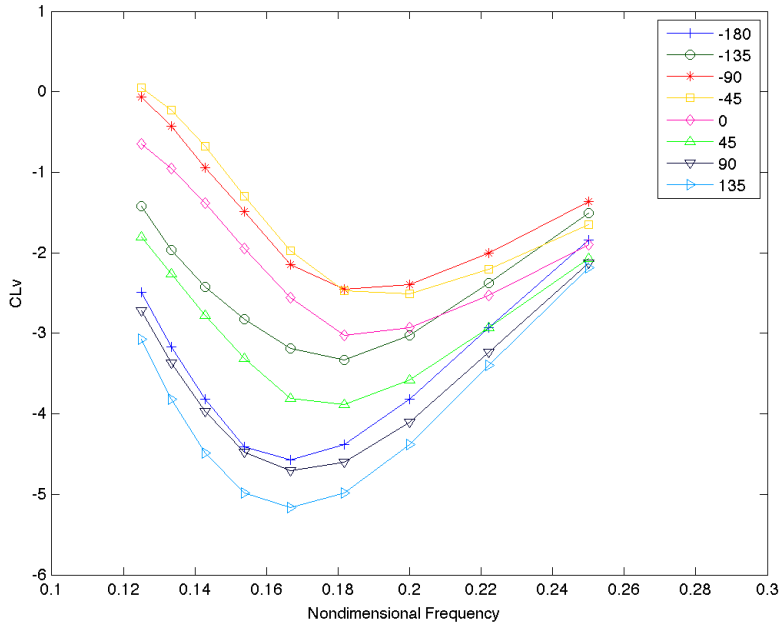

Figure A-48: Lift coefficients in phase with velocity C_{Lv} X 0.45 Y 1.25

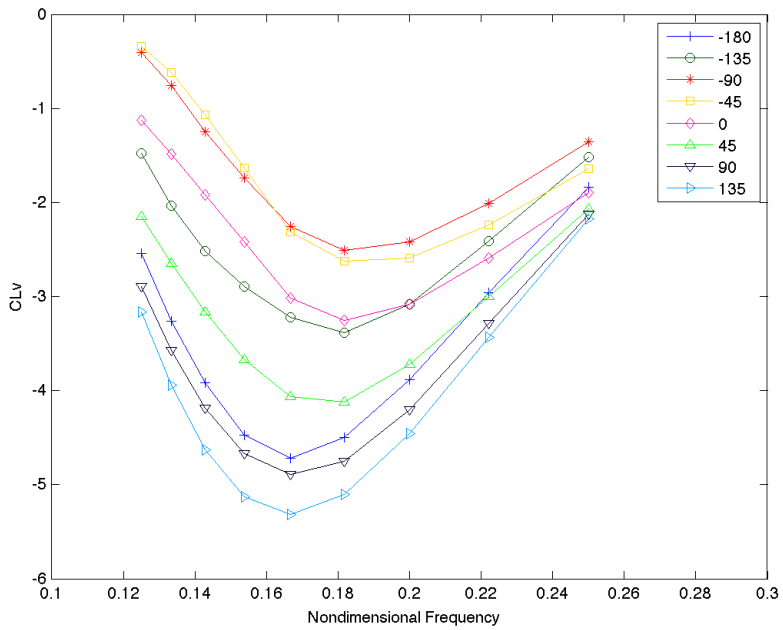

Figure A-49: Lift coefficients in phase with velocity C_{Lv} X 0.45 Y 1.5

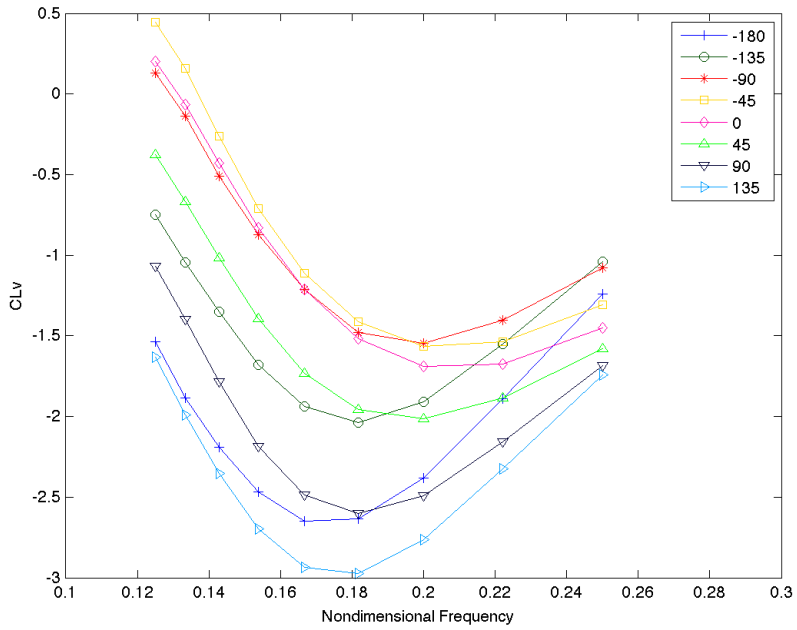

Figure A-50: Lift coefficients in phase with velocity C_{Lv} X 0.6 Y 0.15

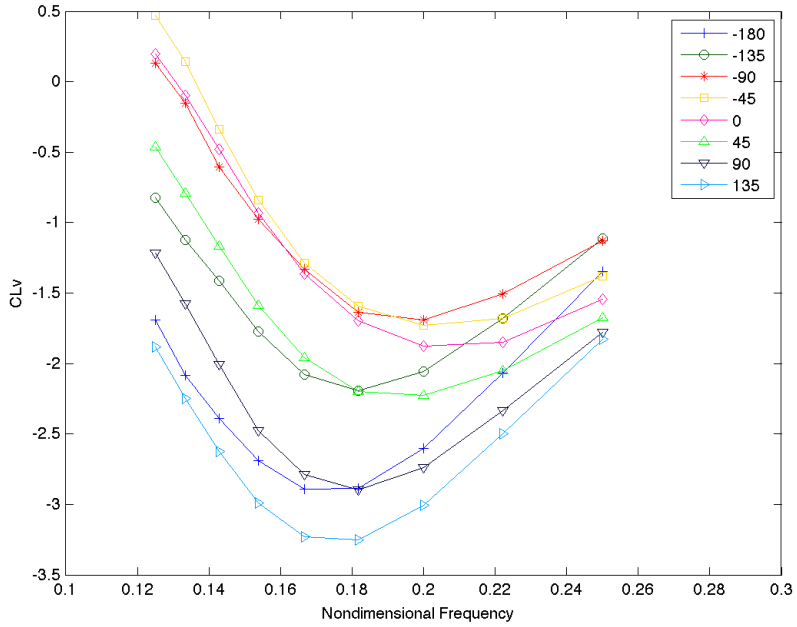

Figure A-51: Lift coefficients in phase with velocity C_{Lv} X 0.6 Y 0.25

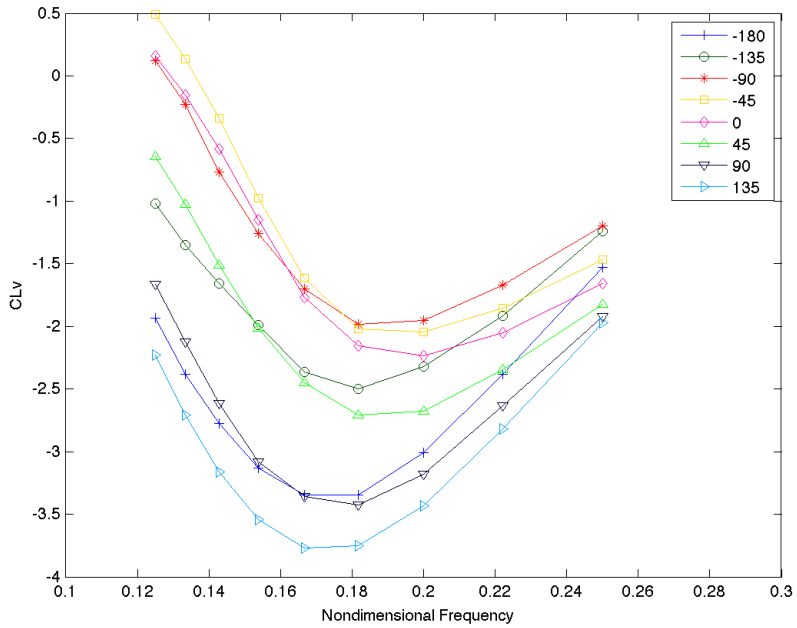

Figure A-52: Lift coefficients in phase with velocity C_{Lv} X 0.6 Y 0.5

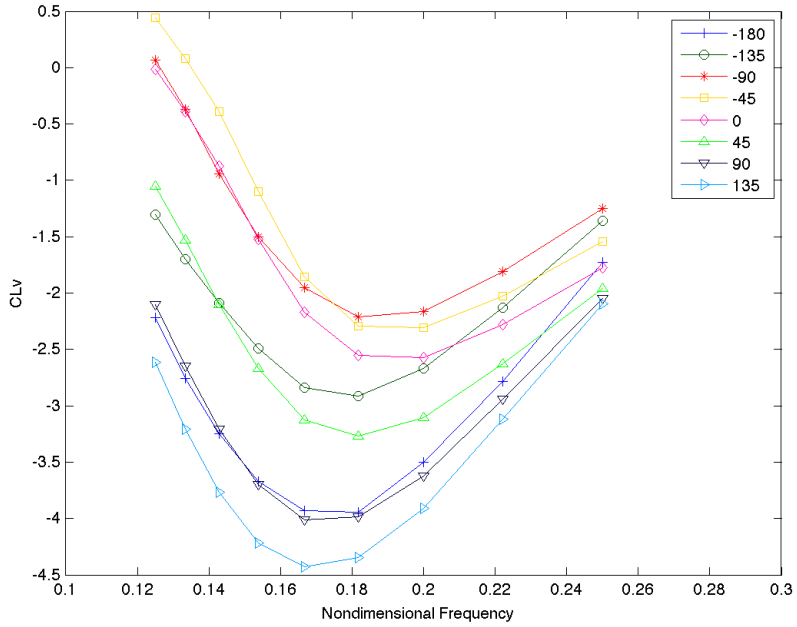

Figure A-53: Lift coefficients in phase with velocity C_{Lv} X 0.6 Y 0.75

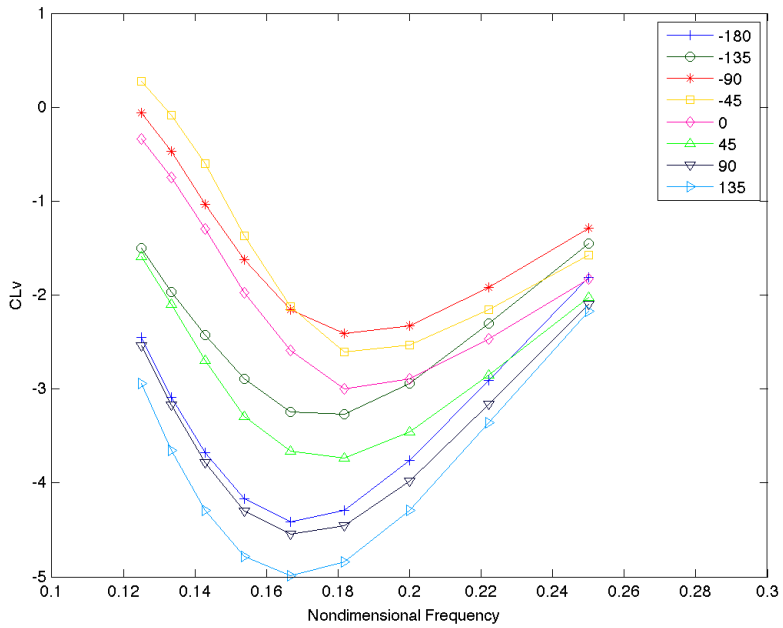

Figure A-54: Lift coefficients in phase with velocity C_{Lv} X 0.6 Y 1

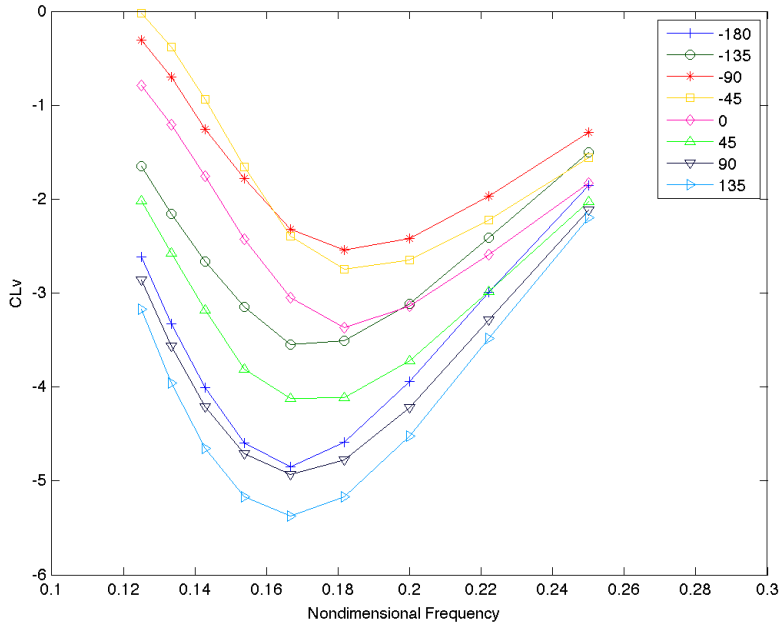

Figure A-55: Lift coefficients in phase with velocity C_{Lv} X 0.6 Y 1.25

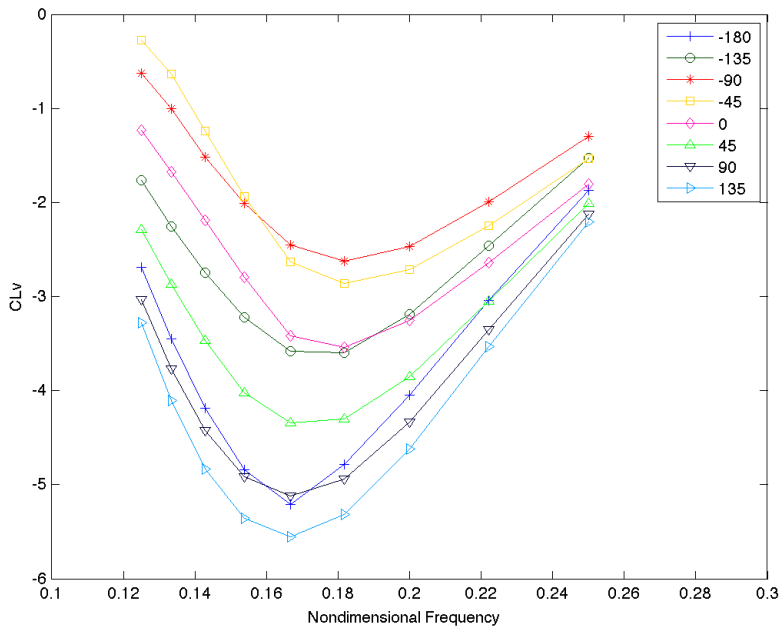

Figure A-56: Lift coefficients in phase with velocity C_{Lv} X 0.6 Y 1.5

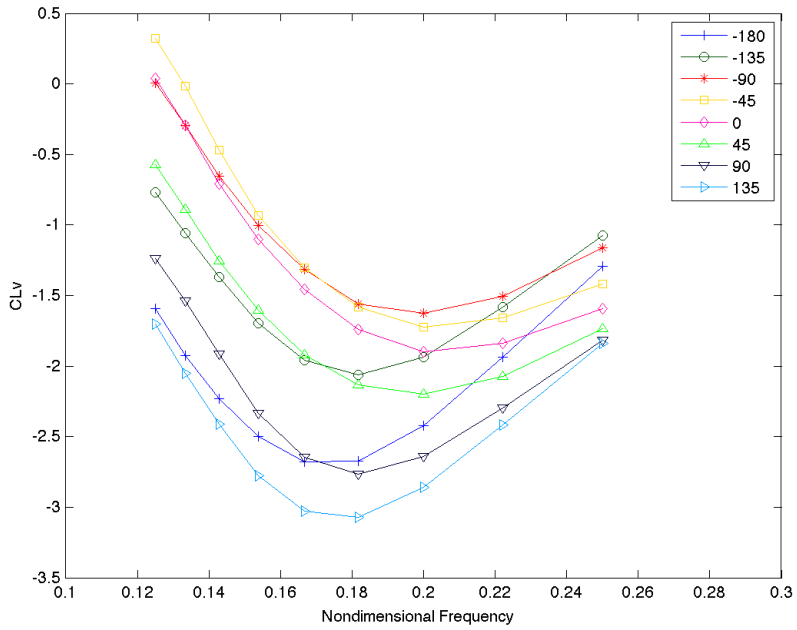

Figure A-57: Lift coefficients in phase with velocity C_{Lv} X 0.75 Y 0.15

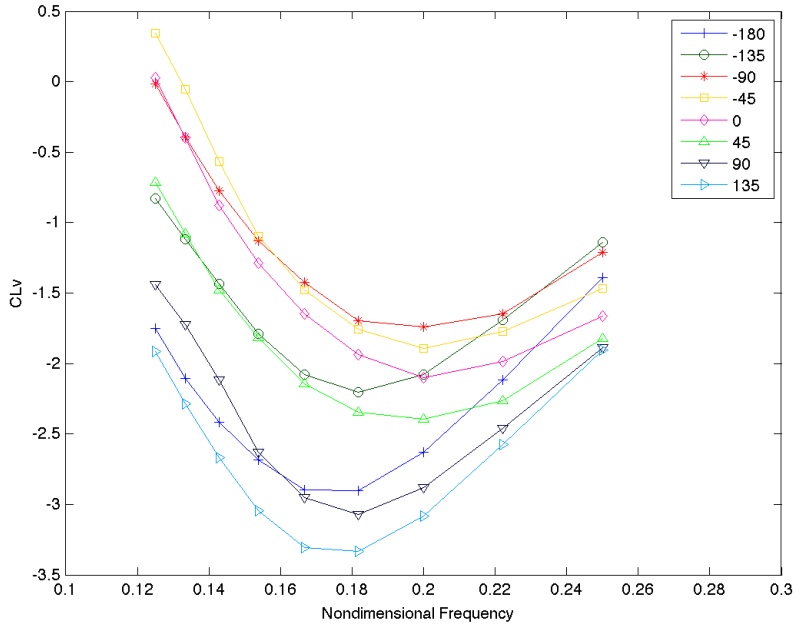

Figure A-58: Lift coefficients in phase with velocity C_{Lv} X 0.75 Y 0.25

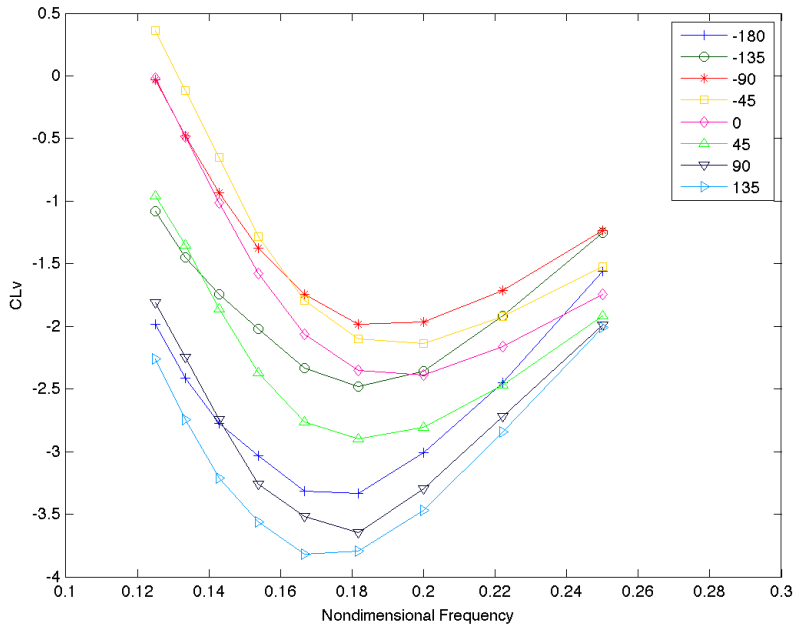

Figure A-59: Lift coefficients in phase with velocity C_{Lv} X 0.75 Y 0.5

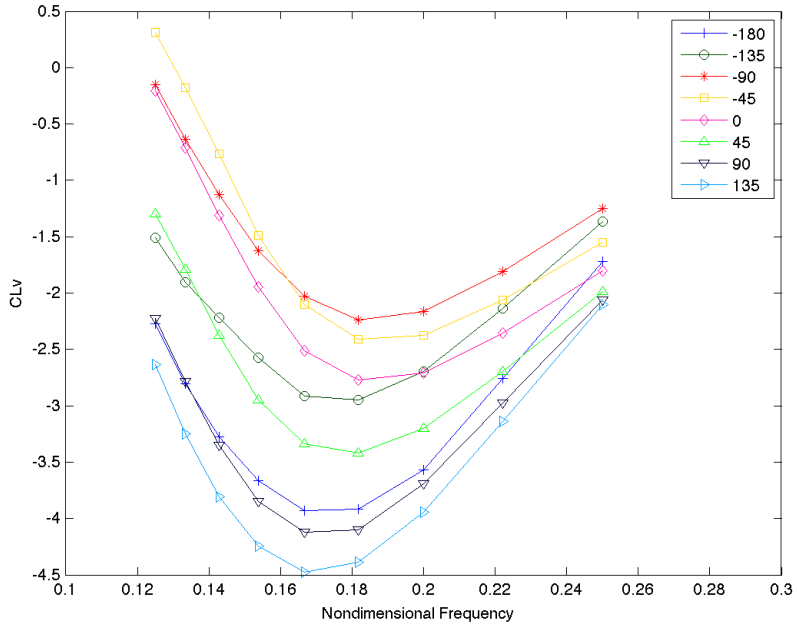

Figure A-60: Lift coefficients in phase with velocity C_{Lv} X 0.75 Y 0.75

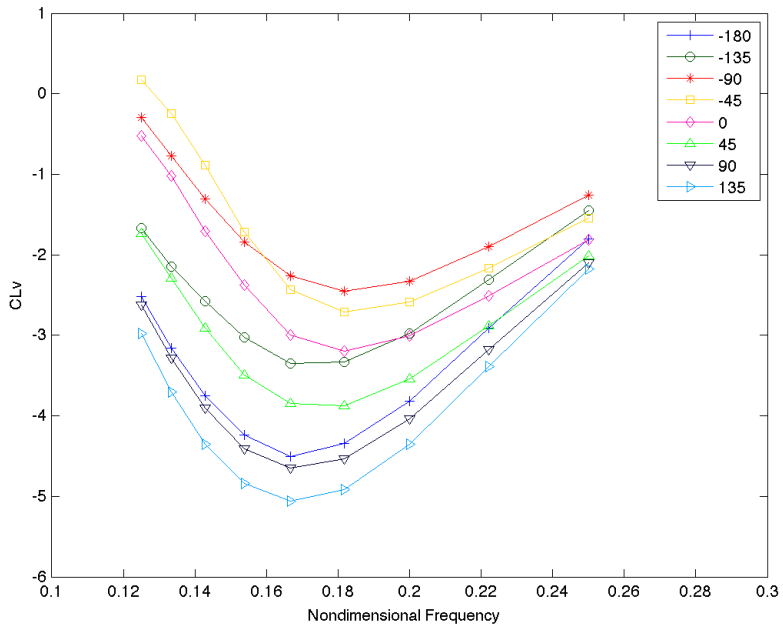

Figure A-61: Lift coefficients in phase with velocity C_{Lv} X 0.75 Y 1

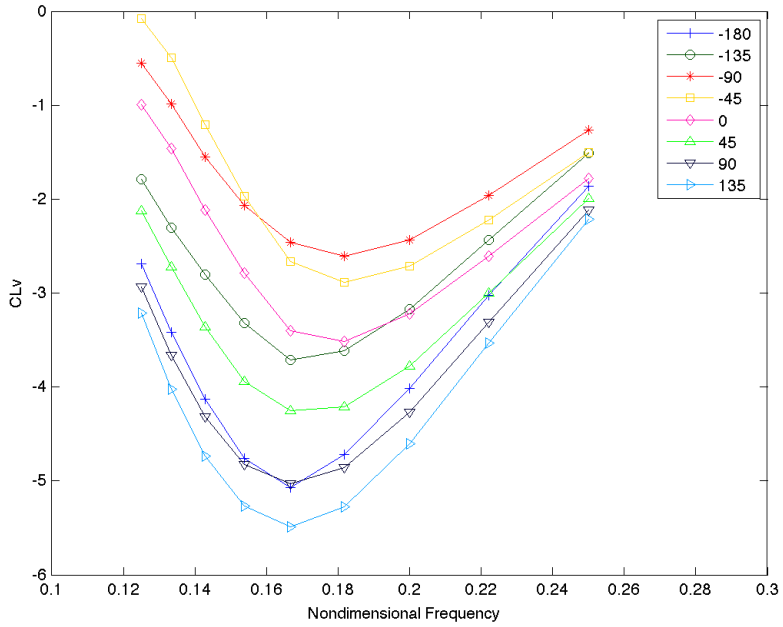

Figure A-62: Lift coefficients in phase with velocity C_{Lv} X 0.75 Y 1.25

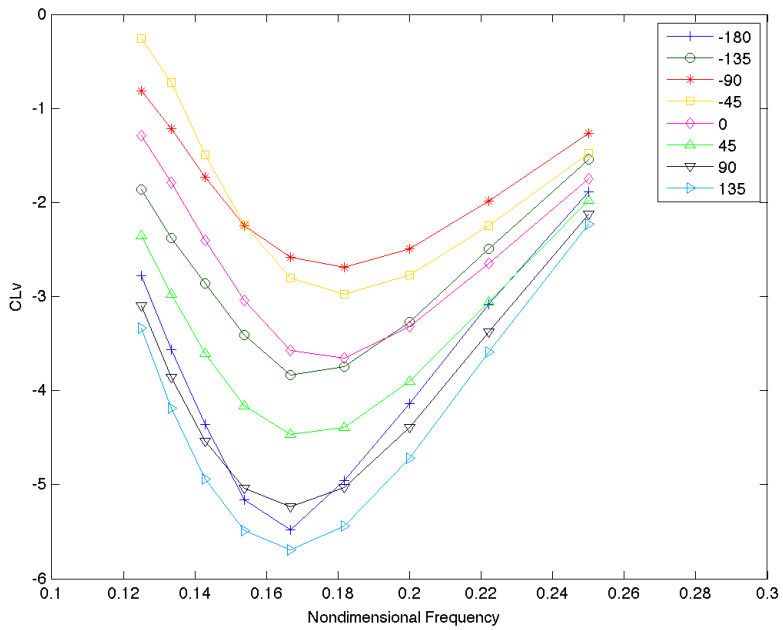

Figure A-63: Lift coefficients in phase with velocity C_{Lv} X 0.75 Y 1.5

A.2 Drag Coefficients in Phase with Velocity C_{Dv}

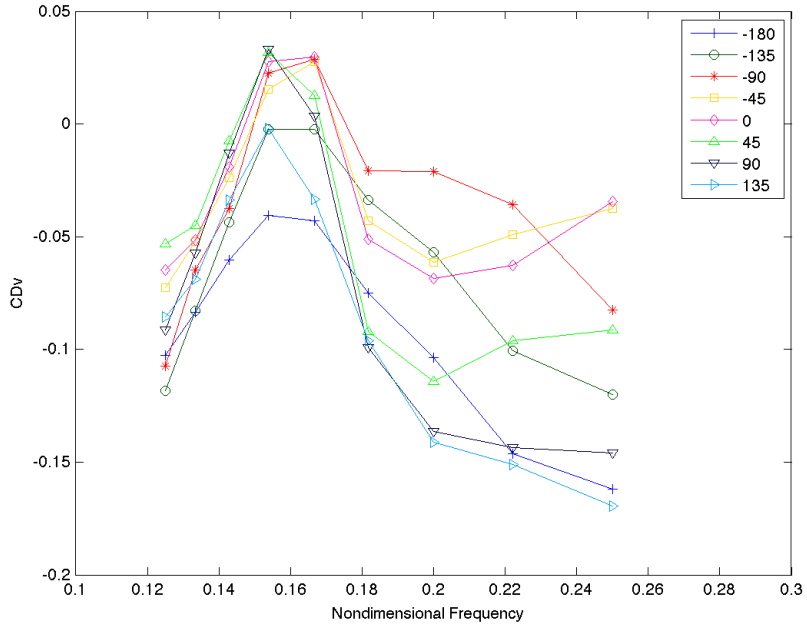

Figure A-64: Drag coefficients in phase with velocity C_{Dv} X 0.05 Y 0.15

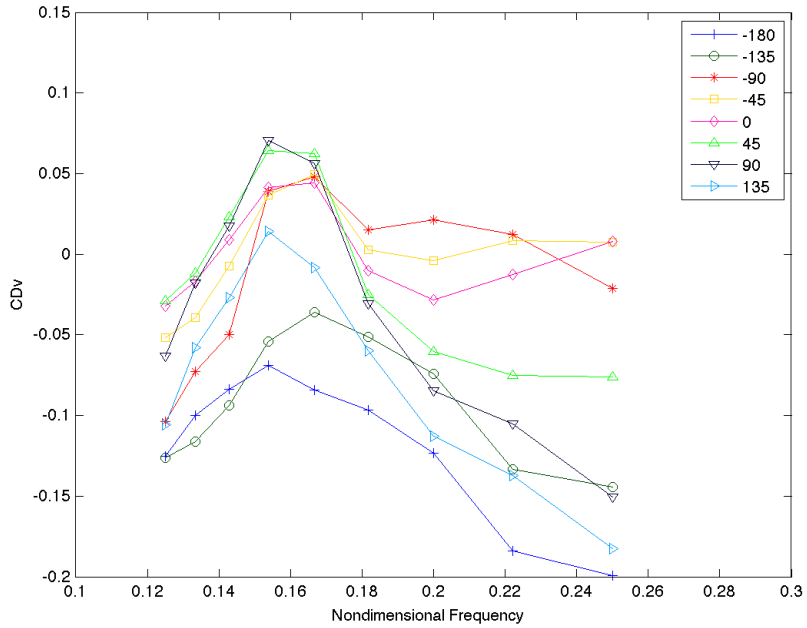

Figure A-65: Drag coefficients in phase with velocity C_{Dv} X 0.05 Y 0.25

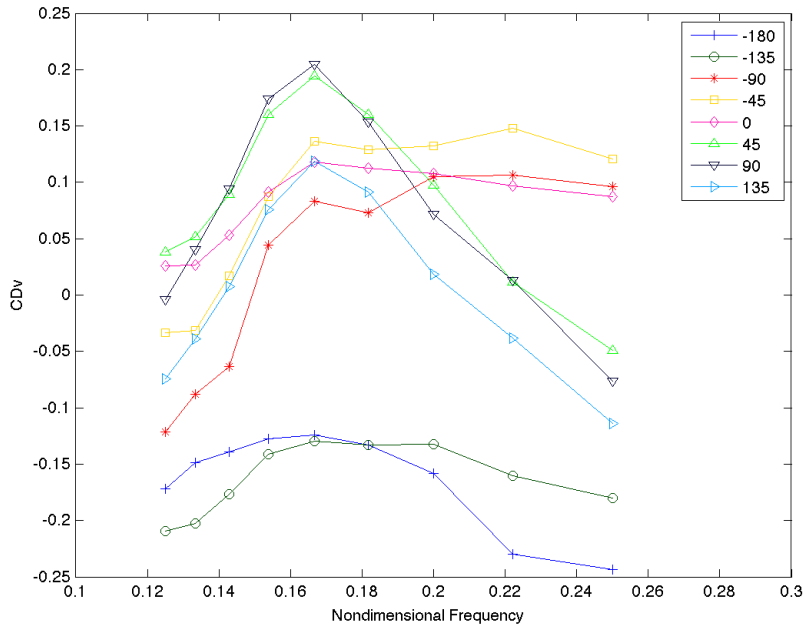

Figure A-66: Drag coefficients in phase with velocity C_{Dv} X 0.05 Y 0.5

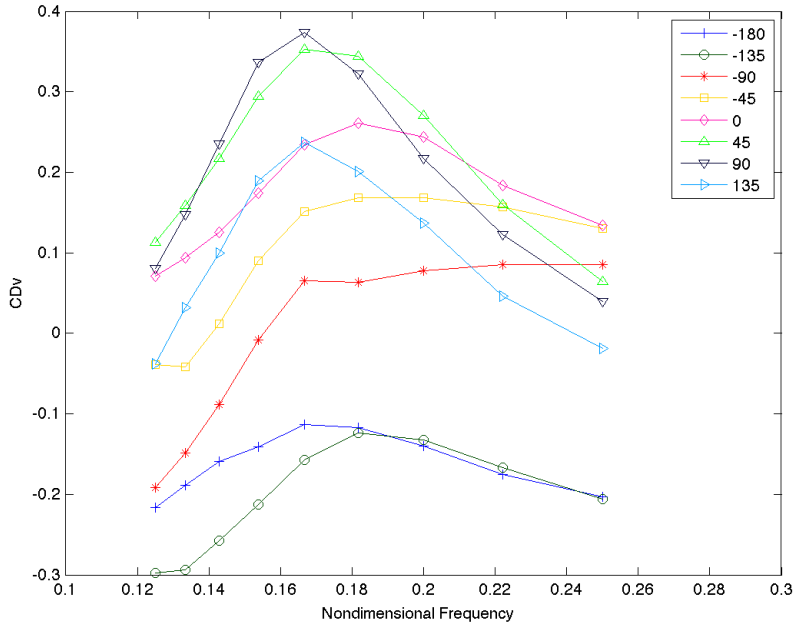

Figure A-67: Drag coefficients in phase with velocity C_{Dv} X 0.05 Y 0.75

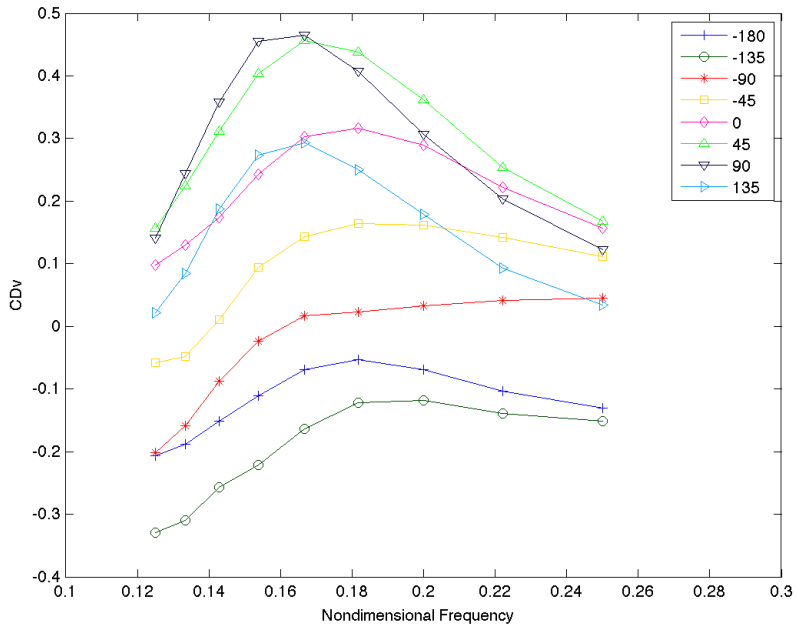

Figure A-68: Drag coefficients in phase with velocity C_{Dv} X 0.05 Y 1

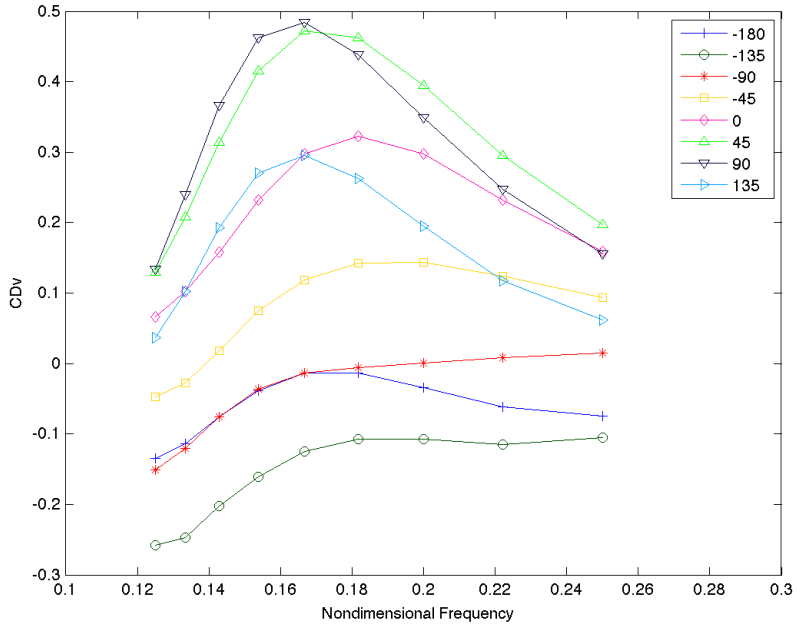

Figure A-69: Drag coefficients in phase with velocity C_{Dv} X 0.05 Y 1.25

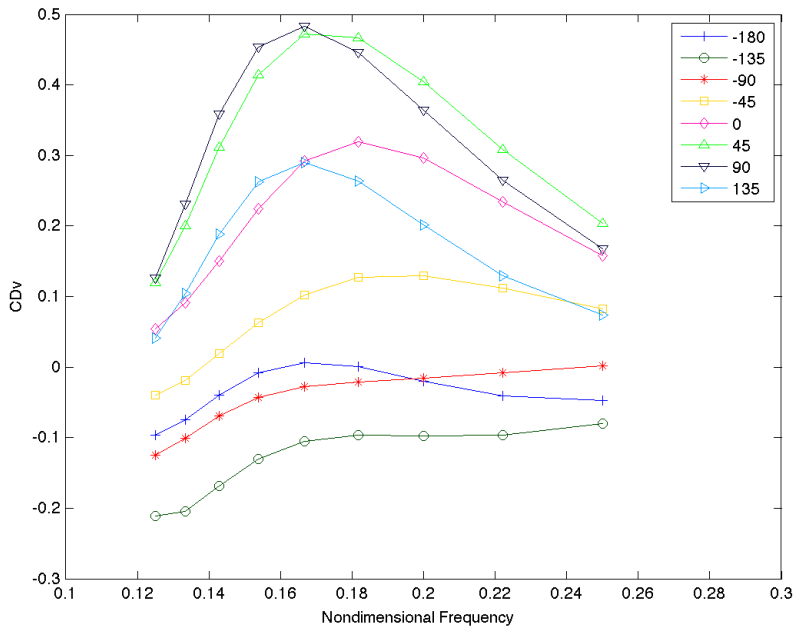

Figure A-70: Drag coefficients in phase with velocity C_{Dv} X 0.05 Y 1.5

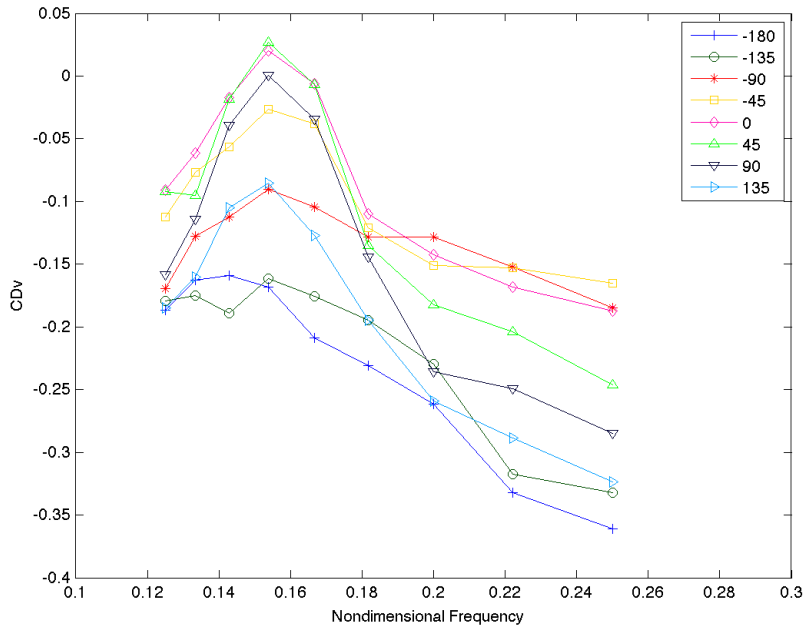

Figure A-71: Drag coefficients in phase with velocity C_{Dv} X 0.1 Y 0.15

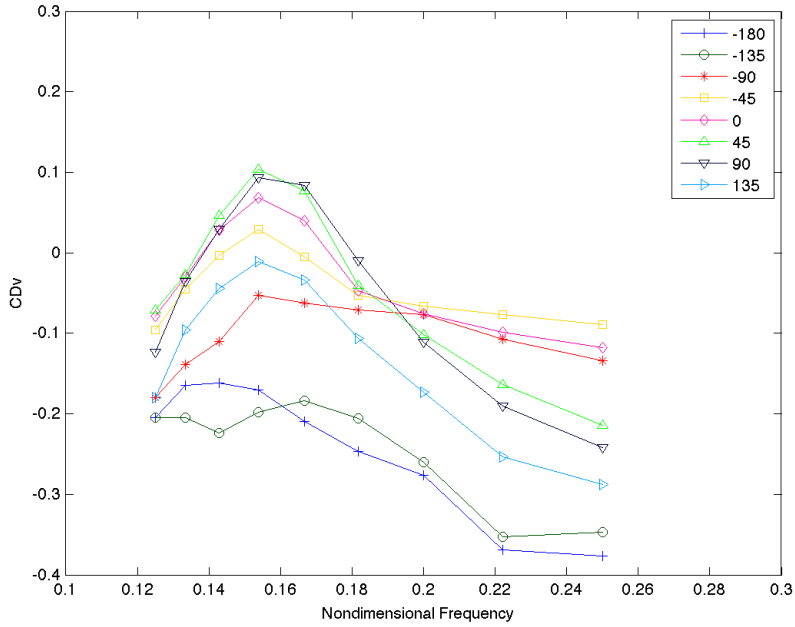

Figure A-72: Drag coefficients in phase with velocity C_{Dv} X 0.1 Y 0.25

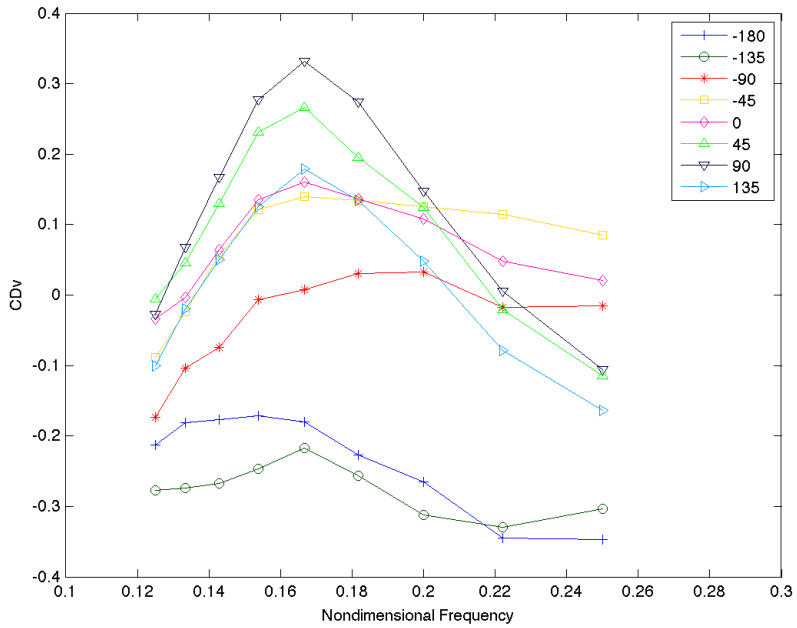

Figure A-73: Drag coefficients in phase with velocity C_{Dv} X 0.1 Y 0.5

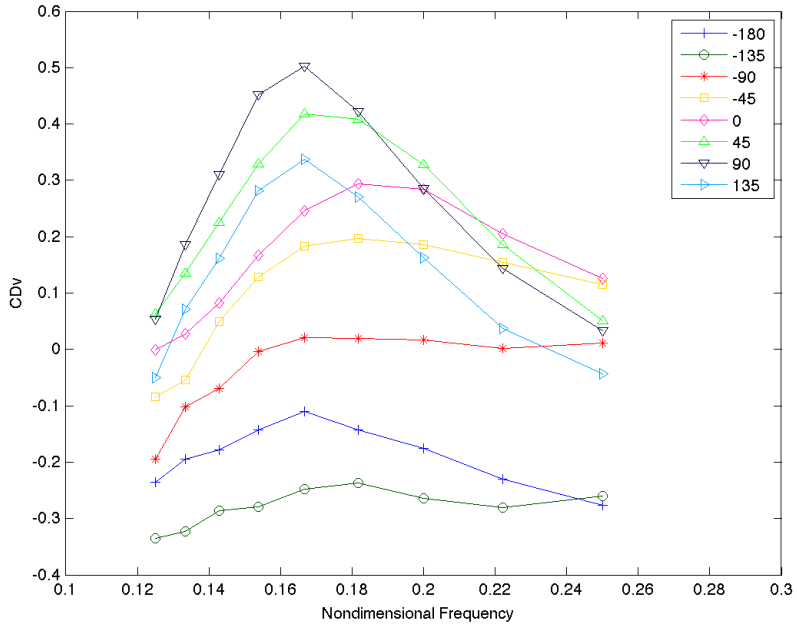

Figure A-74: Drag coefficients in phase with velocity C_{Dv} X 0.1 Y 0.75

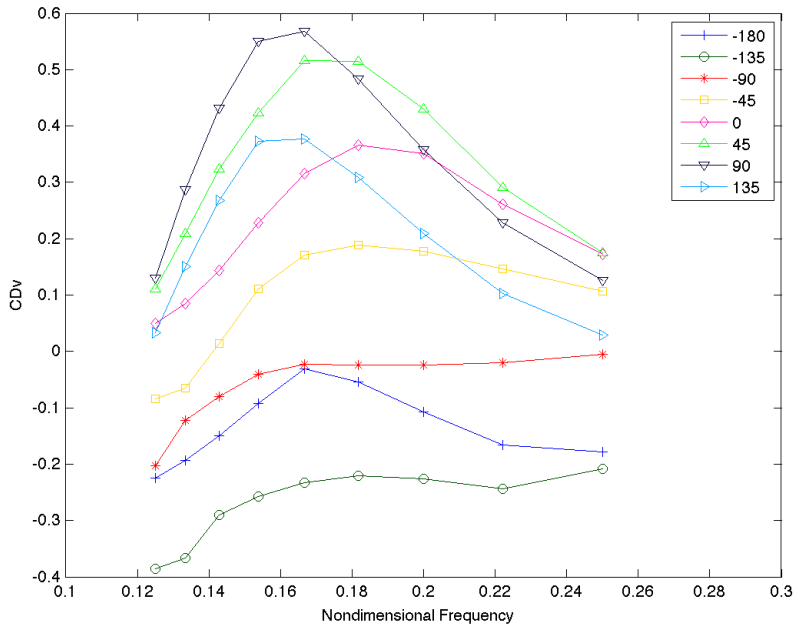

Figure A-75: Drag coefficients in phase with velocity C_{Dv} X 0.1 Y 1

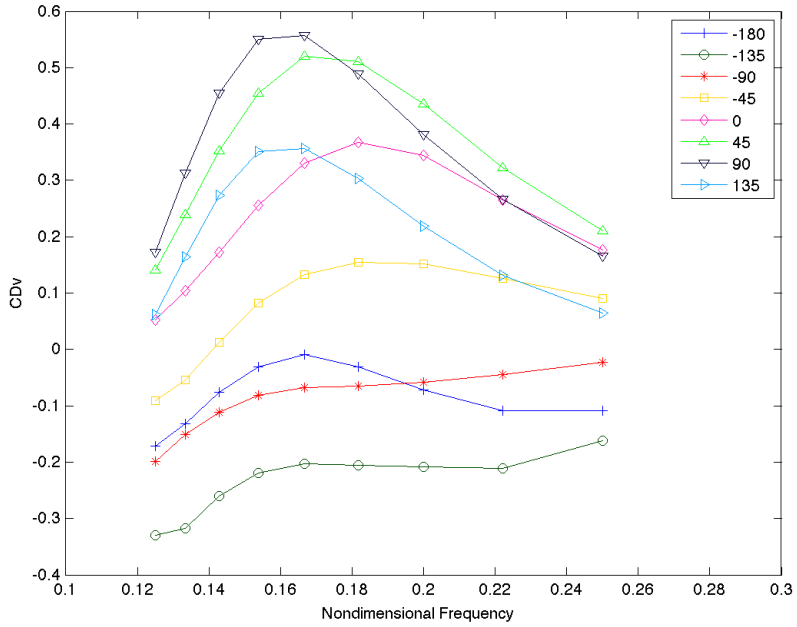

Figure A-76: Drag coefficients in phase with velocity C_{Dv} X 0.1 Y 1.25

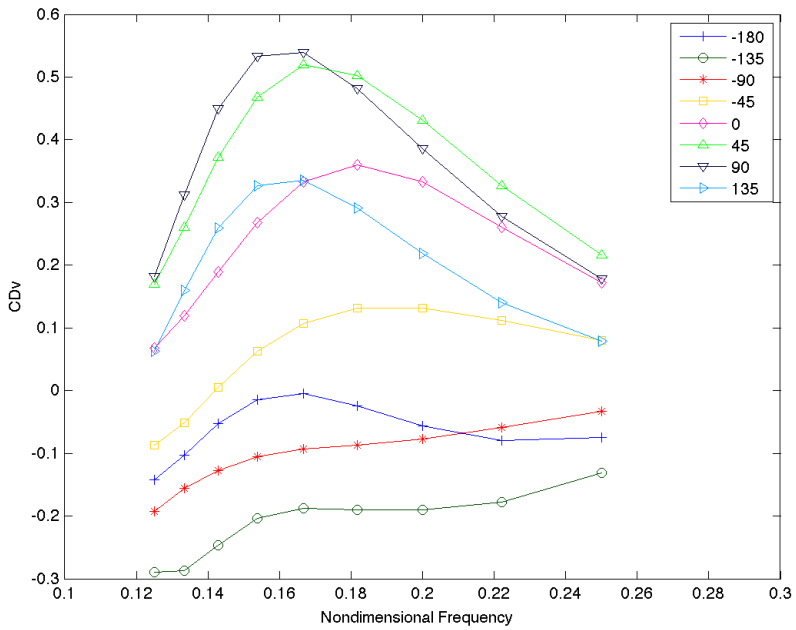

Figure A-77: Drag coefficients in phase with velocity C_{Dv} X 0.1 Y 1.5

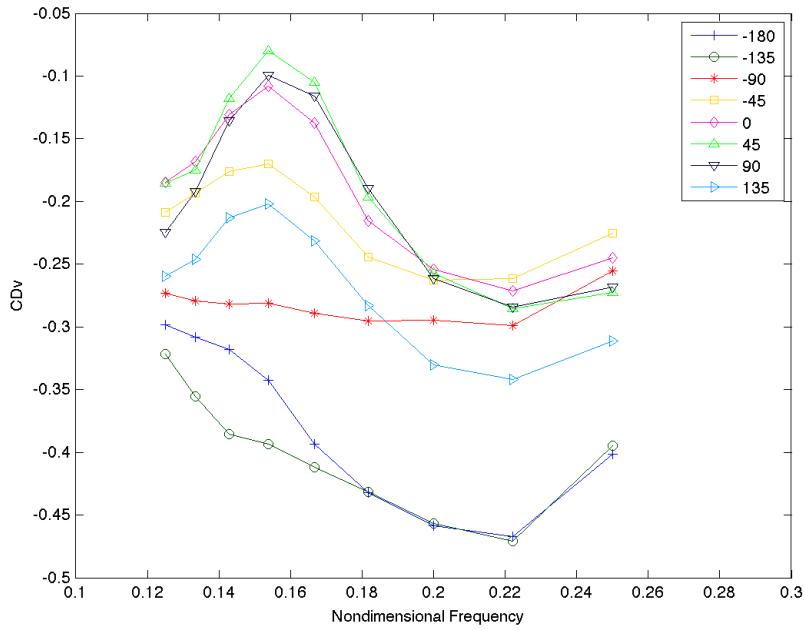

Figure A-78: Drag coefficients in phase with velocity C_{Dv} X 0.15 Y 0.15

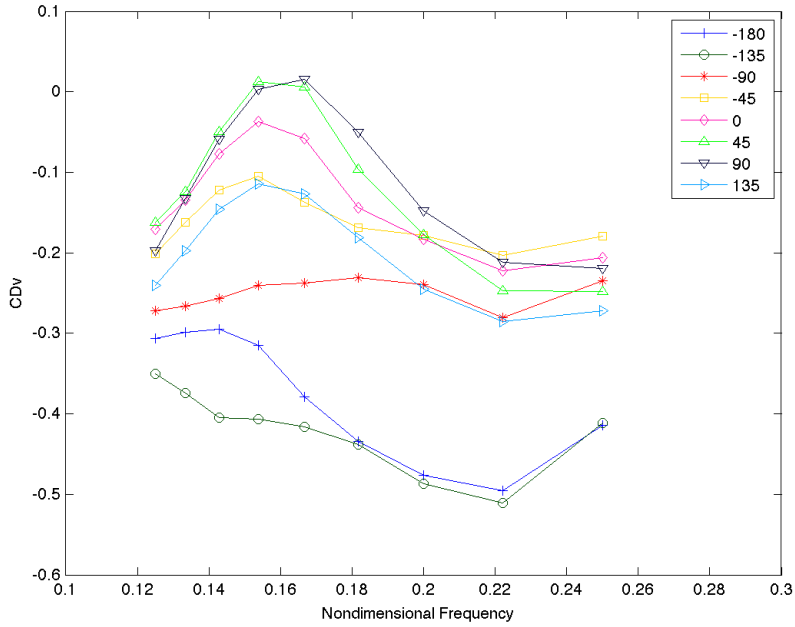

Figure A-79: Drag coefficients in phase with velocity C_{Dv} X 0.15 Y 0.25

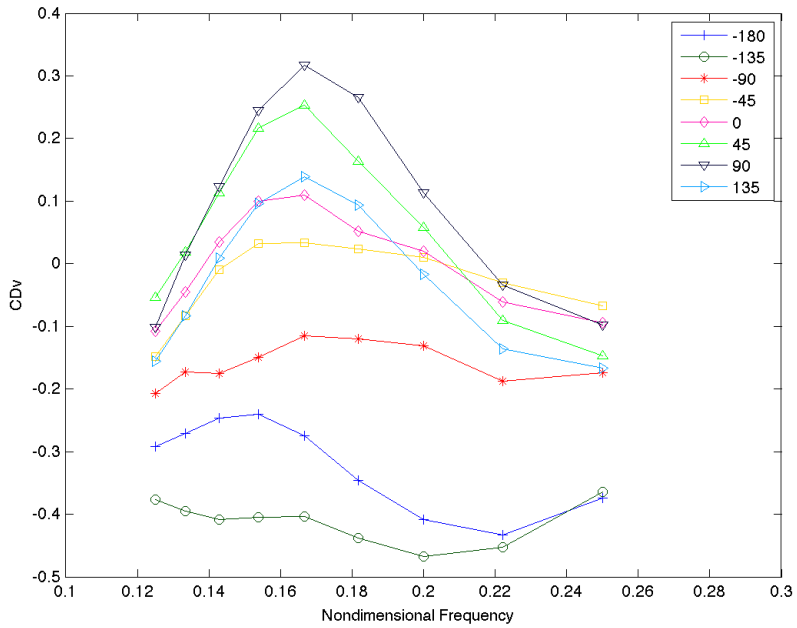

Figure A-80: Drag coefficients in phase with velocity C_{Dv} X 0.15 Y 0.5

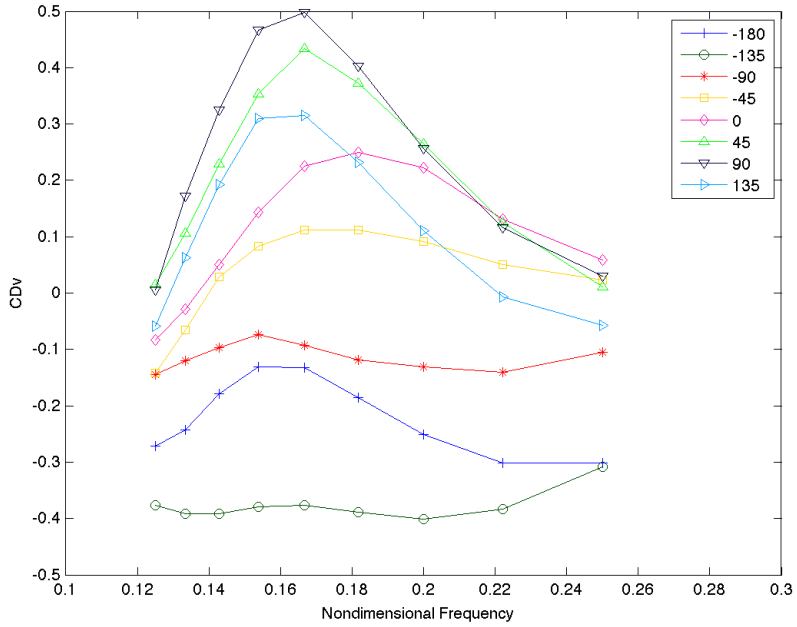

Figure A-81: Drag coefficients in phase with velocity C_{Dv} X 0.15 Y 0.75

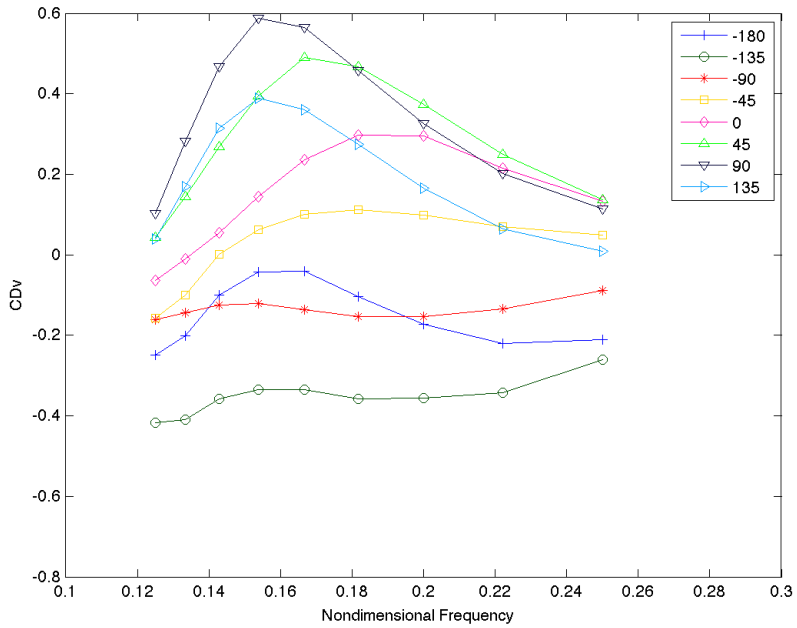

Figure A-82: Drag coefficients in phase with velocity C_{Dv} X 0.15 Y 1

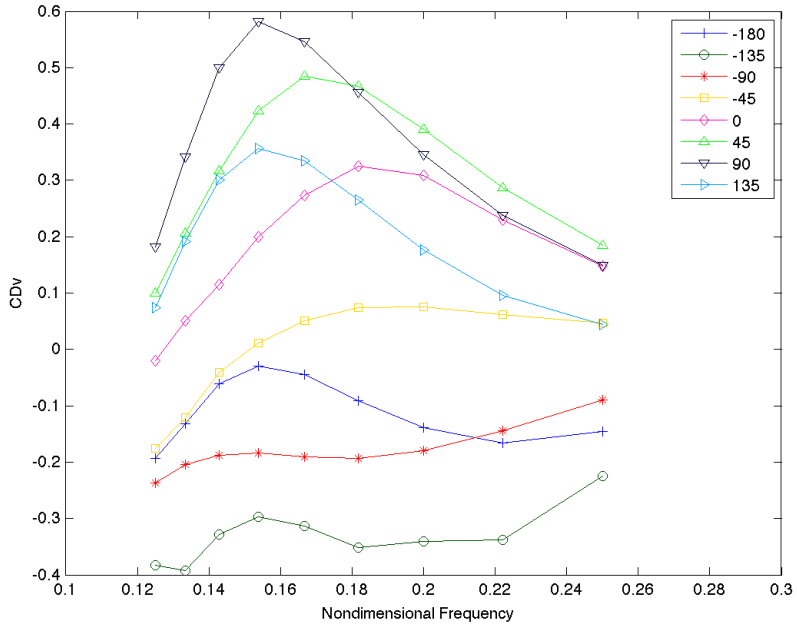

Figure A-83: Drag coefficients in phase with velocity C_{Dv} X 0.15 Y 1.25

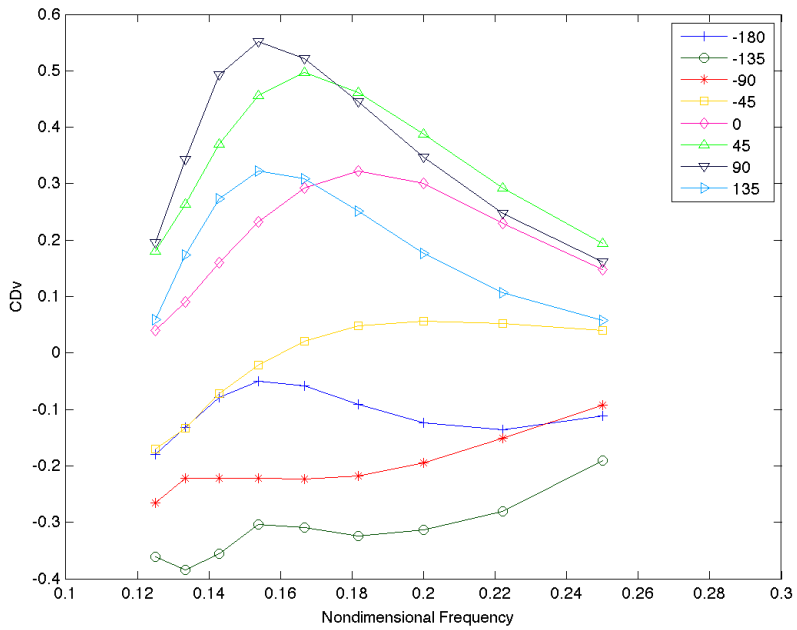

Figure A-84: Drag coefficients in phase with velocity C_{Dv} X 0.15 Y 1.5

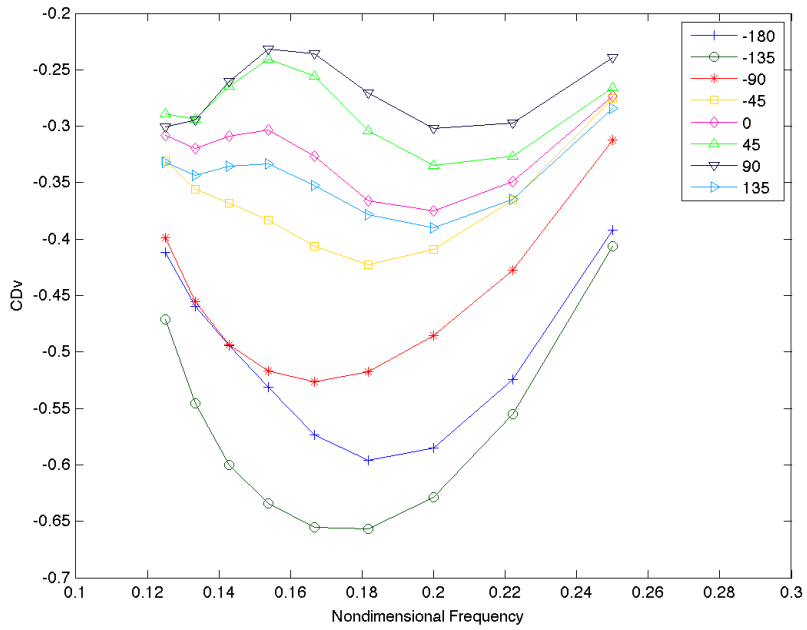

Figure A-85: Drag coefficients in phase with velocity C_{Dv} X 0.2 Y 0.15

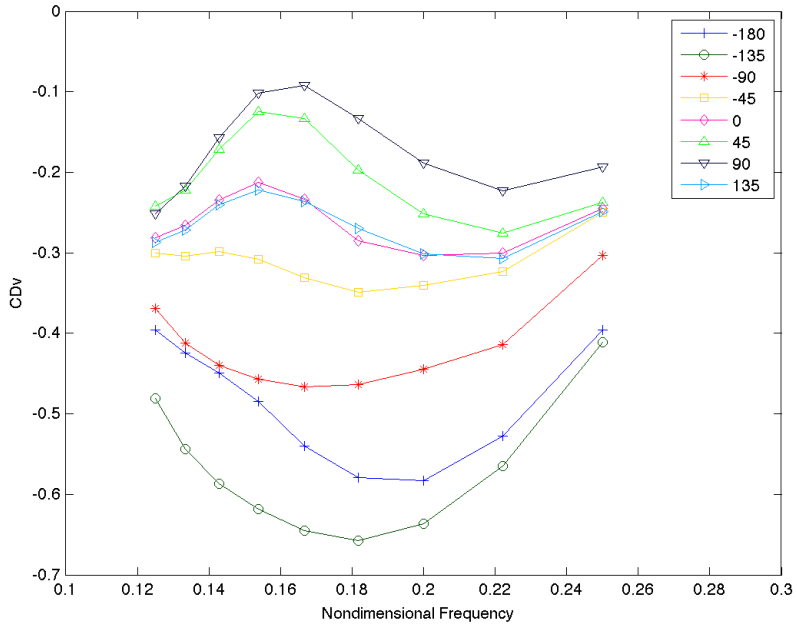

Figure A-86: Drag coefficients in phase with velocity C_{Dv} X 0.2 Y 0.25

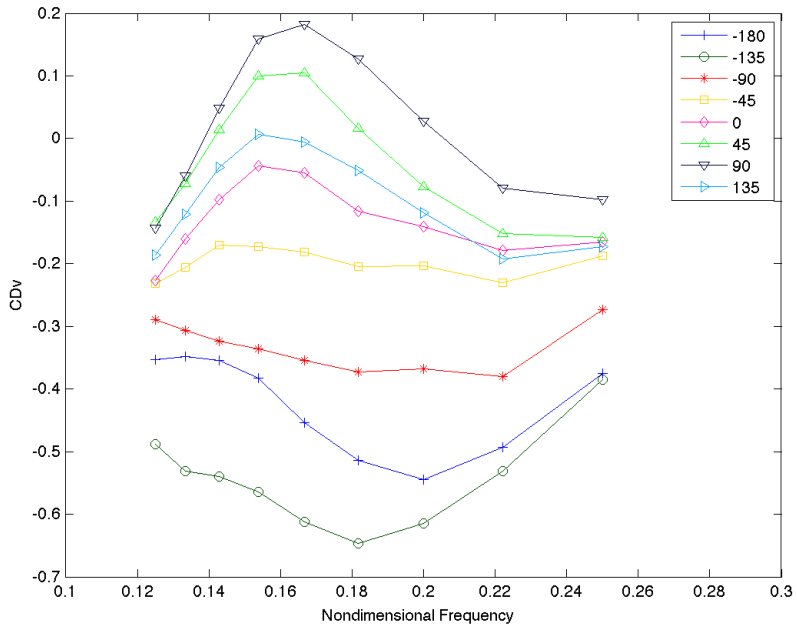

Figure A-87: Drag coefficients in phase with velocity C_{Dv} X 0.2 Y 0.5

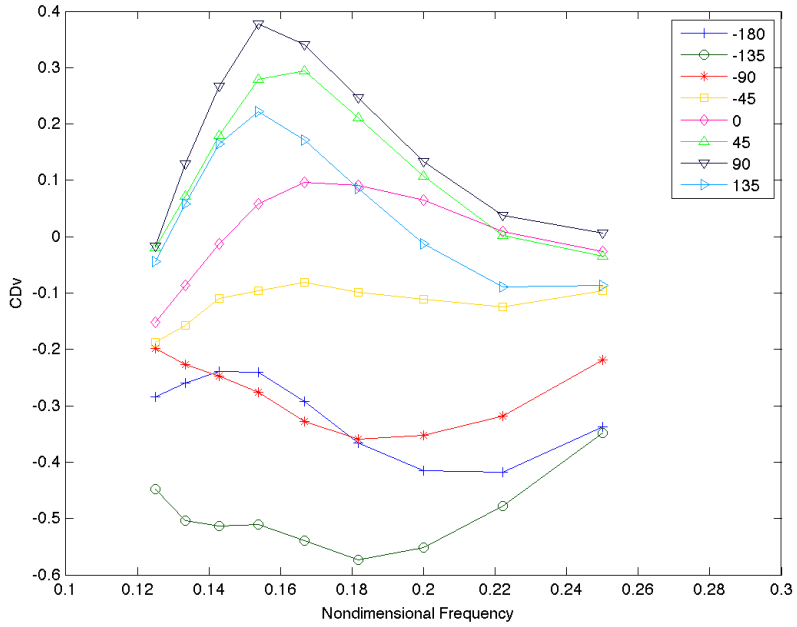

Figure A-88: Drag coefficients in phase with velocity C_{Dv} X 0.2 Y 0.75

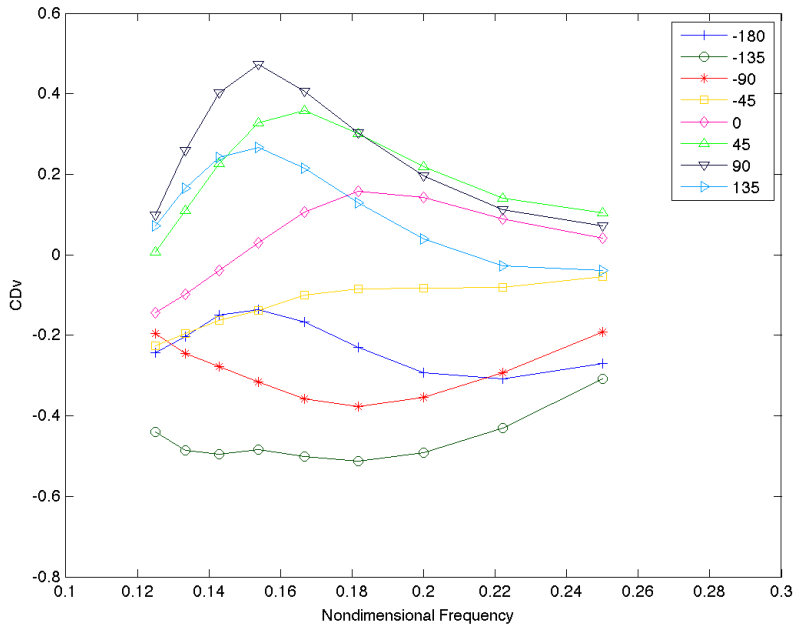

Figure A-89: Drag coefficients in phase with velocity C_{Dv} X 0.2 Y 1

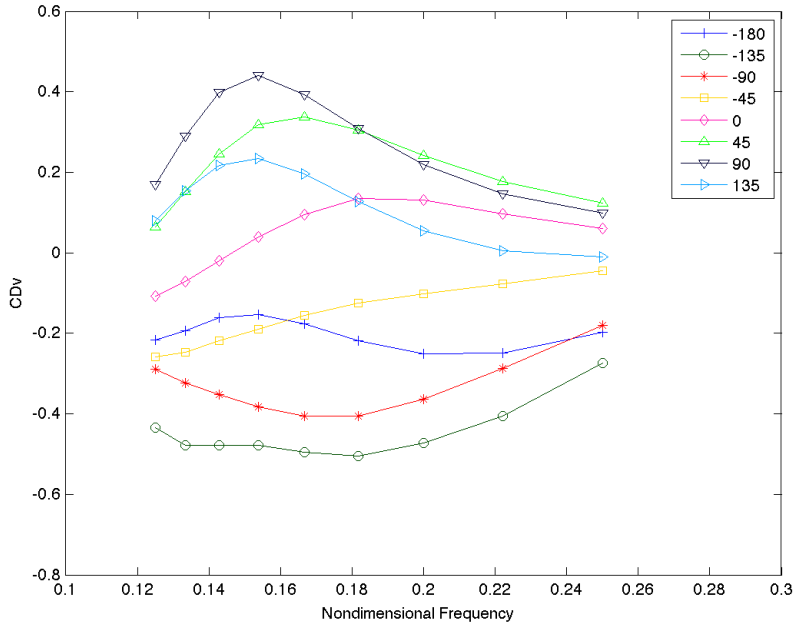

Figure A-90: Drag coefficients in phase with velocity C_{Dv} X 0.2 Y 1.25

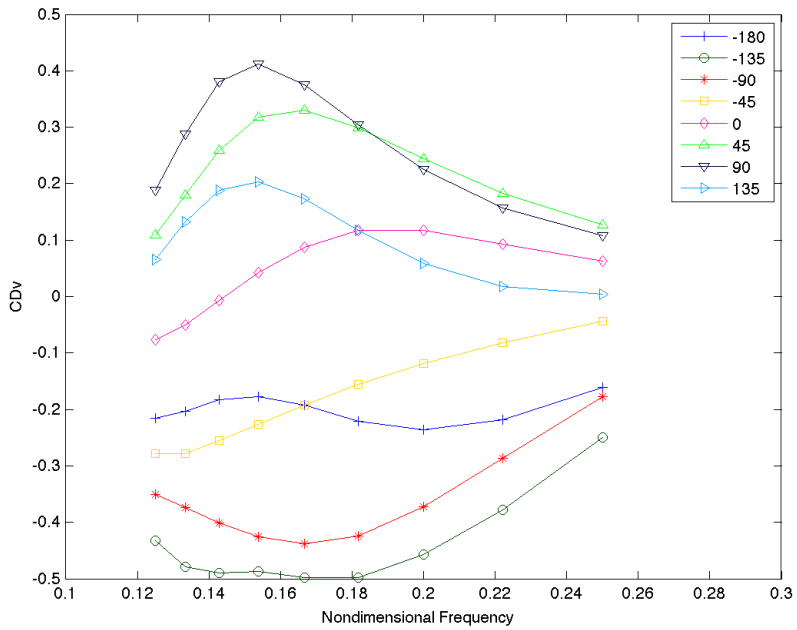

Figure A-91: Drag coefficients in phase with velocity C_{Dv} X 0.2 Y 1.5

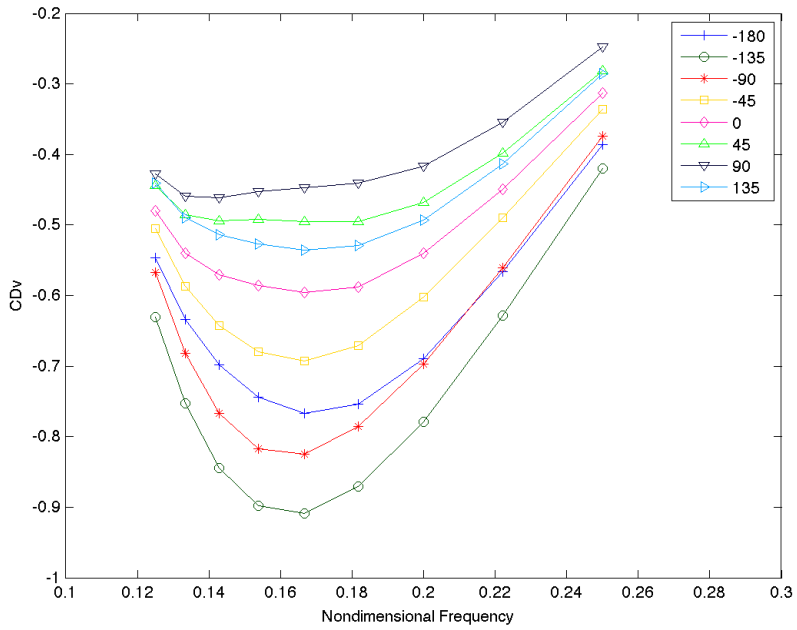

Figure A-92: Drag coefficients in phase with velocity C_{Dv} X 0.25 Y 0.15

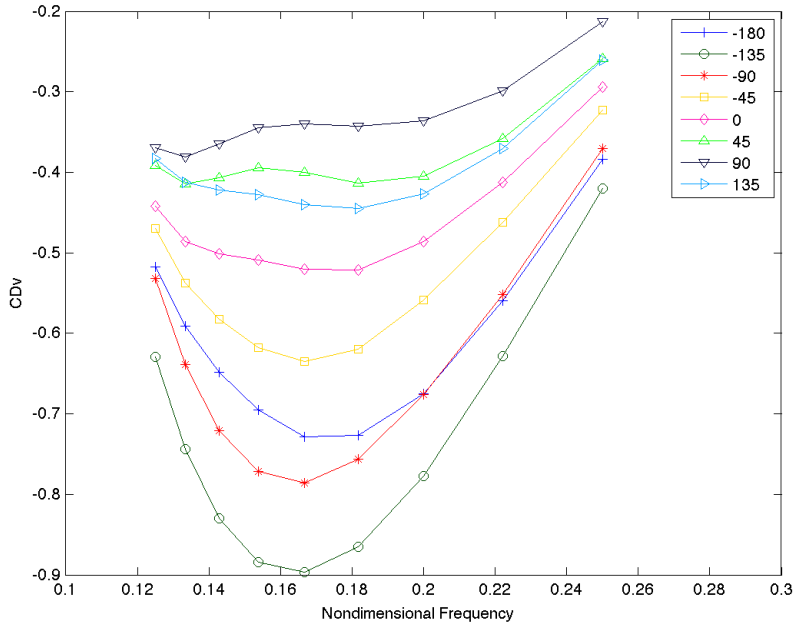

Figure A-93: Drag coefficients in phase with velocity C_{Dv} X 0.25 Y 0.25

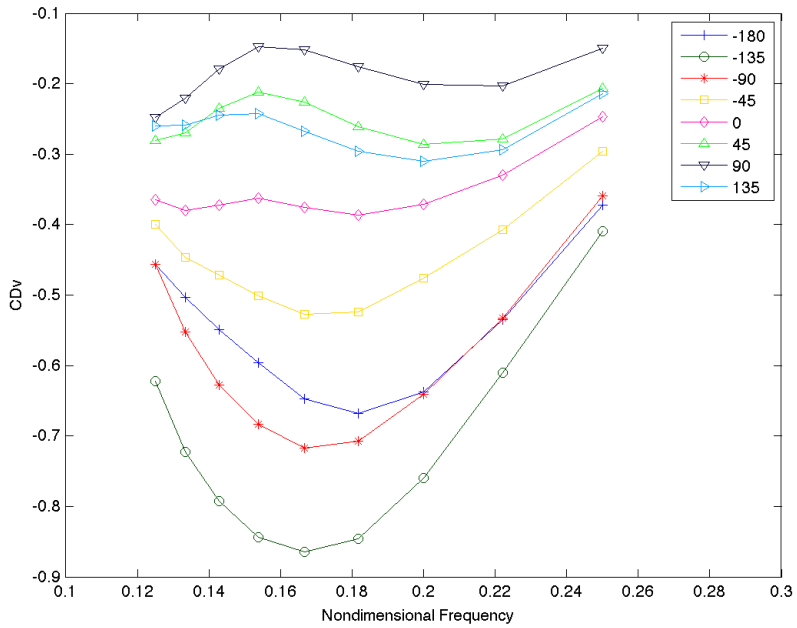

Figure A-94: Drag coefficients in phase with velocity C_{Dv} X 0.25 Y 0.5

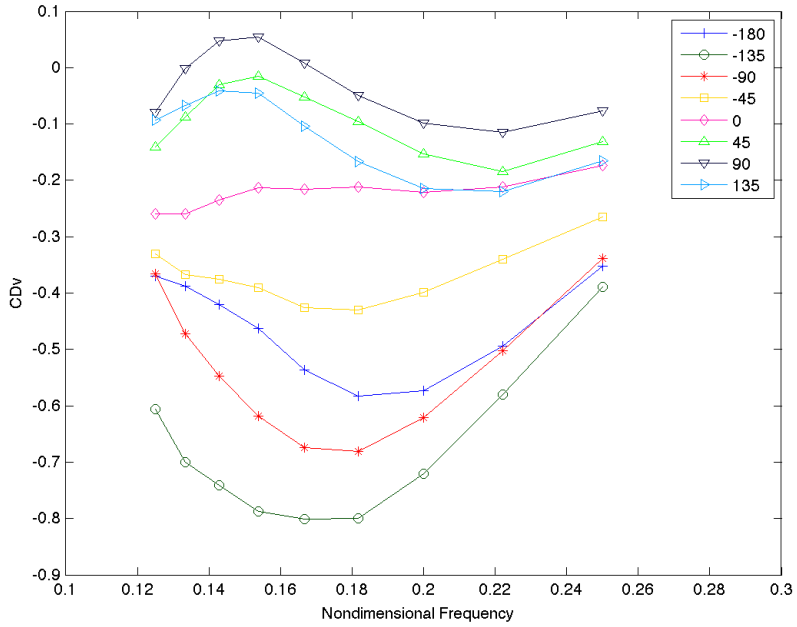

Figure A-95: Drag coefficients in phase with velocity C_{Dv} X 0.25 Y 0.75

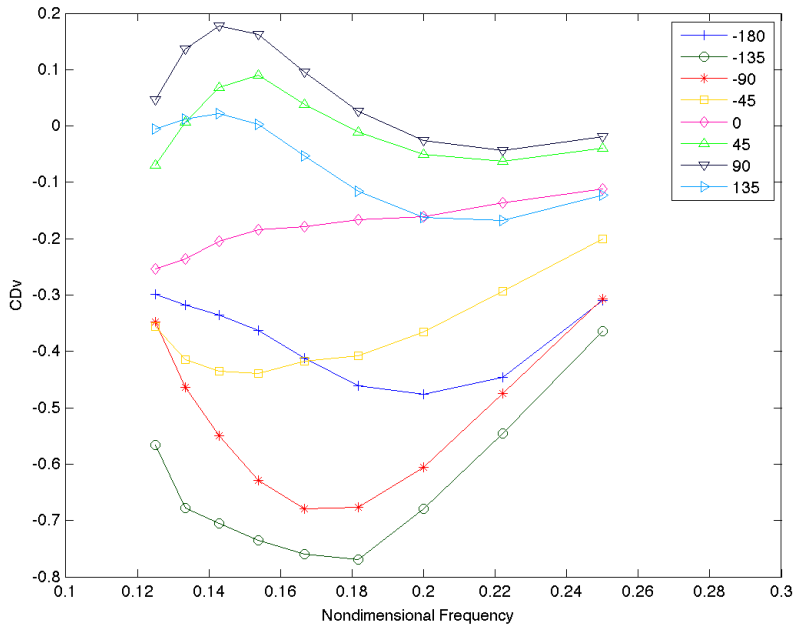

Figure A-96: Drag coefficients in phase with velocity C_{Dv} X 0.25 Y 1

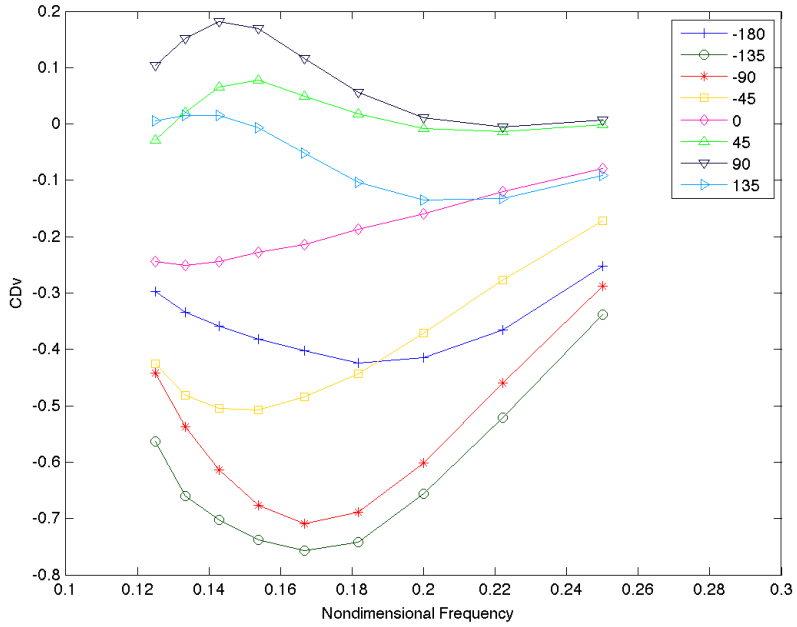

Figure A-97: Drag coefficients in phase with velocity C_{Dv} X 0.25 Y 1.25

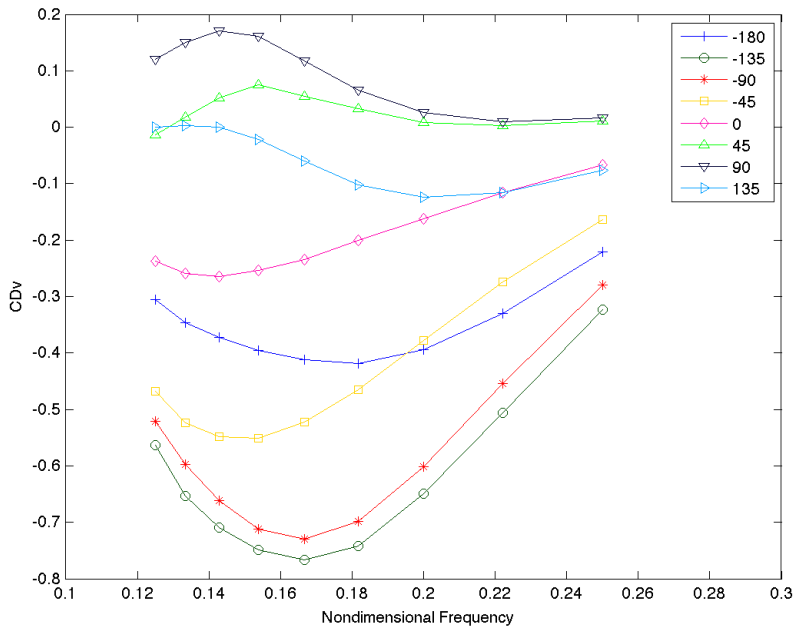

Figure A-98: Drag coefficients in phase with velocity C_{Dv} X 0.25 Y 1.5

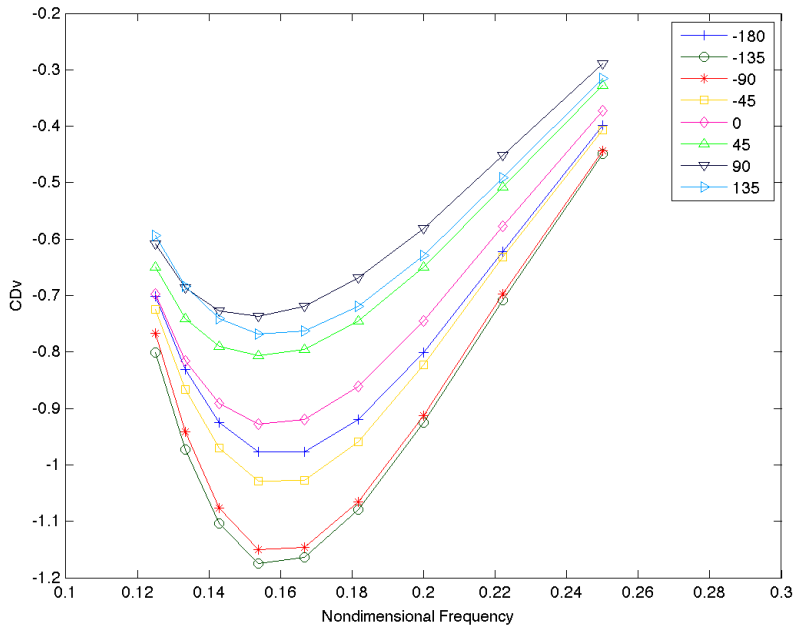

Figure A-99: Drag coefficients in phase with velocity C_{Dv} X 0.3 Y 0.15

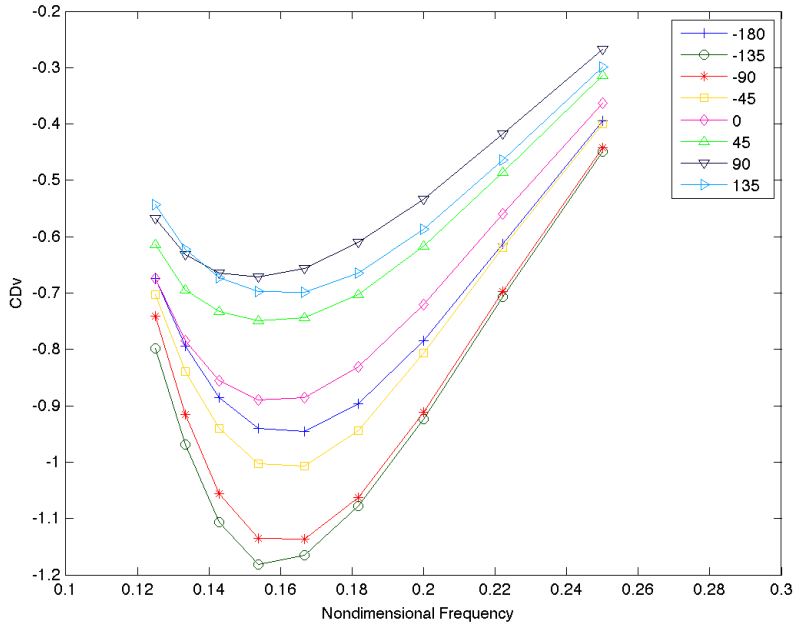

Figure A-100: Drag coefficients in phase with velocity C_{Dv} X 0.3 Y 0.25

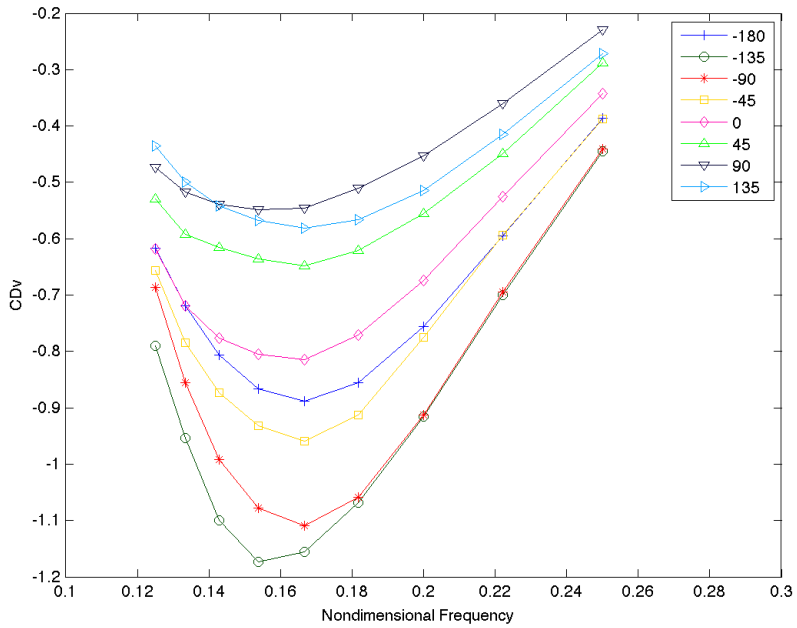

Figure A-101: Drag coefficients in phase with velocity C_{Dv} X 0.3 Y 0.5

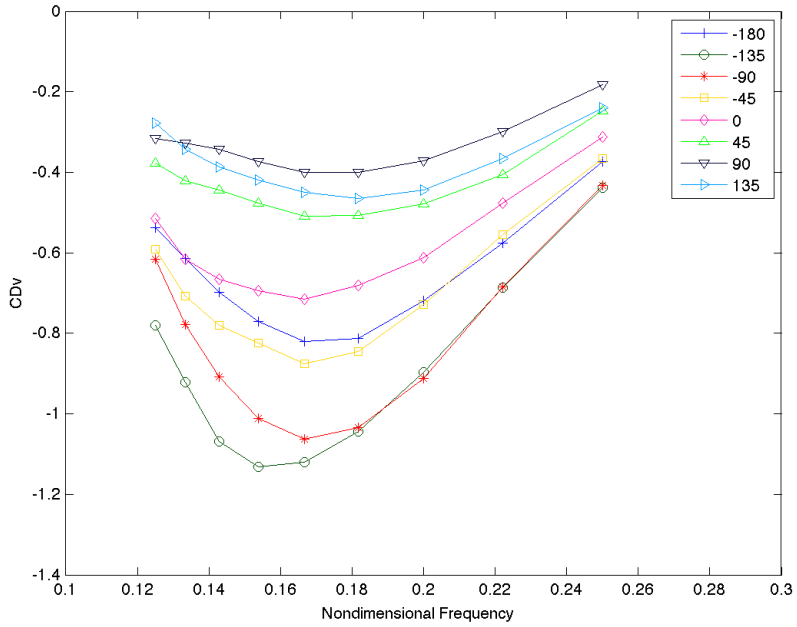

Figure A-102: Drag coefficients in phase with velocity C_{Dv} X 0.3 Y 0.75

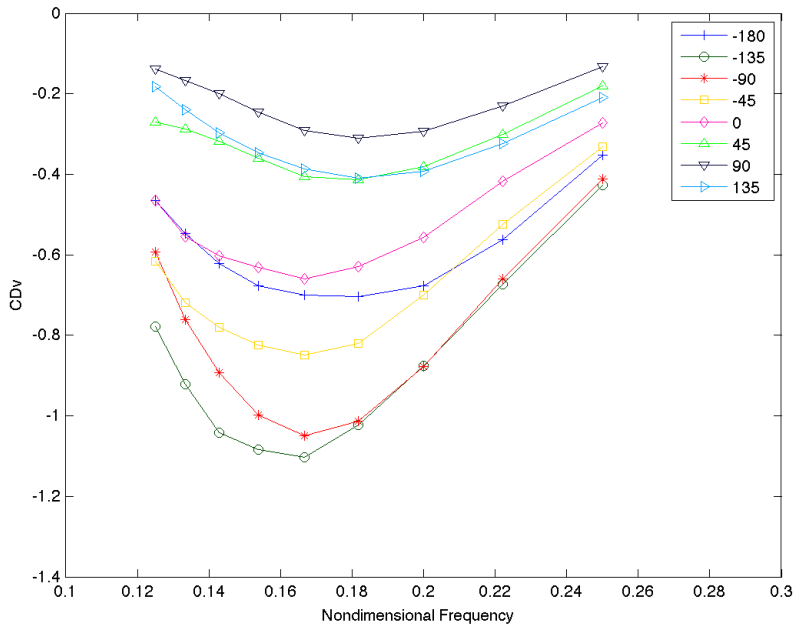

Figure A-103: Drag coefficients in phase with velocity C_{Dv} X 0.3 Y 1

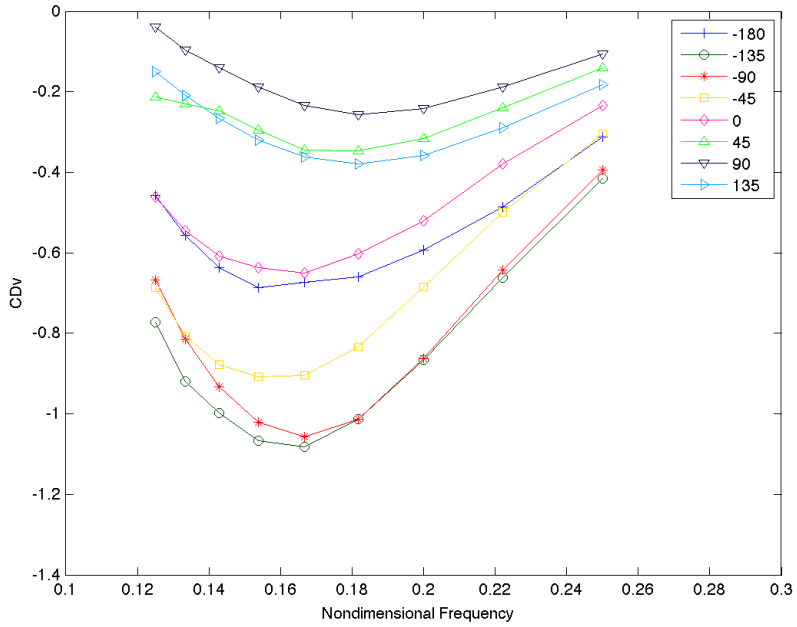

Figure A-104: Drag coefficients in phase with velocity C_{Dv} X 0.3 Y 1.25

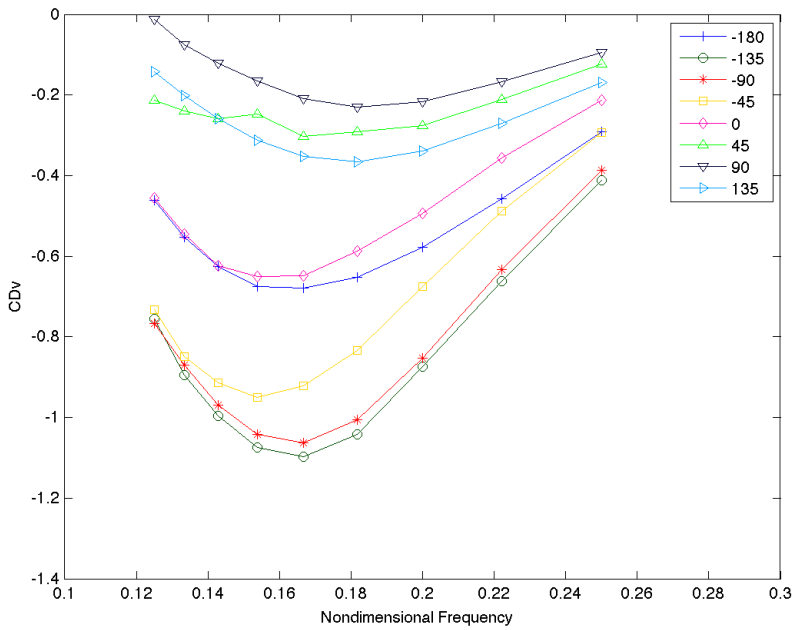

Figure A-105: Drag coefficients in phase with velocity C_{Dv} X 0.3 Y 1.5

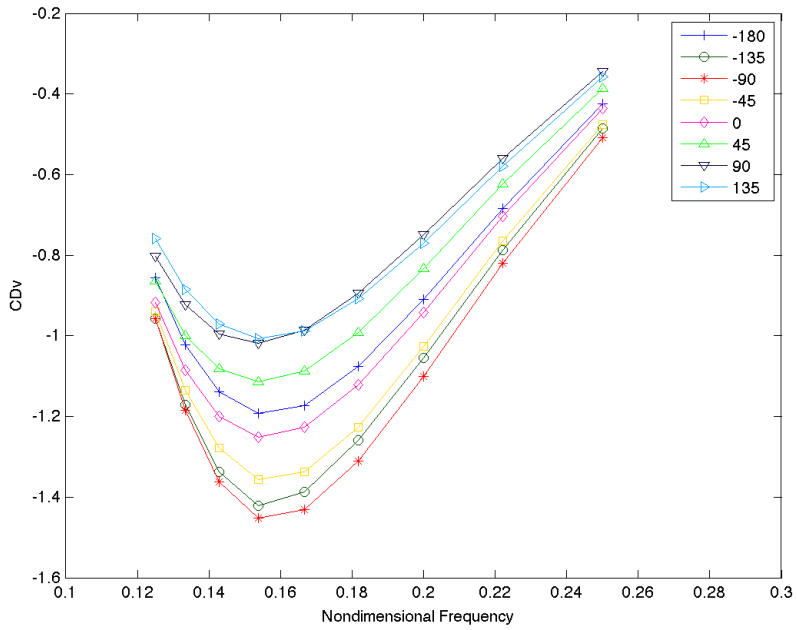

Figure A-106: Drag coefficients in phase with velocity C_{Dv} X 0.45 Y 0.15

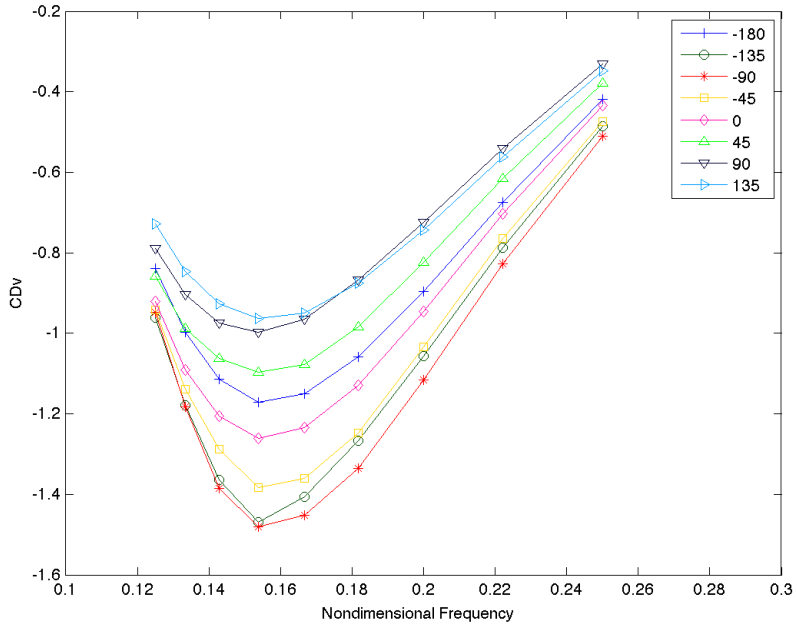

Figure A-107: Drag coefficients in phase with velocity C_{Dv} X 0.45 Y 0.25

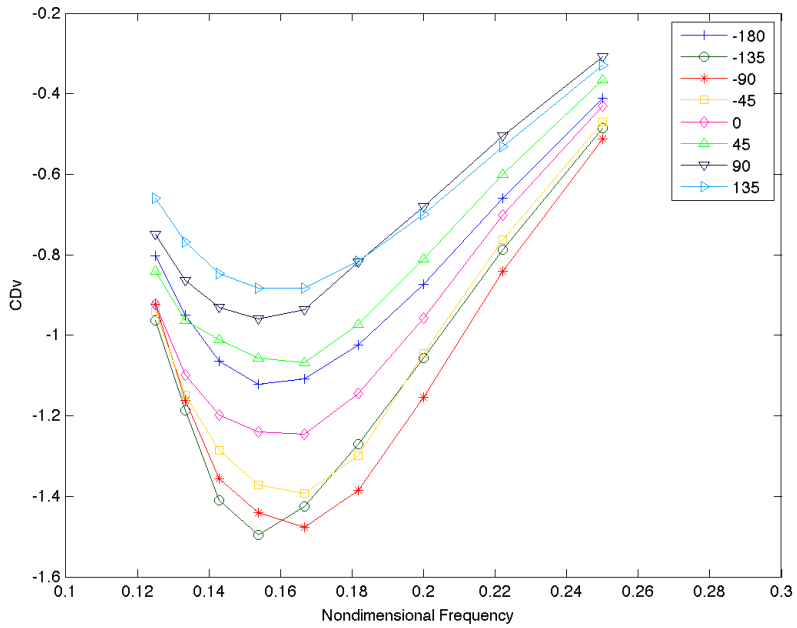

Figure A-108: Drag coefficients in phase with velocity C_{Dv} X 0.45 Y 0.5

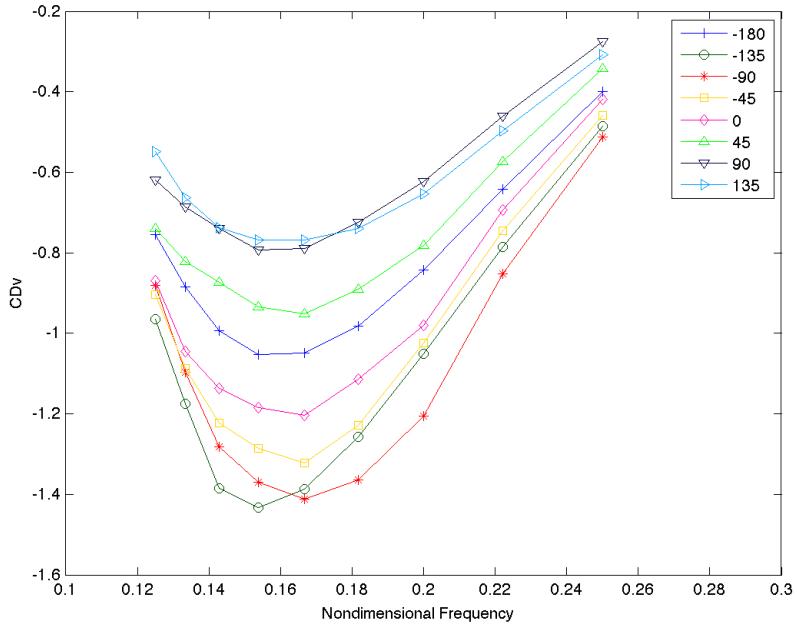

Figure A-109: Drag coefficients in phase with velocity C_{Dv} X 0.45 Y 0.75

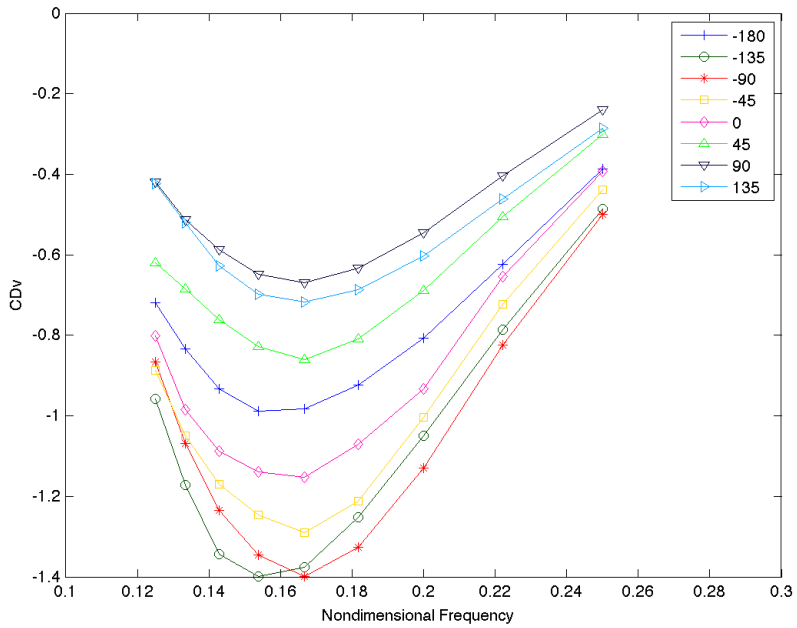

Figure A-110: Drag coefficients in phase with velocity C_{Dv} X 0.45 Y 1

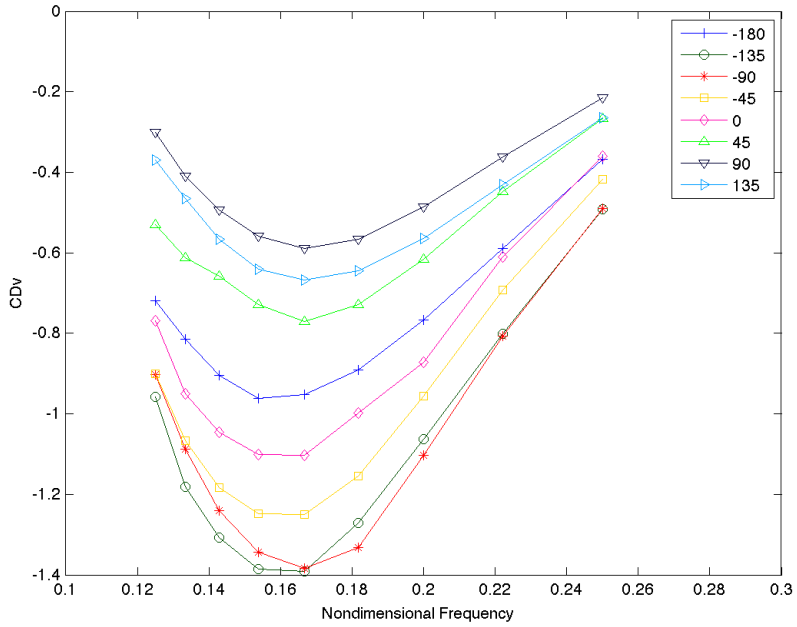

Figure A-111: Drag coefficients in phase with velocity C_{Dv} X 0.45 Y 1.25

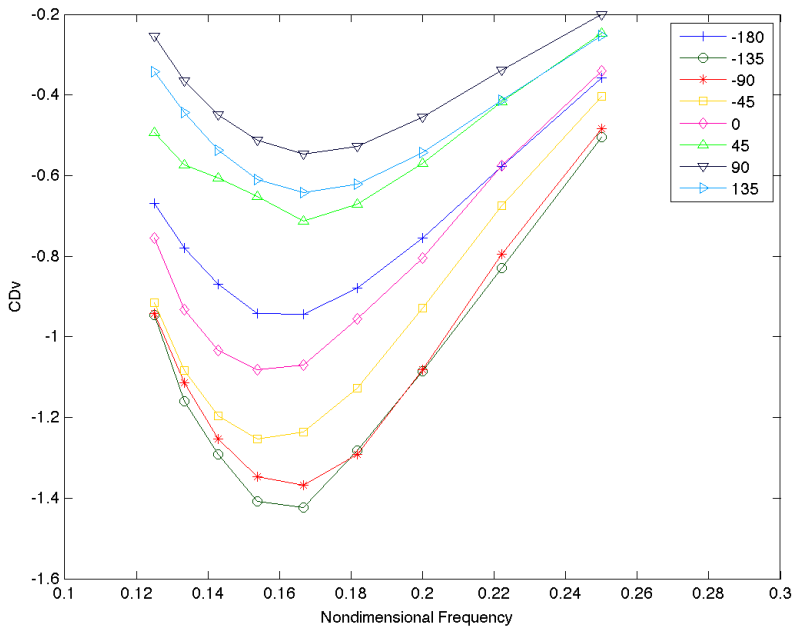

Figure A-112: Drag coefficients in phase with velocity C_{Dv} X 0.45 Y 1.5

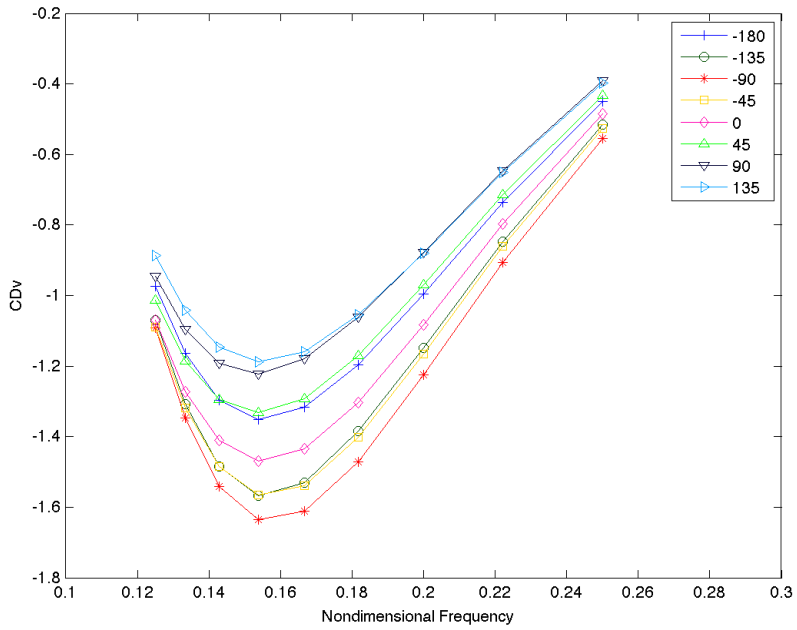

Figure A-113: Drag coefficients in phase with velocity C_{Dv} X 0.6 Y 0.15

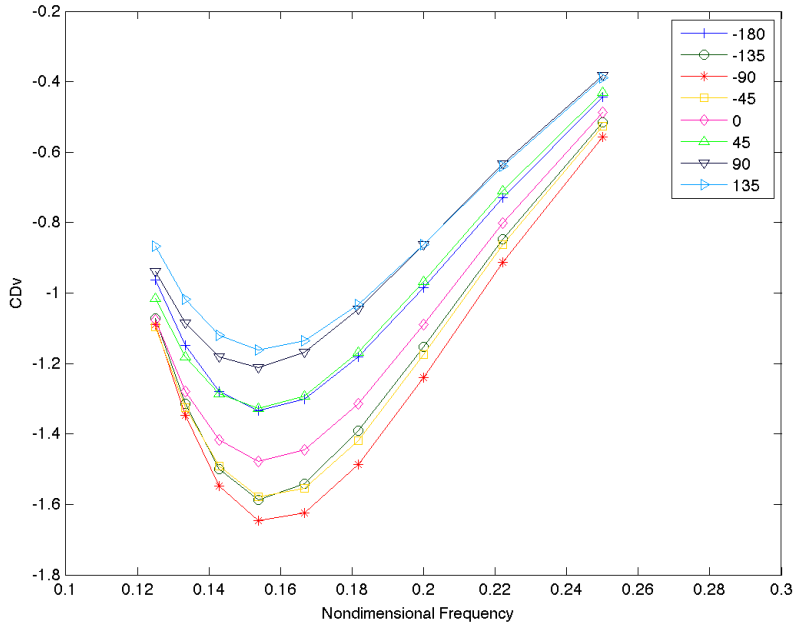

Figure A-114: Drag coefficients in phase with velocity C_{Dv} X 0.6 Y 0.25

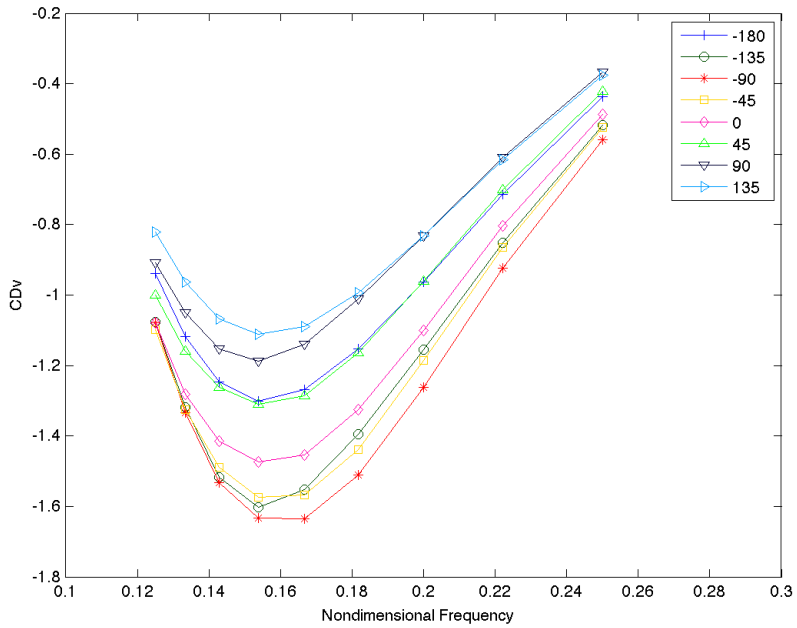

Figure A-115: Drag coefficients in phase with velocity C_{Dv} X 0.6 Y 0.5

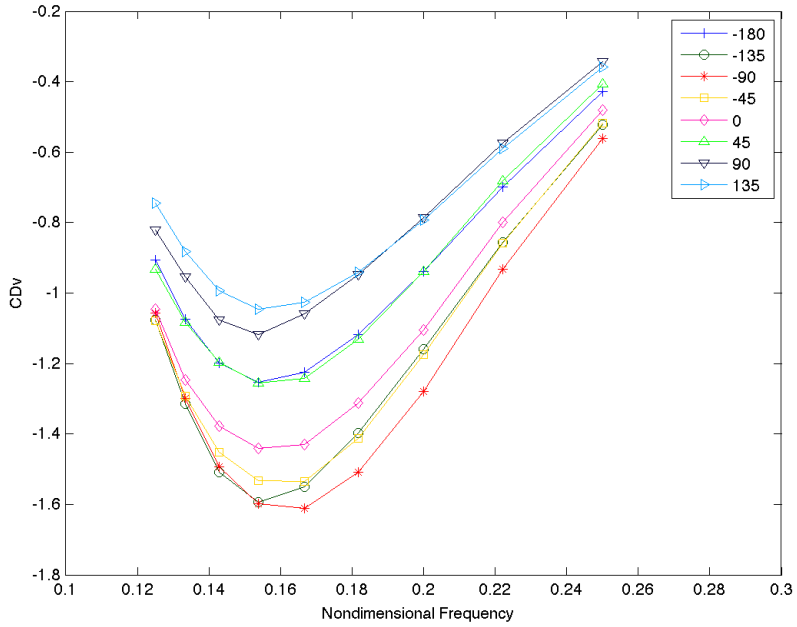

Figure A-116: Drag coefficients in phase with velocity C_{Dv} X 0.6 Y 0.75

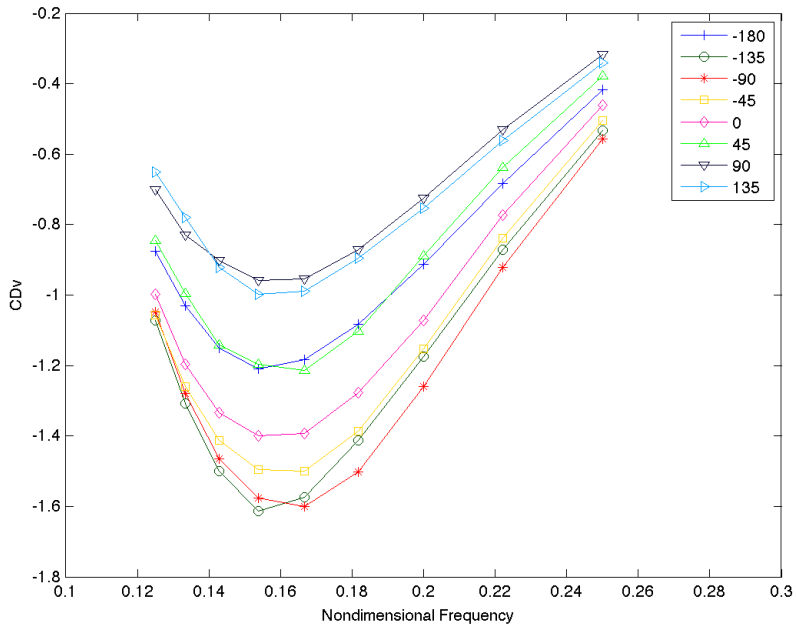

Figure A-117: Drag coefficients in phase with velocity C_{Dv} X 0.6 Y 1

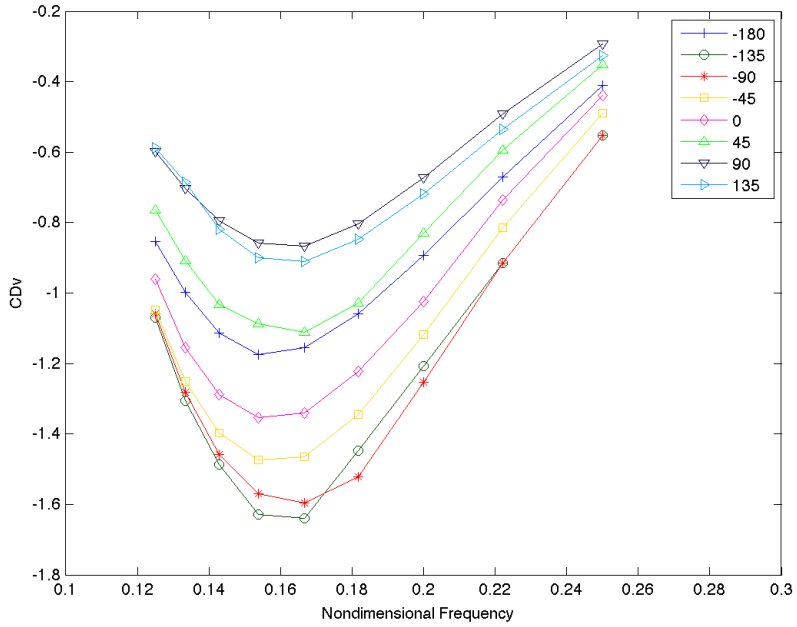

Figure A-118: Drag coefficients in phase with velocity C_{Dv} X 0.6 Y 1.25

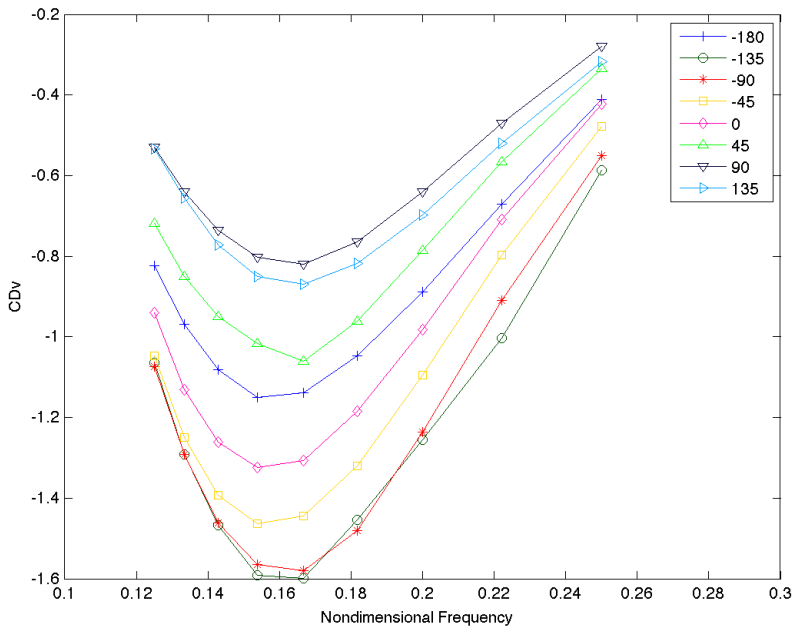

Figure A-119: Drag coefficients in phase with velocity C_{Dv} X 0.6 Y 1.5

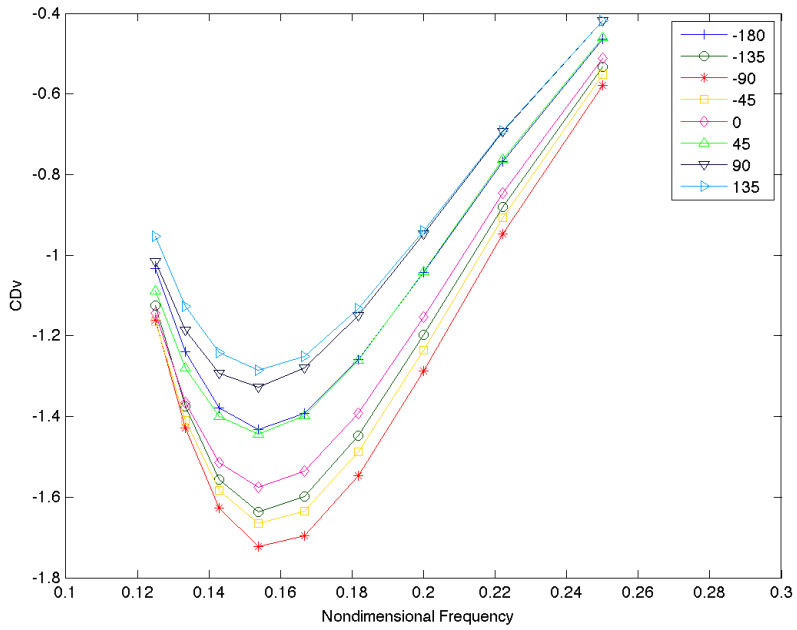

Figure A-120: Drag coefficients in phase with velocity C_{Dv} X 0.75 Y 0.15

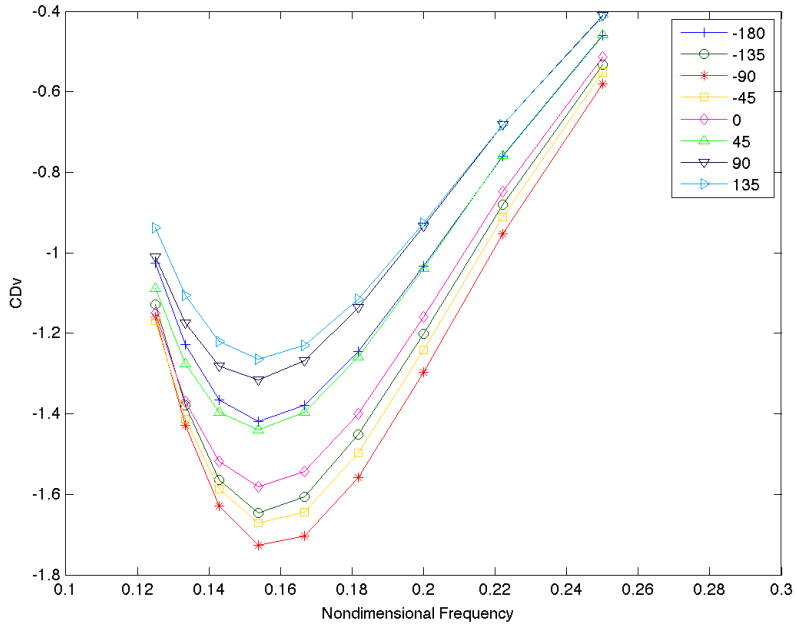

Figure A-121: Drag coefficients in phase with velocity C_{Dv} X 0.75 Y 0.25

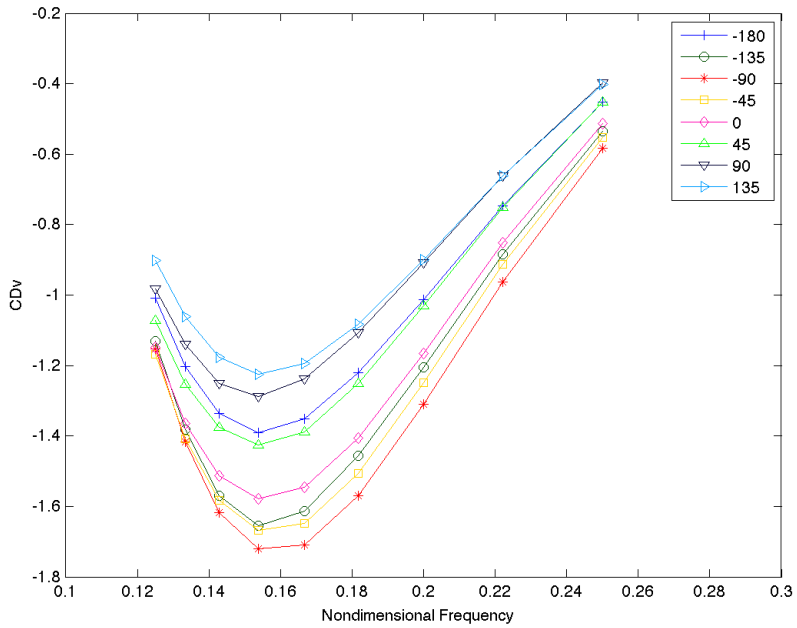

Figure A-122: Drag coefficients in phase with velocity C_{Dv} X 0.75 Y 0.5

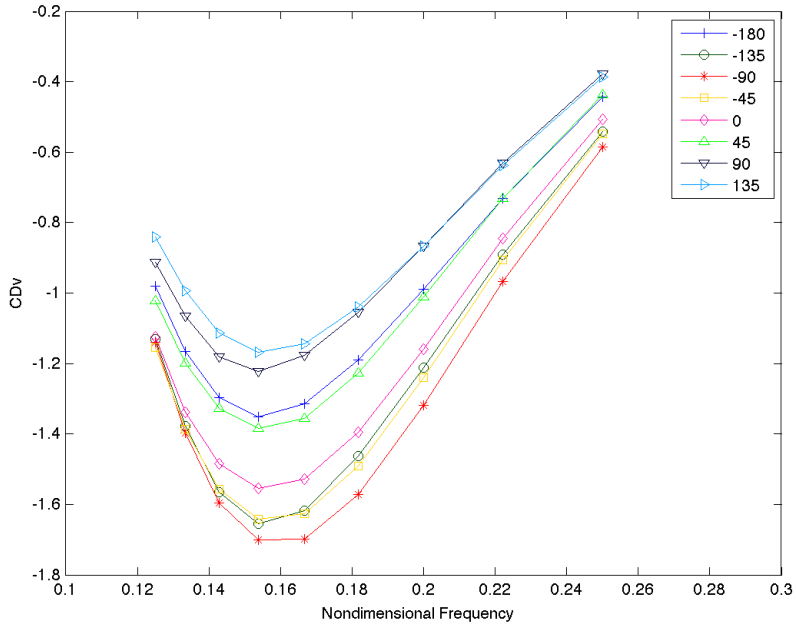

Figure A-123: Drag coefficients in phase with velocity C_{Dv} X 0.75 Y 0.75

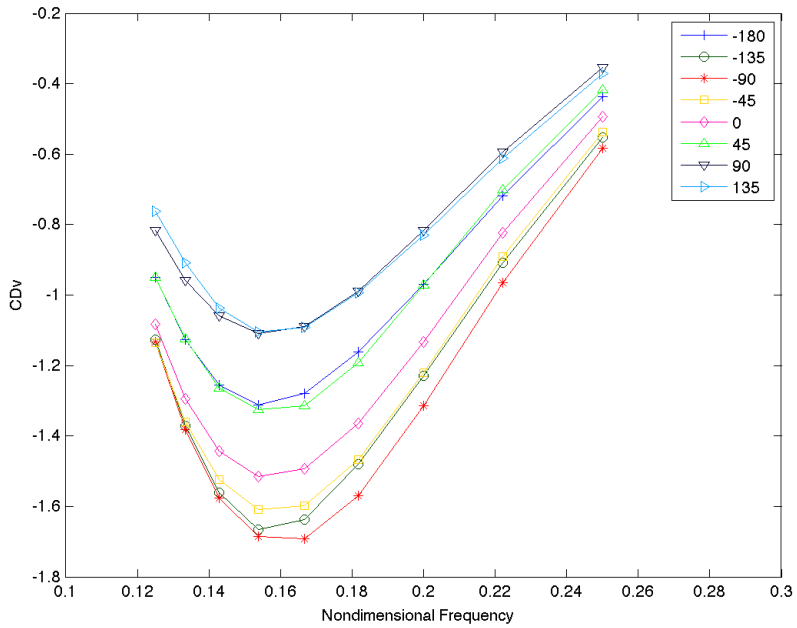

Figure A-124: Drag coefficients in phase with velocity C_{Dv} X 0.75 Y 1

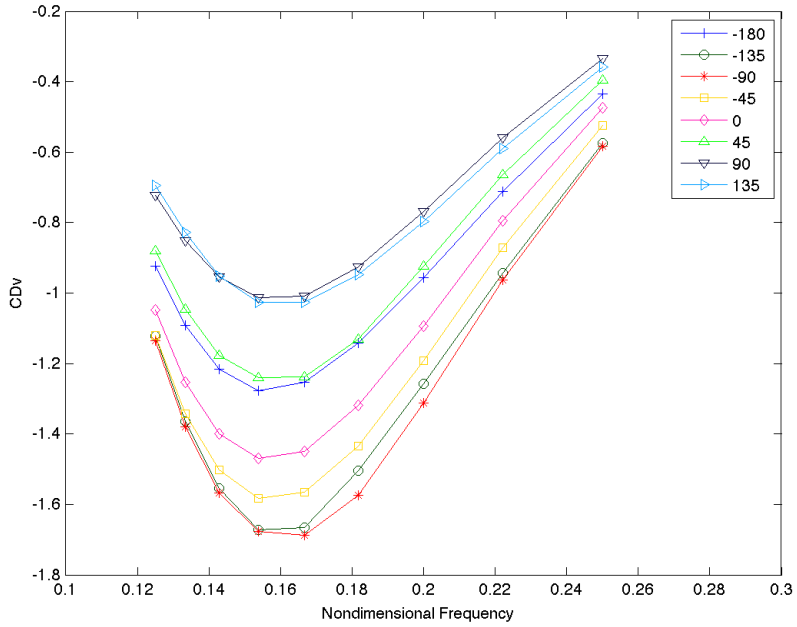

Figure A-125: Drag coefficients in phase with velocity C_{Dv} X 0.75 Y 1.25

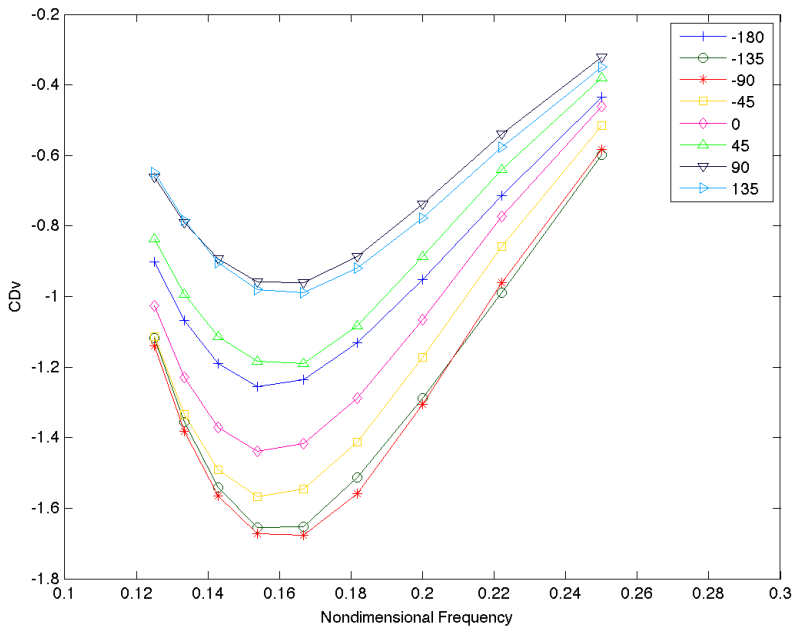

Figure A-126: Drag coefficients in phase with velocity C_{Dv} X 0.75 Y 1.5

A.3 Crossflow Added Mass Coefficients $C_{m,CF}$

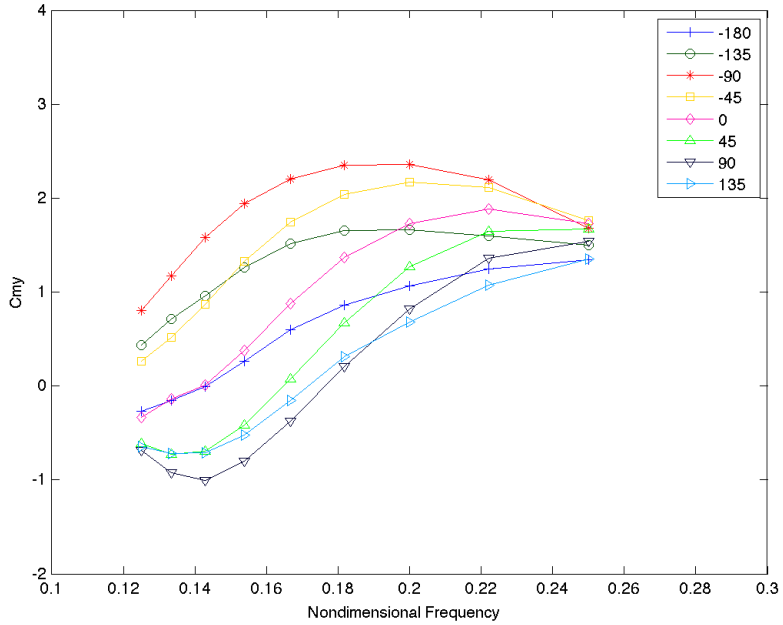

Figure A-127: Crossflow added mass coefficients $C_{m,CF}$ X 0.05 Y 0.15

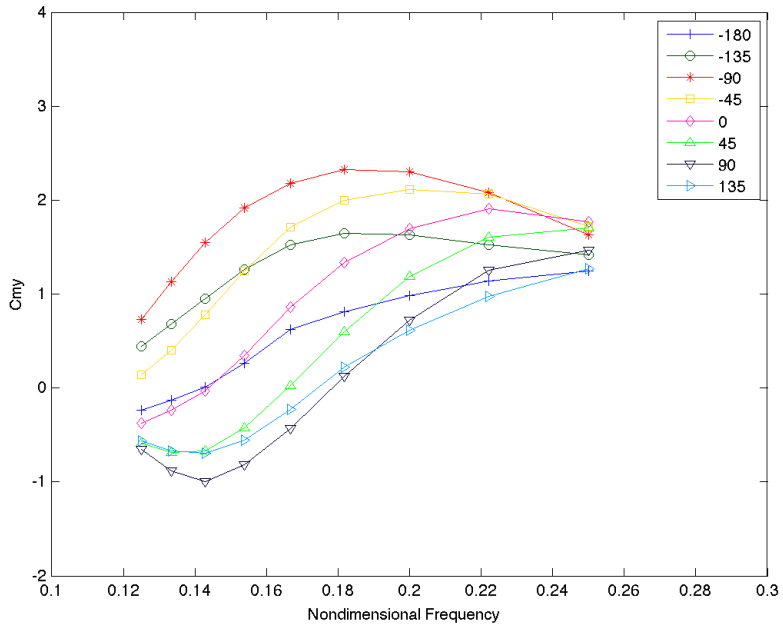

Figure A-128: Crossflow added mass coefficients $C_{m,CF}$ X 0.05 Y 0.25

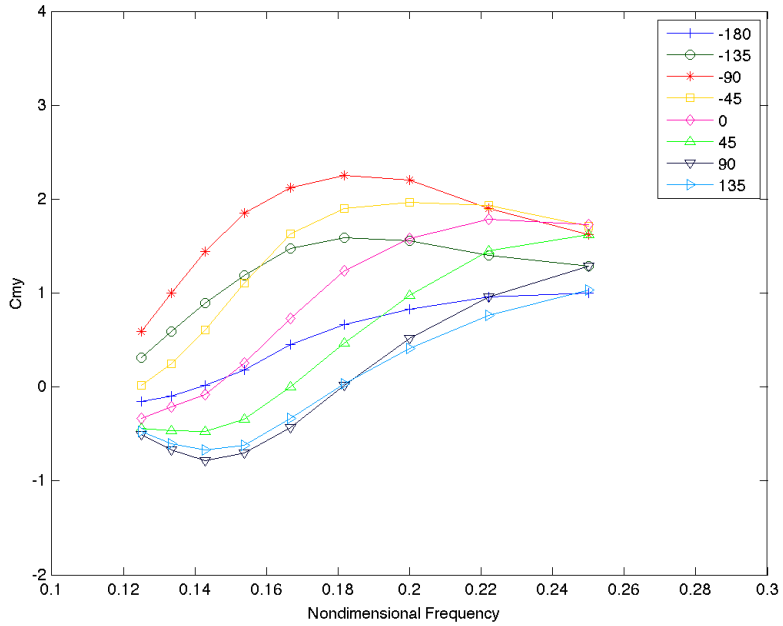

Figure A-129: Crossflow added mass coefficients $C_{m,CF}$ X 0.05 Y 0.5

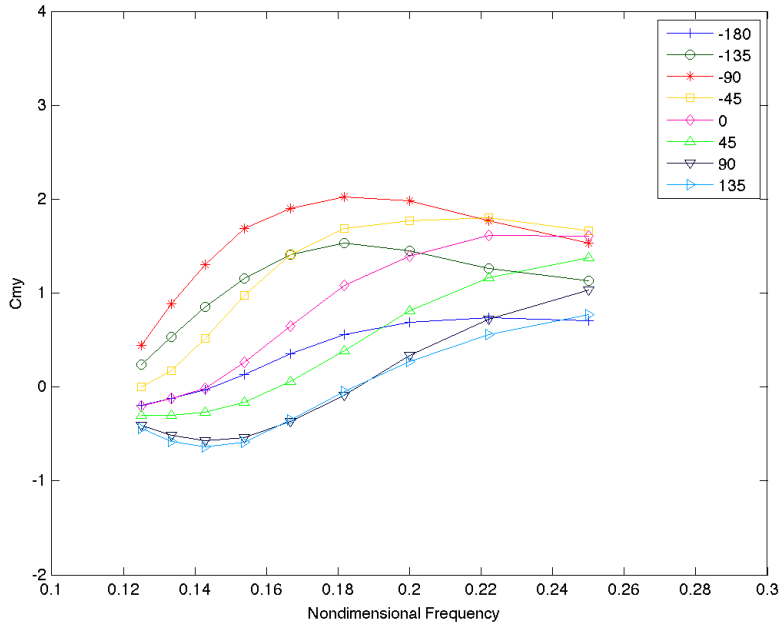

Figure A-130: Crossflow added mass coefficients $C_{m,CF}$ X 0.05 Y 0.75

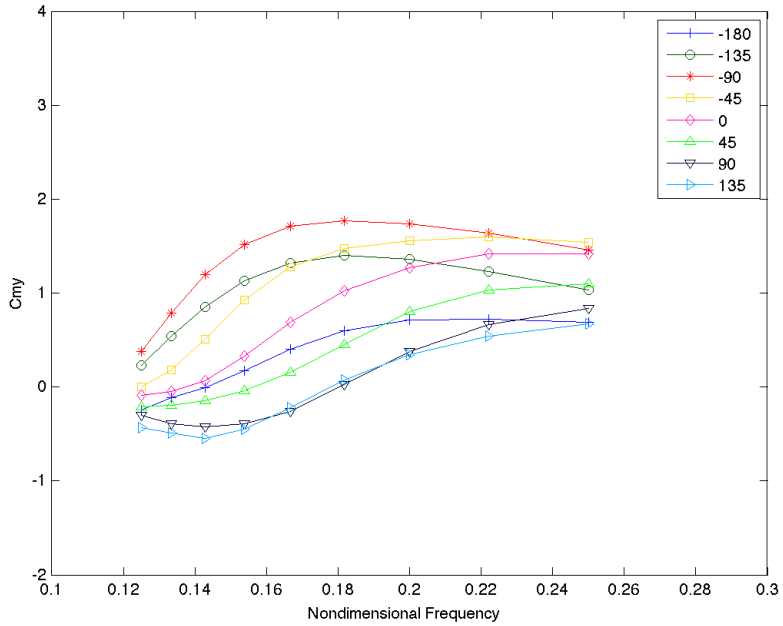

Figure A-131: Crossflow added mass coefficients $C_{m,CF}$ X 0.05 Y 1

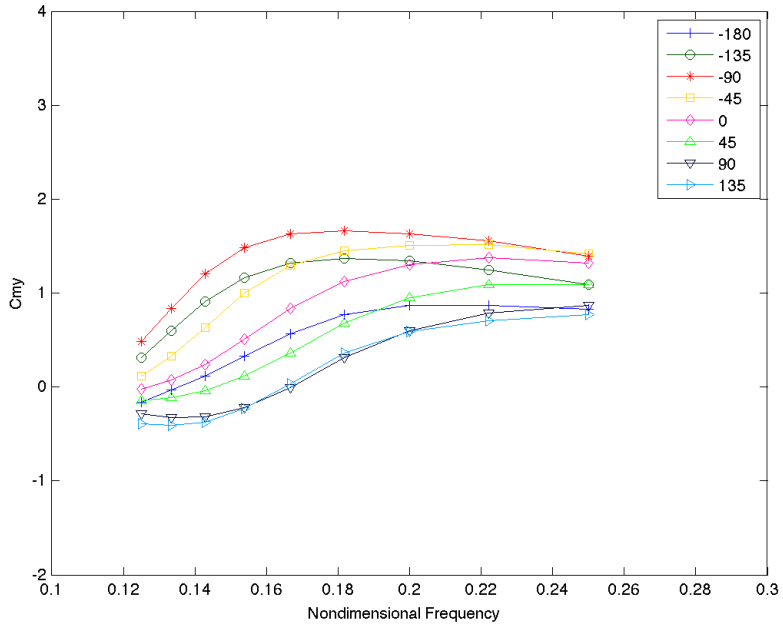

Figure A-132: Crossflow added mass coefficients $C_{m,CF}$ X 0.05 Y 1.25

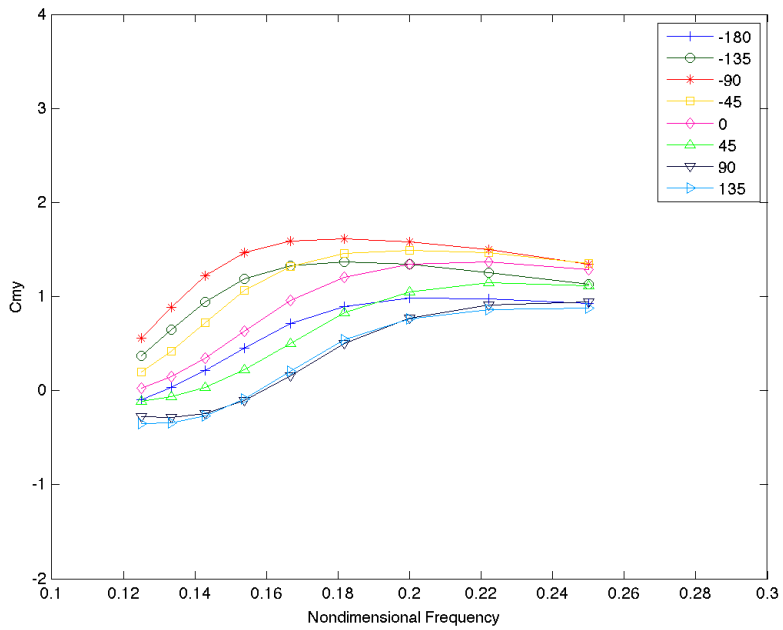

Figure A-133: Crossflow added mass coefficients $C_{m,CF}$ X 0.05 Y 1.5

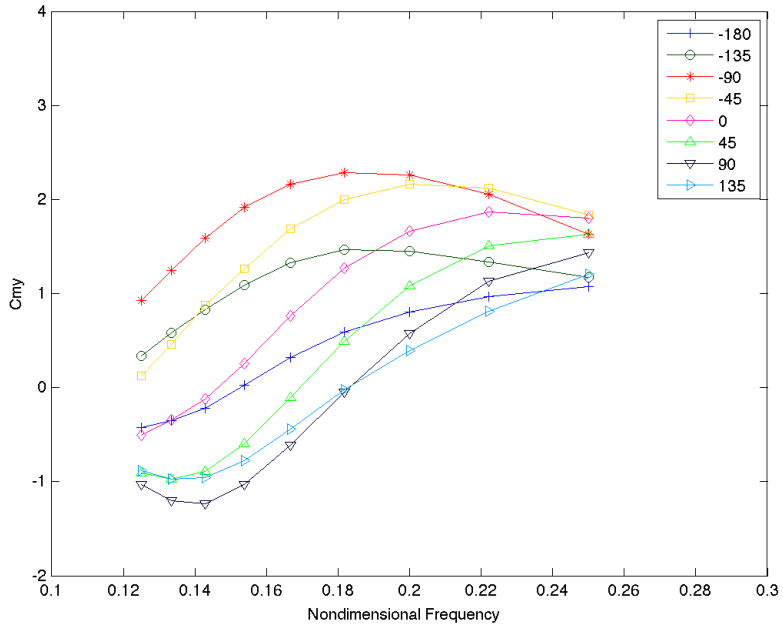

Figure A-134: Crossflow added mass coefficients $C_{m,CF}$ X 0.1 Y 0.15

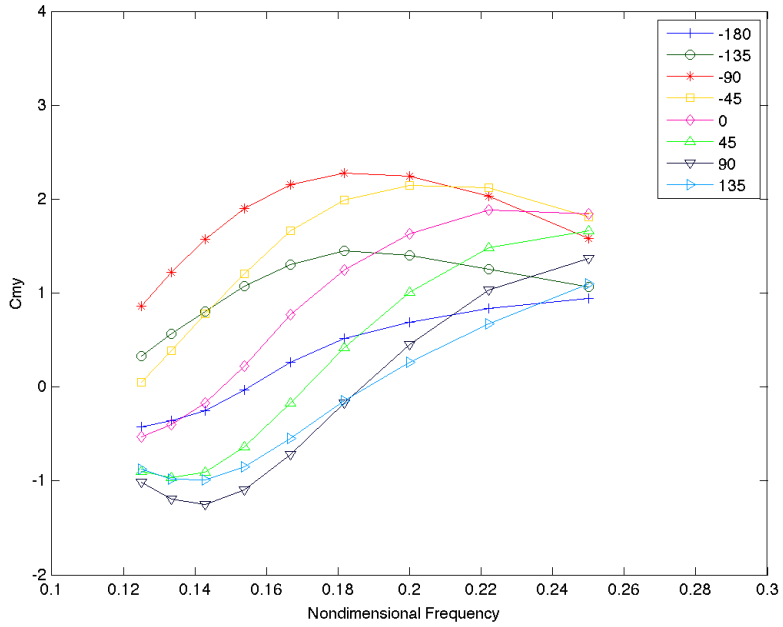

Figure A-135: Crossflow added mass coefficients $C_{m,CF}$ X 0.1 Y 0.25

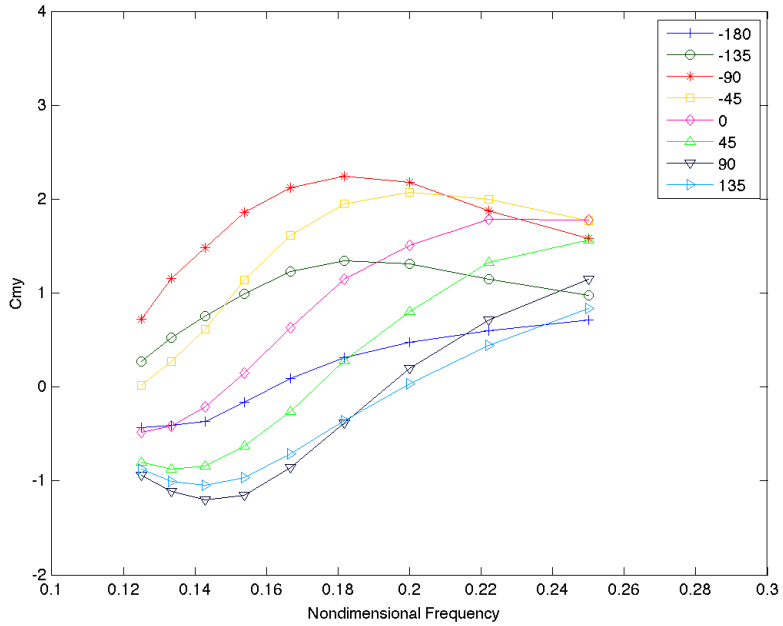

Figure A-136: Crossflow added mass coefficients $C_{m,CF}$ X 0.1 Y 0.5

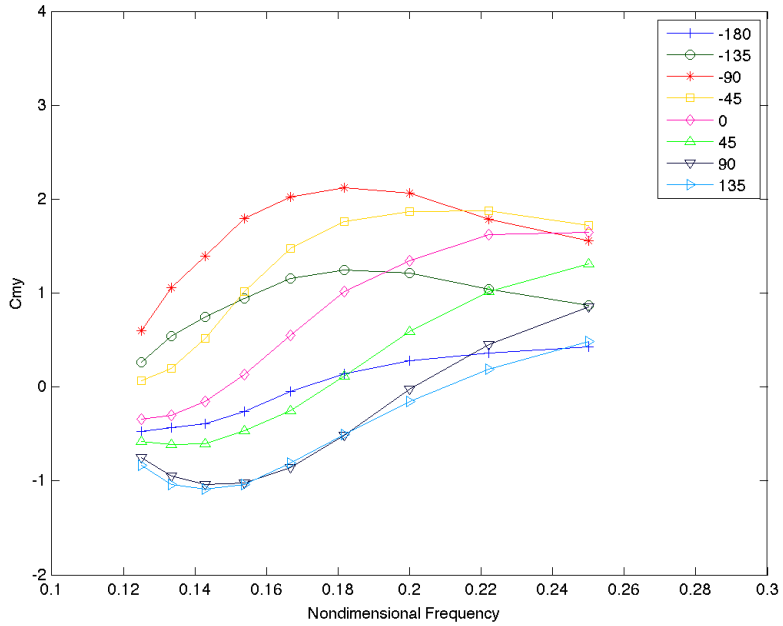

Figure A-137: Crossflow added mass coefficients $C_{m,CF}$ X 0.1 Y 0.75

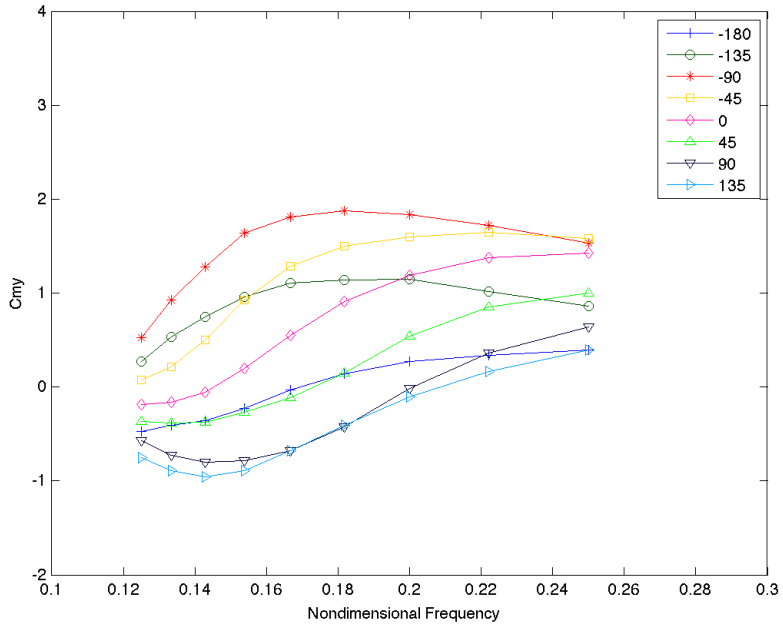

Figure A-138: Crossflow added mass coefficients $C_{m,CF}$ X 0.1 Y 1

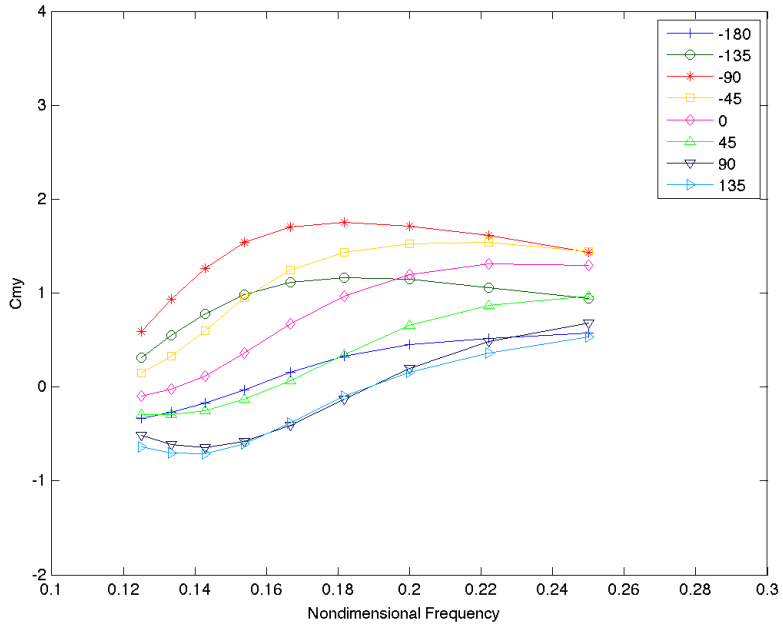

Figure A-139: Crossflow added mass coefficients $C_{m,CF}$ X 0.1 Y 1.25

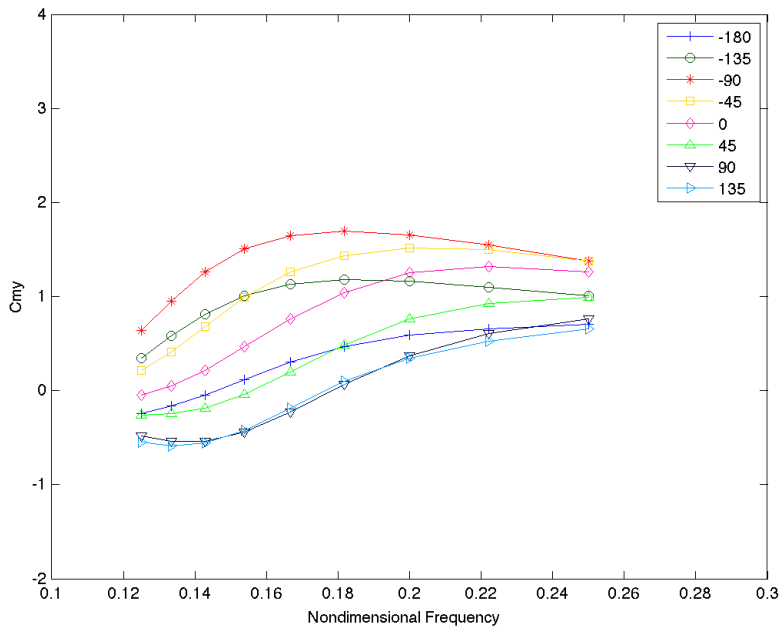

Figure A-140: Crossflow added mass coefficients $C_{m,CF}$ X 0.1 Y 1.5

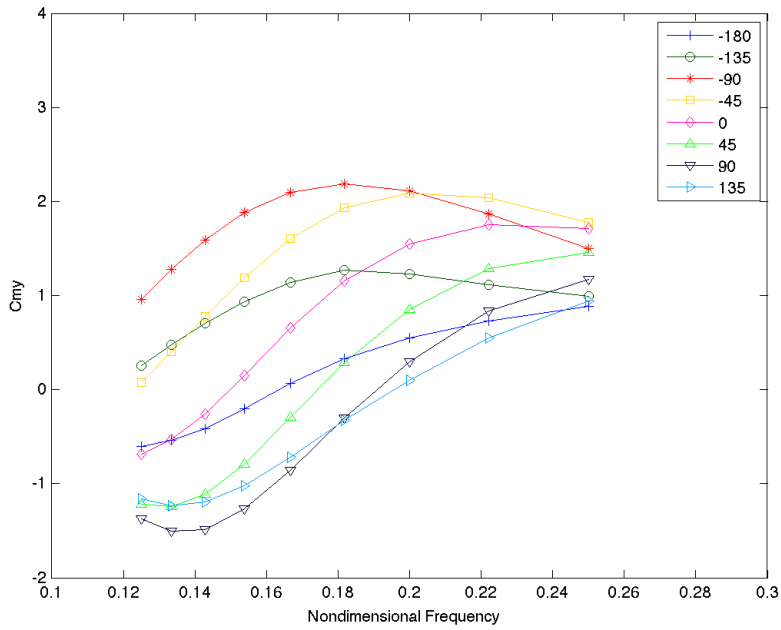

Figure A-141: Crossflow added mass coefficients $C_{m,CF}$ X 0.15 Y 0.15

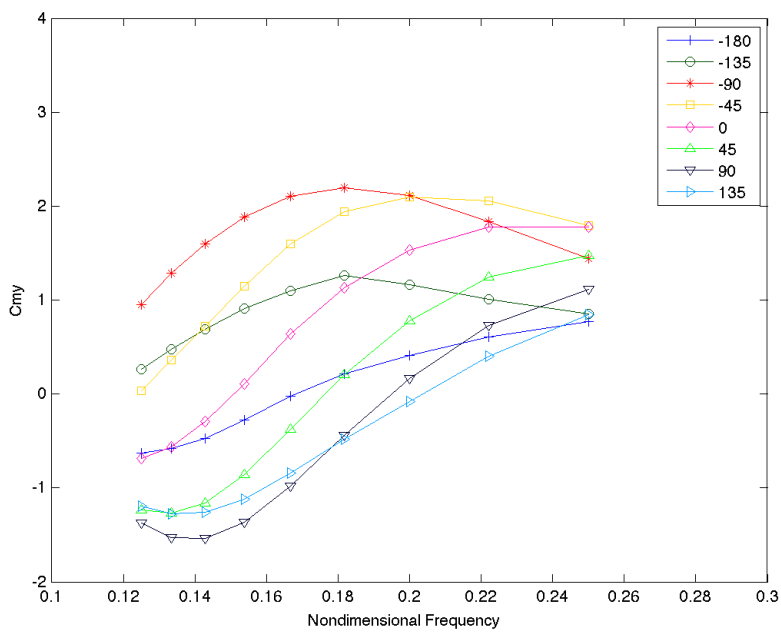

Figure A-142: Crossflow added mass coefficients $C_{m,CF}$ X 0.15 Y 0.25

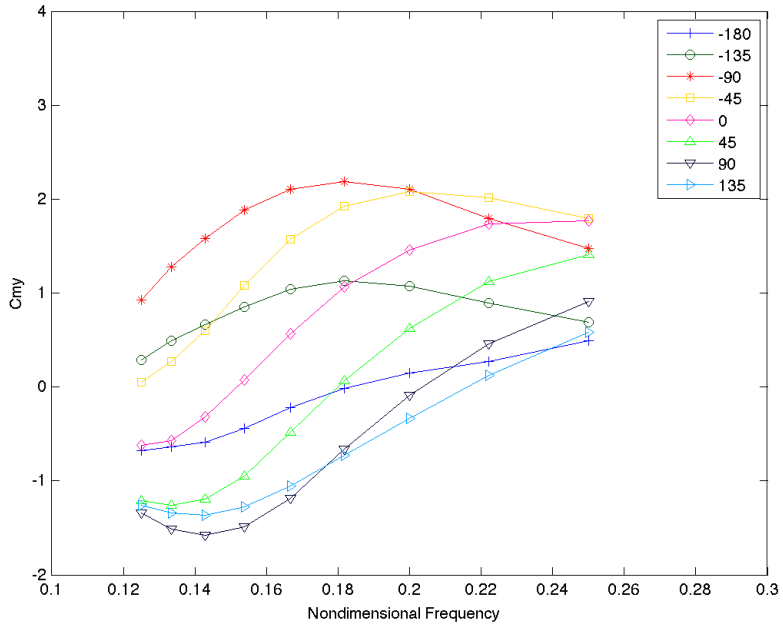

Figure A-143: Crossflow added mass coefficients $C_{m,CF}$ X 0.15 Y 0.5

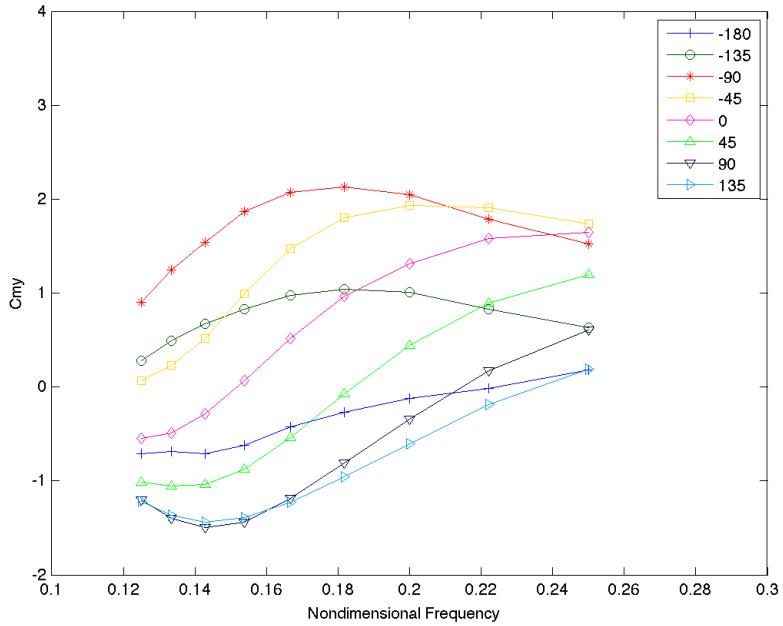

Figure A-144: Crossflow added mass coefficients $C_{m,CF}$ X 0.15 Y 0.75

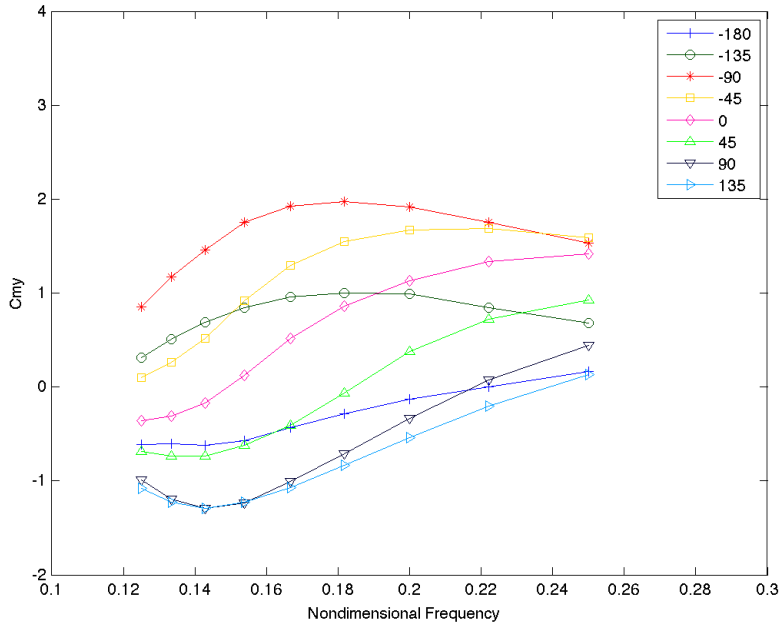

Figure A-145: Crossflow added mass coefficients $C_{m,CF}$ X 0.15 Y 1

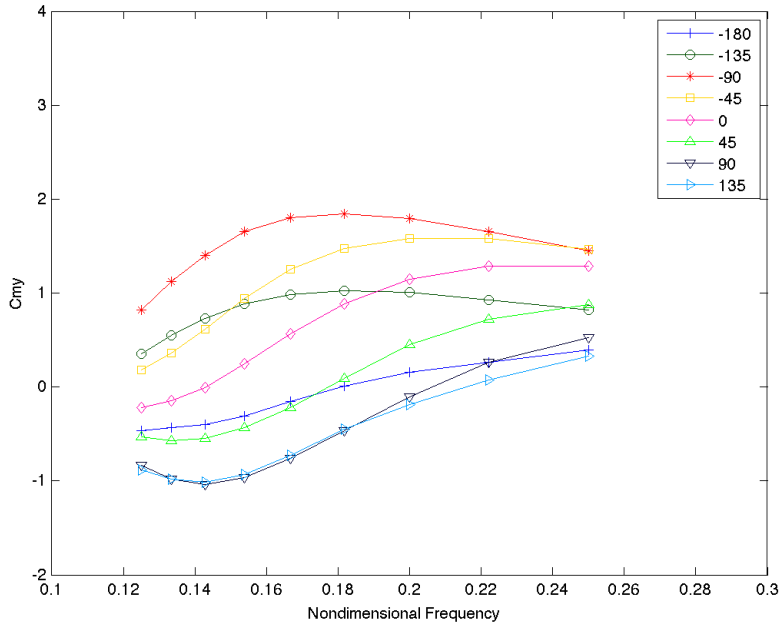

Figure A-146: Crossflow added mass coefficients $C_{m,CF}$ X 0.15 Y 1.25

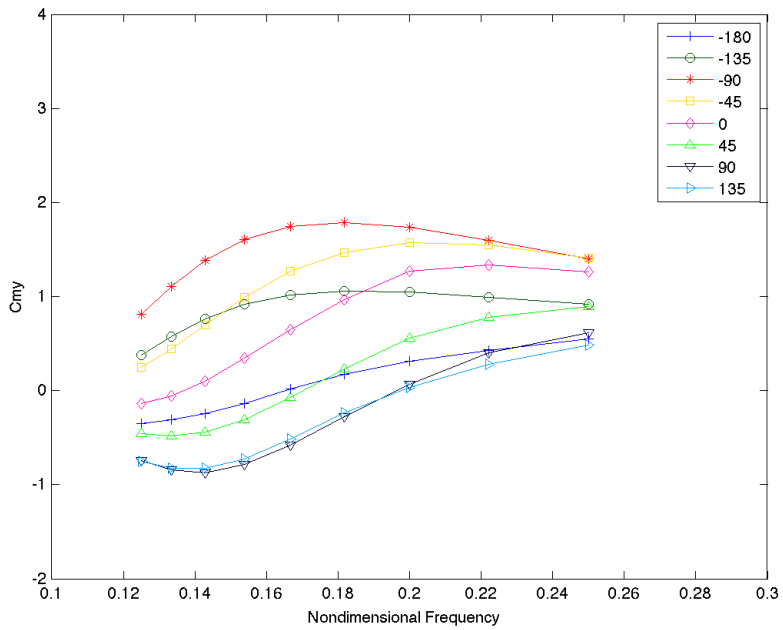

Figure A-147: Crossflow added mass coefficients $C_{m,CF}$ X 0.15 Y 1.5

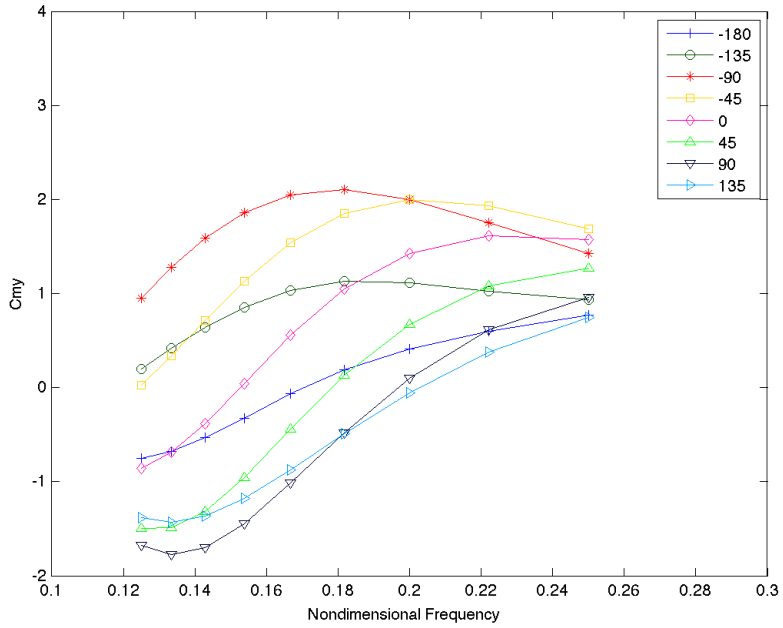

Figure A-148: Crossflow added mass coefficients $C_{m,CF}$ X 0.2 Y 0.15

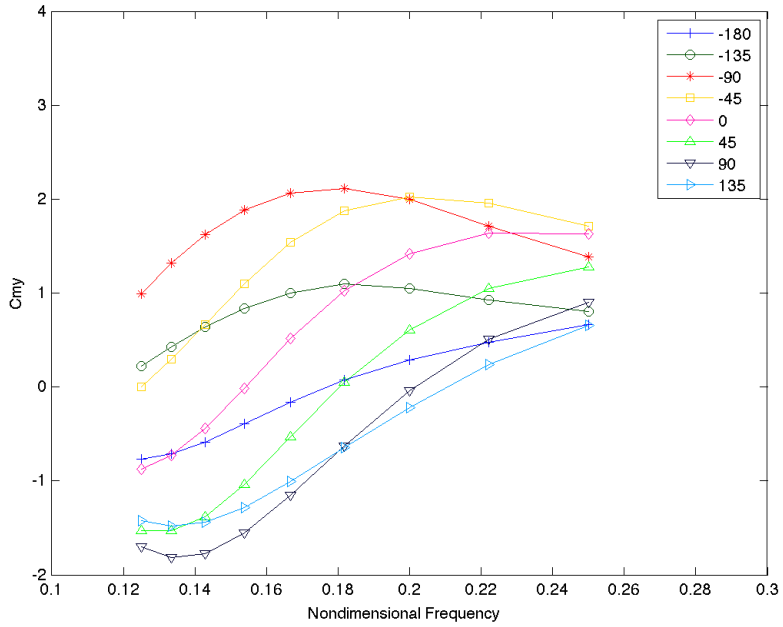

Figure A-149: Crossflow added mass coefficients $C_{m,CF}$ X 0.2 Y 0.25

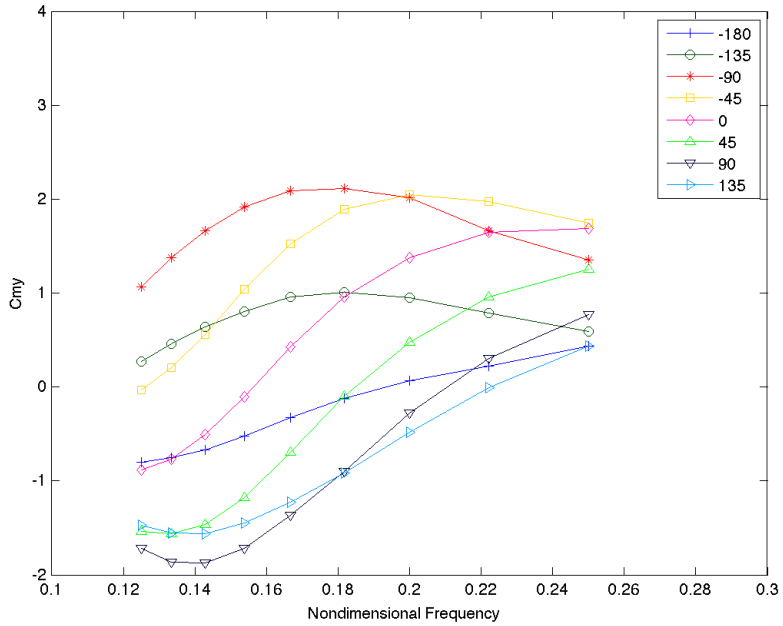

Figure A-150: Crossflow added mass coefficients $C_{m,CF}$ X 0.2 Y 0.5

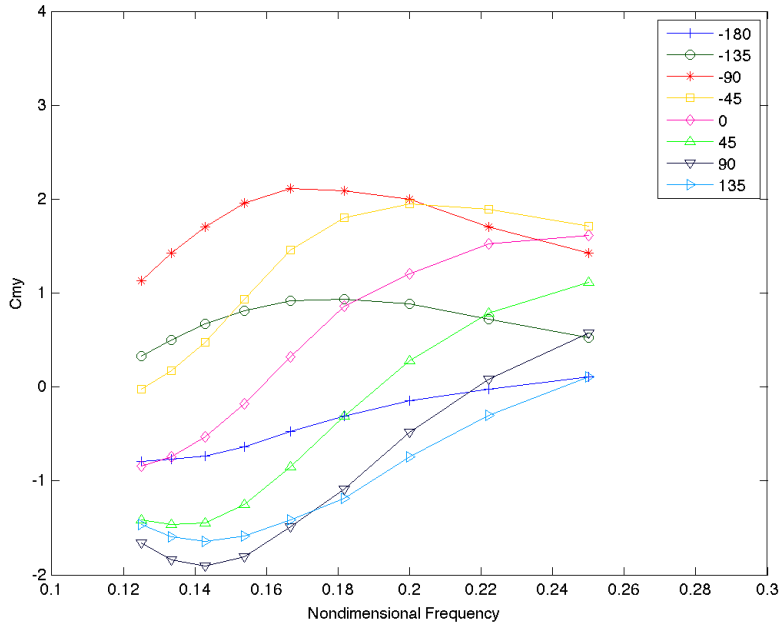

Figure A-151: Crossflow added mass coefficients $C_{m,CF}$ X 0.2 Y 0.75

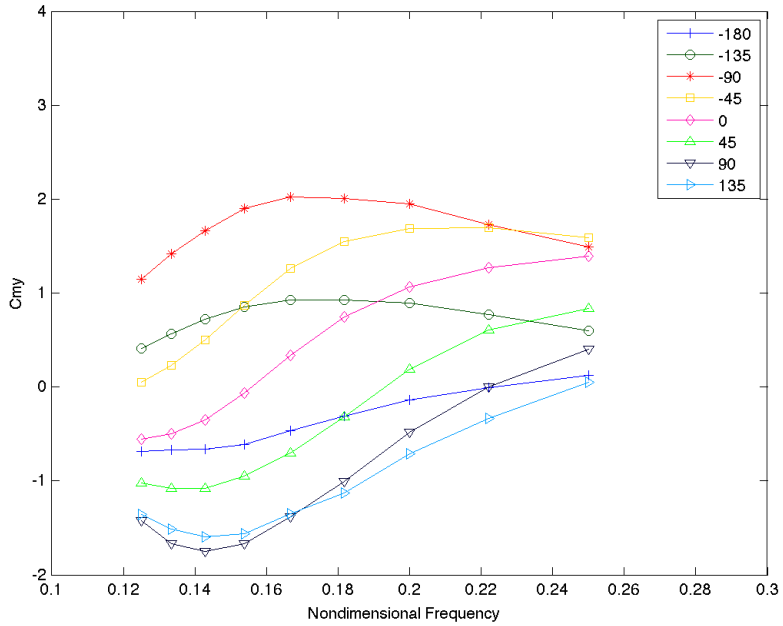

Figure A-152: Crossflow added mass coefficients $C_{m,CF}$ X 0.2 Y 1

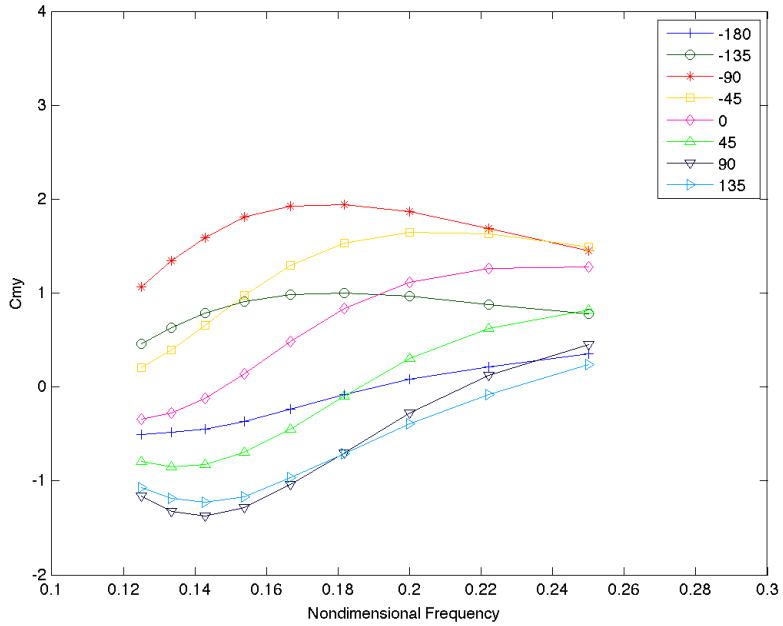

Figure A-153: Crossflow added mass coefficients $C_{m,CF}$ X 0.2 Y 1.25

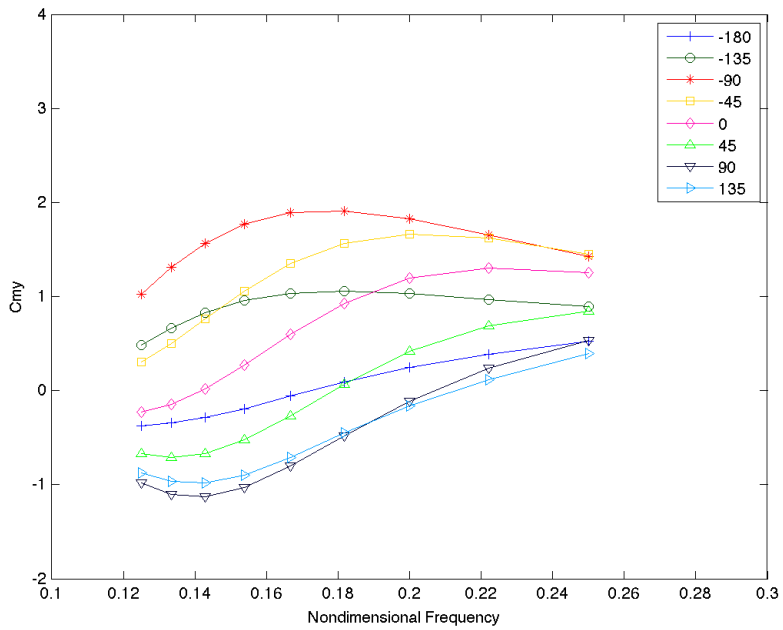

Figure A-154: Crossflow added mass coefficients $C_{m,CF}$ X 0.2 Y 1.5

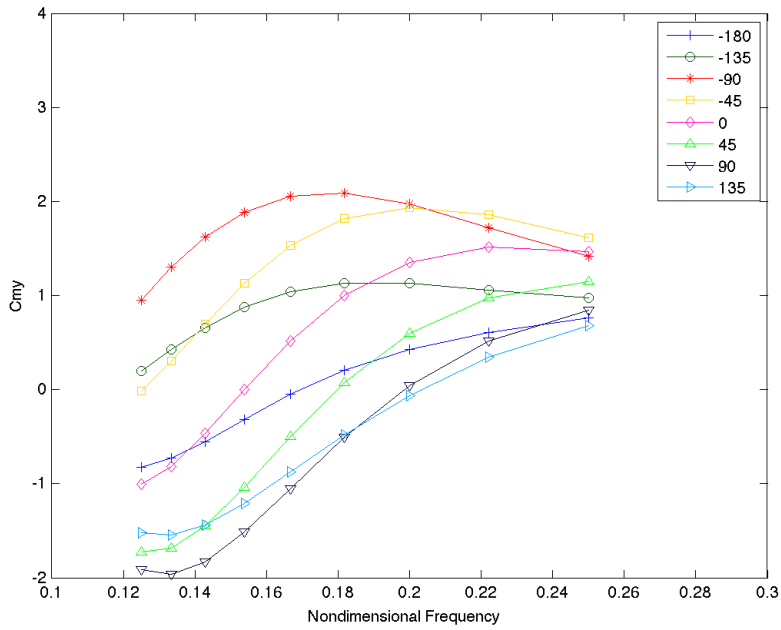

Figure A-155: Crossflow added mass coefficients $C_{m,CF}$ X 0.25 Y 0.15

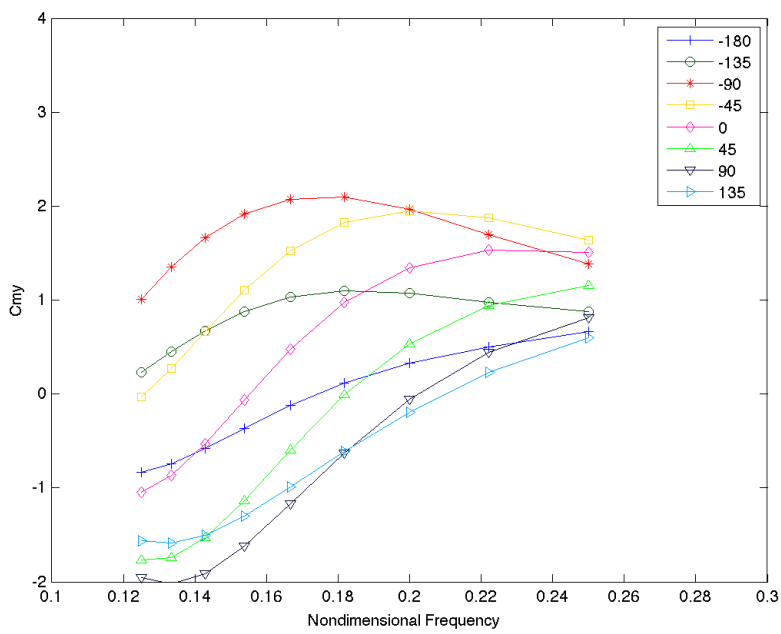

Figure A-156: Crossflow added mass coefficients $C_{m,CF}$ X 0.25 Y 0.25

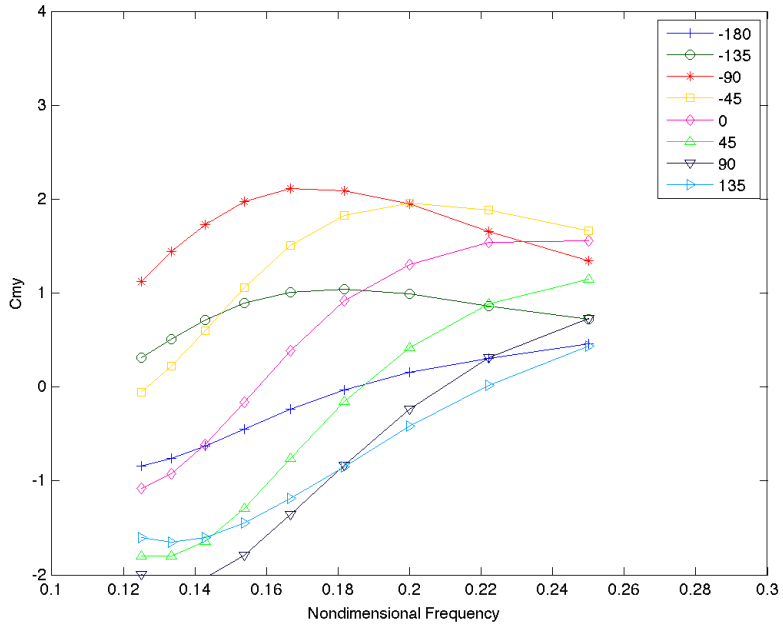

Figure A-157: Crossflow added mass coefficients $C_{m,CF}$ X 0.25 Y 0.5

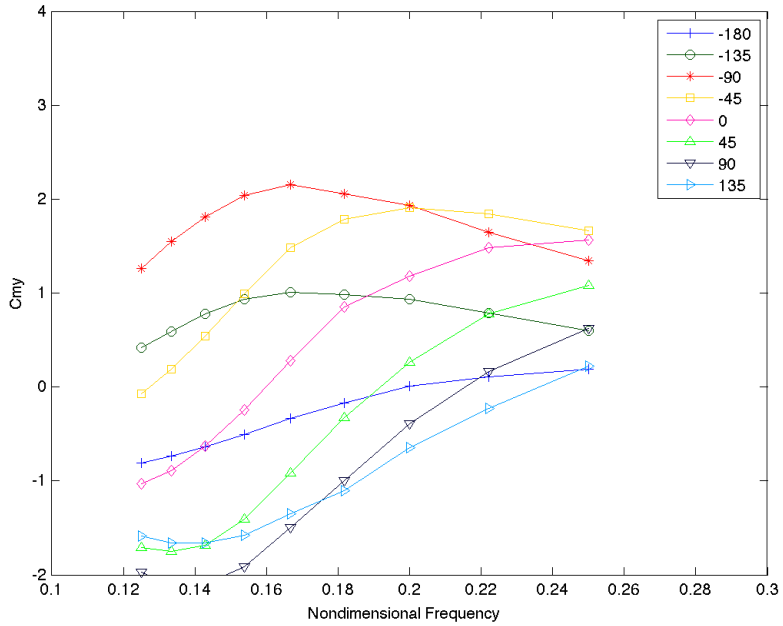

Figure A-158: Crossflow added mass coefficients $C_{m,CF}$ X 0.25 Y 0.75

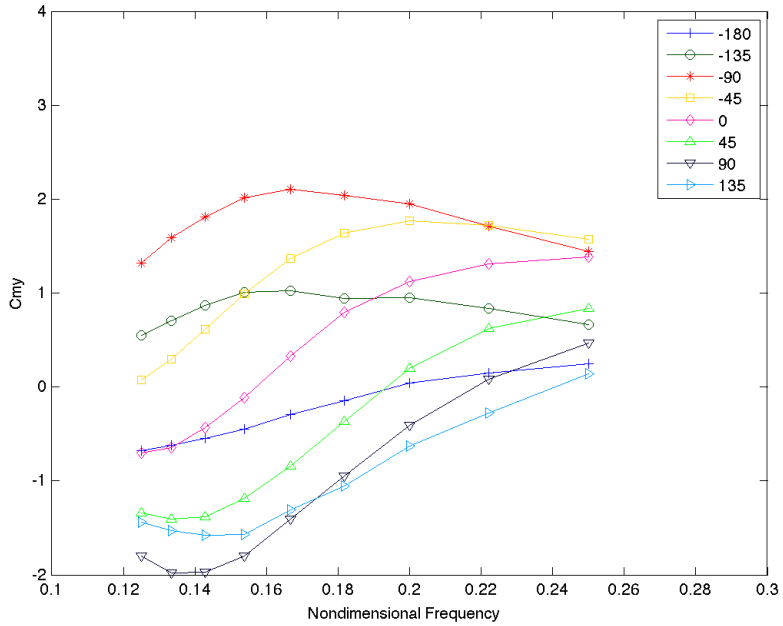

Figure A-159: Crossflow added mass coefficients $C_{m,CF}$ X 0.25 Y 1

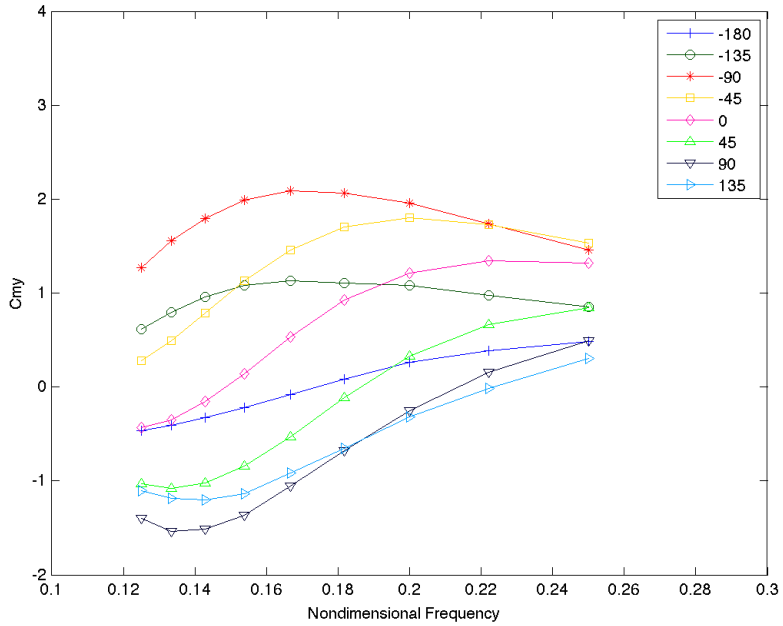

Figure A-160: Crossflow added mass coefficients $C_{m,CF}$ X 0.25 Y 1.25

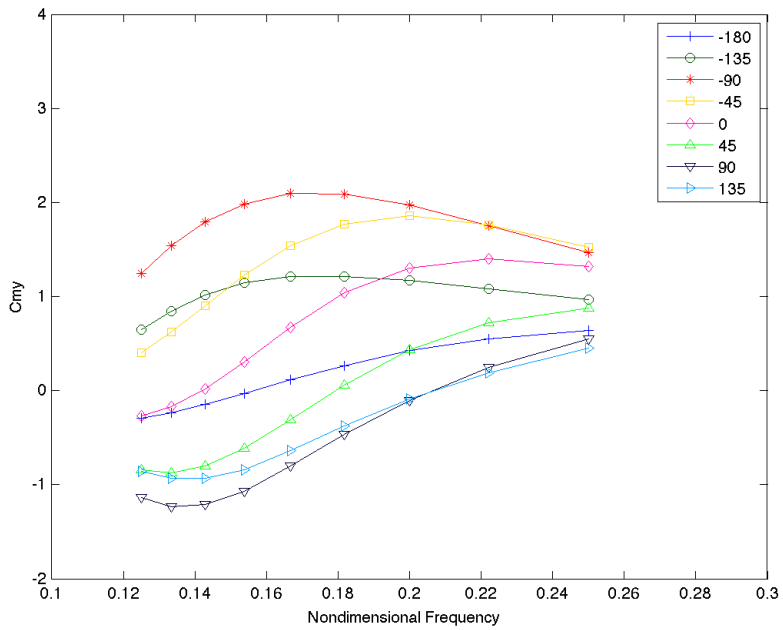

Figure A-161: Crossflow added mass coefficients $C_{m,CF}$ X 0.25 Y 1.5

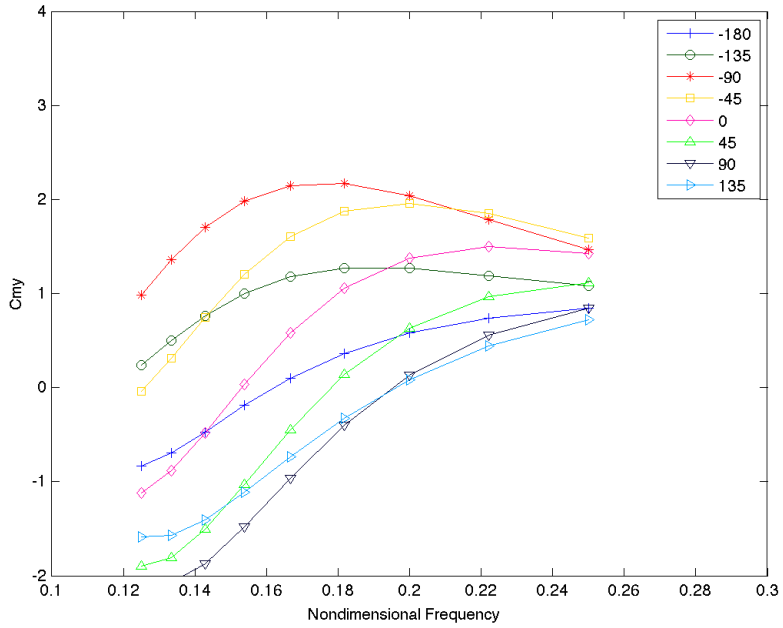

Figure A-162: Crossflow added mass coefficients $C_{m,CF}$ X 0.3 Y 0.15

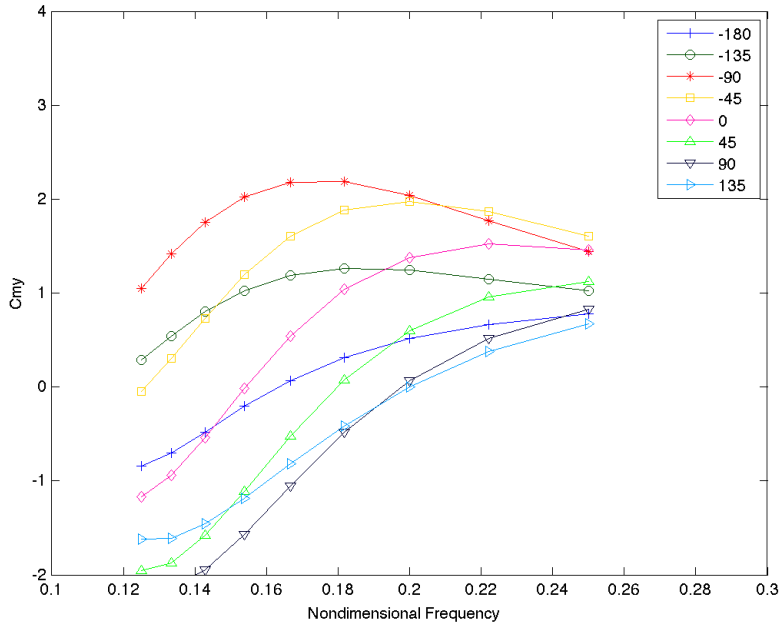

Figure A-163: Crossflow added mass coefficients $C_{m,CF}$ X 0.3 Y 0.25

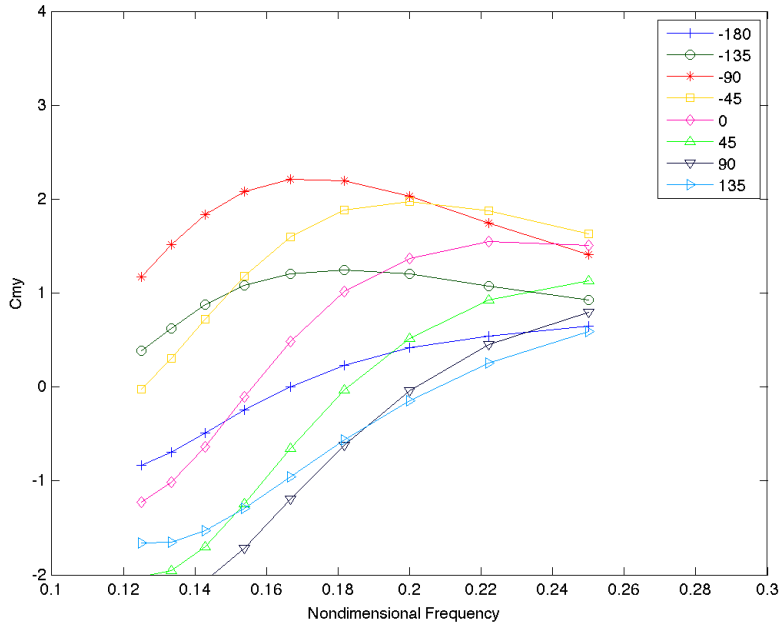

Figure A-164: Crossflow added mass coefficients $C_{m,CF}$ X 0.3 Y 0.5

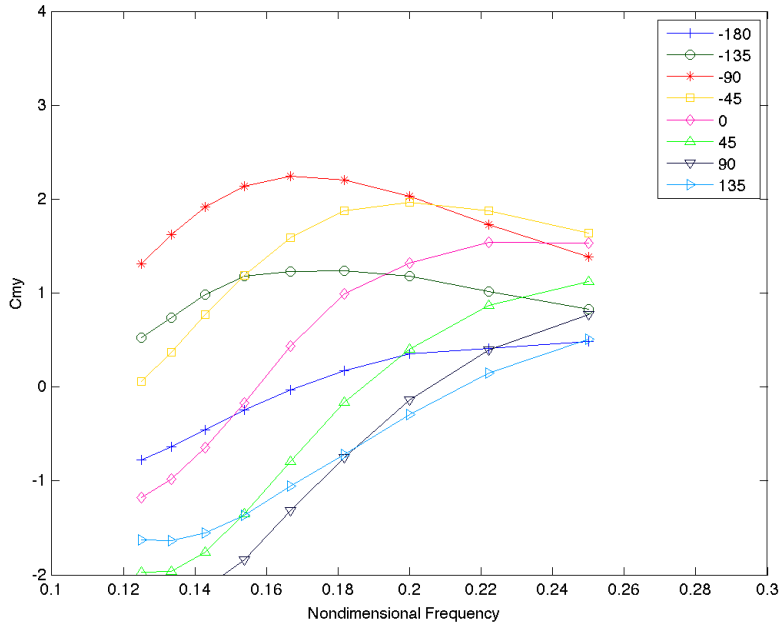

Figure A-165: Crossflow added mass coefficients $C_{m,CF}$ X 0.3 Y 0.75

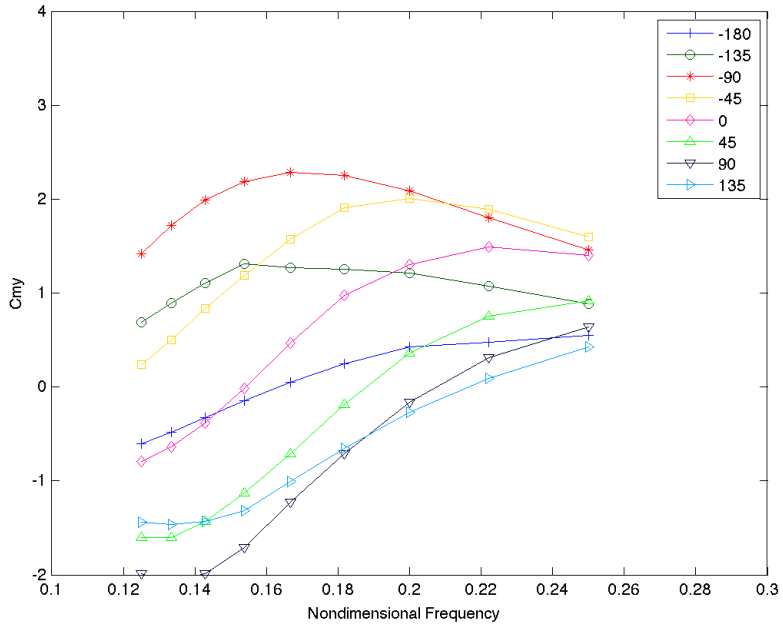

Figure A-166: Crossflow added mass coefficients $C_{m,CF}$ X 0.3 Y 1

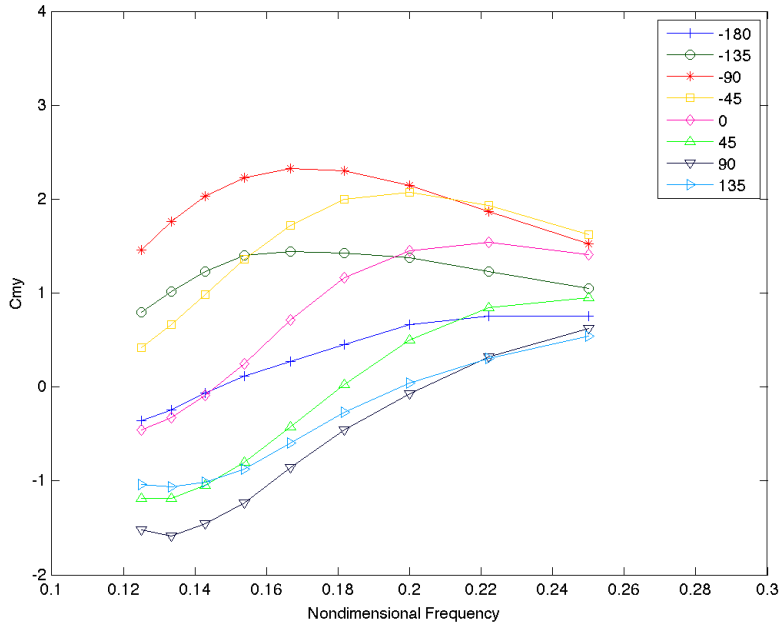

Figure A-167: Crossflow added mass coefficients $C_{m,CF}$ X 0.3 Y 1.25

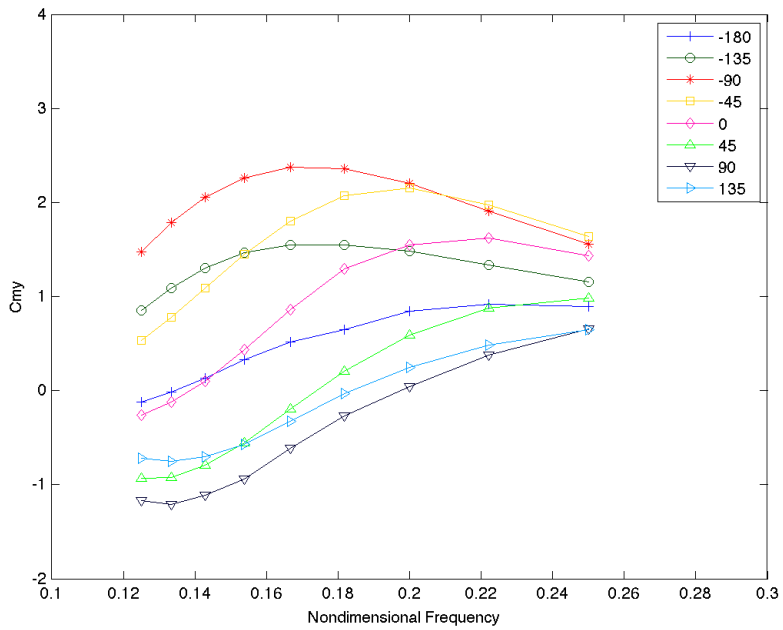

Figure A-168: Crossflow added mass coefficients $C_{m,CF}$ X 0.3 Y 1.5

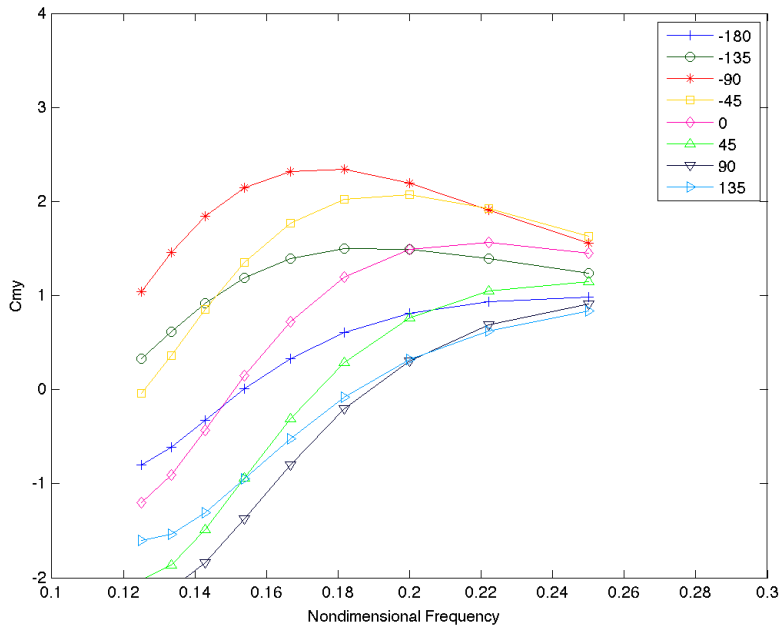

Figure A-169: Crossflow added mass coefficients $C_{m,CF}$ X 0.45 Y 0.15

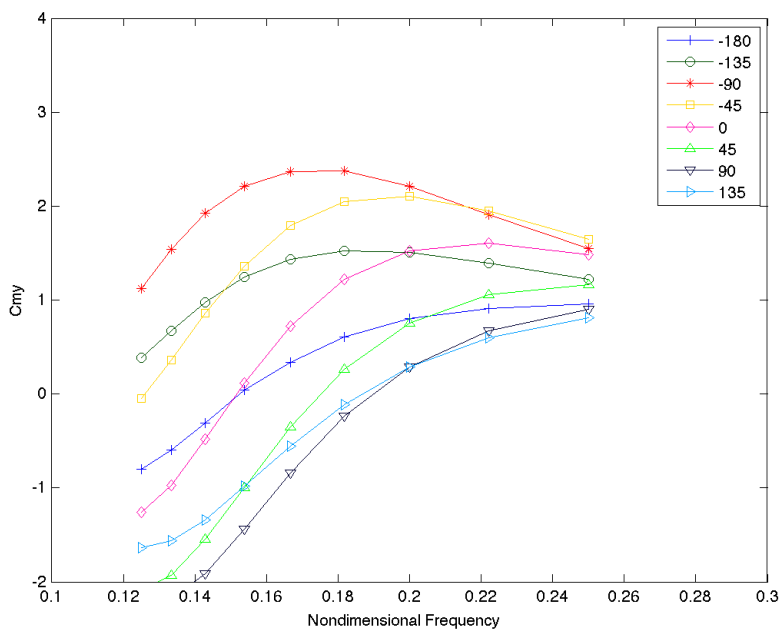

Figure A-170: Crossflow added mass coefficients $C_{m,CF}$ X 0.45 Y 0.25

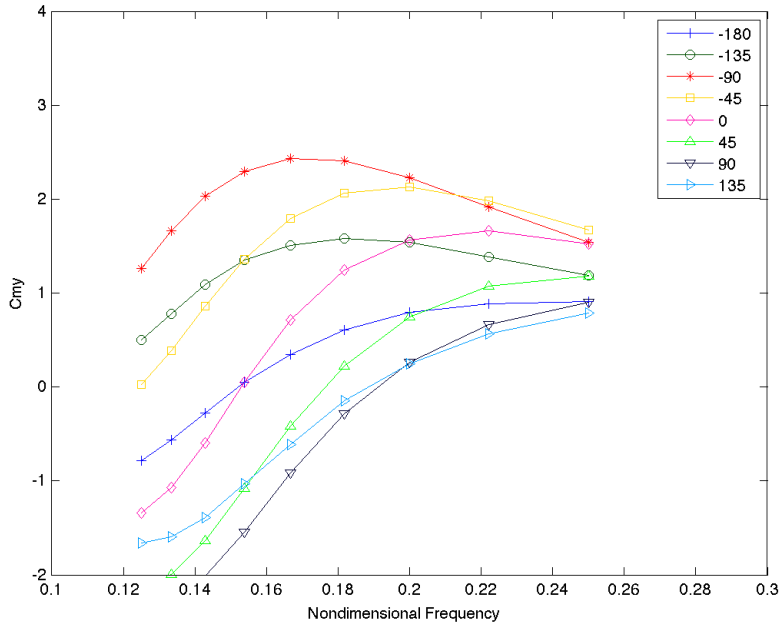

Figure A-171: Crossflow added mass coefficients $C_{m,CF}$ X 0.45 Y 0.5

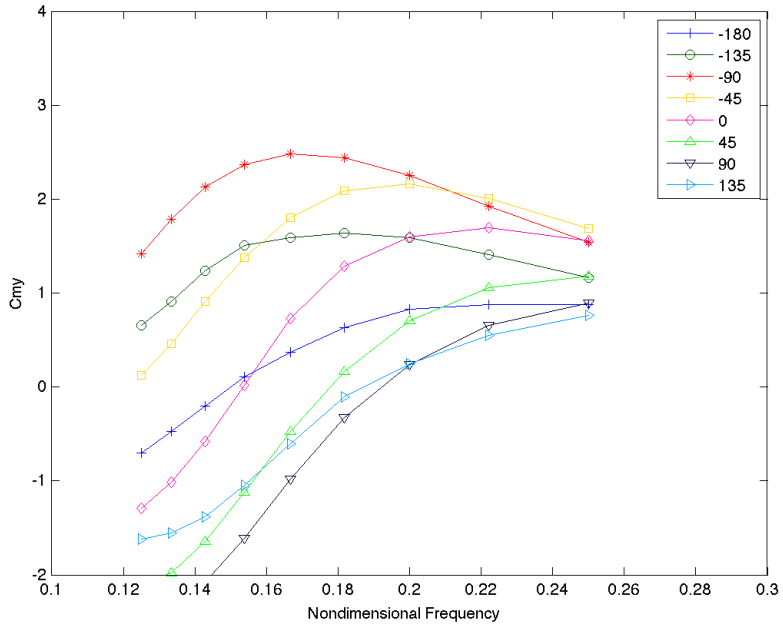

Figure A-172: Crossflow added mass coefficients $C_{m,CF}$ X 0.45 Y 0.75

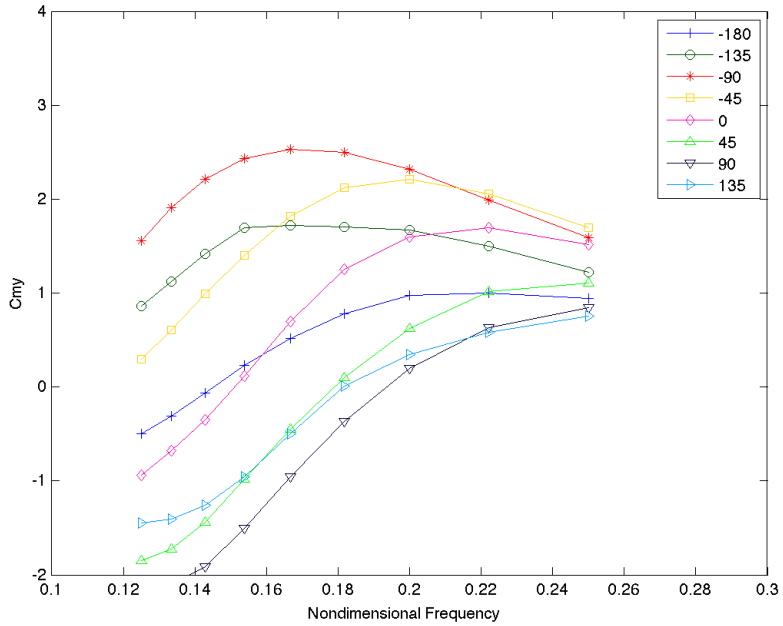

Figure A-173: Crossflow added mass coefficients $C_{m,CF}$ X 0.45 Y 1

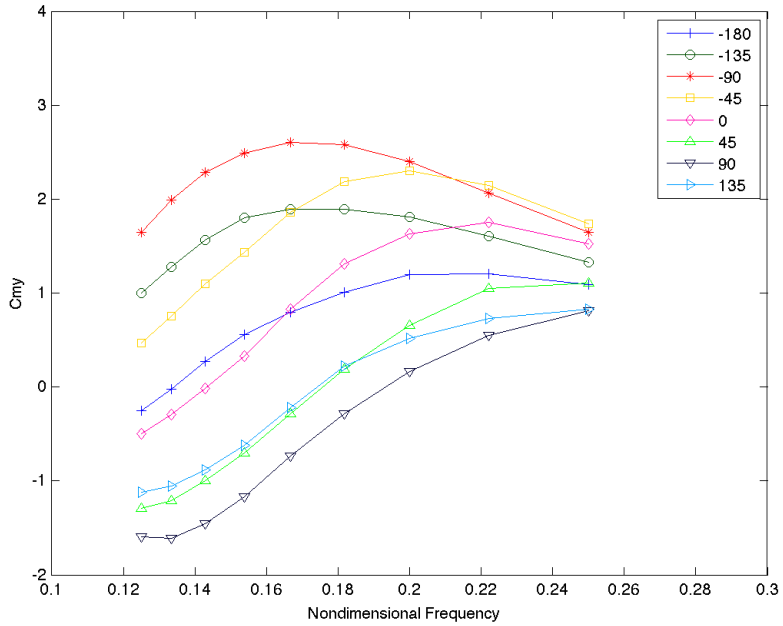

Figure A-174: Crossflow added mass coefficients $C_{m,CF}$ X 0.45 Y 1.25

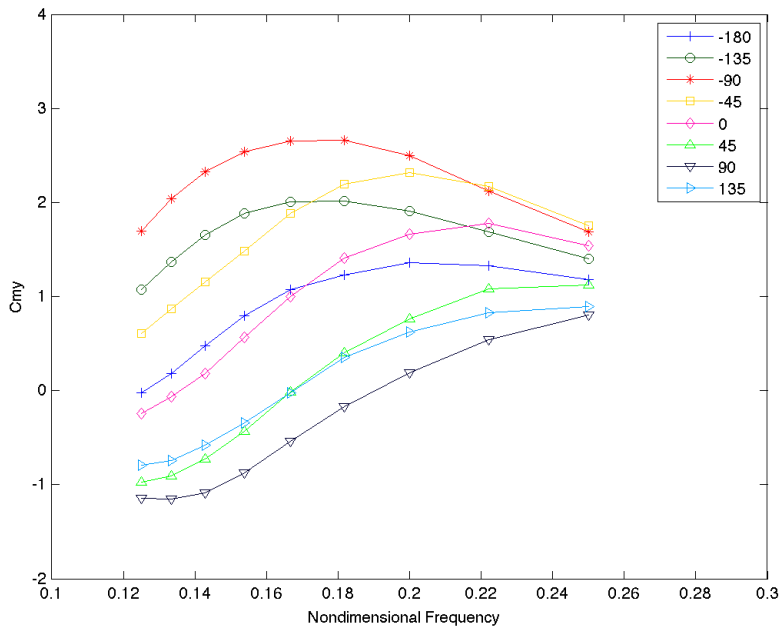

Figure A-175: Crossflow added mass coefficients $C_{m,CF}$ X 0.45 Y 1.5

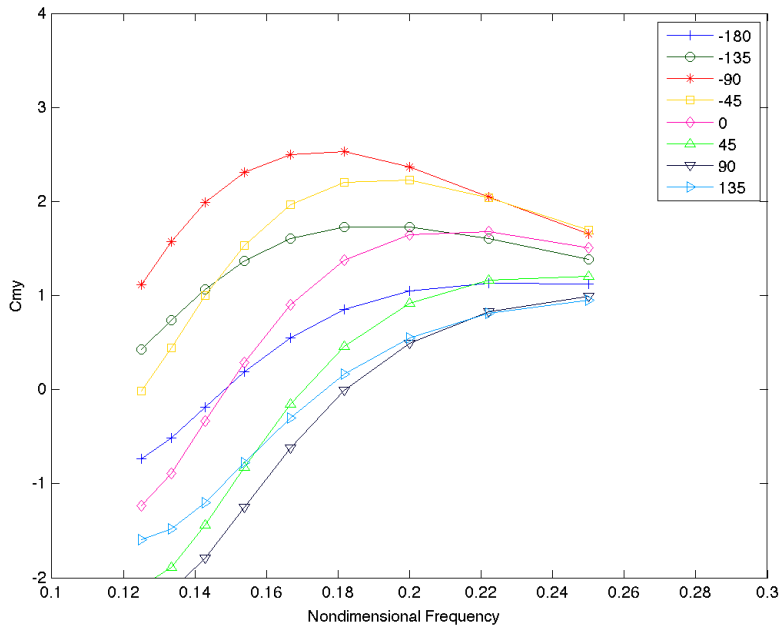

Figure A-176: Crossflow added mass coefficients $C_{m,CF}$ X 0.6 Y 0.15

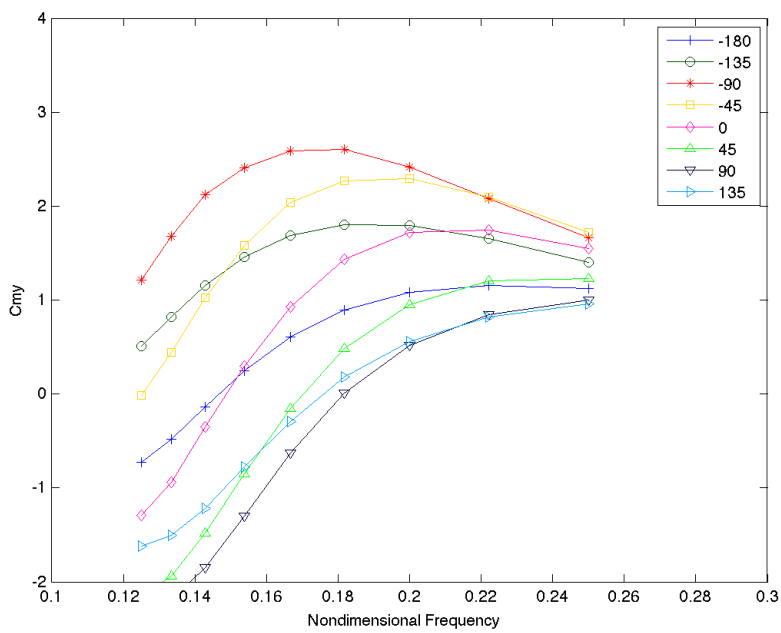

Figure A-177: Crossflow added mass coefficients $C_{m,CF}$ X 0.6 Y 0.25

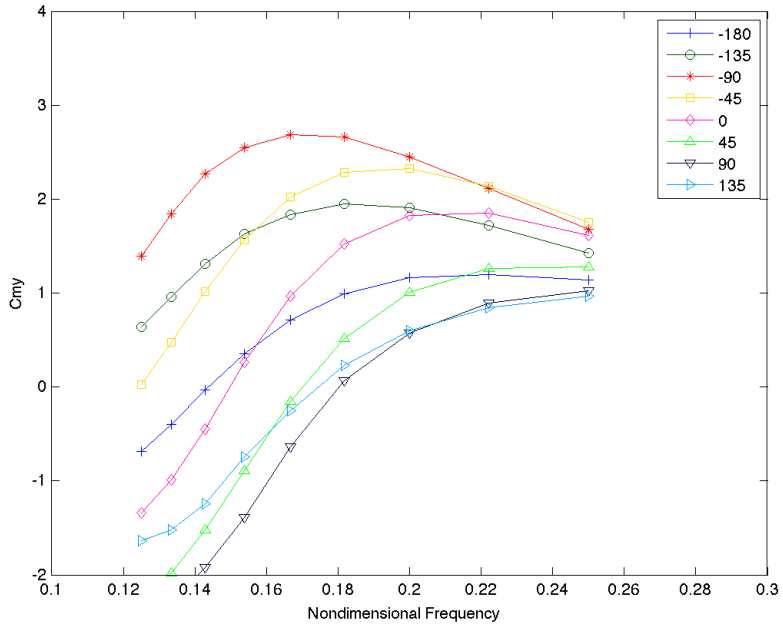

Figure A-178: Crossflow added mass coefficients $C_{m,CF}$ X 0.6 Y 0.5

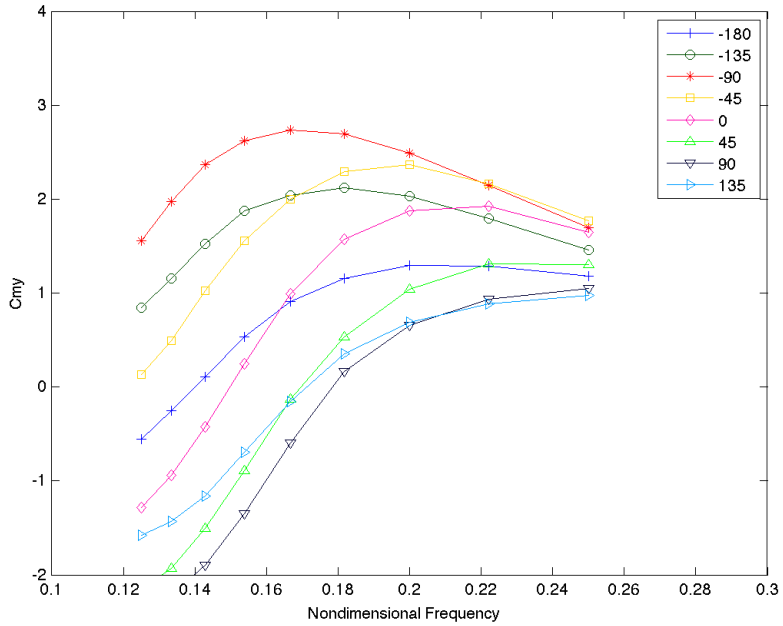

Figure A-179: Crossflow added mass coefficients $C_{m,CF}$ X 0.6 Y 0.75

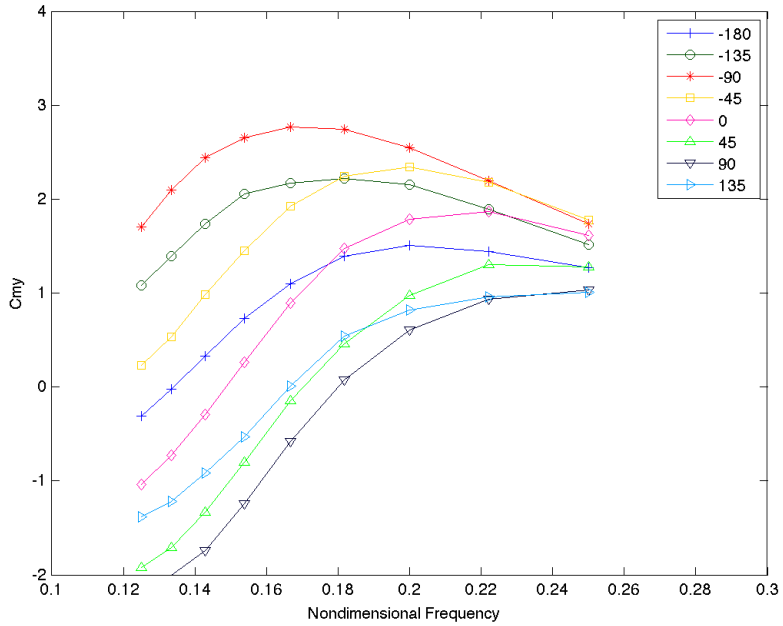

Figure A-180: Crossflow added mass coefficients $C_{m,CF}$ X 0.6 Y 1

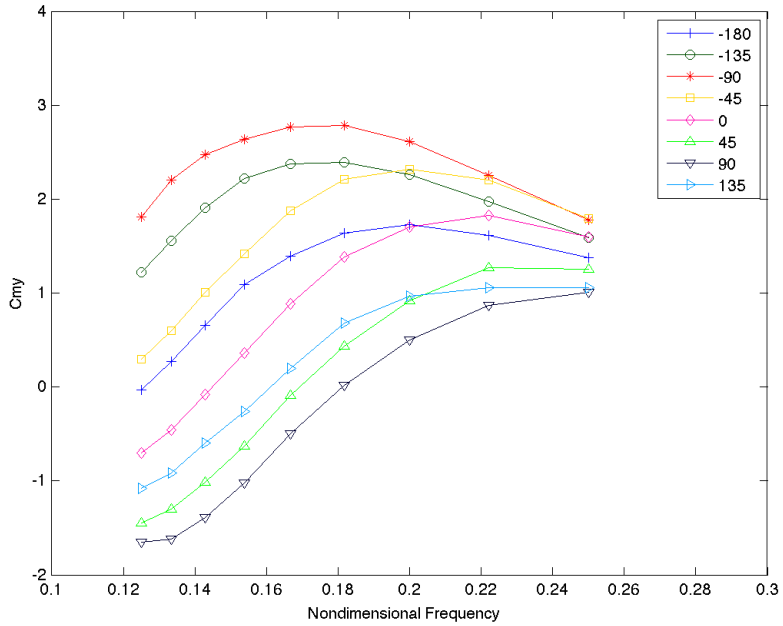

Figure A-181: Crossflow added mass coefficients $C_{m,CF}$ X 0.6 Y 1.25

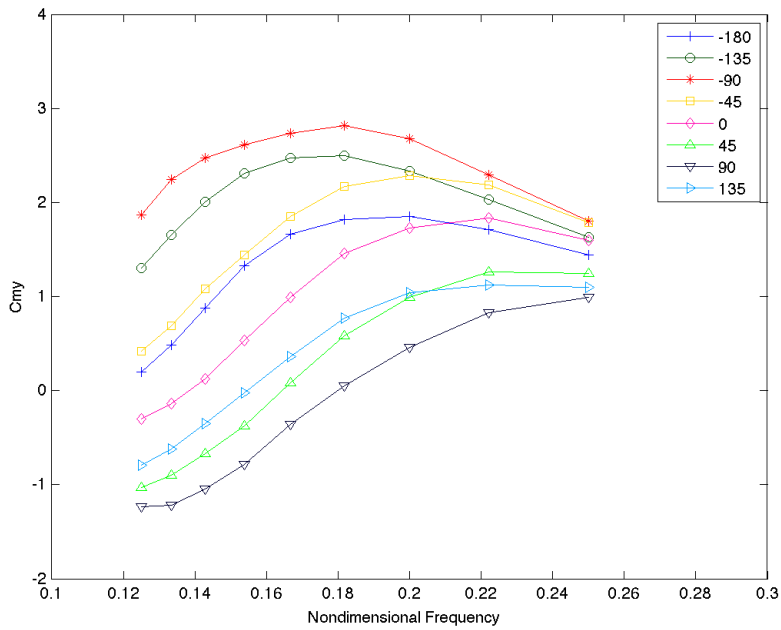

Figure A-182: Crossflow added mass coefficients $C_{m,CF}$ X 0.6 Y 1.5

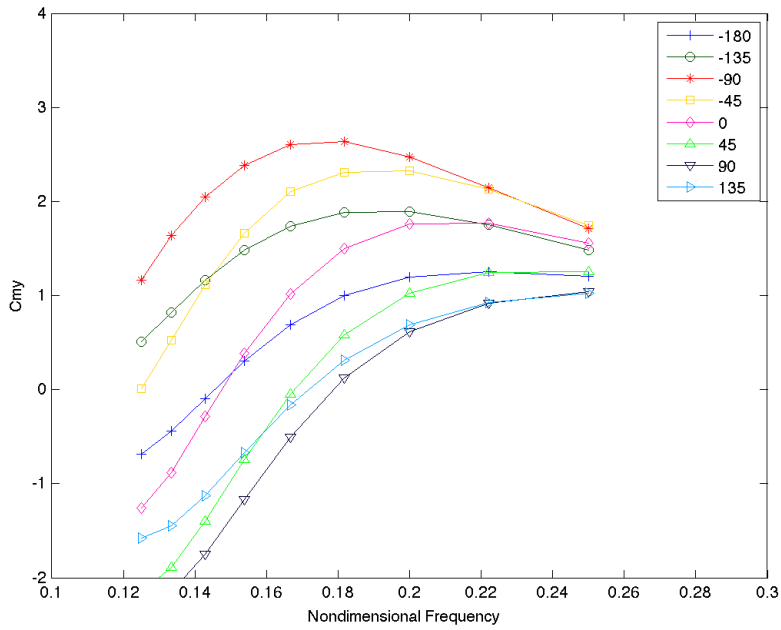

Figure A-183: Crossflow added mass coefficients $C_{m,CF}$ X 0.75 Y 0.15

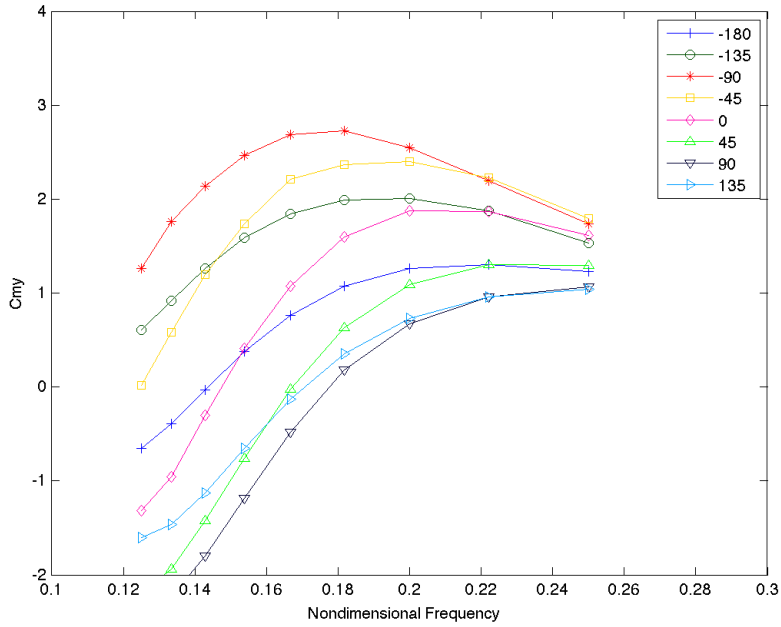

Figure A-184: Crossflow added mass coefficients $C_{m,CF}$ X 0.75 Y 0.25

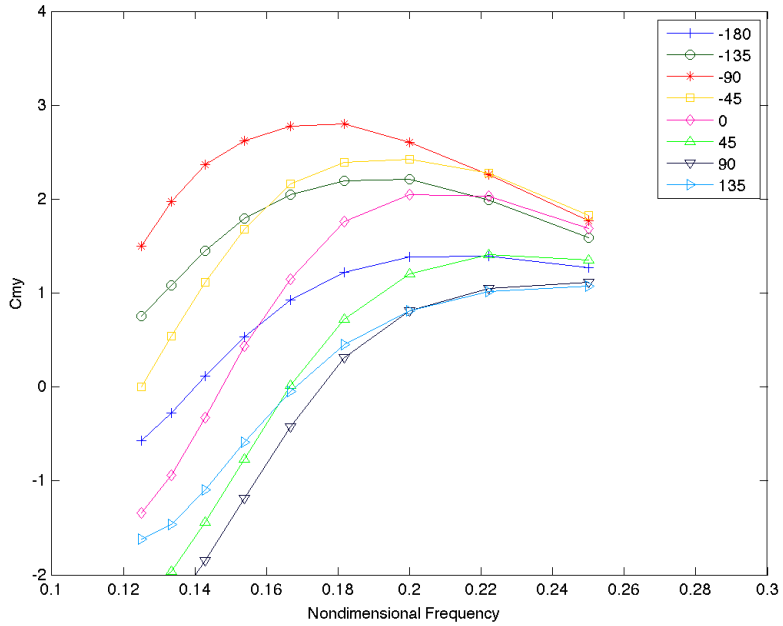

Figure A-185: Crossflow added mass coefficients $C_{m,CF}$ X 0.75 Y 0.5

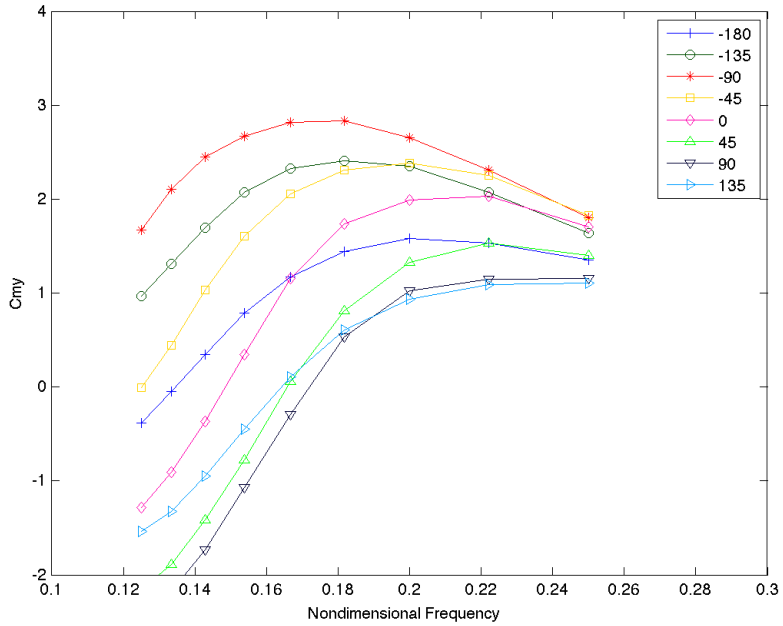

Figure A-186: Crossflow added mass coefficients $C_{m,CF}$ X 0.75 Y 0.75

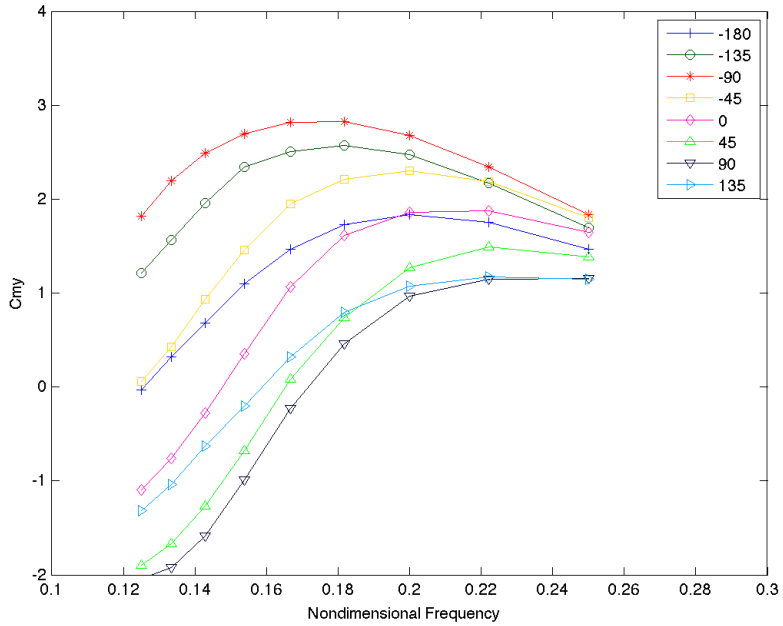

Figure A-187: Crossflow added mass coefficients $C_{m,CF}$ X 0.75 Y 1

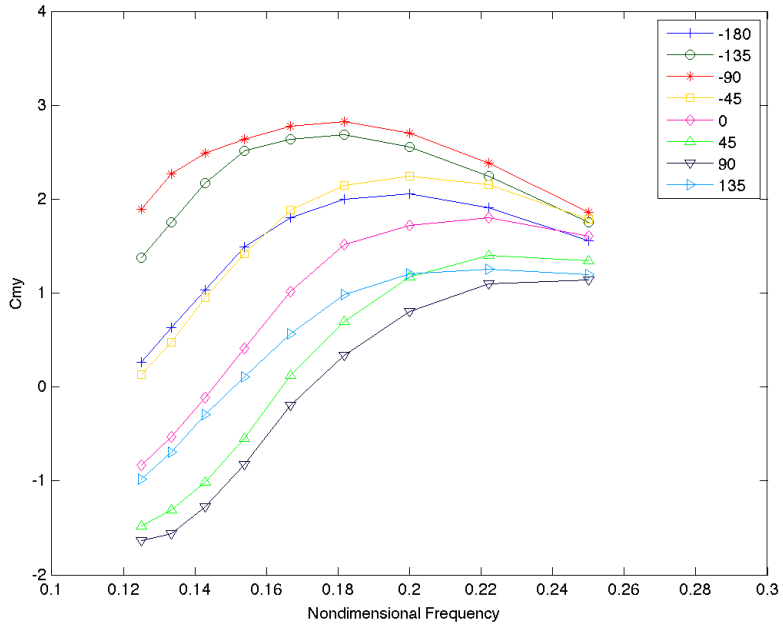

Figure A-188: Crossflow added mass coefficients $C_{m,CF}$ X 0.75 Y 1.25

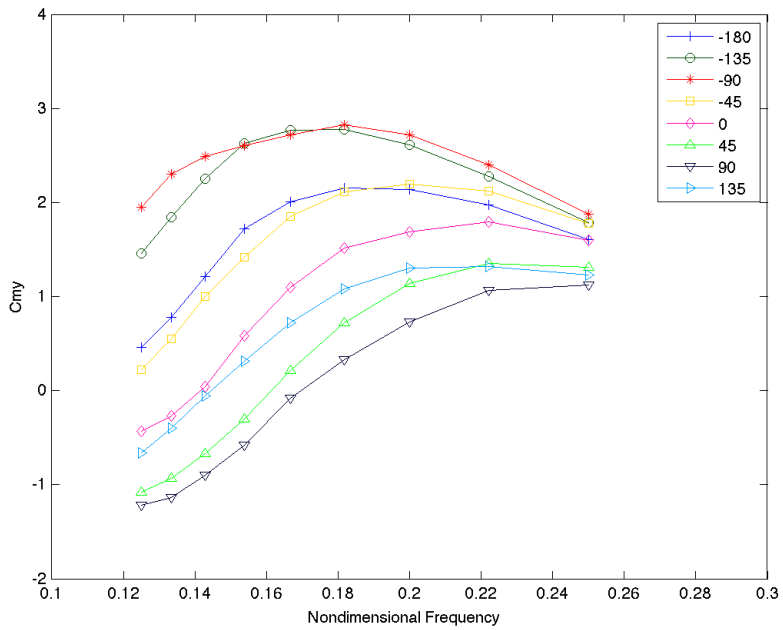

Figure A-189: Crossflow added mass coefficients $C_{m,CF}$ X 0.75 Y 1.5

A.4 Inline Added Mass Coefficients $C_{m,IL}$

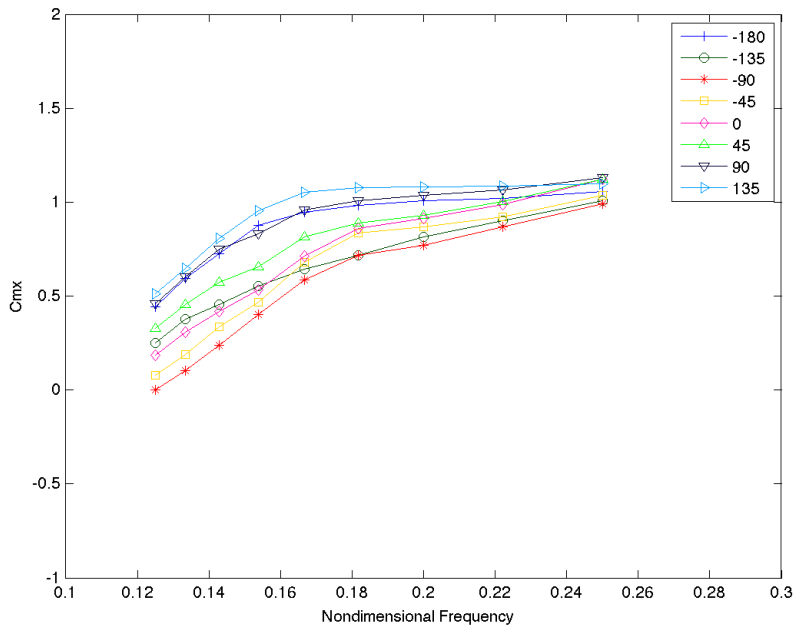

Figure A-190: Inline added mass coefficients $C_{m,IL}$ X 0.05 Y 0.15

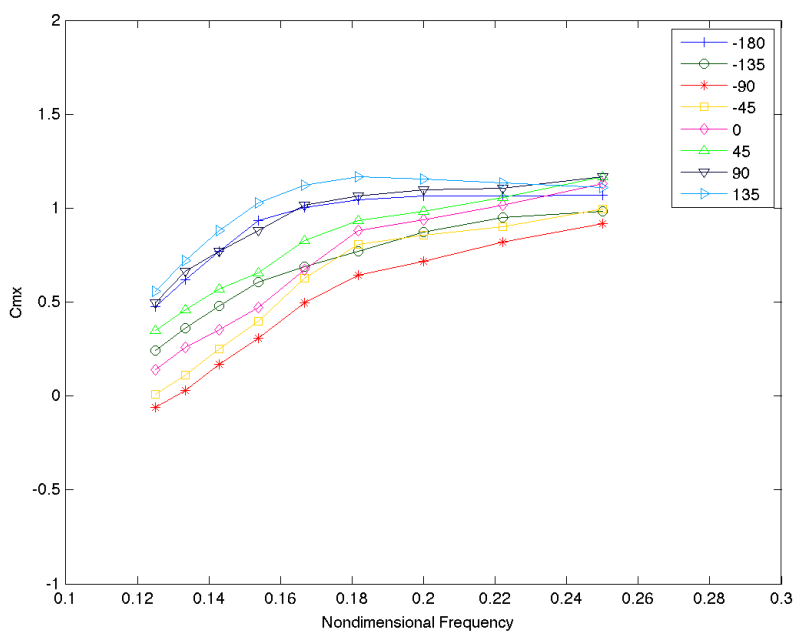

Figure A-191: Inline added mass coefficients $C_{m,IL}$ X 0.05 Y 0.25

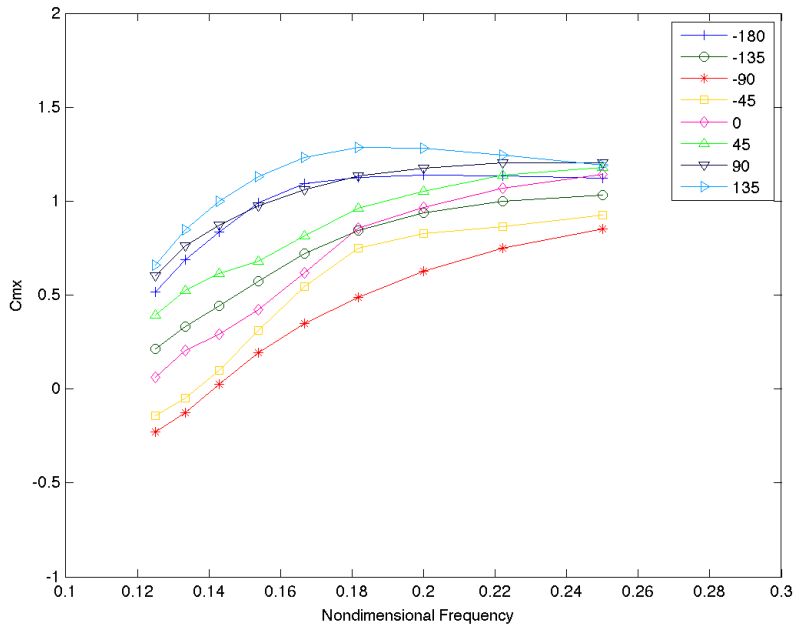

Figure A-192: Inline added mass coefficients $C_{m,IL}$ X 0.05 Y 0.5

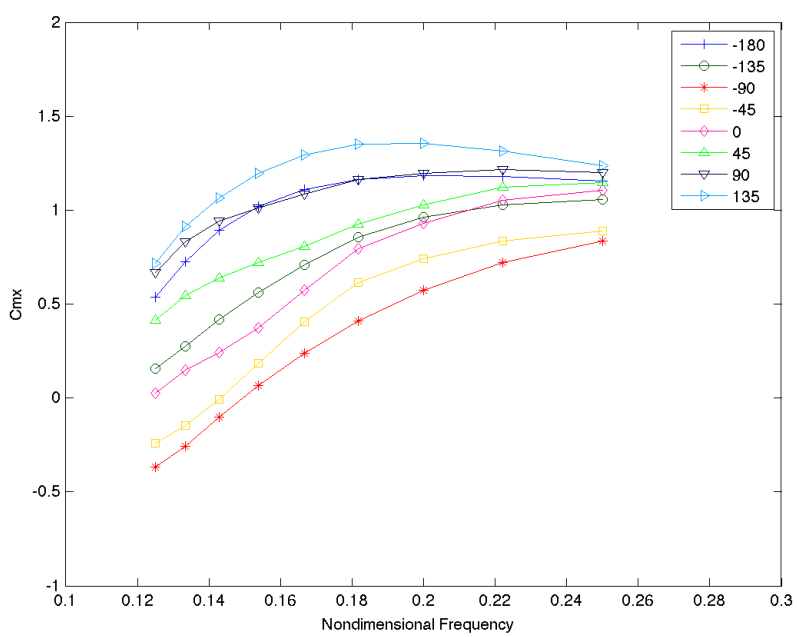

Figure A-193: Inline added mass coefficients $C_{m,IL}$ X 0.05 Y 0.75

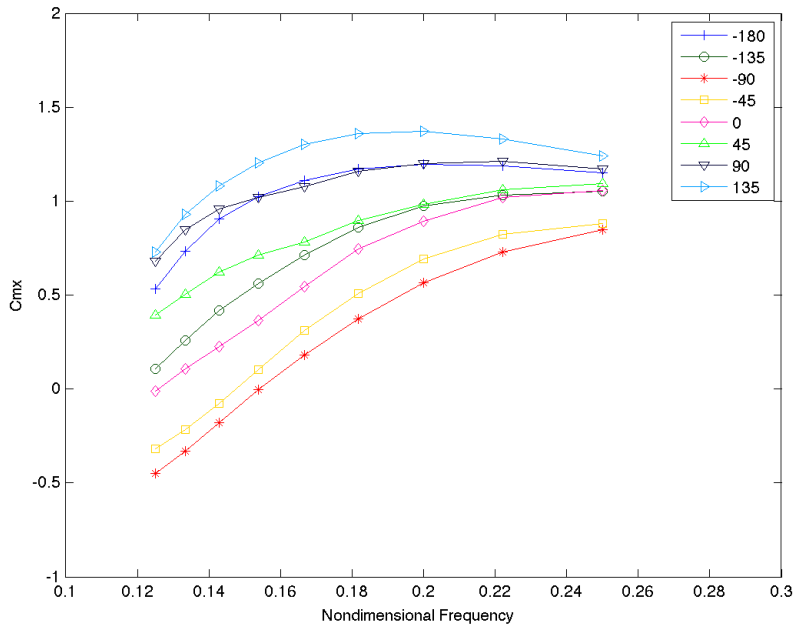

Figure A-194: Inline added mass coefficients $C_{m,IL}$ X 0.05 Y 1

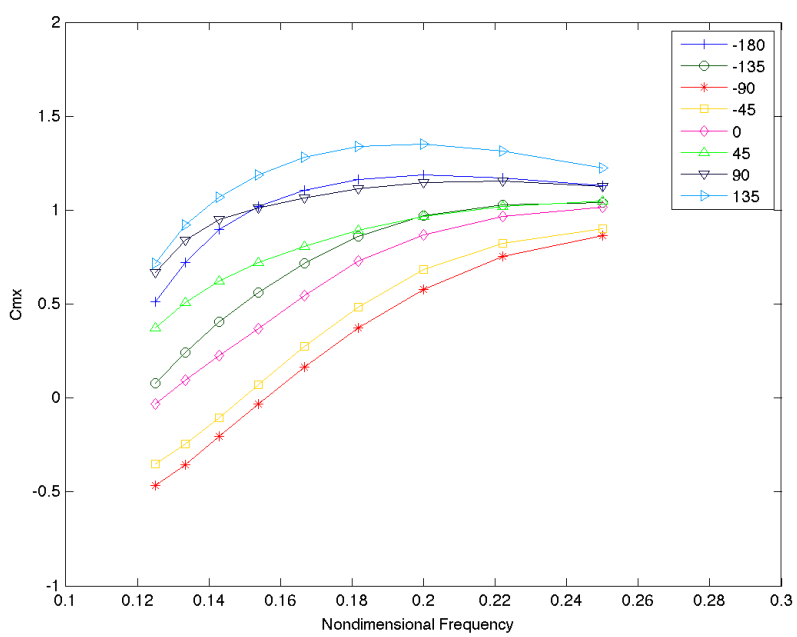

Figure A-195: Inline added mass coefficients $C_{m,IL}$ X 0.05 Y 1.25

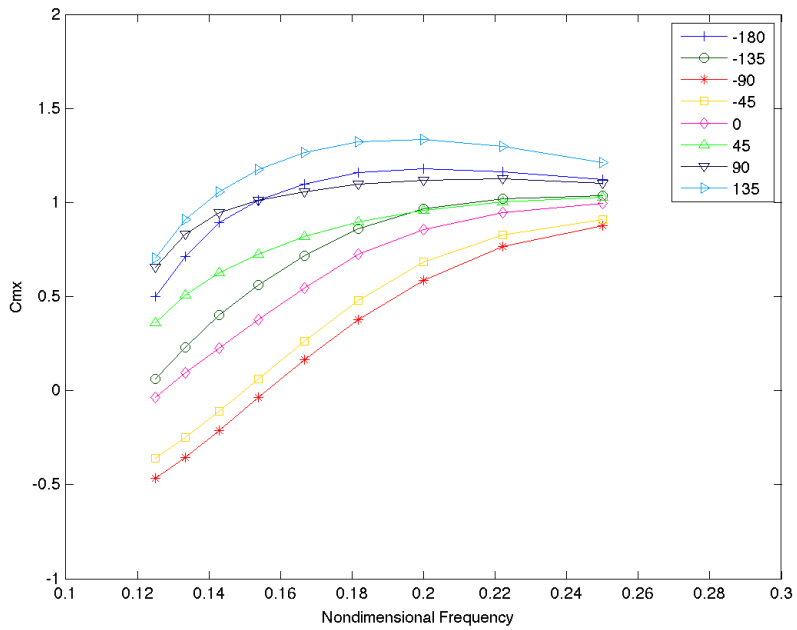

Figure A-196: Inline added mass coefficients $C_{m,IL}$ X 0.05 Y 1.5

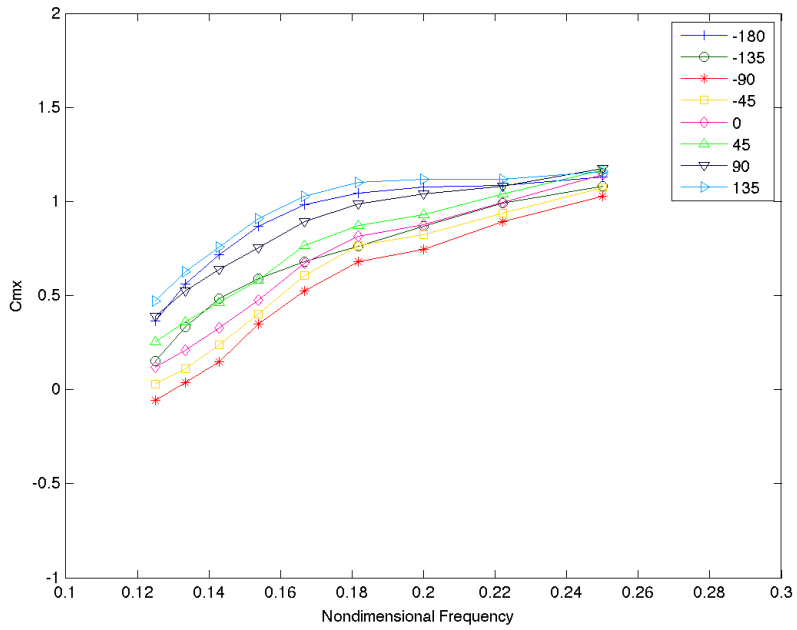

Figure A-197: Inline added mass coefficients $C_{m,IL}$ X 0.1 Y 0.15

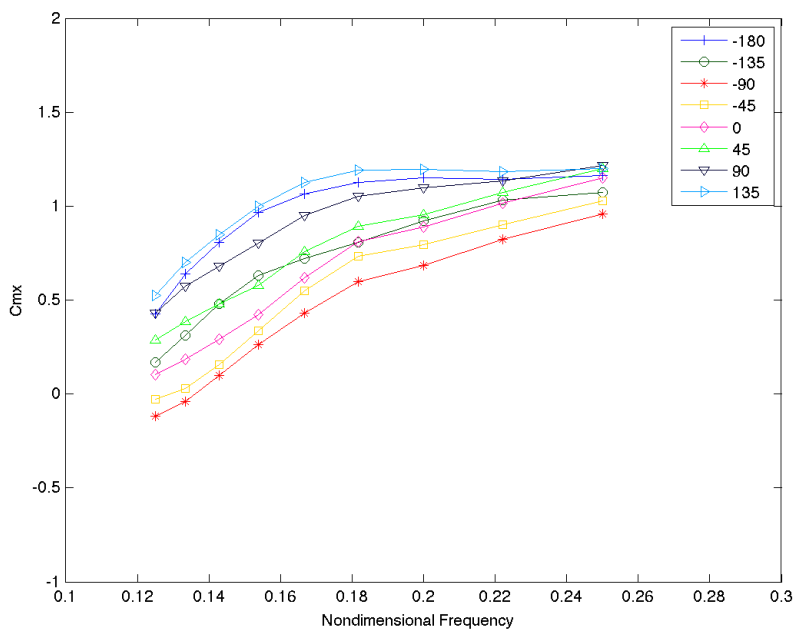

Figure A-198: Inline added mass coefficients $C_{m,IL}$ X 0.1 Y 0.25

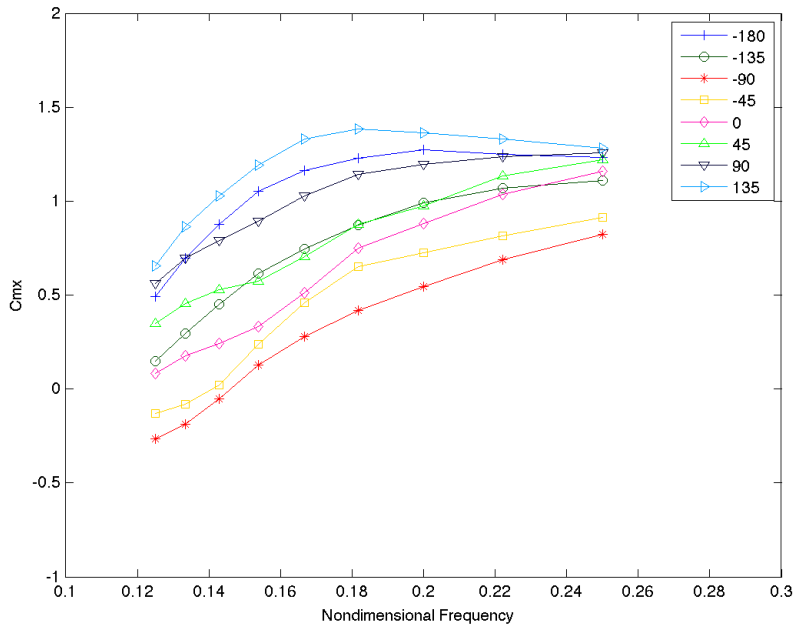

Figure A-199: Inline added mass coefficients $C_{m,IL}$ X 0.1 Y 0.5

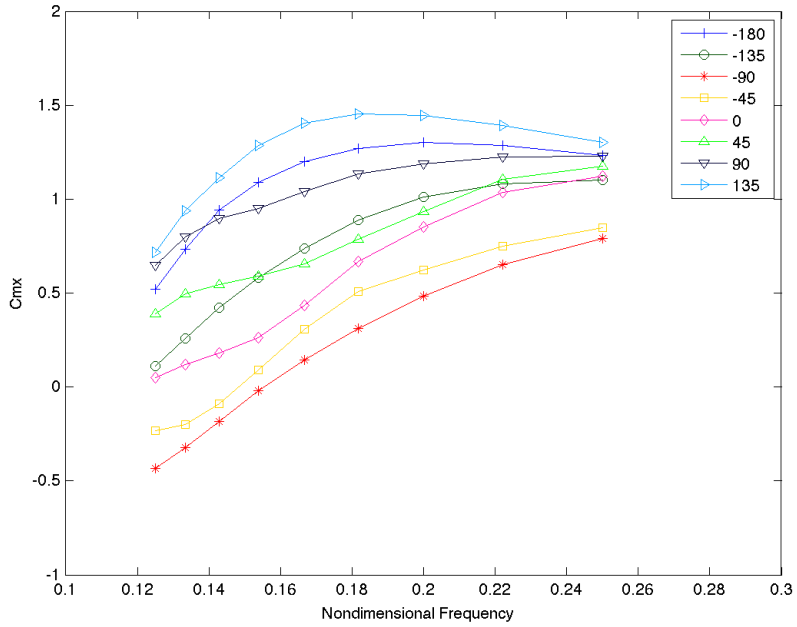

Figure A-200: Inline added mass coefficients $C_{m,IL}$ X 0.1 Y 0.75

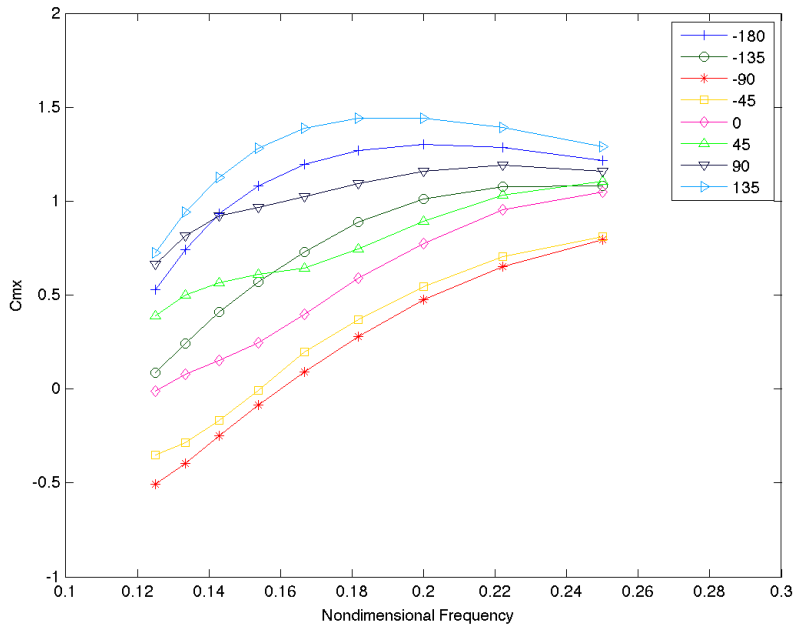

Figure A-201: Inline added mass coefficients $C_{m,IL}$ X 0.1 Y 1

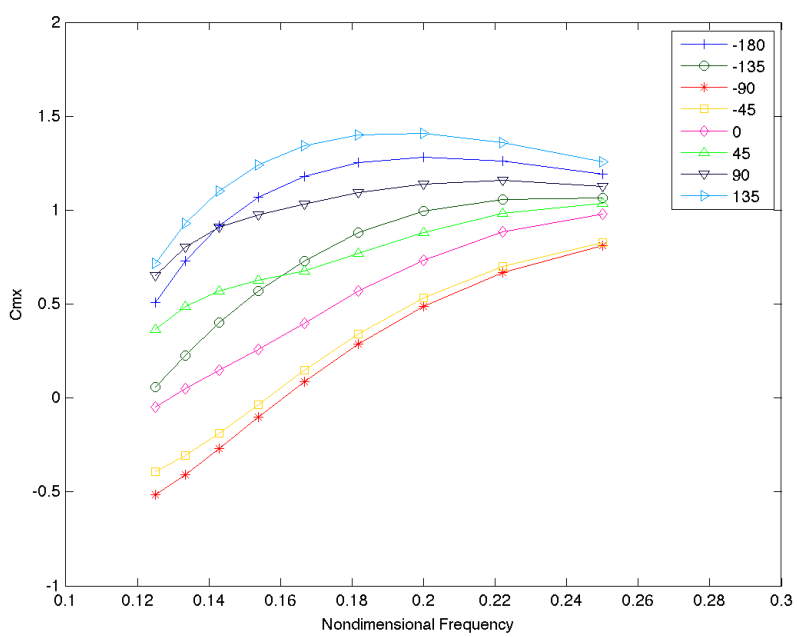

Figure A-202: Inline added mass coefficients $C_{m,IL}$ X 0.1 Y 1.25

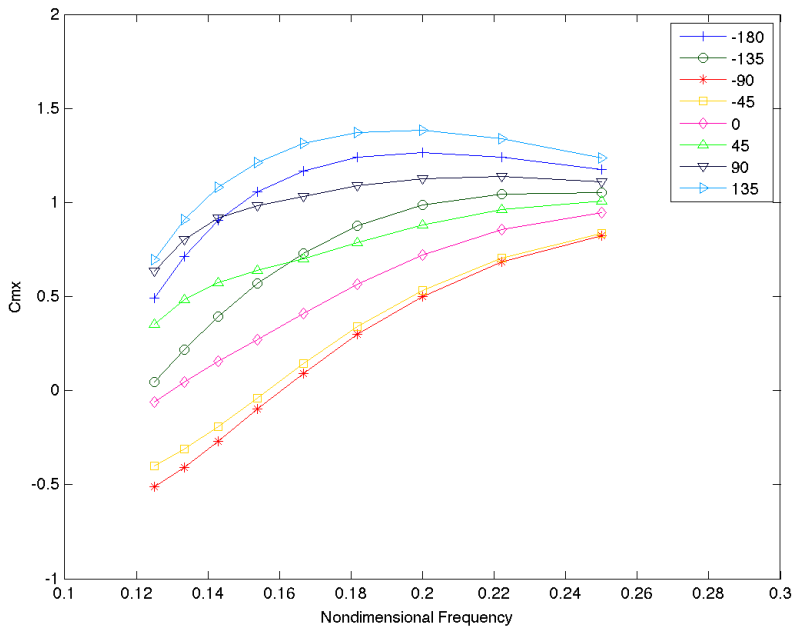

Figure A-203: Inline added mass coefficients $C_{m,IL}$ X 0.1 Y 1.5

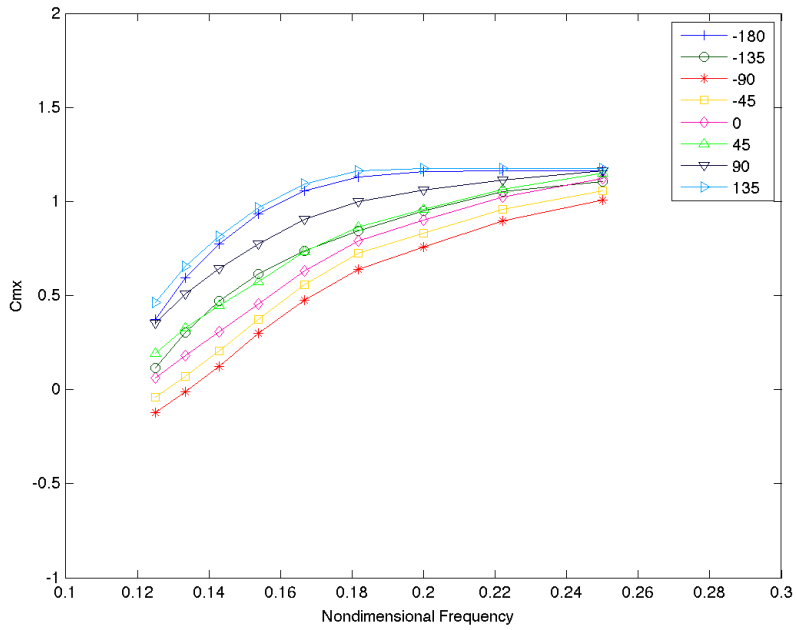

Figure A-204: Inline added mass coefficients $C_{m,IL}$ X 0.15 Y 0.15

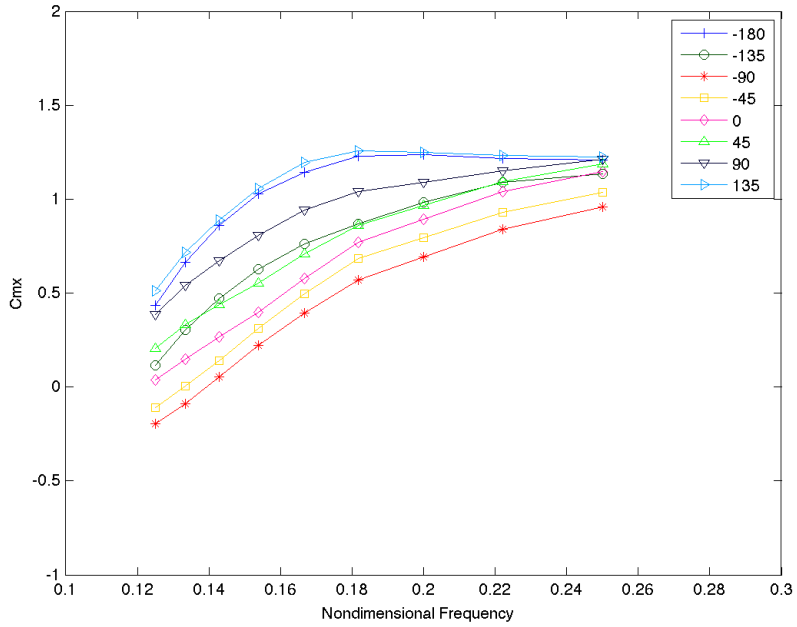

Figure A-205: Inline added mass coefficients $C_{m,IL}$ X 0.15 Y 0.25

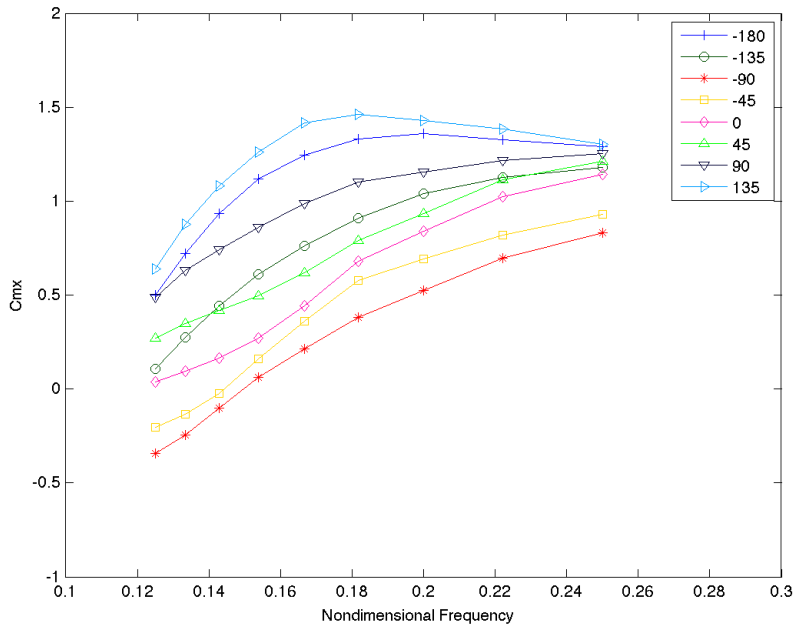

Figure A-206: Inline added mass coefficients $C_{m,IL}$ X 0.15 Y 0.5

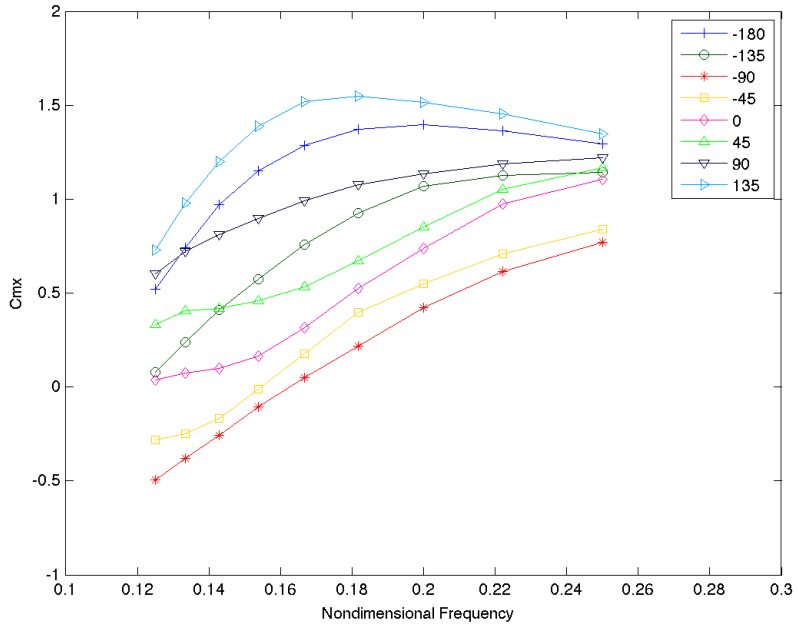

Figure A-207: Inline added mass coefficients $C_{m,IL}$ X 0.15 Y 0.75

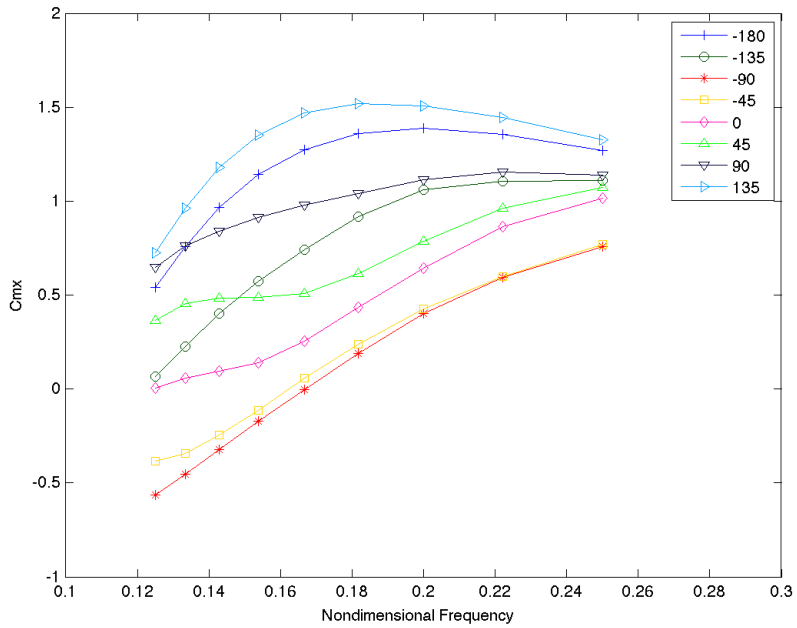

Figure A-208: Inline added mass coefficients $C_{m,IL}$ X 0.15 Y 1

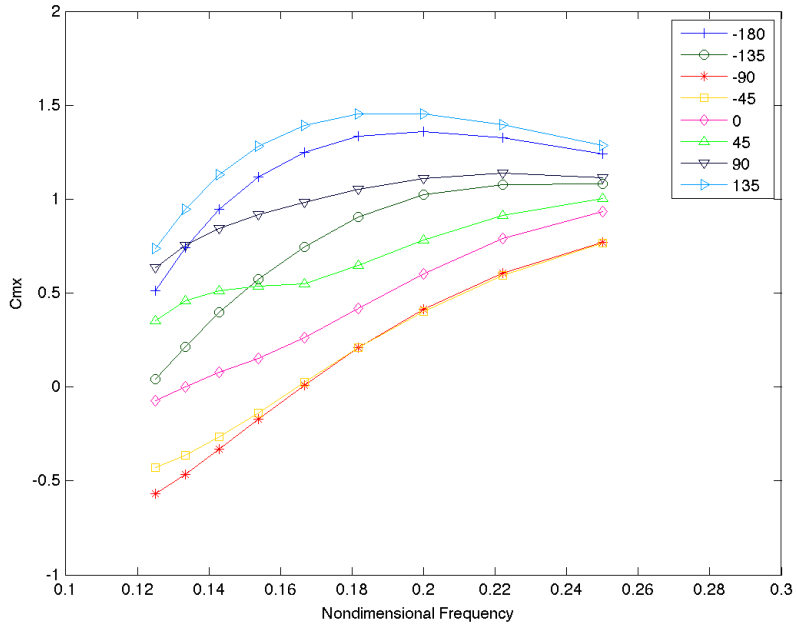

Figure A-209: Inline added mass coefficients $C_{m,IL}$ X 0.15 Y 1.25

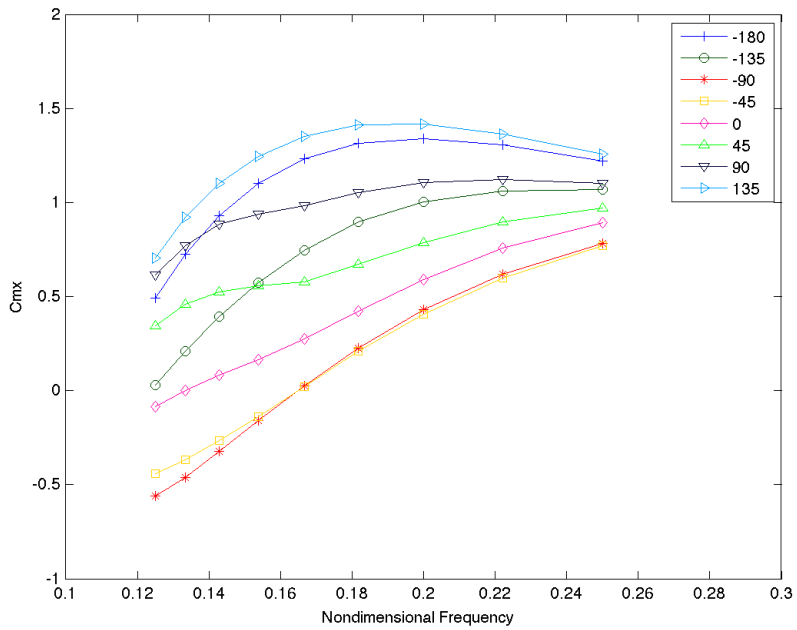

Figure A-210: Inline added mass coefficients $C_{m,IL}$ X 0.15 Y 1.5

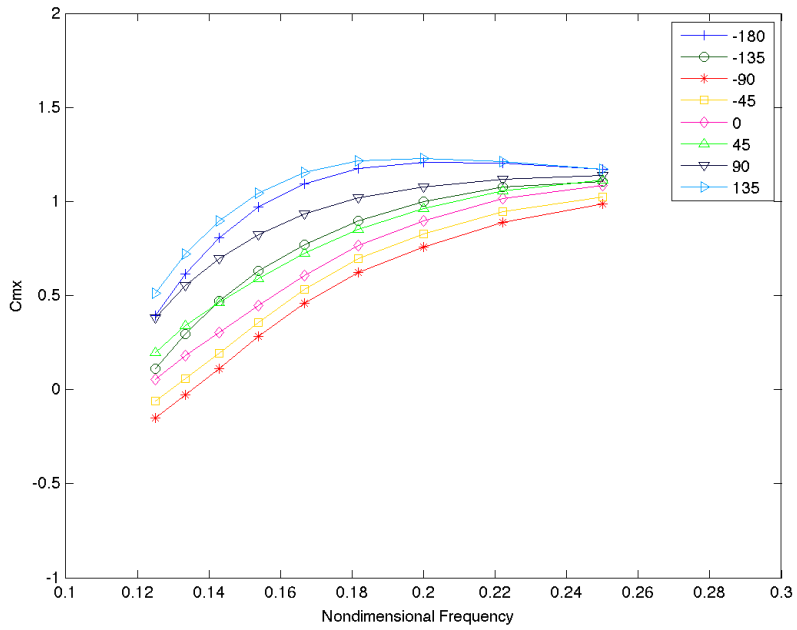

Figure A-211: Inline added mass coefficients $C_{m,IL}$ X 0.2 Y 0.15

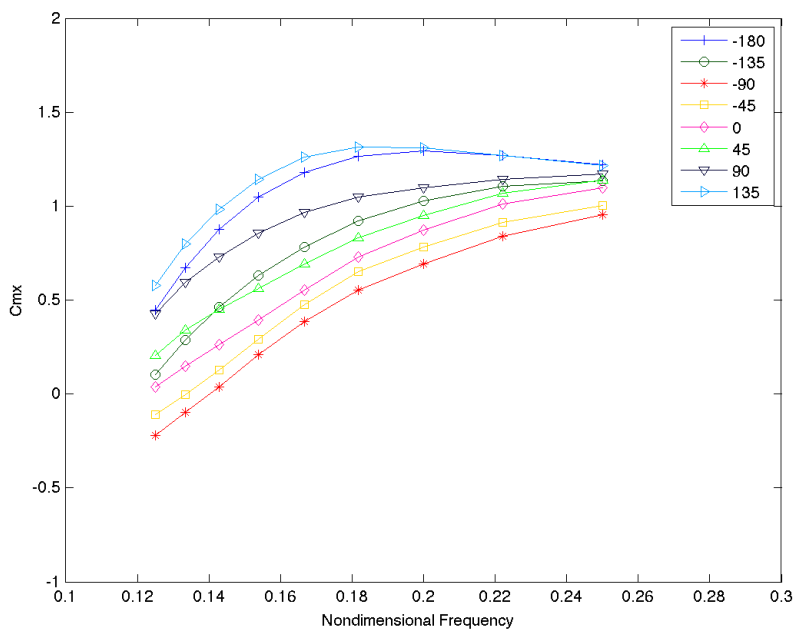

Figure A-212: Inline added mass coefficients $C_{m,IL}$ X 0.2 Y 0.25

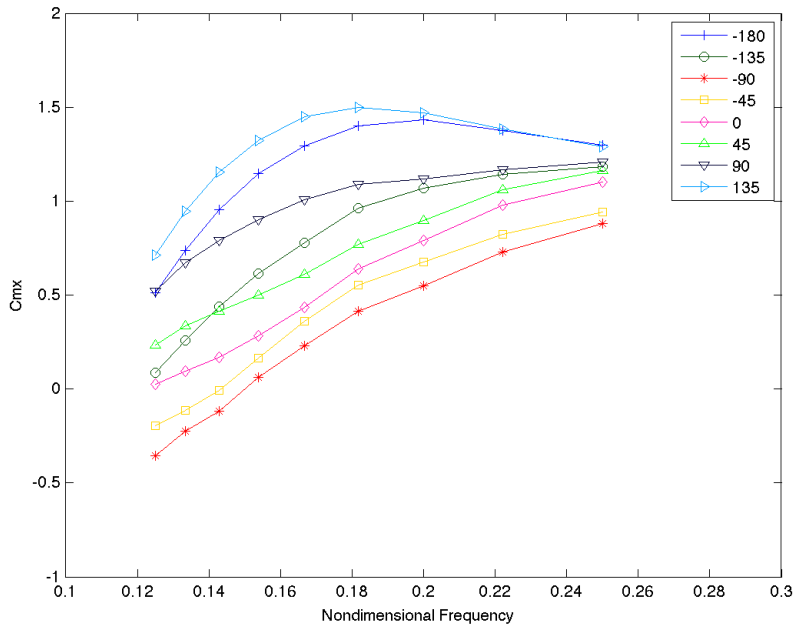

Figure A-213: Inline added mass coefficients $C_{m,IL}$ X 0.2 Y 0.5

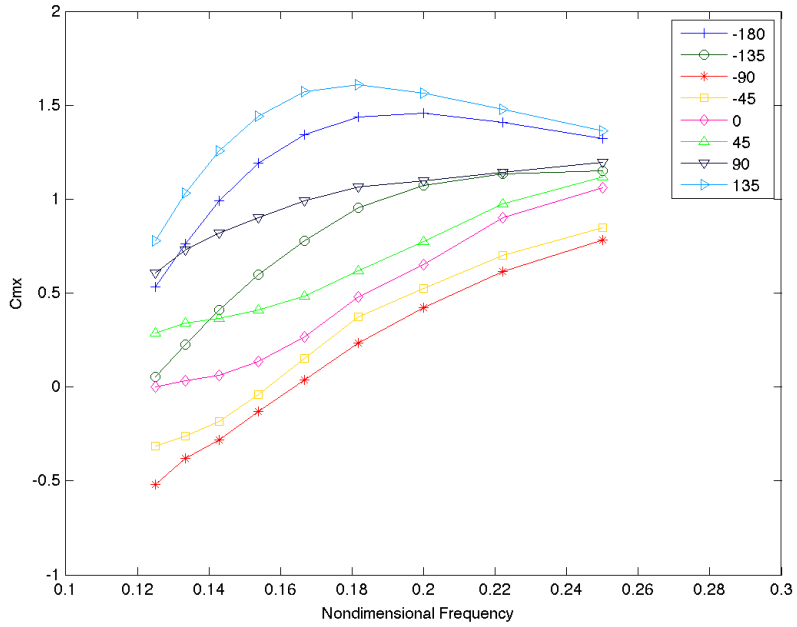

Figure A-214: Inline added mass coefficients $C_{m,IL}$ X 0.2 Y 0.75

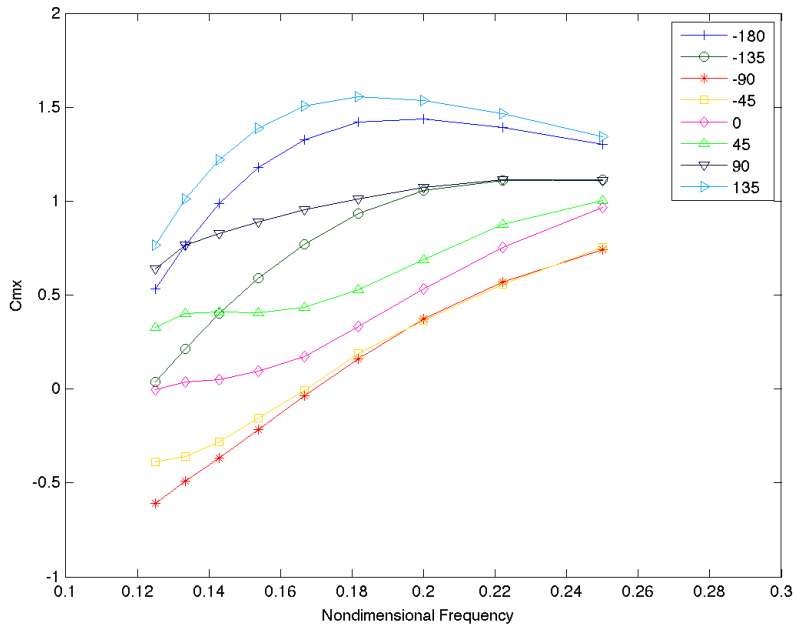

Figure A-215: Inline added mass coefficients $C_{m,IL}$ X 0.2 Y 1

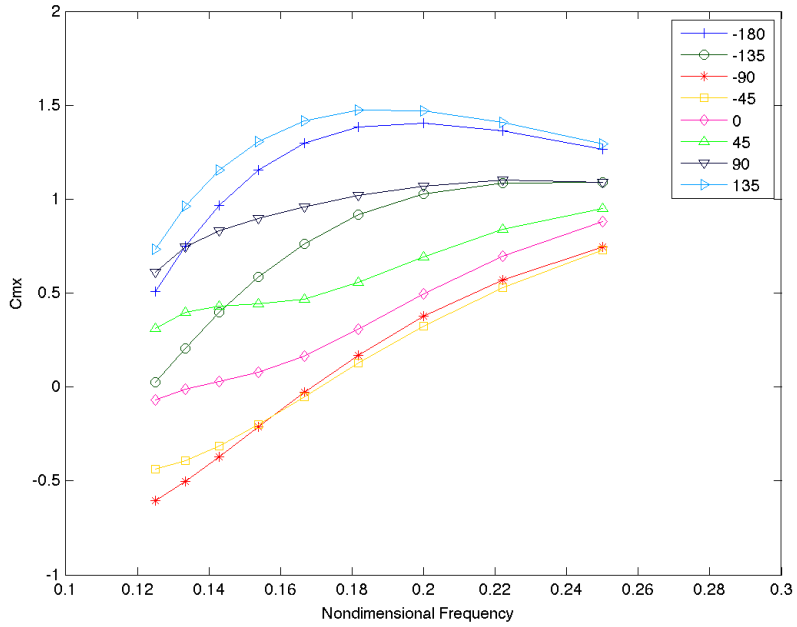

Figure A-216: Inline added mass coefficients $C_{m,IL}$ X 0.2 Y 1.25

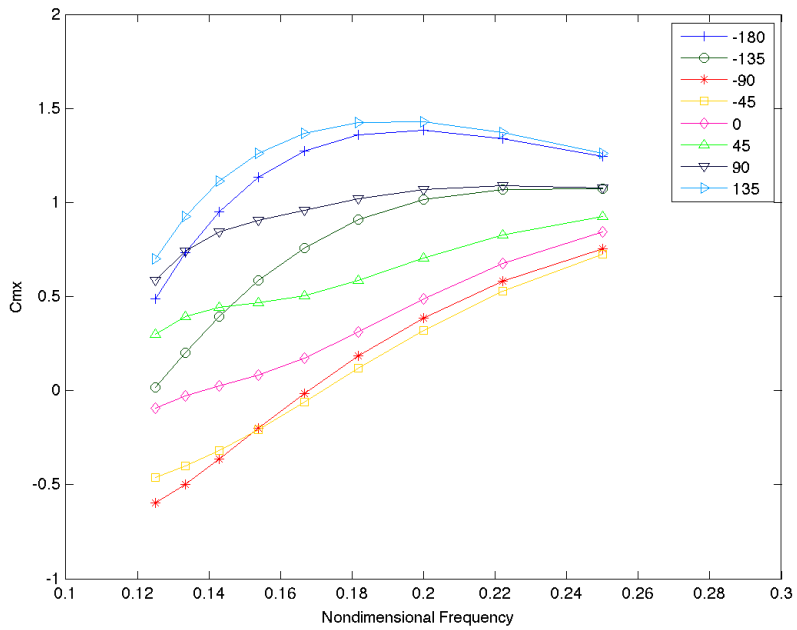

Figure A-217: Inline added mass coefficients $C_{m,IL}$ X 0.2 Y 1.5

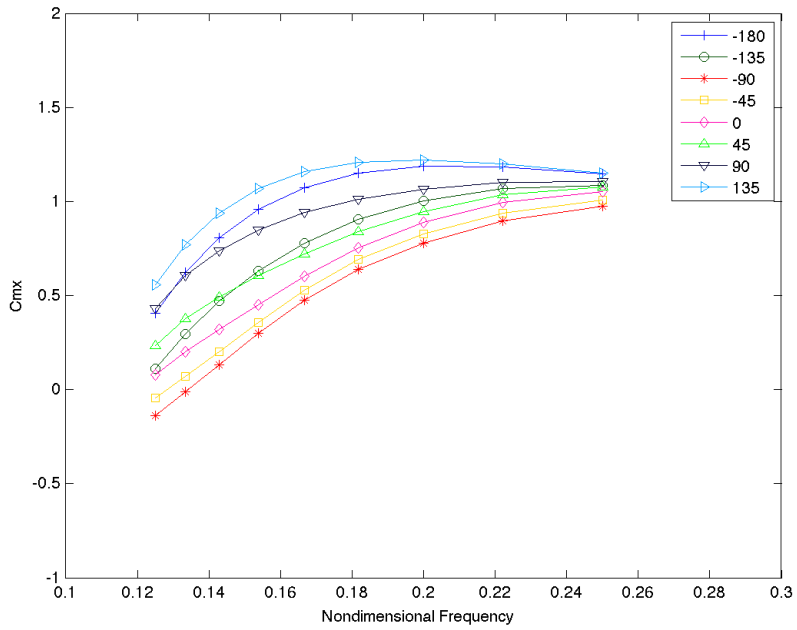

Figure A-218: Inline added mass coefficients $C_{m,IL}$ X 0.25 Y 0.15

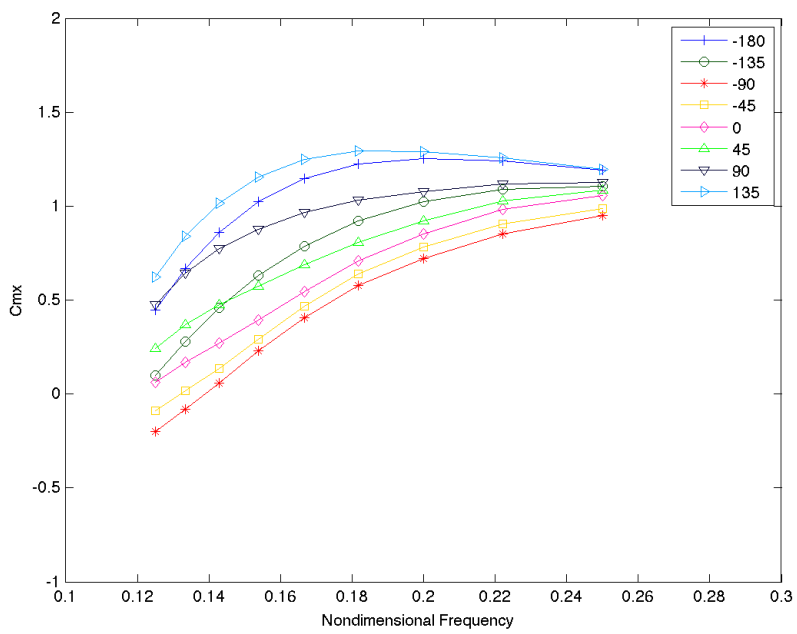

Figure A-219: Inline added mass coefficients $C_{m,IL}$ X 0.25 Y 0.25

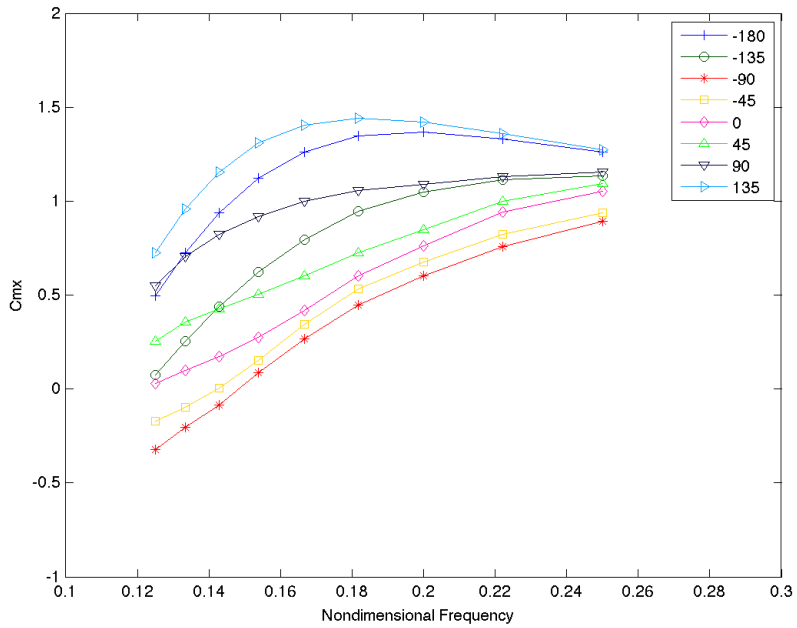

Figure A-220: Inline added mass coefficients $C_{m,IL}$ X 0.25 Y 0.5

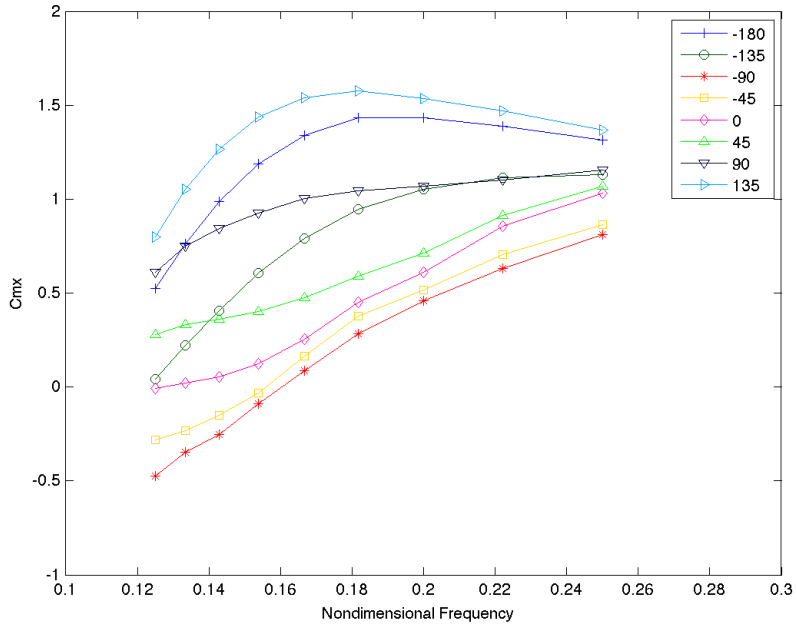

Figure A-221: Inline added mass coefficients $C_{m,IL}$ X 0.25 Y 0.75

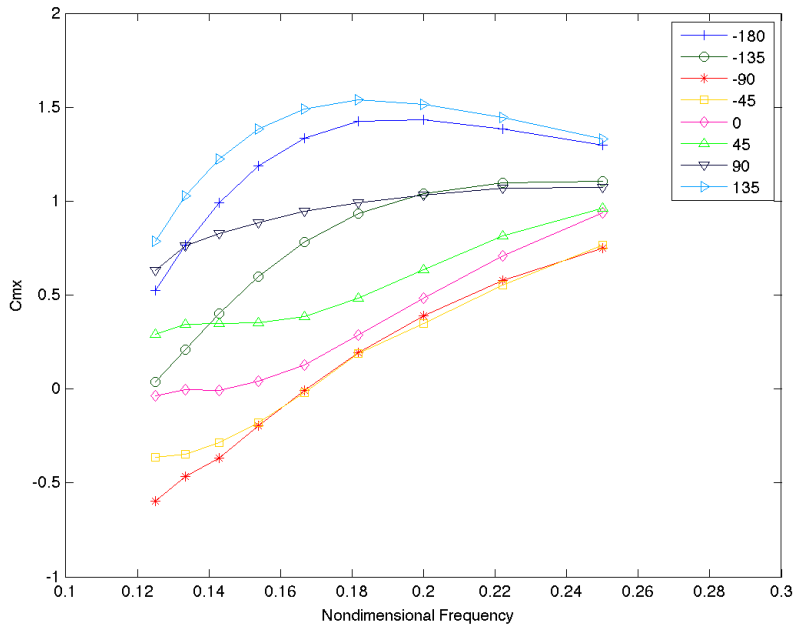

Figure A-222: Inline added mass coefficients $C_{m,IL}$ X 0.25 Y 1

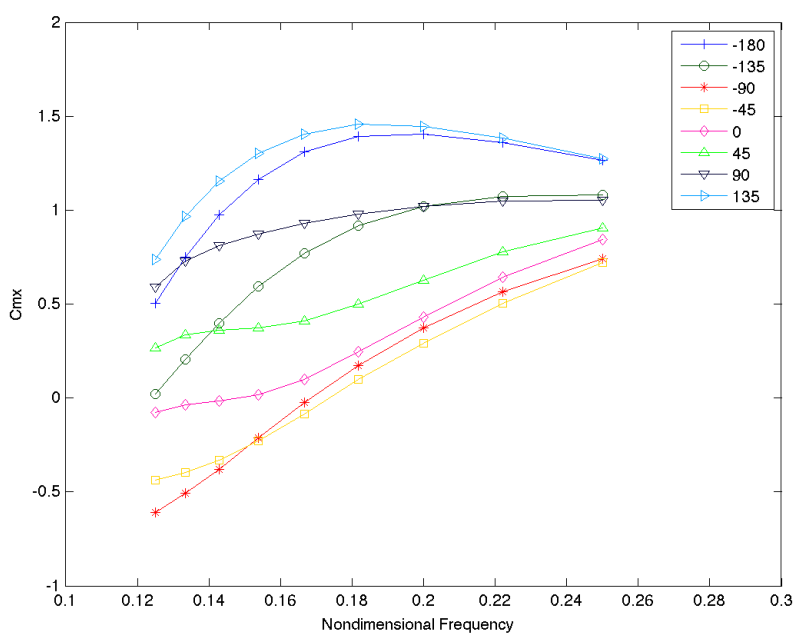

Figure A-223: Inline added mass coefficients $C_{m,IL}$ X 0.25 Y 1.25

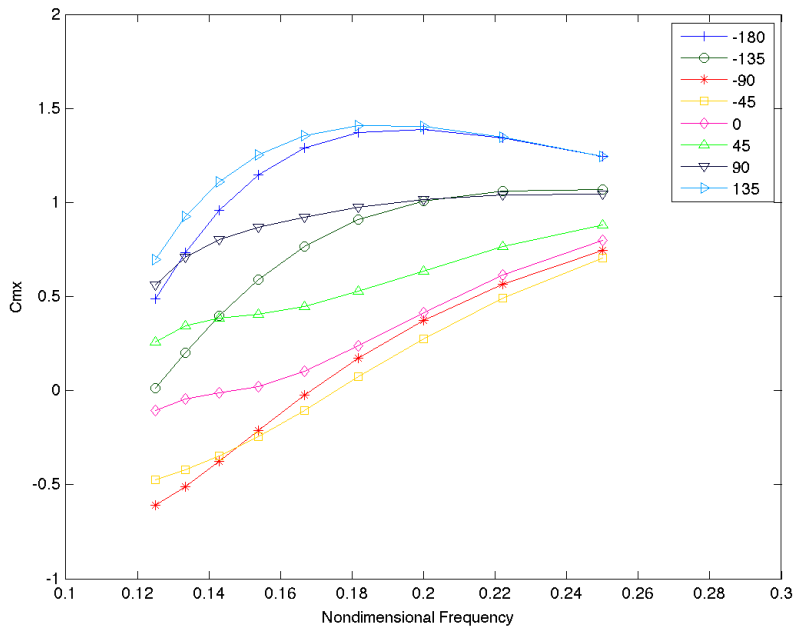

Figure A-224: Inline added mass coefficients $C_{m,IL}$ X 0.25 Y 1.5

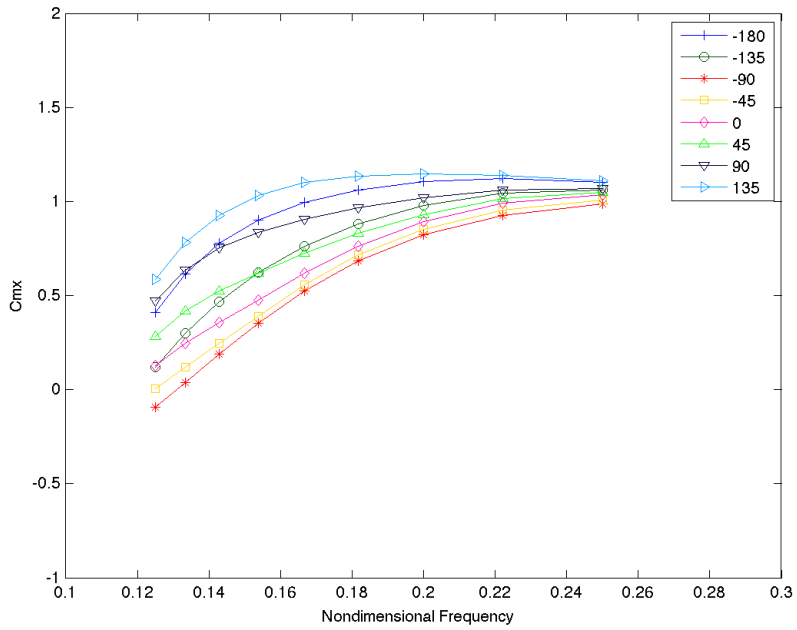

Figure A-225: Inline added mass coefficients $C_{m,IL}$ X 0.3 Y 0.15

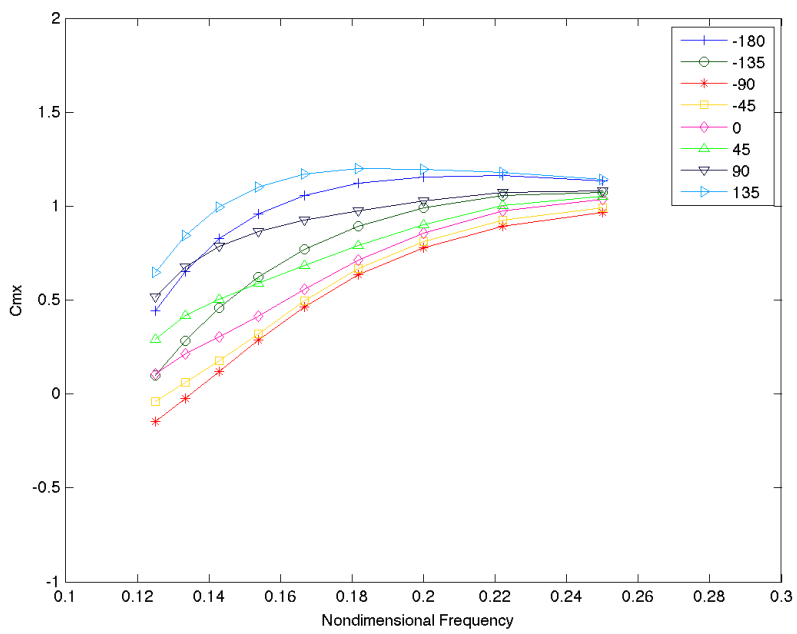

Figure A-226: Inline added mass coefficients $C_{m,IL}$ X 0.3 Y 0.25

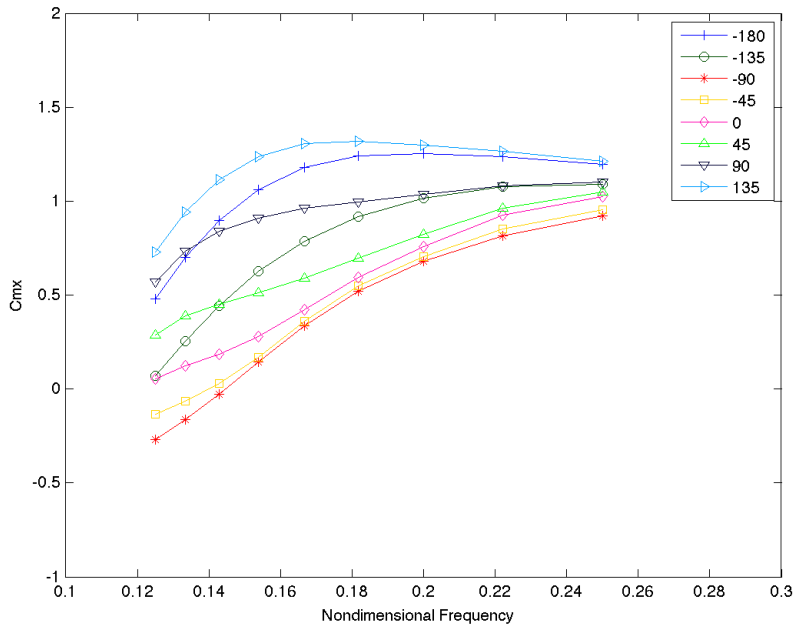

Figure A-227: Inline added mass coefficients $C_{m,IL}$ X 0.3 Y 0.5

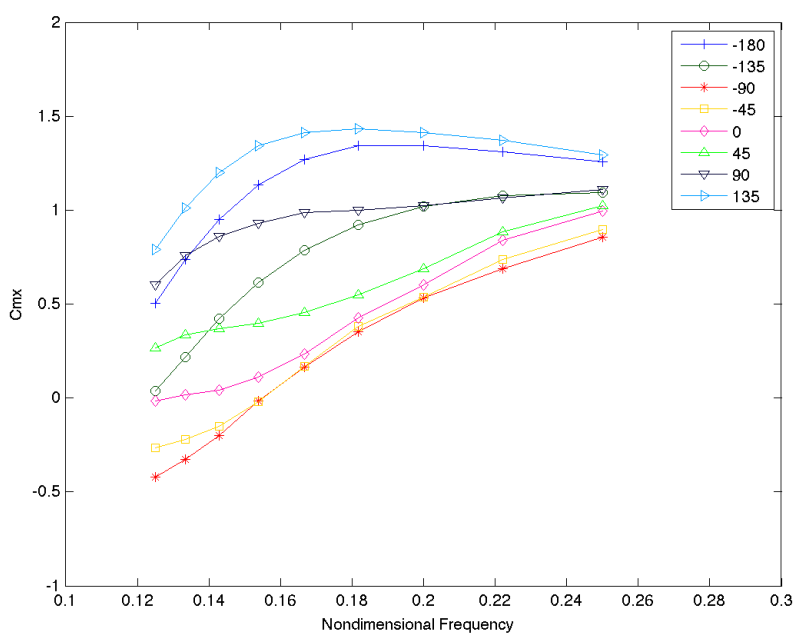

Figure A-228: Inline added mass coefficients $C_{m,IL}$ X 0.3 Y 0.75

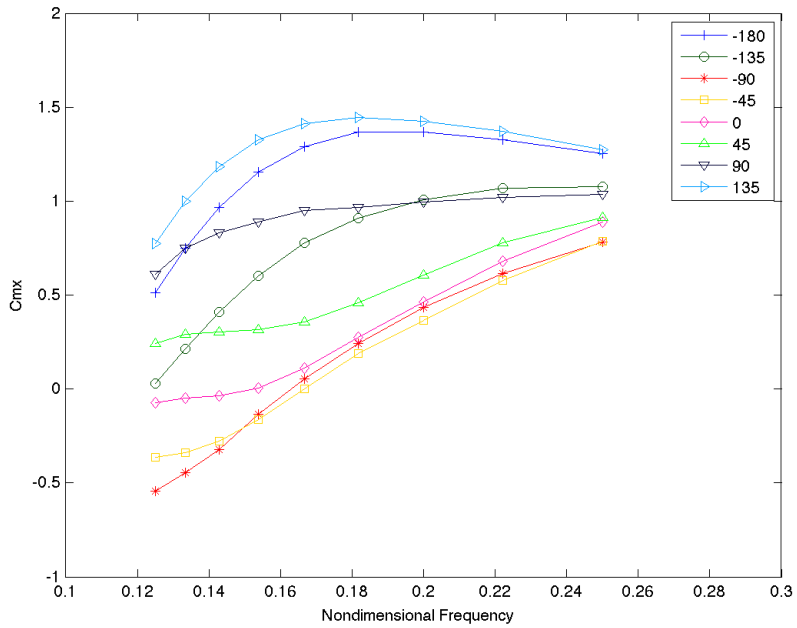

Figure A-229: Inline added mass coefficients $C_{m,IL}$ X 0.3 Y 1

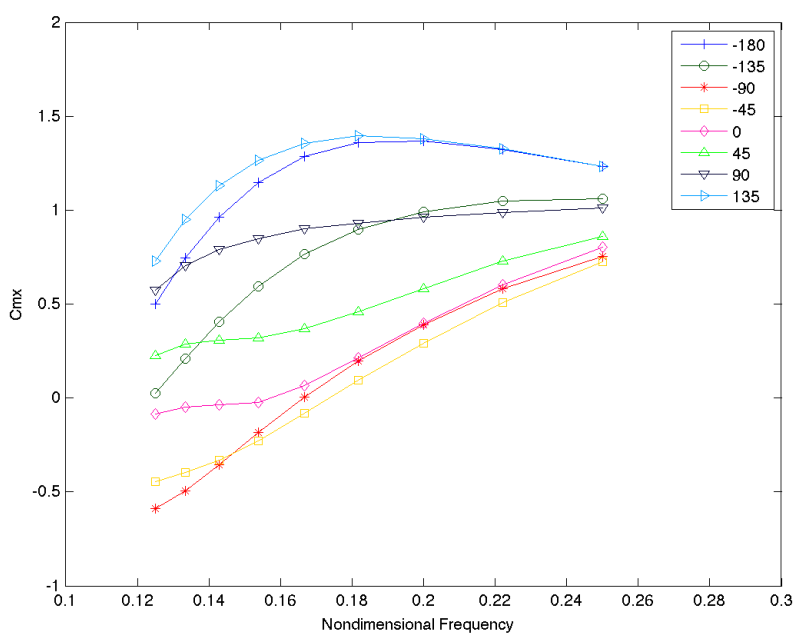

Figure A-230: Inline added mass coefficients $C_{m,IL}$ X 0.3 Y 1.25

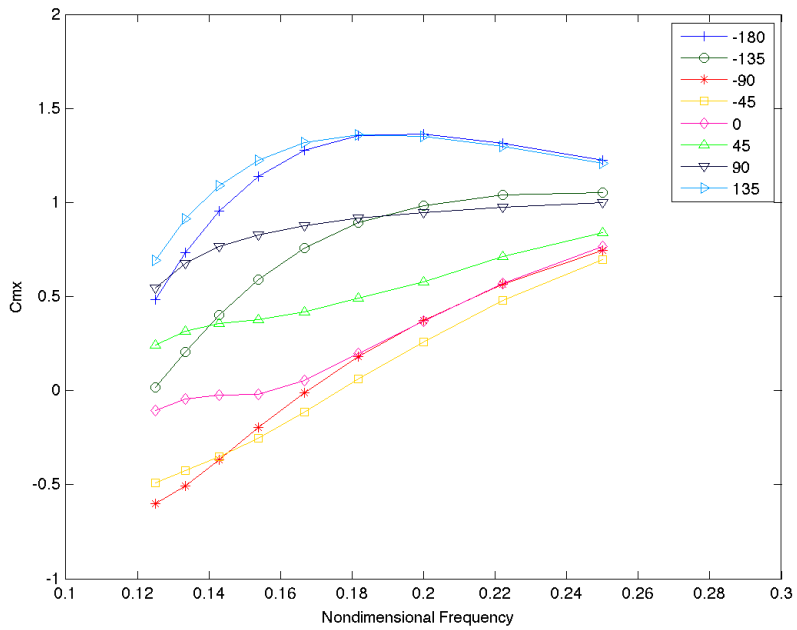

Figure A-231: Inline added mass coefficients $C_{m,IL}$ X 0.3 Y 1.5

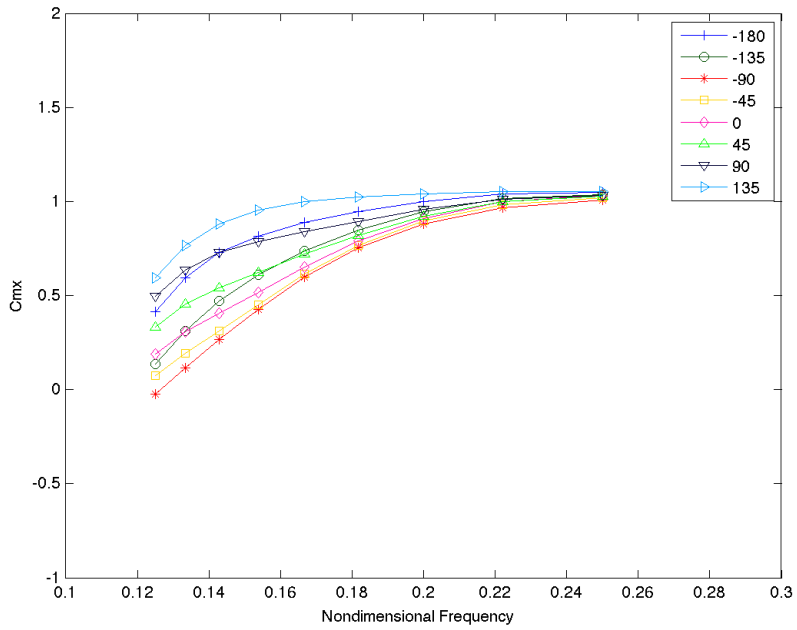

Figure A-232: Inline added mass coefficients $C_{m,IL}$ X 0.45 Y 0.15

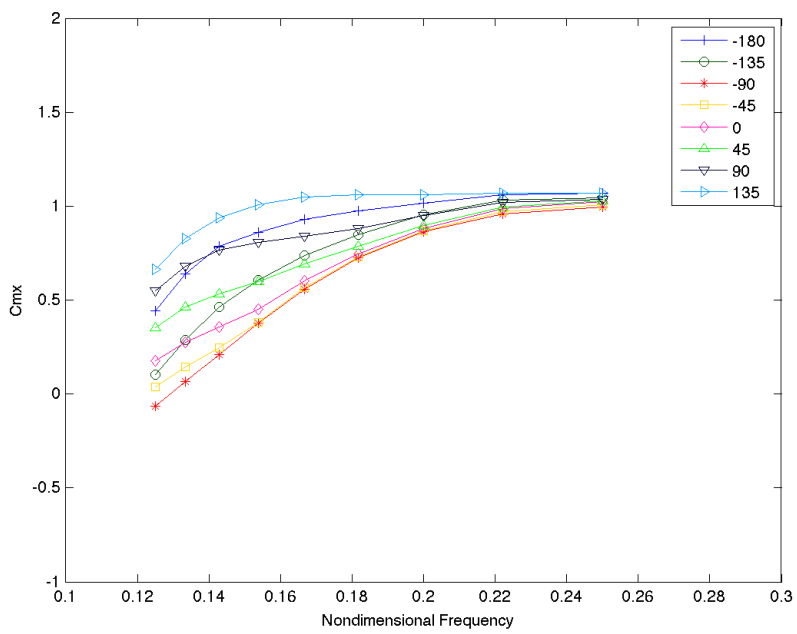

Figure A-233: Inline added mass coefficients $C_{m,IL}$ X 0.45 Y 0.25

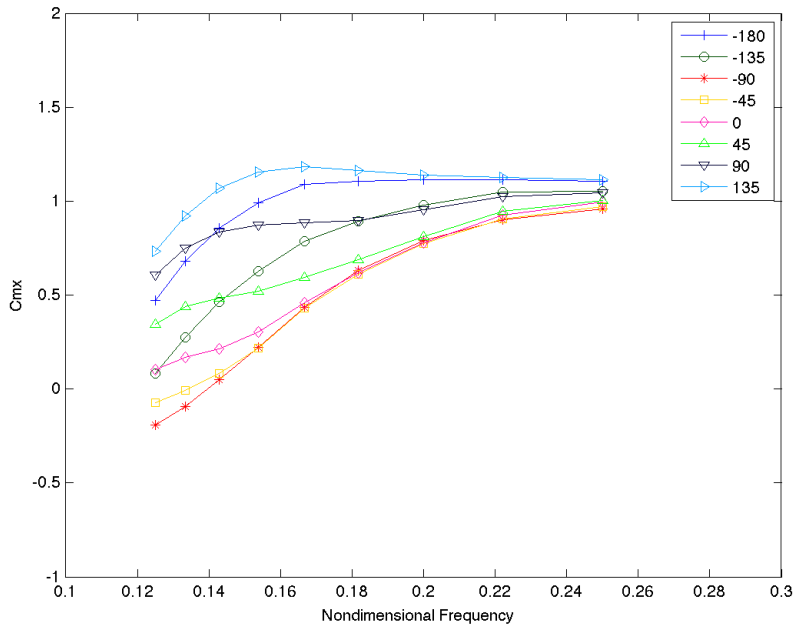

Figure A-234: Inline added mass coefficients $C_{m,IL}$ X 0.45 Y 0.5

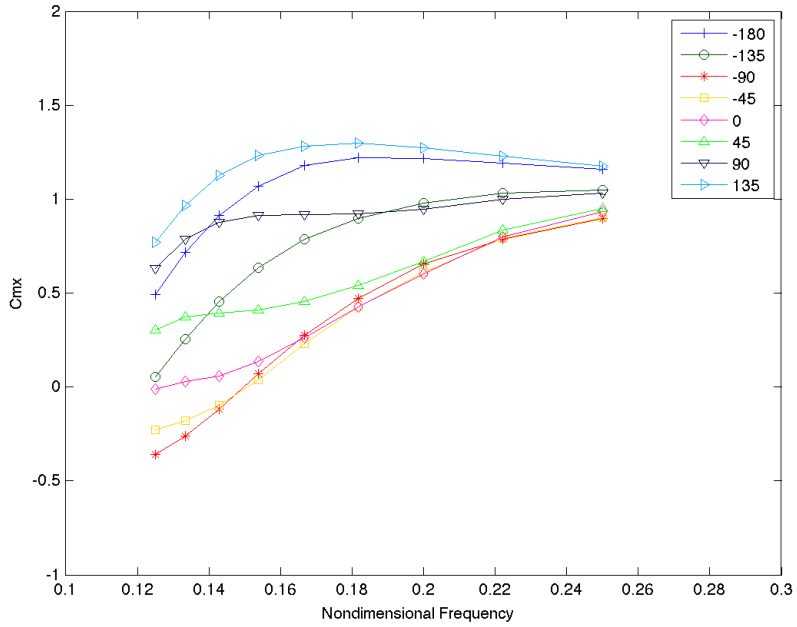

Figure A-235: Inline added mass coefficients $C_{m,IL}$ X 0.45 Y 0.75

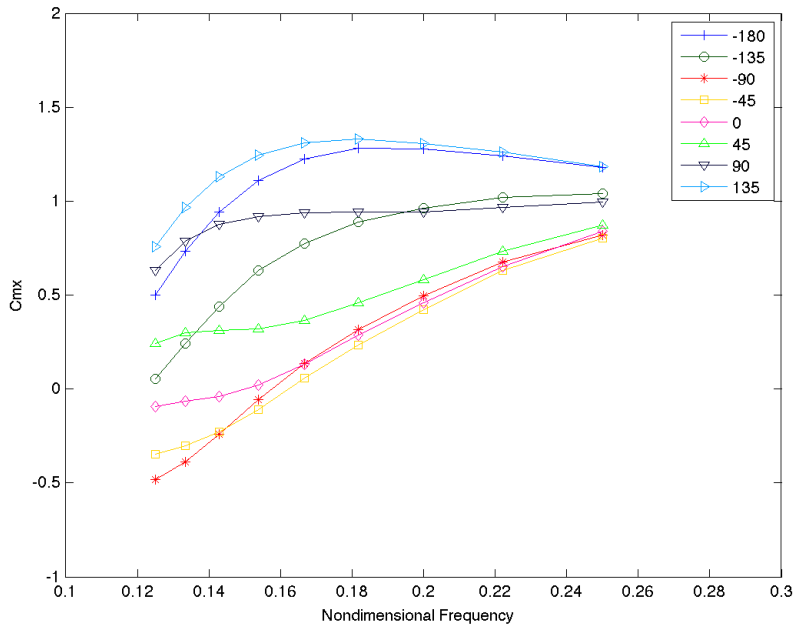

Figure A-236: Inline added mass coefficients $C_{m,IL}$ X 0.45 Y 1

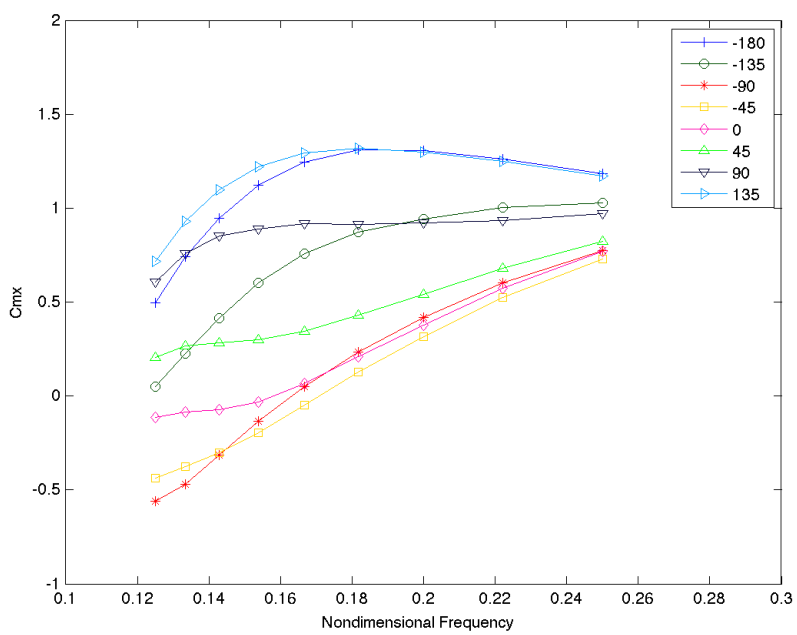

Figure A-237: Inline added mass coefficients $C_{m,IL}$ X 0.45 Y 1.25

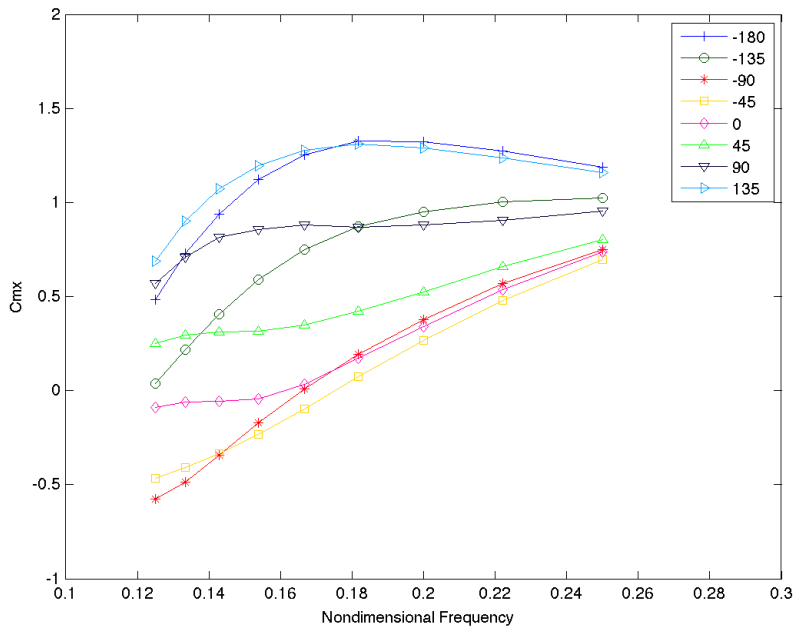

Figure A-238: Inline added mass coefficients $C_{m,IL}$ X 0.45 Y 1.5

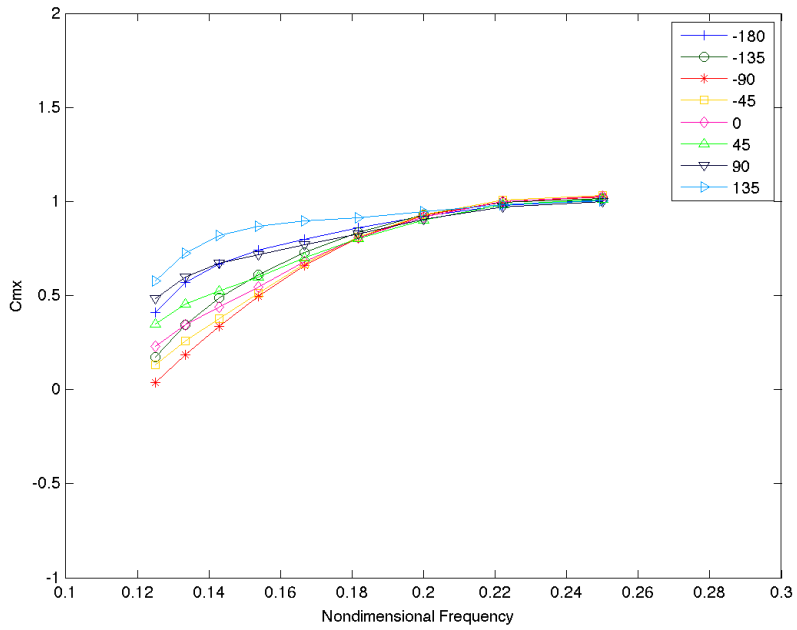

Figure A-239: Inline added mass coefficients $C_{m,IL}$ X 0.6 Y 0.15

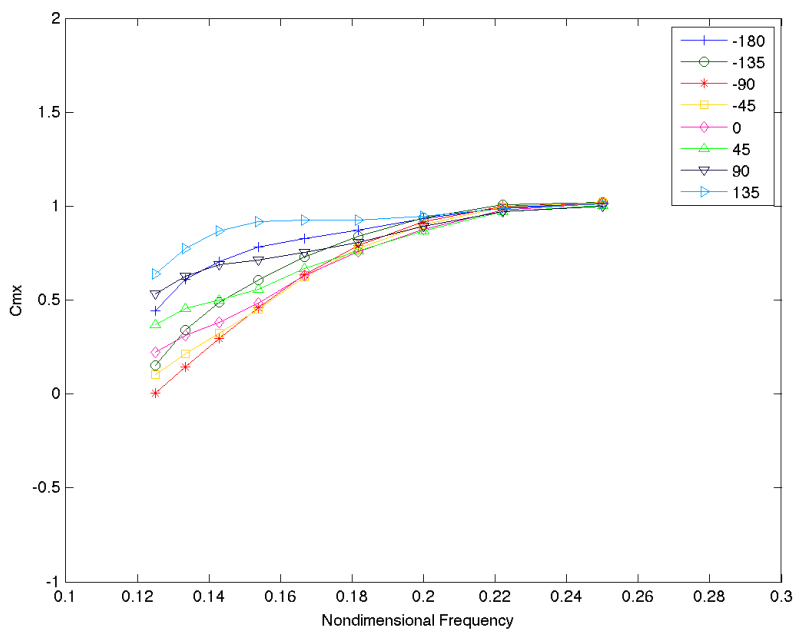

Figure A-240: Inline added mass coefficients $C_{m,IL}$ X 0.6 Y 0.25

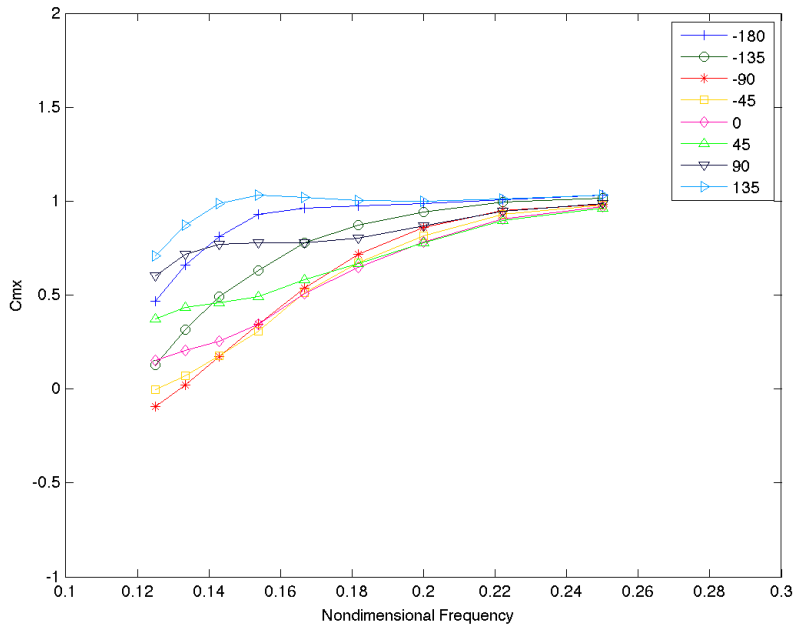

Figure A-241: Inline added mass coefficients $C_{m,IL}$ X 0.6 Y 0.5

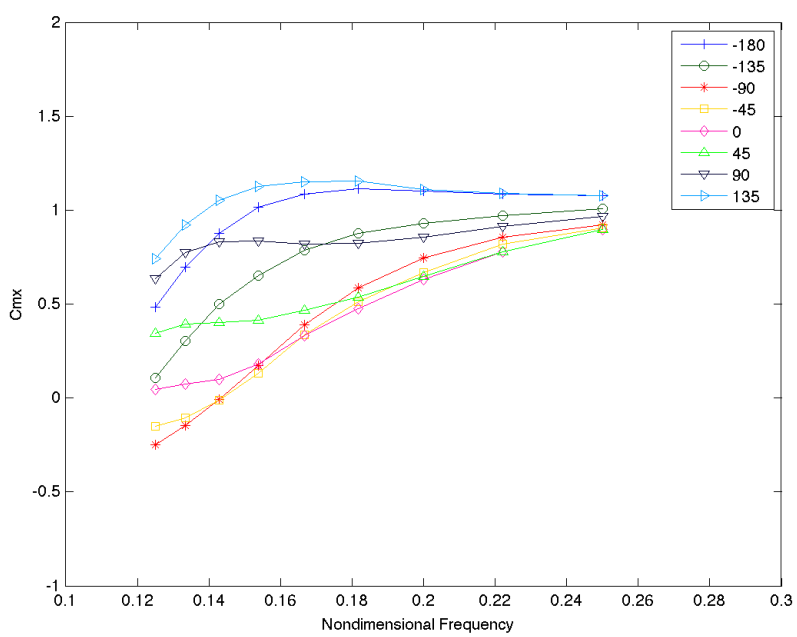

Figure A-242: Inline added mass coefficients $C_{m,IL}$ X 0.6 Y 0.75

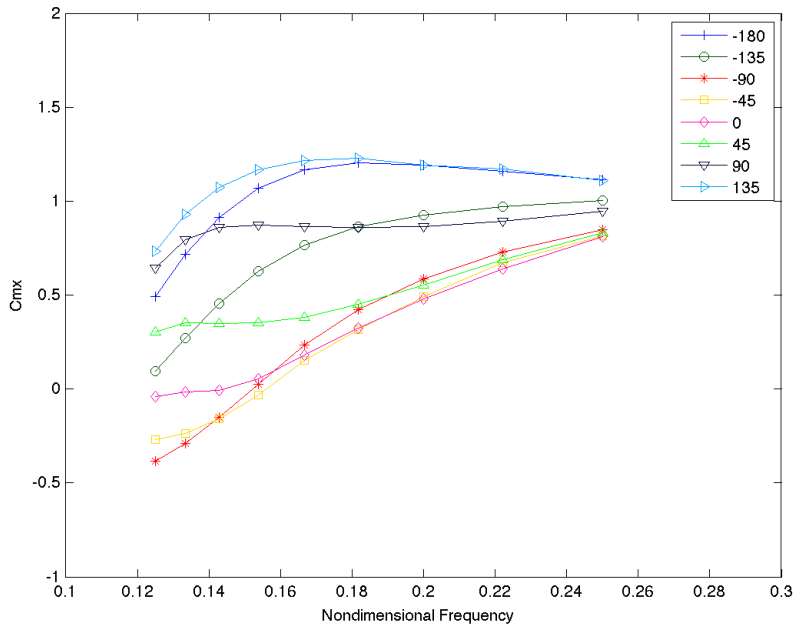

Figure A-243: Inline added mass coefficients $C_{m,IL}$ X 0.6 Y 1

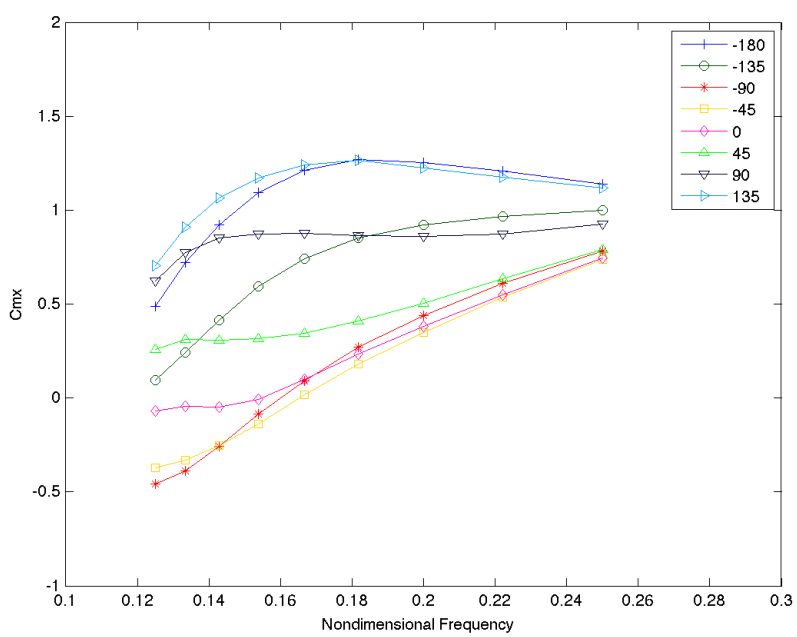

Figure A-244: Inline added mass coefficients $C_{m,IL}$ X 0.6 Y 1.25

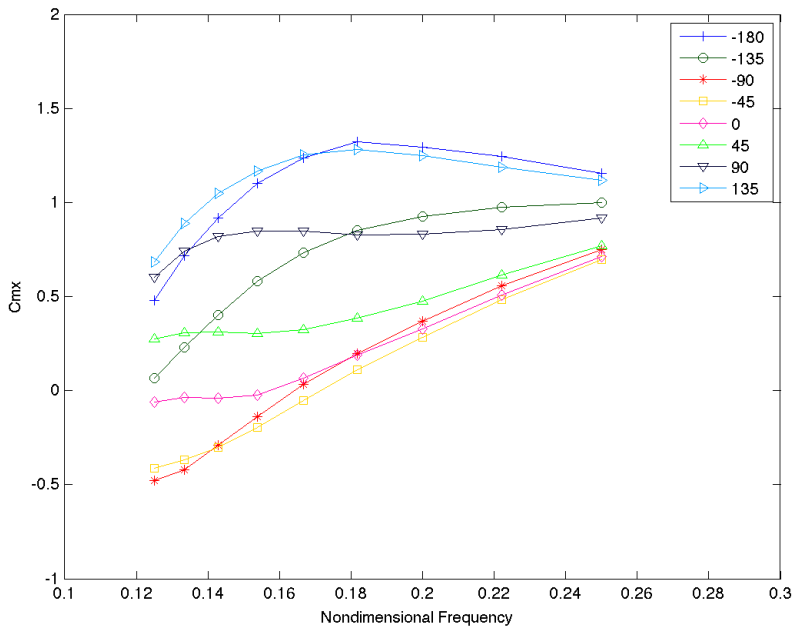

Figure A-245: Inline added mass coefficients $C_{m,IL}$ X 0.6 Y 1.5

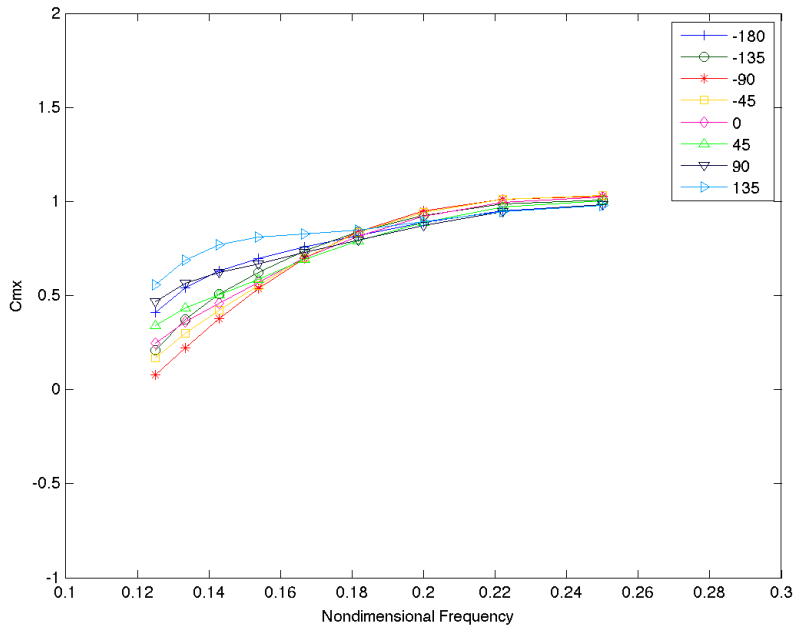

Figure A-246: Inline added mass coefficients $C_{m,IL}$ X 0.75 Y 0.15

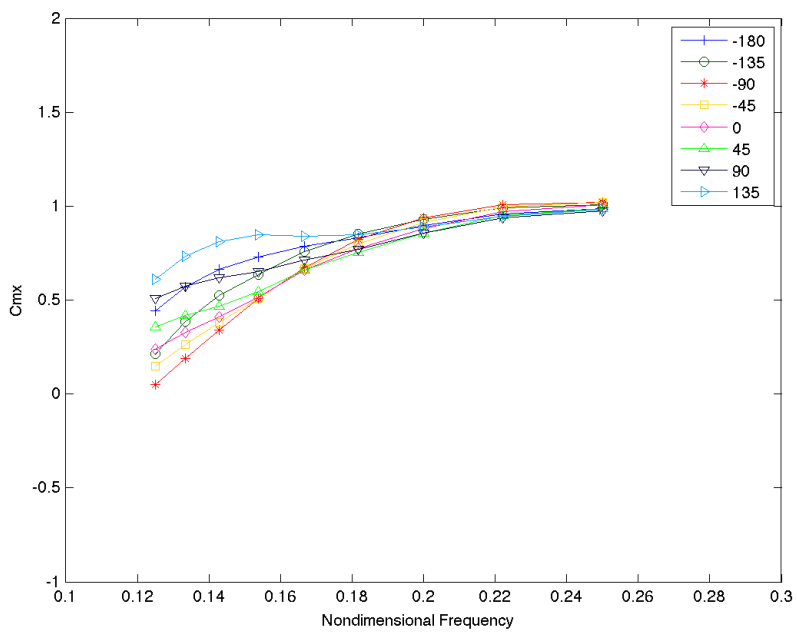

Figure A-247: Inline added mass coefficients $C_{m,IL}$ X 0.75 Y 0.25

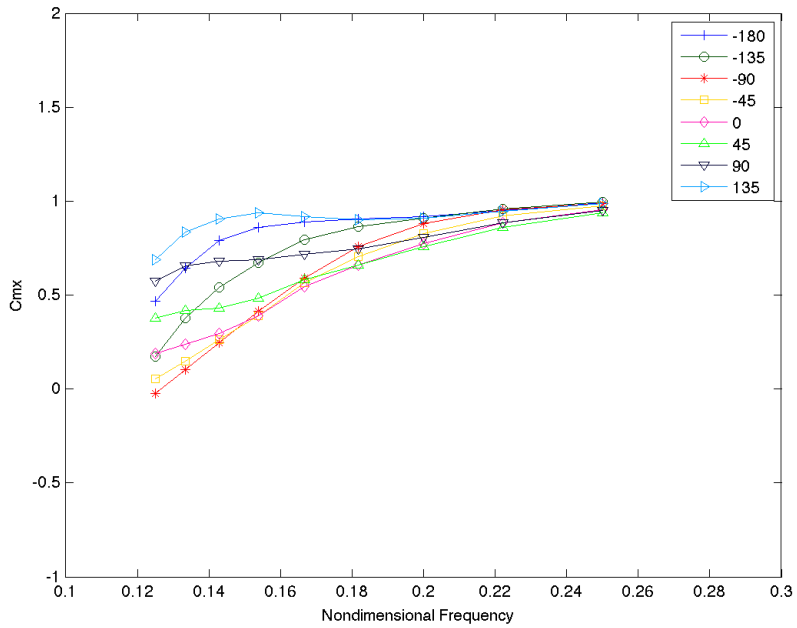

Figure A-248: Inline added mass coefficients $C_{m,IL}$ X 0.75 Y 0.5

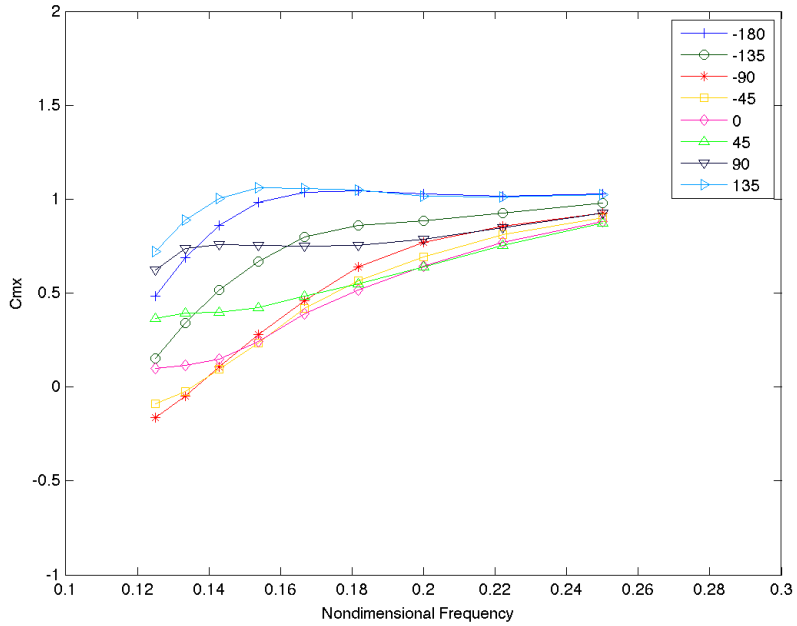

Figure A-249: Inline added mass coefficients $C_{m,IL}$ X 0.75 Y 0.75

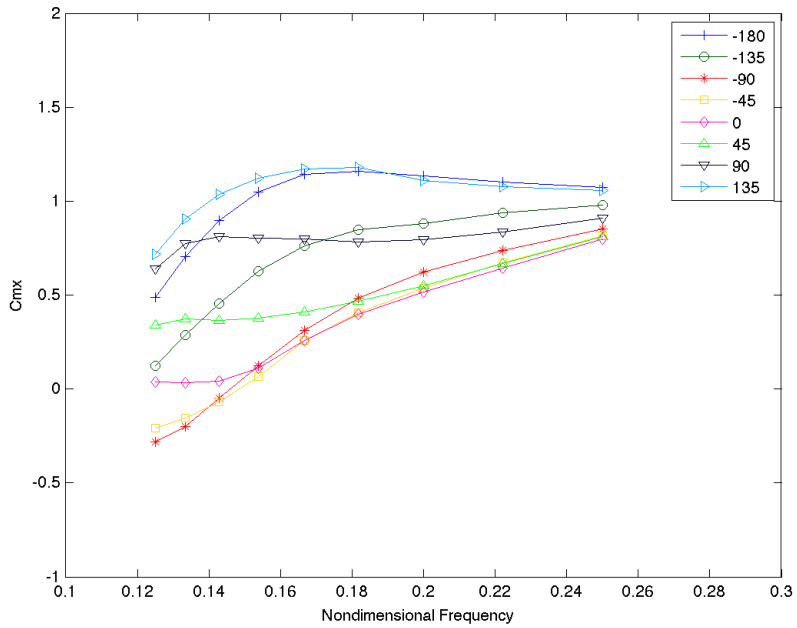

Figure A-250: Inline added mass coefficients $C_{m,IL}$ X 0.75 Y 1

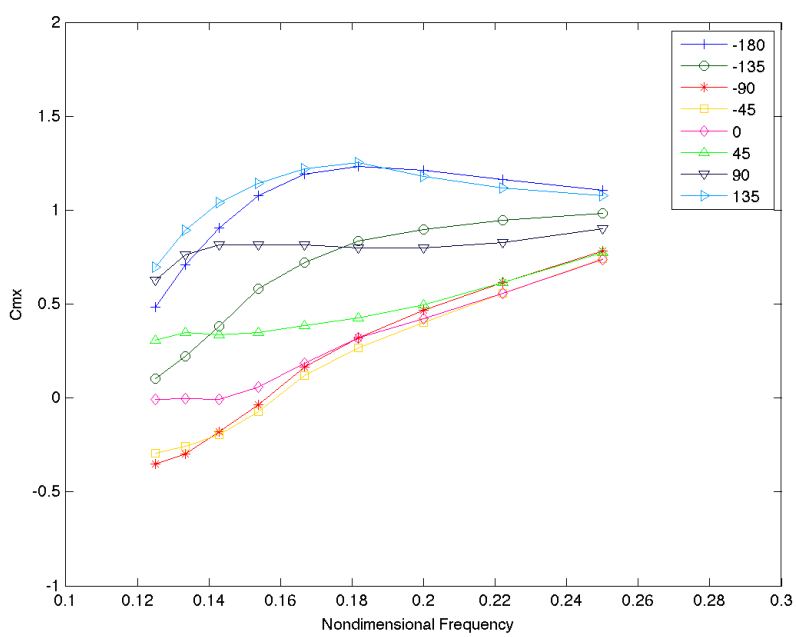

Figure A-251: Inline added mass coefficients $C_{m,IL}$ X 0.75 Y 1.25

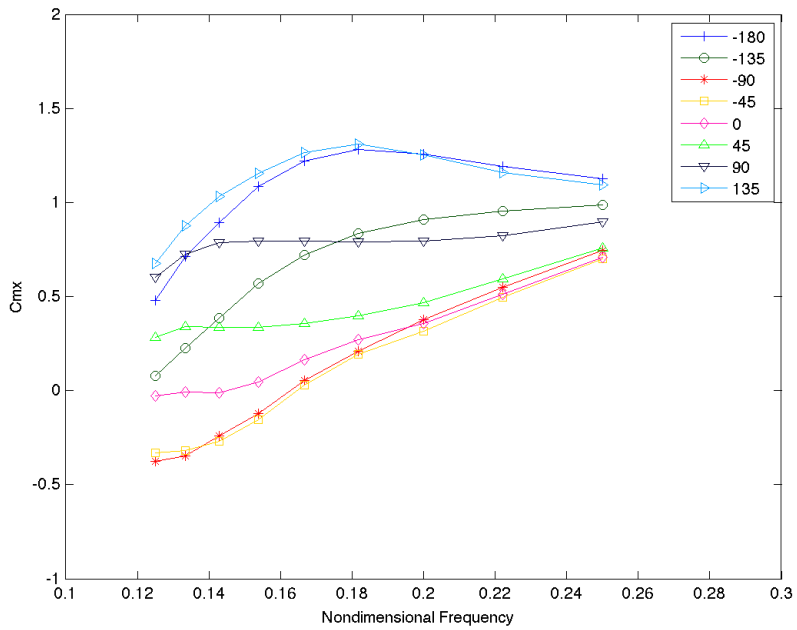

Figure A-252: Inline added mass coefficients $C_{m,IL}$ X 0.75 Y 1.5

Bibliography

[1] K. H. Aronsen. *An experimental investigation of in-line and combined in-line and cross-flow vortex induced vibrations*. PhD thesis, NTNU, 2007.

[2] K. H. Aronsen and C. M. Larsen. Hydrodynamic coefficients from in-line viv experiments. In *Proceedings of the 24th International Conference on Offshore Mechanics and Arctic Engineering OMAE*, 2005.

[3] K. H. Aronsen and C. M. Larsen. Hydrodynamic coefficients for in-line vortex induced vibrations. In *Proceedings of the 26th International Conference on Offshore Mechanics and Arctic Engineering OMAE*, 2007.

[4] G. S. Baarholm, C. M. Larsen, and H. Lie. On fatigue damage accumulation from in-line and cross-flow vortex-induced vibrations on risers. *Journal of Fluids and Structures*, 22(1):109 – 127, 2006.

[5] P. W. Bearman. Vortex shedding from oscillating bluff bodies. *Annual Review of Fluid Mechanics*, 16(1):195–222, 1984.

[6] R.E.D. Bishop and A.Y Hassan. The lift and drag forces on a circular cylinder. In *Proceedings of the Royal Society of London*, number 277 in A, pages 32–50, 1963.

[7] R. D. Blevins. *Flow Induced Vibration*. Van Nostrand Reinhold Company, New York, NY, 1990.

[8] B. Bourguet, Y. Modarres-Sadeghi, G. E. Karniadakis, and M. S. Triantafyllou. Wake-body resonance of long flexible structures is dominated by counter-clockwise orbits. *Physical Review Letters*, 107(134502), 2011.

[9] H. Braaten and H. Lie. Riser high mode VIV tests. Technical Report Main Report no. 512394.00.01, Norwegian Marine Technology Research Institute., 2004.

[10] N. Cagney and S. Balabani. Wake modes of a cylinder undergoing free streamwise vortex-induced vibrations. *Journal of Fluids and Structures*, Available online 19 January 2013, ISSN 0889-9746, 10.10 16/j.jfluidstructs.2012.12.004., 2013.

[11] J. Carberry, R. Govardhan, J. Sheridan, D. Rockwell, and C. H. K. Williamson. Wake states and response branches of forced and freely oscillating cylinders. *European Journal of Mechanics B/Fluids*, 23:89–97, 2004.

[12] J. Carberry, J. Sheridan, and D. Rockwell. Controlled oscillations of a cylinder: A new wake state. *Journal of Fluids and Structures*, 17:337–343, 2003.

[13] J. Carberry, J. Sheridan, and D. Rockwell. Controlled oscillations of a cylinder: Forces and wake modes. *Journal of Fluid Mechanics*, 538:31–69, 2005.

[14] J. R. Chaplin, P. W. Bearman, Y. Cheng, E. Fontaine, J. M. R. Graham, K. Herfjord, F. J. Huera Huarte, M. Isherwood, K. Lambrakos, C. M. Larsen, J. R. Meneghini, G. Moe, R. J. Pattenden, M. S. Triantafyllou, and R. H. J. Willden. Blind predictions of laboratory measurements of vortex-induced vibrations of a tension riser. *Journal of Fluids and Structures*, 21(1):25 – 40, 2005. Fluid-Structure and Flow-Acoustic Interactions involving Bluff Bodies.

[15] F. Chasparis. Vortex-induced motions of marine risers: Straked force database extraction and transient response analysis. Master's thesis, Massachusetts Institute of Technology, Department of Mechanical Engineering, June 2009.

[16] F. Chasparis, Y. Modarres-Sadeghi, F. S. Hover, M. S. Triantafyllou, Y. Contantinides, and H. Mukundan. Hydrodynamic data extraction from field data. In *Proceedings of the 28th International Conference on Offshore Mechanics and Arctic Engineering OMAE*, Honolulu, Hawaii, USA, 2009.

[17] F. Chasparis, Y. Modarres-Sadeghi, F. S. Hover, M. S. Triantafyllou, M. Tognarelli, and P. Beynet. Lock-in, transient and chaotic response in riser VIV. In *Proceedings of the 28th International Conference on Offshore Mechanics and Arctic Engineering OMAE*, Honolulu, Hawaii, USA, 2009.

[18] L. Christian. *Mechanical Vibration and Shock*, volume Vol.4. Taylor & Francis, New York, NY., 2002.

[19] J. M. Dahl. *Vortex-induced vibration of a circular cylinder with combined in-line and cross-flow motion.* PhD thesis, Massachusetts Institute of Technology, 2008.

[20] J. M. Dahl, F. S. Hover, M. S. Triantafyllou, S. Dong, and G. E. Karniadakis. Resonant vibrations of bluff bodies cause multivortex shedding and high frequency forces. *Phys. Rev. Lett.*, 99(14):144503, Oct 2007.

[21] J. M. Dahl, F. S. Hover, M. S. Triantafyllou, and O. H. Oakley, Jr. Dual resonance in vortex-induced vibrations at subcritical and supercritical reynolds numbers. *Journal of Fluid Mechanics*, 643:395–424, 1 2010.

[22] J. M. Dahl, F. S. Hover, and M.S. Triantafyllou. Two degree of freedom VIV of a circular cylinder in subcritical flow condition. In E. de Langre and F. Axisa, editors, *Proceedings of the 8th International Conference on Flow Induced Vibrations*, Paris, July 2004.

[23] J. M. Dahl, F. S. Hover, and M.S. Triantafyllou. Two-degree-of-freedom vortex-induced vibrations using a force assisted apparatus. *Journal of Fluids and Structures*, 22:807–818, 2006.

[24] S. Dong and G. E. Karniadakis. DNS of flow past a stationary and oscillating cylinder at re = 10,000. *Journal of Fluids and Structures*, 20:519–531, 2005.

[25] S. Dong and G. E. Karniadakis. Suppressing the fluctuating lift on a circular cylinder. *Journal of Fluid Mechanics*, page Under Review, Received 2006.

[26] M. Van Dyke. *An Album of Fluid Motions*. Parabolic Press, Inc., Stanford, CA, 1982.

[27] S. Fielding. University of Manchester Lecture Notes: Laminar Boundary Layer Theory.

[28] R. Gopalkrishnan. *Vortex-Induced Forces on Oscillating Bluff Cylinders*. Doctor of science in oceanographic engineering, Massachusetts Institute of Technology and Woods Hole Oceanographic Institution, February 1993.

[29] R. N. Govardhan and C. H. K. Williamson. Defining the 'modified griffin plot' in vortex-induced vibration: Revealing the effect of reynolds number using controlled damping. *Journal of Fluid Mechanics*, 561:147–180, 2006.

[30] O. M. Griffin and G. H. Koopman. The vortex-excited lift and reaction forces on resonantly vibrating cylinders. *Journal of Sound and Vibration*, 53:435–448, 1977.

[31] N. Jauvtis and C. H. K. Williamson. Vortex-induced vibration of a cylinder with two degrees of freedom. *Journal of Fluids and Structures*, 17:1035–1042, 2003.

[32] N. Jauvtis and C. H. K. Williamson. A high-amplitude 2t mode of vortex formation, and the effects of non-hamonic forcing in vortex-induced vibration. *European Journal of Mechanics B/Fluids*, 23:107–114, 2004.

[33] G. Karniadakis and S. Sherwin. *Spectral/hp Element Methods for CFD*. Oxford Univ. Press, 2 edition, 1990.

[34] A. Khalak and C. H. K. Williamson. Dynamics of a hydroelastic cylinder with very low mass and damping. *Journal of Fluids and Structures*, 10:455–472, 1996.

[35] A. Khalak and C. H. K. Williamson. Motions, forces and mode transitions in vortex-induced vibrations at low mass-damping. *Journal of Fluids and Structures*, 13:813–851, 1999.

[36] R. King. Vortex-excited oscillations of a circular cylinder in steady currents. In *Offshore Technology Conference Proceedings*, number OTC 1948, 1974.

[37] C. M. Larsen, H. Lie, E. Passano, R. Yttervik, J. Wu, and G. S. Baarholm. VIVANA theory manual, version 3.7. Technical report, MARINTEK report, Trondheim, Norway, 2009.

[38] L. Lee, D. Allen, Pontaza J. P., F. KOPP, and V. JHINGRAN. In-line motion of subsea pipeline span models experiencing vortex-shedding. In *Proceedings of the ASME 2009 28th International Conference on Ocean, Offshore and Arctic Engineering OMAE2009*, Honolulu, Hawaii, USA, 2009.

[39] E. Lehn. VIV suppression tests on high l/d flexible cylinders main report. Technical report, 2003.

[40] L.M. Milne-Thompson. *Theoretical Hydrodynamics*. The McMillan Company, New York, 1960.

[41] MIT. VIV data repository.

[42] R. L. Mitchell and D. A. McPherson. Generating nonstationary random sequences. *IEEE Trans. Aero., Elec. Sys, AES-17*, 4:553– 560, 1981.

[43] Y. Modarres-Sadeghi, F. Chasparis, M. S. Triantafyllou, M. Tognarelli, and P. Beynet. Chaotic response is a generic feature of vortex-induced vibrations of flexible risers. *Journal of Sound and Vibration*, 330:2565–2579, 2011.

[44] Y. Modarres-Sadeghi, H. Mukundan, J. M. Dahl, F. S. Hover, and M. S. Triantafyllou. The effect of higher harmonic forces of fatigue life of marine risers. *Journal of Sound and Vibration*, 329:43–55, 2010.

[45] Y. Modarres-Sadeghi, A. Patrikalakis, H. Zheng, M. S. Triantafyllou, M. Tognarelli, and P. Beynet. Mode competition, chaotic motion and traveling waves in riser vortex induced vibrations. In *Proceedings of the IUTAM Symposium on Bluff Body Wakes and Vortex-Induced Vibrations (BBVIV)*, Capri Island, Italy, June 22-25, 2010.

[46] Y. Modarres-Sadeghi, M. S. Triantafyllou, and F. S. Hover. Fatigue life calculations of risers by taking into account the higher harmonic force components. In *Proceedings of the International Society of Offshore and Polar Engineering - ISOPE 2008*, Vancouver, July 2008.

[47] G. Moe and Z. J. Wu. The lift force on a cylinder vibrating in a current. *Journal of Offshore Mechanics and Arctic Engineering*, 112:297–303, nov 1990.

[48] T. L Morse and C. H. K. Williamson. Employing controlled vibrations to predict fluid forces on a cylinder undergoing vortex-induced vibration. *Journal of Fluids and Structures*, 22(6-7):877–884, 2006.

[49] H. Mukundan. *Vortex-induced vibrations of marine risers: motion and force reconstruction from field and experimental data*. PhD thesis, Massachusetts Institute of Technology, Department of Mechanical Engineering, June 2008.

[50] H. Mukundan, F. Chasparis, F. S. Hover, and M. S. Triantafyllou. Optimal lift coefficient databases from riser experiments,. *Journal of Fluids and Structures*, 26:160–175, 2009.

[51] D. J. Newman and G. E Karniadakis. A direct numerical simulation study of flow past a freely vibratingcable. *Journal of Fluid Mechanics*, 344:95–136, 1997.

[52] J. N. Newman. *Marine Hydrodynamics*. The MIT Press, Cambridge, MA, 1977.

[53] F. Noca, D. Shiels, and D. Jeon. A comparison of method for evaluating time-dependent fluid dynamic forces on bodies, using only velocity fields and their derivatives. *Journal of Fluids and Structures*, 13:551–578, 1999.

[54] A. Ongoren and D. Rockwell. Flow structure from an oscillating cylinder, part 1 . mechanisms of phase shift and recovery in the near wake. *Journal of Fluid Mechanics*, 191:197–223, 1988.

[55] E. Passano, C. M. Larsen, and J. Wu. VIV of free spanning pipelines: Comparison of response from semi-empirical code to model tests. In *Proceedings of the ASME 2010 29th International Conference on Ocean, Offshore and Arctic Engineering*, Shanghai, China, 2010.

[56] R. Price, H. Zheng, Y. Modarres-Sadeghi, and M. Triantafyllou. Effect of higher stress harmonics and spectral width on fatigue damage of marine risers. In *Proceedings of OMAE 2011*, Rotterdam, The Netherlands, June 19 - 24, 2011.

[57] S. Rao. *Mechanical Vibrations*. Prentice Hall, New York, 2003.

[58] T. Sarpkaya. Transverse oscillations of a circular cylinder in uniform flow. Technical Report NPS-69SL77071, Naval Postgraduate School, Mechanical Engineering, Monterey, California, July 1977.

[59] T. Sarpkaya. Vortex induced oscillations. *Journal of Applied Mechanics*, 46:241–258, 1979.

[60] T. Sarpkaya. Hydrodynamic damping, flow-induced oscillations, and biharmonic response. *ASME Journal of Offshore Mechanics and Arctic Engineering*, 117:232–238, 1995.

[61] T. Sarpkaya. A critical review of the intrinsic nature of vortex-induced vibrations. *Journal of Fluids and Structures*, 19(4):389 – 447, 2004.

[62] O. Smogeli. Design and evaluation of a force-feedback control system for VIV experiments. Sivilingenior, NTNU and MIT, July 2002.

[63] J. L. Szwalek and C. M. Larsen. Reynolds number effects on hydrodynamic coefficients for in-line vortex induced vibrations. In *Proceedings of the 28th International Conference on Offshore Mechanics and Arctic Engineering, OMAE*, Estoril, Portugal, 2008.

[64] B. T. Tan, M. C. Thompson, and K. Hourigan. Evaluating fluid forces on bluff bodies using partial velocity data. *Journal of Fluids and Structures*, 20:5–24, 2005.

[65] G. S. Triantafyllou. Vortex induced vibrations of long cylindrical structures. In *Summer Meeting ASME*, Washington, DC, USA, 1998.

[66] G. S. Triantafyllou, M. S. Triantafyllou, and C. Chryssostomidis. On the formation of vortex street behind stationary cylinders. *Journal of Fluid Mechanics*, 170:461–477, 1986.

[67] M. S. Triantafyllou. MIT Course Design Principles for Ocean Vehicles Lecture Notes.

[68] M. S. Triantafyllou. The dynamics of taut inclined cables. *Journal of Mechanics and Applied Mathematics*, 37:421–440, 1984.

[69] M. S. Triantafyllou. *VIVA: Programs for Calculating Riser Vortex Induced Oscillations and Fatigue Life.* Massachusetts Institute of Technology, Testing Tank Facility, Cambridge, MA, 2006.

[70] M. S. Triantafyllou, G. S. Triantafyllou, Y. Tein, and B. Ambrose. Pragmatic riser VIV analysis. In *Offshore Technology Conference*, Houston, TX, May 1999.

[71] A. D. Trim, H. Braaten, H. Lie, and M. A. Tognarelli. Experimental investigation of vortex-induced vibration of long marine risers. *Journal of Fluids and Structures*, 21(3):335 – 361, 2005. Marine and Aeronautical Fluid-Structure Interactions - Marine Acoustics.

[72] M. F. Unal, J. C. Lin, and D. Rockwell. Force prediction by piv imaging: A momentum-based approach. *Journal of Fluids and Structures*, 11:965–971, 1997.

[73] J. K. Vandiver. Dimensionless parameters important to the prediction of vortex-induced vibration of long, flexible cylinders in ocean currents. *Journal of Fluids and Structures*, 7(5):423–455, July 1993.

[74] J. K. Vandiver. *SHEAR7 User Guide*. Department of Ocean Engineering, Massachusetts Institute of Technology, Cambridge, MA, USA., 2003.

[75] J. K. Vandiver and T. Y. Chung. Hydrodynamic damping on flexible cylinders in sheared flow. *Journal of Waterway, Port, Coastal, and Ocean Engineering*, 115(2):154–171, 1989.

[76] J. K. Vandiver, H. Marcollo, S. Fantone, V. Jaiswal, V. Jhingran, and S. Swithenbank. DeepStar 7402 Miami 2004 Riser Report. Technical report, Massachusetts Institute of Technology, Department of Ocean Engineering, 2004.

[77] J. K. Vandiver, S Swithenbank, V. Jaiswal, and V. Jungran. Fatigue damage from high harmonic mode number vortex-induced vibration. In *ASME Offshore Mechanics and Arctic Engineering Conference*, Hamburg, German, 2006.

[78] C. H. K. Williamson and R Govardhan. Vortex-induced vibrations. *Annual Review of Fluid Mechanics*, 36:413–455, 2004.

[79] P. H. Wirsching and M. C. Light. Fatigue under wide band random stresses. *Journal of the Structural Division*, 106(7):1593–1607, July 1980.

[80] P.H. Wirsching and A. Shehata. Fatigue under wide band random stresses using the rain-flow method. *J. Eng. Mater. Technol.*, 99(3):205–211, 1977.

[81] D. K. P. Yue. MIT Course Marine Hydrodynamics Lecture Notes.

[82] H. Zheng, Y. Modarres-Sadeghi, J. M. Dahl, and M.S. Triantafyllou. Inline-crossflow coupled vortex induced vibrations of long flexible cylinders. In *the Proceedings of 31st International Conference on Ocean, Offshore and Arctic Engineering (OMAE 2012)*, Rio de Janeiro, Brazil, 2012.

[83] H. Zheng, R. Price, Y. Modarres-Sadeghi, G. S. Triantafyllou, and M. S. Triantafyllou. Vortex-induced vibration analysis (VIVA) based on hydrodynamic databases. In *Proceedings of the 30th International Conference on Ocean, Offshore and Arctic Engineering (OMAE 2011)*, Rotterdam, The Netherlands, June 19-24, 2011.

[84] H. Zheng, R. Price, Y. Modarres-Sadeghi, and M. S. Triantafyllou. On increased fatigue damage of marine risers due to the higher harmonic force components and chaotic vortex induced vibrations. *manuscript submitted to Journal of Sound and Vibration*, 2013.

[85] H. Zheng, R. Price, Y. Modarres-Sadeghi, and M. S. Triantafyllou. A systematic approach to understanding the influence of high-harmonic and chaotic vortex-induced vibrations on fatigue damage of flexible risers. In *Proceedings of the 22nd International Offshore and Polar Engineering Conference*, Rhodes, Greece, June 1722, 2012.